

Durham E-Theses

Preparation and characterisation of n-CdS/p-CdTe thin film solar cells.

Bayhan, Murat

How to cite:

Bayhan, Murat (1994) *Preparation and characterisation of n-CdS/p-CdTe thin film solar cells.*, Durham theses, Durham University. Available at Durham E-Theses Online: <http://etheses.dur.ac.uk/1697/>

Use policy

The full-text may be used and/or reproduced, and given to third parties in any format or medium, without prior permission or charge, for personal research or study, educational, or not-for-profit purposes provided that:

- a full bibliographic reference is made to the original source
- a [link](#) is made to the metadata record in Durham E-Theses
- the full-text is not changed in any way

The full-text must not be sold in any format or medium without the formal permission of the copyright holders.

Please consult the [full Durham E-Theses policy](#) for further details.

Academic Support Office, Durham University, University Office, Old Elvet, Durham DH1 3HP
e-mail: e-theses.admin@dur.ac.uk Tel: +44 0191 334 6107
<http://etheses.dur.ac.uk>

The copyright of this thesis rests with the author.
No quotation from it should be published without
his prior written consent and information derived
from it should be acknowledged.

**Preparation and Characterisation of n-CdS/p-CdTe
Thin Film Solar Cells.**

by

Murat Bayhan

Presented in Candidature for the Degree of

Doctor of Philosophy

in the

Physics Department, University of Durham.

April, 1994

i



10 AUG 1994

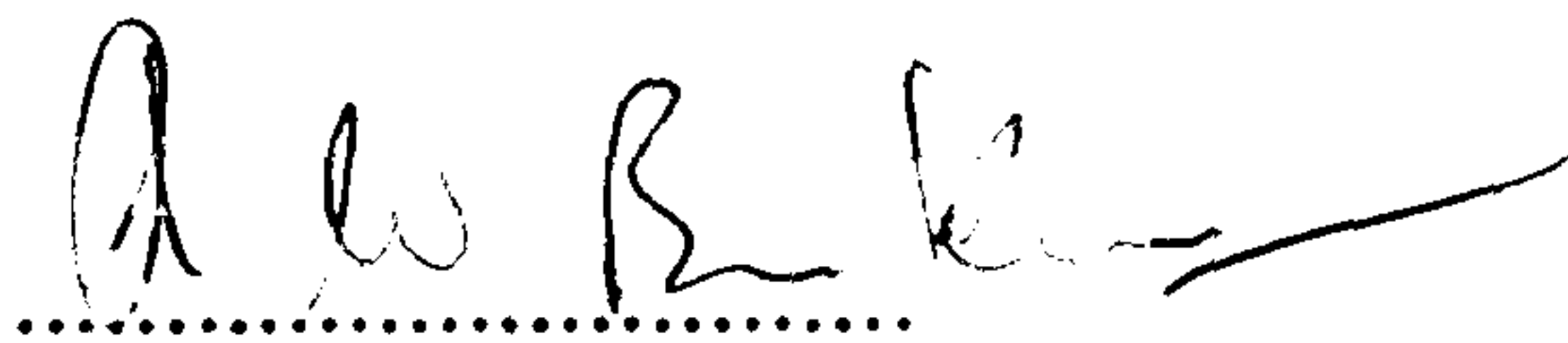
To my parents
and my wife, Habibe

Copyright

Copyright © 1994 by Murat Bayhan. The copyright of this thesis rest with the author. No quotation from it should be published without Murat Bayhan's prior written consent and information derived from it should be acknowledged.

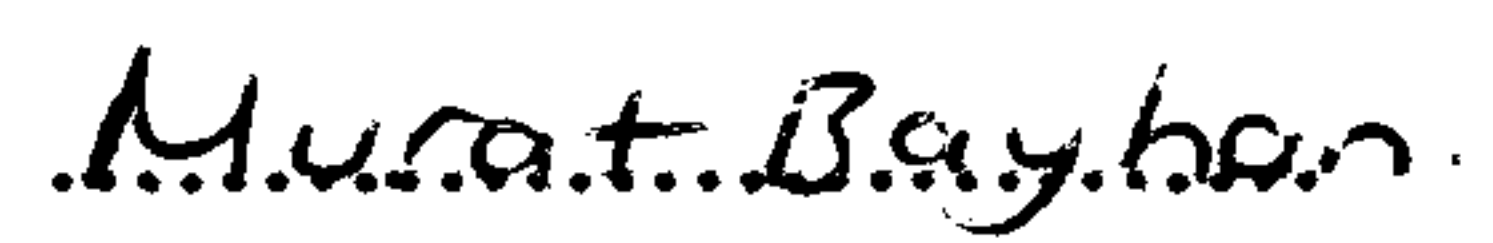
Declaration

I declare that the work reported in this thesis, unless otherwise stated, was carried out by the candidate, that is has not previously been submitted for any degree and that it is not currently being submitted for any other degree.

A handwritten signature in black ink, appearing to read 'A. W. Brinkman', written over a dotted line.

Dr.A.W.Brinkman

Supervisor

A handwritten signature in black ink, appearing to read 'Murat Bayhan', written over a dotted line.

Murat Bayhan

Candidate

Abstract

The optical, structural, and electrical properties of CdTe and CdS thin films grown by vacuum deposition were investigated. Thin film and bulk single crystal CdTe/CdS solar cells were also studied.

In both CdTe and CdS layers, transmission spectra displayed a well defined absorption edge corresponding to the bandgap energy. In the case of CdTe layers, heat treatment in air resulted in a steeper absorption edge that was shifted to longer wavelengths. Additional long wavelength extinction was thought to be due to scattering at grain boundaries and other structural defects. The average transmission in CdS layers was $\sim 91\%$ at wavelengths above the absorption edge.

Layer structure was assessed using XRD and RHEED. These revealed that the CdTe and CdS layers showed $\{111\}$ and $\{0002\}$ preferred-orientation respectively. For the CdTe layers, heat treatment in air resulted in increase in grain sizes. Both CdTe and CdS layers displayed columnar growth with tilted growth axis. Impurity depth profiling by SIMS showed that elements such as, Si, Na, Cl, Al, Cu, Cr and K were present in both CdTe and CdS layers.

As-grown CdTe layers were slightly p-type, but highly resistive ($\rho \cong 10^8 \Omega\text{-cm}$). Air heat treated layers resulted in a more pronounced Seebeck effect, possibly due to oxygen related Cd vacancy formation. Sb doped layers were either of high or very low resistivity suggesting the formation of metallic precipitates. The resistivities of Cl_2 pre- and post doped thin layers were not significantly less than heat treated undoped layers suggesting that it was the heat treatment process that was important. Temperature dependent Hall measurements showed that the mobility could be explained in terms of the grain boundary trapping model in which carrier transport is considered to be dominated by grain boundary scattering. Positron trapping experiments showed that heat treatment in air lead to a reduction in the divacancy concentration. Au contacts to CdTe showed ohmic behaviour but with high contact resistance. In view of the high electron affinity of CdTe, it proved necessary to use a high diffusivity acceptor impurity such as Cu to form a p^+ layer under the Au contact.

As-grown CdS layers exhibited n-type conductivity (i.e. 10^{-2} – $10^{-3} \Omega^{-1}\text{cm}^{-1}$). The introduction of In during deposition reduced the resistivity by up to 3 orders of magnitude.

Illuminated I–V characteristics of undoped bulk single crystal CdTe/CdS cells displayed relatively poor photovoltaic performance resulting in low efficiencies (i.e. $\sim 3\%$). Low FF values indicated that the resistivity of the bulk was quite high. The higher values of J_{sc} and V_{oc} of the cell with Au/P contacts could be attributed to back-surface field effects at the contact/CdTe interface. Values of series resistance were quite high, but reduced by ~ 2 orders of magnitude under illumination.

Illuminated I–V characteristics of undoped CdTe/CdS thin film cells exhibited very poor cell performance. The use of CdCl_2 in the post-growth doping and predoping processes resulted in a small improvement to cell performance. Best cell efficiencies were obtained from $\text{CdS/CdTe:Cl}_2(0.1\%)$ –(pre-doped and BP contacted) cells (i.e. $\eta(\%) \sim 1.2$).

Acknowledgements

It gives me a great pleasure to acknowledge those people who contributed to the preparation of this thesis. I would like to, first of all, express my appreciation and gratitude for the valuable guidance and helpful encouragement of my supervisor, Dr.A.W.Brinkman. I am also indebted to Dr.K.Durose for his valuable discussions and help in structural characterisation, and instruction in the use of the electron microscopes. I would also like to thank, with sadness, the late Professor J.Woods whose sudden death was a great loss to science, for his support and suggestions. I am also grateful to Dr.J.Lewis for his great help with the optical transmission measurements and to Dr.H.Al-Allak for many useful discussions.

I wish to record my appreciation of BP Solar Ltd. for supporting the project and carrying out some PV and SIMS measurements, and also to Dr.E.Özsan and Dr.Ş.Öktik for their useful suggestions. Thanks are also due to Dr.C.Corbel and Dr.L.Liszkay for carrying out the positron trapping experiments and their helpful discussions.

Thanks should also go to all members of the technical staff of the department, especially to Mr.N.Thompson, Mr.H.Kelly, C.Pearson and Mr.D.Pattinson for their friendship and technical support. Special thanks go to Mr.R.Hardy for his help with the XRD measurements.

I would also like to express my appreciation to the Scientific and Technical Research Council of Turkey for the award of a research studentship and for providing financial support. Thanks are also due to University of Durham for additional financial help.

On a more personal note, I wish to express my gratitude to my parents for their many sacrifices and understanding over the years, and to my friends Abdalla, Aziz, Michelle, Dawn and Vangelis, for their close friendship and kindness. Finally, special thanks go to my wife, Habibe, and my parents-in-law for their understanding, patience, kindness and support.

Contents

1	Introduction.	1
1.1	Introduction.	1
1.2	Solar Energy and Solar Cells.	2
1.3	The History of Photovoltaic Solar Cells.	3
1.4	Photovoltaic Solar Cell Devices.	5
1.5	CdTe Based Solar Cells.	7
1.6	n-CdS/p-CdTe Thin Film Solar Cells.	8
1.7	Present Work.	9
1.8	References.	10
2	Scientific Background.	13
2.1	Introduction	13
2.2	Solar Spectrum.	13
2.3	Spectral Dependence of Solar Cells.	14
2.4	Solar Cell Theory.	16
2.4.1	Formation of Energy Band Diagrams.	17
2.4.2	Photovoltaic Effect.	18
2.4.3	Solar Cell Parameters.	21
2.5	CdTe Thin Film Solar Cells.	22
2.5.1	Design and Processing of CdS/CdTe Solar Cells.	23
2.5.2	Issues Regarding Large-Scale Manufacturing.	26
2.5.3	The Cost Potential of CdTe Thin Film Cells.	26
2.5.4	Environmental and Health Aspects.	27
2.6	References.	28
3	Bulk Single Crystal and Thin Film CdTe Growth, and CdTe/CdS Solar Cell Fabrication.	31
3.1	Introduction.	31
3.2	Physical Vapour Deposition.	31
3.2.1	Growth Theory.	32
3.2.2	Basic Modes of Thin Film Growth.	33
3.3	Material Properties of CdTe and CdS.	35
3.3.1	Physical Properties of CdTe.	35

3.3.2	Physical Properties of CdS.	40
3.4	Fabrication of p-CdTe/n-CdS Solar Cells.	42
3.4.1	Preparation of Starting Materials.	44
3.4.2	Cleaning of Glass Substrate Surfaces.	44
3.4.3	n-CdS/or p-CdTe Thin Film Deposition.	45
3.4.4	Metallic (Au or In) Evaporation.	46
3.5	Fabrication of CdS/CdTe Bulk Single Crystal Cells.	47
3.5.1	CdTe Crystal Growth.	47
3.5.2	Sample Orientation and Preparation.	48
3.6	References.	49
4	Characterisation Techniques.	55
4.1	Introduction.	55
4.2	Optical Characterisation.	55
4.3	Structural Characterisation.	56
4.3.1	Reflection of High Energy Electron Diffraction.	56
4.4	Structural Characterisation.	57
4.4.1	Scanning Electron Microscope.	59
4.4.2	X-Ray Diffraction.	60
4.5	Electrical Characterisation.	61
4.5.1	Resistivity and Hall Coefficient Measurements.	61
4.5.2	Dark and Illuminated I-V Characteristics.	62
4.5.3	Capacitance-Voltage Measurements.	63
4.5.4	Spectral Response Measurements.	64
4.6	Secondary Ion Mass Spectroscopy (SIMS).	65
4.7	Positron Trapping At Small Vacancy Clusters.	67
4.7.1	Positron Beam Technique.	67
4.8	References.	68
5	Optical Characterisation of Polycrystalline CdTe and CdS Thin Films.	70
5.1	Introduction.	70
5.2	For films of uniform thickness (Flat Film Analysis).	71
5.2.1	Determination of n_f and α_f in weak absorption region.	72
5.2.2	Determination of n_f and α_f in strong absorption region.	73
5.2.3	Determination of film thickness.	74

5.3	Effects of non-uniform thickness.	76
5.4	Correction for slit-width.	77
5.5	Variation in Refractive Index n_f	78
5.6	Optical properties of as-grown CdTe thin films.	78
5.6.1	Determination of thickness, d	79
5.6.2	Determination of Refractive Index, n_f	80
5.6.3	Determination of α_f , and k_f	81
5.6.4	Determination of Urbach's constant, E_0	88
5.6.5	Determination of dielectric constants, ϵ_1 and ϵ_2	88
5.7	Heat treated CdTe thin films.	90
5.8	Cl ₂ Doped CdTe thin films.	94
5.8.1	Cl ₂ Dipped films.	95
5.8.2	Cl ₂ Predoped films.	98
5.8.3	Effect of Cl ₂ doping.	98
5.9	Optical properties of CdS thin films.	103
5.10	Conclusions.	107
5.11	References.	108
6	Structural Properties of CdTe and CdS Thin Films.	111
6.1	Introduction.	111
6.2	X-Ray Diffraction.	111
6.2.1	X-Ray Diffraction Assessments of CdTe Thin Films.	112
6.2.2	X-Ray Diffraction Assesment of CdS Thin Films.	116
6.3	RHEED Assessment.	117
6.4	Scanning Electron Miscoscopy (SEM) Assessments.	121
6.4.1	Morphology.	121
6.4.2	Energy Dispersive Analysis by X-Rays (EDAX).	122
6.5	Secondary Ion-Mass Spectroscopy (SIMS) Analysis.	127
6.6	Conclusions.	130
6.7	References.	133
7	Electrical Properties of CdTe and CdS Thin Films.	135
7.1	Introduction.	135
7.2	Carrier Mobility and Scattering Mechanisms.	135
7.2.1	Carrier Transport in Bulk Single Crystals.	136

7.2.2	Carrier Transport in Polycrystalline Thin Films.	139
7.3	Electrical Properties of CdTe Thin Films.	141
7.3.1	Metal Ohmic Contacts.	141
7.3.2	Resistivity and Hall Measurements.	143
7.4	Electrical Properties of CdS Thin Films.	154
7.4.1	Metal Ohmic Contacts.	154
7.4.2	Resistivity and Hall Measurements.	154
7.5	Positron Trapping in CdTe Thin Films.	155
7.5.1	Principles of Trapping at Small Vacancy Clusters.	157
7.5.2	Positron Trapping Analysis.	159
7.6	ITO/CdTe:Cl ₂ Diodes.	165
7.6.1	Diode Preparation and Characterisation.	166
7.7	Conclusions.	168
7.8	References.	169
8	Bulk Single Crystal CdTe/CdS Solar Cells.	173
8.1	Introduction.	173
8.2	Device Fabrication.	173
8.3	Dark I-V Characteristics.	174
8.3.1	Room Temperature I-V Characteristics.	174
8.3.2	Temperature Dependent I-V Characteristics.	175
8.4	Illuminated I-V Characteristics.	179
8.5	Determination of Device Series and Shunt Resistance. . .	181
8.5.1	Capacitance-Voltage Characteristics.	191
8.6	Conclusions.	192
8.7	References.	193
9	n-CdS/p-CdTe Thin Film Solar Cells.	195
9.1	Introduction.	195
9.2	I-V Characteristics.	195
9.2.1	Undoped cells.	195
9.2.2	Cl ₂ doped cells.	198
9.3	Determination of Series and Shunt Resistances.	210
9.4	Spectral Response.	214
9.5	Optical Properties.	215

9.6	C-V Characteristics.	217
9.7	Conclusion.	220
9.8	References.	221
10	Conclusion.	222
10.1	Introduction.	222
10.2	Thin Film Characterisation.	222
10.2.1	Optical properties.	222
10.2.2	Structural properties.	224
10.2.3	Electrical properties.	226
10.3	Solar Cell Characterisation.	227
10.3.1	Bulk single crystal cell characterisation.	227
10.3.2	Polycrystalline thin film cell characterisation.	229
10.4	Final Conclusion and Future Work.	231
	A Determination of Optical Constants Using Transmission	
	Spectrum Only.	233

LIST OF FIGURES

2.1	Solar spectrum (After [1]).	14
2.2	Sun's Declination Angles.	15
2.3	A Solar Cell Configuration.	16
2.4	Solar Cell Efficiency vs Bandgap Energy Values.	17
2.5	Energy Band Diagram of n-CdS/p-CdTe Cell.	18
2.6	Current-Voltage Characteristics of a p-n Junction Diode in the Dark and Under Illumination.	23
3.1	Basic growth processes; a: island, b: layer-by-layer, and c: Stranski-Krastanov type.	34
3.2	Crystal Structure of CdTe.	36
3.3	The flow chart for the production of n-CdS/p-CdTe Solar Cells.	43
3.4	The schematic diagram of the chamber fixtures; 1-Source (CdTe) crucible, 2-Dopant crucible (Sb, CdCl ₂), 3-Source filament, 4-Dopant filament, 5-Shutter, 6-Source thermocouple, 7-Dopant ther- mocouple, 8-Heated chimney, 9-Substrate, 10-Substrate heater, 11- Substrate thermocouple, 12-Thickness monitor head.	45
3.5	Typical CdTe thin film growth characteristic.	47
4.1	Schematic diagram of the optical system of the PE Lambda 19 spectrophotometer.	56
4.2	Diffraction geometry in RHEED.	57
4.3	Schematic diagram of the basic functional features of a scan- ning electron microscope.	60
4.4	A schematic diagram of Durham solar simulator.	63

4.5	Schematic diagram of system used for the spectral response measurements.	64
5.1	Schematic diagram for a system consisting of an absorbing thin film on a thick finite transparent substrate.	71
5.2	Transmission spectrum for a typical $1.705\mu\text{m}$ thick film of CdTe on a glass substrate.	72
5.3	Band-pass vs wavelength characteristics of PE L19 spectrophotometer in visible and infrared region.	78
5.4	Transmission spectrum for a typical $2.175\mu\text{m}$ thick film of CdTe on a glass substrate.	80
5.5	Refractive index, n_f , vs wavelength characteristic of a typical as-grown CdTe layer.	83
5.6	Extinction coefficient, k_f , vs wavelength characteristic of a typical as-grown CdTe layer.	83
5.7	Absorption coefficient, α_f vs wavelength characteristic of a typical as-grown CdTe layer.	83
5.8	α_f^2 vs $h\nu$ characteristic of a typical as-grown CdTe thin layer in the strong absorption region.	84
5.9	$\alpha_f^{2/3}$ vs $h\nu$ characteristic of a typical as-grown CdTe thin layer in the strong absorption region.	84
5.10	α_f vs $h\nu$ characteristic of bulk single crystal and as-grown CdTe thin layer in the strong absorption region.	86
5.11	Gap-states, $\alpha_{bulk} - \alpha_f$ vs $h\nu$ characteristic of a typical as-grown CdTe layer.	86
5.12	$\log(\alpha_f)$ vs $h\nu$ characteristics of a typical as-grown CdTe layer.	88
5.13	Real part of the dielectric constant, ϵ_1 , vs wavelength of a typical as-grown CdTe thin layer.	89
5.14	Imaginary part of the dielectric constant, ϵ_2 , vs wavelength of a typical as-grown CdTe thin layer.	89
5.15	A typical transmission spectrum of a heat treated CdTe thin layer.	90
5.16	Refractive index, n_f , vs wavelength characteristic of a typical heat treated CdTe layer.	90

5.17	Extinction coefficient, k_f , vs wavelength characteristic of a typical heat treated CdTe layer.	90
5.18	Absorption coefficient, α_f vs wavelength characteristic of a typical heat treated CdTe layer.	90
5.19	α_f^2 vs $h\nu$ characteristic of a typical heat treated CdTe thin layer in the strong absorption region.	90
5.20	α_f vs $h\nu$ characteristic of bulk single and heat treated CdTe thin film in the strong absorption region.	94
5.21	Gap-states, $\alpha_{bulk} - \alpha_f$ characteristic of a typical heat-treated CdTe thin layer.	95
5.22	A typical transmission spectrum of a Cl ₂ dipped CdTe thin layer.	95
5.23	Refractive index, n_f vs wavelength characteristic of a typical Cl ₂ dipped CdTe thin layer.	95
5.24	Extinction coefficient, k_f vs wavelength characteristic of a typical Cl ₂ dipped CdTe thin layer.	95
5.25	Absorption coefficient, α_f vs wavelength characteristic of a typical Cl ₂ dipped CdTe thin layer.	95
5.26	A typical transmission spectrum of a Cl ₂ pre-doped CdTe thin layer.	99
5.27	Refractive index, n_f vs wavelength characteristic of a typical Cl ₂ pre-doped CdTe thin layer.	99
5.28	Extinction coefficient, k_f vs wavelength characteristic of a typical Cl ₂ pre-doped CdTe thin layer.	99
5.29	Absorption coefficient, α_f vs wavelength characteristic of a typical Cl ₂ pre-doped CdTe thin layer.	99
5.30	α_f vs $h\nu$ characteristics of bulk single and Cl ₂ dipped CdTe thin layer in the strong absorption region.	99
5.31	Gap-states, $\alpha_{bulk} - \alpha_f$ characteristic of a typical Cl ₂ dipped CdTe thin layer.	99
5.32	α_f vs $h\nu$ characteristics of bulk single and Cl ₂ pre-doped CdTe thin layer in the strong absorption region.	99
5.33	Gap-states, $\alpha_{bulk} - \alpha_f$ characteristic of a typical Cl ₂ pre-doped CdTe thin layer.	99

5.34	A typical transmission spectrum for a typical $0.6\mu\text{m}$ thick film of CdS on a glass substrate.	104
5.35	Refractive index, n_f vs wavelength characteristic of a typical as-grown CdS thin layer.	104
5.36	Extinction coefficient, k_f vs wavelength characteristic of a typical as-grown CdS thin layer.	104
5.37	Absorption coefficient, α_f vs wavelength characteristic of a typical as-grown CdS thin layer.	104
5.38	α_f vs $h\nu$ characteristic of a typical as-grown CdS thin layer.	104
5.39	α_f^2 vs $h\nu$ characteristic of a typical as-grown CdS thin layer in the strong absorption region.	104
5.40	$\log(\alpha_f)$ vs $h\nu$ characteristic of a typical as-grown CdS thin layer.	104
6.1	X-ray diffraction spectrum of an as-grown CdTe thin film.	113
6.2	Grain size vs substrate temperature characteristic of as-grown CdTe thin film.	114
6.3	X-ray diffraction spectrum of a heat treated CdTe thin film.	115
6.4	X-ray diffraction spectrum of an as-grown CdS thin film.	117
6.5	RHEED pattern from an as-grown CdTe thin film grown on glass at a substrate temperature of 150°C	120
6.6	RHEED pattern from an as-grown CdS thin film grown on glass at a substrate temperature of 220°C	120
6.7	Secondary emission micrograph of an as-grown CdTe thin layer surface grown on glass at a substrate temperature of 200°C , magn.=10K	122
6.8	Secondary emission micrograph of a cross section through an as-grown CdTe thin film grown on glass at a substrate temperature of 200°C , magn.=10K.	122
6.9	Secondary emission micrograph of a CdTe:Cl ₂ thin layer surface grown on glass by co-evaporation of CdTe and CdCl ₂ , magn.=10K.	122
6.10	Secondary emission micrograph of a CdTe:Cl ₂ thin layer surface grown on glass by dipping into CdCl ₂ /Methanol solution, magn.=200.	122

6.11	Secondary emission micrograph of a CdTe:Cl ₂ thin layer surface grown on glass by dipping into CdCl ₂ /Methanol solution, magn.=5K.	122
6.12	Secondary emission micrograph of an as-grown CdS thin layer surface grown on glass at a substrate temperature of 220°C, magn.=20K.	122
6.13	Secondary emission micrograph of a cross section through an as-grown CdS thin film grown on glass at a substrate temperature of 220°C, mag. = 20K.	122
6.14	EDAX scan of an as-grown CdTe thin layer surface grown on glass at a substrate temperature of 220°C.	126
6.15	EDAX scan of an as-grown CdS thin layer surface grown on glass at a substrate temperature of 220°C.	126
6.16	EDAX scan of a CdTe:Cl ₂ thin layer surface grown on glass by co-evaporation of CdTe and CdCl ₂	126
6.17	EDAX scan of a CdTe:Cl ₂ thin layer surface grown on glass by dipping into CdCl ₂ /Methanol solution; whole surface.	126
6.18	EDAX scan of a CdTe:Cl ₂ thin layer surface grown on glass by dipping into CdCl ₂ /Methanol solution; on the CdCl ₂ island.	126
6.19	SIMS impurity depth profile of an as-grown/heated CdTe thin film.	129
6.20	SIMS impurity depth profile of a co-evaporated CdTe:Cl ₂ thin film.	129
6.21	SIMS impurity depth profile of a ITO/CdS/CdTe structure on glass substrates.	131
6.22	SIMS impurity depth profile of a co-evaporated ITO/CdS/CdTe:Cl ₂ structure on glass substrates.	131
7.1	Grain Boundary Trapping Model (Seto's [13]).	141
7.2	$\log(J)$ vs $\log(V)$ characteristics of Au contact to CdTe thin layer.	143
7.3	$\log(\sigma)$ vs T^{-1} characteristic of a typical CdTe:Cl ₂ thin layer, ($3 < T < 400\text{K}$).	145
7.4	$\log(\sigma)$ vs T^{-1} characteristic of a typical CdTe:Cl ₂ thin layer, ($10 < T < 400\text{K}$).	145

7.5	$\log(\sigma T^{1/2})$ vs T^{-1} characteristic of typical CdTe:Cl ₂ thin layer, 3<T<400K.	146
7.6	$\log(\sigma T^{1/2})$ vs T^{-1} characteristic of typical CdTe:Cl ₂ thin layer, 10<T<400K.	146
7.7	μ vs T characteristic of a typical CdTe:Cl ₂ thin layer.	147
7.8	$\log(\mu)$ vs $\log(T)$ characteristic of a typical CdTe:Cl ₂ thin layer.	148
7.9	$\log(\mu T^{-1/2})$ vs T^{-1} characteristic of a typical CdTe:Cl ₂ thin layer, 3<T<400K.	148
7.10	$\log(\mu T^{-1/2})$ vs T^{-1} characteristic of a typical CdTe:Cl ₂ thin layer, 200<T<400K.	149
7.11	$\log(\mu T^{1/2})$ vs T^{-1} characteristic of a typical CdTe:Cl ₂ thin layer, 3<T<400K.	149
7.12	$\log(\mu T^{1/2})$ vs T^{-1} characteristic of a typical CdTe:Cl ₂ thin layer, 10<T<400K.	150
7.13	$\log(\mu T^{1/2})$ vs T^{-1} characteristic of a typical CdTe:Cl ₂ thin layer, 50<T<400K.	150
7.14	p vs T characteristic of a typical CdTe:Cl ₂ thin layer.	152
7.15	$\log(p T^{-1/2})$ vs T^{-1} characteristic of a typical CdTe:Cl ₂ thin layer, 3<T<400K.	152
7.16	$\log(p T^{-1/2})$ vs T^{-1} characteristic of a typical CdTe:Cl ₂ thin layer, 20<T<400K.	153
7.17	R_H vs T characteristic of a typical CdTe:Cl ₂ thin layer.	153
7.18	$\log(\sigma)$ vs T^{-1} characteristic of an undoped and In-doped CdS:In thin layer, 80<T<400K.	156
7.19	$\log(\sigma T^{1/2})$ vs T^{-1} characteristic of In-doped CdS:In thin layer, 80<T<400K.	156
7.20	Valence annihilation parameter, S_f , as a function of incident posit- ron energy in CTC thin film.	161
7.21	Valence annihilation parameter, S_f , as a function of incident posit- ron energy in CTD1 thin film.	161
7.22	Valence annihilation parameter, S_f , as a function of core an- nihilation parameter, W_f in CdTe thin films.	162

7.23	The relative change in the annihilation parameter, W_f , compared to the bulk.	163
7.24	The relative change in annihilation parameter, S_f , compared to the bulk.	163
7.25	$\log(J)$ vs V characteristics of a typical ITO/CdTe:Cl ₂ /Au Schottky diode at 300K.	167
7.26	$\log(J_o T^{-2})$ vs T^{-1} characteristic of ITO/CdTe:Cl ₂ /Au Schottky diode at 300K.	167
7.27	C^{-2} vs V characteristics of ITO/CdTe:Cl ₂ /Au Schottky diode at 300K.	168
8.1	Room temperature $\log(I)$ vs V characteristic of CdTe/CdS cells with Au and Au/P contacted.	174
8.2	Possible current transport mechanisms in CdTe/CdS cells.	177
8.3	$\log(I_f)$ vs V characteristic of CdTe/CdS cell with Au contact at several temperatures.	178
8.4	$\log(J_o)$ vs T (a) and $\log(J_o)$ vs T^{-1} (b) characteristic of CdTe/CdS cell with Au contact.	180
8.5	Illuminated I-V characteristic of CdTe/CdS cells with Au and Au/P contacts under an illumination intensity of about 90mW/cm ²	180
8.6	Illuminated I-V characteristic of CdTe/ CdS cell with Au contact at two different illumination intensities.	183
8.7	Illuminated I-V characteristic of CdTe/ CdS cell with Au/P contact at two different illumination intensities.	183
8.8	Equivalent circuit diagrams of a cell under (a) open circuit, V_{oc} and (b) short circuit I_{sc} conditions.	183
8.9	$\log(I_{sc})$ vs V_{oc} characteristic of CdTe/CdS cell with Au and Au/P contacts.	183
8.10	Series resistance components of a single bulk crystal CdTe/CdS cell.	187
8.11	Illuminated I-V characteristic of CdTe/CdS cell with Au contact after eliminating R_s and R_{sh} resistances, a: plain cell, b: $R_{sh} \rightarrow \infty$, c: $R_s \rightarrow 0$, d: both (b and c).	188

8.12	Illuminated I-V characteristic of CdTe/CdS cell with Au/P contact after eliminating R_s and R_{sh} resistances., a: plain cell b: $R_{sh} \rightarrow \infty$, c: $R_s \rightarrow 0$, d: both (b and c).	189
8.13	C^{-2} vs V characteristic of CdTe/CdS cell with Au contact at several temperatures.	191
9.1	Dark $\log(I_f)$ vs V characteristic of a typical undoped CdTe/CdS cell at room temperature.	196
9.2	I-V characteristic of an undoped CdTe/CdS cell under an illumination of about 90mW/cm ² using CdTe source temperatures of a: 650°C, b: 750°C, and c: 800°C.	196
9.3	I-V characteristic of an undoped CdTe/CdS cell with Au and Au/Cu contact under an illumination of about 90mW/cm ²	198
9.4	Dark $\log(I_f)$ -V characteristic of co-evaporated CdS/CdTe:Cl ₂ cell.	200
9.5	I-V characteristic of co-evaporated CdS/CdTe:Cl ₂ cell under an illumination of about 90mW/cm ²	200
9.6	Dark $\log(I_f)$ -V characteristic of co-evaporated CdS/CdTe:Cl ₂ cell.	200
9.7	I-V characteristic of co-evaporated CdS/CdTe:Cl ₂ cell under an illumination of about 90mW/cm ²	200
9.8	Dark $\log(I_f)$ -V characteristic of co-evaporated CdS/CdTe:Cl ₂ cell.	200
9.9	Dark $\log(I_r)$ -V characteristic of co-evaporated CdS/CdTe:Cl ₂ cell.	200
9.10	$\log(J_o)$ vs T characteristic of a co-evaporated CdTe/CdS cell.	201
9.11	Dark $\log(I_f)$ vs V characteristic of a pre-doped CdS/CdTe:CdCl ₂ (5%) cell.	205
9.12	I-V characteristic of a pre-doped CdS /CdTe:CdCl ₂ (5%) cell under an illumination of 90mW/cm ²	205
9.13	Dark $\log(I_f)$ vs V characteristic of a pre-doped CdS/CdTe:CdCl ₂ (0.1%) cell.	205
9.14	I-V characteristic of a pre-doped CdS/ CdTe:CdCl ₂ (0.1%) cell under an illumination of 90mW/cm ²	205

9.15	I-V characteristics of a pre-doped CdS/CdTe: CdCl ₂ (0.1%) BP contacted cell after eliminating R_{sh} and R_s , a: Plain cell, b: $R_{sh} \rightarrow \infty$, c: $R_s \rightarrow 0$, d: both (b and c).	206
9.16	I-V characteristic of an undoped and Cl ₂ doped (by dipping) cell under an illumination of 90mW/cm ²	210
9.17	I_f vs ΔV characteristic of an undoped CdS/CdTe cell.	212
9.18	I_f vs ΔV characteristic of a co-evaporated CdS/CdTe cell.	212
9.19	$\log(I_f)$ vs V characteristic of an undoped CdS/CdTe cell be- fore and after eliminating R_s	213
9.20	$\log(I_f)$ vs V characteristic of an undoped CdS/CdTe cell be- fore and after eliminating R_s	213
9.21	V_{oc} as a function of photon energy of a co-evaporated CdS/CdTe: Cl ₂ cell.	215
9.22	V_{oc} as a function of photon energy of a CdCl ₂ coated CdS/CdTe: Cl ₂ cell.	215
9.23	Normal incidence transmission spectra of a: ITO, b: CdS/ITO, and c: CdTe/CdS/ITO structures on glass sub- strates.	217
9.24	C vs T characteristic of a co-evaporated CdS /CdTe: Cl ₂ cell.	218
9.25	C^{-2} vs V characteristic of a co-evaporated CdS/ CdTe: Cl ₂ cell.	219
9.26	C^{-2} vs V characteristic of BP contacted pre-doped CdS/CdTe: CdCl ₂ (0.1%) cell.	219
A.1	Schematic diagram for a system consisting of an absorbing thin film on a thick finite transparent substrate.	234
A.2	Transmission spectrum for a dielectric (or semiconducting) thin layer on a glass substrate.	236

LIST OF TABLES

1.1	Materials and efficiencies (%) of solar cells with module costs estimated for different annual production rates.	4
2.1	Current Status of High-Efficiency Thin Film CdS/CdTe Solar Cell.	24
2.2	International Module Results.	27
3.1	Structural Properties of zincblende-CdTe at 300K, [†] at melting point, ZB: Zincblende, WZ: Wurtzite.	36
5.1	Thickness values obtained by different measurement of tech- niques, (i.e. \bar{d}_1 = Direct measurement by α -step, \bar{d}_2 = Graph- ical method, \bar{d}_3 = Interference fringe method, \bar{d}_4 = Multiple beam interferometer method).	80
5.2	Optical bandgap E_g and ξ for both allowed and forbidden di- rect transitions for a typical as grown CdTe layer.	84
5.3	Published optical bandgap values for thin film CdTe.	86
5.4	Published optical bandgap values for bulk single crystal CdTe.	86
5.5	Dielectric constants of bulk single crystal and thin film CdTe grown here.	90
6.1	XRD data for a typical as-grown CdTe thin film.	112
6.2	Approximate grain sizes of thin CdTe layers, before and after annealing in air (400°C, 30 min).	116
6.3	X-ray diffraction data for *: TeO ₂ (Tellurite); [†] : Te ₃ O ₄ (Paratellurite).	119
7.1	Resistivity and Hall measurement results for low resistivity CdTe:Sb thin layers.	144

7.2	Resistivity and Hall measurement results of a typical undoped CdS and In doped CdS:In thin layer at room temperature.	155
7.3	Annihilation parameters, W_f , S_f and S_s ; diffusion length, L_+ ; and trapping rates, κ_d , in CdTe layers. CTA: glass, as-grown; CTB: glass, heated; CTC: dipped followed by annealing; CTD1: ITO/glass, as-grown; CTD2: ITO/glass, heated; and ZD16 MBE control layer.	160
7.4	Experimental and theoretical core annihilation probability (F_i^c) in CdTe that is: defect-free, contains monovacancies and contains divacancies.	164
8.1	n and J_o values of undoped p-CdTe/n-CdS cell with two different contacts.	175
8.2	J_o , A , and n for the Au/p-CdTe/n-CdS cell at different temperatures.	179
8.3	The slope, B and activation energy, ΔE values for undoped CdTe cells with Au and Au/P contacts.	179
8.4	Solar cell parameters, i.e. V_{oc} , J_{sc} , FF, and η for the cells with Au and Au/P contacts respectively.	181
8.5	R_s values (i.e., in Ohm, normalized to a unit area of 1cm^2) of undoped single crystal p-CdTe/n-CdS cells with two different contacts, i.e. Au and Au/P determined by various methods.	186
8.6	R_{sh} values (i.e., in Ohm, normalized to a unit area of 1cm^2) of the undoped bulk single crystal p-CdTe/n-CdS cells with two different contacts, i.e. Au and Au/P determined by various methods.	186
8.7	Re-calculated solar parameters for the cell with Au contact after removing R_s and R_{sh} effects.	190
8.8	Re-calculated solar parameters for the cell with Au/P contact after removing R_s and R_{sh} effects.	190
8.9	Acceptor density, N_A , intercept voltage, V_i , and depletion width, W_o , values of a typical undoped p-CdTe/n-CdS/In cell.	192
9.1	Values of J_o , n and A for a typical co-evaporated cell as a function of temperature.	204

9.2	Probable cell parameters after eliminating R_s and R_{sh} resistances for a typical pre-doped BP contacted cell.	209
9.3	R_s values (i.e., in Ohm, normalized to a unit area of 1cm^2) of some cells calculated by methods a, b, and c.	210
9.4	R_{sh} values (i.e., in Ohm, normalized to a unit area of 1cm^2) of the some cells calculated by the methods a and b.	214
10.1	n_f , E_g , and, ΔE_g values of CdTe thin layers. * Least-squares fitting in the region of weak absorption, λ measured in μm	224
10.2	Resistivity and Hall effect results for CdTe thin layers doped with Sb and Cl_2	227
10.3	Resistivity and Hall effect results for undoped and In doped CdS thin layers.	227
10.4	R_s and R_{sh} resistance results (i.e., in Ohm, normalized to a unit area of 1cm^2) obtained from the dark and illuminated I-V characteristics.	229
10.5	Junction parameters of undoped bulk single crystal and Cl_2 doped thin film n-CdS/p-CdTe cells, R_{sh} and R_{sh} are in Ohm and were normalized to a unit area of 1cm^2	230
10.6	Solar cell parameters for undoped bulk single crystal and Cl_2 doped thin film n-CdS/p-CdTe cells under illumination of $\sim 90\text{mW}/\text{cm}^2$, R_{sh} and R_{sh} are in Ohm and were normalized to a unit area of 1cm^2	230
10.7	Photovoltaic potential of undoped bulk single crystal and Cl_2 doped n-CdS/p-CdTe cells after eliminating of R_s and R_{sh} resistances (i.e. $R_s \rightarrow 0$ and $R_{sh} \rightarrow \infty$), † (Au/P) contacted, * pre-doped BP contacted.	231

Chapter I

Introduction.

1.1 Introduction.

The direct conversion of sunlight to electricity in terrestrial photovoltaic devices has great potential, as a sustainable, non-polluting renewable source of energy thus providing a contribution towards meeting the increasing energy demands of the future and lessening the dependence on fossil and nuclear fuels. The driving force for the interest in photovoltaic conversion is the realisation that the traditional fossil fuel resources are not only limited, but that they also contribute in an unpredictable and possibly irreversible way to climatic changes through the emission of CO_2 (i.e. warming-up of the lower atmosphere, the so called *greenhouse effect*). In addition, acid rain produced from power station emissions on the western seaboard of Europe is believed to be responsible for severe deforestation problems in Norway and Sweden. The response to impending shortages of fossil fuels has been to develop nuclear power based on the fission of uranium, which is also a limited resource. However, all nuclear fission processes yield radioactive wastes which have to be contained. At the present time, the safety of nuclear reactors and containment of nuclear wastes remain unsolved problems and the well known disasters at Chernobyl and Three Mile Island have led to increased public concern which is likely to limit further development of nuclear sources of power.

In terms of energy availability, conventional and nuclear sources must be considered adequate for the time being. Moreover alternative renewable energy sources (photovoltaic, tidal, wave, wind etc.) are still relatively expensive and with the exception of hydroelectric power have yet to be integrated into national power schemes to any significant effect. This is particularly true for photovoltaic solar energy sources, despite a drop in cost by nearly a factor of ten over the last few years [1]. However, the increasing environmental damage and the expense of associated environmental protection, not to mention the large cost incurred in decommissioning nuclear power stations, have led to a reappraisal of the true cost

of conventional and nuclear power generation. In these changed circumstances, alternative energy sources become more competitive in cost terms as well as in environmental terms. Thus the major objectives of research and development programmes within the renewable energy and photovoltaic industry have been to reduce costs even further by improving efficiency, stability, lifetime, etc. In the early 1970's the solar power industry was regarded with scepticism, the nuclear industry taking a leading role. It was however the oil crisis in the late 1970's that changed the picture, causing investment in the renewable energy industries with subsequent impressive technological advances and dramatic price reductions. As non-renewable energy prices have risen, renewable energy systems have become an increasingly competitive energy source for terrestrial applications.

1.2 Solar Energy and Solar Cells.

The sun, as a source of energy has many advantages over other conventional resources. Its energy is "free", non-polluting, inexhaustible and is evenly distributed across the earth's surface. On a bright summer day at noon, the solar energy on 1m^2 of the earth's surface is about 900W [2]. If say 15% of this could be converted into useable electric power, then it would be sufficient to power one 100W bulb, or a television set, for example. One obvious way of harnessing the sun's energy is through the direct conversion of sunlight into electricity using photovoltaic solar cells. These devices utilise the opto-electronic properties of semiconductor materials to generate an electromotive force (e.m.f.) as a result of the absorption of the sun's radiation. When the incident photons have an energy greater than or equal to the bandgap of the semiconducting material, electron-hole pairs are generated in the semiconductor and if these can be separated by an internal electric field (which may be created by forming a junction between different semiconductor materials), and subsequently collected, then an e.m.f. is produced which can drive a current around an external circuit.

Sunlight has a wide spectral range, so there are large inherent losses in conversion by a single bandgap material and the maximum theoretical efficiency is limited to about 28% (see section 2.3). If the sunlight were to be absorbed by a cascade of solar cells tuned to different parts of the solar spectrum, then in principle, over two thirds of the available energy could be converted into electricity. However,

cascaded solar cells are difficult to interconnect and at the moment expensive, and it is unlikely that such advanced solar cells will become available for general use in the short and medium term.

Presently, available commercial solar cells are based on single crystal Si p-n junctions and a 10x10 cm array consisting of several Si cells connected in parallel, can generate about 4A at 0.5V dc in full sunlight (i.e. a nominal irradiance of 1kWm^{-2}). To obtain a more useful output, cells are generally connected in series in an encapsulated package, termed a *module* to give an output of 4A at 15V dc, and such modules are now the standard commercial product. For higher power, modules are connected in series and/or parallel in an array to give the required output. When costs are quoted, they are usually module costs per unit peak output, W_p (i.e. measured at a solar irradiance of 1kWm^{-2} , similar to Sahara Desert Summer noon). However, the total cost of a photovoltaic (PV) system includes not only the module cost, but the costs of support structures, wiring, electronic control and conditioning and construction etc as well (i.e. balance of-system, BOS costs).

Although, the vast majority of commercially available cells are based on crystalline Si (single and polycrystalline), there are a number of major problems associated with its use in this context. Silicon is a poor absorber of light with a bandgap energy that is not well matched to the solar spectrum. Consequently volume (and therefore weight) requirements are high and a range of alternative thin film amorphous and polycrystalline systems have been developed as potential replacements. These include amorphous silicon (α -Si), CuInSe_2 , and CdTe . In addition, the use of concentrator cells where sunlight is focused by mirrors onto smaller areas, therefore requiring correspondingly smaller areas of solar cell, are under development. These types of device tend to be based on the more expensive but highly efficient GaAs and related systems. The present performance of the different types of solar cell is shown in Table 1.1. This also gives the estimated production cost of the cells at various annual production rates.

1.3 The History of Photovoltaic Solar Cells.

It has been over 150 years since Becquerel in 1839 first discovered that a photovoltage was developed when light was directed onto one of the electrodes

in an electrolyte solution [3]. Adams and Day [4] were the first to observe the effect in a solid (selenium), about forty years later. A number of other early solid-state workers including Lange [5], Grandahl [6], and Schottky [7] did pioneering work on selenium and Cu_2O photovoltaic cells. These cells while exhibiting a strong photovoltaic effect could not provide an efficiency of better than 1% in the conversion of solar energy. However, in 1954, a Si p-n junction solar cell with an efficiency of 6% was developed at Bell Laboratories, and these cells were first used in Vanguard I, a US satellite launched in 1958. In the same year, Reynolds, Leies, Antes and Marburger [8] also reported about 6% solar-conversion efficiency in p- Cu_2S /n-CdS cells.

Cell Material	Best Cell $\eta(\%)$	Module $\eta(\%)$	Module Costs (£W_p)		
			1MW _p pa	10MW _p pa	100MW _p pa
Single Crystal Si.	24	16	3	1.5	1.0
Polycrystalline Si.	18	12	3	1.2	0.8
Amorphous Si.	14	4	2	1.0	0.4
CuInSe_2	16.8	>10	2	1.0	0.4
CdTe	15.8	>10	2	1.0	0.4
Concentrator Cells					
Silicon	27	15-19	4	1.5	0.8
GaAs	29	3	3	1.2	0.7
Tandem (cascade) Cells	37	4	4	1.0	0.5

Table 1.1 — Materials and efficiencies (%) of solar cells with module costs estimated for different annual production rates.

In 1955, a group at RCA undertook to determine what the optimum semiconductor bandgap energy for photovoltaic solar conversion would be. This theoretical study suggested that the optimum bandgap should be about 1.55 eV [9] (subsequent studies have revised this value downwards -the most recent estimate is 1.28 eV [10]) and a number of possible materials with bandgaps close to this have since been studied for use in solar cells. However, it was found experimentally that other

factors, such as diffusion length, stability and absorption coefficient were equally important, and in fact constrain the range of suitable materials to a relatively small number, of which the following have proved to be the most promising:

- III-V Group materials: InP (1.25 eV), GaAs (1.4 eV),
- II-VI Group materials: CdTe (1.45 eV), CdSe (1.7 eV),
- I-III-VI₂ Group materials: CuInSe₂ (1.1 eV), CuInS₂ (1.5 eV).

The oil crises of the early 1970's led to a reappraisal of the use of solar energy for terrestrial power generation. The first mention of central station solar power generation came in 1974 [11], and a design for the former was published in 1975 [12]. This used concentrated sunlight to heat boilers producing steam, which then powered a conventional steam turbine/rotating generator unit. The University of Delaware, however, was the first to document the prospects for large-scale use of photovoltaic solar energy, and to investigate an experimental residential application of PV modules [13]. The University Solar One home had a very small array of photovoltaic cells that were used to study the correlation of solar energy with typical daily residential electric loads. Energy from the PV array was used to charge batteries that supplied energy to dc loads within the home. These developments resulted in the construction of a 1MW demonstrator central power station located in Hesperia, California and built by the Southern California Edison Co. This plant used two-axis tracking flat-plate arrays of Si photovoltaic cells. Performance data (published in 1985 [14]) showed that the average energy output from the plant was 7372 kWh per day. The plant was termed "reliable" with capacity factors ranging from 12% on an "overcast" January day to 37% in July 1983. Other plants have since been constructed in Carissa Plains (USA), Davros (Italy) and in the Swiss Alps. These experimental stations have highlighted a number of particular difficulties with photovoltaic power generation, for example the issue of short term fluctuations in output caused by moving clouds etc. These factors will clearly have to be addressed before the large scale use of PV in power generation becomes practical.

1.4 Photovoltaic Solar Cell Devices.

Although this thesis is concerned with the n-CdS/p-CdTe solar cell, a brief survey of other solar cell structures will be given here. For the last two decades, a considerable volume of research has been directed to the fabrication of high efficiency solar cells. This has succeeded in producing single crystal concentrator Si and GaAs based cells with efficiencies in excess of 24% [15] and 28% [16] respectively. However, these are too expensive for use in large scale terrestrial applications due to their high costs. Much of the interest in GaAs is attributed to their potential for use in tandem (or cascade) cell structures (e.g., GaAs/InGaP) with potential efficiencies of 27% [17]. These structures are, however, complex and employ a large number of component layers. Epitaxial layers of GaAs grown directly on Si substrates have the potentially attractive feature of reducing the cost as well as enabling a III-V/Si monolithic two bandgap technology. Although a large lattice mismatch of 4% gives rise to a large dislocation density in the epilayer, efficiencies of $\sim 12\%$ have been reported [18].

The progress in conventional Si cell technology has exceeded all expectation, and in fact early calculations which assumed that the Si devices were planar homojunctions suggested theoretical maximum efficiencies of around 20%. However, the latest cells using a variety of innovative techniques in non-planar structures have achieved efficiencies that are better than this and calculations of theoretical efficiency for these structures now indicate values of about 30% [19]. In addition, new technologies are being developed which avoid the high cost of solar-grade Si wafer preparation e.g.,

- Casting the Si directly into ribbons or wafers,
- Formation of thin crystalline films of Si on a ceramic substrate,
- Use of Si droplets to produce micro-cells which are then attached to a flexible substrate in a solar “sandpaper”.

The first commercially available thin film cells were based on α -Si and have found widespread use in low power applications such as portable calculators, etc. The α -Si cell is in fact an alloy of amorphous silicon with 3% hydrogen (and sometimes fluorine) and has a bandgap of about 1.7 eV. The first solar cells were

subsequently manufactured by RCA, in the US, and by a number of Japanese companies.

When exposed to bright sunlight the performance of α -Si cells degrades, quite quickly at first and then more slowly, until the efficiency falls to about 4%. Electrons and holes do not diffuse readily in α -Si to allow efficient carrier collection, so the cells are designed with thin ($0.1\mu\text{m}$) p- and n-layers, with a thicker ($0.8\mu\text{m}$) intrinsic layer sandwiched between them. Light is absorbed mainly in the intrinsic layer, and the photogenerated carriers move under the junction electric field which permeates the intrinsic layer. The degradation takes place in the intrinsic layer by processes which are still not well understood despite considerable research effort, and as a result interest in α -Si cells is waning.

One of the other alternative thin film materials for solar cell use is CuInSe_2 , which is a group I-III-VI₂ ternary semiconductor with a chalcopyrite structure. The optical bandgap is direct at around 1.1 eV. Optical absorption coefficients are above $2 \times 10^4 \text{cm}^{-1}$ for photon energies higher than 1.1 eV. As a result therefore, a $2\mu\text{m}$ thick film of CuInSe_2 is adequate to absorb about 92% of the incident radiation (i.e. for photons with energy \geq bandgap). The science base of CIS is far below that of the conventional semiconductors, but already cells of 14% efficiency and modules of 11% have been demonstrated by Siemens Solar Industries. The CIS cells have a higher current but a lower voltage than Si cells, and there are large programmes aimed at increasing the voltage. One route is to incorporate about 20% Ga on In sites to produce CuIn/GaSe_2 (CIGS) which has a larger bandgap and generates a higher voltage. CIGS cells of over 10% efficiency have been demonstrated at Stuttgart University, Germany.

1.5 CdTe Based Solar Cells.

Cadmium telluride is a low cost photovoltaic absorber material with a bandgap of 1.47 eV at room temperature, which is close to the optimum value for solar cells [20]. The bandgap is direct with a relatively high optical absorption coefficient (i.e. $\sim 10^4 \text{cm}^{-1}$ at the band edge [21]) which is large enough for the near total absorption of light in a $2\mu\text{m}$ thick film. Modern interest in CdTe dates back to 1947 when Frerichs [22] grew single crystal of CdTe from the vapour phase reaction of cadmium and tellurium in the presence of hydrogen. However, it was D.de Nobel's

work on the effects of deviation from stoichiometry that laid the foundations for the understanding of CdTe (with well defined electrical properties) crystal growth from the melt [23]. The first CdTe solar cells were reported by Vodakov et al [24], and Naumov and Nikoloeva [25] for homojunction cells in the 1960s when efficiencies of 4–5% were obtained. However, other early studies of CdTe revealed that an economical CdTe homojunction terrestrial cell was not feasible, because of the relatively low carrier lifetimes. Nevertheless, Barbe et al [26] produced a shallow homojunction cell with n-CdTe that had an efficiency of 13%.

Due to the difficulties of forming a thin film shallow junction with a high conductivity surface layer and a low surface recombination velocity, it is preferable to form heterojunction solar cells where a transparent, conducting semiconductor is used as a window layer. Several types of CdTe heterojunction cell have been fabricated and investigated during the last two decades in attempts to produce efficient (about 10% or higher) solar cells. Reviews of CdTe based solar cells can be found in [27,28,29].

1.6 n-CdS/p-CdTe Thin Film Solar Cells.

Thin film solar cells are very attractive for flat-plate terrestrial applications because they can be fabricated using potentially low-cost methods which can produce large area substrates in an economical way. The amount of materials used in thin film solar cells is minimal (1–5 μ m thick layers) compared to crystalline Si devices (300 μ m thick). Furthermore, there is no need for wafer slicing, and solar cells may be monolithically integrated on their insulating substrates to fabricate series connected modules of various power output levels. The first thin film n-CdS/p-CdTe heterojunction solar cell was fabricated by Adirovich et al [30] who reported a modest efficiency value of 1% in 1969. The efficiency of these devices was later improved to the 5% range by Bonnet and Rabenhorst [31] who used a high temperature gas transport method to grow the CdTe layers. Demonstration of 5% efficiency for an all-thin film n-CdS/p-CdTe solar cell stimulated further research on the heterojunction structure and these efforts led to the development of cells with over 10% efficiency by the early 1980s.

Another advantage of thin film CdTe is its potential efficiency. For instance, α -Si cells appear to have a relatively limited efficiency potential. This is partly

because of the known light-induced degradation, but also poor electronic quality of α -Si materials. The comparison with CuInSe₂ is less obvious. CdTe has a large bandgap closer to the theoretical optimum for simple PV devices (single junction cells) whereas CuInSe₂ has a smaller less optimum bandgap. This means that in the ideal case CdTe cells will be characterised by high open-circuit voltage, and modest short-circuit current while CuInSe₂ cells will be the reverse. The theoretical maximum efficiencies for both cells are very close and in practice, it will be the relative difficulty and cost of manufacture that will determine which system will be superior. Both should be able to make 15% efficiency for manufactured modules. However since CdTe cells have higher voltages, they will retain their efficiencies much better.

1.7 Present Work.

This work was aimed at investigations of the CdS and CdTe thin layers, and characterisation of bulk single crystal and thin film p-CdTe/n-CdS solar cells. The thesis begins with a general discussion of world energy needs and the role of renewable energy sources, mainly photovoltaic power generation. A short review of the history of photovoltaic cells together with a general overview of present developments is given. Chapter II introduces the relevant scientific background for the solar cells. Chapter III discusses thin film growth (i.e. in the case of physical vapour deposition), preparation of CdTe bulk single crystals, and the fabrication of CdTe based solar cells (i.e. bulk single crystal and thin film). The details of the experimental set-up and characterisation techniques employed are provided in chapter IV.

Chapter V is concerned with determination of the optical constants (i.e. refractive index, extinction and absorption coefficients) and optical bandgap energies of the CdS and CdTe thin layers, using transmission spectra only (i.e. Swanepoel method). The effects of heat treatment and doping on their optical properties are also given. Chapter VI describes structural investigations of the layers employing X-ray diffraction, SEM, EDAX, RHEED and SIMS. The electrical properties of the layers are presented in chapter VII including a discussion of the carrier scattering mechanisms in CdTe:Cl₂ thin layers. Chapters VIII and IX contain the photovoltaic properties of both bulk single crystal CdTe/CdS and thin film

CdTe/CdS solar cells. Bulk single crystal CdTe/CdS cells were characterised in an attempt to obtain a basic understanding of the device properties and to compare with CdTe/CdS thin film solar cells. Final conclusions are discussed in chapter X.

1.8 References.

1. T.Matsuoka, H.Yagi, Y.Waki, K.Houma, S.Sakai, Solar Cells, **29**, 361 (1990).
2. D.M.Paul and N.E.Stirewalt, in "*A Guide to the Photovoltaic Revolution*", Rodale Press, Emmaus, Pa **7** (1985).
3. E.Becquerel, Compt.Rend, **9**, 561 (1839).
4. W.G.Adams and R.E.Day, Proc.Roy.Soc.London **A25**, 113 (1877).
5. B.Lange, Zeit.Phys., **31**, 139 (1930).
6. O.Grandahl, Rev.Mod.Phys., 51141 (1937).
7. W.Schottky, Zeit.Phys., **31**, 913 (1930).
8. D.C.Reynolds, G.Leies, L.L.Antes, and R.E.Marburger, Phys.Rev., **96**, 533 (1954).
9. J.J.Loferski, J.Appl.Phys., **27** 777 (1956) and Proc. IEEE **51**, 672 (1963).
10. A.W.Brinkman, "CdTe Based Solar Cells", EMIS, Data Review, to be published, 1994.
11. S.Karaki, D.S.Ward, G.O.G.Lof, IEEE Transaction on Power Apparatus and Systems, Vol. PAS-93, No:6, 1737 (1974).
12. J.C.Powel, Proceedings of IEEE Power Engineering Society **A75**, 1 (1975).
13. D.B.Miller, K.W.Boer, Proceedings of IEEE Power Engineering Society **A75**, 417 (1975).
14. N.W.Patapoff, D.R Mattijetz, Transactions on Power Apparatus Band System, PAS-104, No:8 2020, (1985).
15. M.A Green 10th European Photovoltaic Solar Energy Conf. Lisbon, (1991).

16. B-C.Chung, G.F.Virshup, J.C.Schultz, IEEE Proc. of 21st Photovoltaic Specialist Conf., 179 (1990).
17. A.Geelen, P.R.Hageman, W.Gabrielse, L.J.Giling, 10th European Photovoltaic Solar Energy Conf., Lisbon (1991).
18. M.F.Viela, A.Leycuras, European Photovoltaic Solar Energy Conf., Lisbon (1991).
19. J.L.Gray, R.J.Schwartz, IEEE 17th Photovoltaic Specialists Conf., Kissimmee, Florida, 1984.
20. S.M.Sze, "*Physics of Semiconductor Devices*", New York; Wiley & Sons, p.790, 1981.
21. K.W.Mitchell, A.L.Fahrenbruch, R.H.Bube., J.Appl.Phys., 48 829 (1977).
22. R.Frerichs, Phys.Rev., **72**, 594, (1947).
23. D.de Nobel, Philips.Res.Rep., **15** 361 (1959).
24. Yu.A.Vodakov., G.A.Lomakina, G.P.Naumov and Yu.P. Maslakovets, Sov. Phys. Solid State, **2**, 1 (1960).
25. G.P.Naumov and O.V.Nikolaev, Fiz.Tverd Tela, **3**, 3748, (Eng. Transl. Sov. Phys Solid State, **3**, 2718 (1962).
26. M.Barbe, F.Bailly, D.Lincot and G.Cohen-Solal, IEEE Photovoltaic Specialists Conf, 1133 (1982).
27. R.H.Bube, Solar Cell, **23**, 1 (1988).
28. T.L.Chu, "*Current Topics in Photovoltaics*", Vol **3**, 235 (1988).
29. K.Zweibel, R.L.Mitchell and A. Herhann, Proc. 18th IEEE Photovoltaic Specialists Conf., 1393 (1985).
30. E.I. Adirovich, Y.M.Yuabov and G.R.Yagudaev, Sov.Phys. Semicond., **3** 61 (1969).

31. D.Bonnet and H.Rabenhorst, Proc. 9th IEEE Photovoltaic Specialists Conf., New York, 129 (1972).

Chapter II

Scientific Background.

2.1 Introduction

In this chapter the scientific background will be described. General aspects of solar irradiation relevant to solar cells will be discussed. A brief review of the background theory for heterojunction solar cells will then be given. Finally a brief review of the CdTe thin film solar cell will be presented.

2.2 Solar Spectrum.

The solar spectrum at the surface of the earth depends critically on the atmosphere. The spectral distribution depends not only on the composition of the atmosphere, but also on the optical path length. The solar flux density spectrum shown in Fig.2.1 extends from the ultraviolet through the visible to the far infrared. A quantity called the solar constant is used as a measure of the available solar power and is defined as the rate at which energy is received on unit area surface of the outer atmosphere perpendicular to the sun's direction. In free space at the earth's mean distance from the sun, the value is 1353 Wm^{-2} . The proportion of the available solar power that actually reaches the earth's surface is determined by factors such as the water content, turbidity, ozone content, cloudiness, haziness, and ground reflections.

Another important parameter is the sun's declination angle which determines the path length through the atmosphere. This geometric effect is described by specifying the zenith angle of the sun, z , the angle between the earth-sun radius and the normal to the earth's surface, as illustrated in Fig.2.2. The path length through the atmosphere is described in terms of an equivalent air mass, m_r (where $m_r \equiv \sec(z)$), thus specific solar spectra are generally labelled $\text{AM}m_r$ (read air mass m_r). $\text{AM}0$ corresponds to the solar spectrum in outer space. $\text{AM}1$ and $\text{AM}1.5$ represent solar spectra with integrated intensities of 100Wm^{-2} and

95Wm^{-2} respectively and correspond to the irradiance through a standard atmosphere when the sun is at angles of 0° and 48.19° with the normal to the earth's surface (a standard atmosphere is one in which there is 2cm of precipitable water and zero aerosol turbidity). It should be noted that the reduction in irradiance at AM1.5 (compared to AM1) is only 5Wm^{-2} because this is a global irradiance that includes contributions from scattered radiation as well as from the direct (i.e. unscattered) beam.

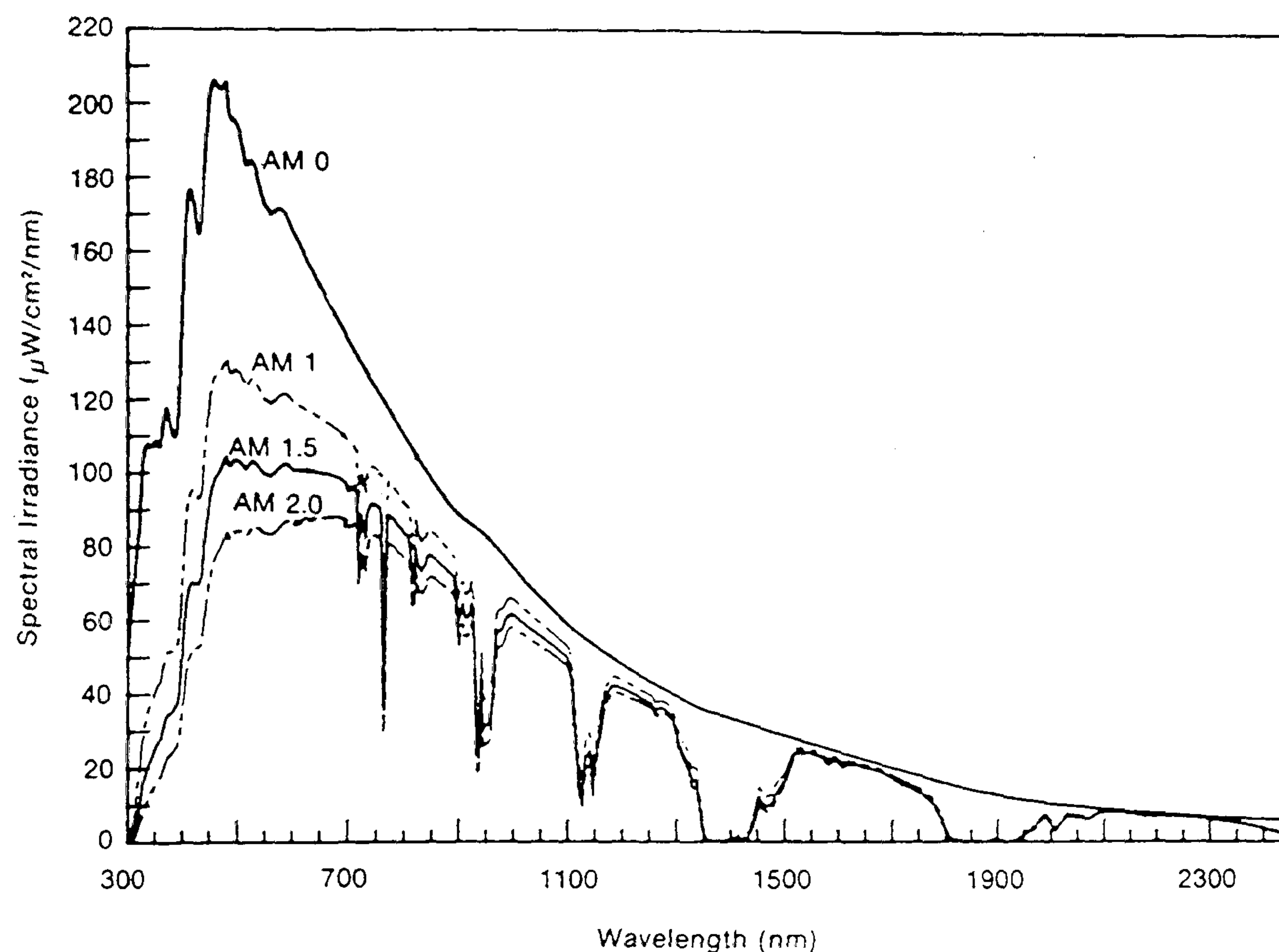


Figure 2.1 — Solar spectrum (After [1]).

2.3 Spectral Dependence of Solar Cells.

The typical configuration of a heterojunction solar cell is given in Fig.2.3. It generally comprises a top window layer composed of a semiconductor with a large bandgap through which the light can pass without attenuation to the junction, and an absorber layer consisting of a semiconductor with a high absorption coefficient and a bandgap energy matched to the solar spectrum.

The absorber is generally chosen to be the p-type material because of the larger diffusion lengths for minority carriers (i.e. electrons) in p-type semiconductors. Ohmic contacts are made to both semiconductor layers and that to the window layer must obviously be transparent (either a transparent conducting oxide e.g., ITO, or a grid structure as illustrated in Fig.2.3).

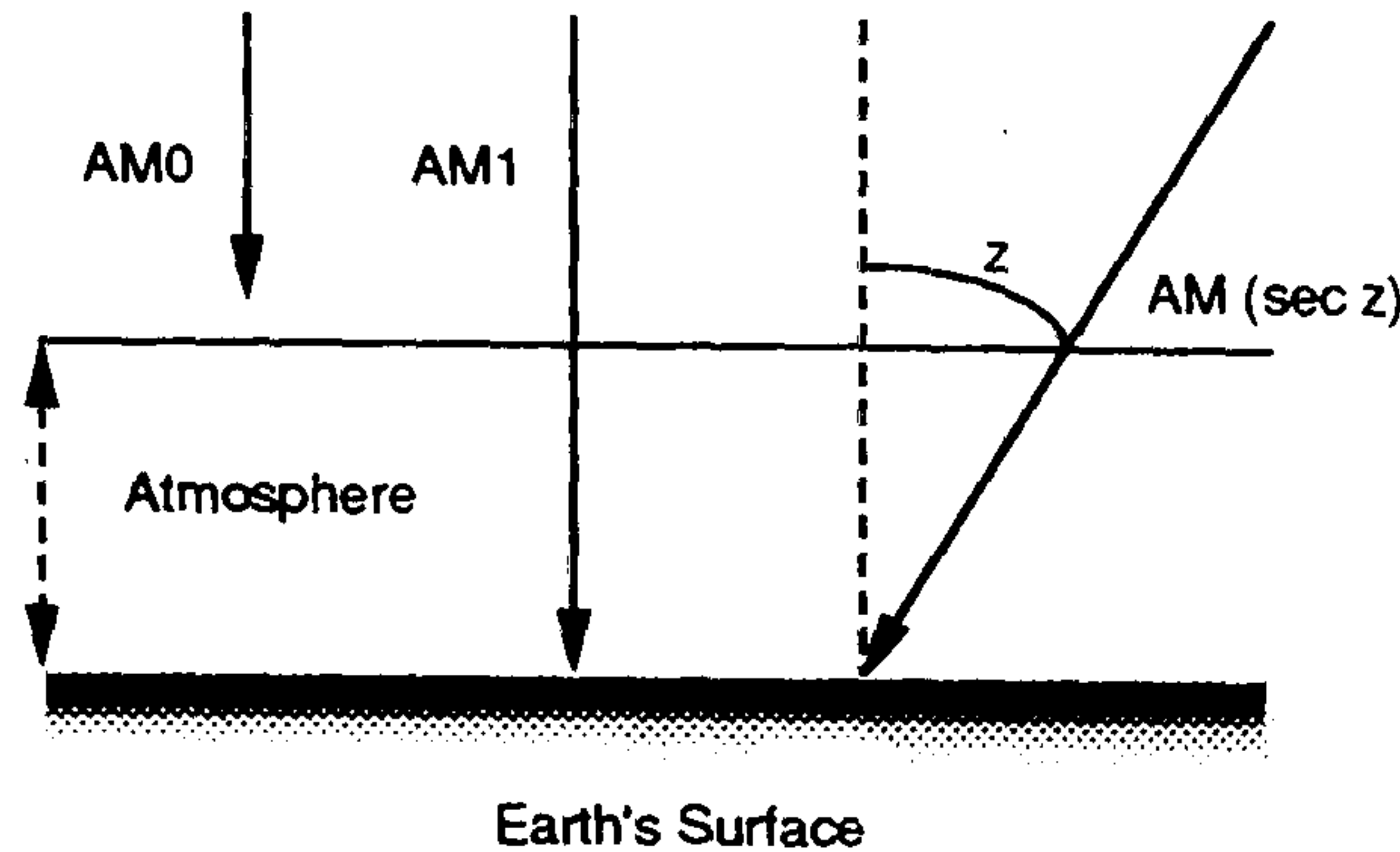


Figure 2.2 — Sun's Declination Angles.

In choosing the semiconductor for a solar cell application there are a number of material parameters that need to be considered, including the optical bandgap, absorption coefficient, diffusion length, doping characteristics, lattice parameter and surface state activity. The most fundamental parameter is the bandgap energy, E_g of the absorber semiconductor. For a given value of E_g , only photon energies $h\nu \geq E_g$ will be absorbed and in the ideal case contribute to the photocurrent. In principle a photon of energy $h\nu > E_g$ will excite an electron into the conduction band with energy $h\nu$. However, this electron will be thermalised down to the bottom of the conduction band very rapidly dissipating the excess energy as heat and that proportion of the incident energy is then lost. As a consequence there is always a trade off between having a small energy gap to absorb a larger fraction of the solar spectrum and a larger energy gap to ensure that the photogenerated carriers have higher energy (i.e. voltage). The variation of ideal efficiency vs absorber layer bandgap energy is illustrated in Fig.2.4. The optimum bandgap energy varies with the air mass number, because the solar spectrum also changes with air mass number, but at AM1.5 the optimum bandgap is about 1.3 eV [2].

Electron-hole pairs generated in the junction region are immediately separated by the built-in field. However, electron-hole pairs generated outside the depletion

region must first diffuse to the junction before charge separation can take place. Any that recombine before this stage will not contribute to the photocurrent. Thus the minority carrier diffusion length L_n (electron) or L_p (hole) is an important parameter in determining collection efficiency, and depends on the crystallinity, defect content, and stoichiometry of the material involved. It should be as large as possible, to maximise the effective active volume of the semiconductor.

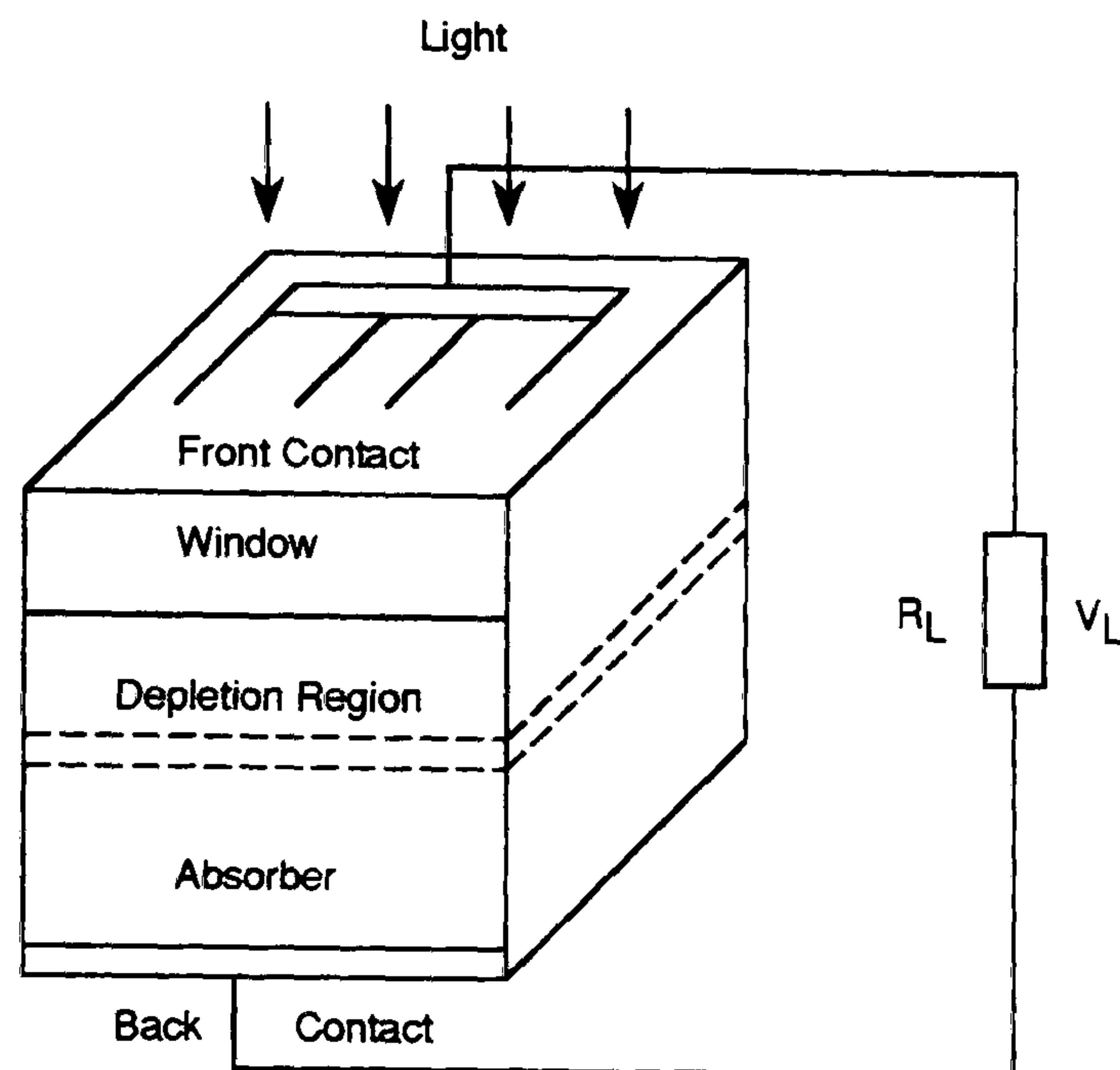


Figure 2.3 — A Solar Cell Configuration.

The incorporation of dopants has a profound effect on the absorption coefficient, diffusion length and bandgap [3]. In order to obtain good efficiencies, high levels of doping are required in order to reduce the internal resistance, however excessive doping can lead to reduced diffusion lengths. A compromise has again to be reached to obtain the optimum performance.

The lattice mismatch between the window and absorber semiconductors can lead to the formation of misfit dislocations and interface states. These act as recombination centres, reducing the photogenerated current crossing the junction. Another less obvious problem that affects the efficiency is the effect of surface states on the window material. Surface states arise from dangling bonds, chemical residues, and oxide layers, and these also lead to the recombination of carriers, thus limiting the cell performance.

2.4 Solar Cell Theory.

This section describes the theoretical background required for understanding the operation of p-n heterojunctions and their applications as solar cells. Detailed analysis of heterojunction theory and its historical review is not presented since it is beyond the scope of the thesis. Instead a qualitative picture of the device concepts and junction characteristics involved is given using mathematical expressions only when necessary.

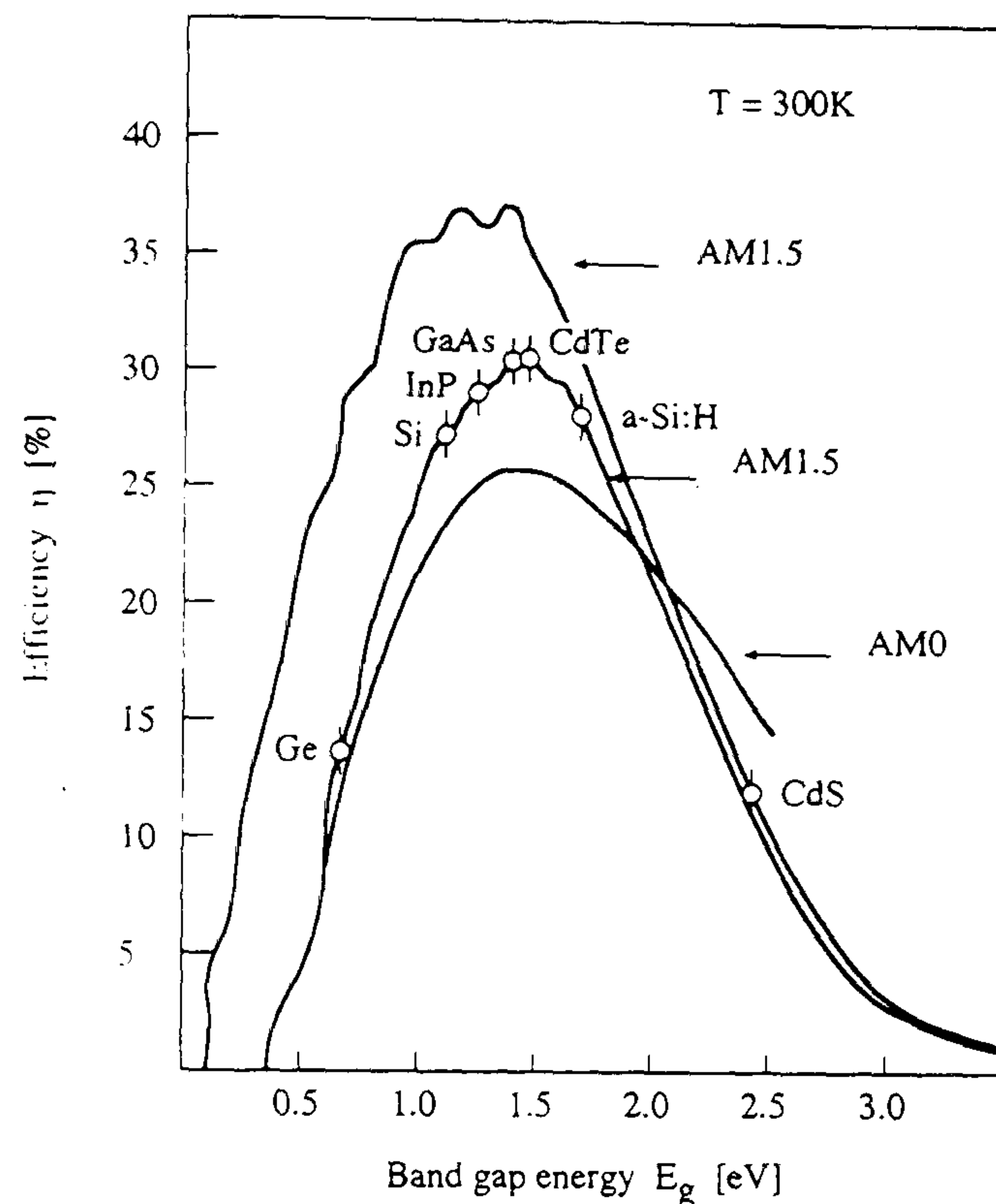


Figure 2.4 — Solar Cell Efficiency vs Bandgap Energy Values.

2.4.1 Formation of Energy Band Diagrams.

Heterojunctions have been extensively reviewed by Milnes and Feucht [4], Sharma and Purhoit [5] and Chopra and Das [6]. The construction of the energy band diagram for the heterojunction proceeds by first drawing the energy diagrams of the two materials separately as in Fig.2.5a (drawn for n-CdS/p-CdTe neglecting the effects of dipoles and interface states -ideal case) and with the vacuum energy in common. As the materials are brought into contact, there is an equalisation of the Fermi level energies and consequently there is an exchange of

electrons and holes between the two semiconductors. This displacement of charge at the interface bends the conduction and valence bands in the semiconductors to form a depletion or space charge region. In addition to the band bending, there will be, in general, discontinuities in the conduction and valence bands at the junction due to the difference in the electron affinities. For an ideal junction, the barrier height, E_b to electron flow is given by [7,8];

$$E_b = E_{g,p} + \Delta E_c - \delta_n - \delta_p \quad [2.1]$$

where ΔE_c is the conduction band discontinuity, $E_{g,p}$ is the bandgap of the p-type material and δ_n , δ_p are the displacements of the Fermi level from the conduction band edge and valence band edge in the n- and p-type materials respectively. Conduction and valence band offsets (i.e. discontinuities) are given by;

$$\Delta E_c = \chi_p - \chi_n \quad [2.2a]$$

$$\Delta E_v = (E_{g,n} - E_{g,p}) - \Delta E_c \quad [2.2b]$$

$E_{g,n}$ is the bandgap of the n-type material, and χ_n and χ_p are the electron affinities of the n- and p-type materials respectively. If the conduction band offset ΔE_c , produces a barrier or “spike” in the conduction band profile, it will limit the electron injection and allow recombination at the interface to dominate the current flow. In the band profile for the n-CdS/p-CdTe heterojunction, illustrated in Fig.2.5, the conduction band line-ups do not result in the formation of such a spike and the discontinuity does not therefore impede current flow in this system.

2.4.2 Photovoltaic Effect.

When a forward bias is applied to a p-n junction (i.e. as in Fig.2.5), the barrier height potential is reduced, and majority electrons from the n-side and majority holes from the p-side diffuse over their respective barriers to the opposite sides where they become minority carriers. The current-voltage relation is expressed by the usual diode equation [9];

$$J = J_o \left[\exp\left(\frac{qV}{kT}\right) - 1 \right] \quad [2.3]$$

where J_o is the reverse saturation current density, V is the applied bias voltage, k is the Boltzmann's constant, q is the electronic charge and T is the temperature.

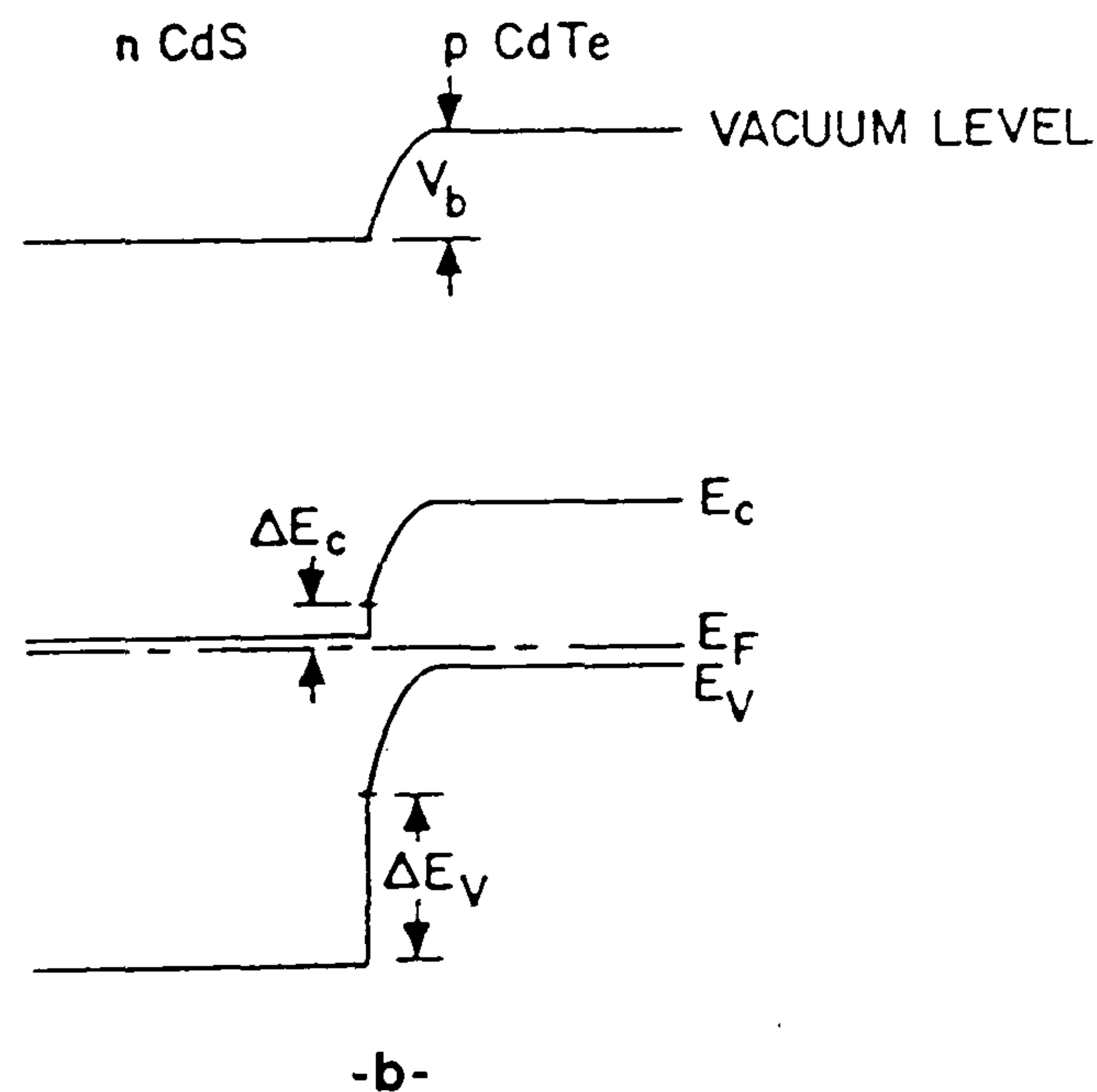
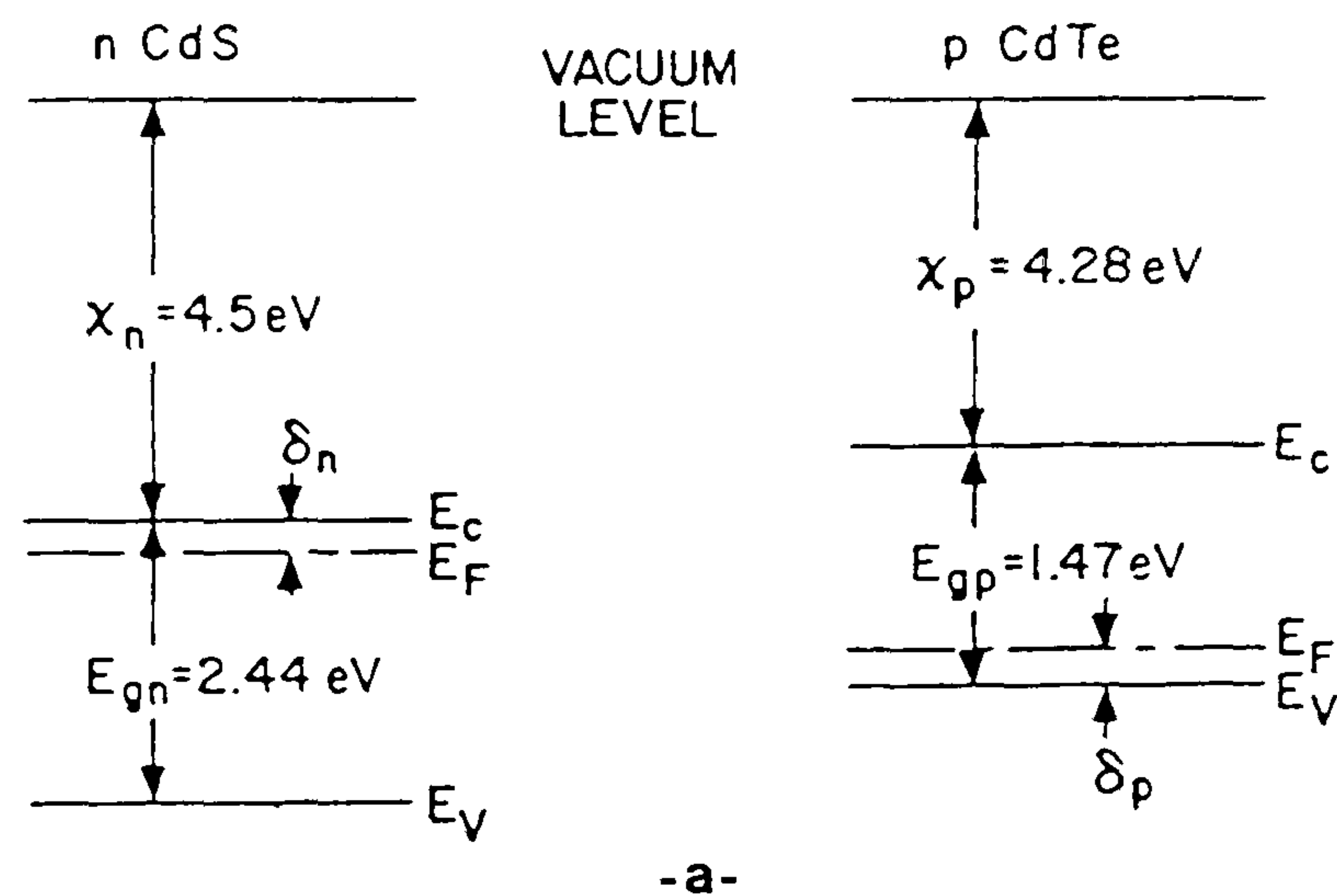


Figure 2.5 — Energy Band Diagram of n-CdS/p-CdTe Cell.

In practice, such a p-n junction diode will not be fully ideal and there will be internal losses due to the recombination of electrons and holes at defects etc. Thus the ideal diode equation is normally modified to;

$$J = J_o \left[\exp\left(\frac{qV}{nkT}\right) - 1 \right] \quad [2.4]$$

where n is an ideality factor which takes account of these effects. When the diode is illuminated excess electron-hole pairs are created in both regions. As a proportion of the total current density, the increase in the majority carriers is very small. For the minority carriers however, the proportional increase is large and this leads to a pronounced change in the reverse current. Thus the diode current in the forward direction may then be expressed as [10];

$$J = J_o \left[\exp\left(\frac{qV}{nkT}\right) - 1 \right] - J_L \quad [2.4]$$

where J_L is the total light generated current density (i.e. integrated over incident wavelength and neglecting recombination losses).

The total photocurrent arriving at the junction is the sum of contributions from absorption in the depletion region (J_w) and the bulk (J_b), giving;

$$J_L = J_w + J_b \quad [2.6]$$

If the incident total intensity at the junction is ϕ_o then;

$$J_w = qa_o \int_{\lambda_1}^{\lambda_2} \phi_o(\lambda) \left[1 - \exp[-\alpha(\lambda) W] \right] d\lambda \quad [2.7]$$

where a_o , $\alpha(\lambda)$, W and λ_1 and λ_2 are the quantum efficiency, absorption coefficient, depletion width and wavelength limits for the absorption. As stated earlier only charge carriers generated within one diffusion length (L) from the depletion region edge can contribute to the photocurrent, so therefore;

$$J_b = qa_o \int_{\lambda_1}^{\lambda_2} \phi_o(\lambda) \exp[-\alpha(\lambda) W] \left\{ 1 - \exp[-\alpha(\lambda) L] \right\} d\lambda \quad [2.8]$$

combining Eq.2.7 and Eq.2.8 gives the total photocurrent as;

$$J_L = J_w + J_b = qa_o \int_{\lambda_1}^{\lambda_2} \phi_o(\lambda) \left\{ 1 - \exp[-\alpha(\lambda) (W + L)] \right\} d\lambda \quad [2.9]$$

This is often expressed in terms of [11];

$$J_L \cong qa_o \int_{\lambda_1}^{\lambda_2} \phi_o(\lambda) \left\{ 1 - (1 + \alpha(\lambda) L)^{-1} \exp[-\alpha(\lambda) W] \right\} d\lambda \quad [2.10]$$

where the exponential term in Eq.2.8 has been expanded to first order. In practice the current is reduced by recombination at the interface by a fraction $[1 + \frac{s}{\mu E}]^{-1}$ where s , μ and E are the recombination velocity, minority carrier mobility and junction electric field. The actual photocurrent density, J_{ph} is;

$$\begin{aligned} J_{ph} &= \left[1 + \frac{s}{\mu E}\right]^{-1} J_L \\ &= qa_o \left[1 + \frac{s}{\mu E}\right]^{-1} \int_{\lambda_1}^{\lambda_2} \phi_o(\lambda) \left\{1 - (1 + \alpha(\lambda) L)^{-1} \exp[-\alpha(\lambda) W]\right\} d\lambda \end{aligned} \quad [2.11]$$

The spectral response of a solar cell is often given as the ratio of photogenerated carriers collected per incident photon at a particular wavelength;

$$\frac{J_{ph}(\lambda)}{q\phi_o(\lambda)} = \left[1 + \frac{s}{\mu E}\right]^{-1} \left\{1 - \exp[\alpha(W + L)]\right\} \quad [2.12]$$

The spectral response of a solar cell is one of the important performance characteristics and gives a good indication of the quality of particular cell.

2.4.3 Solar Cell Parameters.

The performance of solar cells is typically described in terms of open-circuit voltage, V_{oc} , short-circuit current density, J_{sc} , fill factor, FF and efficiency, η . These parameters are useful, intuitive, easily measured, and used as universal figures of merit although they should always be quoted with respect to the illumination intensity (i.e. AM1.5 etc.).

Short Circuit Current Density, J_{sc} : This is the photocurrent flowing through the junction at zero applied bias. In ideal conditions, it is equal to the total light generated current density J_L and is proportional to the incident photon flux in the bandpass window. In essence, the short circuit current density is determined by the spectrum of the light source and the spectral response of the device.

Open Circuit Voltage, V_{oc} : The open circuit voltage is the output voltage of the device under illumination when zero current is flowing through the junction. The open circuit voltage of the cell is directly related to the bandgap of the semiconductor through the barrier height at the junction and is often expressed in terms of

the total light generated current density, J_L , the reverse saturation current density, J_o and the diode ideality factor, n as [7];

$$V_{oc} = \frac{nkT}{q} \ln \left[\frac{J_L}{J_o} + 1 \right] \quad [2.13]$$

It might appear from Eq.2.13 that high values of n are desirable in obtaining high V_{oc} but this is not so. Large values of n indicate poor diode quality leading in turn to larger values of J_o . Consequently the open circuit voltage is in fact reduced. In contrast, in an ideal junction, n is equal to unity but J_o will be a minimum and V_{oc} attains its highest value.

Fill Factor, FF : The fill factor is the ratio of the maximum actual output power to the product of V_{oc} and J_{sc} . It describes the rectangularity or squareness of the photovoltaic output characteristics. The fill factor is mainly determined by the value of n , the series resistance R_s and shunt resistance R_{sh} of the cell (see section 8.5). A high shunt resistance and low values of n and R_s are required for a high fill factor. High values of fill factor imply a high utilisation of the available current and voltage.

Efficiency, η : This parameter describes the overall cell performance and can be expressed as [7];

$$\eta = \frac{J_{sc} V_{oc}}{P_{in}} FF \quad [2.14]$$

where P_{in} is the incident radiation power density, and is usually expressed in mW/cm². A typical current-voltage characteristic of a p-n junction diode in the dark and under illumination is shown in Fig.2.6.

2.5 CdTe Thin Film Solar Cells.

The development of CdTe thin film photovoltaics has reached a stage where it can be considered a leading candidate for cost competitive photovoltaic electricity generation. Achievements such as high cell and module efficiencies and the existence of pilot production facilities have placed CdTe in the first rank of the thin film cells alongside CuInSe₂.

In addition, CdTe technology has an important advantage in that a variety of low-cost methods can be used to make quality layers. The low capital costs of these

processes make it relatively easy to begin scaling up CdTe solar cell manufacturing. The achievements that have brought CdTe to its current state of development can be categorised in terms of efficiency, cost and reliability. The performance of thin film CdTe solar cells is given in Table 2.1.

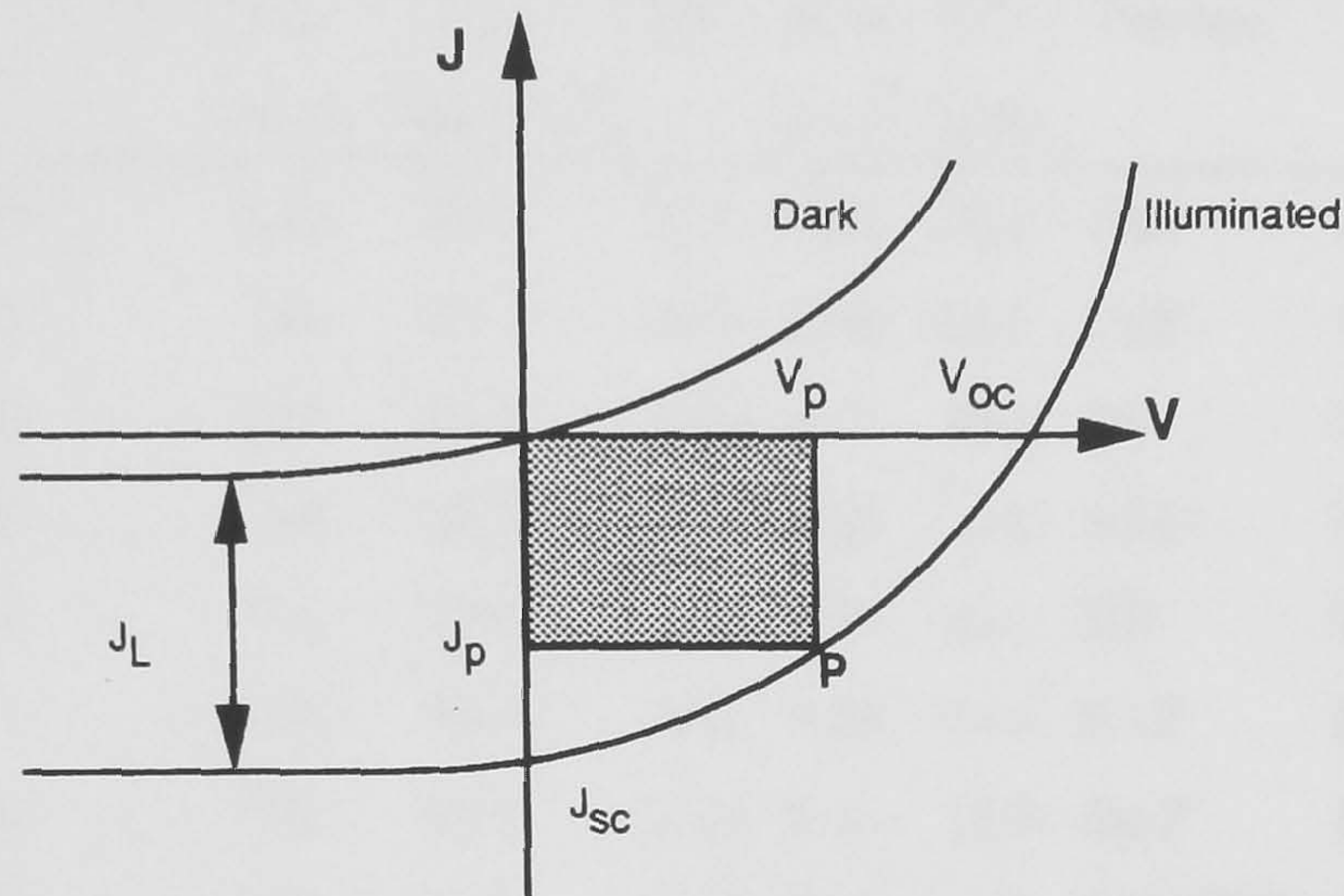


Figure 2.6 — Current-Voltage Characteristics of a p-n Junction Diode in the Dark and Under Illumination.

High efficiency thin film CdTe solar cells generally have the *superstrate* device configuration. In this design the substrate is usually glass coated with a transparent conducting oxide (TCO), which forms one of the cell contacts. The TCO is typically an indium tin oxide (ITO), or a F- or Sb- doped oxide (TO) giving a sheet resistance of 5–10 Ω/sq . A very thin ($<0.2\mu\text{m}$) film of CdS is deposited onto the TCO to form an n-type window layer. The p-type absorber layer ($2\text{--}4\mu\text{m}$) is then deposited onto the CdS to form the p-n heterojunction and a back contact is then applied to the CdTe to complete the structure.

2.5.1 Design and Processing of CdS/CdTe Solar Cells.

The CdS window layers are generally undoped with resistivity values of $10\text{--}10^3 \Omega\text{-cm}$ under illumination depending upon the stoichiometry and the deposition technique. There is, in principle, no limitation on the methods that can be

employed for CdS deposition and a wide range of techniques including low temperature methods (i.e. $T < 100^\circ\text{C}$), such as electrodeposition and solution growth; medium temperature (i.e. $150^\circ\text{C} < T < 250^\circ\text{C}$), such as vacuum evaporation; and high temperature (i.e. $T > 250^\circ\text{C}$), such as screen printing (Sc.P), spray pyrolysis (Sp.P) and close-space sublimation (CSS) have been used successfully.

Cell Structure	V_{oc} (mV)	J_{sc} (mA/cm ²)	FF	Area (cm ²)	Eff. η (%)	Process	Group, Ref.
G/TO/CdS/CdTe	843	25.1	0.75	1.05	15.8	CSS	J.Britt, USF. [12]
G/TO/CdS/CdTe	850	24.4	0.70	1.08	14.6	CSS	Chu, USF. [13]
G/TO/CdS/CdTe	819	23.5	0.74	0.02	14.2	ED	BP Solar. [14]
G/TO/CdS/CdTe	804	23.8	0.73	0.12	14.0	ALD	Micro.Chem. [15]
G/TO/CdS/CdTe	720	27.9	0.65	0.02	13.1	ED	Univ.of Queens. [16]
G/CdS/CdTe	750	28.0	0.61	0.78	12.8	Sc.P	Matsushita [17]
G/TO/CdS/CdTe	783	25.0	0.67	0.31	12.3	Sp.P	Photon Energy [18]
G/TO/CdS/CdTe	756	24.5	0.64	0.08	11.9	MOCVD	George Techn. [19]
G/ITO/CdS/CdTe/ZnTe	767	22.4	0.70	1.07	11.2	ED	Ametek. [20]
G/ITO/TO/CdS/CdTe	745	22.6	0.65	0.4	11.0	CSS	Batt. Europe [21]
G/ITO/CdS/CdTe	789	20.1	0.69	0.19	11.0	VE	Ins.of E.Conv. [22]
G/IO/CdS/CdTe	750	17.0	0.62	0.10	10.5	CSS	Kodak [23]
G/TO/CdTe	663	28.1	0.56	4.00	10.5	CSS	Arco Solar. [24]

G: Glass, TO: Thin oxide, ITO: Indium tin oxide; CSS: Close-Space Sublimation, ED: Electrodeposition, ALD: Atomic Layer Deposition, Sc.P: Screen Printing, Sp.P: Spray Pyrolysis, VE: Vacuum Evaporation, MOCVD : Metal Organic Chemical Vapour Deposition.

Table 2.1 — Current Status of High-Efficiency Thin Film CdS/CdTe Solar Cell.

The thickness of the CdTe film is determined by the partly conflicting requirements for complete absorption of the incident radiation, and by the need to keep the resistance low. The high absorption coefficient of CdTe means that for above bandgap illumination a film of about $2\mu\text{m}$ in thickness is effectively opaque. Consequently, the CdTe film thickness is generally restricted to about this dimension. The two major difficulties in the development of CdTe thin films have been the

problems of p-type doping, and the formation of low resistance contacts. Polycrystalline thin films of CdTe are very difficult to dope with acceptor dopants, because of the self-compensation mechanisms. The relatively open crystal structure and the ionic nature of CdTe allows the easy formation of native vacancy (V_{Cd} , V_{Te}) and interstitial (Cd_i , Te_i) defects which are highly mobile even at low temperatures. These defects interact with the residual impurities in the material causing self compensation, which the presence of grain boundaries in polycrystalline layers further complicates. The films are either doped during growth (e.g., with such as As, Cl_2 etc.) or after growth in a procedure where the CdS/CdTe structure is dipped in $CdCl_2$ /MeOH solution followed by a high temperature heat treatment in air at around 400°C. The $CdCl_2$ layer resulting from the dipping step is thought to act as a flux during the annealing-stage, promoting re-crystallisation and grain growth when annealing takes place in the presence of oxygen in acceptor doping.

The electron affinity of p-CdTe is rather high (5.78 eV) and a barrier contact forms at the CdTe/metal interface when any of the commonly used metals are deposited on the p-CdTe. Such contacts have a high resistance and are a major cause of losses in the cell. It is for this reason that tunneling junctions are utilised as an ohmic contact to p-CdTe. To achieve good quality electrical contacts, CdTe layers are first etched and conditioned and then an appropriate contact material such as graphite or Ni is applied to the conditioned surface. Commonly used etchants leave a Te-rich surface on the CdTe layer and this low resistivity p^+ region allows the formation of a tunneling contact to the high-resistivity CdTe film [25,26]. A dopant such as Cu or Hg may also be introduced to the contact/CdTe interface to lower the contact resistance [27]. Graphite is so far considered to be the most stable contact to CdTe. Ni is also commonly employed. Excessive amounts of Cu and/or Te at the film/contact interface also give rise to instabilities due to the diffusion of these elements along the grain boundaries.

Experimentally, n-CdS/p-CdTe thin film solar cells seem to suffer from very little degradation. Laboratory cells after 10 years of storage in an unencapsulated state have shown unimpaired values and additional irradiation over four months did not lead to any further degradation [28]. Screen printed and electrodeposited cells have shown similarly high stability and no indication of degradation [29,30]. More

recent systematic testing has confirmed that cells after 14,000 hours of outdoor exposure in Spain suffered virtually no degradation [31].

2.5.2 Issues Regarding Large-Scale Manufacturing.

As discussed above, it is difficult to make low-resistance ohmic contacts to high resistivity p-type CdTe thin films because of the large electron affinity, and commonly tunneling contacts have to be used. Therefore, any variation in the thickness of the tunneling region would be expected to change the electrical characteristics of the contact and hence of the cell. There are many reasons why the width of the tunneling region might change; diffusion of compensating dopant species into the contact area; slow chemical reactions between the etched CdTe surface and the contact material; chemical interactions of the contact interface with the gaseous by-products of the sealants used for module encapsulation; chemisorption of gases such as oxygen at the CdTe/metal contact interface etc. These factors raise questions over the long term stability of CdS/CdTe modules and remain one of the greatest uncertainties over the future development and exploitation of the device. Better ohmic contacts and practical encapsulation methods that eliminate any possible contact instability will have to be developed for the CdTe modules, before viable commercial utilisation can take place. A few industrial companies have started pilot production, the most important of which are listed in Table 2.2.

2.5.3 The Cost Potential of CdTe Thin Film Cells.

The most critical question regarding commercial success is related to the cost. The specific cost in ecu per W_p will determine the competitiveness of the cell in relation to conventional energy sources. The specific cost decreases rapidly upon upscaling of production, and at a production capacity of 100 MW_p (10⁶m² per year), a cost as low as 0.9 ecu/ W_p can be expected. Different production processes may lead to some cost variation, but no significant changes are anticipated. The main pre-requisite for low cost production is a process allowing either fast in-line production via fast deposition or high-capacity parallel production. Gross evaluations of costs are based on categories such as capital costs, material costs, utility costs, and labour cost. The most important conclusions to be drawn are the following;

- Thin films have cost advantages based on reduced materials, handling, and utilities costs.
- All thin films have relatively similar materials costs if feed stock materials are used well.
- Capital costs although important are not dominant.
- Module efficiencies are the most important determinant of final thin film costs.

Company	Process	Cell Area(cm ²)	Efficiency(%)
Matsushita (Japan)	Sc.P	1200	8.1
Photon Energy (US)	Sp.P	838	7.3
British Petroleum (U.K.)	ED	900	10.1
Microchemistry (Finland)	ALD	in	progress
Antec (Germany)	CSS	in	progress

Table 2.2 — International Module Results.

2.5.4 Environmental and Health Aspects.

Being a heavy metal, Cd has to be considered a potentially hazardous material. Its binding energy in CdTe is quite high, so that Cd is only liberated at temperatures above 900°C, limiting the risk-potential to strong fires in application. However, Cd is a widely used element in, for example, the manufacture of secondary cells and the health hazards and necessary control measures are well known. In addition the technology for recycling spent modules already exists and it should be a relatively straightforward matter to contain any environmental risks. Within the last 10 years, a group of health and environmental experts at Brookhaven Laboratories in the US have conducted a detailed analysis of these questions [32]. The main conclusion of these studies was;

“Cadmium-containing modules do not present any major new hazard to health or the environment, especially if reasonable management strategies are implemented. Furthermore, as an alternative to existing energy options which are by themselves far more stressful to health and the environment, cadmium-containing modules could reduce the important energy-related health and environmental hazards”.

In around 25 years of research at various laboratories, the technology of CdTe films has advanced to a stage that the production of CdTe as the active material for thin film solar cells is a realistic possibility. Thin film cells with high photocurrents can already be made. These favourable properties are confirmed by the fact that single crystalline CdTe cells, even after intense study, do not show significantly better photovoltaic properties: the maximum efficiency achieved was 15% in single crystal [33] versus 15.8% in film [12]. It is moreover one of the few cells that can be produced with efficiencies above 10% using low cost, scaleable techniques.

2.6 References.

1. C.J.Riordan, *Solar Cells*, **18**, 223 (1986).
2. Principal Conclusions of the American Physical Society Study Group on Solar Photovoltaic Energy Conversion, New York: American Society, 1979.
3. H.J.Hovel, "*Solar Cells*", Academic Press (1975).
4. A.G.Milnes, D.L.Feucht, "*Heterojunctions and Metal- Semiconductor Junctions*", Academic Press, New York, (1972).
5. B.L.Sharma, R.K.Purhoit, "*Semiconductor Heterojunctions*", Pergamon Press (1974).
6. K.L.Chopra, S.R.Das, "*Thin Film Solar Cells*", Plenum, (1983).
7. A.L.Fahrenbruch, R.H.Bube, "*Fundamentals of Solar Cells*", Academic Press (1983).
8. H.J.Hovel, "*Semiconductors and Semimetals*", Vol.11, Academic Press (1975).
9. A.S Grove, "*Physics and Technology of Semiconductor Devices*", Wiley, New-York (1967).
10. H.J.Möller, "*Semiconductors for Solar Cells*", Artech House, Inc., Norwood, U.S.A., 1993.
11. K.W.Mitchell, "*Evaluation of the CdS/CdTe Heterojunction Solar Cell*", Garland Publishing, Inc., New York & London, 1979.

12. J.Britt, C.Ferekides, Appl.Phys.Lett., **62** 2851 (1993).
13. T.L.Chu, S.S.Chu, Int.J.Solar Energy **12** 121 (1992).
14. J.M.Woodcock, A.K.Turner, M.E.Ozsan and J.G.Summers, 22th IEEE Photovoltaic Specialists Conf., 842 (1991).
15. J.Skarp, Y.Koskinen, S.Lindfors, A.Rautiainen, T.Suntola, Proc 10th Photovoltaic Solar Energy Conf., 567 (1991).
16. C.G.Morris., P.G.Tanner and A.Tooszer, 21th IEEE Photovoltaic Specialists Conf., 575 (1990).
17. S.Ikegami and A.Nakano, Int.J.Solar Energy, **Vol 12** (1992).
18. S.Ikegami, Solar Cells, **23**, 89 (1988).
19. A.Rohatgi, Int.J.Solar Energy, **Vol 12**, (1992).
20. P.V.Meyers and C.H.Liu., Proc. 8th Photovoltaic Solar Energy Conf., 1588 (1988) and Solar Cells, **23**, 59 (1988).
21. D. Bonnet, B. Henrichs, H. Richter, 22th IEEE Photovoltaic Specialists Conf., 1165 (1991).
22. R.W.Birkmire, B.E.McCandless and S.S.Hegedus, Int.J.Solar.Energy, (1992).
23. Y.S.Tyan and E.A.Perez-Albuerne, 16th Photovoltaic Specialists Conf., 794 (1982).
24. K.W.Mitchell, et al., Solar Cells, **23**, 49 (1988).
25. B.M.Basol, "*Method of Forming Ohmic Contacts*", U.S.Patent, 4 456 630 (1984).
26. B.M.Basol, S.S.Ou and O.M.Stafsudd, J.Appl.Phys., **58**, 3809 (1985).
27. B.M.Basol, "*Method of Making Multi-Layer Ohmic Contact to Thin Film P-Type II-VI Semiconductors*", U.S.Patent 4 666 569 (1987).
28. D.Bonnet, Proc. 5th Photovoltaic Solar Energy Conf., 897 (1983).

29. P.V.Meyers, NREL PV ARED 11th Review Meeting, May (1992).
30. A.Nakano, S.Ikegami, H.Matsumoto, H.Uda and Y.Komatsu., Solar Cells **17**, 233 (1986).
31. J.M.Woodcock, A.K.Turner, M.E.Ozsan and J.G.Summer, 22th Photovoltaic Specialists Conference, 842 (1991).
32. P.D.Moskowitz, K.Zweibel and V.M.Fthenakis, Report prepared for the U.S. Depart. of Energy, (Contract No: DE-ACO2-83CH10093), January (1990).
33. P.K.Raychaudhuri, J.Appl.Phys. **62**, 3025 (1987).

Chapter III

Bulk Single Crystal and Thin Film CdTe Growth, and CdTe/CdS Solar Cell Fabrication.

3.1 Introduction.

For many practical applications, thin films rather than bulk crystals are more convenient, if not essential. Due to the high cost of bulk single crystal preparation and difficulties in large scale production, thin film technologies are preferred in commercial device production. Most films, in early work, were put down by vacuum deposition onto polycrystalline or glass substrates, although many other techniques have also been used. A review of the earlier techniques of film deposition used specifically with II-VI compounds has been provided by Shallcross [1], and Cusano [2]. In the 1970s, interest turned increasingly to the growth of epitaxial layers, which means the deposition of an oriented, monocrystalline over-growth of one crystalline substance upon another. Initially, this was done using vapour-phase epitaxy techniques [3] and then liquid-phase epitaxy [4]. More recently, the development of molecular beam epitaxy (MBE) and metal organic vapour-phase epitaxy (MOVPE) have led to the production of high purity layers with potential for large scale commercial exploitation of the diverse interesting properties of compound semiconductors.

3.2 Physical Vapour Deposition.

Physical vapour deposition, PVD is the growth of crystalline films on solid surfaces by condensation of elements and/or compounds from the vapour phase. The most important characteristic feature of PVD techniques is that the transport of vapours from the source to substrate takes place by physical means. It involves three steps;

- 1- Generation of vapours either by thermal evaporation or sublimation, or by cathodic sputtering of appropriate solid sources.
- 2- Transport of the vapourised material from the source to the substrate generally

in a vacuum. During transport, collisions with residual gas molecules can occur depending on vacuum conditions and source to substrate distance.

3- Condensation occurs on the substrate, and finally the crystalline layer is formed by heterogeneous nucleation and film growth.

In pure PVD techniques, the deposits are formed from atomic or molecular units, simply by the physical process of condensation. It should be noted, however, that in practice condensation processes may actually involve a chemical reaction. For instance, when CdTe is evaporated for preparing CdTe films, it dissociates into Cd and Te, and the CdTe films are formed by condensation of this two-component vapour system via a chemical reaction ($\text{Cd} + \text{Te} \rightarrow \text{CdTe}$) on the substrate. In some cases films of multi-component materials, can be prepared by simultaneous condensation of the vapours of the individual components produced from separately controlled sources. This type of PVD process is known as a multi-source or co-evaporation process.

3.2.1 Growth Theory.

While there are many possible techniques that have been used to make thin films, this discussion will be concerned mainly with the growth of films produced by the physical vapour deposition method, since this was used in the course of this work. The basic physical process in vacuum evaporation involves heating the evaporant to a temperature at which its vapour pressure is sufficiently high so that vapourised atoms or molecules will strike a conveniently situated substrate at some desired rate of incidence.

The first attempts to measure quantitatively the rates, at which condensed materials enter the gaseous state were carried out by Hertz, Knudsen, and Langmuir. For all conditions chosen, Hertz found that evaporation rates were proportional to the difference between the equilibrium pressure of an evaporant at the surface temperature of the reservoir p^* and the hydrostatic pressure p acting on that surface. The number of molecules dN_e evaporating from a surface area A_e during the time dt is given by [5];

$$\frac{dN_e}{A_e dt} = (2\pi mkT)^{-1/2}(p^* - p) \quad [3.1]$$

where m is the mass of the evaporant, k is the Boltzman constant, p^* and p are the equilibrium and the hydrostatic pressures respectively. Knudsen later argued that molecules impinging on the evaporating surface may be reflected back into the gas rather than being incorporated back into the source. Consequently, there is a certain fraction $(1 - \alpha_v)$ of the vapour molecules which contribute to the evaporant pressure but not to the net molecular flux from the condensed into the vapour phase. Therefore, the most general form of the evaporation rate is then given by;

$$\frac{dN_e}{A_e dt} = \alpha_v (2\pi m k T)^{-1/2} (p^* - p) \quad [3.2]$$

where α_v is the evaporation coefficient, defined as the ratio of the observed evaporation rate in vacuum to the value theoretically possible according to the Eq.3.1. The mass evaporation rate from the solid surfaces, first shown by Langmuir, is given by;

$$\Gamma = m \frac{dN_e}{A_e dt} = \left(\frac{m}{2\pi k T} \right)^{1/2} (p^* - p) \quad [3.3]$$

where m is the mass of an individual molecule. The directional dependence of the molecules will of course depend on the source. For instance, an ideal Knudsen evaporant cell consisting basically of an enclosed chamber at temperature T that has a small orifice, the mass distribution has a cosine dependence;

$$\frac{dM}{M} = \frac{\cos \phi}{\pi} d\omega \quad [3.4]$$

where dM/M is the fractional amount of mass emitted into solid angle $d\omega$ centred at an angle ϕ with respect to the normal to the plane of the orifice.

3.2.2 Basic Modes of Thin Film Growth.

The general picture of the growth process can be presented step by step as follows;

- 1- The unit species, impinging on the substrate lose their velocity component normal to substrate and are physically adsorbed on its surface.
- 2- Since the adsorbed species initially are not in thermal equilibrium with the substrate, they move over the substrate surface, and interact among themselves, forming bigger clusters. The clusters or the nuclei are thermodynamically unstable

and tend to desorb in a time depending on the deposition parameters. If these are such that a cluster collides with other adsorbed species before desorption, it will grow in size. When a certain critical size is reached, the cluster becomes stable. This step involving the formation of stable, chemisorbed, critically-sized nuclei is called the *nucleation* stage.

3- The critical nuclei grow in number as well as in size until a saturation nucleation density is reached. A nucleus can grow both parallel to the substrates by surface diffusion of the adsorbed species, as well as perpendicular to it by direct impingement of the incident species. The grown nuclei are called *islands*.

4- The next stage in the process of the film formation is the coalescence stage in which the small islands start to merge with neighbouring islands in an attempt to reduce the surface area. This tendency to form bigger islands is termed *agglomeration* and is enhanced by increasing the substrate temperature.

5- Larger islands grow together, leaving channels and holes. The structure of the films at this stage changes from discontinuous island type to porous network type. A completely continuous film is formed by filling of the channels and holes.

Depending on the thermodynamic parameters of the deposit and the substrate surface, the initial nucleation and growth stages may be described as; a-island type, b-layer type, c-mixed type (called Stranski-Krastanov type). This is illustrated in Fig.3.1.

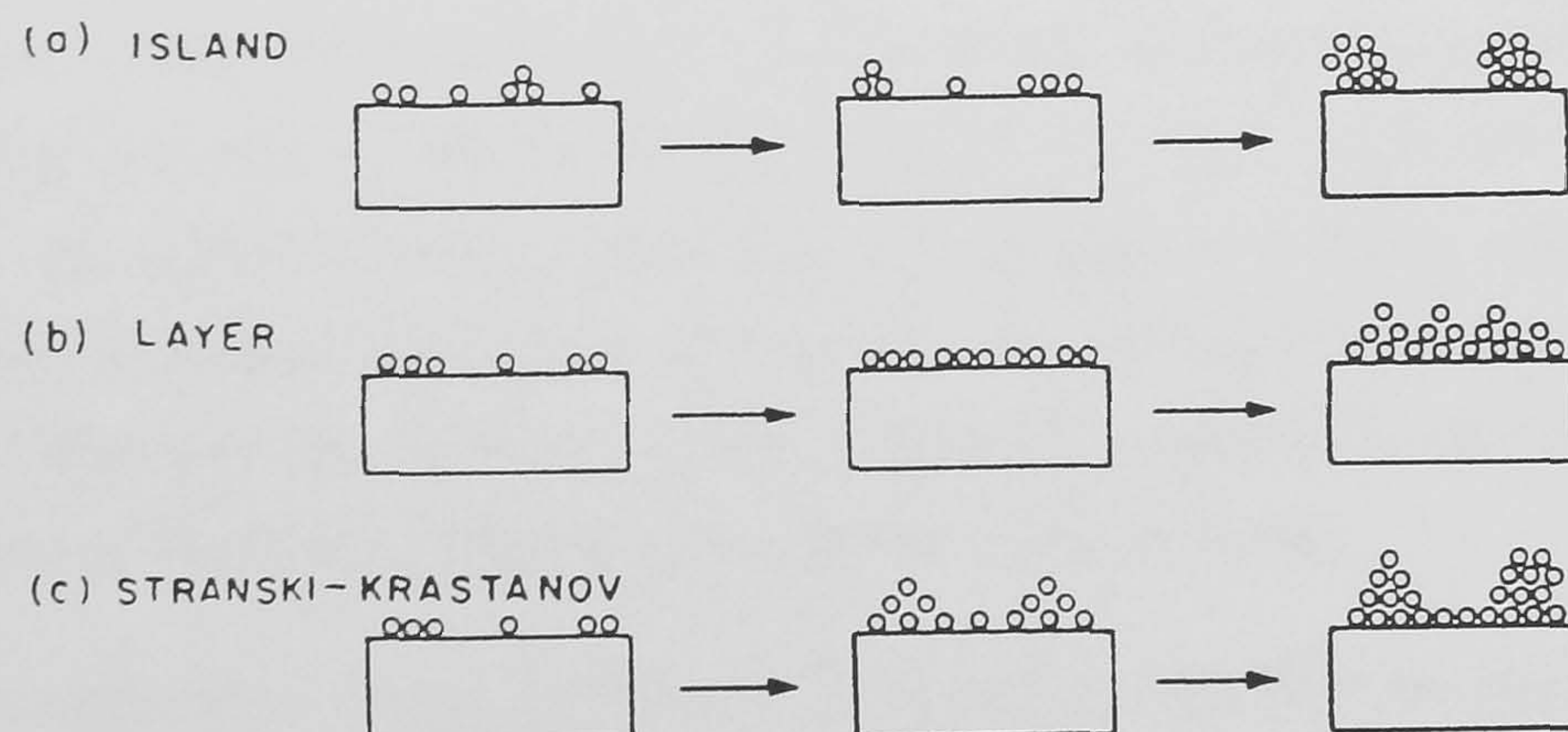


Figure 3.1 — Basic growth processes; a: island, b: layer-by-layer, and c: Stranski-Krastanov type.

3.3 Material Properties of CdTe and CdS.

3.3.1 Physical Properties of CdTe.

CdTe was suggested early on as a possible candidate for a solar cell material due to the good matching of its bandgap with the solar spectrum and the possibility of preparing both n- and p-type CdTe with high conductivity [6,7]. It has the advantage of a high optical absorption coefficient (i.e. $\sim 10^4 \text{cm}^{-1}$ at the band edge [8]), reducing the amount of material required for device fabrication (i.e. $< 5 \mu\text{m}$). Bulk single crystal growth technology of CdTe is relatively well established and researched. A congruent melting point of only 1092°C and the resulting moderate vapor pressures permit the growth of crystals by the modified Bridgman [9] and vertical zone refining [10] techniques and travelling heater method [11]. Importantly, CdTe thin films can be prepared by a variety of techniques, such as physical vapour deposition [12,13], electrodeposition [14,15], close-space sublimation [16,17], screen printing [18,19], molecular beam epitaxy [20] etc.

3.3.1.1 Structural Properties.

The cubic zinc blende structure is the stable form for bulk single crystals of CdTe at atmospheric pressure. In this structure each atom is tetrahedrally coordinated with four nearest neighbors of the other element. Fig.3.2 shows a model of the zinc blende structure. The vertical direction in the figure is parallel to a $[111]$ axis. There are two types of $\{111\}$ planes that alternate with each other, one consisting entirely of atoms of one element and the other consisting entirely of atoms of the other element, while the $\{110\}$ planes contain equal numbers of the two kinds of atoms. Thus one surface of a $\{111\}$ -oriented sample of CdTe will be composed entirely of Cd atoms, (conventionally referred to as the $\{111\}$ A face) and the other of Te atoms (referred to as the $\{\bar{1}\bar{1}\bar{1}\}$ B face).

The currently best value of the cubic lattice parameter at room temperature is 6.481\AA [21] although this value is subject to change due to deviations from stoichiometry. Medvedev et al. [22] obtained a value of 6.482\AA ($\pm 0.001 \text{\AA}$) for crystals grown from stoichiometric melts. However the lattice constants of crystals grown from Cd-rich and Te-rich solutions are 6.480\AA and 6.488\AA respectively. Although the zinc blende structure is the stable form for bulk CdTe at atmospheric

pressure, thin films in both the sphalerite and wurtzite form are common. The presence of the wurtzite form is not surprising since the two crystal systems are closely related and differ only by a lateral displacement of every third pair of {111} plane. Bulk single crystals of the other II-VI compounds are also found in both forms. Some crystal parameters of zinc blende CdTe are tabulated in Table 3.1.

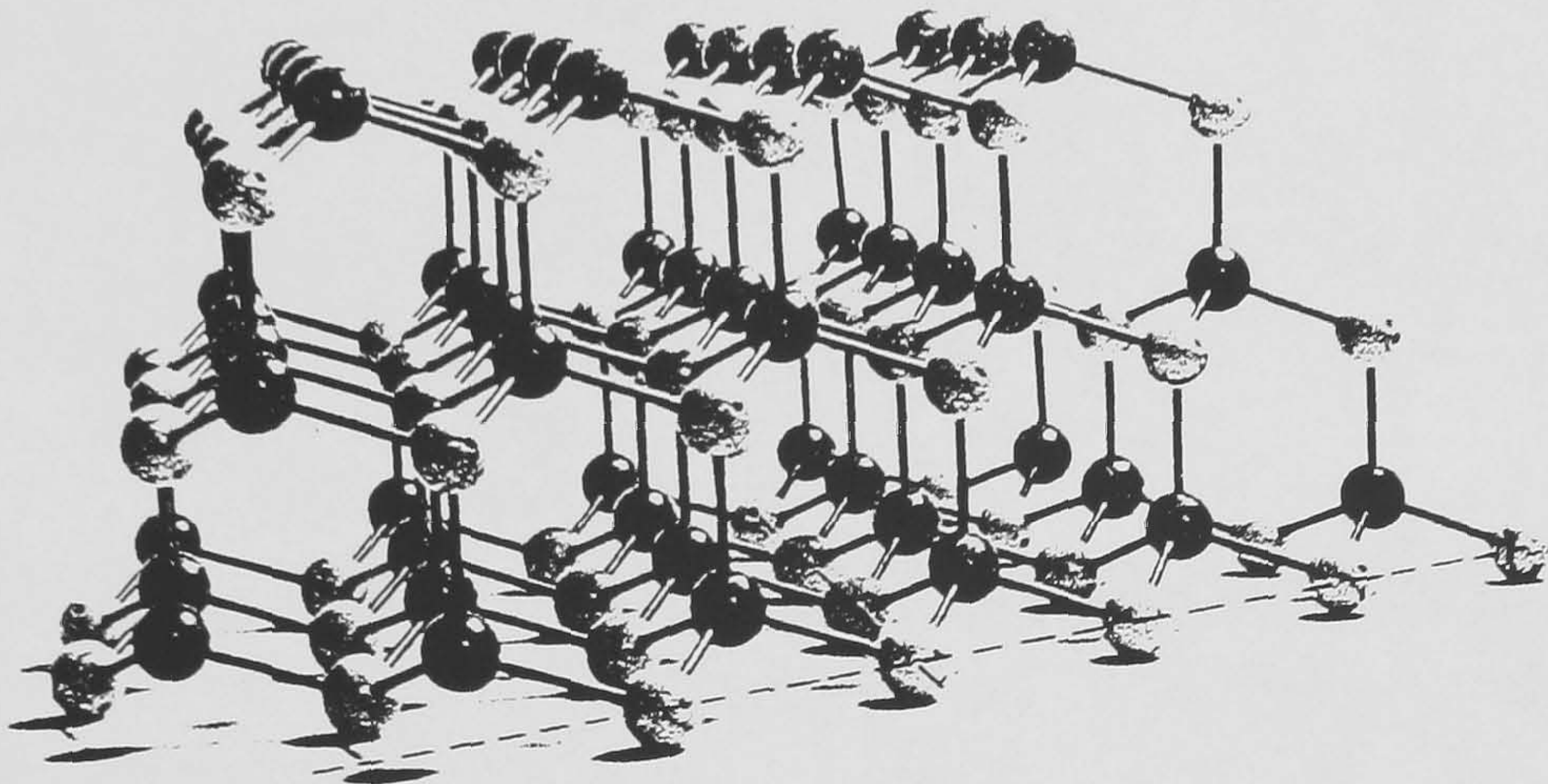


Figure 3.2 — Crystal Structure of CdTe.

Crystal Structure	ZB, WZ
Molecular Weight(g)	240.0
Molecules Per Unit Cell	4
Lattice Constant(Å)	6.481
Molar Volume (cm ³)	40.99
Melting Point(°C)	1092
P [†] _{min} (atm)	0.23

Table 3.1 — Structural Properties of zincblende-CdTe at 300K, [†] at melting point, ZB: Zincblende, WZ: Wurtzite.

3.3.1.2 Electrical Properties.

CdTe is one of the few II-VI compounds that exhibits both p-type and n-type bulk conductivity at relatively high levels of concentration. Its electrical properties are strongly affected by native defects, and in particular by a very high degree of self-compensation [23]. Doping of bulk single crystal CdTe is well developed, although the mechanisms for incorporation remain somewhat controversial. Discussions of doping in CdTe are given by Zanio [24], Kroger [25], and Strauss [26]. Growth under excess Te (at low Cd pressure) gives hole densities up to about 10^{16}cm^{-3} through the formation of acceptor-like Cd vacancies and/or Te interstitials. Conversely, growth under high Cd pressure produces either insulating crystals, or n-type material with donor densities up to about 10^{17}cm^{-3} , due to Cd interstitials or Te vacancies [27].

The group V elements P, As, and Sb are acceptor-like dopants and presumably substitute for Te. Gu et al. [28] have reported the growth from the melt of P-doped bulk crystals with hole concentrations of 5×10^{16} to $6 \times 10^{17}\text{cm}^{-3}$, mobilities of 24 to $39\text{ cm}^2\text{V}^{-1}\text{s}^{-1}$ and ionization energies between 36 and 60 meV at room temperature. The group IB elements such as Cu, Ag, Au, Na and Li can also provide acceptors, presumably substituting for Cd, with ionization energies reported in the range from 0.3 to 0.4 eV. Li can be introduced either during crystal growth or by subsequent diffusion, giving significantly higher carrier densities, up to 10^{19}cm^{-3} [29,30]. Popova and Polivka [31] have obtained p-type CdTe with hole concentrations (at 300K) as high as $1 \times 10^{18}\text{cm}^{-3}$ and resistivities as low as $0.01\ \Omega\text{-cm}$, among the highest so far reported for p-type CdTe, by means of Cu diffusion. The hole density is limited by self-compensation [32,33] and the electrical activity of the dopant depends on the microstoichiometry.

Two types of donor impurities have been identified in CdTe; the Group III elements Al, Ga, and In which presumably substitute for Cd, and the Group VII halogens Cl, Br, and I, which probably substitute for Te. The highest carrier concentration at room temperature that can be obtained by doping with Ga is about $4 \times 10^{17}\text{cm}^{-3}$ while concentrations of about $2 \times 10^{18}\text{cm}^{-3}$ can be obtained with the other elements. However, the problems of doping CdTe polycrystalline thin films are more severe and adequate control is often difficult to achieve. This is

because the oppositely charged grain boundary states effectively compensate the dopant. The effective carrier density is substantially reduced by the presence of the grain boundary depletion regions and the mobility is strongly reduced by the grain boundary barriers. CdTe thin films can be doped n-type using In, during growth or subsequently by diffusion, with carrier densities of $2 \times 10^{17} \text{cm}^{-3}$ for epitaxial growth on BaF_2 and $5 \times 10^{15} \text{cm}^{-3}$ for polycrystalline films grown on Corning 7059 glass [34].

Attempts at doping CdTe thin films p-type during growth have been less successful. Anthony et al. [35] obtained p-type films with $N_A \cong 10^{15} - 10^{16} \text{cm}^{-3}$ without extrinsic doping by control of substrate temperature for close-space vapour transport (CSVV) growth. Chu et al. [36] reported that the introduction of P and As during CVD, gave a p-type resistivity of $200 \Omega\text{-cm}$ with carrier densities of about 10^{16}cm^{-3} , but depended on close control of CdTe stoichiometry. Anthony et al. [37] found no transport of As, Cu, or Na by hot wall vacuum evaporation (HWVE). Introduction of Sb during growth yielded either no change in carrier density, or at high Sb pressures, an abrupt change to high conductivity material, suggesting metallic Sb precipitation. Photo-assisted molecular beam epitaxy (PAMBE), developed by R.N.Bicknell [38,39] was used to obtain Sb and As doped p-type CdTe epilayers on $\{100\}$ -oriented bulk single crystal CdTe substrates with hole concentrations of $2.8 \times 10^{18} \text{cm}^{-3}$ and $6 \times 10^{18} \text{cm}^{-3}$, while the hole mobilities were 81 and $65\text{--}74 \text{cm}^2 \text{V}^{-1} \text{s}^{-1}$ at room temperature respectively. They also obtained In doped n-type CdTe epilayers grown at a substrate temperature 230°C , with room temperature carrier concentrations of $2 \times 10^{16} - 6 \times 10^{17} \text{cm}^{-3}$, and electron mobilities ranging from $450\text{--}800 \text{cm}^2 \text{V}^{-1} \text{s}^{-1}$.

More recently, due to difficulties in extrinsic p-type doping of polycrystalline CdTe films with common dopants, CdCl_2 was introduced to improve the quality of the films both structurally and opto-electronically. Heat treatment of as-grown layers in an oxygen containing atmosphere at about 400°C causes type-conversion in such films (i.e. n-type \rightarrow p-type with or without CdCl_2 , known as type-conversion/junction formation process [40]). CdCl_2 , on the other hand, improves grain size and conductivity. As-grown CdTe thin films exhibit in general very high resistivity (i.e. $\sim 10^8 \Omega\text{-cm}$).

3.3.1.3 Optical Properties.

The electronic band structure of CdTe (using a pseudopotential technique) showed the absolute extrema of the valence and conduction bands to occur at $k=0$, classifying CdTe as a direct gap material. The optical bandgap is 1.606 eV at liquid helium temperatures, and the spin-orbit splitting between the valence bands at γ is 0.91 eV. The second lowest conduction band edge is located at the L-point, 1.35 eV above the lowest. The reflectance measurements of Thomas [41] and of Marple [42] showed that as the temperature was increased from liquid helium temperature the bandgap decreased very slowly up to about 20K, then began to decrease more rapidly, and between 80 and 150K decreased linearly, at a rate of $-3.5 \times 10^{-4} \text{ eVK}^{-1}$. Extrapolation to 300 K gave a bandgap energy equal to 1.520 eV, in good agreement with the value of 1.529 eV obtained by Camassel [43] by extrapolation of their piezoreflectance results for the interval between 77 and 145 K. The absorption edge obtained by Marple [44] at several temperatures for bulk single crystal CdTe showed that mechanical damage significantly increased the lower absorption coefficients and led to a marked curvature of the absorption edge. This effect probably in fact explained why early workers interpreted their data as evidence for an indirect energy gap in CdTe.

Data of Deutsch [45] for the absorption coefficient of CdTe as a function of reduced frequency, defined as the ratio of photon frequency to the longitudinal optical phonon frequency, which is 168 cm^{-1} for CdTe, showed that the absorption coefficient is 10^{-2} cm^{-1} at about $21 \mu\text{m}$ which is due probably to interactions with the lattice phonons. However, the absorption coefficient rises sharply to $\sim 10^4 \text{ cm}^{-1}$ at the optical band edge ($\lambda \cong 0.82 \mu\text{m}$).

For photon energies between the optical absorption edge and the onset of lattice phonon absorption, (i.e. corresponding to wavelengths between about 0.9 and $30 \mu\text{m}$) the optical absorption of CdTe results primarily from the interaction between photons and various types of defects, if free carriers are regarded as electronic defects. For a given carrier concentration, the absorption coefficient exhibits the λ^m dependence characteristic of intraband free-carrier absorption, with value of m ranging from 2.7 to 3.4 rather than the classical "Drude square law" dependence.

Optical constants, n and k of thin polycrystalline CdTe films have been determined by Thutupalli and Tomlin [46] over the wavelength range 0.3 to $3.0\mu\text{m}$ from normal-incidence reflectance and transmittance spectrum. Analysis of the absorption spectrum revealed that CdTe films possess a direct bandgap of 1.50 eV and exhibit a spin-orbit splitting of the valence band of 0.88 eV. An indirect bandgap of 1.82 eV is also observed. The temperature dependence of the bandgap energy was analysed using the Kramers-Kronig technique by D.Poelman et al. [47]. The bandgap energy was determined as the position of the maximum derivative of the extinction coefficient. The resulting thin film bandgap was;

$$E_g(\text{eV}) = 1.626 - 3.25 \times 10^{-4}T \quad (T \text{ in } K) \quad [3.5]$$

and valid between 123–623K. This gives a value of $E_g=1.5285$ eV at 300K.

3.3.2 Physical Properties of CdS.

CdS is one of the most extensively investigated semiconductor materials with a variety of potential uses in producing optical electronic devices, such as detectors and images. Bulk single crystal growth techniques include growth from vapour and melt [48], Bridgmann [49], and iodine vapour transport [50]. CdS thin films have been prepared by a variety of techniques including physical vapour deposition [51,52], close-space sublimation [53,54], spray pyrolysis [55,56], chemical vapour deposition [57], anodization [58], molecular beam epitaxy [59] etc.

3.3.2.1 Structural Properties.

CdS is a binary compound which crystallizes in two allotropic forms with the wurtzite and zincblende structures. The wurtzite and zincblende structures are both characterised by tetrahedral lattice sites, and as a consequence their nearest-neighbor environment is identical. It is generally believed that CdS dissociates completely on heating according to: $\text{CdS} \rightarrow \text{Cd} + \frac{1}{2}\text{S}_2$, with some higher aggregates of S, and that no CdS molecules exist in the vapour. However, Caveney [60] has reported that a recognizable proportion of the vapour is in the form of CdS molecules. CdS thin films, grown by physical vapour deposition at substrate and source temperatures of 200 to 250°C and 800– 1050°C respectively exhibit the wurtzite crystal structure and usually in a strongly preferred orientation with the

{0002} plane parallel to the substrate (i.e. the c-axis approximately perpendicular to the substrate [61]). In fact, Hall [62] has pointed out that as-deposited CdS films normally have a c-axis that is tilted about 19° normal to the substrate. Epitaxial growth of thin film CdS has been observed on GaAs, CdTe, Ge, and InP substrates. Epi-layers of hexagonal CdS have been deposited by VPE [63] on {111}, {110} and {100} faces of InP. Solution grown CdS layers can be obtained in different structures [64] depending on the deposition conditions with grain sizes up to $0.1\mu\text{m}$.

3.3.2.2 Electrical Properties.

CdS can only be made n-type, any attempt to incorporate acceptor impurities, such as Cu and Ag results in self-compensation by non-metal vacancies. Thus n-type CdS is readily formed by growth under non-stoichiometric conditions in an excess pressure of Cd vapour (Cd-rich); such bulk crystals may be regarded as self-doped. In fact, of course, the non-stoichiometry can be changed by heating in Cd- or S-vapour, although heating in S-vapour does not produce p-type conductivity. Substituting Cl, Br, or I for S, and Al, Ga, or In for Cd creates shallow donor levels in the range of 0.03 eV from conduction band. However Cu and Ag produce acceptor levels, 0.6–1.0 eV above the valence band [65]. The alkali metals Na, K, and Li are also acceptor type impurities resulting in shallow levels. The room temperature electron and hole mobilities are about 300 and $10\text{ cm}^2\text{V}^{-1}\text{s}^{-1}$ respectively in good quality bulk single crystals.

Depending on the method and growth conditions, the electrical properties of CdS films vary over a wide range. CdS films grown by vacuum evaporation usually have resistivities and carrier concentrations in the range of $1\text{--}10^3$ and $10^{16}\text{--}10^{18}\text{cm}^{-3}$ [66,67] respectively. The films are always n-type and the conductivity is dominated by the deviation from stoichiometry (i.e. Cd:S ratio) which implies the films grow with S vacancies or excess Cd. In thin films resistivity values as low as $10^{-3}\Omega\text{-cm}$ and mobility of $90\text{ cm}^2\text{V}^{-1}\text{s}^{-1}$ have been obtained on In-doped (1.5%) layers. Several workers [68,69] have studied the transport mechanism in evaporated films. Deppe and Kassing [70] have suggested that the electrical properties are dependent on dominant deep impurity level caused by S-vacancies. At low concentrations ($<10^{17}\text{cm}^{-3}$) a discrete level equal to 0.6 eV has been obtained.

As-evaporated CdS films are not photo-sensitive. However, Cu-diffused CdS films exhibit significant amounts of photoconductivity. Undoped, epitaxial CdS films grown by MBE [59] exhibit a resistivity of $10^5 \Omega\text{-cm}$. CVD grown epitaxial films exhibit as-deposited resistivities between 10-100 $\Omega\text{-cm}$ [57]. Annealing in H_2/Ar at 400°C reduces the resistivity to values between 0.01 and 0.05 $\Omega\text{-cm}$.

3.3.2.3 Optical Properties.

The maximum of the valence band and the minimum of the conduction band are situated at the centre of the Brillouin zone, $k=0$ making CdS a direct gap semiconductor. The lowest conduction band is associated with the Cd 5s levels and the highest valence band with the S 3p levels [71]. The optical properties of CdS films are determined to a large extent by their microstructure, hence, by the deposition conditions. Thin evaporated CdS films are smooth and specularly reflecting. Khwaja and Tomlin [72] have determined the optical constants n and k of evaporated films over the wavelength range of 0.25 to $2.0\mu\text{m}$ by reflectance and transmittance taking into account the surface roughness. Their analysis yielded direct transitions in the range of 2.42 to 2.82 eV and combined direct and indirect transitions beyond 2.82 eV. The n and k values are observed to be dependent on the substrate temperature.

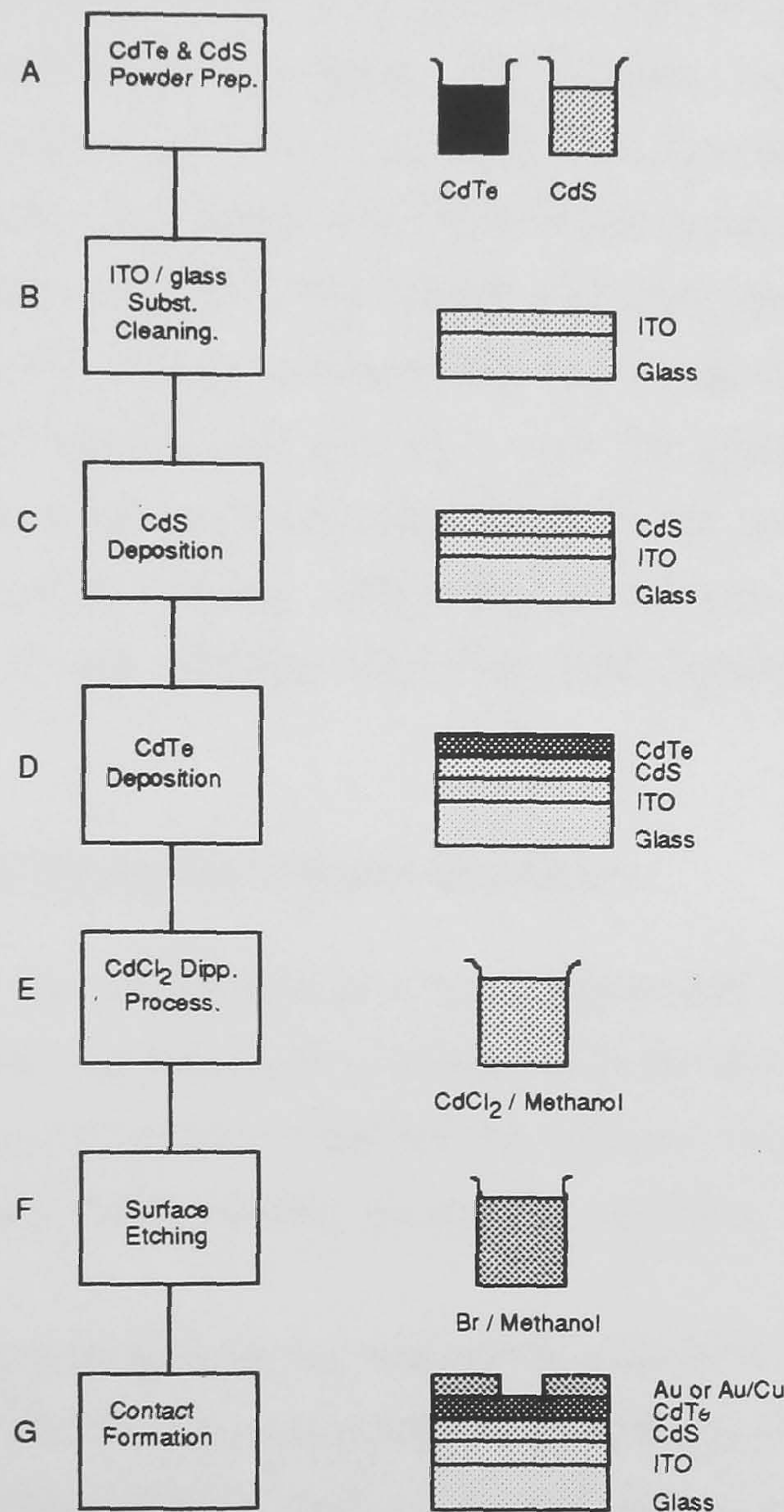
3.4 Fabrication of p-CdTe/n-CdS Solar Cells.

In this work, the n-CdS/p-CdTe solar cells were prepared by vacuum deposition. The cell production procedure can be given as;

- 1- ITO-coated glass substrates were first cleaned following the chemical procedure given in section 3.4.2.
- 2- $0.5\text{--}0.75\mu\text{m}$ thick CdS was evaporated onto the ITO-coated glass substrate followed by CdTe deposition.
- 3- The glass/ITO/CdS/CdTe structure was either first dipped into $\text{CdCl}_2/\text{Methanol}$ solution (i.e. dipping into 1% $\text{CdCl}_2/\text{Methanol}$ solution for about 1-2 sec and then drying in N_2 flow) followed by heat treatment in air at 400°C for about 30 min resulting in grain growth and increase in the conductivity of the CdTe layer or given only the heat treatment.
- 4- The structure (i.e. CdTe surface side) was first etched with 0.1-0.2% Br-Methanol

solution to leave a Te or at least Te-rich surface and significantly lowering the resistivity of a thin layer adjacent to the surface of the CdTe, then a thin layer of Au was deposited by evaporation.

5- Finally the device was annealed in N₂ at 300°C for about 15 min to improve the contact formation. Detailed information about the cleaning the substrate surfaces, thin film deposition, contact formation and the flow chart for the production of p-CdTe/n-CdS solar cells is shown in Fig.3.3.



A- Powder Preparation: - CdTe was grown in house by direct combination of Cd and Te, and crushed in pestle and mortar (NB: pre-doped CdTe material was prepared using CdCl₂, Cd, Te or CdCl₂ and CdTe), and CdS was supplied by Johnson Matthey Ltd, B- ITO /glass substrate cleaning (by chemical etching), C- CdS deposition by PVD, D- CdTe deposition by PVD, E- CdCl₂-dipping followed by heat treatment (NB: this step was omitted if CdTe layers were initially doped either during the deposition of CdTe or by pre-doping) F- Surface etching prior to contact formation, G- Metallic contact deposition, Au or Au /Cu.

Figure 3.3 — The flow chart for the production of n-CdS/p-CdTe Solar Cells.

3.4.1 Preparation of Starting Materials.

The CdTe starting material used in this work was synthesised in house by direct combination of high purity double zone refined Cd and Te (99.9999%) supplied by M.C.P. Electronic Materials Ltd. A charge of about 450g of Cd and Te in stoichiometric proportions was loaded into a cleaned silica tube sealed at one end. The tube was evacuated to a pressure of 10^{-5} torr and left to outgas for about 12 hours. The tube was then sealed using an oxy-acetylene gas torch and placed into a horizontal high temperature furnace. The furnace temperature was increased steadily to 940°C over a period of an hour and thereafter maintained at that temperature for 3 days. The charge was then cooled down slowly over several hours. This produced a solid lump of CdTe which was then crushed in a marble pestle and mortar to form the source material for the preparation of CdTe thin films. Cl₂ doped CdTe starting material was also made by synthesis of CdTe and CdCl₂ compounds using the same procedure described above, but using different furnace temperatures and synthesis times. CdS starting material supplied by "Specpure", Johnson Matthey Ltd was used for thin film CdS deposition onto glass and ITO coated glass.

3.4.2 Cleaning of Glass Substrate Surfaces.

The cleaning of the substrates is a very important, but also a very difficult and delicate operation. In this work, plain glass (used for individual layer studies) and ITO-coated glass substrates supplied by Chance Propper Ltd and Hoya Inc. respectively were used. The cleaning procedure used for the plain glass substrates was as follows;

- 1- The glass substrates were first pre-washed in a solution of 5% Decon 90 (surfactant) in deionised water at room temperature to dislodge the gross contamination.
- 2- Refluxing in Trichloroethylene and iso-propyl alcohol for about 4 hours each in order to remove the grease and other organic contamination.
- 3- Washing in hot solution of 5% Decon 90-deionised water solution.
- 4- Washing in warm solution of 0.1 Mol Nitric acid to leach out alkali metals (i.e. Na, Ag etc.).
- 5- Ultrasonic bath in iso-propyl alcohol and deionised water about 15 min to rinse the layer.

6- Second rinse in deionised water. The glass substrates were rinsed in deionised water following each step. ITO-coated glass substrates were cleaned by the procedure given above, but only following the steps 1, 5 and 6.

3.4.3 n-CdS/or p-CdTe Thin Film Deposition.

Two oil diffusion pumped high vacuum systems were used for the deposition of CdTe and CdS thin films. The lowest obtainable pressure with these system using a liquid nitrogen cold trap were around 4×10^{-5} and 5×10^{-6} torr respectively. The schematic diagram of the chamber fixtures is shown in Fig.3.4.

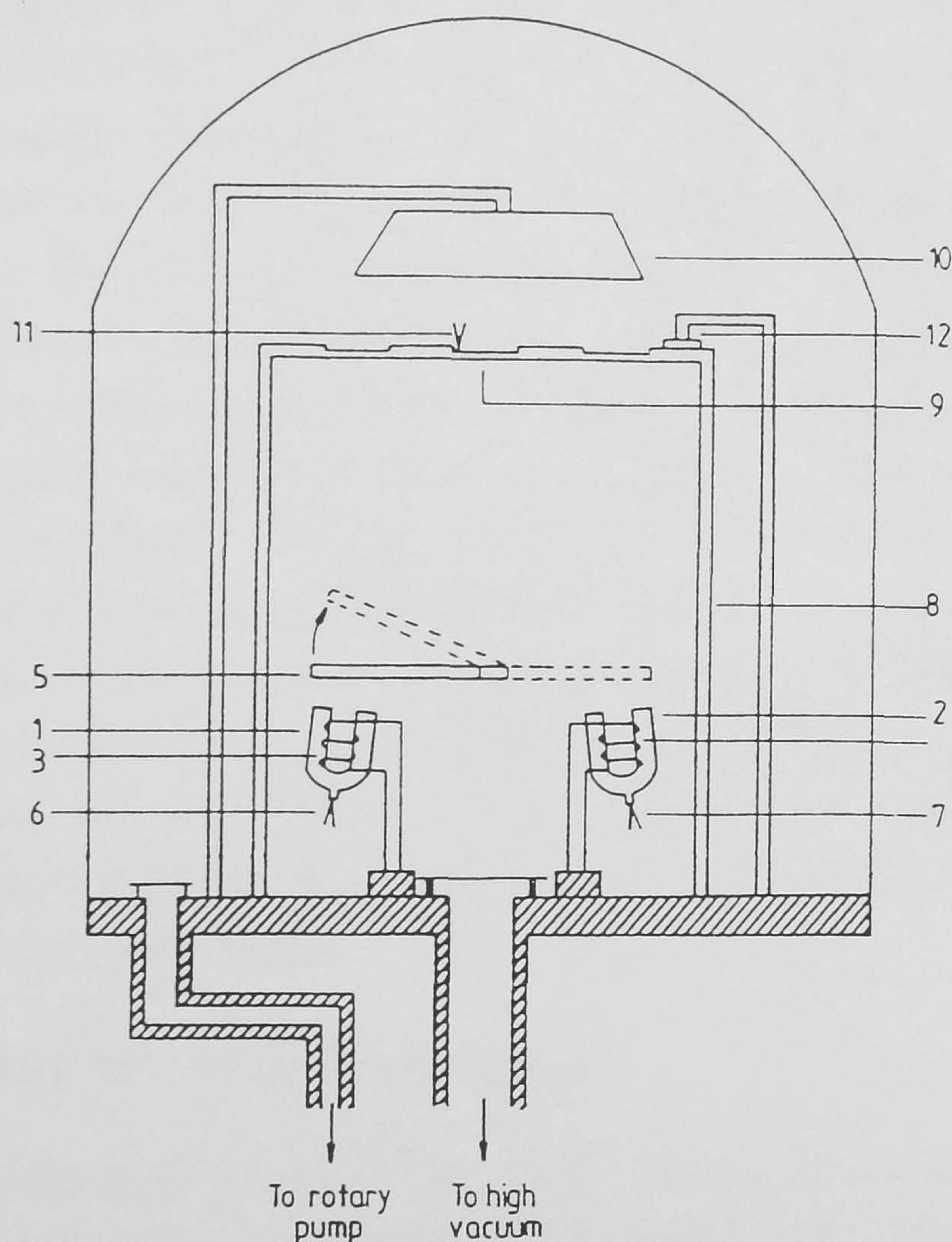


Figure 3.4 — The schematic diagram of the chamber fixtures;

1-Source (CdTe) crucible, 2-Dopant crucible (Sb, CdCl₂), 3-Source filament, 4-Dopant filament, 5-Shutter, 6-Source thermocouple, 7-Dopant thermocouple, 8-Heated chimney, 9-Substrate, 10-Substrate heater, 11-Substrate thermocouple, 12-Thickness monitor head.

A silica glass crucible wound with tungsten wire was used as an evaporator cell for both sources and dopants. The temperatures of the source and dopant were measured with Pt/Pt-13%Rh thermocouples placed in a recess in the bottom of the crucible, and controlled by Eurotherm programmable temperature controllers (Type:818). The substrates were heated from the rear by a 750W quartz-halogen lamp while the substrate temperature was measured by a Pt/Pt-13%Rh thermocouple and was also automatically controlled using a Eurotherm programmable temperature controller. The volume between the source and substrate was surrounded by a stainless steel cylindrical tube and a hot-wall chimney 15 cm long in order to minimize the radiation losses and prevent contamination on the lamp. A shutter was placed over the evaporation cells to start and stop the evaporation. After charging the source and the dopant, a piece of silica-wool was inserted into the source crucible to prevent the “spitting” of the charge onto the substrates, at high evaporation rates. Glass substrates cleaned as described in section 3.4.2 were dried in a flow of N_2 and inserted into the substrate holder together with the mask. The substrate thermocouple was placed on top of the glass substrate. After the system was pumped down, the source, dopant, hot-wall chimney and substrate were heated up to their characteristic temperatures. When steady evaporation conditions were achieved, the shutter was opened to start the evaporation. The schematic temperature versus time characteristics of the growth process is shown in the Fig.3.5. When the required thickness had been deposited, the deposition was stopped by closing the shutter, following which, the source and substrate temperatures were gradually reduced to room temperature. Usually the cycle took about 40 minutes for CdTe and an hour for CdS to grow approximate thicknesses of $2\mu\text{m}$ and $0.6\mu\text{m}$ respectively.

3.4.4 Metallic (Au or In) Evaporation.

The evaporation of Au (or In) for ohmic contact formation to CdTe(or CdS) was made in dedicated high vacuum evaporator systems. The device was placed on a mask which was mounted on the substrate plate above the source. A piece of Au or In was cut and put on a molybdenum boat. The source temperature was gradually increased keeping the shutter closed. When steady state conditions were attained, the mechanical shutter was opened to expose the substrates to the Au or In vapour. When deposition was completed (typically 30 – 40 min) the shutter

was closed and the source heating switched off. Finally, substrates were allowed to cool down to room temperature before being removed from the vacuum system for the characterisation and/or further processing.

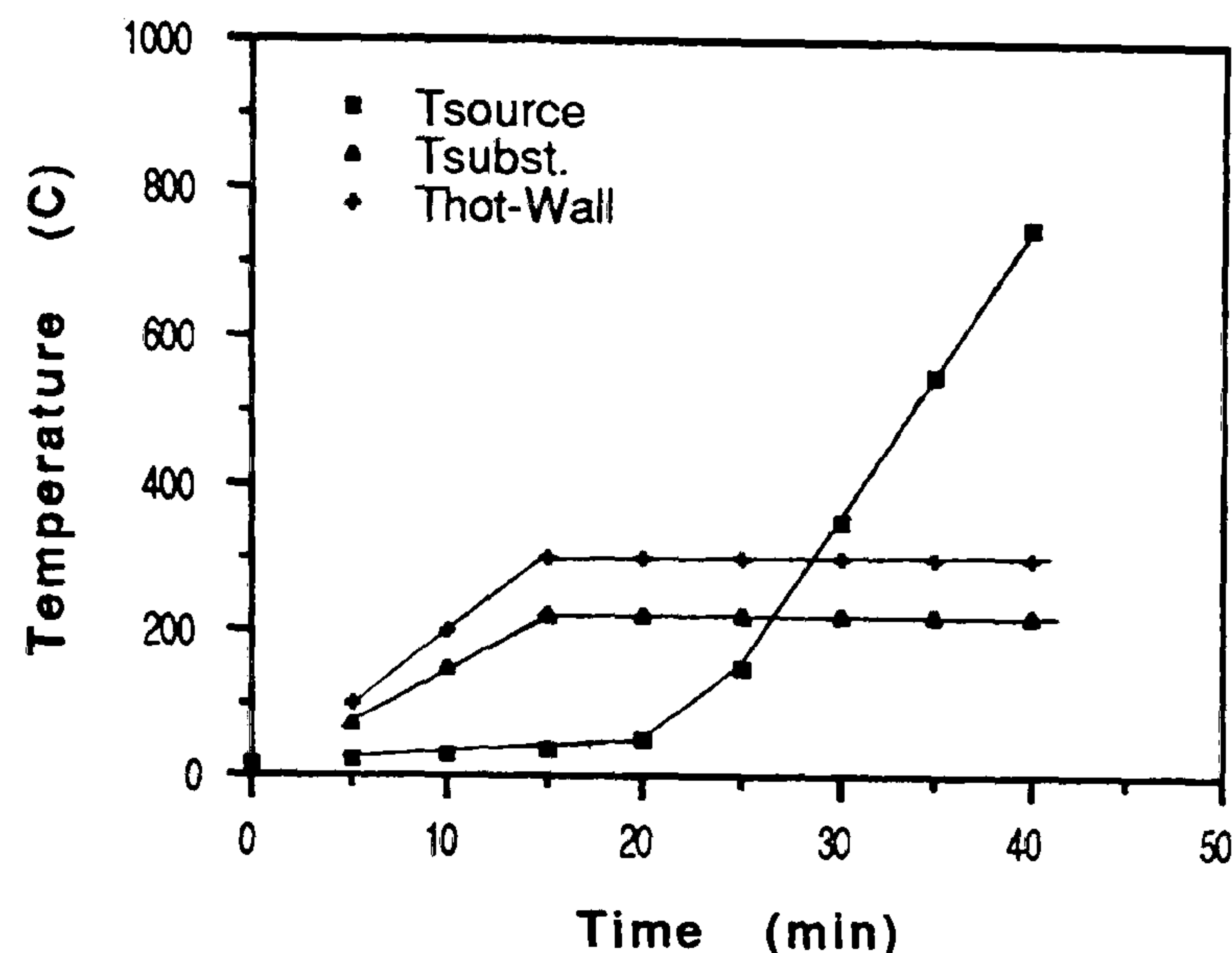


Figure 3.5 — Typical CdTe thin film growth characteristic.

3.5 Fabrication of CdS/CdTe Bulk Single Crystal Cells.

3.5.1 CdTe Crystal Growth.

Bulk single crystal CdTe crystal substrates used in the present study were grown in-house by a vapour phase technique originally developed by Clark and Woods [73] for CdS and adapted for CdTe. A specially designed growth tube was used to grow the crystals. The tube consisted of a silica-capsule in which was fitted a conical growth tip. A small bore tube formed a tail which provided some control of the constituent partial pressures during growth.

A measured quantity of synthesised polycrystalline charge of the CdTe prepared as described in section 3.4.1 was loaded into the growth capsule and an appropriate amount of Te was placed in the tail to enhance the growth [74]. The tube was then evacuated to a pressure of 10^{-6} mbar and allowed to outgas for a

day before it was sealed. The sealed tube was suspended vertically in a double zone furnace. Initially the tube was placed in the furnace with the growth tip at the highest temperature, to sublime any CdTe debris away from the growth tip before growth began. The tube was then pulled through the furnace at a rate of ~ 15 mm per day, until a temperature gradient of $\sim 50^\circ\text{C}$ was established between the charge and the growth tip. The pulling was then stopped and the tube allowed to remain in this position for a week. Finally, the temperature of the main furnace was gradually reduced to room temperature over 3 days. The reservoir furnace, which was independently controlled was switched off when the temperature of the main furnace had fallen to that of the reservoir. With this technique, CdTe boules up to 29 mm in diameter and 5 cm in length could be grown from a charge of 150g.

3.5.2 Sample Orientation and Preparation.

The most efficient n-CdS/p-CdTe solar cells were the ones deposited either onto {111} or {221} surfaces of CdTe [75,76]. CdTe crystals were therefore oriented parallel to the {111} direction using the Laue x-ray method, and cut into 1.8–1.2 mm thick wafers using a diamond saw. The slices were further cut into small dice with dimensions of $5 \times 5 \text{ mm}^2$. The cutting process from the bulk crystals left saw damage on the free surface which needed to be removed by polishing (i.e. subsequent mechanical and chemical treatments). The dice were first subjected to an intensive bath in acetone in order to remove grease and traces of glue resulting from the sawing process. Mechanically, the dice were polished with α -alumina powder in a decreasing sequence of particle sizes, starting with 600 grit and ending with $0.05 \mu\text{m}$ particle size in 4–5 steps. This process leaves a specular surface finish.

The CdTe dice were then mounted using wax onto the end of a PTFE shaft, which in turn was mounted (sliding fit) in a cylindrical housing. Excess wax was wiped off the upper surface and edges using hot trichloroethene. A PTFE-fibre glass pad was placed in the bottom of a circular dish containing 2% Br-Methanol solution and the CdTe polished 3 min. The method is close to a contactless polish, since the arrangement traps a very thin layer of Br-Methanol solution between the substrate and the pad. Finally the dice were given a complete methanol wash and dried in N_2 . To release the dice from the shaft, they were submerged in hot trichloroethene to dissolve the wax. Acetone was then used to dissolve traces of

the trichloroethene from the dice, this was followed by methanol to remove the acetone. The acetone-methanol wash sequence was repeated three times followed by a final dry with N₂. Mirror-like surfaces were obtained using this method.

Cu and P were used as the injecting contact dopant in attempts to obtain ohmic contacts to the CdTe substrates. A thin layer of the contact dopant was deposited onto the pad polished surface of the dice, which was then heated (200–300°C) in a N₂-atmosphere to diffuse in the Cu or P and create a p⁺ layer at the back surface. Finally Au was deposited on the p⁺ layer.

The back contact surface of the cell was coated with lacomit varnish and the other CdTe surface was pad-polished using 2% Br-Methanol solution in the same way in order to produce a fresh CdTe surface. Substrates were then loaded into the CdS evaporation system, and a thin layer of CdS (<1μm) deposited as outlined in section 3.4.3. Finally an In metallic layer was deposited on the CdS in two steps; firstly an ultra thin In layer was evaporated onto as-grown CdS, followed by a small and thicker spot contact, where the former serves as a charge collector and the later serves as the contact pad to the cell. After deposition of the In contact, the cell was coated (on both front and back surfaces) with lacomit varnish and immersed in HCl to remove any CdS or In deposits from the sides of the device in order to prevent shunt leakage current paths. After the lacomit was removed from the surfaces, the dice was mounted using Ag-paste onto a Cu plate which had been etched in dilute HCl, and dried with N₂ flow, for easy of handling.

3.6 References.

1. F.V.Shallcross, RCA Rev., **27** (1967) 572.
2. D.A.Cusano, "*Physics and Chemistry of II-VI Compounds*", eds. M.Aven and J.S.Prener, North-Holland, Amsterdam (1967) 706.
3. H.Hartmann, J.Crystal.Growth, **31** (1975) 323.
4. J.B.Mullin, S.J.C.Irvine and P.J.Ashen, J.Cryst.Growth, **55** (1981) 92.
5. L.I.Maissel, in L.I.Maissel, R.Glang, (Eds.), "*Handbook of Thin Film Technology*", McGraw-Hill, New York (1970), chap.1.

6. P.Rappaport, RCA Rev., **20** (1959) 373.
7. J.J.Loferski, J.Appl.Phys., **27** (1956) 777.
8. K.W.Mitchell, A.L.Fahrenbruch, R.H.Bube, J.Appl.Phys., **48** (1977) 829.
9. N.R.Kyle, J.Electrochem.Soc., **118** (1971) 1791.
10. M.R.Lorenz, R.E.Halsted, J.Electrochem.Soc., **110** (1963) 343.
11. R.Triboulet, Y.Marfing, A.Cornet and P.Siffert, J.Apply.Phys. **45** (1974) 2759.
12. P.Sharps, A.L.Fahrenbruch, A.Lopez-Otero, M.Schofthaler, and R.H.Bube, Proc. of 21st IEEE Photovoltaic Specialists Conf., (1990) 493.
13. R.W.Birkmire, B.E.McCandless and S.S.Hegedus, Int. J. Solar Energy, **12** (1992) 145.
14. B.M.Basol, Solar Cells, **23** (1988) 115.
15. P.V.Meyers and C.H.Liu, Proc. 8th Photovoltaic Solar Energy Conf. (1988) 1588.
16. Y.S.Tyan and E.A.Perez-Albuerne, 16th Photovoltaic Specialist Conference (1982) 794.
17. K.W.Mitchell et al., Solar Cells, **23** (1988) 49.
18. S.Ikegami, Solar Cells, **23** (1988) 89.
19. I.Clemminck, M.Bulgelman, M.Casteleyn and B.Depuydt, Int.J. Solar Energy, **12** (1992) 67.
20. A.Rohatgi, S.A.Ringel, R.Sudharsanan and H.C.Chou, 22th Photovoltaic Specialists Conference (1991) 962.
21. M.G.Williams, R.D.Tomlinson and M.J.Hampshire, Solid State Commun., **7** (1969) 1831.

22. S.A.Medvedev, Yu.V.Klevkov, K.V.Kiselevo and N.N. Sentyurina, *Izv. Akad. Nauk SSSR Neorg Mater.*, **8** (1972) 1210, (Engl. Transl., *Inorg. Mater.*, **8** (1964)).
23. Y.Marfaing, *Prog. Crystal Growth Charact.*, **4** 317 (1981).
24. K. Zanio, in R. K. Willardson and A.C. Beer (eds.), *"Semiconductor and Semimetals"*, Vol.13, Academic Press, New York (1978), Chap.3.
25. F.A.Kroger, *Rev.Phys.Appl.*, **12** (1977) 205.
26. A.J.Strauss, *Rev.Phys.Appl.*, **12** (1977) 167.
27. K. Zanio, in R. K. Willardson and A.C. Beer (eds.), *"Semiconductor and Semimetals"*, Vol.13, Academic Press, New York (1978), p.129.
28. J.Gu, T.Kitahara, K.Kawakami and T.Sakaguchi, *J.Appl.Phys.*, **46** (1975) 1184.
29. B.L.Crowder and W.N.Hammer, *Phys.Rev.*, **150** (1966) 541.
30. C.T.Lee and R.H.Bube, *J.Appl.Phys.*, **54** (1983) 7041 and **58** (1985) 880.
31. M.Popova and P.Polivka., *Czech.J.Phys.*, **B23** (1973) 110.
32. C.Canali, G.Ottaviani, R.O.Bell and F.V.Wald, *J. Phys. Chem. Solids.*, **35** (1974) 1405.
33. F.A.Selim and F.A.Kroger, *J.Electrochem.Soc.*, **124** (1977) 401.
34. W.Huber, A.L.Fahrenbruch, C.Fortmann and R.H.Bube, *J.Appl.Phys.*, **54** (1983) 4038.
35. T.C.Anthony, A.L.Fahrenbruch, M.G.Peters and R.H.Bube, *J.Appl.Phys.*, **57** (1985) 400.
36. T.L.Chu, S.S.Chu, F.Firszt, H.A.Naseem and R.Stawski, *J.Appl.Phys.*, **58** (1985) 1349.
37. T.Anthony, C.Fortmann, W.Huber, R.H.Bube and A.L.Hahrenbruch, *Proc. 17th IEEE Photovoltaic Specialists Conf., Kissimmee, FL*, (1984) 827.

38. R.N.Bicknell, N.C.Giles and J.F.Schetzina, J.Vac.Sci.Technol., **B5** (3) (1987) 701.
39. R.N.Bicknell, N.C.Giles and J.F.Schetzina, J.Vac.Sci.Technol., **A5** (5) (1987) 3059.
40. B.M.Basol, Int.J.Solar Energy, **12** (1992) 25.
41. D.G.Thomas, J.Appl.Phys., **32** (Supp.) (1961) 2298.
42. B.Segal, Phys.Rev, **150** (1966) 734.
43. J.Camassel, D.Auvergne, H.Mathieu, R.Triboulet and Y.Marfing., Solid State Commun., **13** 63 (1973).
44. D.T.F. Marple, Phys.Rev., **150** (1966) 728.
45. T.F.Deutsch., J.Phys.Chem.Solids, **34** (1973) 2091.
46. G.K.M. Thutupalli, S.G. Tomlin, J.Phys. D:Appl Phys., **9** 128 (1976).
47. D.Poelman and J.Vennick, J.Phys.D:Appl.Phys., **21** (1988) 1004.
48. W.E.Mechalf and R.H.Fahring., J.Electrochem.Soc., **105** (1958) 719.
49. A.G.Fischer, J.Electrochem.Soc., **117** 410 (1970).
50. R.Nische, N.V.Boelsterli and N.Lichtensteiger., J.Phys. and Chem.Sol., **21** (1961) 199.
51. N.Romeo, G.Sberveglieri and L.Terricone, Thin Solid Films, **55** (1978) 413.
52. L.C.Burton, T.Hench, G.Storti and G.Haacke, J.Electrochem.Soc., **123** (1976) 1741.
53. K.Mitchell, A.L.Fahrenbruch and R.H.Bube, J.Vac.Sci. Technol., **12** (1975) 909.
54. A.Yoshikawa and Y.Sakai, J.Appl.Phys., **45** (1974) 3521.
55. F.Dutault. Ph.D Thesis, L.'Universite de Haute Alsace et L Universite Louis Pasteur de Strasbourg (1979).

56. M.S.Alaee and M.D.Rauhani, J.Electronic Mat., **8** (1979) 289.
57. M.Arienzo and J.J.Loferski, Proc. 2nd EC Photovoltaic Solar Energy Conference (Eds., R.Van.Overstraeten and W.Palz), Berlin (1979) p.361.
58. J.Vedel, M.Soubeyrand and E.Castel, J.Electrochem.Soc., **124** (1977) 177.
59. D.C.Cameron, W.Duncan and W.M.Tsang, Thin Solid Films, **58** (1979) 61.
60. R.J.Caveney, J.Cryst.Growth, **7** (1970) 102.
61. A.Amith, J.Vac.Sci.Technol., **15** (1978) 353.
62. R.B.Hall, Proc.Int. Workshop on "Cadmium Sulphide Solar Cells and Other Abrupt Heterojunctions" (Eds., K.W.Boer and J.D. Meakin), Delaware (1975) p.284.
63. K.Ito and T.Ohsawa, Jpn.J.Appl.Phys., **16** (1977) 11.
64. I.Kaur, D.K.Pandya and K.L.Chopra, J.Electrochem.Soc., **127** (1981) 943.
65. R.H.Bube, "*Photoconductivity of Solids*", R.E.Krieger, Publishing Company, Huntingdon, New York, (1978).
66. S.R.Das, Ph.D Thesis, Indian Institute of Technology, Delhi (1978).
67. G.H.Hewing and W.H.Blass, Thin Solid Films, **45** (1977).
68. C.Wu and R.H.Bube, J.Appl.Phys., **45** (1974) 648.
69. N.G.Dhere and N.R.Parikh, Thin Solid Films, **60** (1979) 257.
70. R.Deppe and R.Kassing, Proc. 7th Int.Vac.Congress and 3rd Int.Conf.Solid Surfaces, Vienna (1977) p.1927.
71. T.K.Bergstresser, M.L.Cohen, Phys.Rev., **164** (1967) 1069.
72. E.Khwaja and S.G.Tomlin, J.Phys. D:Appl.Phys., **8** (1975) 581.
73. L.Clark and J.Woods, J.Crystal Growth, **3** (1968) 126.
74. K.Durose, G.J.Russell and J.Woods, J.Crystal Growth, **72** (1985) 85.

75. K.Yamaguchi, H.Matsumota, N.Nakayama and S. Ikegami, Jpn. J. Appl. Physics, **15** (1976) 1575.
76. G.R.Awan, A.W.Brinkman, G.J.Russell and J.Woods, J.Crystal Growth, **85** (1987) 477.

Chapter IV

Characterisation Techniques.

4.1 Introduction.

This chapter describes the experimental techniques employed in the analysis of the thin layer materials and devices. In principle there were four main areas of characterisation; optical transmission, structural assessment, electrical characterisation and thickness measurement. The essential details of the equipment used for the optical transmission measurements are given in section 4.1. Various structural assessment techniques including reflection high energy electron diffraction (RHEED), scanning electron microscopy (SEM), energy dispersive analysis by x-rays, and x-ray diffraction (XRD) used to analyse the layer crystallinity, surface morphology and grain size are described in section 4.3. Electrical techniques used to characterise thin layer and device performance, including resistivity and Hall coefficient, current-voltage (I-V), capacitance-voltage (C-V), and spectral response (SR) are given in section 4.4. Finally a brief description of the equipment used in determining thin film thickness is given in section 4.5.

4.2 Optical Characterisation.

The optical constants (i.e. complex refractive index, n_c and absorption coefficient α_f) of the thin layers were determined under normal incidence in the wavelength range 400–2500 nm using a PE Lambda 19 double-beam spectrophotometer. It is designed to operate in the ultra violet (UV), visible (VIS) and near infra red (NIR) spectral ranges and permits transmission, absorption and reflection measurements to be made. Two radiation sources, a deuterium lamp, and a halogen lamp cover the working wavelength range of the spectrophotometer. Depending on the wavelength, the collimated light beam strikes either the UV/VIS grating or the NIR grating. It is then split into two beams, one of which passes through the sample while the other produces a reference. A photomultiplier is used in the UV/VIS range while a PbS detector is used in the NIR range. In the sample

plane, each beam is 10 mm high. The beam band-width (i.e. spectral bandpass) changes between 6–2 nm in the wavelength range of 2500–750 nm. A schematic diagram of the optical system of a PE L19 spectrophotometer is shown in Fig.4.1.

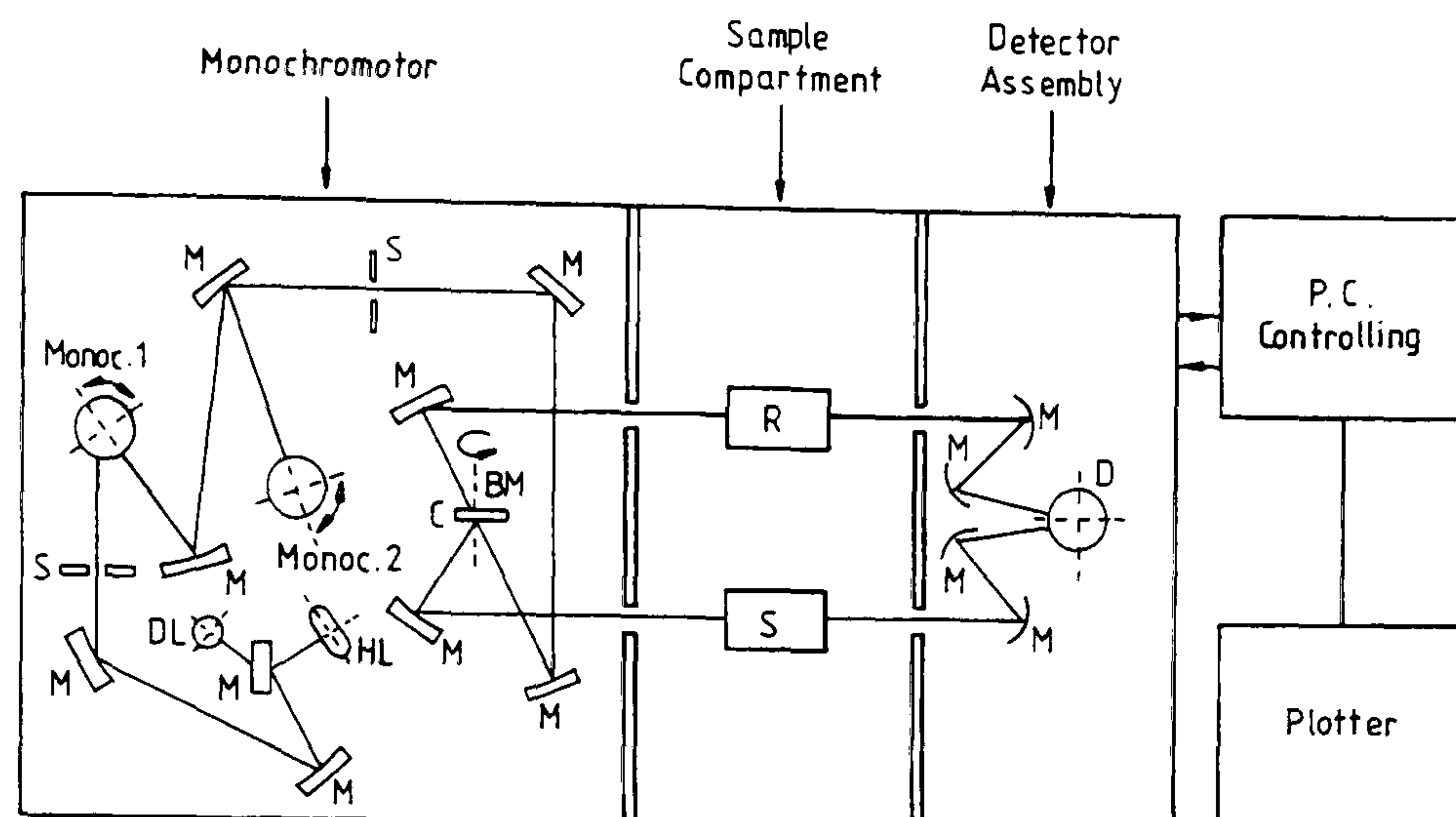


Figure 4.1 — Schematic diagram of the optical system of the PE Lambda 19 spectrophotometer.

4.3 Structural Characterisation.

4.3.1 Reflection of High Energy Electron Diffraction.

Reflection High Energy Electron Diffraction (RHEED) entails the diffraction of a monochromatic beam of high energy from the atomic planes at the surface of a crystalline specimen at glancing incidence. The electron beam penetration depth is extremely small and very dependent on the surface morphology, making RHEED a highly surface sensitive, and non-destructive technique. RHEED patterns may provide information on a number of different aspects including, crystal orientation, interplanar spacing, crystal structure, and the texture of the specimen surface.

The wavelength, λ (in Angstroms) of the electron accelerated through a potential difference V (given in volts) is given by the expression [1];

$$\lambda = \sqrt{\frac{150}{V(1 + 10^{-6}V)}} \text{ \AA} \quad [4.1]$$

Thus for the energy range used (80kV-120kV), the associated wavelength of the electrons varies from 0.12 to 0.04Å. The requirement for *Bragg* diffraction is that,

$$\lambda = 2d_{hkl} \sin \theta_B \quad [4.2]$$

where d_{hkl} is the interplanar spacing and θ_B is the Bragg angle. For most semiconductors, d_{hkl} is typically of the order of 4Å, so only those crystal planes inclined at less than a few degrees to the surface of the specimen will diffract the electron beam. The diffraction geometry employed in RHEED is illustrated in Fig.4.2.

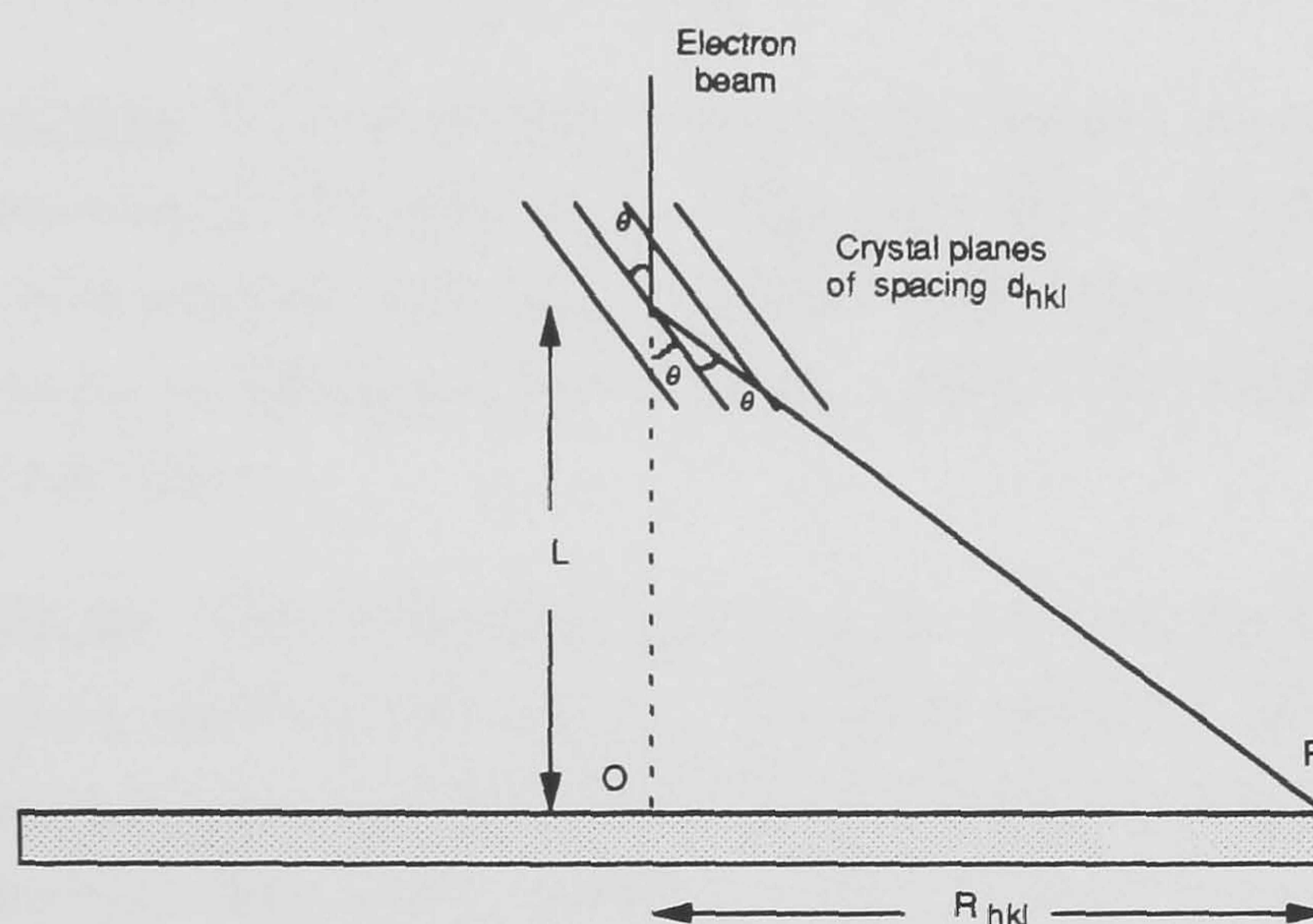


Figure 4.2 — Diffraction geometry in RHEED.

4.4 Structural Characterisation.

The incident electron beam strikes the crystal planes $\{hkl\}$ at the Bragg angle θ_B , to form a diffraction spot, P on a photographic plate placed at a distance L from the sample. Thus from simple geometry;

$$R_{hkl} = L \tan 2\theta_B \cong 2L\theta_B \quad [4.3]$$

for small angles and R_{hkl} is the distance from the central spot. Combining Eq.4.2 and Eq.4.3 gives;

$$\lambda L \cong R_{hkl} d_{hkl} \quad [4.3a]$$

where λL is the *camera constant* which is a constant for a given set of diffraction conditions. The value of L is determined by reference to a standard specimen of known crystal structure and lattice parameter. The nature of the specimen surface may be deduced from the shape of the diffraction patterns and in general may be divided into 5 categories;

Diffuse Pattern: The diffraction pattern consists of a set of broad, diffuse semi-circles. Such patterns arise from structures with no crystalline order (i.e. amorphous) or with a low degree of long range order or that are microcrystalline i.e. that have an extremely small grain size.

Ring Patterns: If the grain size of the sample is larger than that which can give rise to broadening of the diffraction rings, then the resulting diffraction pattern will consist of a number of sharp continuous rings, which become less continuous and more *spotty* as the grain size increase. Grains are randomly oriented with respect to each other.

Arc Patterns: The diffraction patterns are characterised by concentric arcs (i.e. subtending angles at the centre, $<180^\circ$) of intensity instead of semicircular rings, and indicate that, although the layer is still polycrystalline, individual grains display preferred orientation in relation to the direction of the electron beam. The length of the arcs is a measure of the misorientation of the grains (i.e. degree of preferred orientation).

Single Crystal Patterns: Single crystals give rise to either discrete spot or Kikuchi patterns which can provide information relating to the evaluation of the crystal structure, the determination of its lattice parameters, and a qualitative assessment of the surface. Kikuchi patterns are only obtained from a flat single crystals with very good lattice perfection.

Streak Patterns: Where the specimen is monocrystalline with a very flat surface, then the diffraction spots become elongated along a direction perpendicular to the shadow edge. In addition streaking along other directions may often indicate planar defects or very specific faceting along preferred directions.

The origin and interpretation of many types of diffraction pattern is fully discussed in a review article by G.J. Russell [2]. In the present study a JEM 120

TEM (capable of operating at 80,100, and 120kV) fitted with a RHEED stage was used routinely in the structural assessment of thin film samples.

4.4.1 Scanning Electron Microscope.

Scanning electron microscope (SEM) techniques are well suited for the characterisation of semiconductor morphology, since they provide high spatial resolution, and the simultaneous availability of a variety of modes and forms of contrast allow a wide range of analysis to be completed [3]. The construction, modes of operation and uses of the scanning electron microscopy are described in detail in the textbooks by Goldstein et al [4,5] and Holt et al [6].

Routine assessment of the surface morphology and compositional analysis of layers was performed using a Cambridge Stereoscan S600 SEM. The basic components of the SEM are shown schematically in Fig.4.3 and briefly consist of an electron gun, lens systems, detectors, visual and recording cathode ray tubes (CRT's) and associated electronics. The microscope is essentially an electron probe instrument which makes use of a focused electron beam that has been accelerated through voltages up to 25kV (in the case of the S600).

The electron gun is composed of a heated tungsten cathode maintained at a high negative potential in a Wehnelt cylinder configuration. Two condenser lenses and an objective lens are used to form a fine electron beam which is focused onto the specimen surface. Scan coils enable the electron beam to be deflected in a raster over the specimen, which is maintained at earth potential. Normally the SEM is used in secondary emission mode where the secondary electrons ejected by the primary incident electron beam are collected and detected. The resulting electrical signals are amplified and fed to the grid of a synchronously scanned display CRT. Thus the variation in the strength of the signal is recorded as a variation in brightness on the CRT screen and hence contrast on the micrographs. A number of interactions occur in various parts of the excitation region of the specimen due to electron bombardment and they may be detected and analysed. Useful effects include;

- 1- Secondary electrons which may be collected to form a magnified image of the specimen surface (i.e. secondary emission (SE) mode). These secondary electrons have energies <50 eV and provide topographical contrast.

2- X-rays emitted due to relaxation of electrons excited by the electron beam into higher orbitals. This takes place up to a depth of a few microns beneath the surface and forms the basis of Energy Dispersive Analysis by X-rays (EDAX). It may be used to analyse the elemental species present in the sample. Quantitative analysis and light element (such as H, C, O, etc.) detection were not available on the EDAX used in the course of this study.

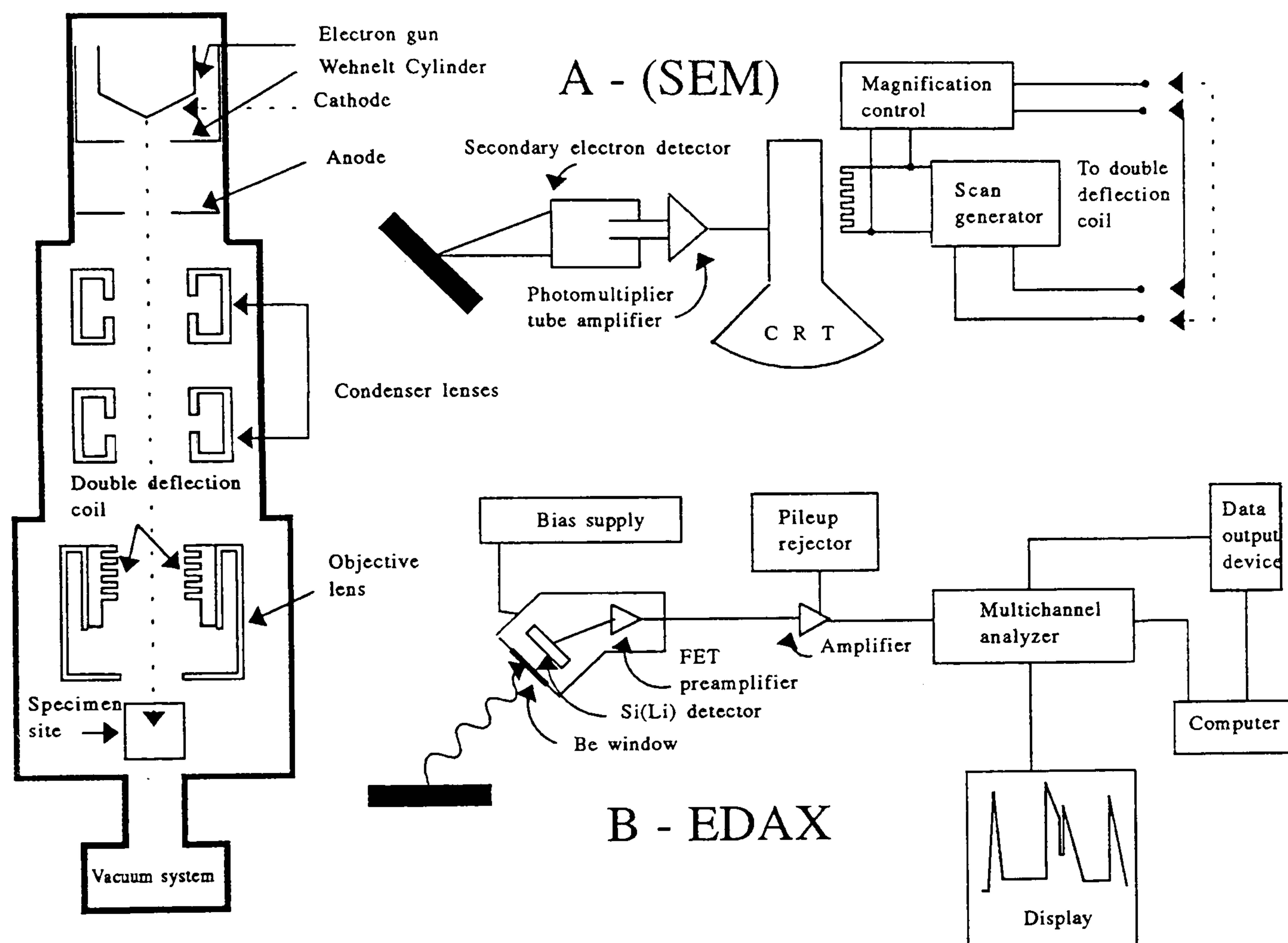


Figure 4.3 — Schematic diagram of the basic functional features of a scanning electron microscope.

4.4.2 X-Ray Diffraction.

X-ray diffraction (XRD) is a basic tool in the structural analysis of the materials. A very useful comprehensive treatment of X-ray diffraction theory can be

obtained from Klug & Alexander [7] and Cullity [8]. In the present study, structural characterisation of the thin layers (CdTe and CdS) was performed by X-ray diffractometry. This was used to assess grain size as well as general crystal quality.

4.4.2.1 X-Ray Diffractometry.

A collimated monochromatic beam of X-rays striking a crystalline material will be diffracted according to Bragg's law. Thus if a narrow acceptance angle detector (i.e. fitted with appropriate collimating slits) is used, the angle of a given diffracted beam can be measured directly. Scanning the detector over a range of angles will map the diffracted rays in that region of angular space. A proportional counter is driven at a constant angular velocity through increasing values of $2\theta_B$ until the whole angular range is scanned. The counter and specimen are mechanically coupled so that a rotation of the counter through $2\theta_B$ degrees is automatically accompanied by a rotation of the specimen through θ_B degrees. The counter is connected to an analogue recorder whose speed is synchronized with that of the detector so that the x-axis is calibrated in terms of $2\theta_B$. The diffraction record (i.e. intensity versus diffraction angle, $2\theta_B$) typically consists of a spectrum of narrow peaks corresponding to angles which fulfil the Bragg condition. These peaks can be easily converted into lattice spacings, d_{hkl} , of crystalline materials present applying Bragg's law. A Philips PW1130, 3kW generator/diffractometer assembly employing a Cu anode was used for XRD in the present study. The radiation was then passed through an nickel filter to give monochromatic ($\text{Cu}_{K\alpha}$) radiation of wavelength 1.5418 Å. The diffracted beam was detected using a sealed proportional counter, operating at 1550V.

4.5 Electrical Characterisation.

4.5.1 Resistivity and Hall Coefficient Measurements.

The resistivity, ρ , and Hall coefficient, R_H of thin layers of known thickness were measured using the Van-der Pauw method [9]. Van-der Pauw has shown that the resistivity and Hall coefficient of a thin layer of known thickness but arbitrary shape can be measured by means of four ohmic contacts labeled A , B , C and D of negligible size and positioned anywhere on the periphery of the sample. Four different resistances are measured, denoted by $R_{AB,CD}$ (where the first pair of

subscripts denote the current terminals and the second subscript pair identify the voltage terminals). This has the advantage over the usual 4 point probe technique in that it is not necessary to know the geometrical dimensions apart from the thickness which is generally more easily measured. The resulting resistivity, ρ of the sample is given by any adjacent pair of resistances, i.e. for $R_{AB,CD}$ and $R_{BC,DA}$

$$\rho = \frac{\pi d [R_{AB,CD} + R_{BC,DA}]}{2 \ln 2} f \left[\frac{R_{AB,CD}}{R_{BC,DA}} \right] \quad [4.4]$$

where d is the layer thickness and the function f is a correction term satisfying the relationship;

$$\frac{R_{AB,CD} - R_{BC,DA}}{R_{AB,CD} + R_{BC,DA}} = \frac{f}{\ln 2} \operatorname{arccosh} \left[\frac{\exp \left[\frac{\ln 2}{f} \right]}{2} \right] \quad [4.4a]$$

The correction function, f is a function of the ratio of the two adjacent resistance and is close to 1 if the resistances are similar. The resistance between two adjacent contacts was obtained from the slope of the I-V graph. The measurements were then repeated with the current in the reverse direction, to check the ohmicity of the contacts.

The Hall coefficient, R_H was determined from the change in resistance $R_{AC,BD}$ following a change in the magnetic field ΔB perpendicular to the plane of the sample using;

$$R_H = \frac{d}{\Delta B} \Delta R_{AC,BD} \quad [4.5]$$

The Hall mobility of a semiconductor, μ_H can be defined as [10];

$$\mu_H = R_H \sigma \quad [4.6]$$

where σ is the dark conductivity.

A constant current source, made in house and a Hewlett Packard HP3456a DVM with an input impedance of $>10^{10}\Omega$ was used to measure the current and voltage respectively. An electromagnet was provided with a constant current of 2A at 200V to give a magnetic flux density of 0.16T at the center of the pole gap. All parameters were controlled and the data analysed by an Acorn Archimedes microcomputer, a detailed discussion of which has been previously reported [11].

4.5.2 Dark and Illuminated I-V Characteristics.

Dark I-V measurements were carried out using a Keithley electrometer (Model A195) which contains a high impedance voltmeter, a low impedance ammeter and a dc calibrated power supply (Time Electronics, model 2003). Detailed temperature dependent I-V characteristics were measured using the same circuitry, except that the sample was mounted in a Oxford DN1704 static helium exchange gas, liquid nitrogen (LN_2) cryostat capable of maintaining temperatures between 77–400K. Measurements were made at 0.025 V intervals in order to be able to observe any changes in the current transport mechanism with temperature. Independent ammeters and voltmeters were used to measure the absolute current passing through the sample, and check the bias voltage from the dc power supply respectively.

The photovoltaic output characteristics of the devices were measured under AM1.5 simulated illumination using a solar simulator experimental arrangement as described by Alnajjar [12]. A 1.5 kW quartz halogen strip lamp with a parabolic reflector housing was mounted in a leveled stainless steel frame fitted with a tray containing 2cm deep flowing water, intended to simulate the infrared absorption due to water vapour of the atmosphere. Standard (European) test conditions (temperature 25°C), were maintained in the sample compartment by the aid of a temperature controller. Heating was provided by two resistive heaters and cooling by circulating cooling water. The solar simulator was calibrated to supply AM1.5 illumination, by adjusting the height of the sample below the light source, using a standard silicon PIN diode covering the wavelength range. A general view of the Durham solar simulator is shown in Fig.4.4.

4.5.3 Capacitance-Voltage Measurements.

Capacitance-voltage measurements enabled the determination of free carrier density, and provided estimates of barrier height, and depletion width in junction devices. They also give an indication of interface state density. Capacitance-voltage characteristics were measured manually with a Boonton 72B capacitance meter which operates at 1MHz, together with a dc voltage source. The sample was mounted in a liquid nitrogen cryostat to allow temperature dependent capacitance-voltage measurements (between 77–400K) to be made.

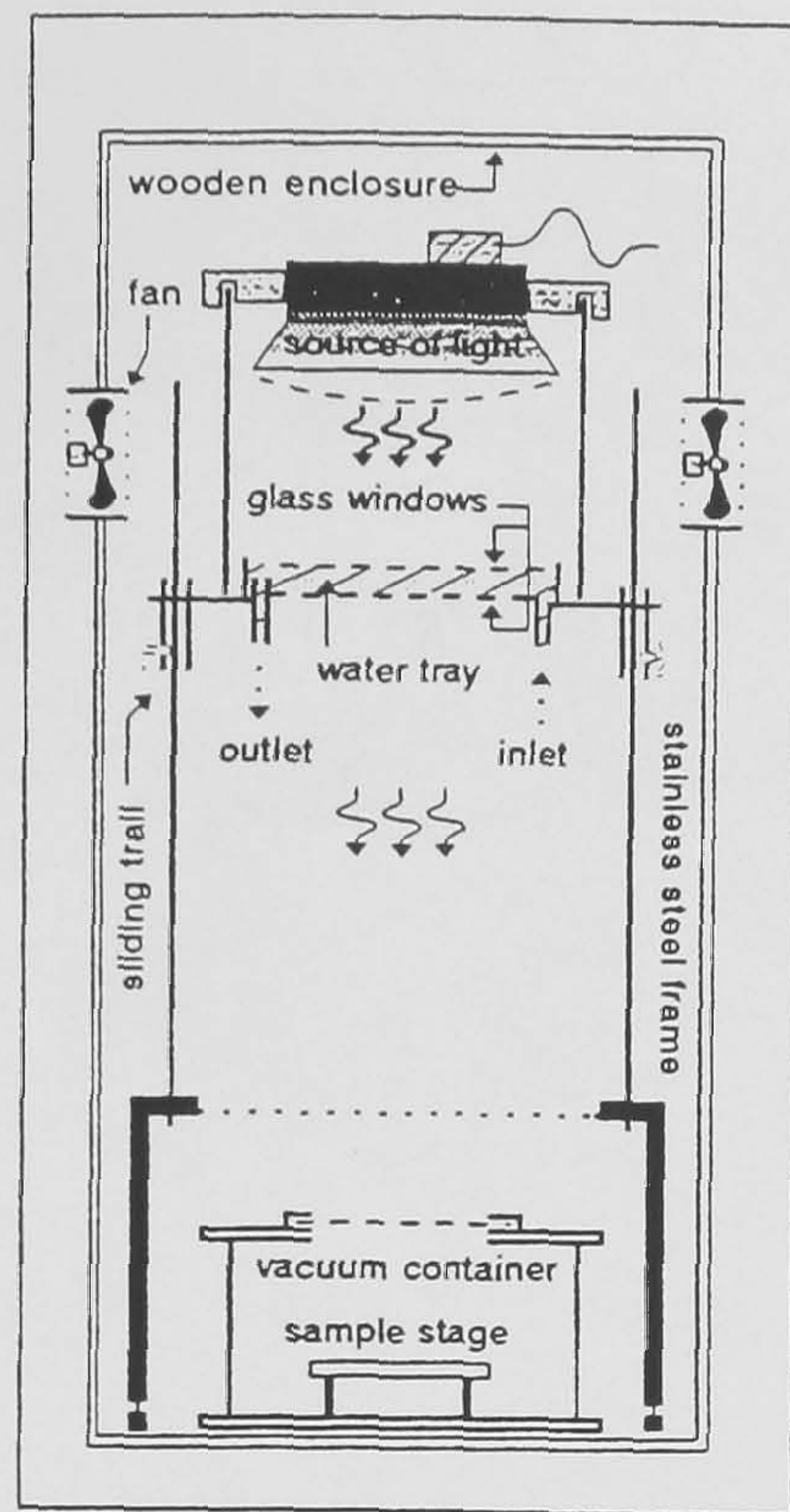


Figure 4.4 — A schematic diagram of Durham solar simulator.

4.5.4 Spectral Response Measurements.

The spectral response of solar cells was measured over the wavelength range $0.4\text{--}2.0\mu\text{m}$ using a Barr and Stroud prism monochromator fitted with a Spectrosil A silica prism. The light source consisted of a 250W, 24V quartz halogen lamp driven by a dc stabilized power supply. A 50/50 beam splitter ensured that light passing through the exit slit illuminated both the sample and a PIN diode reference, thus ensuring calibration of the photoresponse. The PIN diode response was amplified and passed through a comparator in a feedback loop to control the light output to provide constant photon flux illumination at all wavelengths in the range $0.4\text{--}1\mu\text{m}$. (i.e. within the PIN diode response). Fig.4.5 describes the experimental set-up, where it can be seen that the device is mounted in a cryostat with a window for illumination. A Keithley 602 electrometer was used to measure open circuit voltage (input impedance of $10^{14}\Omega$) or a very low impedance for measurements of short circuit current. The output of the electrometer and PIN diode were recorded on a LeCroy digital storage oscilloscope and down loaded where required to a HP plotter.

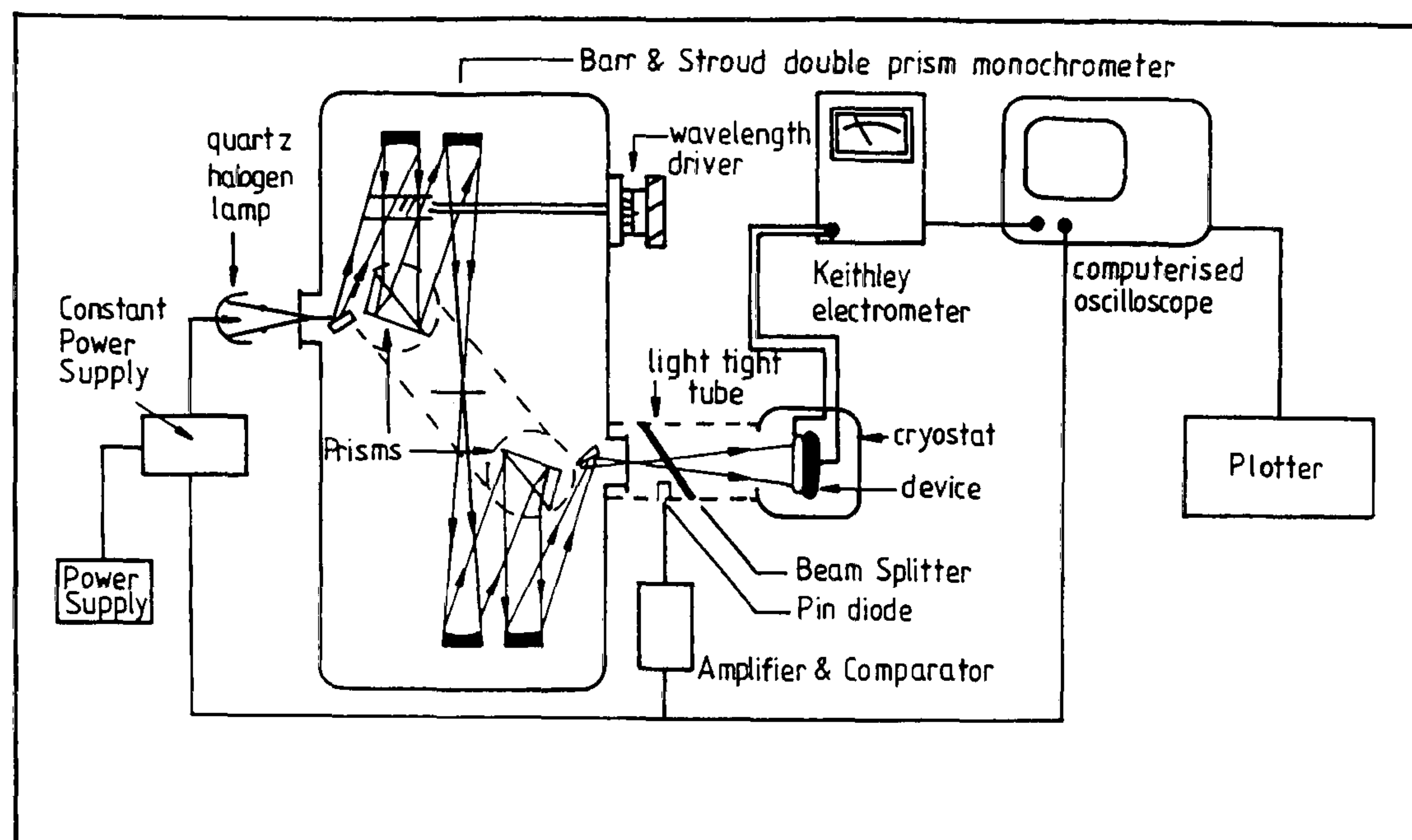


Figure 4.5 — Schematic diagram of system used for the spectral response measurements.

4.6 Secondary Ion Mass Spectroscopy (SIMS).

Secondary ion mass spectroscopy (SIMS) offers extremely high sensitivity quantitative elemental analysis of the chemical structure of surfaces [13]. A limited amount of SIMS analysis was carried out using facilities provided by BP Solar*. The basic principles of a SIMS can be outlined as;

I- Secondary Ion Emission: The sputtering process is the basis of any SIMS analysis. A beam of energetic primary ions impinges onto the solid surface of the sample, causing some atoms to be sputtered off. These sputtered particles can be ejected as atoms or molecules in a neutral, excited or ionised state, but only the ionised species may be used for SIMS analysis.

II- Instrumentation: A typical SIMS system contains an ion gun to provide a source of primary ions, a mass spectrometer with which to detect the secondary ions, a data acquisition system, and a vacuum environment in which to house the

* A solar cell company producing highly efficient thin film n-CdS/p-CdTe solar cells, BP Solar, 12 Brooklands Close, Windmill Road Sunbury-on-Thames, Middlesex TW16 7DX, U.K

ion gun and mass spectrometer. The ion gun consists of an ion source, ion optics to focus and deflect the primary ions, and a mass filter to ensure the purity of primary ion beam. A source of caesium ions is also required for optimum sensitivity for electronegative elements. The ion optics in the ion gun allow the primary ions to be accelerated up to energies of between 1 and 20 keV and focused into spots of between 1 and 50 μm in diameter. A primary beam filter is generally incorporated into the primary ion column to remove any neutral species in the primary beam and also to remove any impurities in the beam which may be present in the ion source area, otherwise the trace level impurities in the primary ion beam may become implanted into the sample and then be detected as a false high background level of that species.

In SIMS systems, two types of mass spectrometer may be used, namely the quadrupole mass spectrometer and the magnetic sector mass spectrometer. The quadrupole mass spectrometer in its basic form comprises four rods to which dc and rf signals are applied; the resulting electric field will allow ions of a given charge to mass ratio entering the quadrupole to follow a stable oscillatory trajectory between the rods and so reach the detector. The quadrupole mass spectrometer offers a high mass range, to greater than 1000 amu, freedom from magnetic fields, compactness and compatibility with other surface analysis techniques in the same vacuum chamber. However, it has a lower capability for high mass resolution than can be achieved with the magnetic sector mass spectrometer. In magnetic sector mass spectrometers the ions are accelerated by a large potential and injected into a uniform magnetic field where they follow circular trajectories dependent on their energy and charge:mass ratio. Different trajectories may be selected by varying either the magnetic field or the accelerating potential. By changing the width of the entrance and exit slits to the magnetic sector, the mass resolution of the mass filter can be adjusted allowing continuous variation of the mass resolution.

III- Quantification: The information contained in a SIMS mass spectrum recorded from the sample can give quantitative information about the sample, providing that it is uniform in composition within the analysed volume. If a second phase is present then the interpretation must be considered qualitative because of the strong matrix effects characteristic of SIMS analysis. Two separate approaches have been developed to quantify SIMS data, one based upon a physical model of

the secondary ion emission process and providing semiquantitative information; the other using a direct reference to calibrated standard samples of similar composition. The latter approach is more accurate but requires a large suite of standard samples to be available.

4.7 Positron Trapping At Small Vacancy Clusters.

Positrons are widely used to study momentum density and crystal imperfections. The annihilation characteristics give information on the electron-positron system which can be directly related to the electronic structure of the medium. The positron technique has many advantages in the study of matter. It provides a nondestructive method, and no special sample preparation is necessary. Several reviews on the use of positrons to the study of condensed matter have been published [14,15].

4.7.1 Positron Beam Technique.

Initially fast positrons annihilate with electrons from the surrounding medium into 511 keV gamma quanta. The annihilation characteristics give information on the electron-positron system which can be directly related to the electronic structure of the medium. There are three conventionally measurable quantities; the positron lifetime, the angular correlation of 2γ annihilation radiation, and the Doppler-broadened annihilation line shape. The angular correlation measurements are widely used to investigate electron momentum densities in metals and alloys. The line shape of the annihilation radiation also reflects the momentum distribution of annihilated electrons.

Positron annihilation in the films was studied as a function of depth by recording the γ - annihilation line $E_\gamma = 511\text{keV} \pm \Delta E_\gamma$, as a function of positron energy E_p . The 511 keV annihilation line is Doppler broadened, ΔE_L , due to the momentum of the annihilating electron-positron pair [16]. Experiments were performed using the variable energy slow positron beam at the Helsinki University of Technology [17]. It is customary to characterise the momentum distribution by using the line shape parameters $S(W)$ defined as the relative number of annihilation events in the centroid (wings) of the 511 keV line. According to the relationship $\Delta E_L = cp_L/2$ where c is the light speed and p_L is the component of the momentum

along the emission direction of the 511 keV γ -rays, annihilations with low(high) momentum electrons contribute to $S(W)$. Annihilations with valence electrons contribute mainly to S whereas annihilation with core electrons contribute to S but predominantly to W . Consequently, the S and W parameters are referred to below as valence and core annihilation parameters respectively.

4.8 References.

1. P.B.Hirsch, "*Electron Microscopy of Thin Crystals*", Butterworths, London, 1965.
2. G.J.Russell, Prog.Crystal Growth and Charact., Vol.5, (1982) 291.
3. D.B.Holt, B.G.Yacobi, "*SEM Micro Characterisation of Semiconductors*", Academic Press, (1989).
4. J.I.Goldstein, H.Yakowitz, D.E.Newbury, E.Lifshin, J.W.Colby and J.R. Coleman, "*Practical Electron Microscopy*", Plenum Press, New York (1975).
5. J.I. Goldstein, D.E. Newbury, P. Echlin, D.C. Joy, C. Fiori and E. Lifshin, "*Scanning Electron Microscopy and X-Ray Micro Analysis, Plenum Press*", New York, (1981).
6. D.B.Holt, M.D.Muir, P.R.Grant and I.M. Boswarva, "*Quantitative Scanning Electron Microscopy*", Academic Press, London, (1974).
7. H.P.Klug and L.E.Alexander, "*X-Ray Diffraction Procedures*", John Wiley & Sons, New York (1974).
8. B.D.Cullity, "*Elements of X-Ray Diffraction, Addison Wesley*", (1956).
9. L.J.van der Pauw, "*Philips Research Reports*", **13**, (1958) 1.
10. S.M.Sze, "*Physics of Semiconductor Devices*", John Wiley& Sons, (1981).
11. J.T.Mullins, Ph.D Thesis, University of Durham, (1990).
12. A.A.A.Alnajjar, Ph.D Thesis, University of Durham, (1992).

13. J.M.Walls, V.G.Ionex, "*Methods of Surface Analysis*", Cambridge University Press, (1989).
14. A.T. Stewart, L.O. Roellig (eds), "*Positron Annihilation*", Academic Press, New York, 1967.
15. I.Ya.Dekhtyar, Phys.Rpt., **C9**, 243 (1974).
16. P. Autojarvi, "*Positrons in Solids*", Topics in Current Physics, **12** 89, Springer, (1979).
17. J.Lahtinen, A.Vehanen, H.Huomo, J.Makinen, P. Huttunen, K. Rytola, M. Bentzon, P. Hautojarvi, Nucl. Instr. Meth. Phys. Res. Sect., **17** 73 (1986).

Chapter V

Optical Characterisation of Polycrystalline CdTe and CdS Thin Films.

5.1 Introduction.

The interaction of electromagnetic radiation with matter has provided over the years an effective and powerful tool for understanding the electronic structure of condensed materials. Maxwell's equations describing the propagation of electromagnetic waves are well established, and serve as the underlying basis for optical studies.

The optical constants, (i.e. complex refractive index n_c and absorption coefficient α) which are of particular significance, are related to the atomic structure of the material and provide a great deal of information about its properties.

Since CdTe and CdS are to be used as the absorber and window layers in a low cost thin film photovoltaic device, it is important to know the complex refractive index n_c and absorption coefficient α as a function of wavelength to predict their photoelectronic behaviour.

Complex refractive index n_c and absorption coefficient α are usually determined by elaborate computer iteration procedures using both the transmission and reflection spectra [1,2,3]. However, here n_c and α have been determined by a simple straightforward process using transmission spectra only [4,5,6].

In this chapter, the methods of calculation for the optical constants of layers of uniform and non-uniform thickness will be discussed first. This will be followed by a description of the optical properties of CdTe and CdS thin films produced by vacuum deposition on plain glass substrates. Finally, the effects on the optical properties of the layers of thin film treatments such as annealing and doping will be presented.

5.2 For films of uniform thickness (Flat Film Analysis).

The practical situation for a thin film on a transparent substrate is shown in Fig.5.1. The film has a thickness, d and a complex refractive index, $n_c = n_f - ik_f$ which is related to the velocity of propagation by $v = c/n_c$ where c is the velocity of the light. We refer here to n_f as the refractive index, and to k_f as the extinction coefficient of the film, which can be expressed in terms of the absorption coefficient α_f , $k_f = \lambda \alpha_f / 4\pi$ where λ is the wavelength of the incident light. The transparent substrate has a thickness several orders of magnitude larger than d , and has refractive index, n_s and absorption coefficient, $\alpha_s \simeq 0$ in the spectral range examined. The refractive index of the surrounding air is taken as $n_o = 1$.

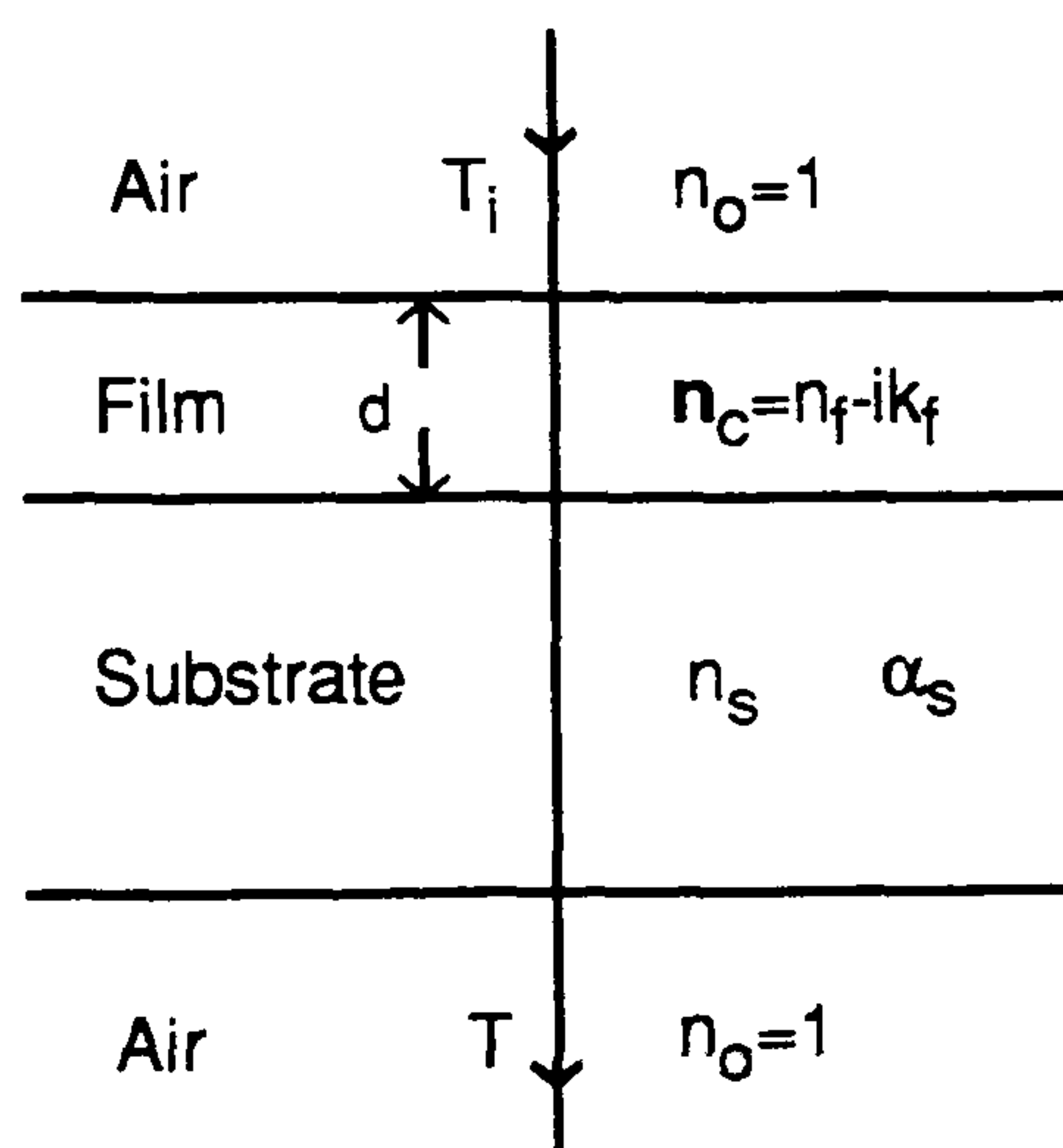


Figure 5.1 — Schematic diagram for a system consisting of an absorbing thin film on a thick finite transparent substrate.

A typical transmission spectrum of an as-grown CdTe thin film measured over the wavelength range 750–2500 nm is shown in Fig.5.2. The spectrum can be roughly divided into two regions as shown on the diagram. In the region of weak absorption, $\alpha_f > 0$, and transmission decreases mainly due to the effect of α_f , and may be determined from the envelopes of the extrema T_M , and T_m , and refractive indices n_f , and n_s . Multiple reflections give rise to the interference fringes. In the region of strong absorption ($\alpha_f \gg 0$), the transmission virtually ceases and the film

becomes opaque. If the interface and surface of the sample were not plane parallel, the transmission would be a smooth curve as shown by T_α in Fig.5.2.

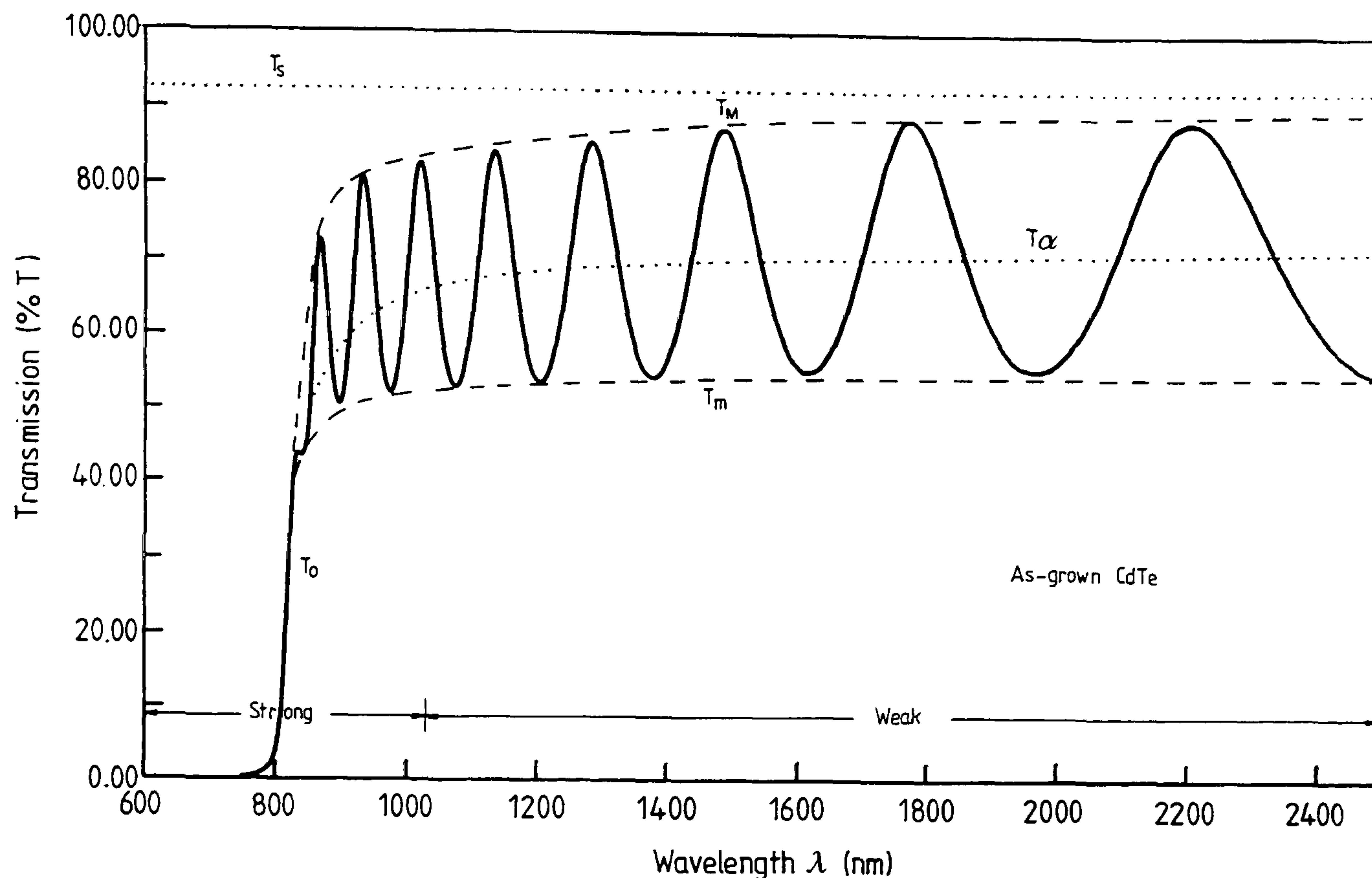


Figure 5.2 — Transmission spectrum for a typical $1.705\mu\text{m}$ thick film of CdTe on a glass substrate.

5.2.1 Determination of n_f and α_f in weak absorption region.

A detailed description of the method [6] including the associated mathematical derivation is given in the Appendix A. For the calculation of n_f in weak absorption region, the extrema of the interference fringes, T_M and T_m , at each wavelength are obtained from the envelope spectrum (note that the transmission spectrum should be taken with reference to air). The refractive index $n_f(\lambda)$ can then be calculated straightforwardly by using the expression A1.15 given in Appendix A;

$$n_f = [N + (N^2 - n_s^2)^{1/2}]^{1/2} \quad [5.1]$$

where,

$$N = 2n_s \frac{T_M - T_m}{T_M T_m} + \frac{n_s^2 + 1}{2} \quad [5.1a]$$

Once $n_f(\lambda)$ is determined, all the constants in Eq.A1.8a-A1.8d are known, and the absorption coefficient $\alpha_f(\lambda)$ may be calculated from;

$$x = \exp(-\alpha_f d) = \frac{F - \left[F^2 - (n_f^2 - 1)^3 (n_f^2 - n_s^2) \right]^{1/2}}{(n_f - 1)^3 (n_f - n_s^2)} \quad [5.2]$$

where,

$$F = \frac{4n_f^2 n_s}{T_M T_m} (T_M + T_m) \quad [5.2a]$$

and x is defined as the attenuation of the incident light. The “Flat Analysis” procedure calculates first the refractive index, n_f called, $n_{[f,raw]}$ in the region of weak absorption by using the Eq.5.1 at each fringe extremum. Then using the graphical procedure outlined in section 5.2.3.1, corrected values of the refractive index, $n_{[f,adj]}$ are calculated and an estimate obtained for the layer thickness, d . Finally the absorption coefficients are determined from Eq.5.2 using the corrected values of refractive index, $n_{[f,adj]}$.

5.2.2 Determination of n_f and α_f in strong absorption region.

In strong absorption region where the interference fringes disappear, it is not possible to calculate $n_f(\lambda)$ and $\alpha_f(\lambda)$ independently, using the transmission spectrum alone. For very large α_f , the three curves T_M , T_m , and T_α (Fig.5.2) converge to a single curve T_o . If the interference effects are ignored, Eq.A1.8 can be rewritten for $x \gg 1$ as;

$$x = \exp(-\alpha_f d) \cong \frac{(n_f + 1)^3 (n_f + n_s^2)}{16n_f^2 n_s} T_o \quad [5.3]$$

In the region of strong absorption, the absorption coefficient, α_f , was calculated from Eq.5.3 using extrapolated values of n_f . This was done by fitting a function of the form, $n_f = a\lambda^{-2} + b$ (first order Cauchy equation, see Appendix A) to values of n_f in the weak absorption region and then using the function to provide the extrapolated values of n_f for use in Eq.5.3. The absorption coefficient, $\alpha_f(\lambda)$ in

the region of strong absorption may in general be written as a function of incident photon energy so that [7];

$$\alpha_f(h\nu) = A(h\nu - E_g)^\xi \quad [5.4]$$

in which ξ is a constant depending on the type of electronic transition, and the coefficient A can be evaluated from [8];

$$A = \frac{q^2(2m_r^*)^{3/2}}{n_f c h^2 m_e^*} \quad [5.4a]$$

where m_r^* is the reduced mass: $1/m_r^* = 1/m_e^* + 1/m_h^*$, m_e^* and m_h^* are the electron and hole effective masses respectively, q is the charge on the electron, c is the speed of light and h is Planck's constant.

5.2.3 Determination of film thickness.

The measurement of the film thickness is difficult and there is no single method that gives the thickness unambiguously. All the available techniques suffer from some degree of uncertainty. It is therefore, better to measure the film thickness, d by a number of different methods in order to allow for the various uncertainties. Film thickness, d can be used to provide a check on the determination of optical constants. The list of the methods is given below as follows;

- 1- Direct Measurement by α -step;
- 2- Graphical Method;
- 3- Interference Fringe Method;
- 4- Multiple Beam Interferometer Method.

5.2.3.1 Direct measurement by α -step.

The thickness, d was obtained by direct measurement using a Tencor α -step 200 which provided measurements of surface profile and thickness. By scribing the layer, a step was formed across which the thickness could be measured. However the substrate may also have been damaged by scribing, resulting in a noticeable error in the thickness measurement especially if the layer was thin.

5.2.3.2 Graphical method.

The graphical method has an appealing simplicity for the calculation of fringe order number, m and thickness, d in the region of the film where the transmission is measured (i.e. the weak absorption region). The basic equation for an interference fringe is given by;

$$2n_f d = m\lambda \quad [5.5]$$

where m is the fringe order number (an integer for a maximum and half integer for a minimum). Suppose the order number m of the first extremum is m_ℓ . Then the adjacent minimum (or maximum) will be $m_\ell + 1/2$. So in general, Eq.5.5 can be rewritten as;

$$2n_f d = \left(m_\ell + \frac{\ell}{2}\right)\lambda, \quad \ell = 0, 1, 2, 3, \dots \quad [5.6]$$

or,

$$2d\left(\frac{n_f}{\lambda}\right) - m_\ell = \frac{\ell}{2} \quad [5.6a]$$

This is in the form of a straight line. In general, m_ℓ will not be known but may be determined by plotting $\ell/2$ versus n_f/λ . A straight line will be obtained with slope, $2d$ and an intercept on the y-axis of $-m_\ell$. The straight line is now redrawn such that it passes exactly through the nearest integer (or half integer if the first extremum is a minimum) value on the y-axis and the thickness, d obtained from the slope (in principle, the values of λ and n_f of only two extrema are necessary to obtain the fringe number, m and thickness, d).

5.2.3.3 Interference fringe method.

If n_{f1} and n_{f2} are the refractive indices at two adjacent maxima (or minima) at λ_1 and λ_2 , it follows from Eq.5.5 that the thickness is given by;

$$d = \frac{\lambda_1 \lambda_2}{2(\lambda_1 n_{f2} - n_{f1} \lambda_2)} \quad [5.7]$$

For this method to be used most successfully, the interference fringe peaks should be widely spaced, thus reducing relative errors. Once, d is determined for each pair of adjacent extrema, an average is calculated, \bar{d}_{av} and used with n_f to determine the order numbers for the extrema.

5.2.3.4 Multiple beam interferometer method.

The film thickness, d can be calculated by measuring fringe displacement, O and fringe spacing, S obtained by placing a half silvered reference mirror on top of a step formed at the junction of the layer and substrate surface at a small angle. Then d is obtained using the formula [9];

$$d = \frac{O}{S} \frac{\lambda}{2} \quad [5.8]$$

where λ is the wavelength of the light, and d is calculated over many fringes.

5.3 Effects of non-uniform thickness.

Inhomogeneties in thin films can have a large influence on the optical transmission spectrum. If not corrected for, this may lead to errors in calculated values of the absorption coefficient, refractive index and film thickness.

In the previous section a thin homogeneous film of uniform thickness, d and complex refractive index, n_c was considered. The effects of thickness variation on the optical constants have been analysed by Swanepoel [10]. He assumed that the thickness varied linearly over the illuminated area so that the thickness could be expressed in the following form, $d = \bar{d} \pm \Delta d$, where Δd refers to the actual variation in thickness from the average thickness \bar{d} . While this is clearly an approximation, it is not an unreasonable one since, in general, the thickness did vary smoothly across the layer (though not necessarily linearly). The experimental measurements must be done in such a way that the same area is illuminated at all wavelengths while ensuring that the slit-width is always kept constant.

The simplest way of treating the transmission spectrum of a non-uniform film is to transform it to the spectrum of a uniform film of the same average thickness \bar{d} . This can be done using the envelopes T'_M and T'_m , T_{M0} and T_{m0} of the non-uniform and equivalent uniform films respectively. The compact relations between the envelopes of the two spectra (see A1.8 in Appendix A) are initially solved simultaneously by using the values of T'_M and T'_m of the spectrum. This requires measurements at the long wavelength limit when $T_{M0} \equiv T_s = 0.92$. In the present case, this was never reached, so this could not be applied to films prepared

here in Durham. In fact, the layers gave values close to bulk single crystal values confirming that the layers were reasonably uniform.

5.4 Correction for slit-width.

A spectrophotometer in practice always has a finite spectral bandpass or slit-width S and a spectral band in the range $\lambda \pm \Delta\lambda$, where $\Delta\lambda = S/2$, is therefore incident on the film. The slit-width of the instrument is not the physical gap between the slit foils of the monochromator which is termed the geometric slit-width. The effect of the finite band-width on the transmission spectrum transmission spectrum is to reduce progressively the fringe amplitude at shorter wavelengths, i.e T_M becomes smaller and T_m larger [6]. The effect can be minimised experimentally by reducing the slit-width S but this reduces the intensity of the incident beam leading to smaller signals and greater noise problems with a consequent loss of accuracy. In practice the effect of S becomes important only when the width of the fringes is of the same order of magnitude as S . Over the wavelength region of interest 750–2500 nm, the band-width of the transmission fringes varied between 200–250 nm while the band-pass changed from 2–6 nm as shown in Fig.5.3. In order to determine whether correction is required, it is first necessary to understand how S will affect the transmission. The change in transmission T , ΔT , due to a change in slit-width is proportional to T and S and inversely proportional to fringe band-width $\Delta\omega$. Theoretical analysis shows the proportionality dependence to be quadratic as written below [6];

$$\Delta T \propto \left(\frac{T S}{\Delta\omega} \right)^2 \quad [5.9]$$

The actual values of ΔT depend on the way in which $\Delta\omega$ is defined. Strictly $\Delta\omega$ is the fringe band-width but in practice because of dispersion $\Delta\omega$ will vary across the transmission spectrum. Thus measured values of $\Delta\omega$ may differ depending on whether they were determined from one period or several periods. If $\Delta\omega$ is simply taken to be wavelength-width between the two neighbouring extrema (i.e. one period) then the corrected values of T_M and T_m can be calculated from the following equations;

$$T_{M,true} = T_{Ms} + \left(\frac{T_{Ms} S}{\Delta\omega_M} \right)^2 \quad [5.10]$$

$$T_{m,true} = T_{ms} - \left(\frac{T_{ms} S}{\Delta\omega_m} \right)^2 \quad [5.11]$$

where,

$$\Delta\omega_{Mi} = \lambda_{m(i-1)} - \lambda_{m(i+1)} \quad [5.11a]$$

and

$$\Delta\omega_{mi} = \lambda_{M(i-1)} - \lambda_{M(i+1)} \quad [5.11b]$$

Calculated $T_{M,true}$ and $T_{m,true}$ values suggest that the slit-width did not materially affect the accuracy. The effect of finite band-width on a spectrum is thus similar to that of a variation in thickness. The equivalence can be expressed formally as [10];

$$\Delta\lambda = \lambda \frac{\Delta d}{d} \quad [5.12]$$

5.5 Variation in Refractive Index n_f .

The variation in the refractive index due to non-uniformity and changes in slit-width of the spectrometer can be written as;

$$n_f = \bar{n}_f + \Delta n_f \quad [5.13]$$

Due to a symmetrical relation between Δd and Δn (since the product nd corresponds to the optical path), the equivalence effect can be expressed as [10];

$$\Delta n_f \cdot d \equiv n_f \cdot \Delta d \quad [5.14]$$

5.6 Optical properties of as-grown CdTe thin films.

The optical constants (i.e. refractive index, n_f , extinction coefficient, k_f and absorption coefficient, α_f) of polycrystalline CdTe films prepared by vacuum deposition were determined under normal incidence over the wavelength range 750–2500 nm using a PE Lambda 19 spectrophotometer, and compared with bulk single crystal values given in the literature [11]. The effects of heat treatments, CdCl₂ dipping and the use of Cl₂ pre-doped CdTe source material on the optical properties of the layers were then investigated and are discussed below.

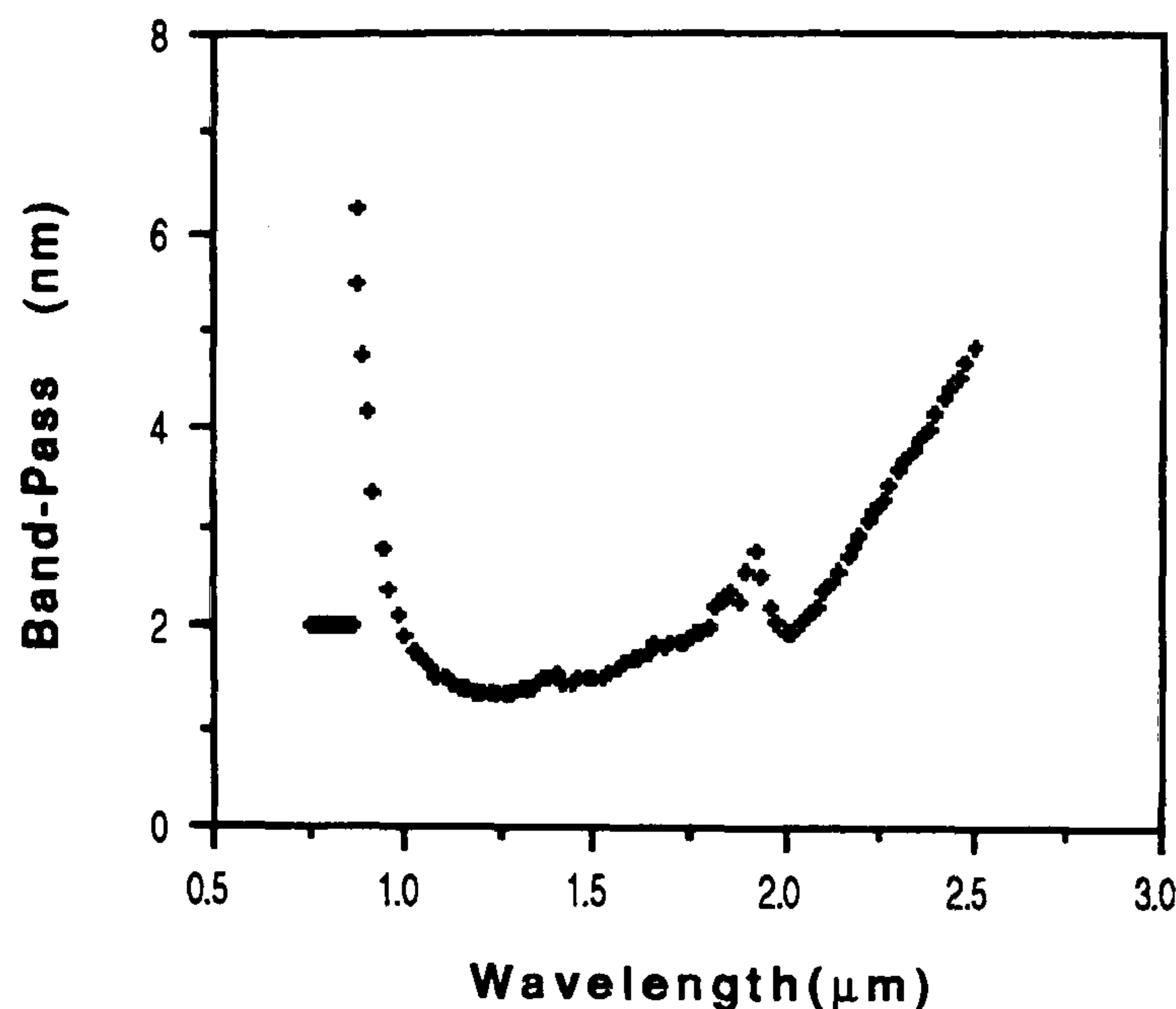


Figure 5.3 — Band-pass vs wavelength characteristics of PE L19 spectrophotometer in visible and infrared region.

5.6.1 Determination of thickness, d .

The thickness values determined by the methods described in section 5.2.3 for as-grown CdTe layers are listed in Table 5.1. The estimates d_1 and d_4 were made by measuring steps at different points on the film and then taking the average. It was thought that thickness might also be measured at the edge of the layer, eliminating the need for scribing the layer. However, since the thickness at the edge of the layer varied smoothly due to the nature of the growth, this was not a suitable approach. It was found that the measured values of d by α -step were slightly different to values obtained by the other methods. One possible reason for the slight differences might be that, as discussed previously, in scribing the layer to form the step, it was always possible that the underlying substrate was scribed as well, resulting in an over-estimate of the layer thickness (note that when a glass substrate was scribed and measured with a α -step 200, the depth of the scribe mark was found to be 10–15 nm).

The graphical method did seem to be more appropriate since one obtained the fringe order number, m straightaway as well as the thickness. The interference fringe method gave very similar values to those obtained by using graphical method. The thickness variation of the layers were also calculated. The change

in the interference fringe peak separation was measured with the layer in two positions, 4 mm apart. Variation in thickness was found to be about 40 nm for a typical CdTe layer, which shows that the layers were quite uniform in thickness.

$\bar{d}_1(\mu m)$	$\bar{d}_2(\mu m)$	$\bar{d}_3(\mu m)$	$\bar{d}_4(\mu m)$
1.691	1.705	1.705	1.710
0.849	0.839	0.839	0.837
0.655	0.664	0.664	0.660
2.175	2.167	2.167	—
2.182	2.158	2.158	—

Table 5.1 — Thickness values obtained by different measurement of techniques, (i.e. \bar{d}_1 = Direct measurement by α -step, \bar{d}_2 = Graphical method, \bar{d}_3 = Interference fringe method, \bar{d}_4 = Multiple beam interferometer method).

5.6.2 Determination of Refractive Index, n_f .

Fig.5.4 shows the normal incidence transmission spectra in the infrared and visible range for a typical CdTe layer. Strong absorption was observed at wavelengths less than 832 nm where the transmission virtually ceased. In the region of weak absorption, sharp interference fringes due to the parallel interfaces of the layer were apparent.

Optical constants and film thickness were determined in the region of weak absorption, using the uniform thickness approach (i.e. “Flat Analysis”) described in section 5.2. Fig.5.5 shows refractive index as a function of wavelength for a typical layer. Refractive index, n_f values were found to be in good agreement with those for bulk single crystal CdTe (about 0.8% lower), confirming that the method for uniform films was appropriate and also that layers were quite uniform in thickness. They showed a quadratic dispersion (i.e. first-order Cauchy equation (i.e. $n_f = a\lambda^{-2} + b$)). Assuming such a function to be appropriate, a least-square fit of the n_f -values yielded (in this example) $n_f = 0.16\lambda^{-2} + 2.66$ (for λ in μm).

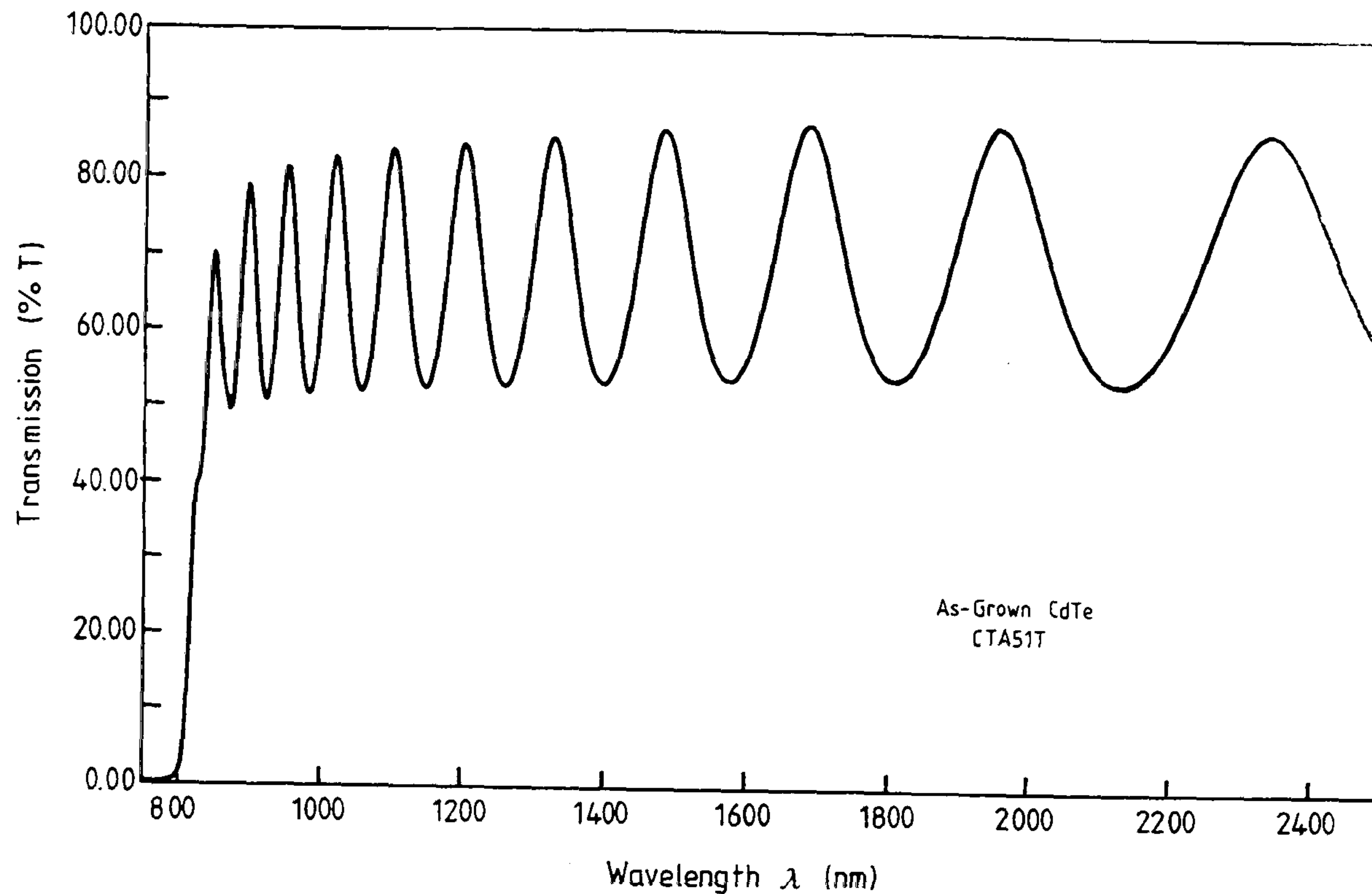


Figure 5.4 — Transmission spectrum for a typical $2.175\mu\text{m}$ thick film of CdTe on a glass substrate.

5.6.3 Determination of α_f , and k_f .

Extinction, k_f and absorption, α_f coefficients (see Fig.5.6 and Fig.5.7) increased progressively as the wavelength decreased. It can be seen that there was some absorption at long wavelengths giving rise to a reduction in the percentage transmission. The reasons for that might be due to;

1- Surface Scattering due to Surface Roughness:

Several authors have treated the effects of surface roughness on the reflectance and transmission of bulk surfaces and thin films, studying in particular, the dominant terms in the ratio of reflectance from a rough surface relative to a smooth surface of the same material [3,12,13]. Szczyrbowski and Czapla [3], for example, found that the effect of surface roughness was significant in InAs thin films in the transparent region, where the absorption coefficients are small. However the CdTe layers grown on glass substrates seemed to be, in general quite smooth with a specular surface

in the as grown condition. Hence it was unlikely that surface scattering played any role.

2- Grain Boundary Scattering and Structural Imperfections (i.e. deviation in stoichiometry, defects and impurities):

The presence of grain boundary and other structural imperfections can lead to spatial fluctuations in the optical constants of a material resulting in such anomalous transmission and reflection values. This is a more complicated problem than surface roughness. The grain boundary may be sufficiently disordered that it is in effect in an amorphous state, or it might form a sink for various impurities which can create internal electric fields. Such fields cause excess absorption at the low energy side of the absorption edge (i.e. Franz-Keldysh effect [14]). Bugnet [15] has studied excess absorption in reactively sputtered polycrystalline ZnS films, and found that excess absorption near the band gap could be attributed to the Franz-Keldysh effect at the grain boundary. However, at longer wavelengths the excess absorption was more probably due to other defects and impurities. The SIMS analysis (section 6.5) showed that CdTe layers grown here contained some unwanted and uncontrolled impurities (such as Si, Al, Na, Fe, Cu, Cr, Cl, K, and S) due possibly to the vacuum environment and glass substrates. Such impurities could give rise to additional absorption at long wavelengths. Due to the polycrystalline nature of the layers which had grain sizes having $<0.1\mu\text{m}$, scattering at grain boundaries would presumably have been occurring. However this would be expected to affect the shorter wavelengths where the grain size was of comparable dimension to the wavelength.

3- Free Carrier Absorption and Reflection:

A free carrier moving inside a band can make a transition absorbing a photon. Such a transition requires an additional interaction with the lattice to conserve the momentum. The change in momentum can be provided by interaction with the lattice by way of phonons or by scattering from ionized impurities [16,17]. Since typical as-grown CdTe layers were slightly *p-type*, it is believed that the effect of free carrier absorption and reflection at long wavelengths were negligible.

As discussed in section 5.2.2 the rate of increase in α_f at the band edge with photon energy ($h\nu$) depends on the type of transition taking place, i.e.

$$\alpha_f \propto (h\nu - E_g)^\xi \quad [5.15]$$

where $\xi = 1/2, 3/2$, for allowed direct and forbidden direct transitions respectively (since CdTe is a direct gap semiconductor, indirect transitions are not important). Clearly, graphs of α^2 vs $h\nu$ if allowed direct transitions are dominant, or $\alpha^{2/3}$ vs $h\nu$ for forbidden direct transitions, will give a straight line with an intercept on the $h\nu$ axis equal to the optical bandgap.

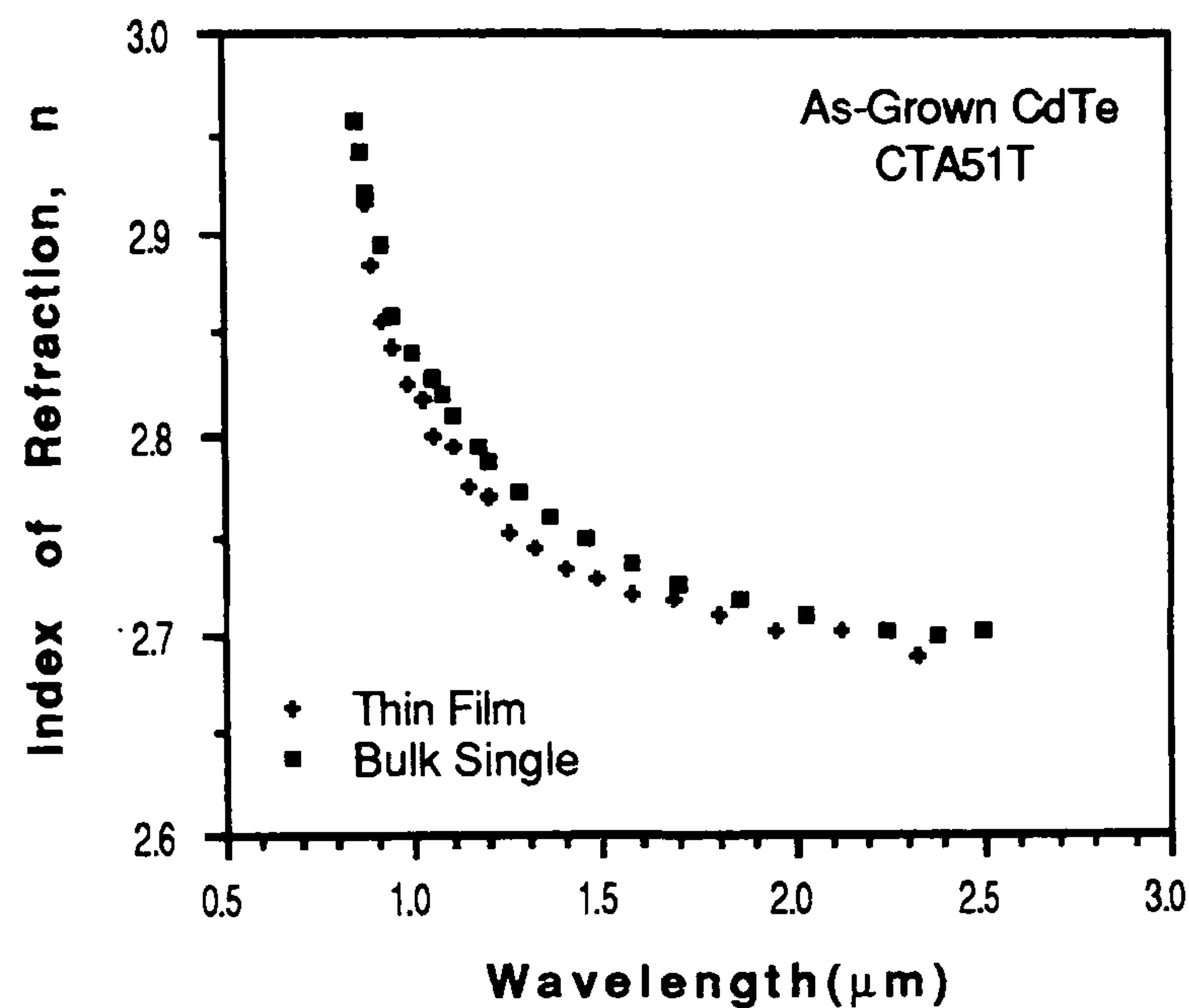


Figure 5.5 — Refractive index, n_f , vs wavelength characteristic of a typical as-grown CdTe layer.

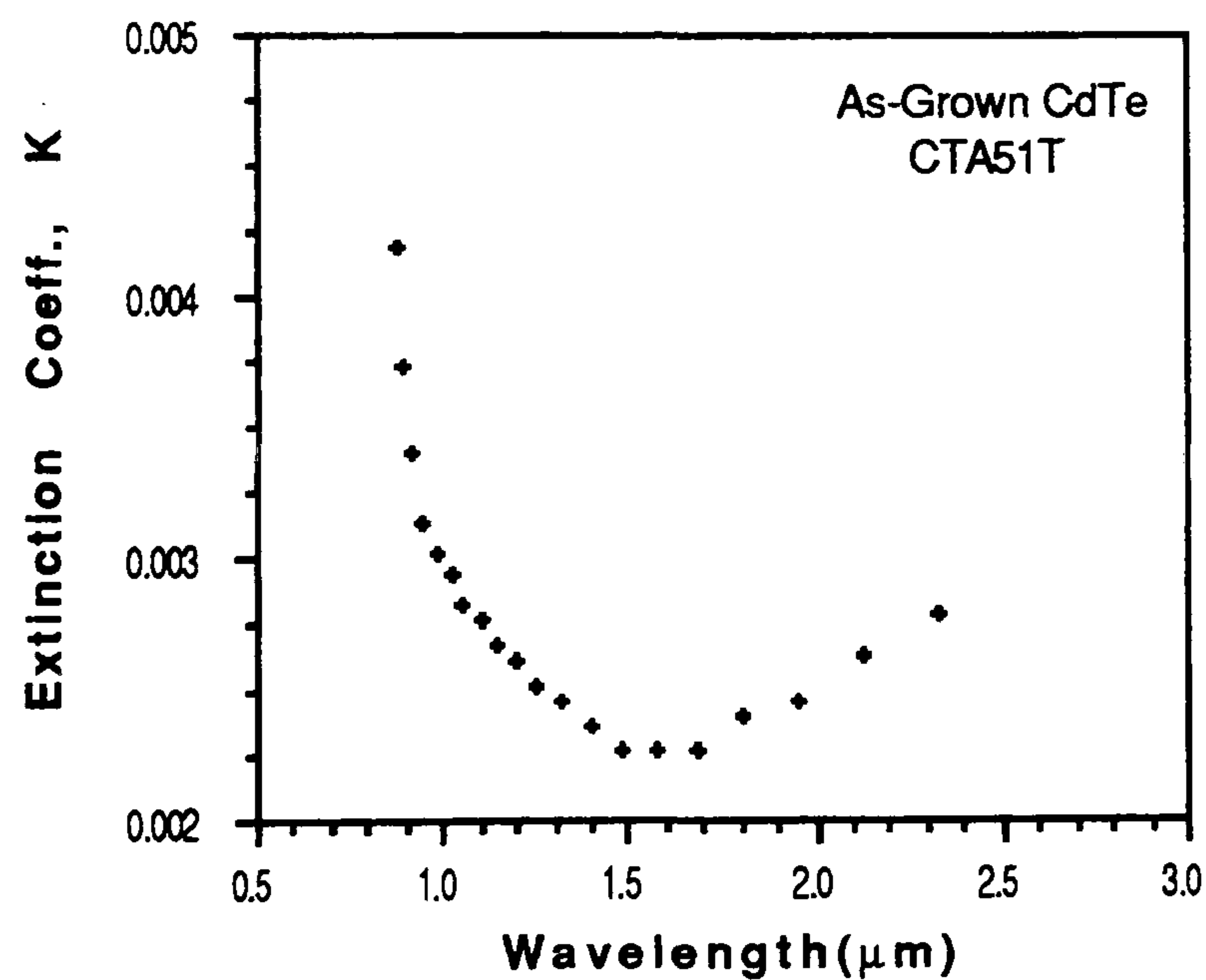


Figure 5.6 — Extinction coefficient, k_f , vs wavelength characteristic of a typical as-grown CdTe layer.

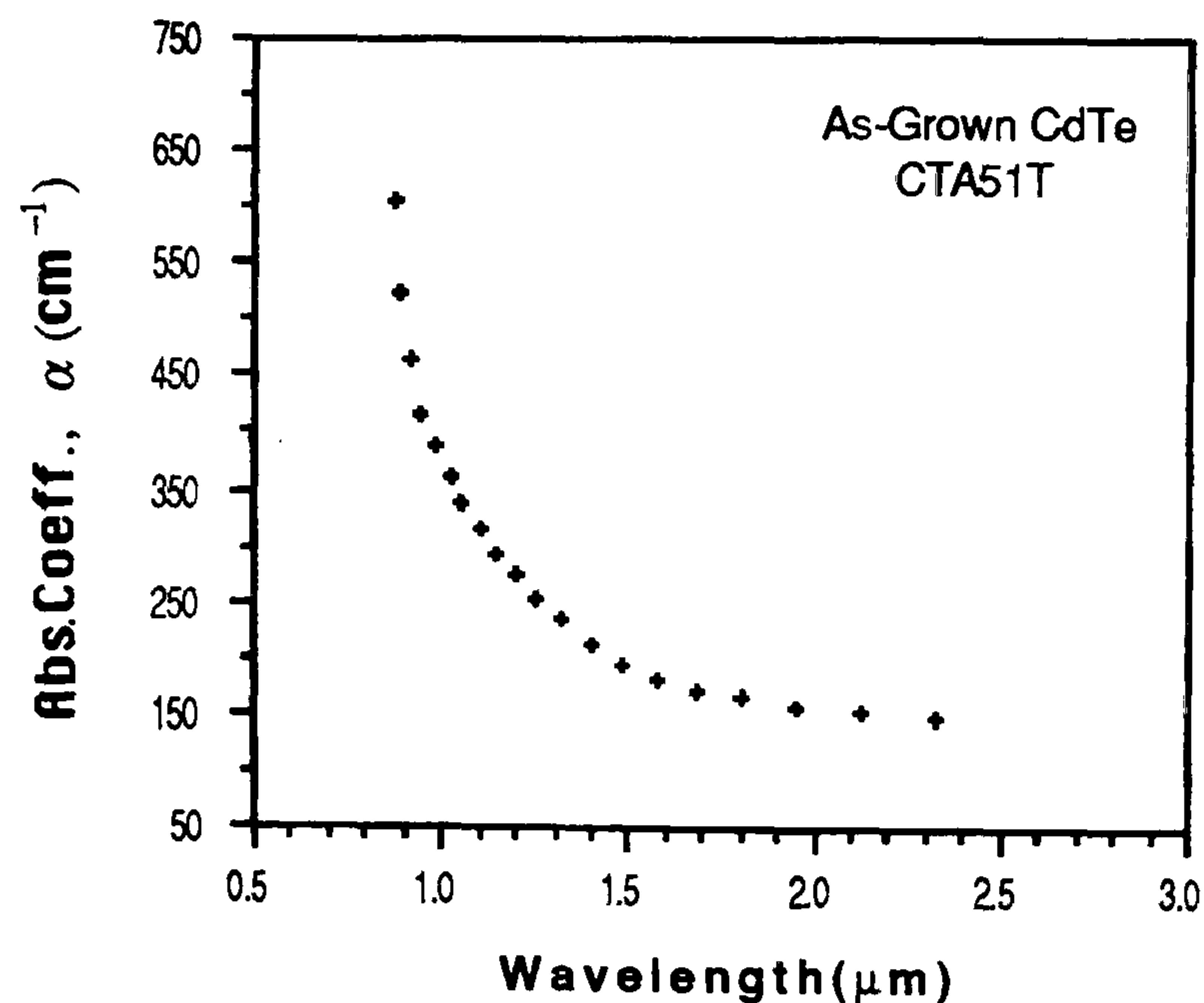


Figure 5.7 — Absorption coefficient, α_f vs wavelength characteristic of a typical as-grown CdTe layer.

Graphs of α^2 vs $h\nu$ and $\alpha^{2/3}$ vs $h\nu$ are drawn in Fig.5.8 and Fig.5.9 and the intercept values are given in Table 5.2. The direct bandgap E_g value of a typical CdTe layer was found to be 1.526 eV corresponding to allowed direct transitions occurring in the band and is similar to literature values (see Table 5.3). The slight differences might be due to different growth techniques and substrate temperatures used.

Transition Type	Index, ξ	Bandgap, E_g (eV)
Allowed Direct	1/2	1.526
Forbidden Direct	3/2	1.503

Table 5.2 — Optical bandgap E_g and ξ for both allowed and forbidden direct transitions for a typical as grown CdTe layer.

Room temperature, optical bandgap, E_g values given in the literature for typical CdTe thin films and bulk single crystals are given in Table 5.3 and Table 5.4 below respectively.

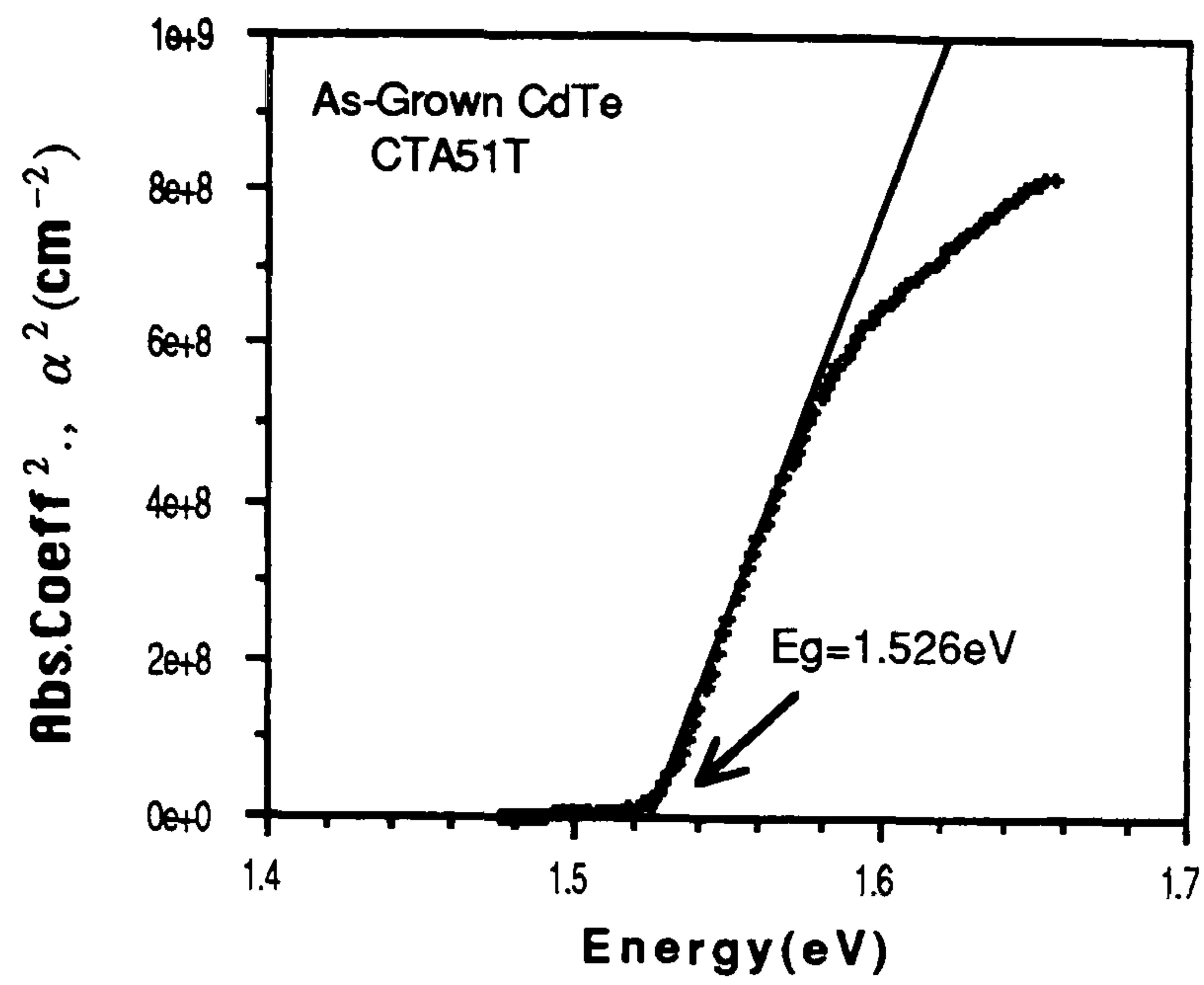


Figure 5.8 — α_f^2 vs $h\nu$ characteristic of a typical as-grown CdTe thin layer in the strong absorption region.

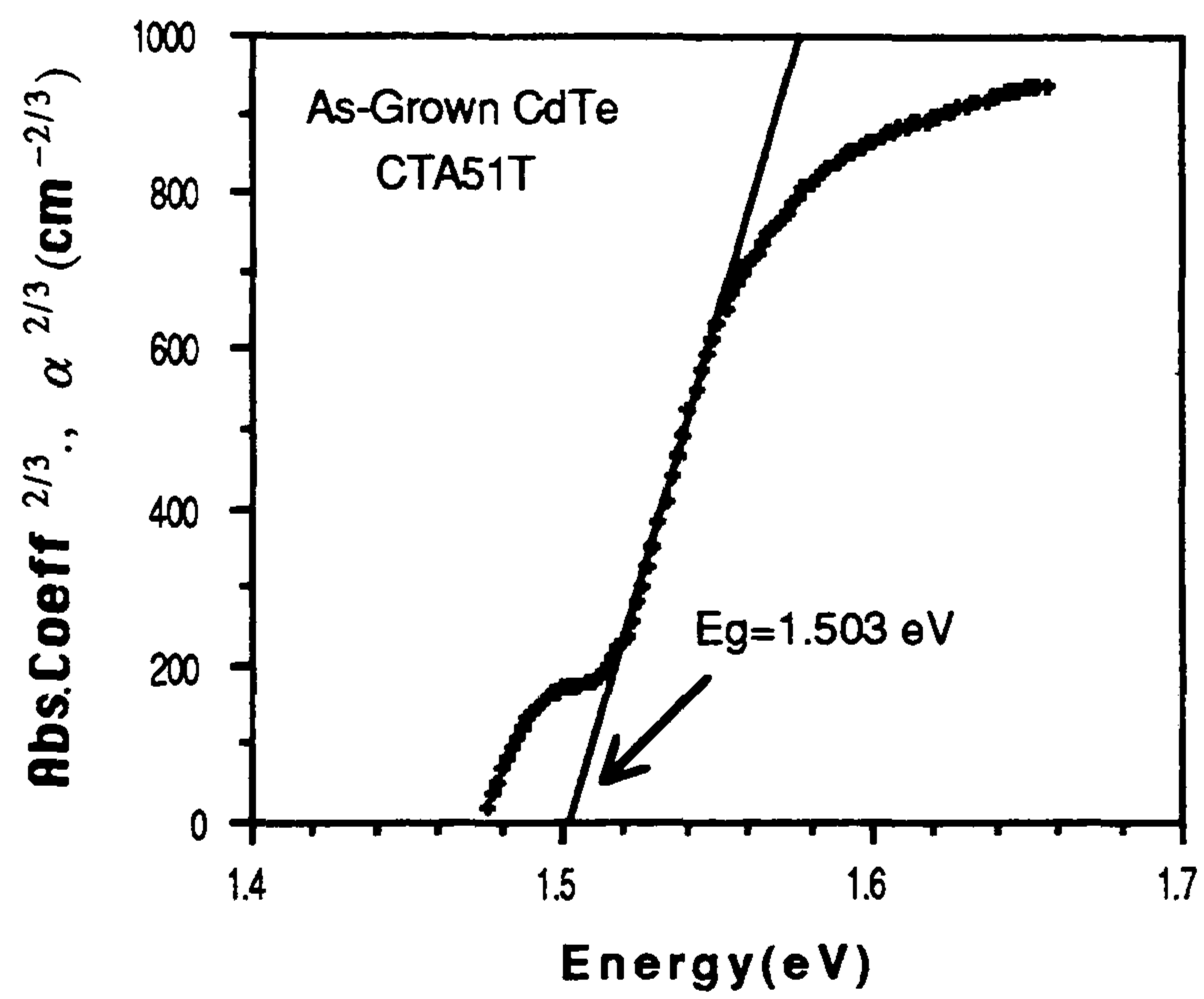


Figure 5.9 — $\alpha_f^{2/3}$ vs $h\nu$ characteristic of a typical as-grown CdTe thin layer in the strong absorption region.

Growth Technique	Subs. Temp.(°C)	E_g (eV)	Reference
Electrodeposition	————	1.510	18
Hot-wall Vac. Evap.	322	1.510	19
Vacuum Evap.	240–280	1.528	20
Vacuum Evap.	200	1.519	21
Vacuum Evap.	300	1.470	22
CVE	540–550	1.500	23

Table 5.3 — Published optical bandgap values for thin film CdTe.

Measurement Technique	E_g (eV)	Reference
Photoconductivity	1.470	24
Absorption	1.500	25
Photovoltaic effect	1.505	26
Thermoreflectance	1.500	27
Electroreflectance	1.495	28
Piezoreflectance	1.529	29

Table 5.4 — Published optical bandgap values for bulk single crystal CdTe.

In the as-grown case the absorption coefficients were consistently less than the bulk single crystal values (Fig.5.10). The difference in the two values of absorption coefficient $\alpha_{diff} \equiv \alpha_f - \alpha_{bulk}$ is shown in Fig.5.11, where, α_f , and α_{bulk} refer to the absorption coefficients of the film and bulk single crystal respectively. The values of α_{diff} reached a minimum at about 1.535 eV which was some 9 meV larger than the optical bandgap of the as-grown film. The origin of this is unclear but could be related to the additional excitonic absorption in the bulk single crystal material. However the temperature is rather high for this to be readily observed.

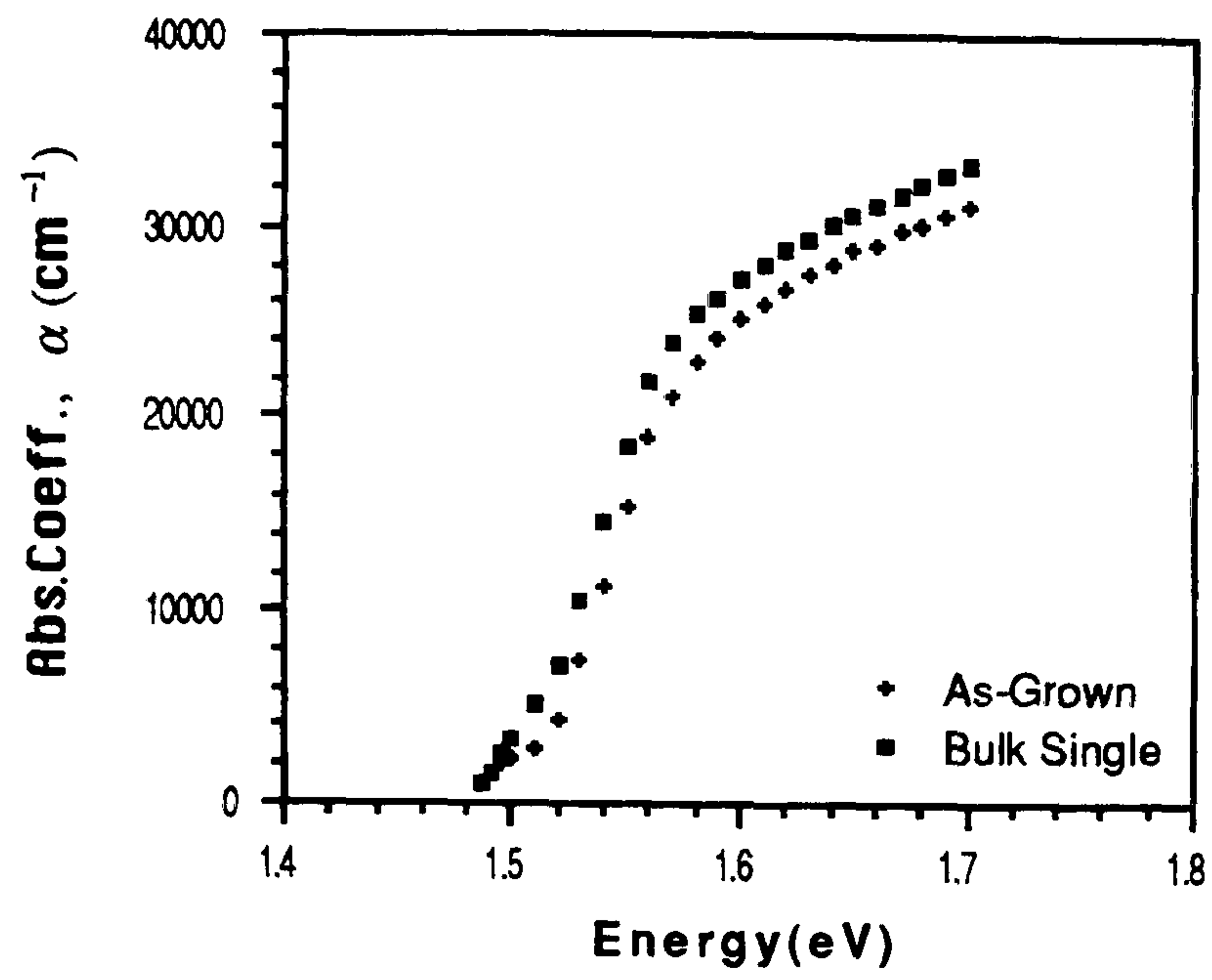


Figure 5.10 — α_f vs $h\nu$ characteristic of bulk single crystal and as-grown CdTe thin layer in the strong absorption region.

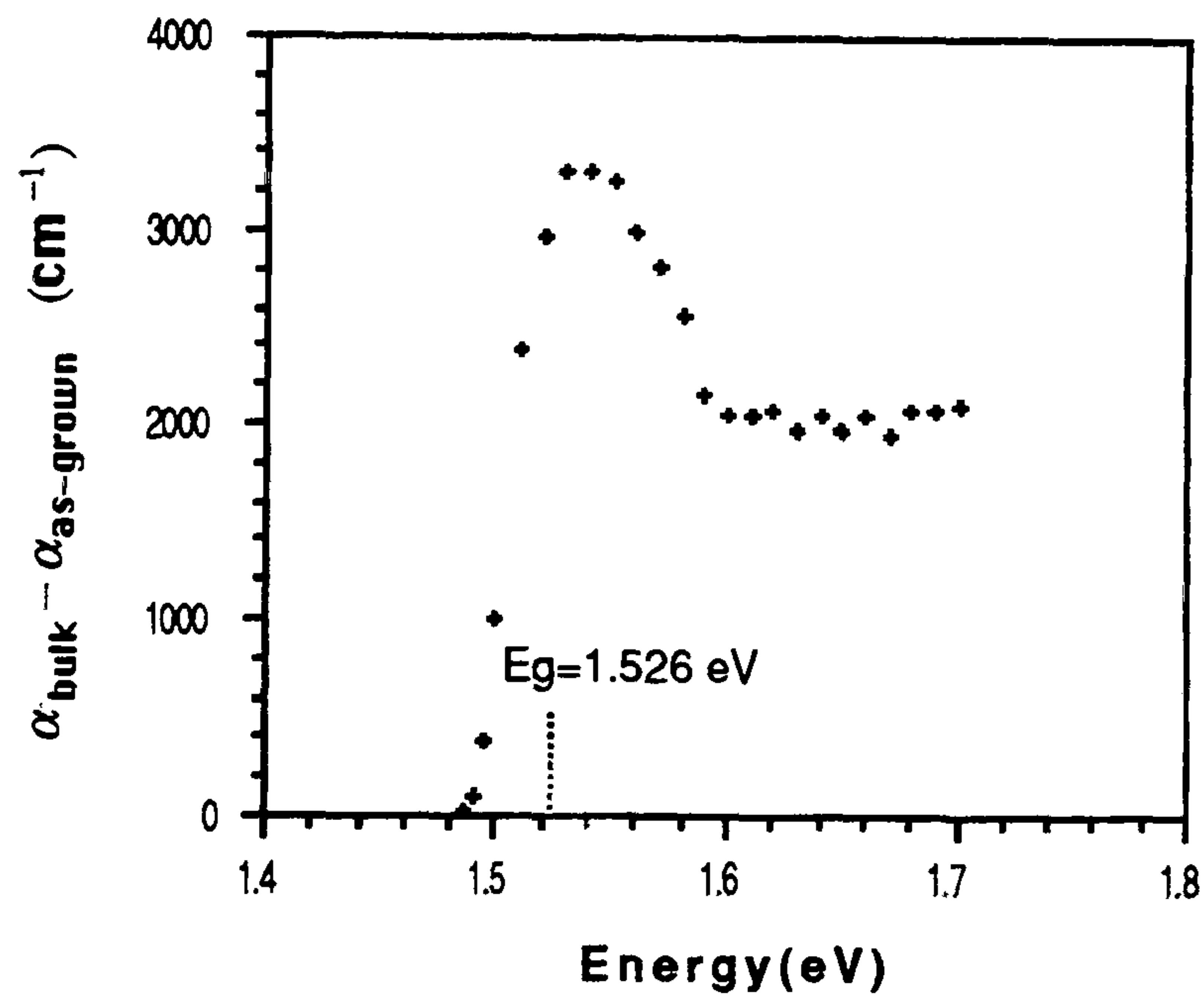


Figure 5.11 — Gap-states, $\alpha_{bulk} - \alpha_f$ vs $h\nu$ characteristic of a typical as-grown CdTe layer.

5.6.4 Determination of Urbach's constant, E_o .

For direct transitions between parabolic bands, the theory predicts a very steeply rising absorption edge, and no absorption below the energy bandgap. In practice, the absorption coefficient increases exponentially near E_g ; an empirical dependence sometimes referred to as *Urbach's Rule* [30]. *Urbach* found that in many materials, $d\ln(\alpha)/d(h\nu) \cong -1/E_o = -1/kT$. The absorption coefficient is plotted on a semilogarithmic plot in Fig.5.12. The slope gave an estimate for E_o of 18.9 meV for a typical CdTe layer which would correspond to a temperature of 219.4 K, somewhat below room temperature. The increased absorption near the bandgap is generally attributed to tail states probably associated with grain boundary states.

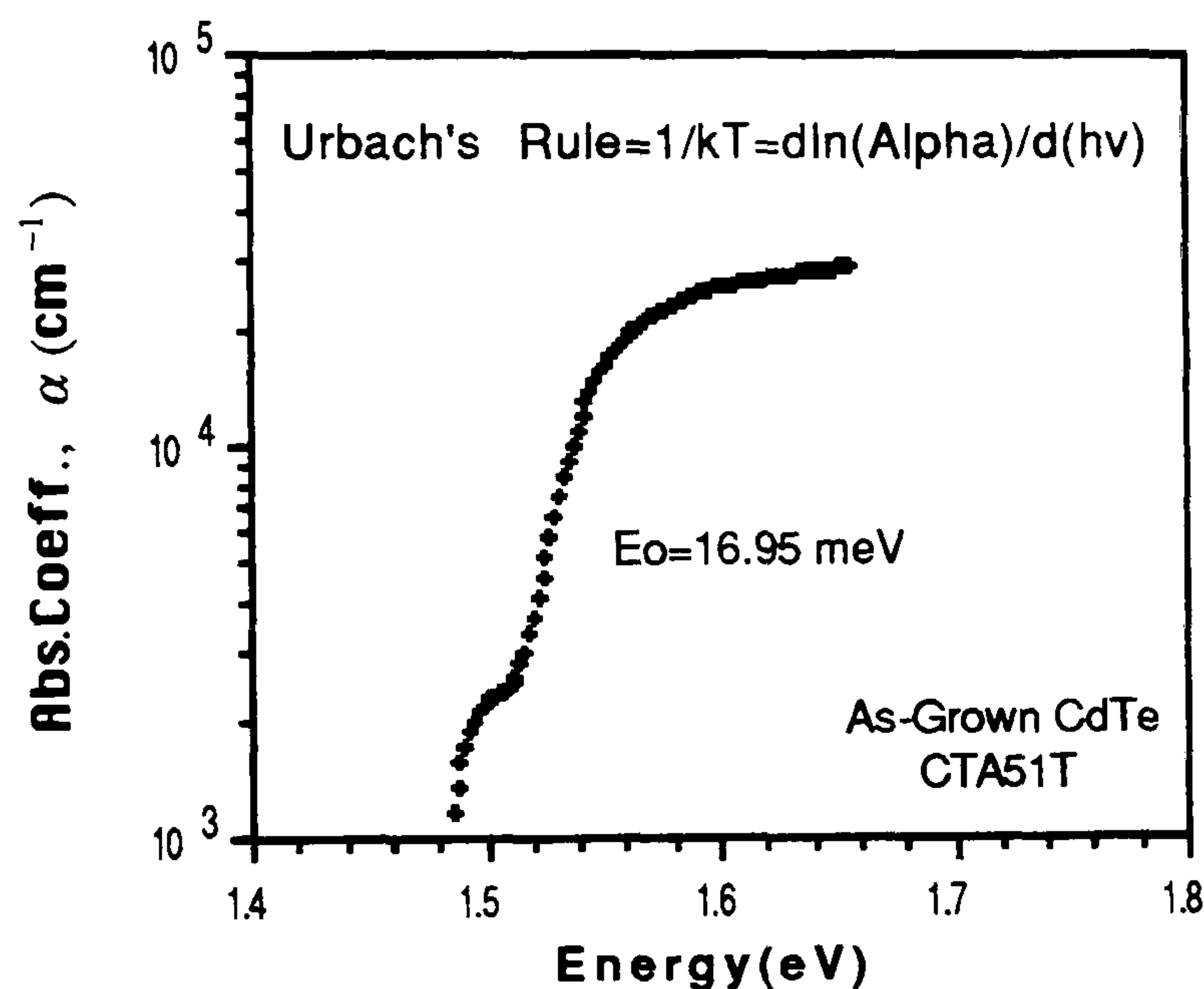


Figure 5.12 — $\log(\alpha_f)$ vs $h\nu$ characteristics of a typical as-grown CdTe layer.

5.6.5 Determination of dielectric constants, ϵ_1 and ϵ_2 .

For a transparent dielectric, the refractive index and extinction coefficient are related to the dielectric constants of the material by;

$$n_f^2 - k_f^2 = \epsilon_1 \quad \text{and} \quad 2n_f k_f = 2\frac{\sigma}{\nu} = \epsilon_2 \quad [5.16]$$

where ε_1 and ε_2 , σ and ν are the real and imaginary parts of the dielectric constant, the conductivity, and the frequency of the incident light respectively.

Fig.5.13 and Fig.5.14 show plots of the real and imaginary parts the of dielectric constant respectively for the same as-grown layer. Since the as-grown layers were quite highly resistive (i.e. $\rho \cong 10^8 \Omega\text{-cm}$) the layer was effectively insulating and $\varepsilon_1 \cong n^2$, $\varepsilon_2 \rightarrow 0$. Values of the relative dielectric constant ε_1 , for bulk single crystal CdTe given in literature are listed below.

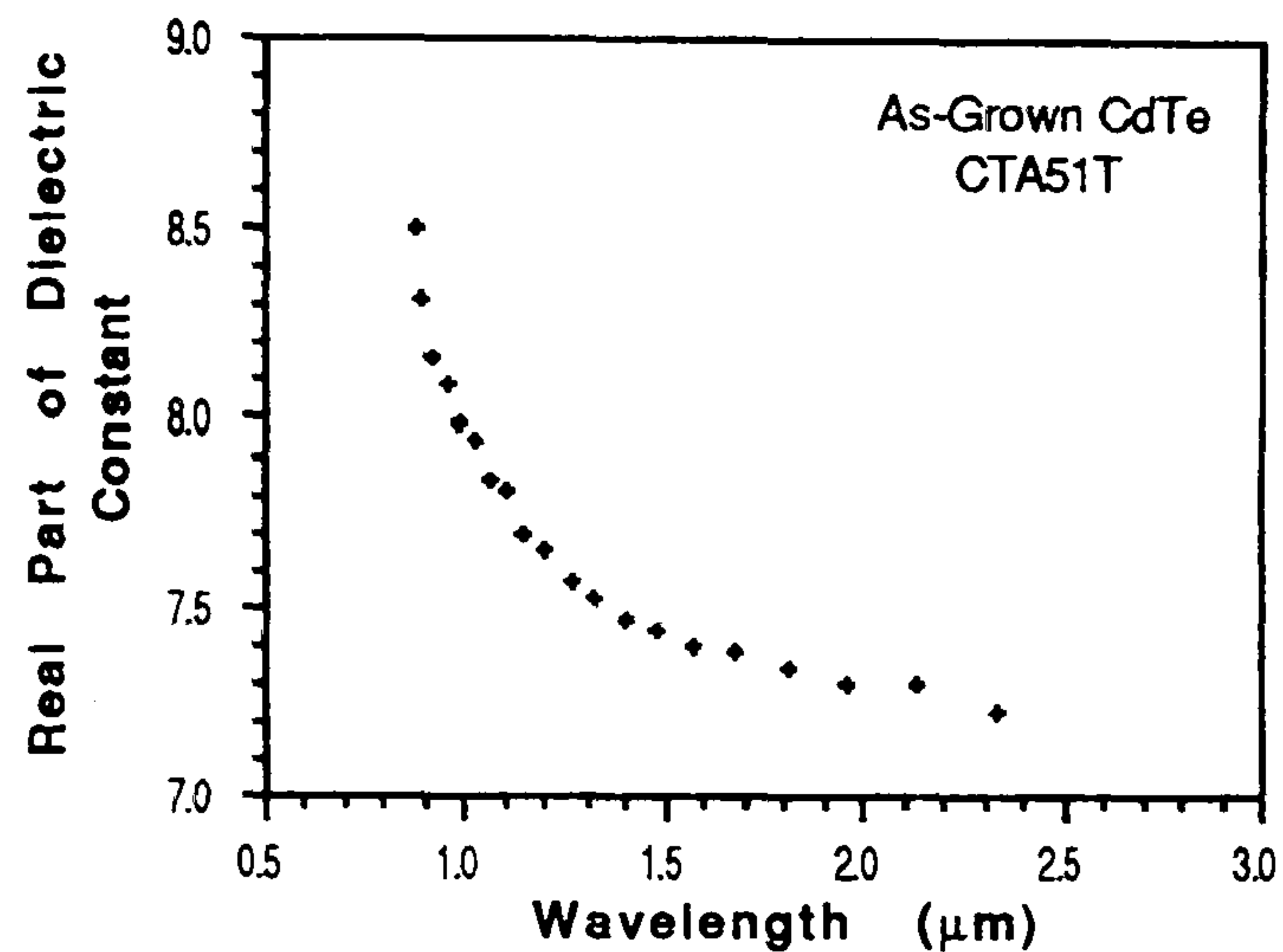


Figure 5.13 — Real part of the dielectric constant, ε_1 , vs wavelength of a typical as-grown CdTe thin layer.

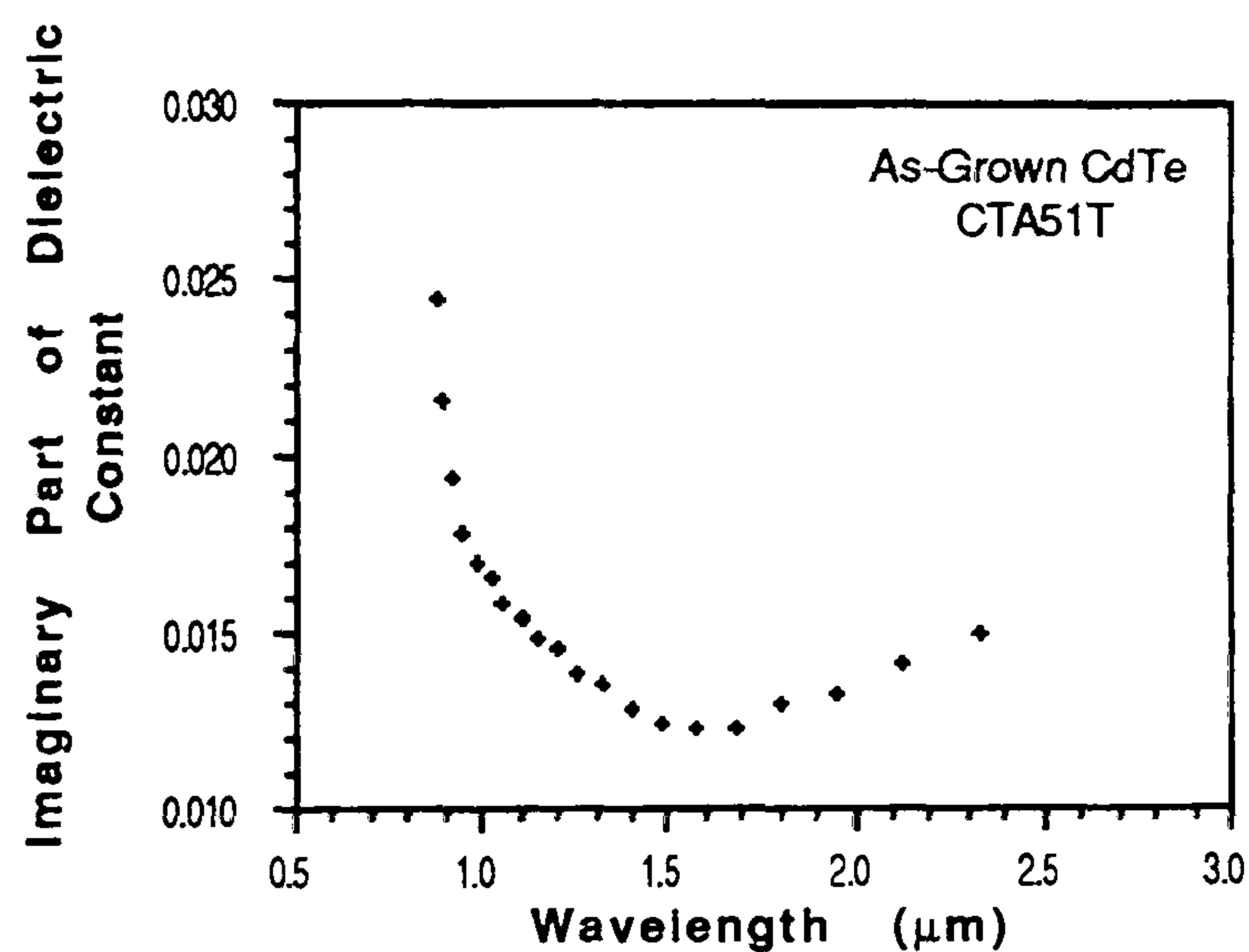


Figure 5.14 — Imaginary part of the dielectric constant, ε_2 , vs wavelength of a typical as-grown CdTe thin layer.

T(K)	$\lambda(\mu\text{m})$	Measurement	ϵ_1	References
100, 300	—	Reflection	7.10	31
77,300	—	Reflection	7.40	32
300	—	Reflection	7.20	33
300	2.5	Transmission(our value)	7.25	—

Table 5.5 — Dielectric constants of bulk single crystal and thin film CdTe grown here.

5.7 Heat treated CdTe thin films.

The optical properties of as-grown CdTe layers heat treated in air at 400°C for about 30 min were measured in the same way, in order to determine the effect of the treatment. Thickness measurements before and after heat treatment showed that there was a noticeable change in the thickness of the layer of about 37.5nm as measured by the α -step and 33.5nm when determined by the interference fringe method (i.e. corresponding to a reduction of 300 bilayers in the [111] direction). There was however, a substantial improvement in the transmission characteristics of the heat treated layers (see Fig.5.15). The absorption edge became much sharper and moved towards longer wavelengths.

The refractive index values of heat the treated layers were found to be in good agreement with bulk single crystal CdTe values (about 0.3% lower, see Fig.5.16). A least-squares fit of the refractive index, using first-order Cauchy equation yielded, $n_f = 0.18\lambda^{-2} + 2.67$ (for λ in μm). The extinction coefficient and absorption coefficients for the same layers are also shown as a function of wavelength in Fig.5.17 and Fig.5.18 respectively. These showed that there was additional absorption occurring near to the band edge ($\lambda \leq 1250$ nm).

The optical bandgap, E_g was estimated to be 1.507 eV (see Fig.5.19) which is 20 meV less than the bandgap value for the as-grown layers, but closer to published values of E_g for bulk single crystal CdTe.

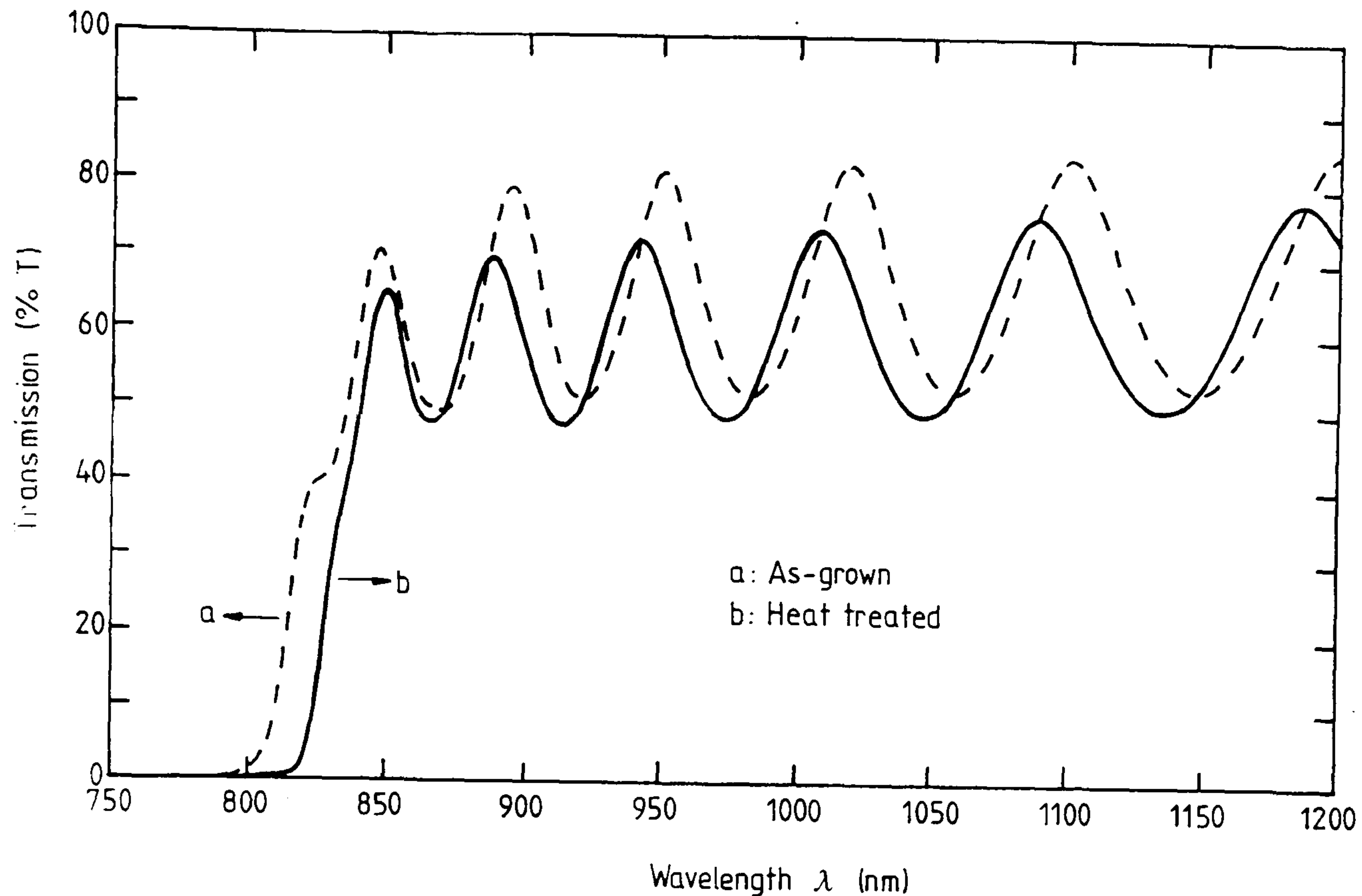


Figure 5.15 — A typical transmission spectrum of a heat treated CdTe thin layer.

In microcrystalline films where the grain size is relatively small, quantum confinement effects can lead to quantum states in the valence and conduction bands, which would open the band gap [34]. This effect has been reported in CdSe films with small grain size [35]. Since the heat treatment was found to result in an average grain size of the CdTe layers of ~ 78 nm to ~ 100 nm, the observed shift at the band edge to lower energy could be explained in terms of the change in grain size. However it is more probable that the heat treatment led to a change in the stoichiometry of the layer due to loss of Cd [36]. This would result in the formation of shallow acceptor levels, giving in some increased optical absorption near the band edge. Similar effects would be associated with oxygen adsorption at grain boundaries [37]. Although it is generally believed that the effect of oxygen is to enhance the p-type characteristics of CdTe films [38], the exact nature of the oxygen-related acceptor states is not well understood.

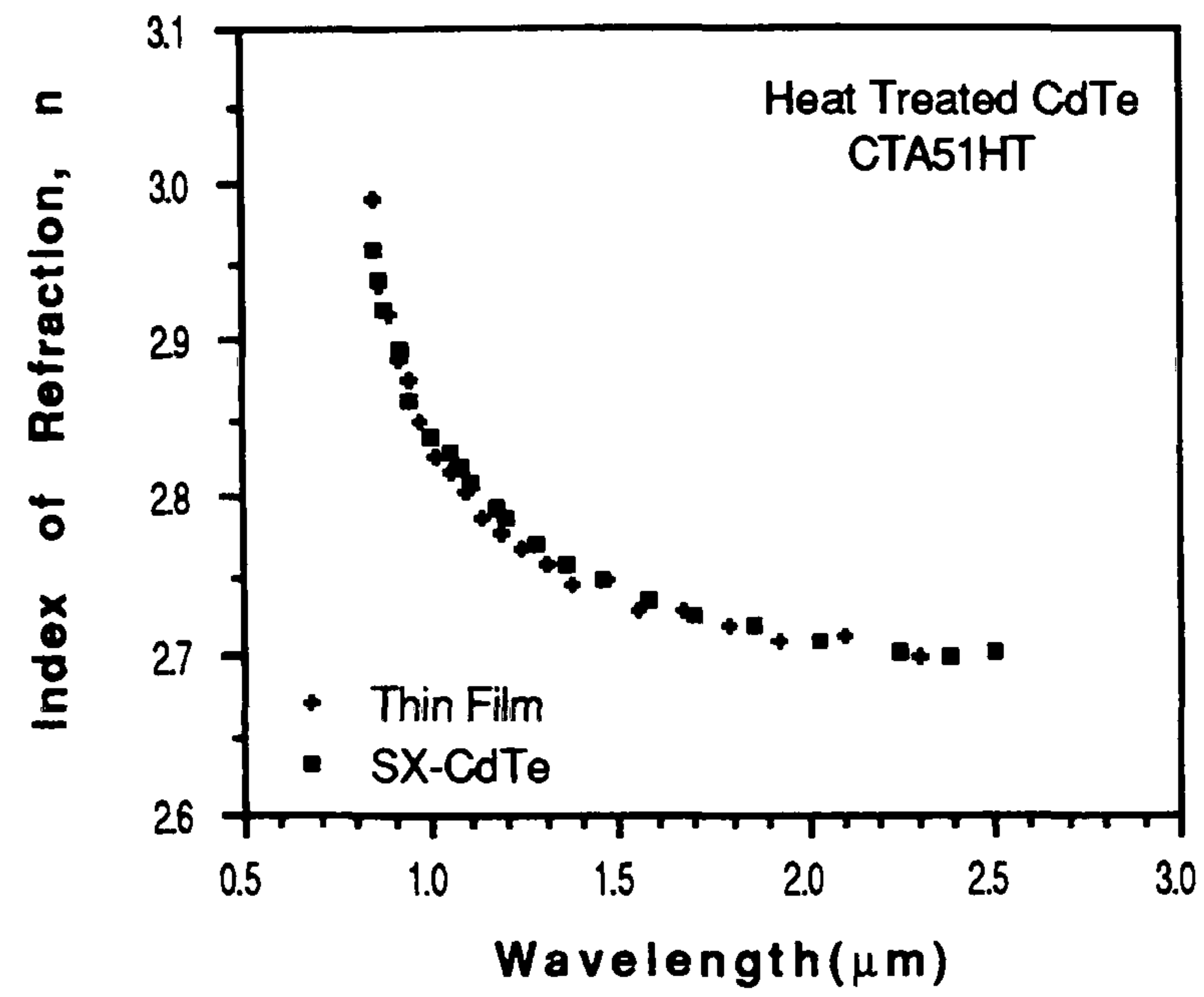


Figure 5.16 — Refractive index, n_f , vs wavelength characteristic of a typical heat treated CdTe layer.

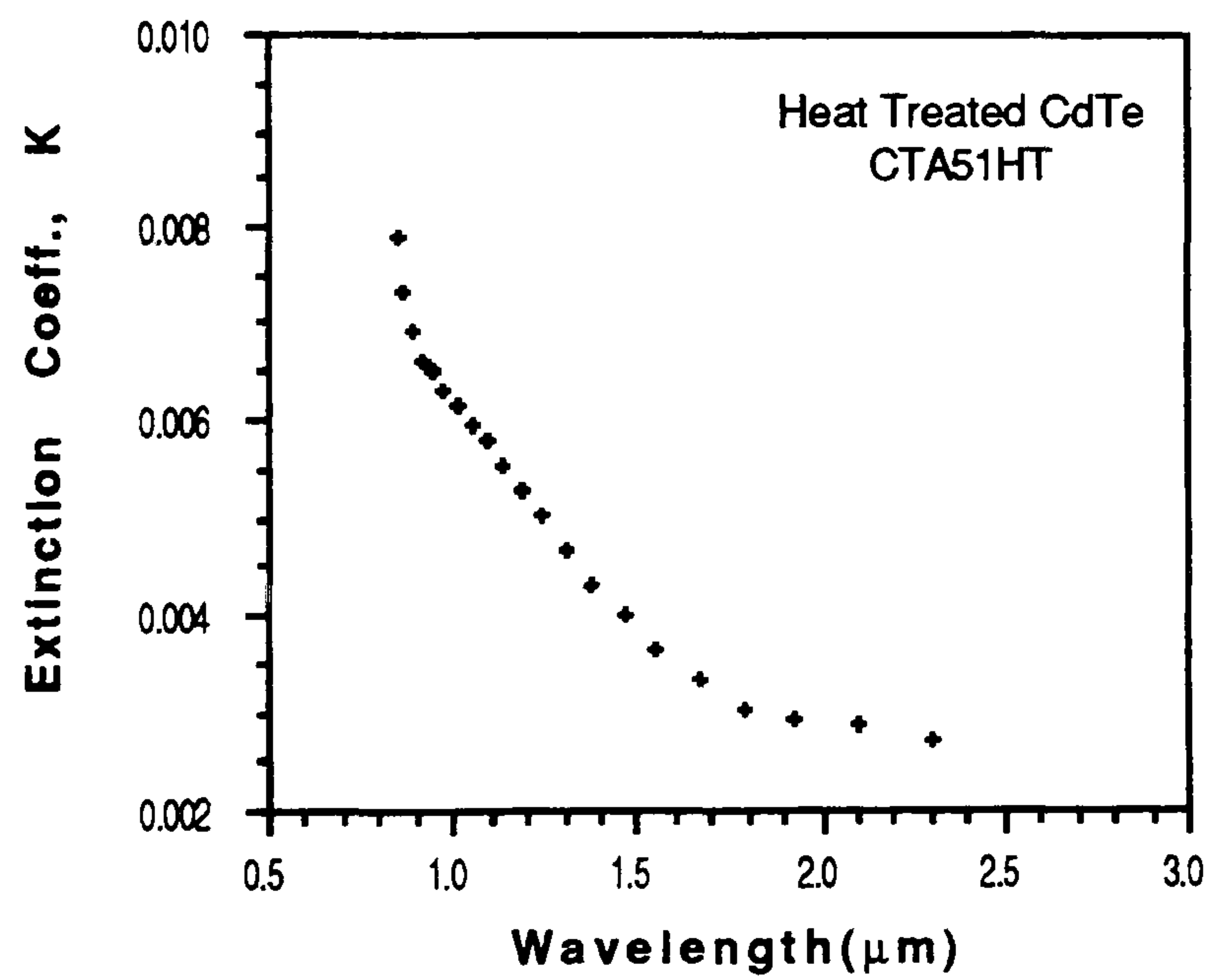


Figure 5.17 — Extinction coefficient, k_f , vs wavelength characteristic of a typical heat treated CdTe layer.

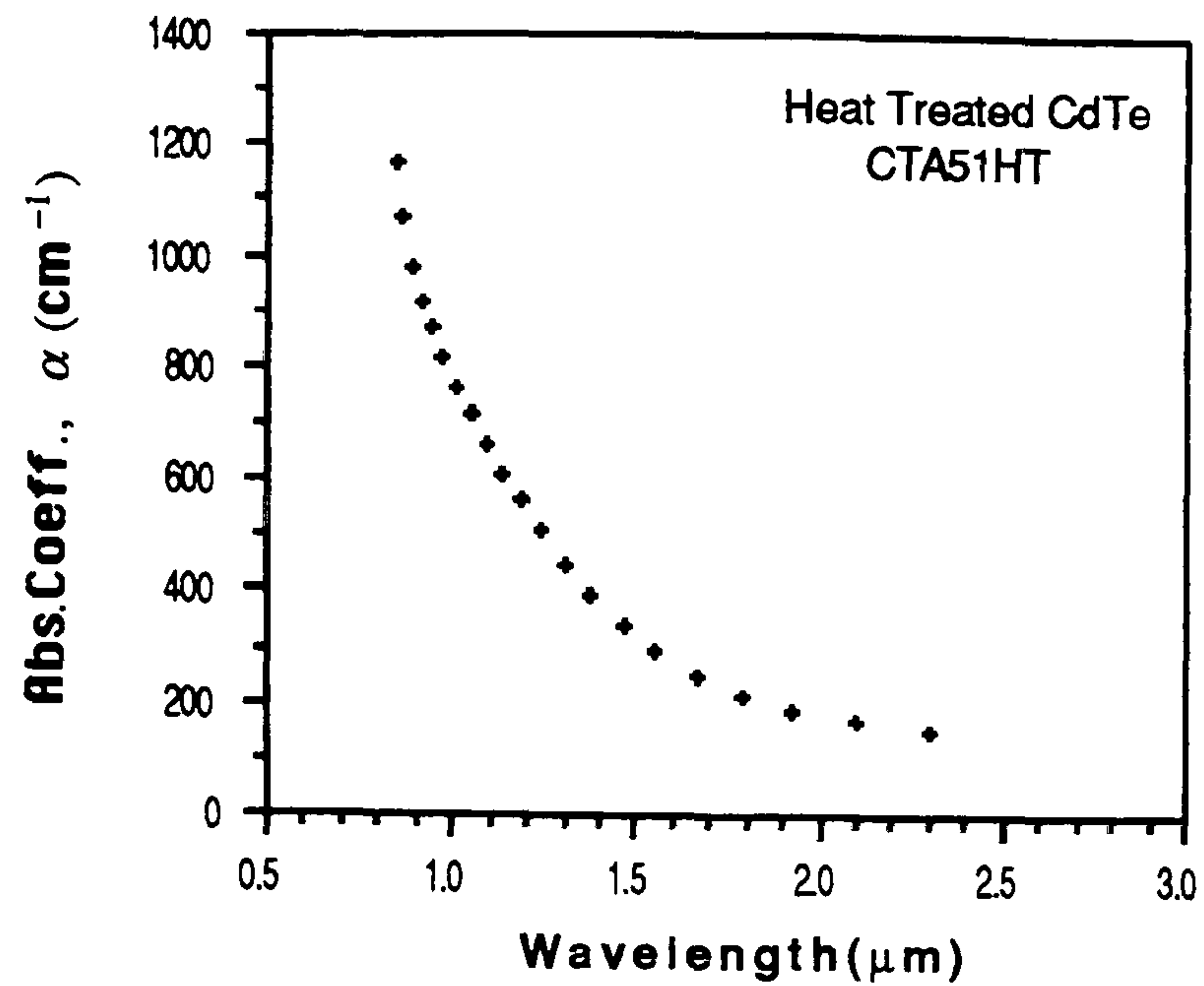


Figure 5.18 — Absorption coefficient, α_f vs wavelength characteristic of a typical heat treated CdTe layer.

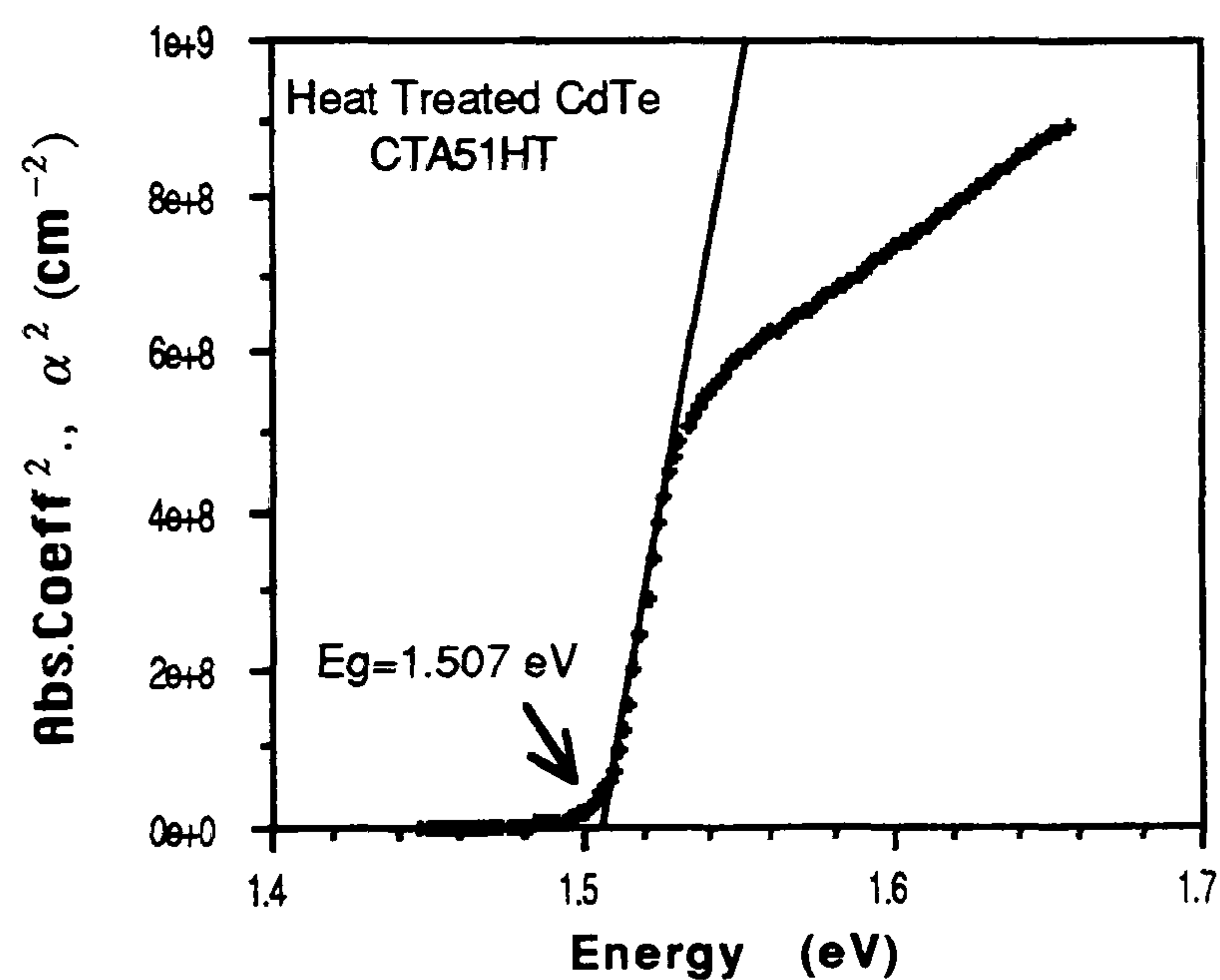


Figure 5.19 — α_f^2 vs $h\nu$ characteristic of a typical heat treated CdTe thin layer in the strong absorption region.

Fig.5.20 shows the absorption coefficient vs energy characteristics of bulk single crystal and heat treated thin films in the strong absorption region. Heat treated layers, unlike as-grown layers showed increased absorption below 1.59 eV, compared to bulk single crystal, but lower absorption at higher photon energies. The difference in absorption coefficients (α_{diff}) is plotted in Fig.5.21 and peaked at about 1.53 eV which was 23 meV higher than the optical bandgap measured for heat treated layers. This behaviour is in marked contrast to that observed with as-grown layers where α_{diff} showed a minimum just above the bandgap, rather than a maximum as seen here.

It is possible that the increased absorption is related to changes of stoichiometry, oxygen absorption, etc induced by the heat treatment, although these would have been expected to generate states within the bandgap (i.e. $< E_g$).

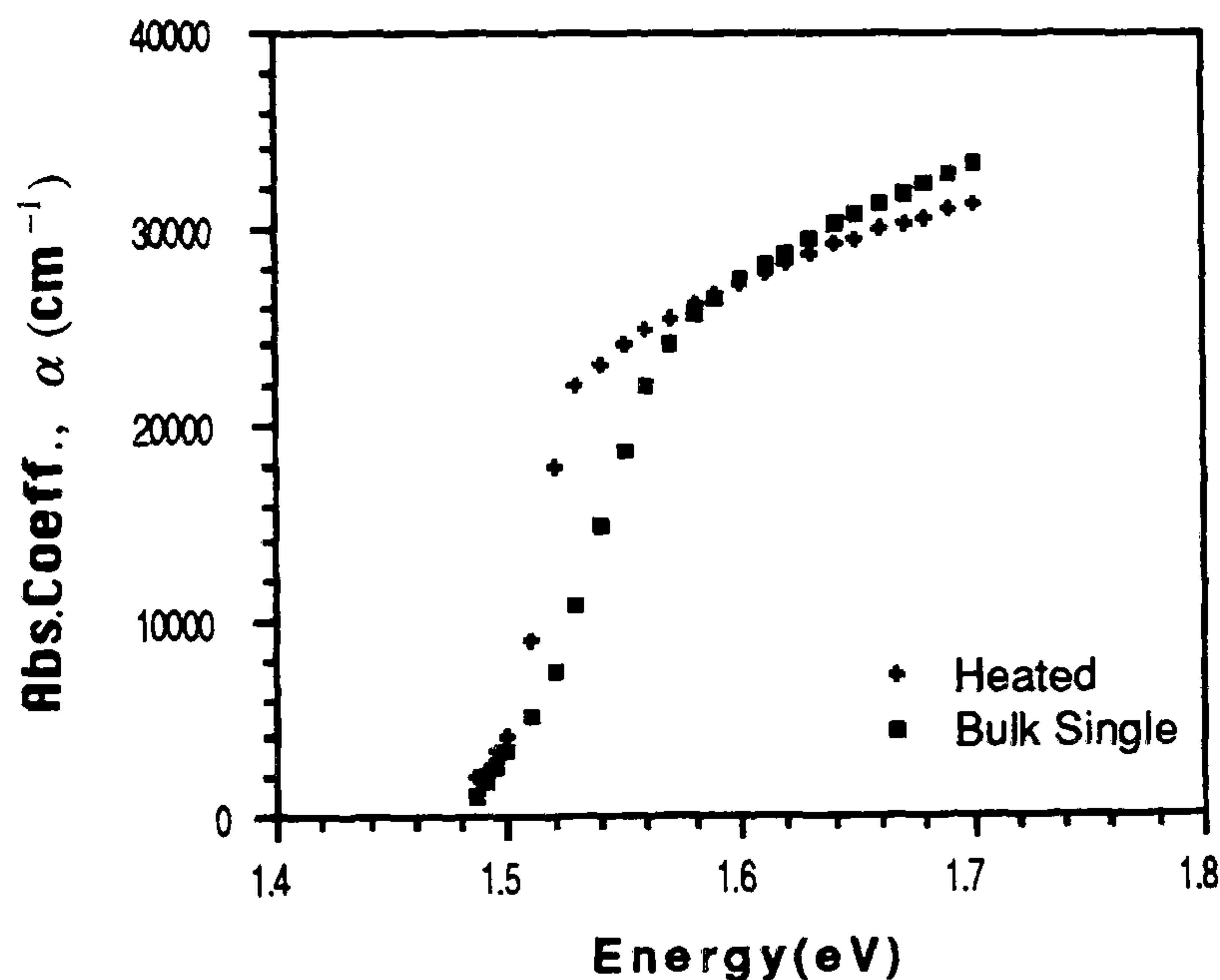


Figure 5.20 — α_f vs $h\nu$ characteristic of bulk single and heat treated CdTe thin film in the strong absorption region.

5.8 Cl₂ Doped CdTe thin films.

CdTe layers were doped with Cl₂ in attempt to reduce the resistivity. Three methods were used as described in section 3.4, namely dipping, predoping and co-evaporation. In the following sections, the optical constants of Cl₂ doped layers

will be determined, discussed, and compared with as-grown, heat treated and bulk single crystal CdTe values.

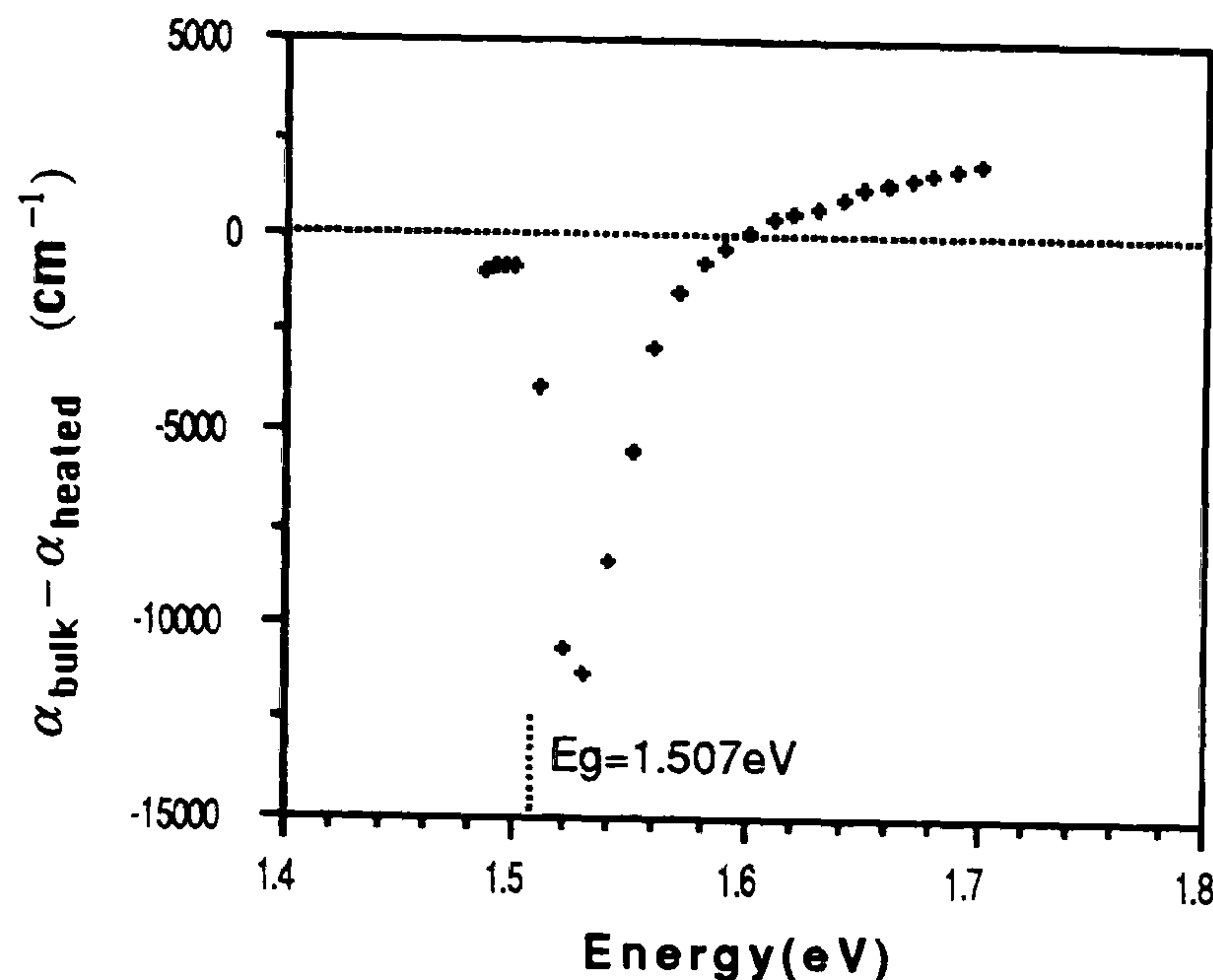


Figure 5.21 — Gap-states, $\alpha_{bulk} - \alpha_f$ characteristic of a typical heat-treated CdTe thin layer.

5.8.1 Cl₂ Dipped films.

Cl₂ dipped layers (i.e. dipped into CdCl₂+Methanol soln., followed by annealing in air at 400°C for about 30 min) showed the same sort of transmission characteristics as the heat treated layers. Fig.5.22, and Fig.5.23–5.25 show normal incidence transmission spectra and the optical constants of a typical dipped layer as a function of wavelength. The refractive index values obtained were in reasonable agreement to bulk single crystal CdTe, (1.6% lower), and a least-squares fit yielded, $n_f = 0.17\lambda^{-2} + 2.63$ (for λ in μm) for a first order Cauchy dispersion. Both extinction and absorption coefficients also showed very similar characteristics to those of heat treated layers.

The optical bandgap was found to be 1.507 eV which was identical to the heat treated films and bulk single crystal CdTe.

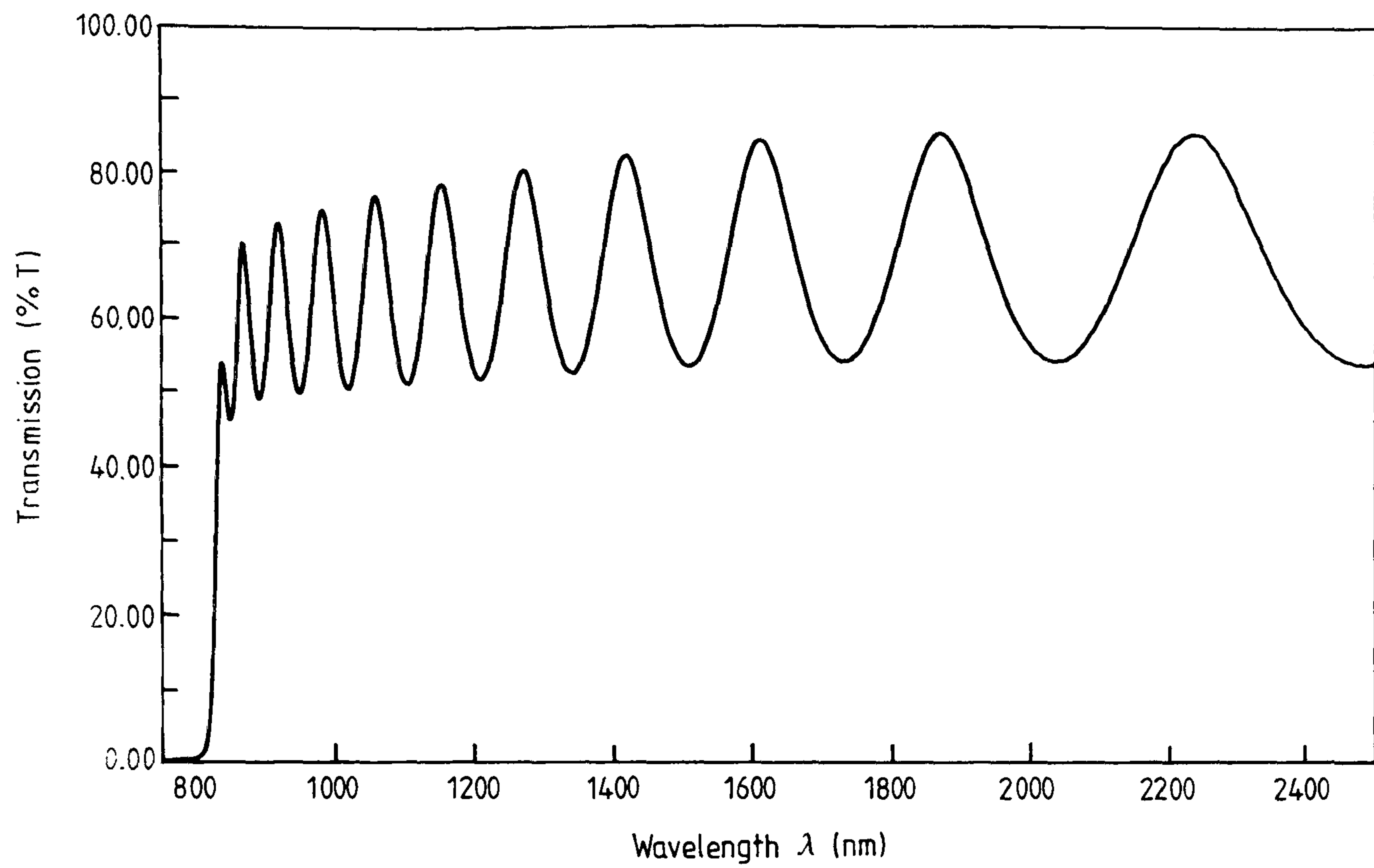


Figure 5.22 — A typical transmission spectrum of a Cl_2 dipped CdTe thin layer.

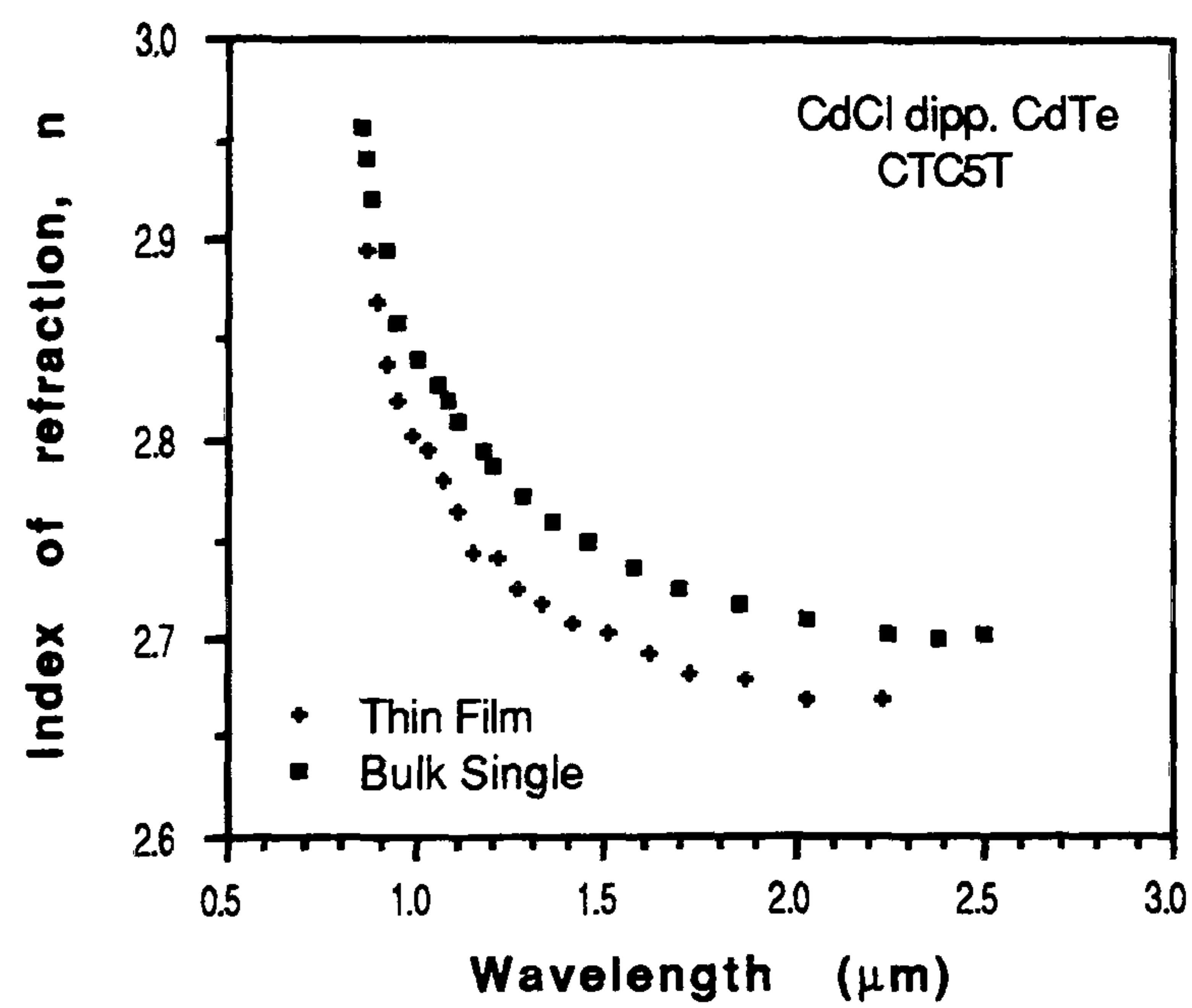


Figure 5.23 — Refractive index, n_f vs wavelength characteristic of a typical Cl_2 dipped CdTe thin layer.

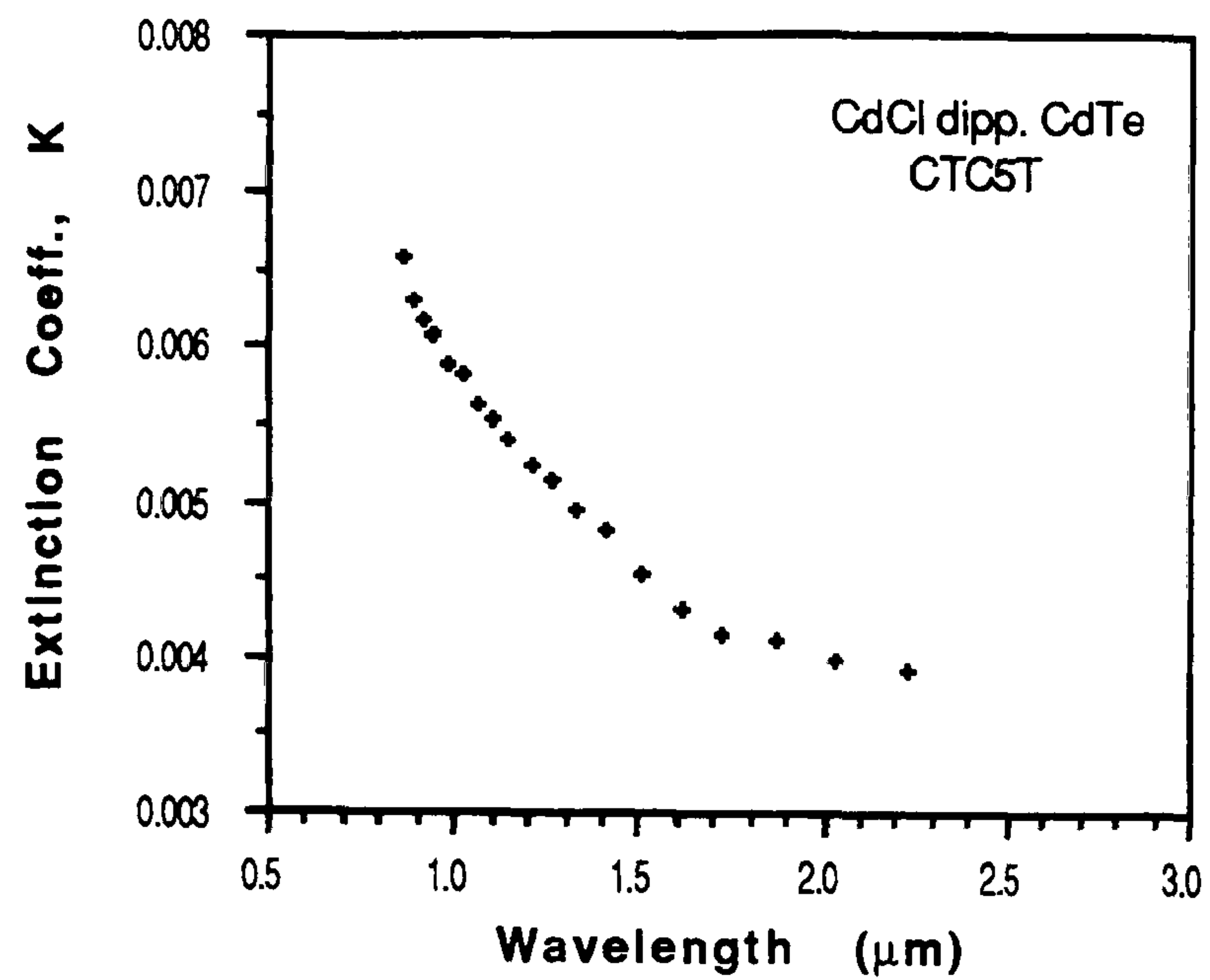


Figure 5.24 — Extinction coefficient, k_f vs wavelength characteristic of a typical Cl_2 dipped CdTe thin layer.

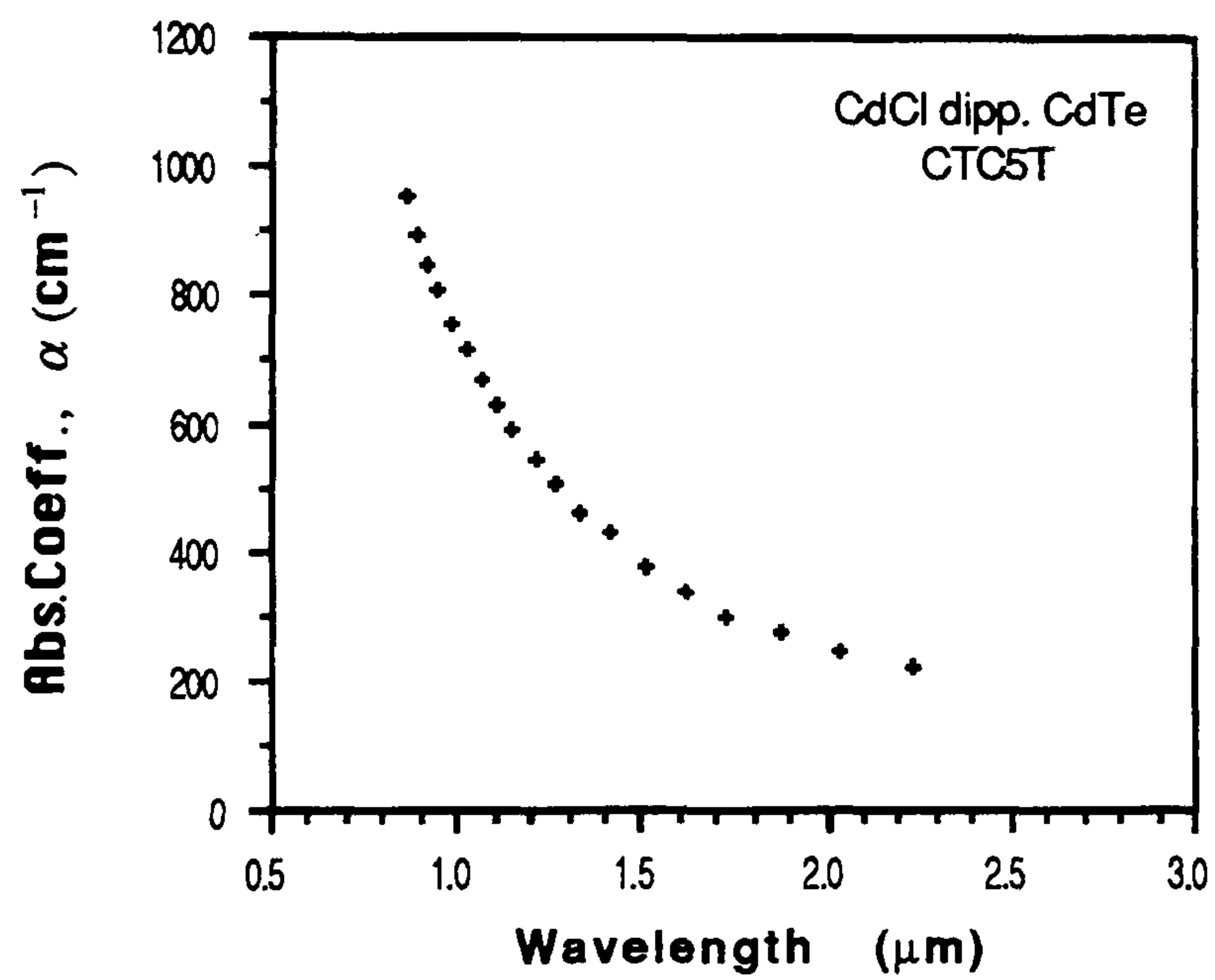


Figure 5.25 — Absorption coefficient, α_f vs wavelength characteristic of a typical Cl_2 dipped CdTe thin layer.

5.8.2 Cl₂ Predoped films.

The layers grown using Cl₂ predoped starting material showed a remarkable change in the transmission (see Fig.5.26). There was a progressive increase in absorption as the wavelength approached the band edge. Fig.5.27–5.29 show the optical constants as a function of wavelength in the region of weak absorption. The refractive index values were calculated just in the spectral region where the interference fringes had not been too seriously affected by additional absorption. They were found to be close to bulk single crystal CdTe values, and fitting (least-squares) to a first-order Cauchy equation yielded $n_f = 0.23\lambda^{-2} + 2.66$ (for λ in μm).

The optical bandgap was estimated to be 1.452 eV, which was quite low compared to the other types layer (e.g., 73.8 meV lower than Cl₂ dipped layers). This could be attributed to the Cl₂ associated centers disturbing the transmission characteristics or to the method leading to erroneous results in the presence of greater absorption.

Fig.5.30 and Fig.5.31 show the absorption coefficients, α_f , α_{bulk} and the difference in absorption coefficients, α_{diff} characteristics of a typical dipped layer. Similar characteristics for predoped layers are also shown in Fig.5.32 and Fig.5.33. The Cl₂ dipped layer showed a peak at about 1.53 eV, in the α_{diff} vs $h\nu$ characteristics, some 23.5 meV higher than the optical bandgap. Conversely, the predoped material had reached its maximum at about 1.49 eV. In the predoped case, the peak could be associated with Cl-related gap states since the maximum lies in the middle of the bandgap.

5.8.3 Effect of Cl₂ doping.

It is clear that Cl₂ dipped layers showed the same properties as heat treated layers, with optical bandgap values that were within experimental error the same. Introducing Cl₂ by dipping followed by annealing in air did not seem to have a noticeable effect on the properties of the layers. It is believed that incorporation and interdiffusion of Cl₂ is a limited process in which annealing might lead to desorption from the surface.

Predoped layers, on the other hand, showed markedly different optical properties with significant absorption, even at long wavelength limits. This may be associated with a Cl-V_{Cd} complex. Then in this case, the following equilibrium reactions might occur [39];



These four different species may also introduce the following levels in the material;

Donor: $[\text{Cl}^+]$, $E_c - 0.02\text{eV}$ [40]

Acceptor: $[\text{V}_{\text{Cd}} \text{Cl}]^-$, $E_v + 0.14 \text{ eV}$ [40] and $V_{\text{Cd}}^{\bar{\bar{}}}$, $E_c - 0.7 \text{ eV}$ [41]

Electron-trap: $[\text{V}_{\text{Cd}} 2\text{Cl}]$, $E_c - 0.06 \text{ eV}$ [40,42].

It is also possible that the pre-doped films were not as dense as the other films and that the optical transmission spectra were therefore affected by scattering and transmission through the pin-holes present in the layers.

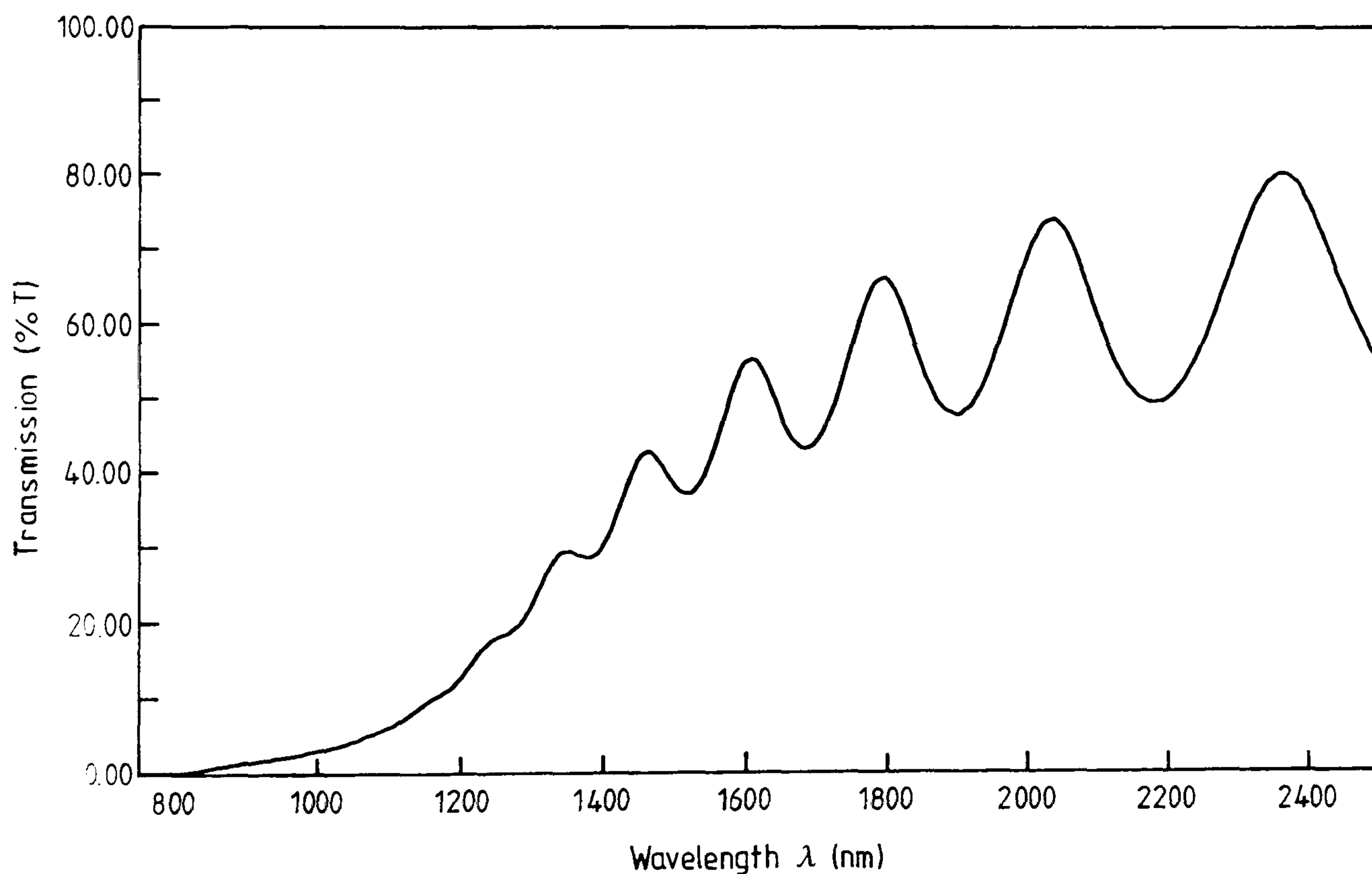


Figure 5.26 — A typical transmission spectrum of a Cl_2 pre-doped CdTe thin layer.

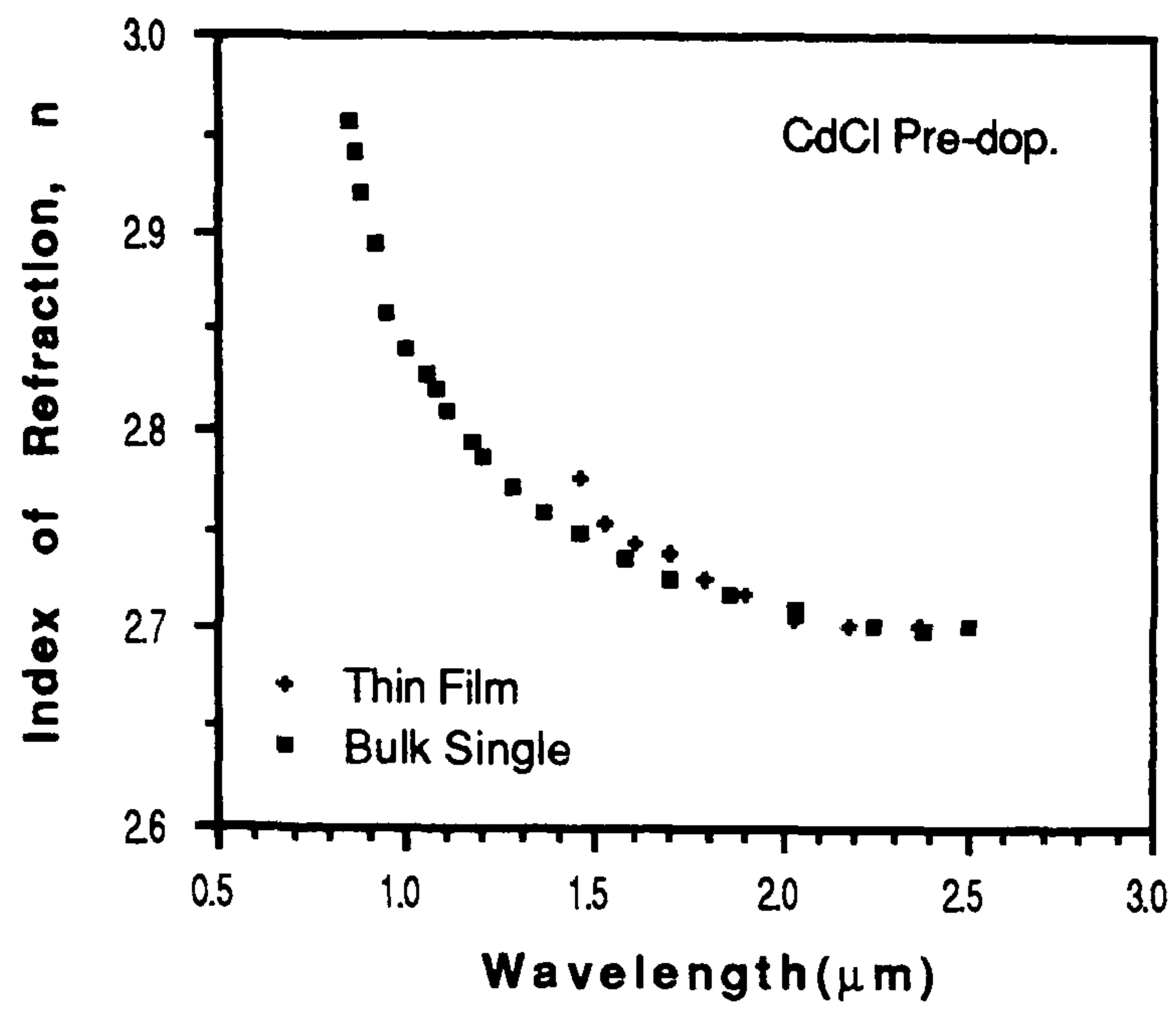


Figure 5.27 — Refractive index, n_f vs wavelength characteristic of a typical Cl_2 pre-doped CdTe thin layer.

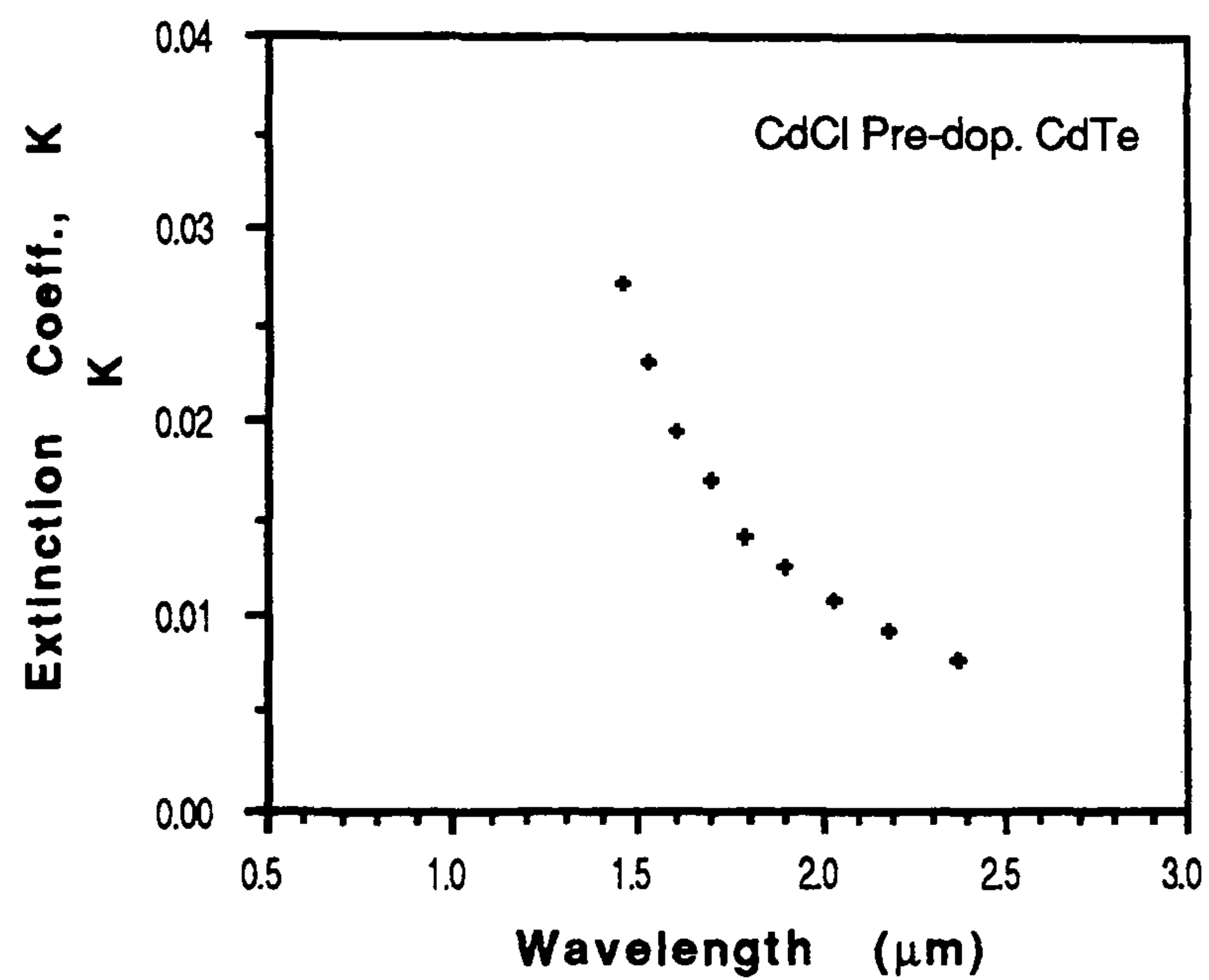


Figure 5.28 — Extinction coefficient, k_f vs wavelength characteristic of a typical Cl_2 pre-doped CdTe thin layer.

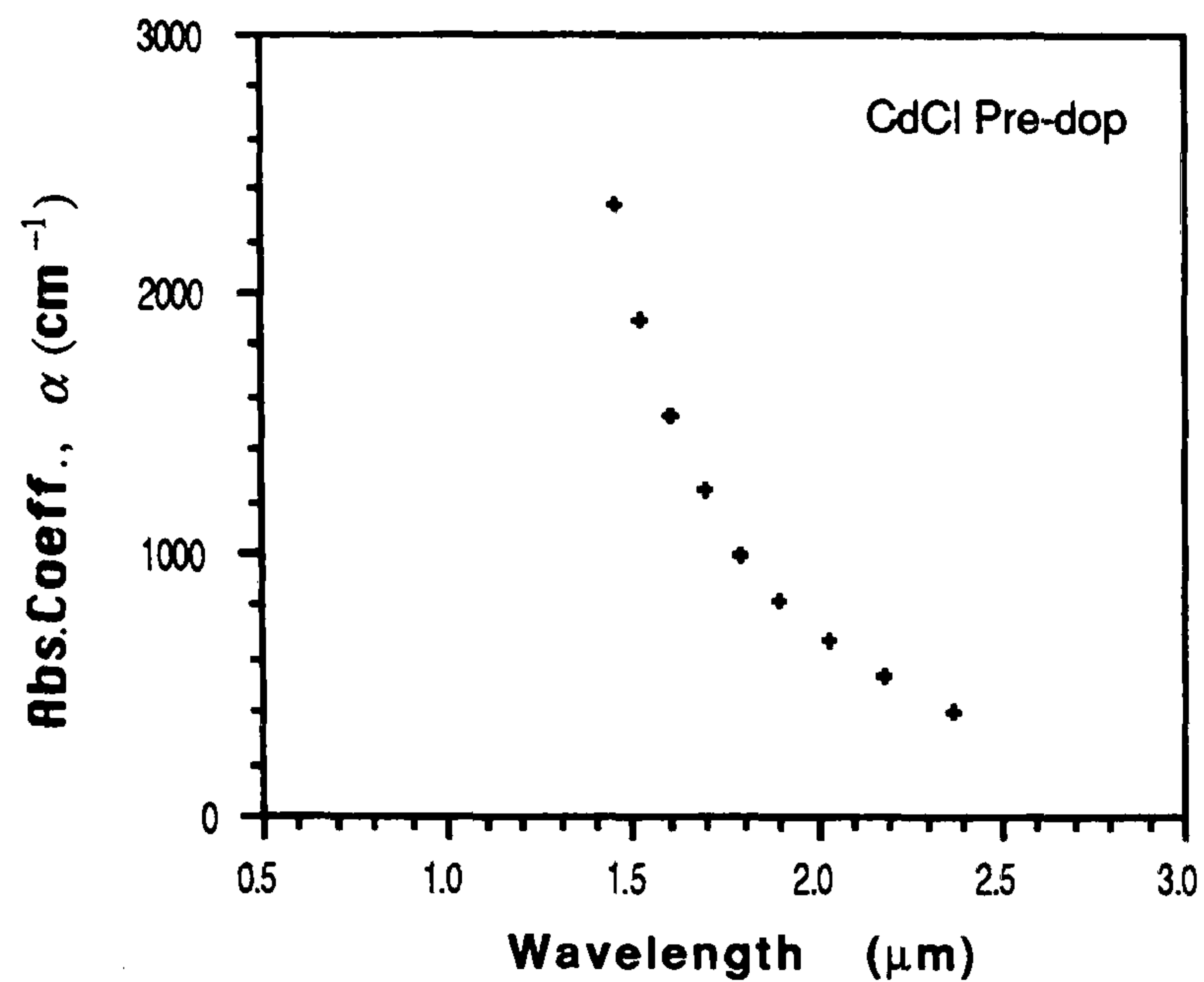


Figure 5.29 — Absorption coefficient, α_f vs wavelength characteristic of a typical Cl_2 pre-doped CdTe thin layer.

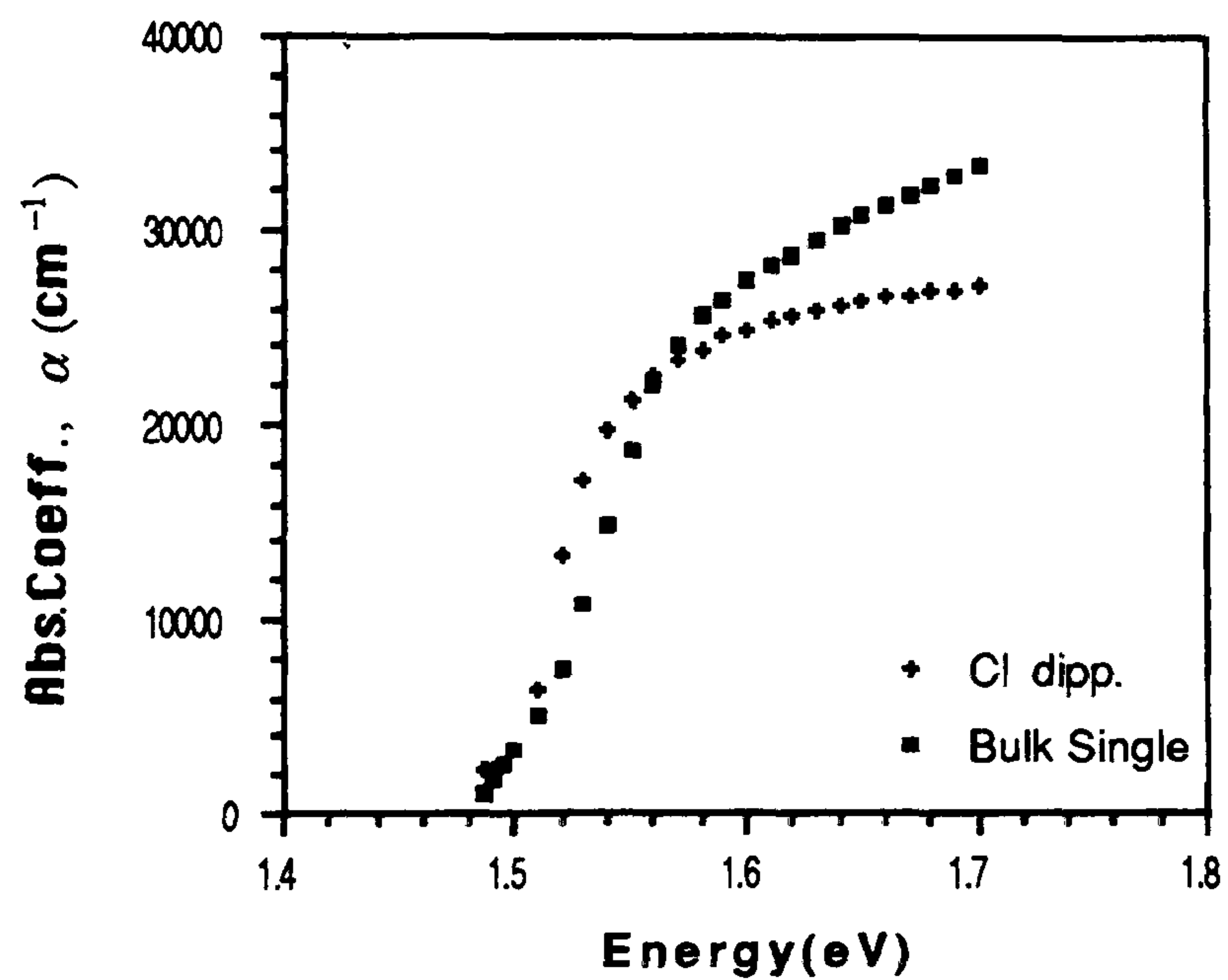


Figure 5.30 — α_f vs $h\nu$ characteristics of bulk single and Cl_2 dipped CdTe thin layer in the strong absorption region.



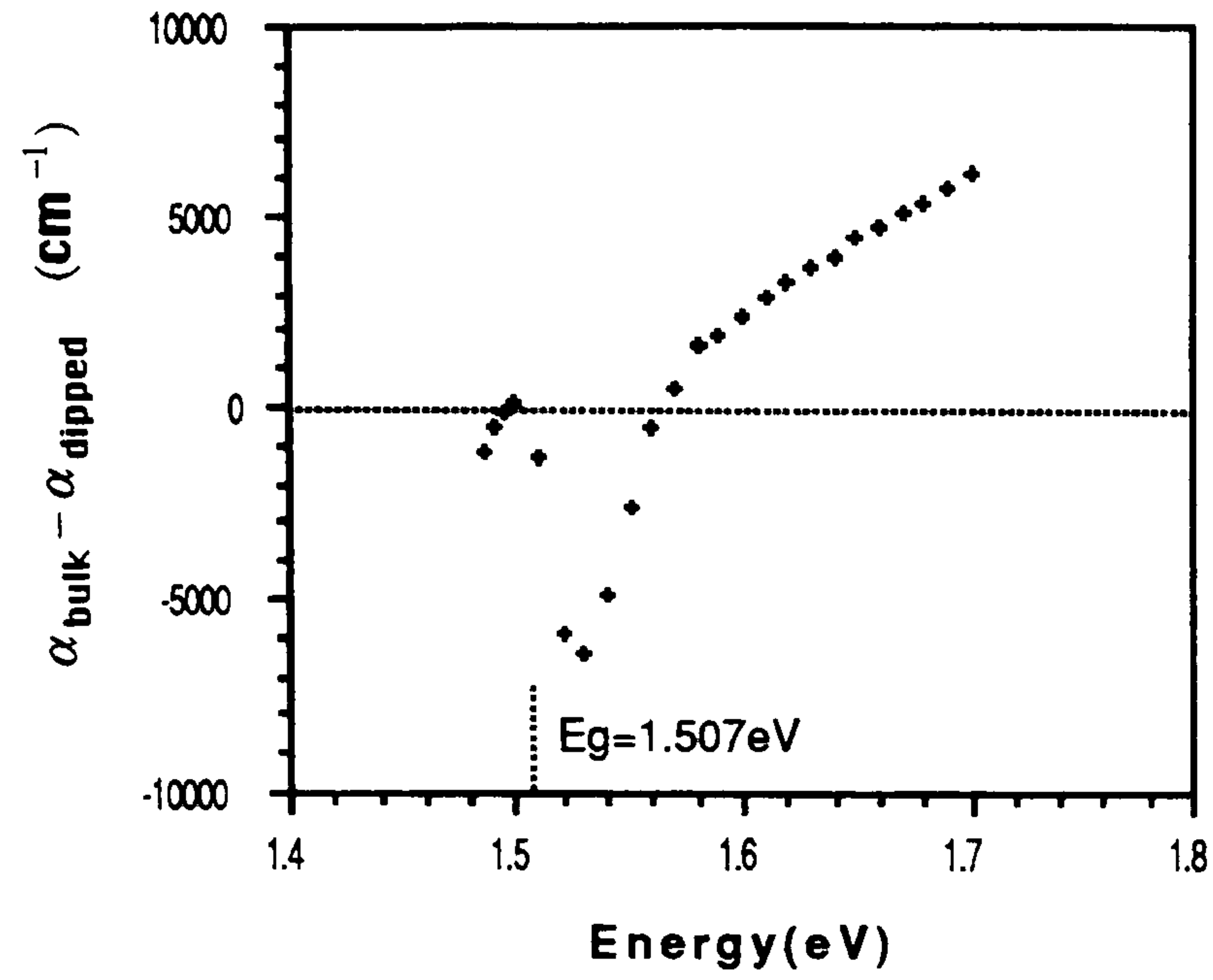


Figure 5.31 — Gap-states, $\alpha_{\text{bulk}} - \alpha_f$ characteristic of a typical Cl_2 dipped CdTe thin layer.

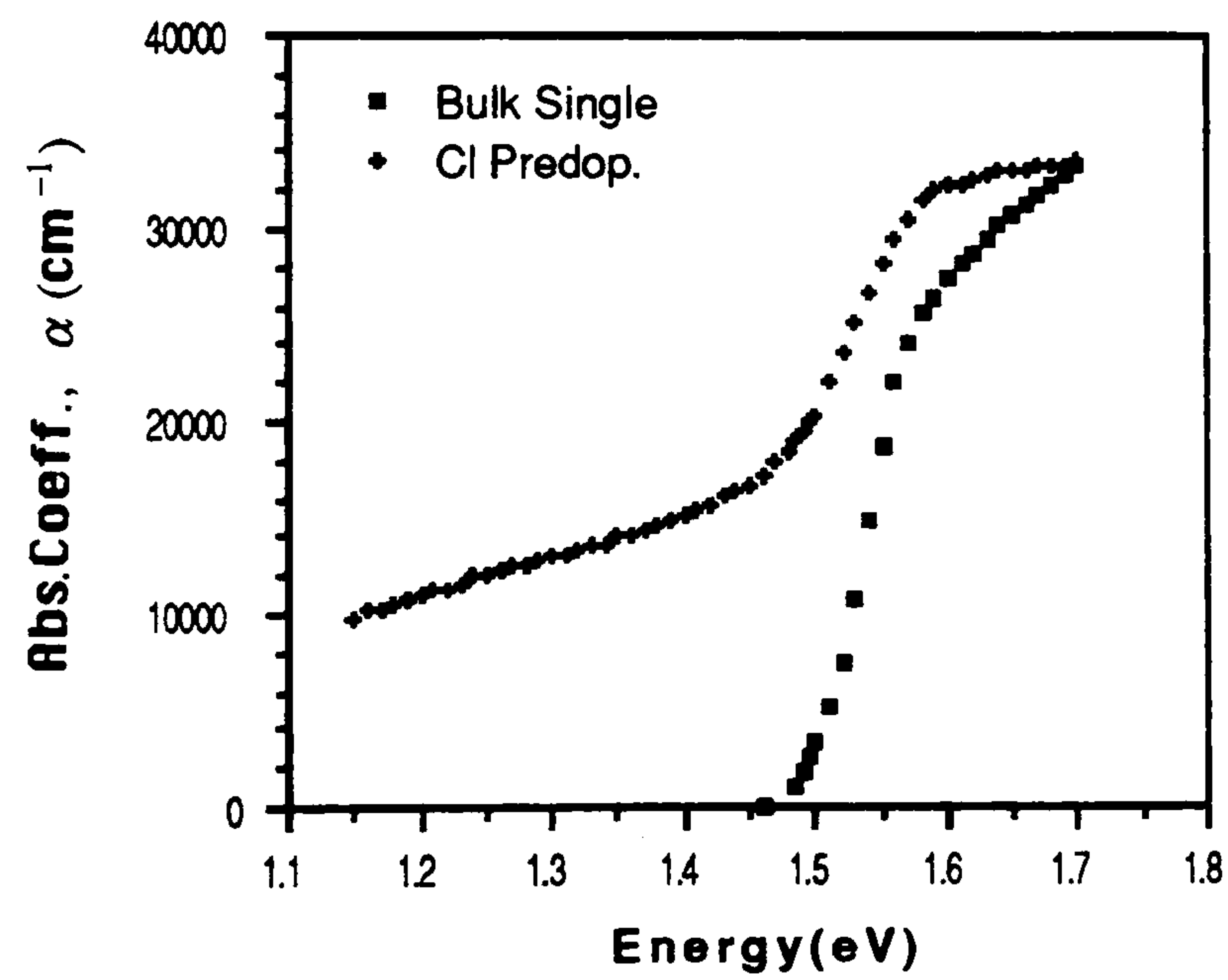


Figure 5.32 — α_f vs $h\nu$ characteristics of bulk single and Cl_2 pre-doped CdTe thin layer in the strong absorption region.

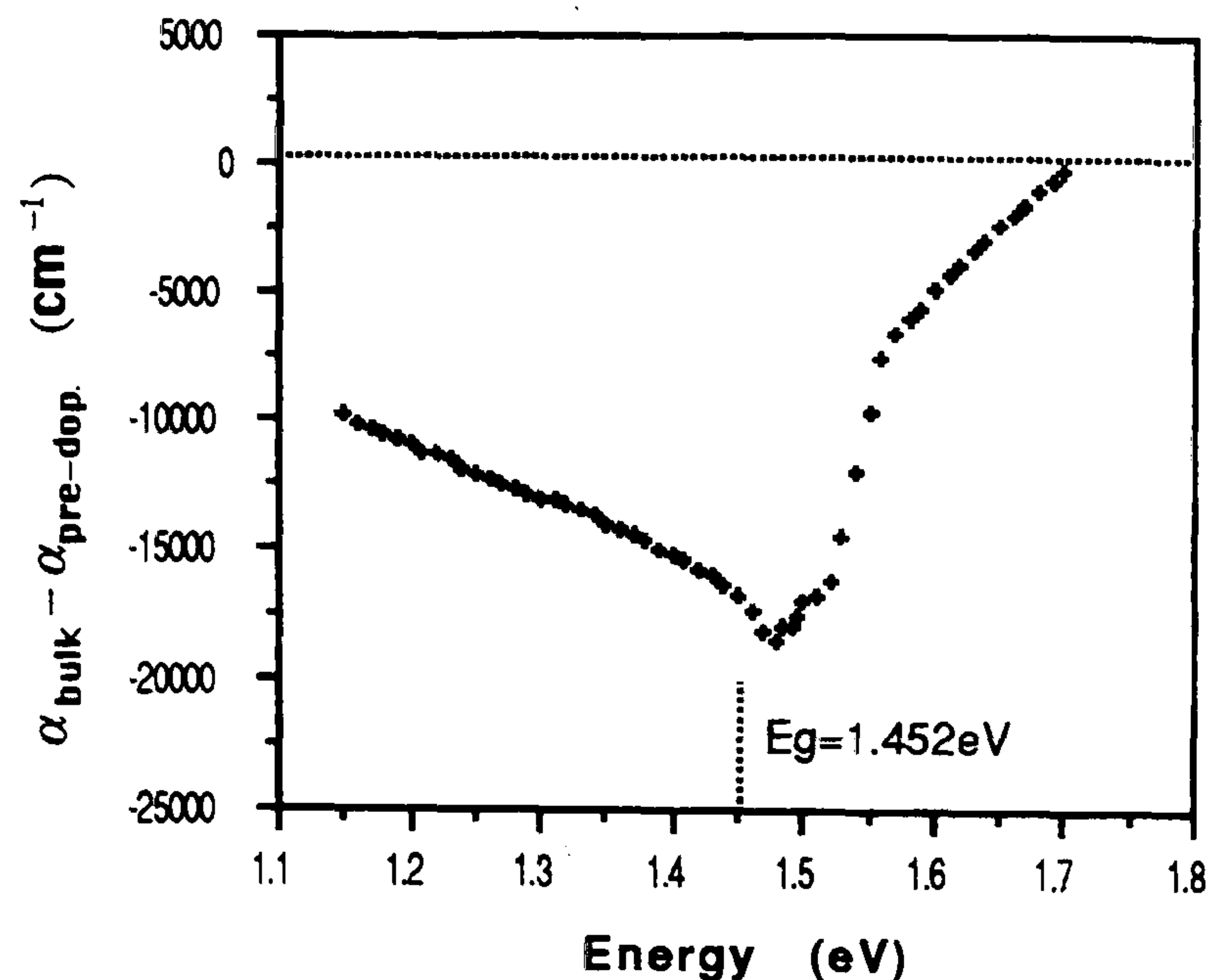


Figure 5.33 — Gap-states, $\alpha_{bulk} - \alpha_f$ characteristic of a typical Cl_2 pre-doped CdTe thin layer.

5.9 Optical properties of CdS thin films.

Optical properties of the polycrystalline CdS thin films were also investigated. Fig.5.34 shows transmission spectra for a typical as-grown CdS layer in the region of 400–2500 nm. Normal incidence transmission through as-grown layers showed a smooth cut-off at about 532 nm in the visible region, and interference fringes due to the parallel plane interface. No additional longwave absorption was observed, with the maximum transmission T_M , approaching that of the glass (i.e. $T_M \cong T_s = 0.92$). Heating the layers at 400°C, for about 30 min in an argon atmosphere did not result in any observable change in the transmission. Optical constants of as-grown layers were determined as a function of wavelength in the usual way and are shown in Fig.5.35–5.37. The least squares fit curve to the refractive index values of a typical as-grown CdS layer yielded $n_f = 5.73 \times 10^{-2} \lambda^{-2} + 2.10$ (λ in μm). Fig.5.38 and 5.39 show α_f and α_f^2 as a function of photon energy in the strong absorption region.

The optical bandgap, E_g was found to be 2.420 eV which is very close to the bulk single crystal CdS value given in the literature of 2.415 eV [43]. The absorption coefficient followed an exponential dependence with photon energy between 2.24

eV and 2.46 eV with an inverse slope E_o (i.e. Urbach Rule) of 50.3 meV, somewhat above room temperature (see Fig.5.40) at 583.5 K.

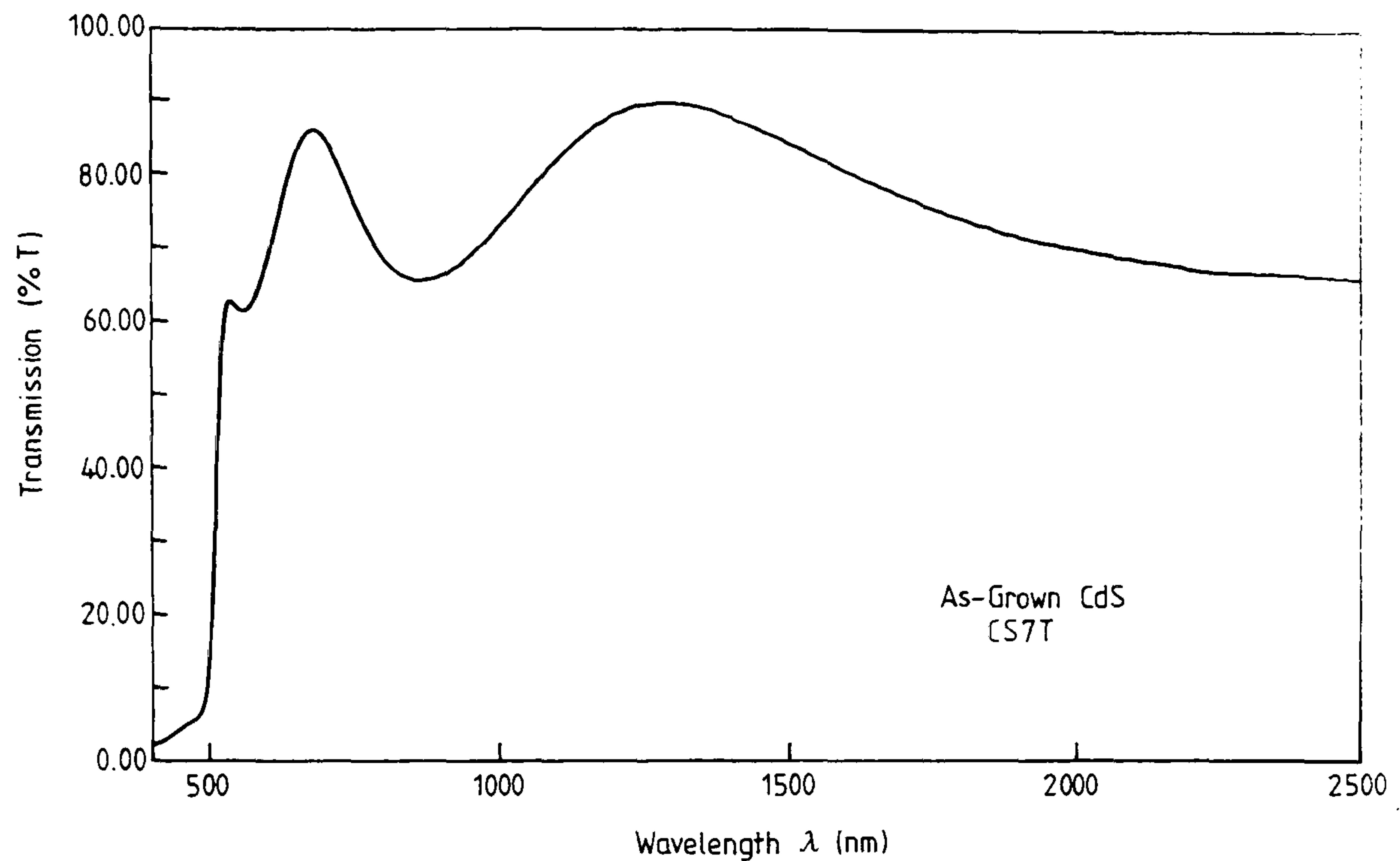


Figure 5.34 — A typical transmission spectrum for a typical 0.6 μm thick film of CdS on a glass substrate.

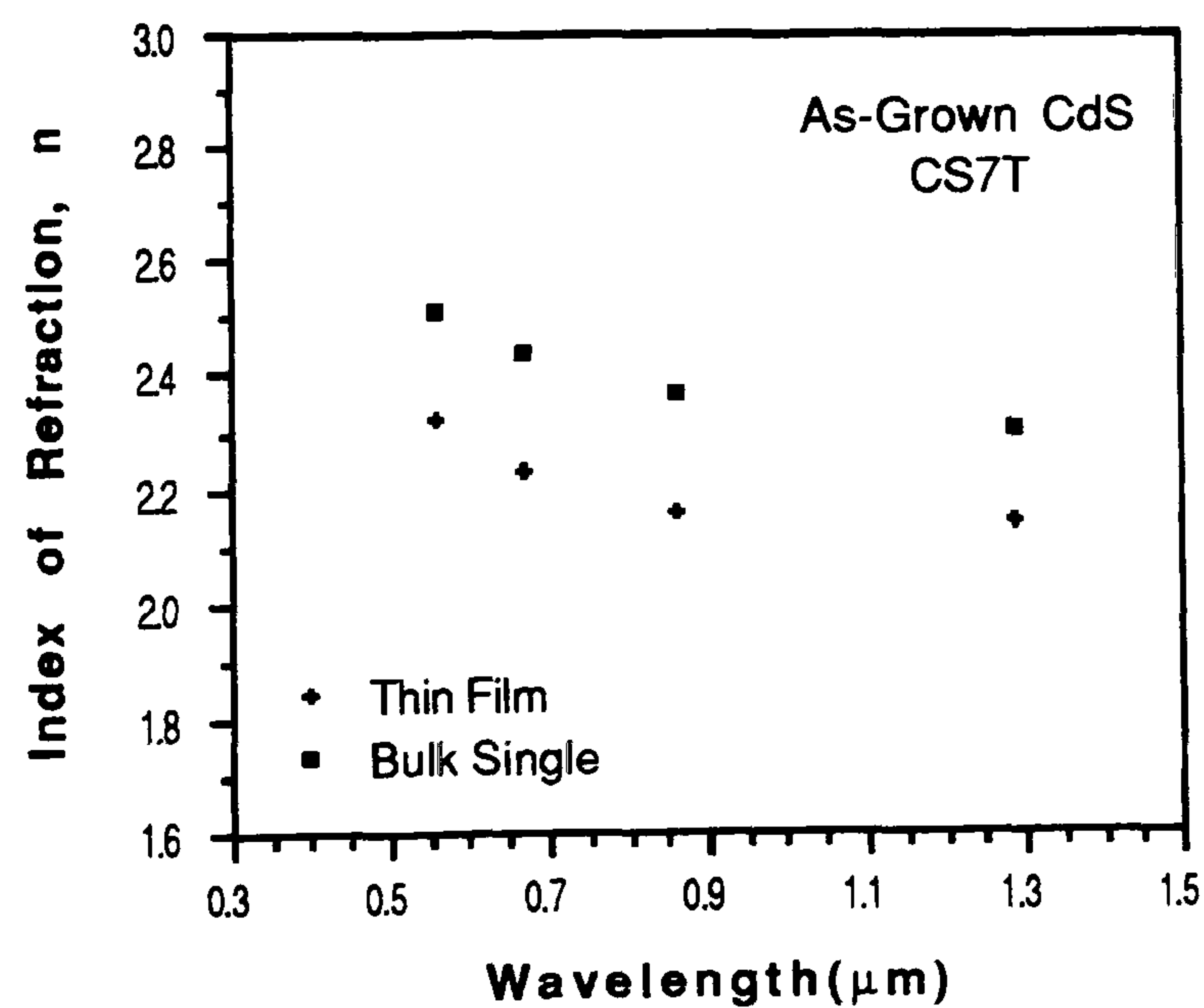


Figure 5.35 — Refractive index, n_f vs wavelength characteristic of a typical as-grown CdS thin layer.

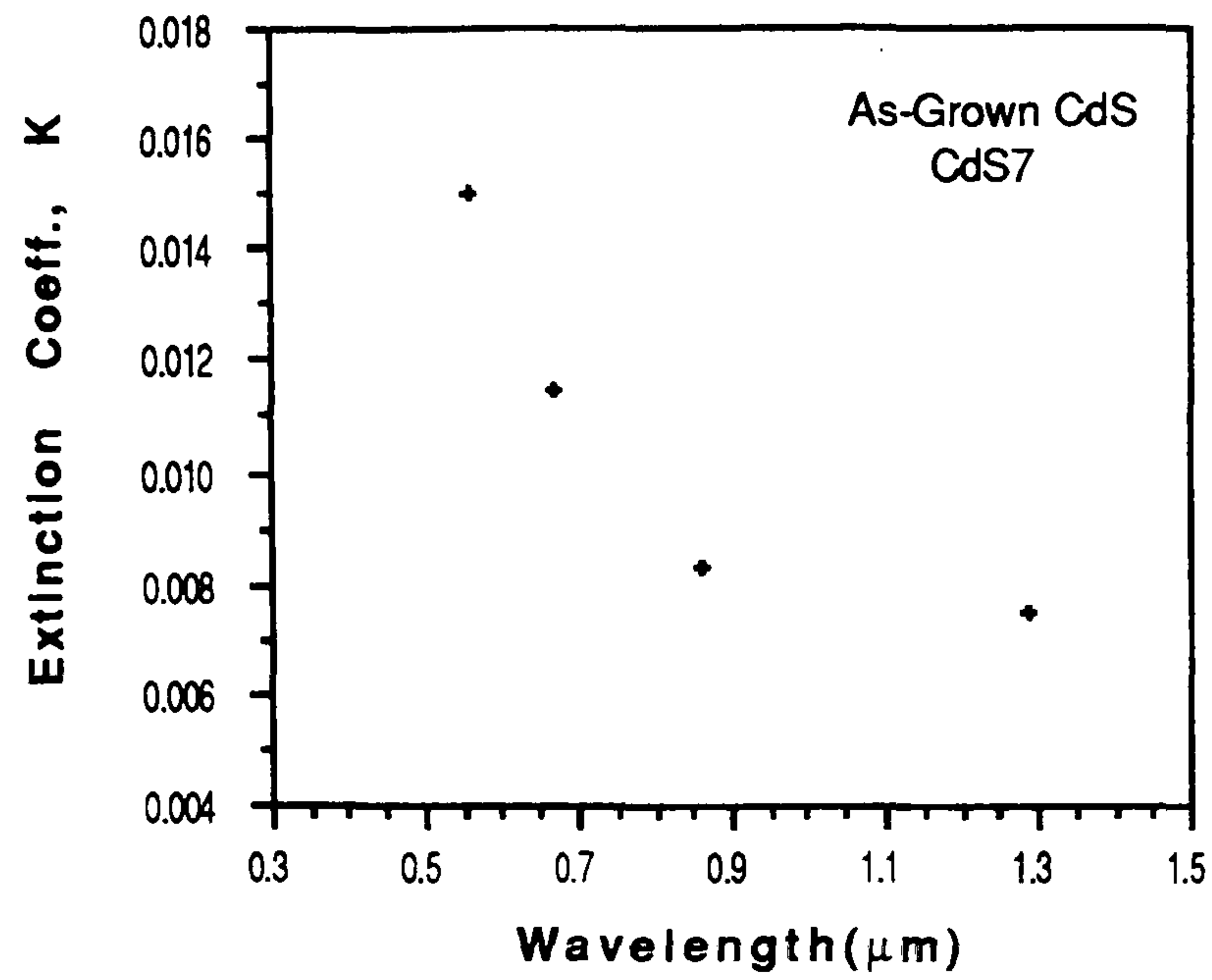


Figure 5.36 — Extinction coefficient, k_f vs wavelength characteristic of a typical as-grown CdS thin layer.

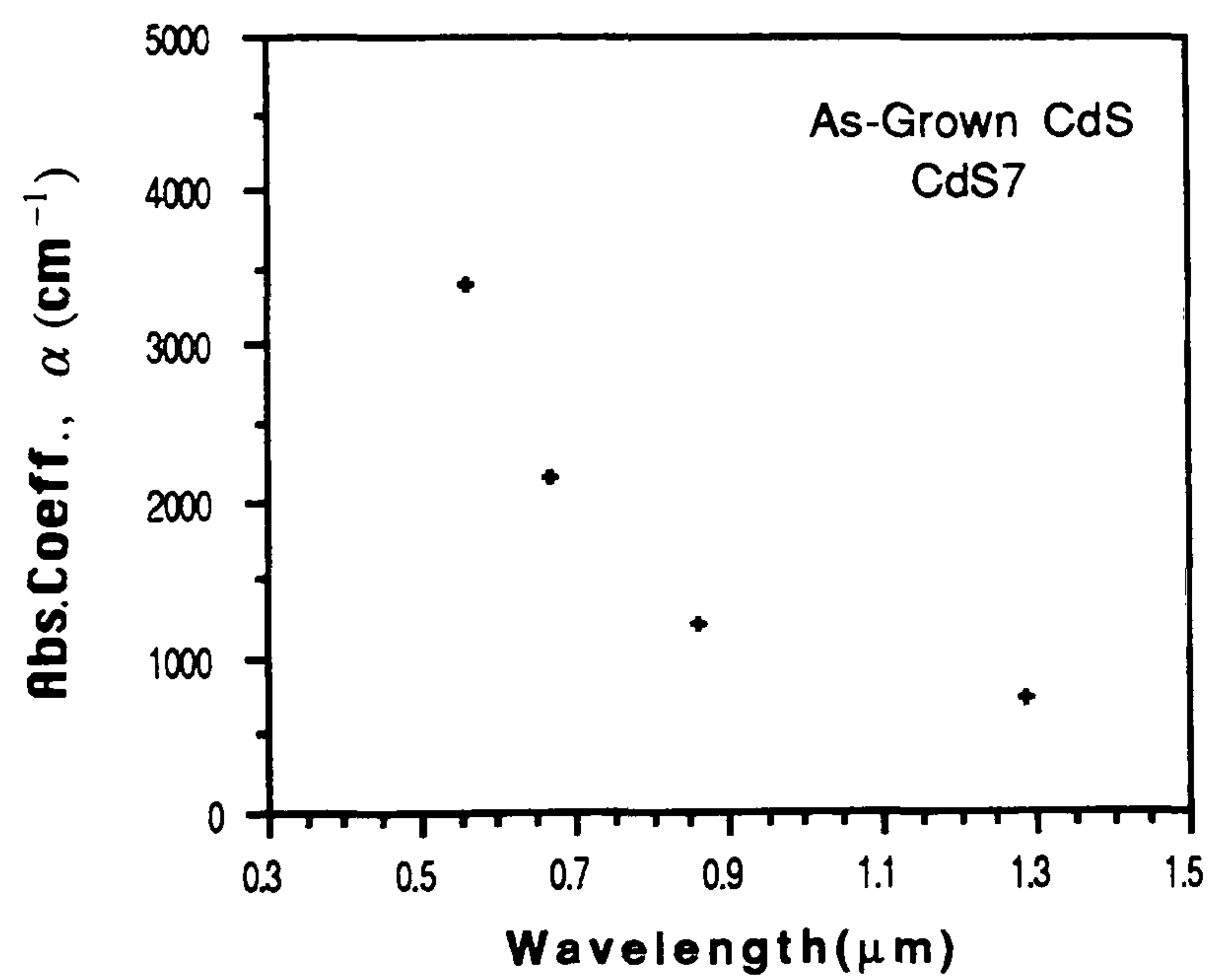


Figure 5.37 — Absorption coefficient, α_f vs wavelength characteristic of a typical as-grown CdS thin layer.

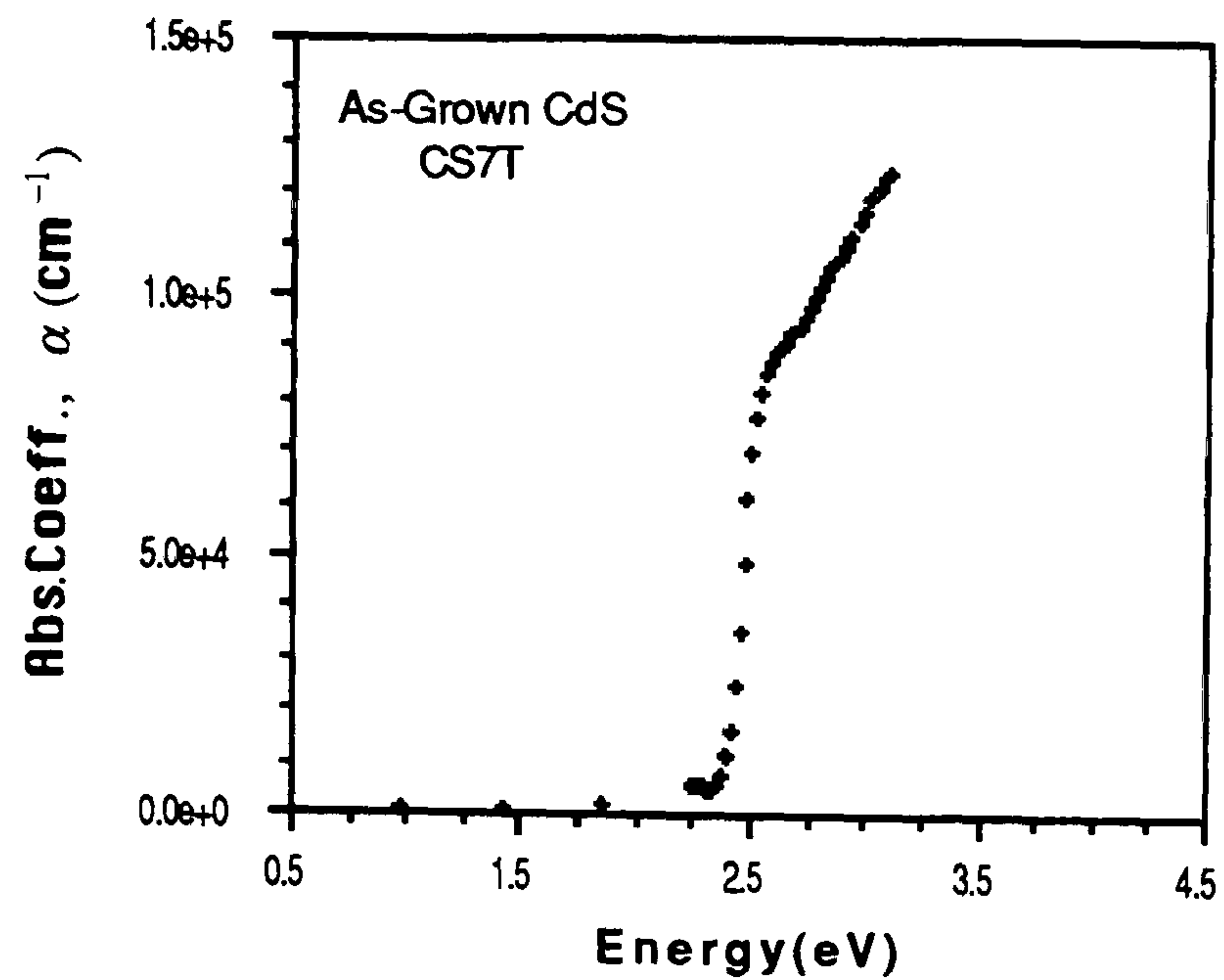


Figure 5.38 — α_f vs $h\nu$ characteristic of a typical as-grown CdS thin layer in the strong absorption region.

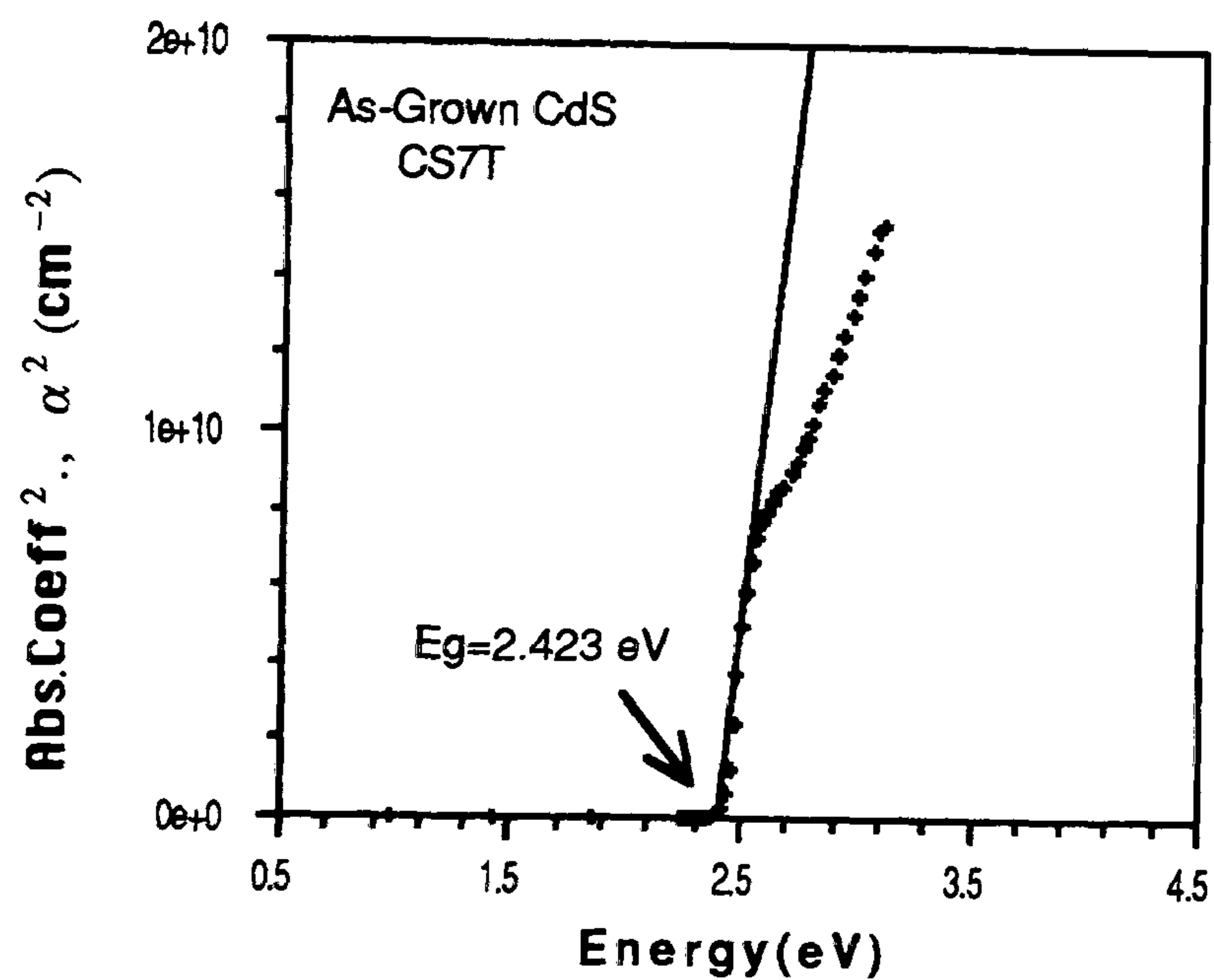


Figure 5.39 — α_f^2 vs $h\nu$ characteristic of a typical as-grown CdS thin layer in the strong absorption region.

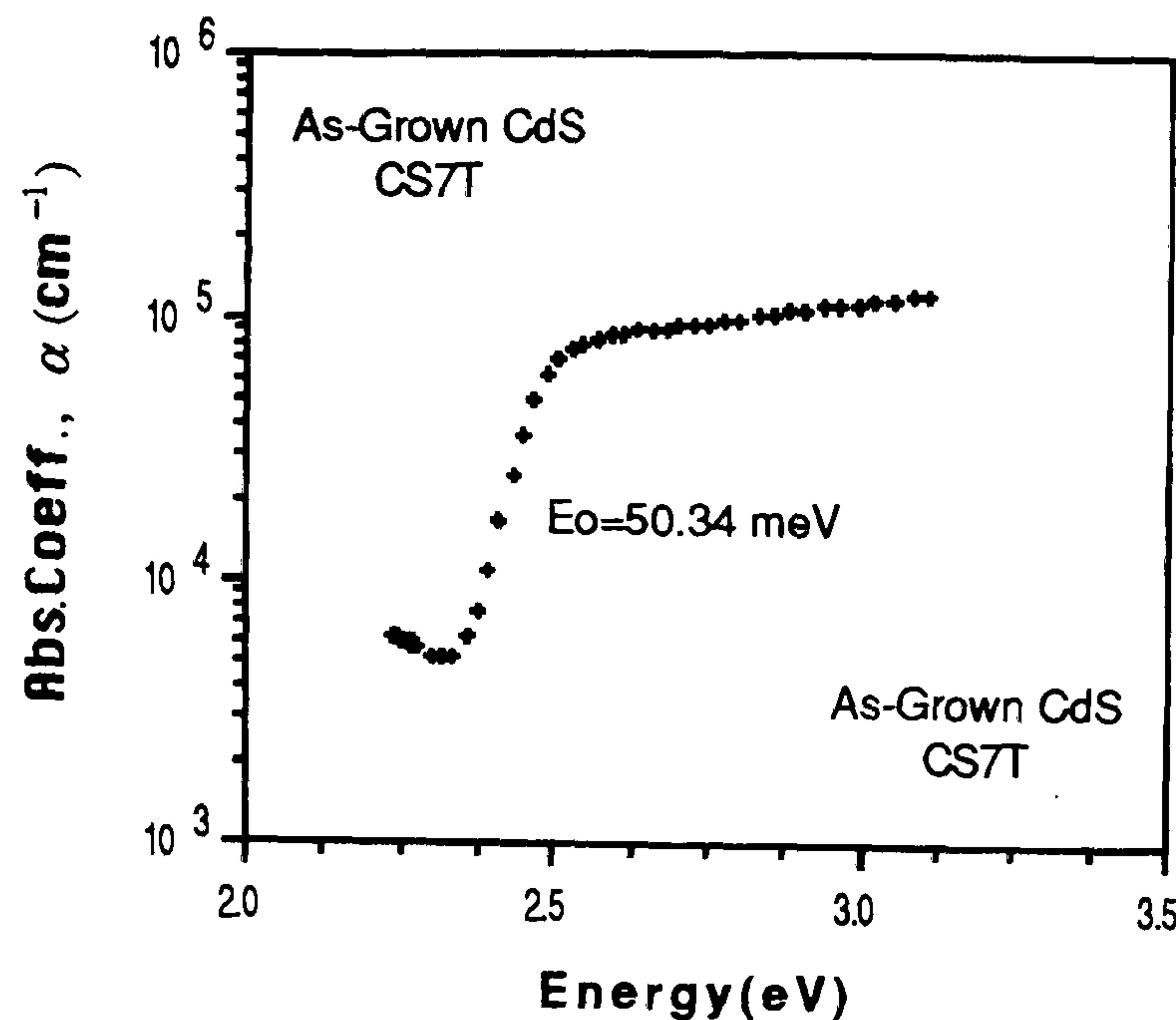


Figure 5.40 — $\log(\alpha_f)$ vs $h\nu$ characteristic of a typical as-grown CdS thin layer.

5.10 Conclusions.

The optical constants of both CdTe and CdS layers were calculated by the Swanepoel procedure using optical transmission spectra only. In the region of weak absorption, sharp interference fringes due to the parallel interface of the layer were usually observed. Refractive index, n_f values were found to be in good agreement with bulk single crystal values, confirming that the method was appropriate and also that the layers were quite uniform in thickness. The dispersion in the refractive index followed a quadratic first order Cauchy trend. Some absorption at long wavelength occurred in CdTe layers, probably due to grain boundary and surface scattering, and structural imperfections. Heat treated and CdCl₂-dipped layers showed a shift in E_g and a much sharper band edge, which could be attributed to the increase in grain size, the change in stoichiometry due to loss of Cd, the formation of shallow oxygen-related acceptor levels, and effects of Cl₂ associated vacancy centres (promoted by the oxygen containing ambient used in the heat treatment). However, layers grown using Cl₂-predoped starting CdTe material showed a progressive increase in absorption, probably due to Cl₂-associated complexes or possibly to film porosity.

As-grown and heat treated CdS layers (i.e. at 300°C about 15 min in Ar) did not show any change in transmission, nor was any additional long wave absorption observed. Values of refractive index were comparable to bulk single crystal values and showed a similar quadratic first order Cauchy dispersion to the CdTe.

5.11 References.

1. S.P.Lyashenko, and V.K.Miloslavskii, Opt. Spectrosc., **16**, 80 (1964).
2. J.Wales, G.J.Lovitt, and R.A.Hill, Thin Solid Films, **1**, 137 (1967).
3. J.Szczyrbowski, and A.Czapla, Thin Solid Films, **46**, 127 (1977).
4. J.C Manifacier, J.Gasiot, and J.P.Fillard, J.Phys., **E9**, 1002 (1976).
5. J.C Manifacier, M.Demurcia, J.P.Fillard, and L.Vicaria, Thin Solid Films, **41**, 127 (1977).
6. R.Swanepoel, J.Phys.E:Sci. Instrum., **16**, 1214, (1985).
7. J.I.Pankove, "*Optical Processes in Semiconductors*", p.36, Prentice Hall, Inc., (1971).
8. J.Bardeen, F.J.Blatt, and L.H.Hall, Proc.of Atlantic City Photoconductivity Conference 1954, J.Wiley and Chapman and Hall 146 (1956).
9. F.L.Pedrotti, L.S.Pedrotti, "*Introduction to Optics*", Prentice-Hall Inc., Englewood Cliffs, Newjersey (1987).
10. R.Swanepoel, J.Phys.E:Sci.Instrum., **17**, 896 (1984).
11. E.D.Palik, "*Handbook of Optical Constants of Solids*", Academic Press, 409 (1985).
12. I.Filinski, Phys.Status.Solidi (b) **49**, 577 (1972).
13. H.E. Bennett and J.M. Bennett, "*Physics of Thin Films*", (G. Hass and R.E. Thun, eds.) **4**, Academic Press, New York, 1 (1967).
14. L.V.Keldysh, Soviet Physics-JETP **7** (1958) 788.

15. P.Bugnet, Rev.Phys.Appl. **Fr.9**, 447 (1974).
16. H.Y.Fan, M.Becker, "*Semiconducting Materials*", Butterworth Scientific Publications Ltd. (1951).
17. H.Y.Fan, W.G.Spitzer, and R.J.Collins, Phys.Rev., **101**, 566 (1956).
18. S.S.Ou and O.M.Stafsudd, and B.M.Basol, J.Appl.Phys. **55**, 3769 (1984).
19. S.Chaudhuri, S.K.Das and A.K.Pal, Thin Solid Films, **147**, 9 (1986).
20. D.Poelman and J.Vennik, J.Phys. D: Apply.Phys. **21**, 1004 (1988).
21. M. Melendez-Lira, S. Jimenez-Sandoval, and I. Hernondez- Calderon. , J. Vac. Sci. Technol. **A7**, 1426 (1989).
22. J.Aranda, J.L. Morenza, J.Esteve and J.M. Cordina, Thin Solid Films., **23**, 120 (1984).
23. T.L.Chu, Solar Cells, **23**, 31 (1988).
24. H.Miyasawa, S.Sugaike, J.Phys.Soc.Japan, **9**, 648 (1954).
25. P.W.Davis, T.S.Shilliday, Phys.Rev. **118**, 1020 (1960).
26. W.G.Spitzer, C.A.Mead., J.Phys.Chem.Solids, **25**, 443 (1964).
27. E.Matatagui, A.G.Thomson, M.Cardona., Phys.Rev **176**, 950 (1968).
28. G.A.Banonas, R.A.Bendoryus, A.Y. Shileika., Soviet Phys. Semiconductors **5**, 329 (1971).
29. J. Camassel., D. Auvergne., H. Mathieu., R. Triboulet, and Y. Marfaing., Solid.State.Comm., **13**, 63 (1973).
30. F.Urbach, Phys.Rev. **92** 1324 (1953).
31. Manabe, A., Mitsuishi, A., Yoshinaga, H., Jpn.J.Appl.Phys., **6**, 593 (1967).
32. J.Baars, F.Sorger, Solid State Commun., **10**, 875 (1972).
33. M.Gorska, W.Nazarewicz, Phys.Status Solidi **B**, 193 (1974).

34. G. Burrafato, G. Giaquinta, N.A. Mancini, A. Pennisi et al., J. Phys. Chem. Solids, **37**, 519 1976.
35. F.Cerdeira, I. Torriani, P.Matisuke, V. Lemos, and F.Decker, Appl.Phys., **A46**, 107 (1988).
36. R.F.C, Farrow, G.R,Jones, G.M,Williams, and I.M,Young, Appl.Phys.Lett., **39**, 954 (1981).
37. C.W,Tang and F.Vazan, J.Appl.Phys., **55**, 3886 (1984).
38. Y.S.Tyan, F.Vazan and T.S. Barge, Proc. 17th IEEE Photovoltaic Specialists Conf., p.840, Kissimmee, FL, (1984).
39. P.Siffert, J.Berger, C.Scharager, A.Cornet, R.Struck, and R.O. Bell, H.B. Serreze, F.V. Wald, IEEE Transactions on Nuclear Science **NS-23**, No: 1, 159 (1976).
40. C.Canali, G.Ottaviani, R.O.Bell and F.V.Wald, J.Phys.Chem.Solids, **35** 1405 (1974).
41. B.M.Vul, V.S.Vavilov, V.S.Lvanov, V.B.Stopachinskii and V.A.Chapnin, Soviet Phys.Semicond., **6**, 1255 (1973).
42. R.D.Bell, Solid State Comm., **16**, 913 (1975).
43. M.P. Lisitsa, L.F. Gudymenko, V.N. Malinko, and S.F. Terekhova, Phys. Stat. Sol. **31**, 389 (1969).

Chapter VI

Structural Properties of CdTe and CdS Thin Films.

6.1 Introduction.

The successful development of any thin film device requires a detailed understanding of the structure, morphology and crystallinity of the component layers. This is essential if a full description of the device behaviour is to be obtained. In the present context cell performance is closely related to crystal grain size and possibly orientation. Hence, a programme of structural assessment was undertaken to determine the relevant structural parameters.

The principal techniques used were x-ray diffraction (XRD) and reflection high energy electron diffraction (RHEED). Assessment by XRD enabled grain size to be obtained as well as a general indication of crystallinity of the CdTe and CdS layers. A qualitative indication of the surface crystallinity and preferred orientation was derived from RHEED studies and together with the XRD results used to determine the optimum growth conditions for the layers.

Morphology was assessed by scanning electron microscopy (SEM) in which compositional analysis was carried out simultaneously using EDAX. In a few samples it was possible to undertake some secondary ion mass spectroscopy (SIMS) in order to identify impurities present in the layers.

6.2 X-Ray Diffraction.

X-ray diffraction (XRD) is particularly useful in the structural analysis of thin film or fine-grained materials which are difficult to study by other means. The analysis requires interpretation of the diffractometer record and this entails firstly identification of the peaks and then conversion of the diffraction angles to interplanar spacings and lattice parameters.

6.2.1 X-Ray Diffraction Assessments of CdTe Thin Films.

Fig.6.1 shows the x-ray diffractometer trace using Ni-filtered $\text{Cu}_{K\alpha}$ radiation with a wavelength of $\lambda=1.5418 \text{ \AA}$ from an as-grown CdTe thin film. A list of the diffraction peaks at values of $2\theta_B$ (θ_B : Bragg angle), associated with corresponding planes of a typical CdTe thin film are given in Table 6.1. Although the diffraction peaks at $2\theta_B$ angles of 23.8° , 46.4° and 76.2° are associated with corresponding planes of cubic CdTe, the peaks at $2\theta_B$ angles of 23.1° , 25.9° , 26.2° , 29.6° and 32.6° could not be so identified. Their origin was not known, but they may have been due to excess Te. It has been suggested that in vacuum evaporation, surface deposits of Te may accumulate due to the higher vapour pressure of Cd [1]. In this respect, it should be noted that the additional peaks are relatively small.

$2\theta_B$	$d_{cal.}(\text{\AA})$	CdTe, Cd or Te	$\{hkl\}$	I/I_o
23.1	3.86	Te	100	
23.8	3.74	CdTe	111	100
25.9	3.44	—		
26.2	3.40	TeO_2	110	
29.6	3.02	TeO_2	040	
32.6	2.75	—		
46.4	1.96	CdTe	311	1.9
76.2	1.25	CdTe	511	2.2

Table 6.1 — XRD data for a typical as-grown CdTe thin film.

The lattice parameter, a_o was calculated by combining the Bragg law and the equation of lattice-spacing between the planes of a cubic crystal such as CdTe, i.e.

$$\lambda = 2d_{hkl} \sin \theta_B \quad [6.1]$$

$$\frac{1}{d_{hkl}^2} = \frac{(h^2 + k^2 + l^2)}{a_o^2} \quad [6.2]$$

where $\{hkl\}$ are the Miller indices. Combining Eq.6.1 and Eq.6.2, one can obtain

$$\sin^2 \theta_B = \frac{\lambda^2}{4a_o^2} \{h^2 + k^2 + l^2\} \quad [6.3]$$

Eq.6.3 predicts, for a particular incident wavelength and for a cubic crystal of unit cell size, a_o , all the possible Bragg angles at which diffraction can occur. For a typical thin layer of cubic CdTe, a_o was calculated to be 6.48Å, 6.48Å and 6.49Å from $2\theta_B$ values associated with diffraction from the $\{111\}$, $\{311\}$ and $\{511\}$ planes respectively.

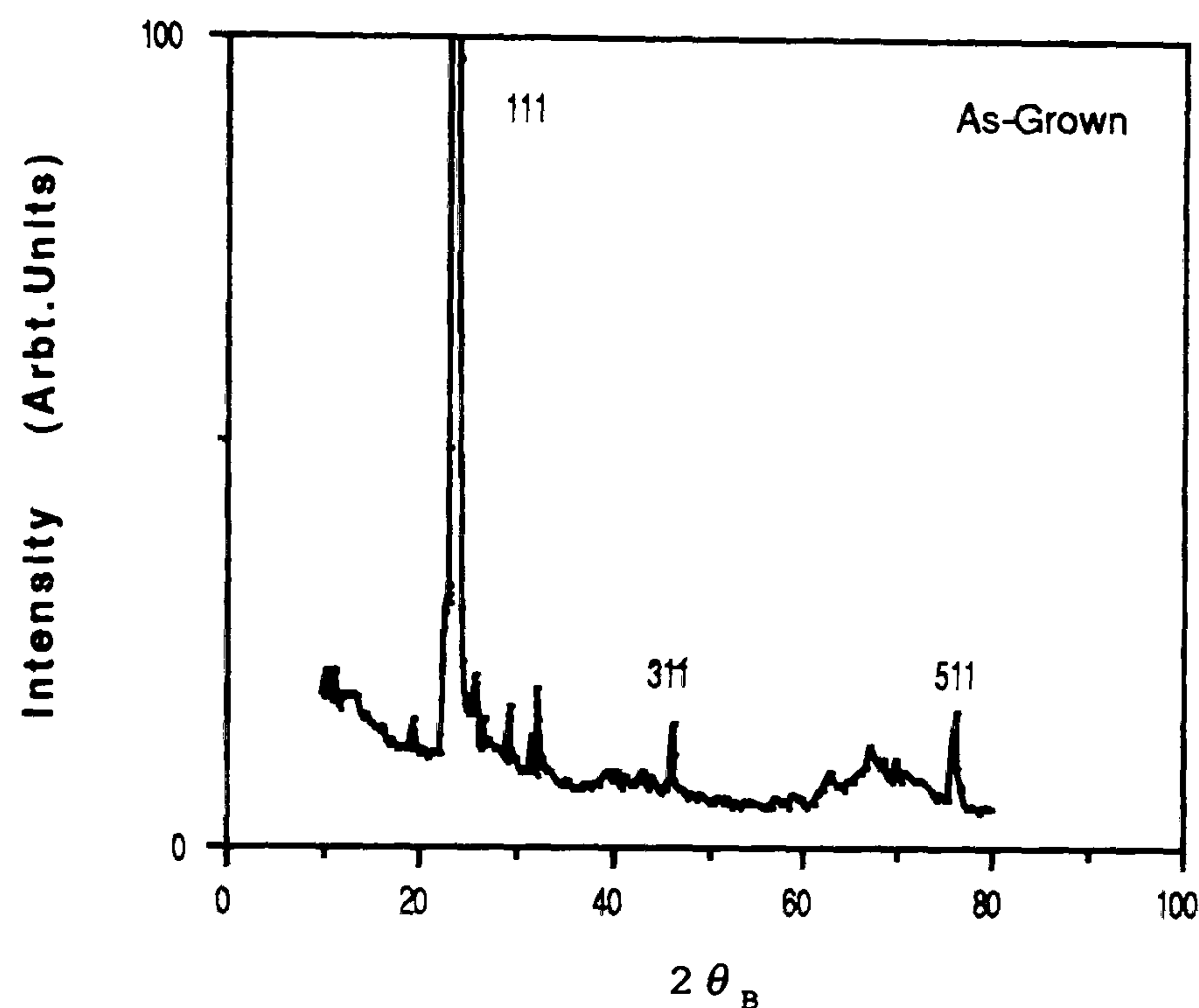


Figure 6.1 — X-ray diffraction spectrum of an as-grown CdTe thin film.

More importantly, x-ray diffraction was used to obtain estimates of grain size (i.e. crystallite size) in the CdTe and CdS thin films. The method relies on the fact that small grains produce line broadening in X-ray diffraction spectra. In order to distinguish the line broadening associated with small grain size, from that

due to the instrument, a reference XRD spectrum was taken from a bulk single crystal of GaAs. As the GaAs was nearly perfect, any line broadening observed can be attributed to instrumental effects and may be used to determine the net broadening, β in the XRD spectra from the CdTe and CdS thin films using;

$$\beta = \sqrt{B^2 - b^2} \quad [6.4]$$

where B is the measured line width (FWHM) and b the instrumental broadening. The grain size, ε_{hkl} can then be obtained from the equation [2,3];

$$\varepsilon_{hkl} = \frac{K \lambda}{\beta \cos \theta_B} \quad [6.5]$$

where K is a shape factor and θ_B is the Bragg angle. K is utilised to take account of the crystallite shape and orientation, and an average value of 0.9 is generally used for polycrystalline films. A plot of a grain size (where ε_{111} was considered) versus substrate temperature is shown in Fig.6.2. Although there was considerable scattering in the values of grain sizes at low substrate temperatures, there was a maximum size of ~ 85 nm at about 215°C substrate temperature, above which the grain size decreased. (i.e. between 220°C and 250°C).

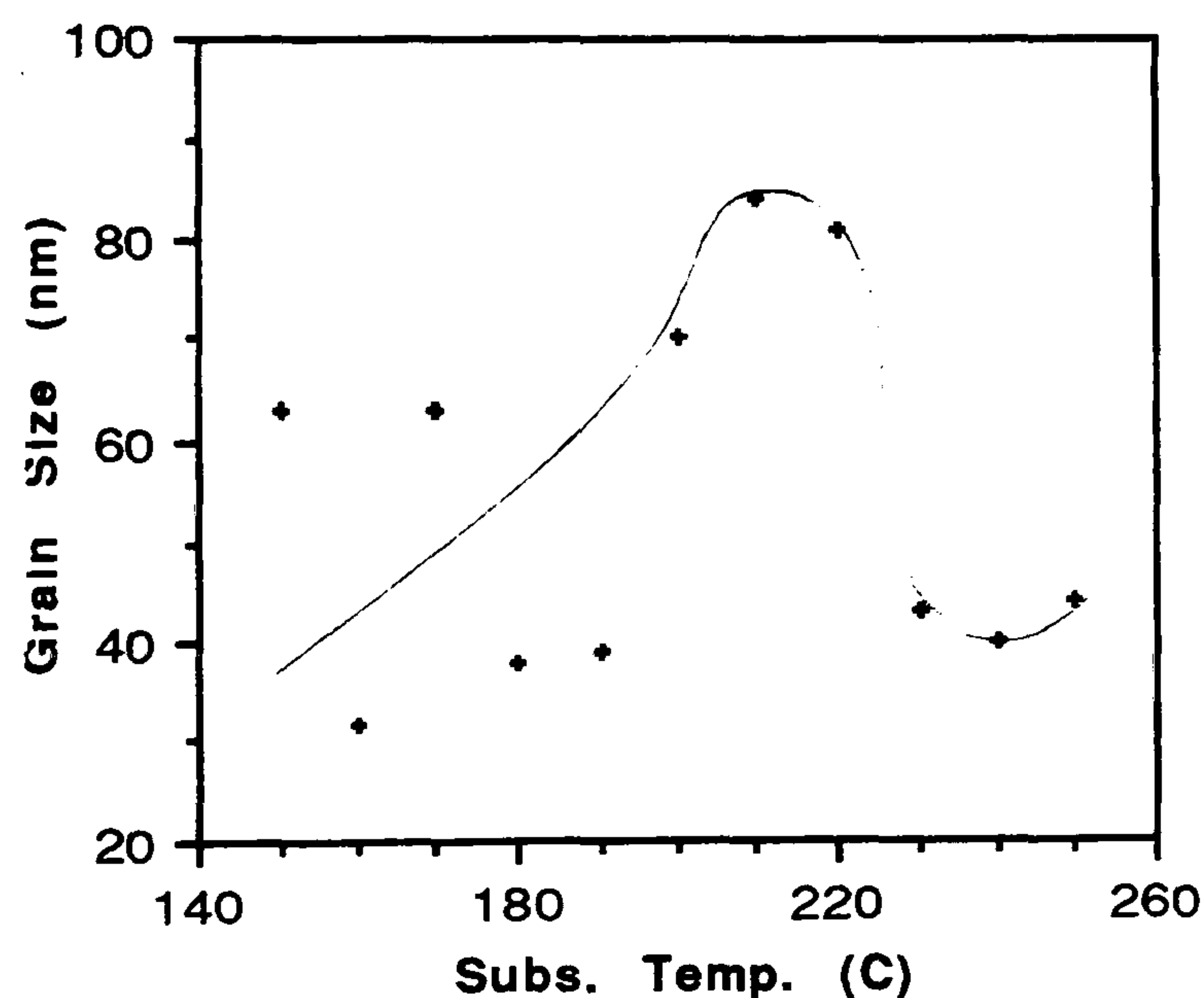


Figure 6.2 — Grain size vs substrate temperature characteristic of as-grown CdTe thin film.

Annealing the CdTe thin layers at 400°C for about 30 min in air showed a dramatic change in the x-ray diffraction pattern as shown in Fig.6.3. The intensity of the {111} diffraction line increased due, probably, to grain growth resulting in a greater degree of preferred ordering. In addition, a peak associated with the {422} planes of cubic CdTe appeared in the x-ray diffraction spectrum. Other diffraction peaks were also observed that could not be related to CdTe, but which could be attributed to pure Te or TeO₂. This was probably due to oxygen from the air reacting with chemi-absorbed residual free Te (i.e. from the deposition) or with Te “liberated” from the dissociation of CdTe by the annealing procedure. However, no diffraction peaks which could be associated with Cd or Cd oxides were observed, suggesting that desorption of Cd atoms or molecules (i.e. since the Cd vapour pressure is larger than the Te vapour pressure) had occurred during annealing.

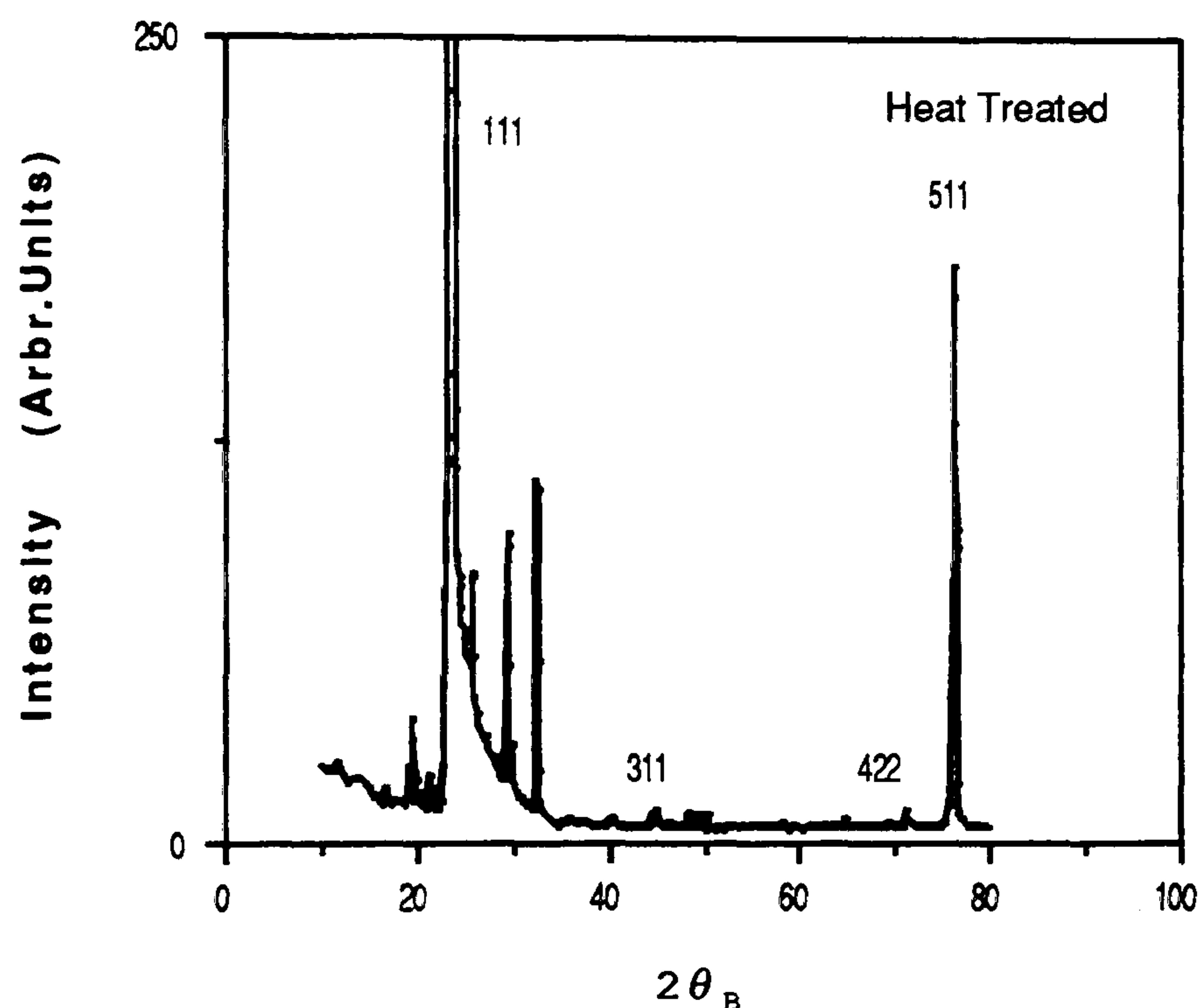


Figure 6.3 — X-ray diffraction spectrum of a heat treated CdTe thin film.

Grain sizes of thin layers annealed at 400°C for about 30 min in air were measured and are tabulated in Table 6.2. This shows that some grain growth had occurred during the heat treatment in air. This is a comparatively low temperature for grain growth/re-crystallisation to occur even in a thin film, suggesting that

grain growth may be more accelerated in the presence of oxygen possibly due to some surface reaction with chemi-absorbed species. The values of grain sizes estimated for the Cl_2 -doped layers (i.e. by pre-doping, co-evaporation, or by dipping) showed little significant change before and after annealing, as shown in Table 6.2. The effects of the heat treatment were quite identical to undoped layers. However, the estimated change in grain size could be larger, i.e. especially for Cl_2 -doped layers due to the limitations of the technique used (i.e. max measurable grain size is $0.1\mu\text{m}$). Interestingly, the intensity of the $\{111\}$ peak for the Cl_2 -dipped layers increased very little after heat treatment. This might be due to the passivation of $\{111\}$ planes by Cl_2 or Cl-V_{Cd} complexes.

Thin Layer	Before(nm)	After(nm)
As-grown CdTe	78	100
CdTe: Cl_2 dipped	86	100
CdTe: Cl_2 co-evap.	81	99
CdTe: Cl_2 predop.	85	99

Table 6.2 — Approximate grain sizes of thin CdTe layers, before and after annealing in air (400°C , 30 min).

X-ray diffraction spectra of CdTe thin layers obtained by co-evaporation of CdCl_2 with CdTe and which had been heat treated at 400°C for about 30 min showed that the layer comprised CdCl_2 and TeCl_2 compounds, as well as CdTe, suggesting that Cl_2 molecules form complexes with Te rather than with Cd.

6.2.2 X-Ray Diffraction Assessment of CdS Thin Films.

The x-ray diffraction spectrum for a typical CdS film grown on glass at a substrate temperature of 220°C is shown in Fig.6.4. There were two principal peaks at $2\theta_B$ equal to 26.5° and 54.6° which correspond to diffraction from the $\{0002\}$ and $\{0004\}$ planes of hexagonal CdS. The former peak was narrow and pronounced while the latter was relatively small (other expected diffraction peaks

could not be seen even at very high sensitivity). This implies that the CdS layers displayed a strong $\{0002\}$ -preferred orientation in the as-grown condition. Such a preferred orientation is commonly seen for CdS thin films [4,5,6]. The intensity of the diffraction peak associated with the $\{0002\}$ planes of the heat treated layers (i.e. at 300°C for about 15 min in N₂) increased moderately. This implies that a degree of preferred orientation was promoted by annealing, possibly due to recrystallisation effects and probable changes in the layer stress [7]. Grain sizes for the CdS layers were estimated by the same technique as was used for the CdTe, and were found to be in the range 40–50 nm. It was observed that grain sizes did not change noticeably before and after heat treatment at 300°C for about 15 min in N₂ atmosphere.

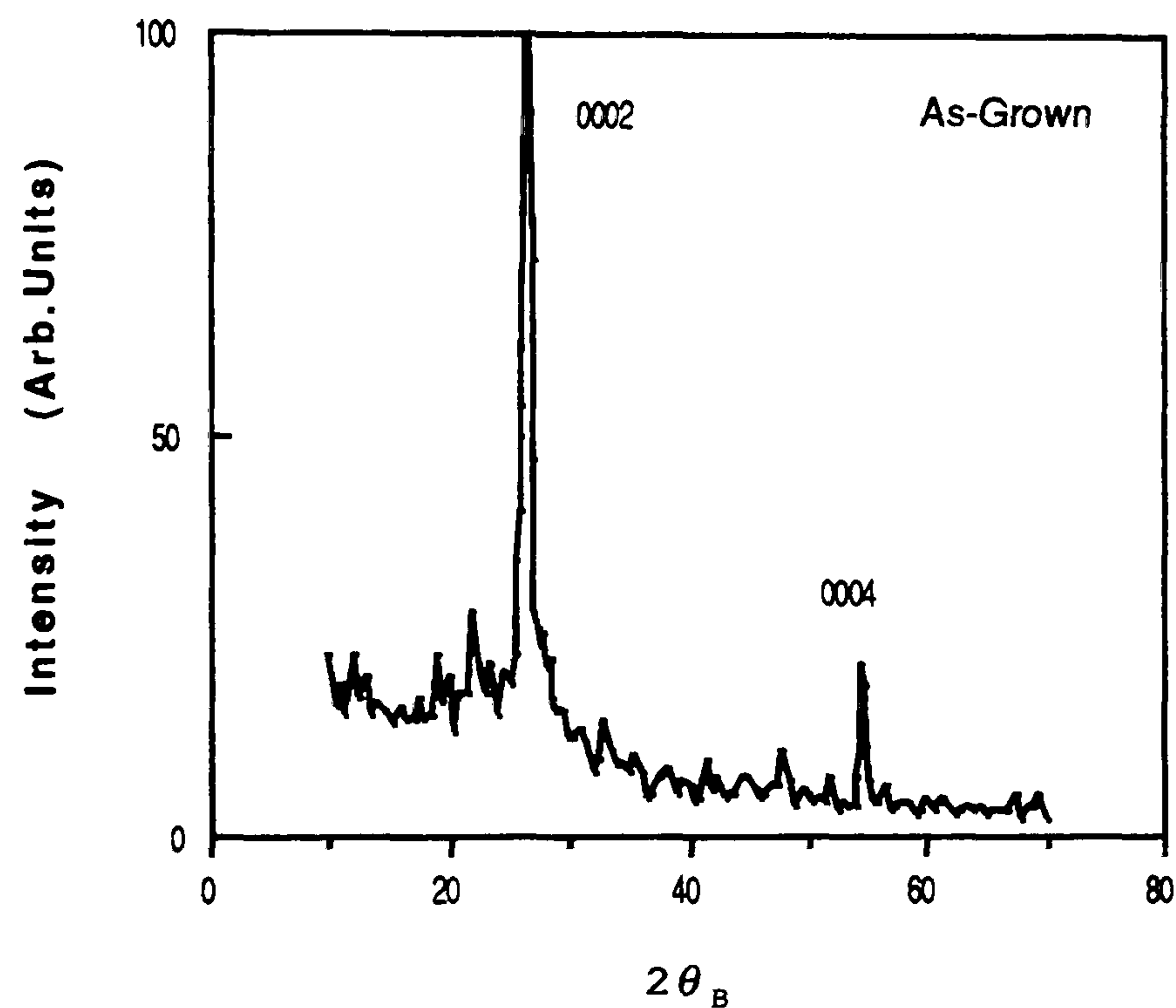


Figure 6.4 — X-ray diffraction spectrum of an as-grown CdS thin film.

6.3 RHEED Assessment.

Reflection high energy electron diffraction patterns were obtained from the surfaces of the CdTe thin films (i.e. first few layers) grown on glass substrates at temperatures between 150°C and 250°C, in order to provide information on the presence of surface films, crystal orientation and degree of preferred orientation of

crystallites at the surface. The surface of layers grown at substrate temperatures $\geq 180^\circ\text{C}$ had a random polycrystalline texture although some evidence of weak $\{111\}$ -preferred orientation was occasionally present. RHEED patterns taken from layers grown at substrate temperatures $\leq 170^\circ\text{C}$ had a distinct $\{111\}$ -preferred orientation which was stronger at the lower growth temperatures. These results show that thin films with a good degree of preferred orientation can be deposited at 150°C – 170°C and that the degree of preferred orientation was decreased if higher substrate temperatures were used. The RHEED patterns of the CdTe thin films were indexed using the *Camera* equation and the inter-planar spacing between planes, d_{hkl} which can be rewritten (see Eq.6.2) as;

$$d_{hkl} = \frac{a_o}{\sqrt{h^2 + k^2 + l^2}} \equiv \frac{a_o}{\sqrt{N_{hkl}}} \quad [6.6]$$

where $N_{hkl} = h^2 + k^2 + l^2$ and combining this with the *Camera* equation gives for one set of planes $\{hkl\}$ planes,

$$R_{hkl} \frac{a_o}{\sqrt{N_{hkl}}} = \lambda L \quad [6.7]$$

and for a different set of planes $\{h'k'l'\}$,

$$R_{h'k'l'} \frac{a_o}{\sqrt{N_{h'k'l'}}} = \lambda L \quad [6.8]$$

hence,

$$R_{hkl} \frac{a_o}{\sqrt{N_{hkl}}} = R_{h'k'l'} \frac{a_o}{\sqrt{N_{h'k'l'}}} \quad [6.9]$$

Combining Eq.6.6 and Eq.6.9, one can easily obtain;

$$\frac{R_{hkl}}{R_{h'k'l'}} = \frac{\sqrt{N_{hkl}}}{\sqrt{N_{h'k'l'}}} = \frac{d_{hkl}}{d_{h'k'l'}} \quad [6.10]$$

Hence, measurement and comparison of the ratios of experimentally observed arc radii (i.e. with respect to the first and brightest arc associated with $\{111\}$ planes)

yielded $\sqrt{N_{hkl}}$ ratios without using a calibration standard. Fig.6.5 shows the indexed pattern for a typical as-grown CdTe thin film grown at a substrate temperature of 150°C on glass substrates. The indices were further confirmed by comparing the angles between the arcs subtended by a given arc with respect to the normal through the principal {111} arc. These are related to the respective Miller indices by the equation [3];

$$\cos \phi = \frac{h_1 h_2 + k_1 k_2 + l_1 l_2}{\sqrt{(h_1^2 + k_1^2 + l_1^2)(h_2^2 + k_2^2 + l_2^2)}} \quad [6.11]$$

All of the measured and calculated angles were in good agreement with the indices in the figure and it was concluded that the film is polycrystalline and the arc pattern contained diffracted intensity analogous to the [112] and [110] beam directions and {111} planes were parallel to the substrate (i.e. there is a {111} preferred orientation).

The RHEED patterns of the heat treated CdTe layers were also investigated. The patterns of arcs were almost identical to those of as-grown {111}-oriented CdTe layers, except for an additional arc which was located just above the {111} arc. Calculation of the d-spacing for this arc yielded 3.24Å which could correspond to the value of d-spacing for either Te or TeO₂. Probable d-spacings obtained from ASTM file for Te and TeO₂ are given in Table 6.3.

As far as the probable errors are concerned, the measured d-spacing of 3.24Å could correspond to either Te(101) or TeO₂(121), although it seems to be closer to the d-spacing for Te(101).

Compound	d-spacing(Å)	hkl
Te	3.23	101
TeO ₂ *	3.28	121
Te ₃ O ₄ †	3.40	110

Table 6.3 — X-ray diffraction data for *: TeO₂ (Tellurite); †: Te₃O₄ (Paratellurite).

Fig.6.6 shows an indexed RHEED pattern for a typical as-grown CdS layer grown at a substrate temperature of 220°C on a glass substrate. The RHEED pattern confirms the polycrystalline nature of the film and the preferred orientation of {0002} determined by XRD (i.e. the x-ray diffraction spectrum had only one strong diffraction peak associated with the {0002} plane). The pattern was indexed by finding the d-spacings and by measuring the relative angles between the planes of $\{h_1k_1l_1\}$ and $\{h_2k_2l_2\}$ which is given for a hexagonal system by [3];

$$\cos \phi = \frac{h_1h_2 + k_1k_2 + \frac{1}{2}(h_1k_2 + h_2k_1) + \frac{3}{4}\frac{a^2}{c^2}l_1l_2}{\sqrt{(h_1^2 + k_1^2 + h_1k_1 + \frac{3}{4}\frac{a^2}{c^2}l_1^2)(h_2^2 + k_2^2 + h_2k_2 + \frac{3}{4}\frac{a^2}{c^2}l_2^2)}} \quad [6.12]$$

and by taking the {0002} arc as a reference. CdS thin films deposited directly onto ITO/glass substrates were also examined by RHEED. The pattern of the arcs was almost identical to those shown for the {0002}-oriented CdS layers on glass substrates. However, even though the preferred orientation was the same for this layer, the arcs were more diffuse indicating that the sample surface was flatter. There were some variations in the samples, and whereas all had {0002} preferred orientation, the degree of diffuseness in the rings (and hence roughness) varied.

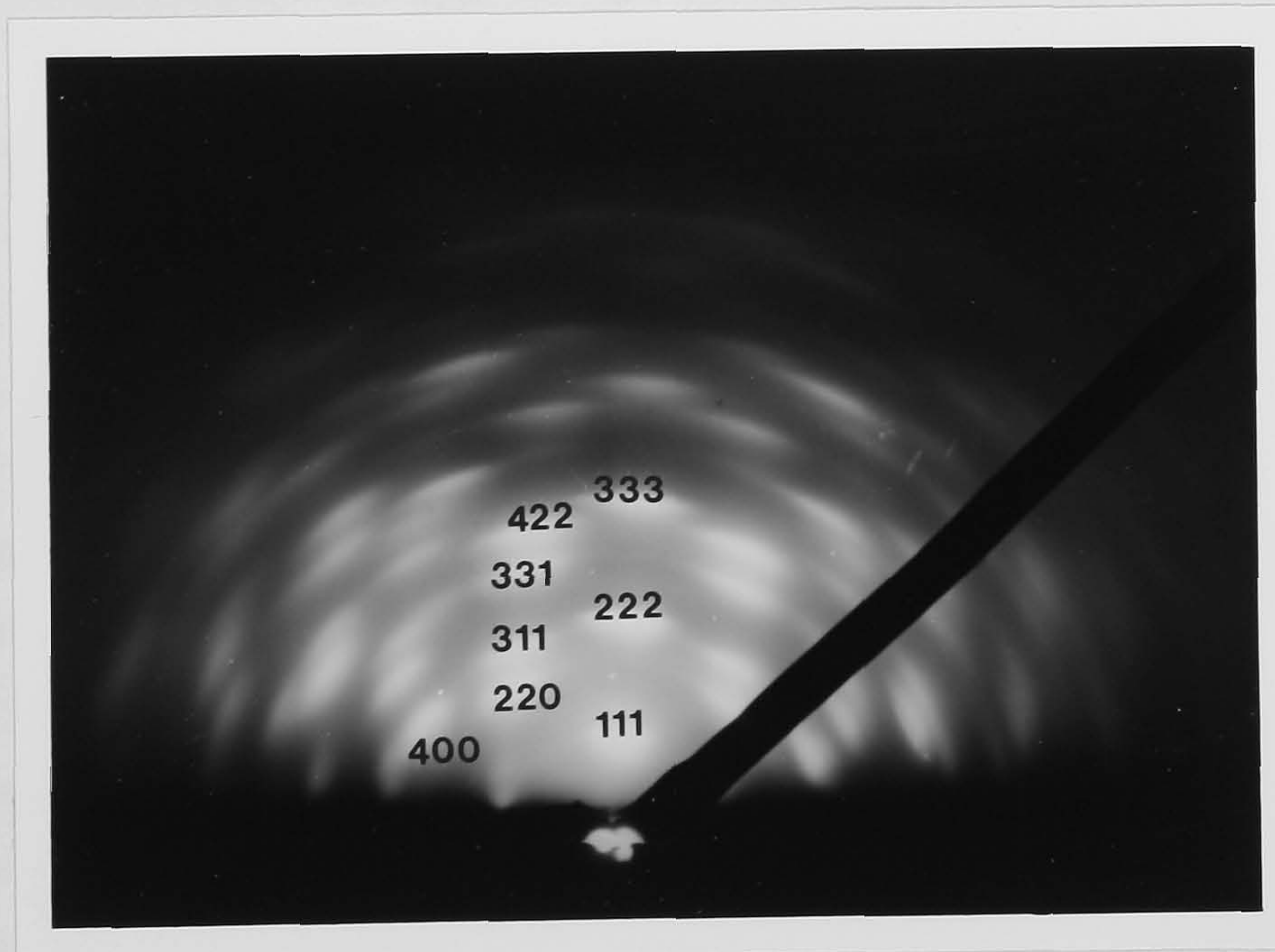


Figure 6.5 — RHEED pattern from an as-grown CdTe thin film grown on glass at a substrate temperature of 150°C.

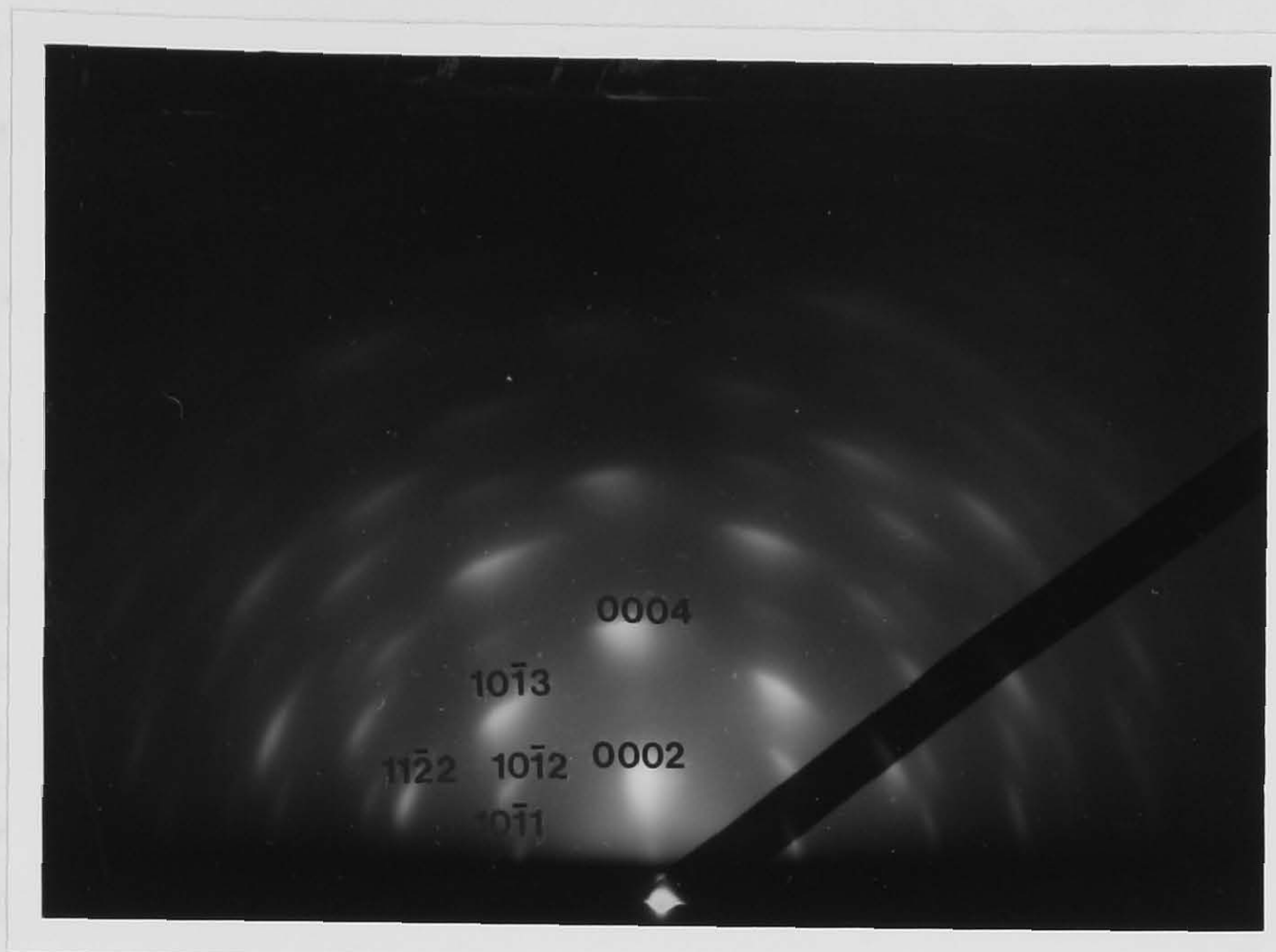


Figure 6.6 — RHEED pattern from an as-grown CdS thin film grown on glass at a substrate temperature of 220°C.

6.4 Scanning Electron Microscopy (SEM) Assessments.

6.4.1 Morphology.

Routine assessment of the surface morphology of thin film layers was performed using the secondary electron (SE) mode of the SEM. As-grown CdTe thin layers showed a smooth surface with distinct pin holes of about $2\mu\text{m}$ in diameter (Fig.6.7). They displayed columnar growth, with the growth axis tilted by about $\sim 15^\circ$, to the substrate normal, as shown by the cross-section in Fig.6.8. However, surface micrographs of the layers grown by co-evaporation of CdTe and CdCl₂ on glass substrates displayed remarkable surface morphologies. Fig.6.9 shows SEM micrograph of a typical CdTe:Cl₂ (by co-evaporation) thin layer grown on plain glass substrates. The surface consisted of larger grains confirming that grain growth occurred during deposition by incorporation of Cl₂ atoms but also larger pores giving rise to a much rougher surface. The films were visually much darker than as-grown and heat treated layers.

Fig.6.10 and 6.11 also show the surface micrographs of CdCl₂-dipped layers (i.e. dipping into CdCl₂/Methanol solution). The distribution of CdCl₂ was not

uniform over the surface with, as can be seen from Fig.6.10, regions of high and low CdCl_2 concentration suggesting that the dipping time and pulling rate (i.e. removing the layer from the solution) could play an important role in achieving uniform doping. Fig.6.11 shows an enlarged image of one of the CdCl_2 islands and shows the porous nature of the deposits which were precipitated out of droplets of the CdCl_2 /Methanol solution.

CdS thin layers showed smooth surfaces with no observable pin holes at least within the resolution of the SEM, about $1\mu\text{m}$ (see Fig.6.12). Fig.6.13 also shows a cross-sectional view of a typical as-grown CdS thin film in which columnar growth has occurred with the growth axis at about $\sim 5^\circ$, to the substrate normal (as seen in the RHEED patterns of these results).

6.4.2 Energy Dispersive Analysis by X-Rays (EDAX).

EDAX scans confirmed that CdTe and CdS thin film layers comprised only Cd & Te and Cd & S respectively. No other elements were observed within its limits of sensitivity (elements with atomic number less than 11 or with concentrations less than 1% would not be detected by the EDAX used here). Fig.6.14 and Fig.6.15 show EDAX scans of typical as-grown CdTe and CdS layers respectively.

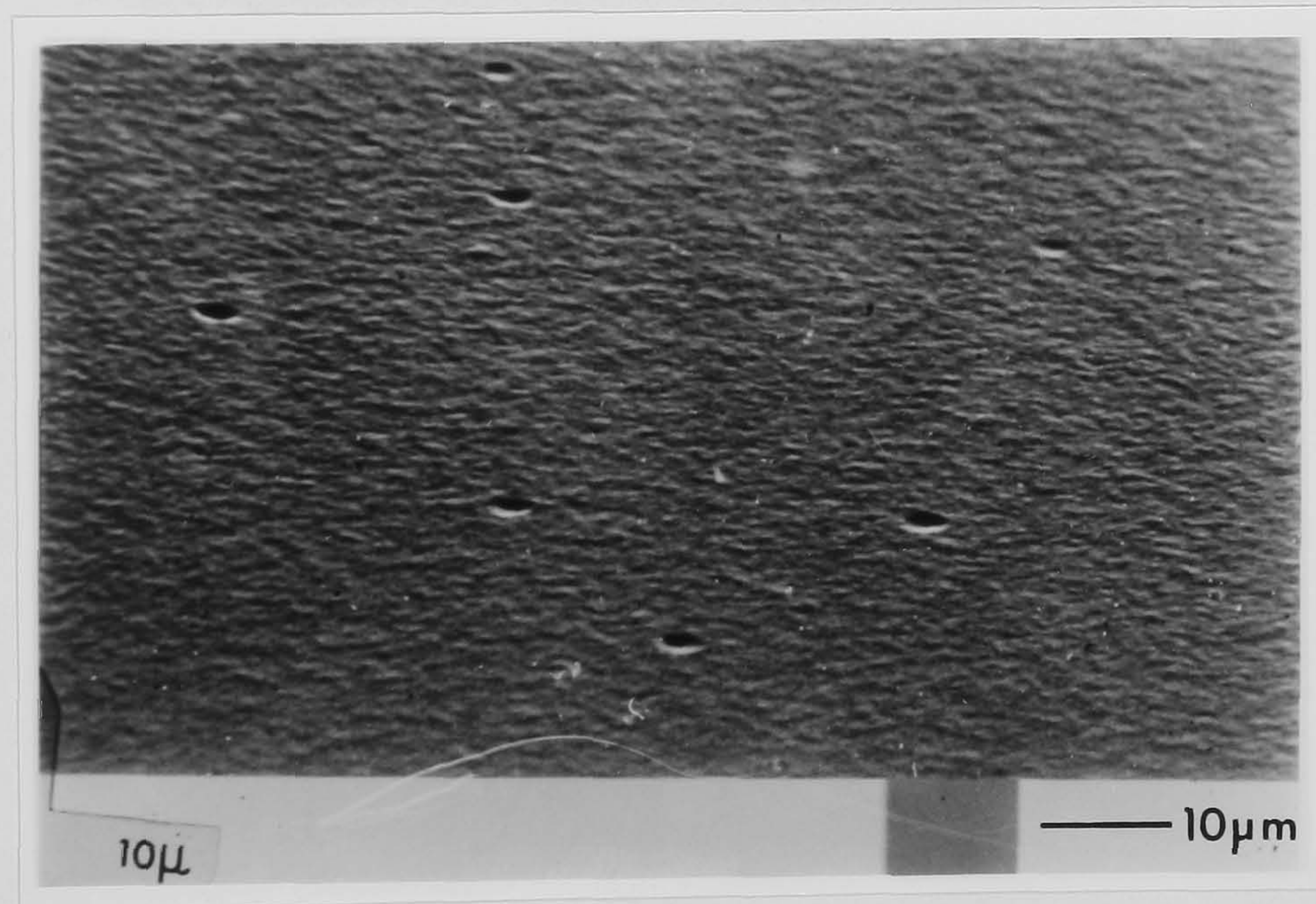


Figure 6.7 — Secondary emission micrograph of an as-grown CdTe thin layer surface grown on glass at a substrate temperature of 200°C , magn.=10K

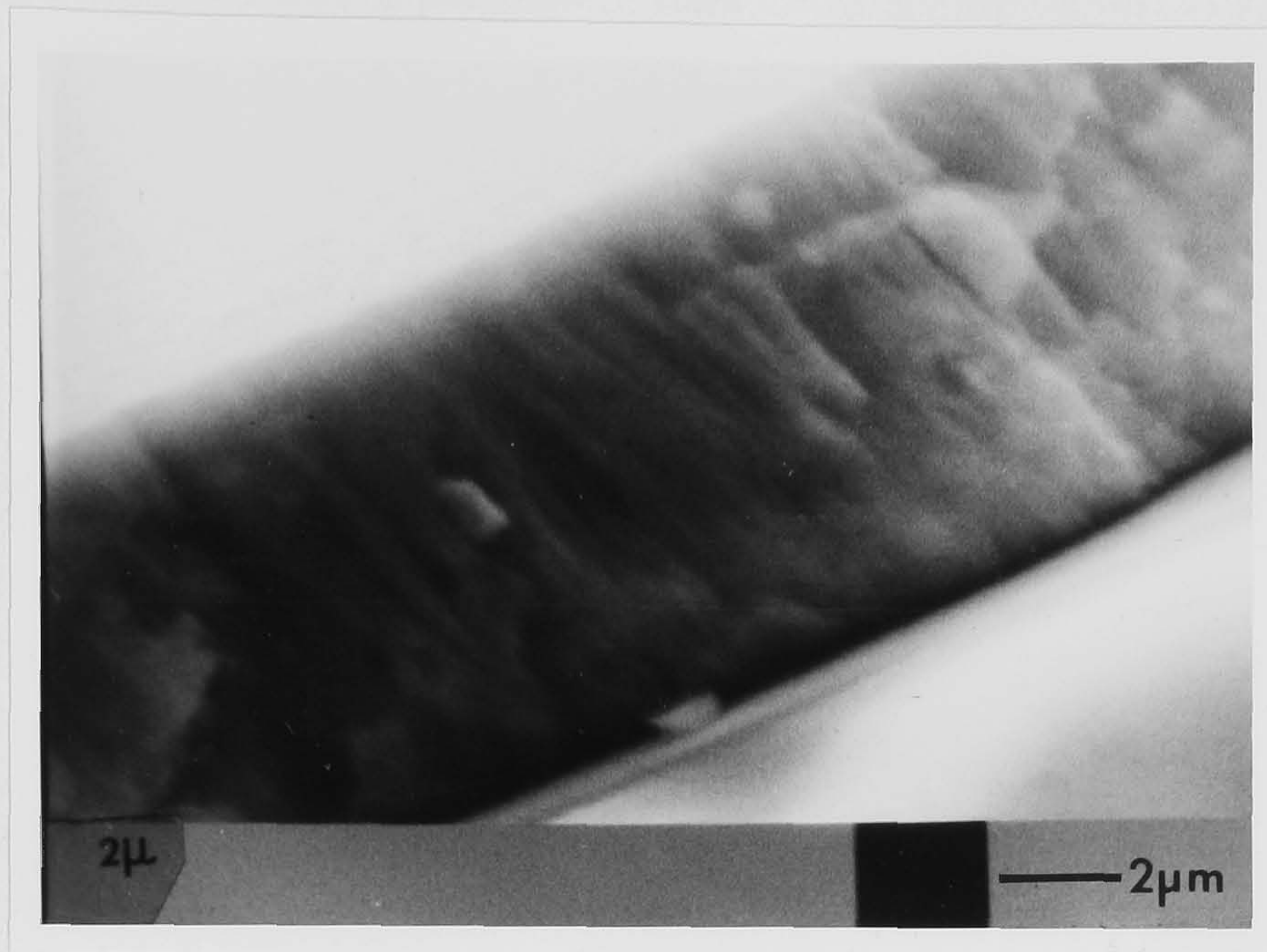


Figure 6.8 — Secondary emission micrograph of a cross section through an as-grown CdTe thin film grown on glass at a substrate temperature of 200°C, magn.=10K.

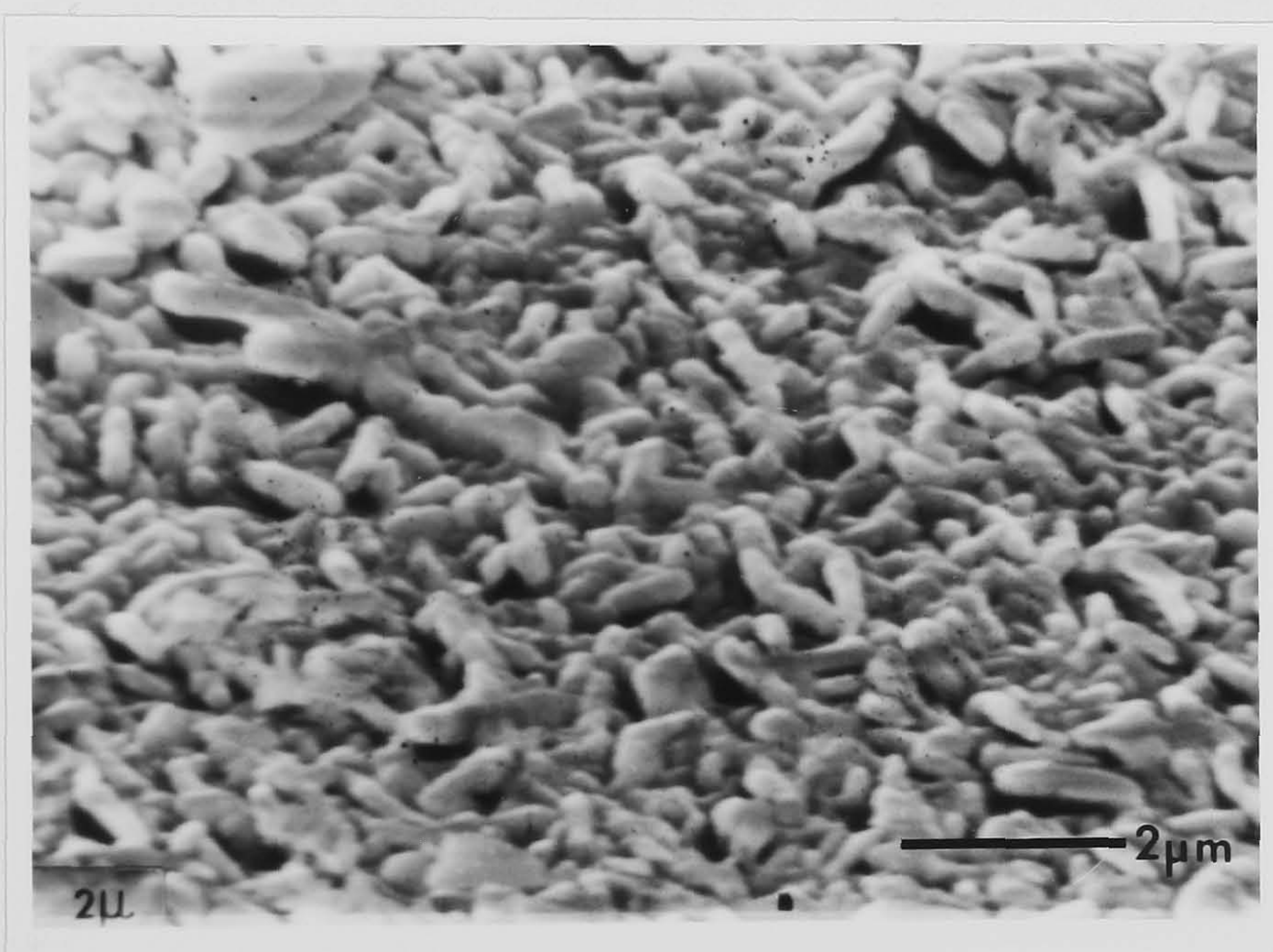


Figure 6.9 — Secondary emission micrograph of a CdTe:Cl₂ thin layer surface grown on glass by co-evaporation of CdTe and CdCl₂, magn.=10K.

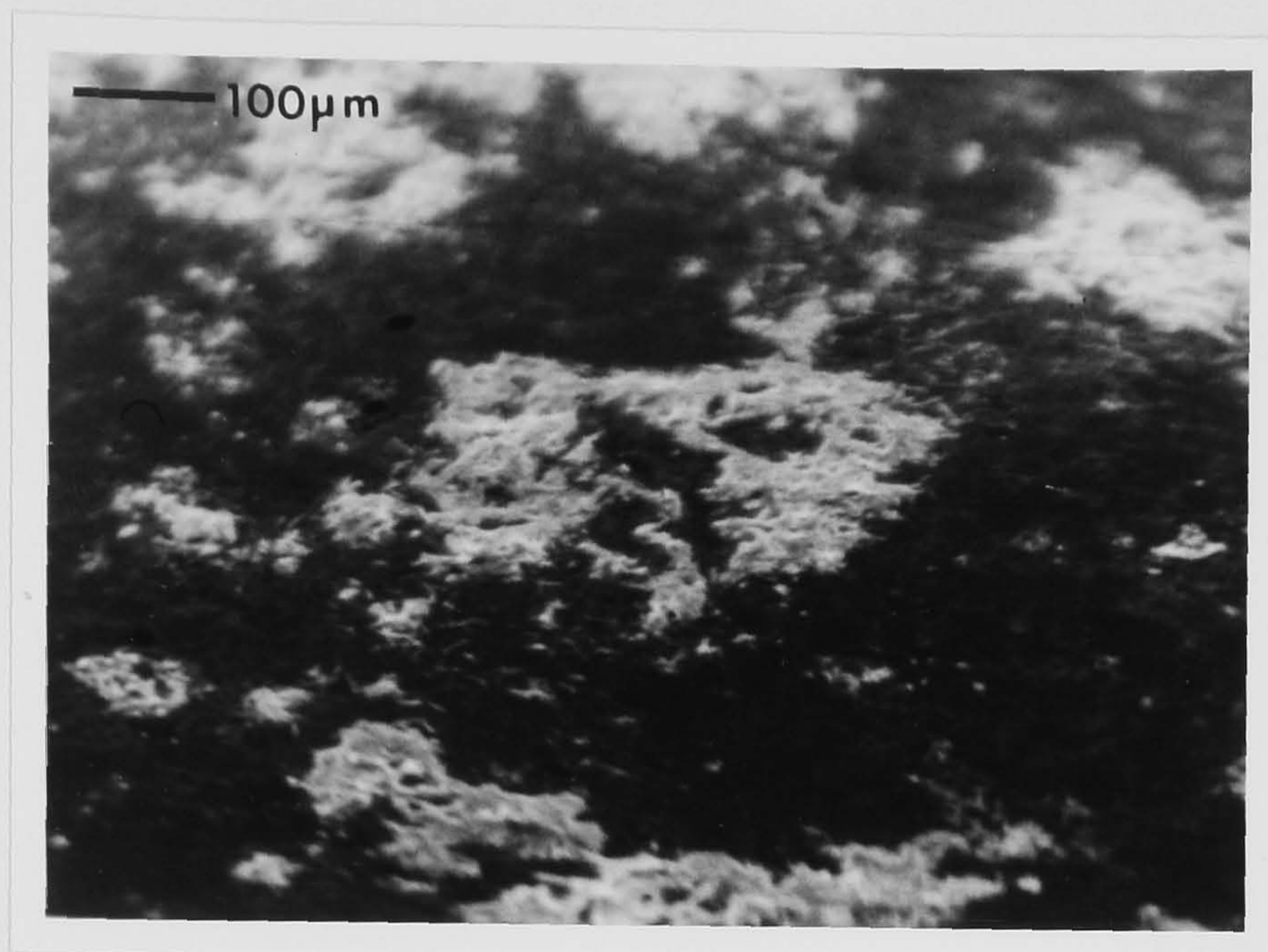


Figure 6.10 — Secondary emission micrograph of a CdTe:Cl₂ thin layer surface grown on glass by dipping into CdCl₂/Methanol solution, magn.=200.

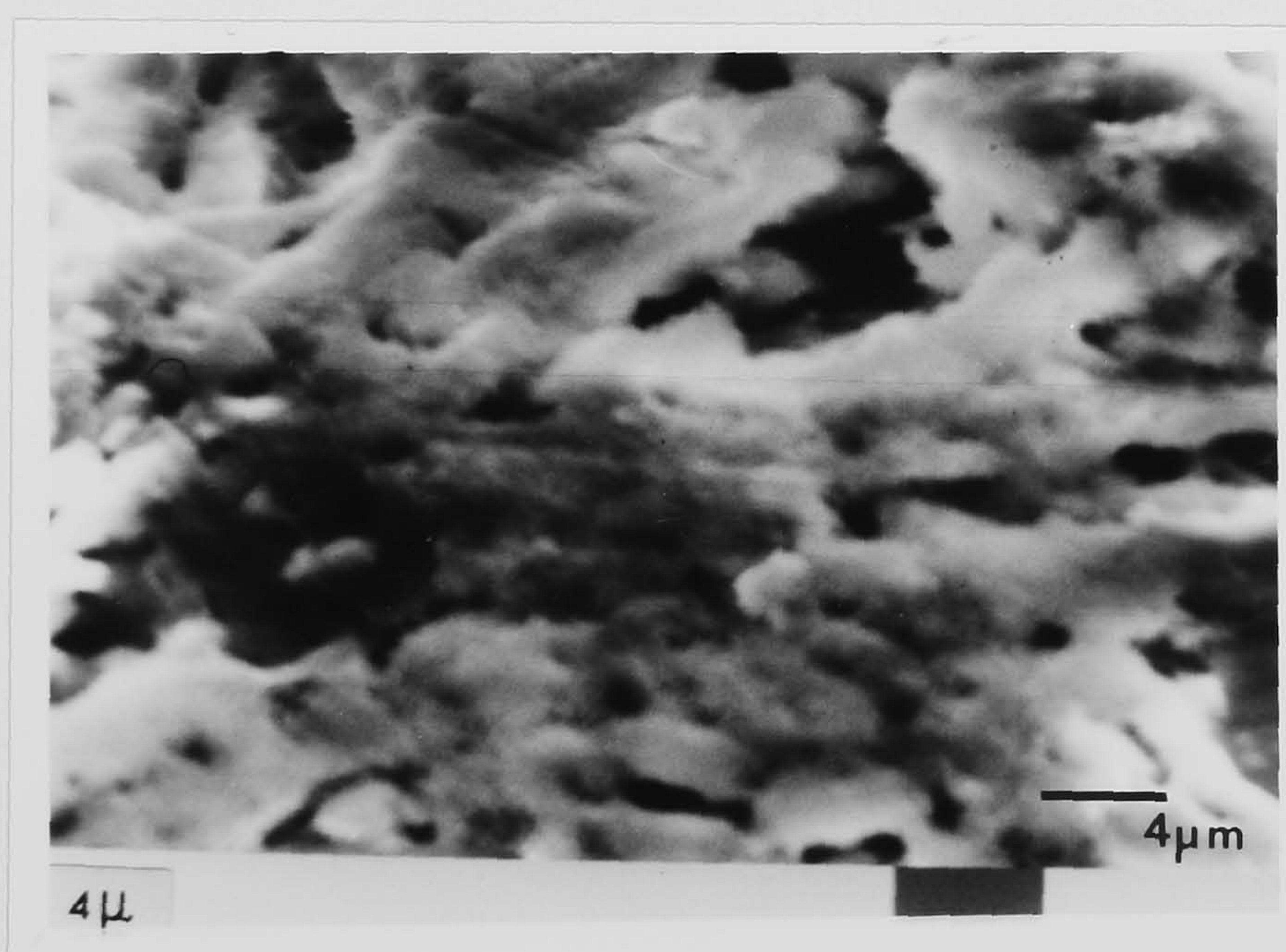


Figure 6.11 — Secondary emission micrograph of a CdTe:Cl₂ thin layer surface grown on glass by dipping into CdCl₂/Methanol solution, magn.=5K.

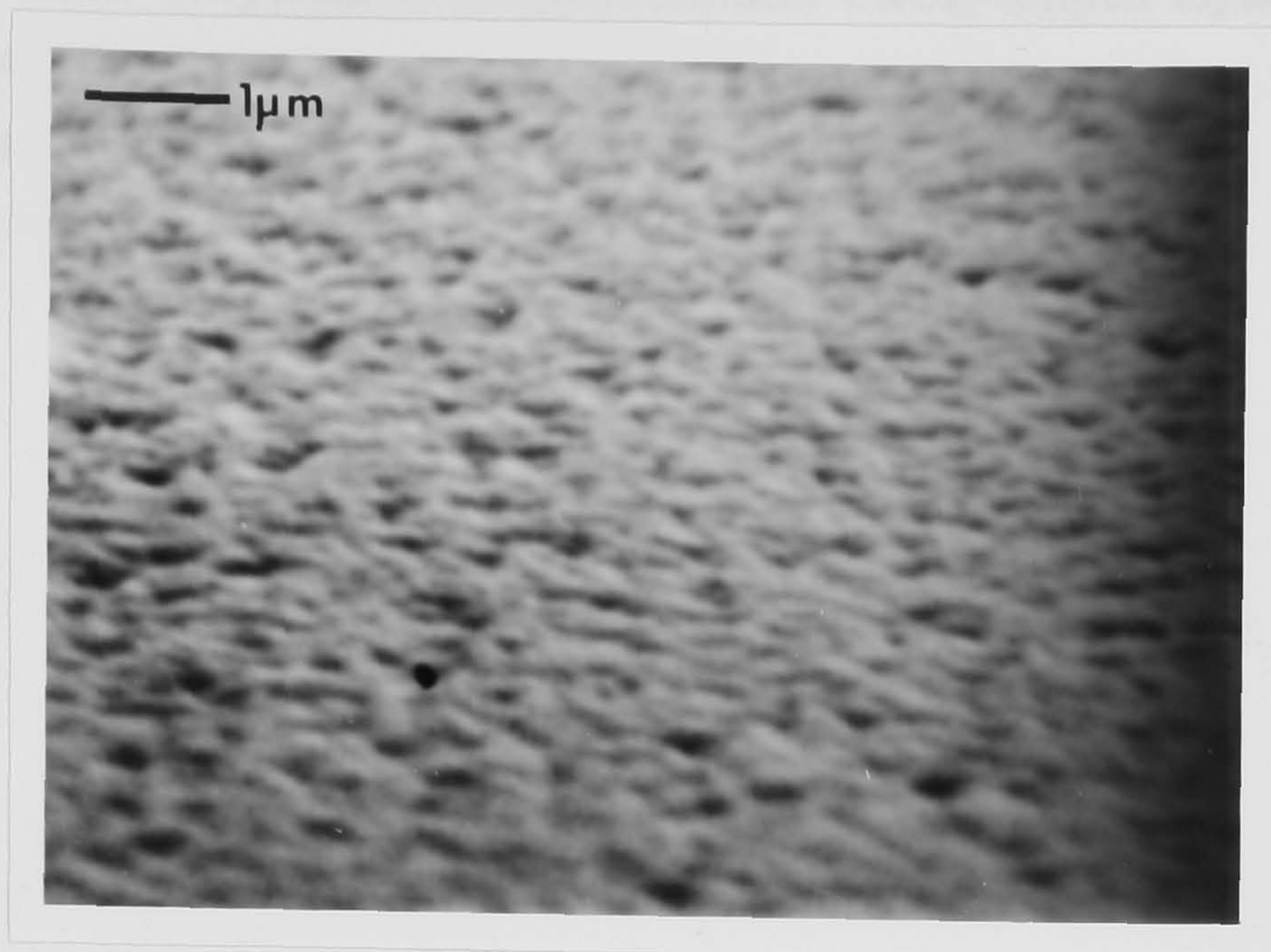


Figure 6.12 — Secondary emission micrograph of an as-grown CdS thin layer surface grown on glass at a substrate temperature of 220°C, magn.=20K.

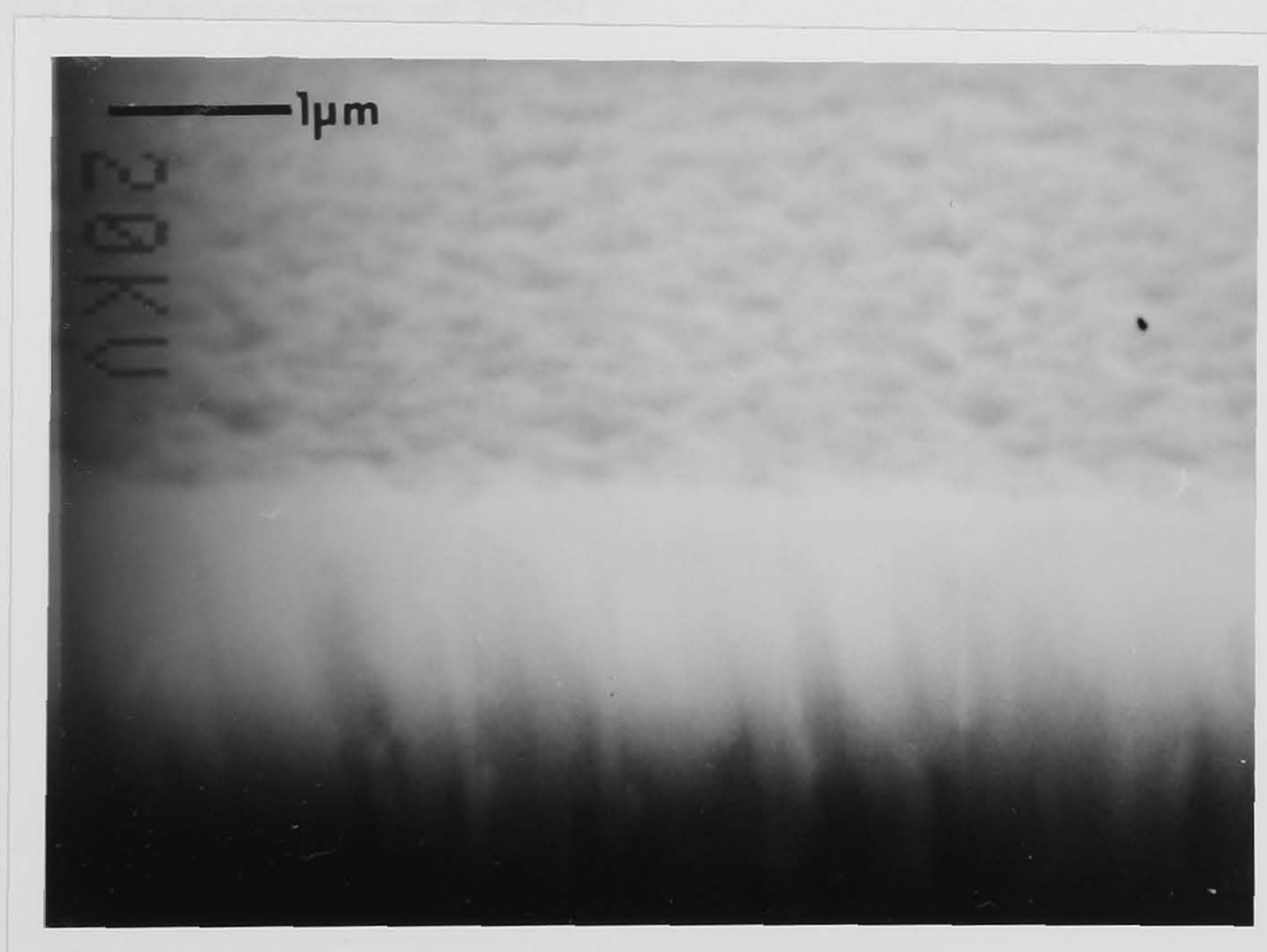


Figure 6.13 — Secondary emission micrograph of a cross section through an as-grown CdS thin film grown on glass at a substrate temperature of 220°C, mag. = 20K.

EDAX scans of typical co-evaporated and CdCl_2 -dipped layers on plain glass substrates are shown in Fig.6.16 and Fig.6.17 and 6.18 respectively. They displayed proportionately higher Cl_2 peaks in the island deposits (see Fig.6.18) confirming that there were CdCl_2 deposits.

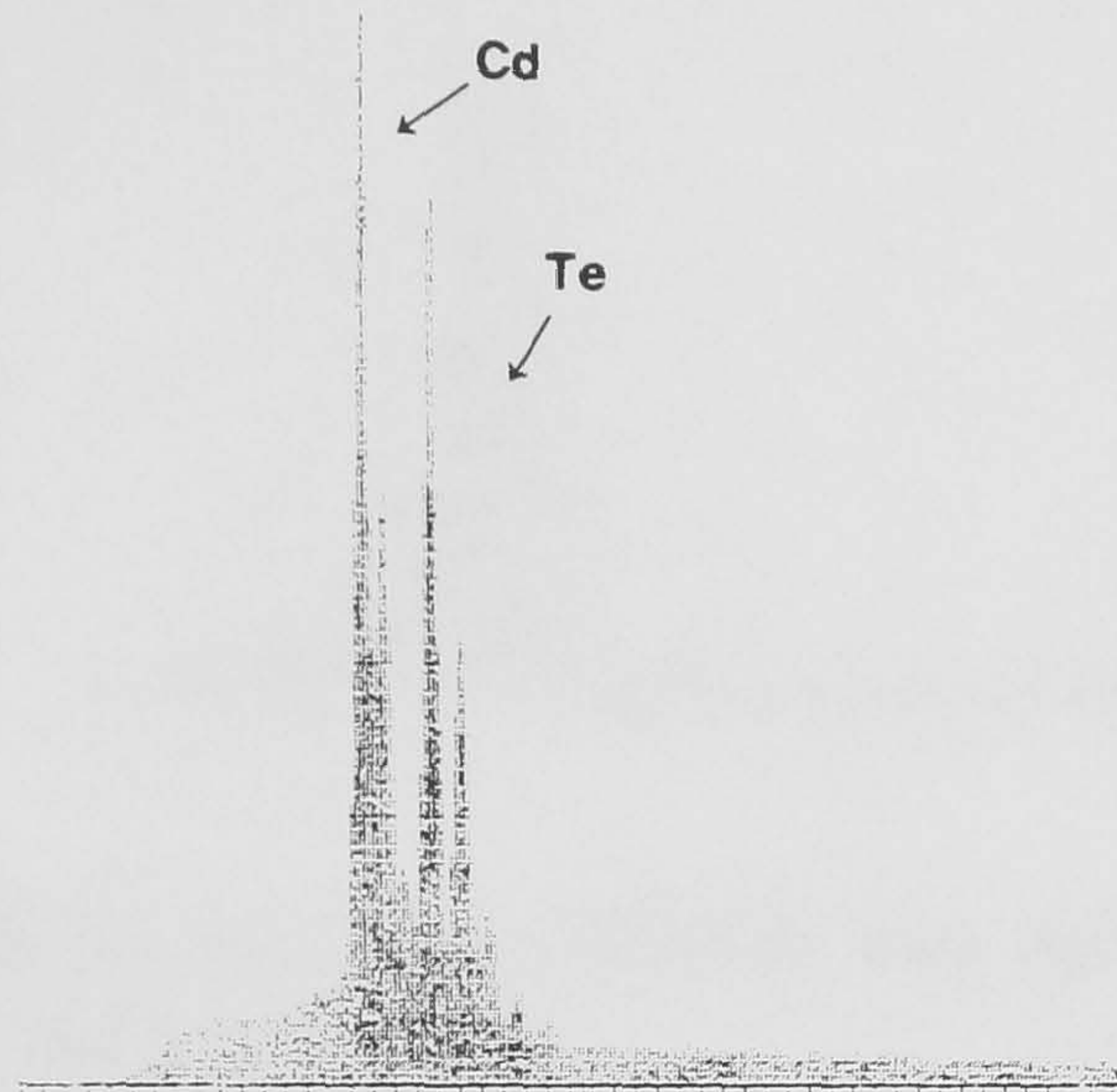


Figure 6.14 — EDAX scan of an as-grown CdTe thin layer surface grown on glass at a substrate temperature of 220°C .

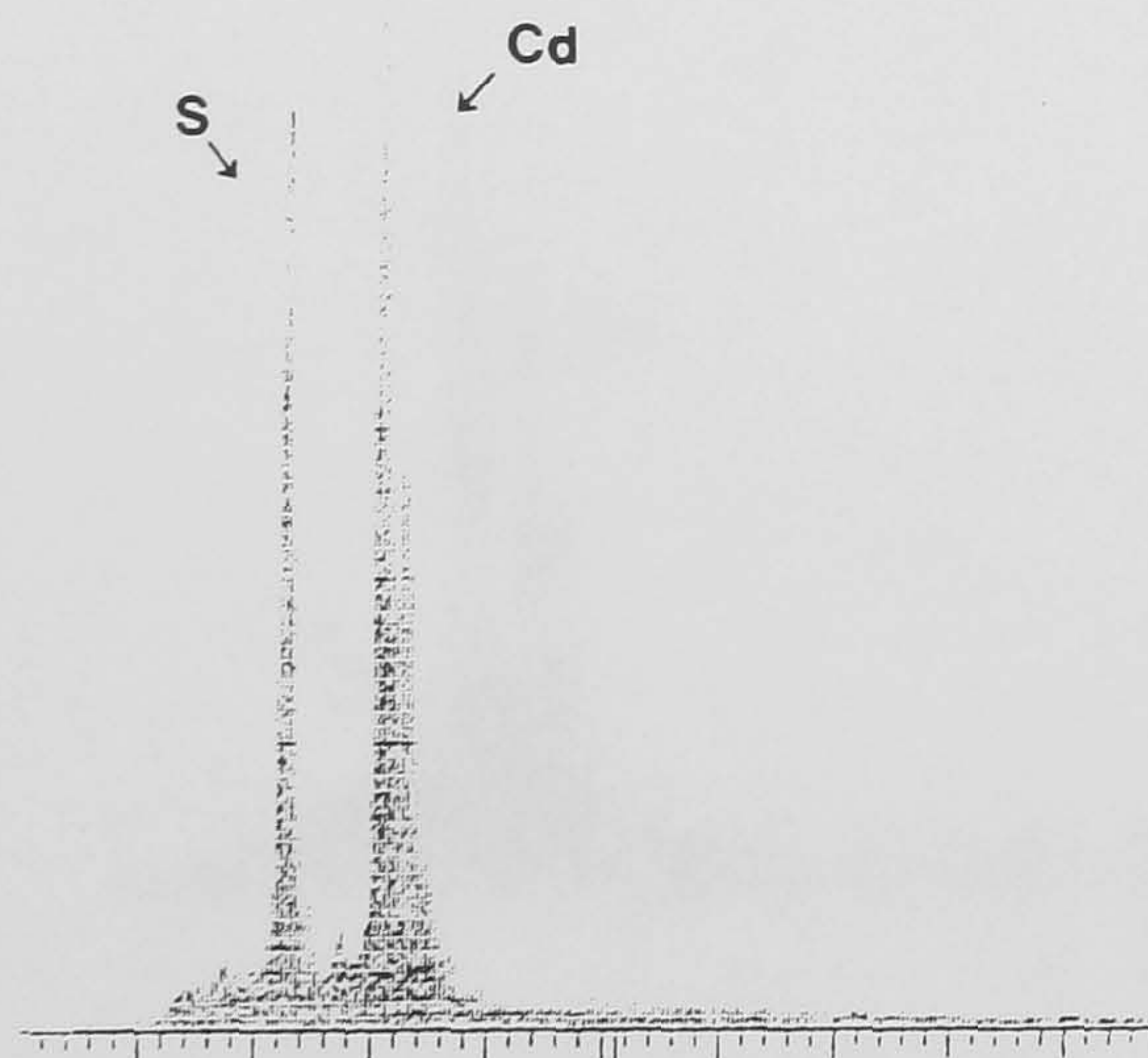


Figure 6.15 — EDAX scan of an as-grown CdS thin layer surface grown on glass at a substrate temperature of 220°C .

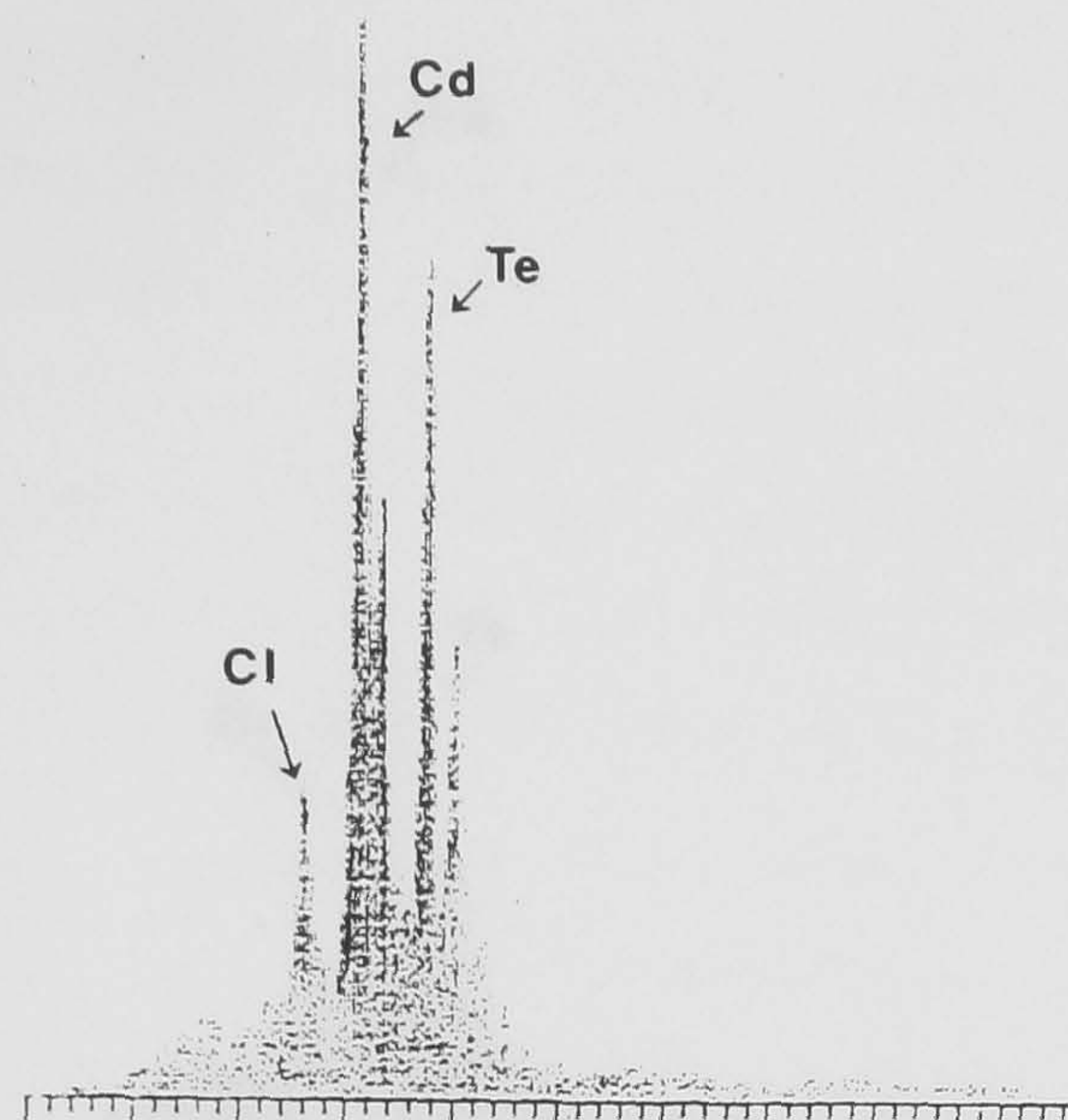


Figure 6.16 — EDAX scan of a CdTe:Cl₂ thin layer surface grown on glass by co-evaporation of CdTe and CdCl₂.

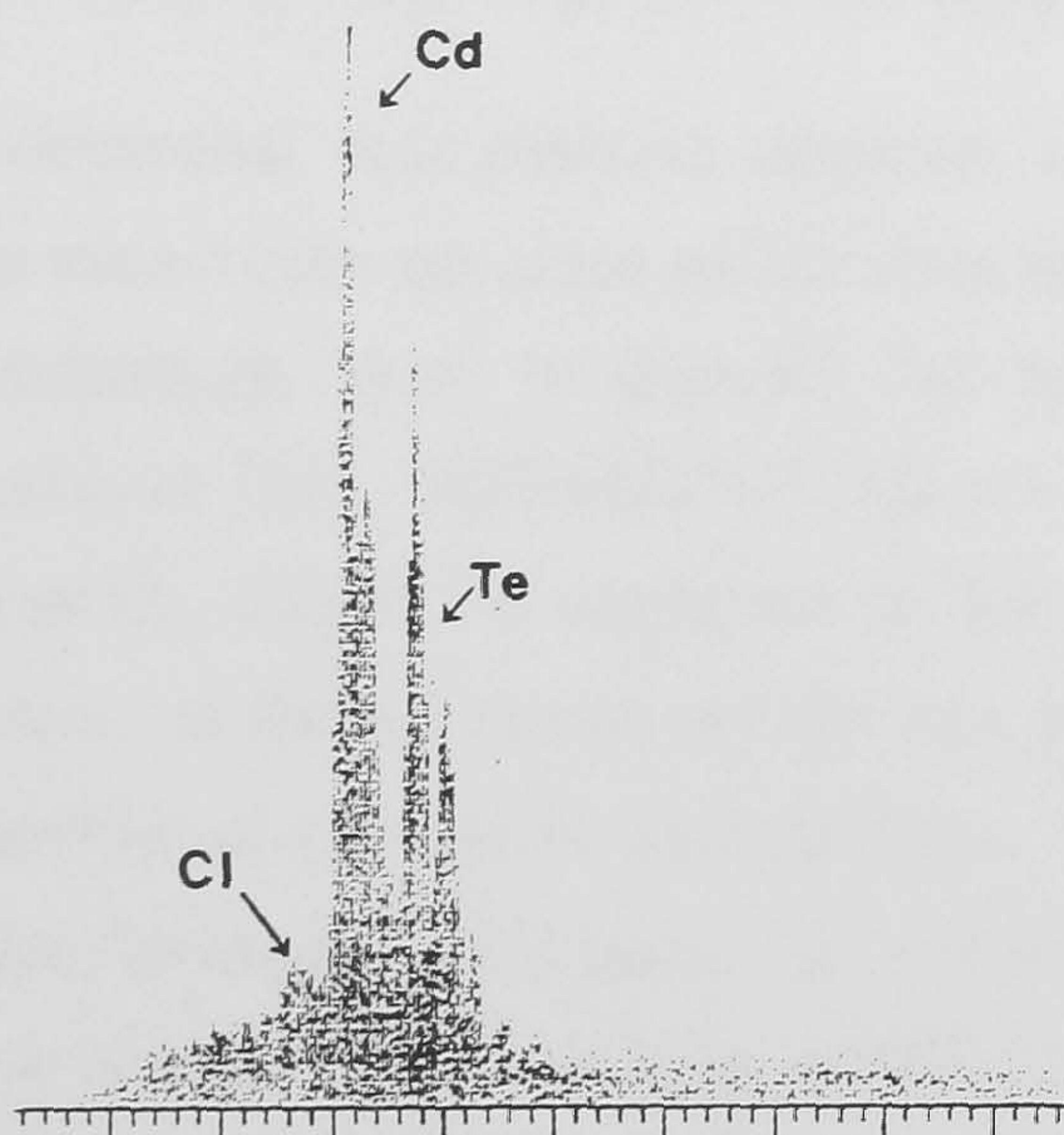


Figure 6.17 — EDAX scan of a CdTe:Cl₂ thin layer surface grown on glass by dipping into CdCl₂/Methanol solution; whole surface.

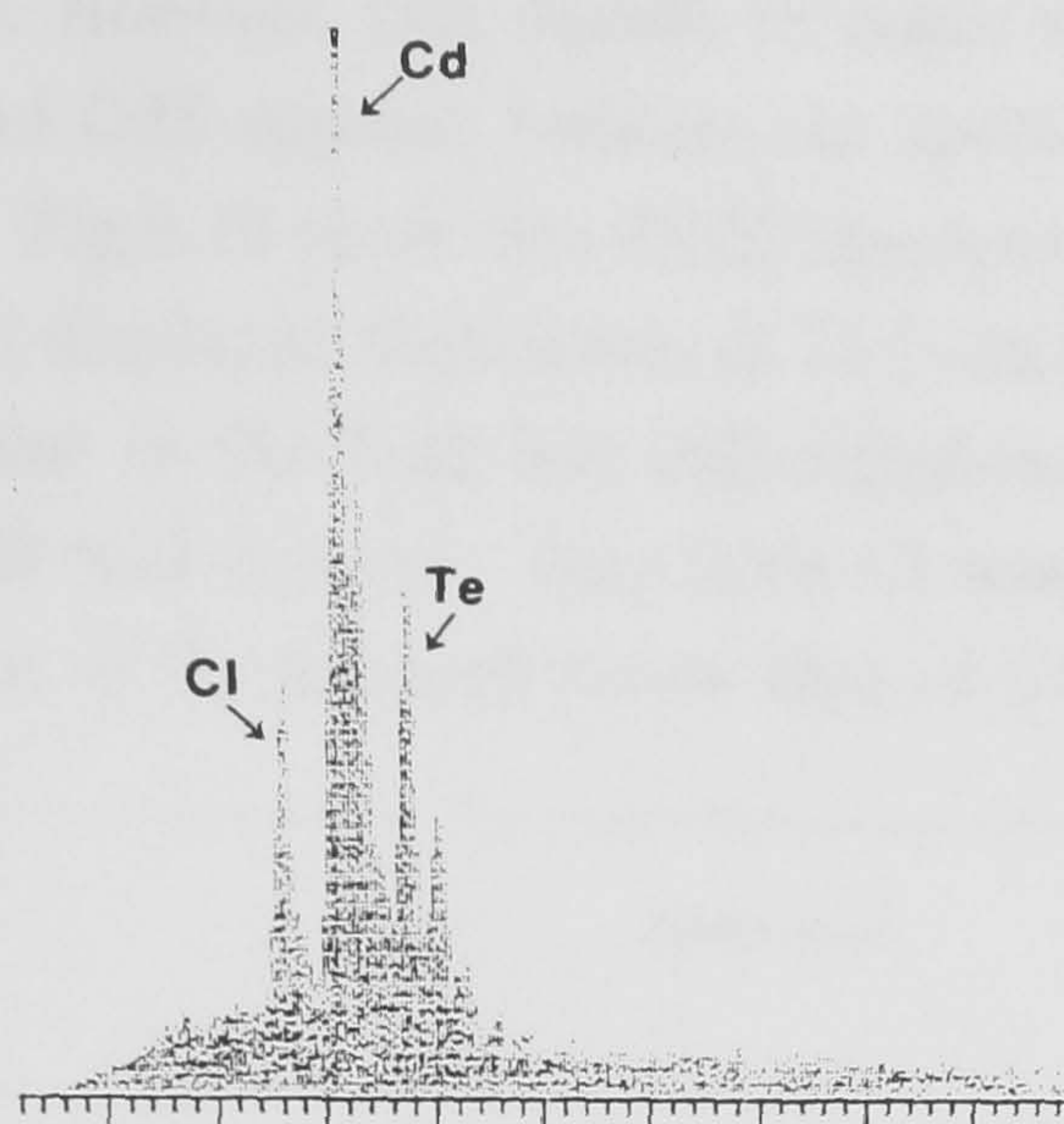


Figure 6.18 — EDAX scan of a CdTe:Cl₂ thin layer surface grown on glass by dipping into CdCl₂/Methanol solution; on the CdCl₂ island.

6.5 Secondary Ion-Mass Spectroscopy (SIMS) Analysis.

A quantitative elemental composition analysis of a few layers of CdTe, CdS and ITO/CdS/CdTe structures on glass substrates was carried using SIMS by BP Solar. The PVD technique, used to deposit the thin layers required relatively high growth temperatures (i.e. $\sim 650\text{--}800^\circ\text{C}$). Hence contamination from the surroundings during growth, might be expected in the layers. Such contamination results in the formation of defect states which can play an important role in the opto-electronic properties of the layers and devices. Fig.6.19 shows a SIMS depth profile of an, as-grown/heated, CdTe layer. In particular, the elements Si and Na displayed relatively a higher concentration profile ($>10^{18}\text{cm}^3$) through the layer than did the rest. This probably originated from the glass substrate and/or desorption off surfaces of the hotter growth fixtures, such as the crucible (silica-glass), etc.

The corresponding spectrum for a co-evaporated film is given in Fig.6.14, and shows the presence of Fe and K in the film. The Cl level was higher than the as-grown/heated film, as might be expected. A SIMS spectrum for a cell structure

(using undoped CdTe and CdS) is given in Fig.6.15. The Cd, S, Te and Sn peaks were easily identified. However, care should be taken when comparing, say the Cd peak in the CdTe and CdS regions, because the sputtering rates in the two compounds are different. Fig.6.16 shows the SIMS spectrum for a CdCl₂ co-evaporated heterostructures, and displayed high levels of Cl ($\sim 2 \times 10^{19} \text{ cm}^{-3}$) in the CdTe layer. The Cl level was lower in the CdS but still significant suggesting that some Cl diffusion into the CdS had occurred. Very little Cl was detected in the ITO layer. Interestingly, the level of Cu was well below that of Cl.

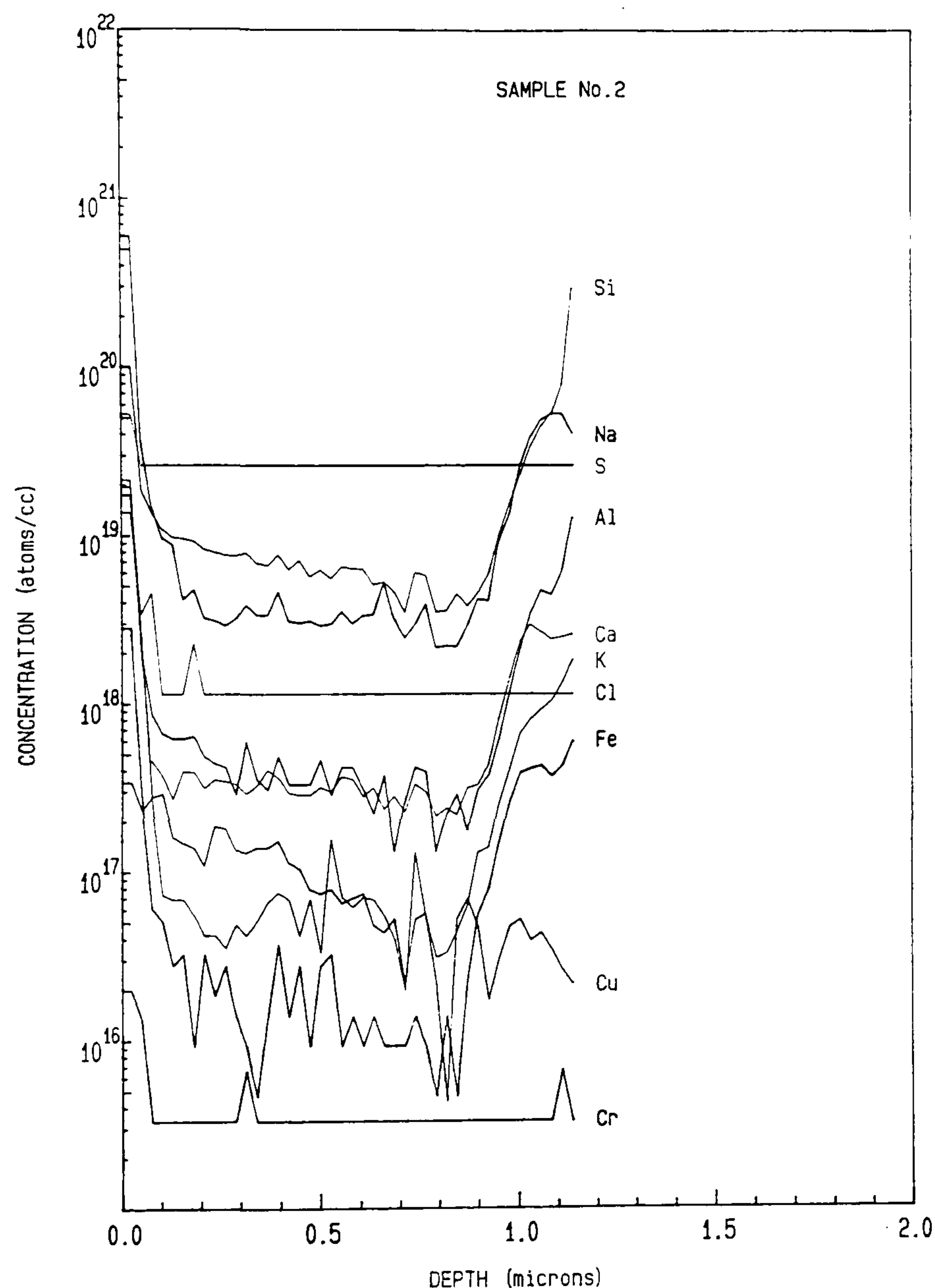


Figure 6.19 — SIMS impurity depth profile of an as-grown/heated CdTe thin film.

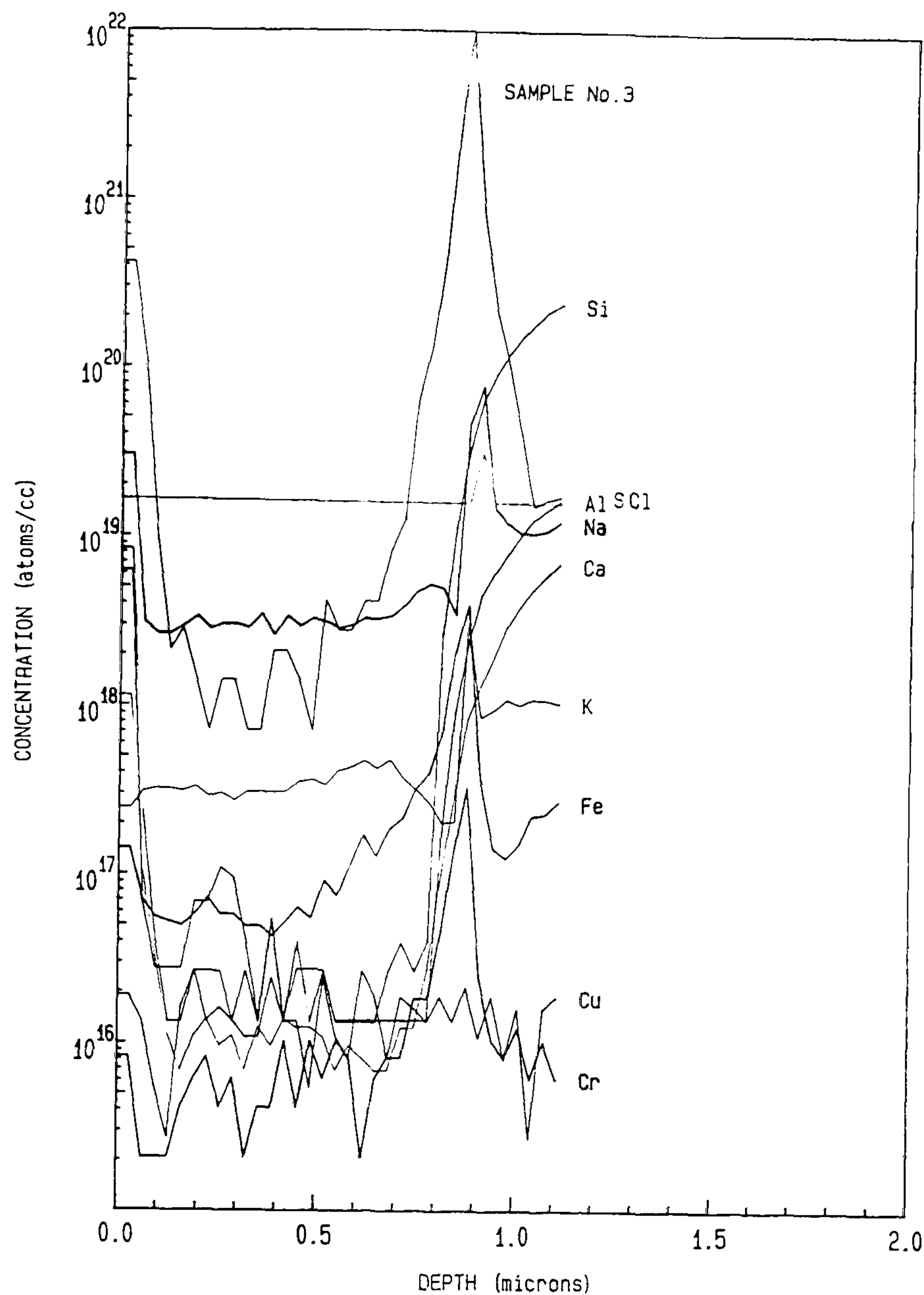


Figure 6.20 — SIMS impurity depth profile of a co-evaporated CdTe:Cl₂ thin film.

6.6 Conclusions.

The structure of CdTe and CdS layers grown by vacuum evaporation were assessed by several methods. XRD spectra of as-grown CdTe layers showed diffraction peaks at values of $2\theta_B$, associated with corresponding planes of cubic CdTe. However, additional peaks, small in intensity, were also seen at $2\theta_B$ values that could not be identified. It is possible that these were due to excess Te. The lattice parameter, a_o , was calculated and was in good agreement with the values for bulk single crystal CdTe. Grain sizes of the layers were estimated by the net broadening in the XRD spectra. Estimated grain sizes of the as-grown CdTe layers

grown at low substrate temperatures showed some scattering in values. However, at $T_{sub}=215^{\circ}\text{C}$, there was a maximum in the grain size.

The intensity of the $\{111\}$ diffraction line of heat treated CdTe layers increased, due probably to grain growth resulting in a greater degree of preferred ordering. In addition, a peak associated with $\{422\}$ planes and others which could be attributed to pure Te or TeO_2 also appeared. This may have been due to chemi-absorbed residual free Te “liberated” from the dissociation of CdTe during the annealing process. Grain sizes of heat treated layers were found to be larger than as-grown layers, confirming that grain growth had occurred during the heat treatment in air. The effects of heat treatment in the presence of Cl_2 during film deposition were found to be identical to those which were undoped.

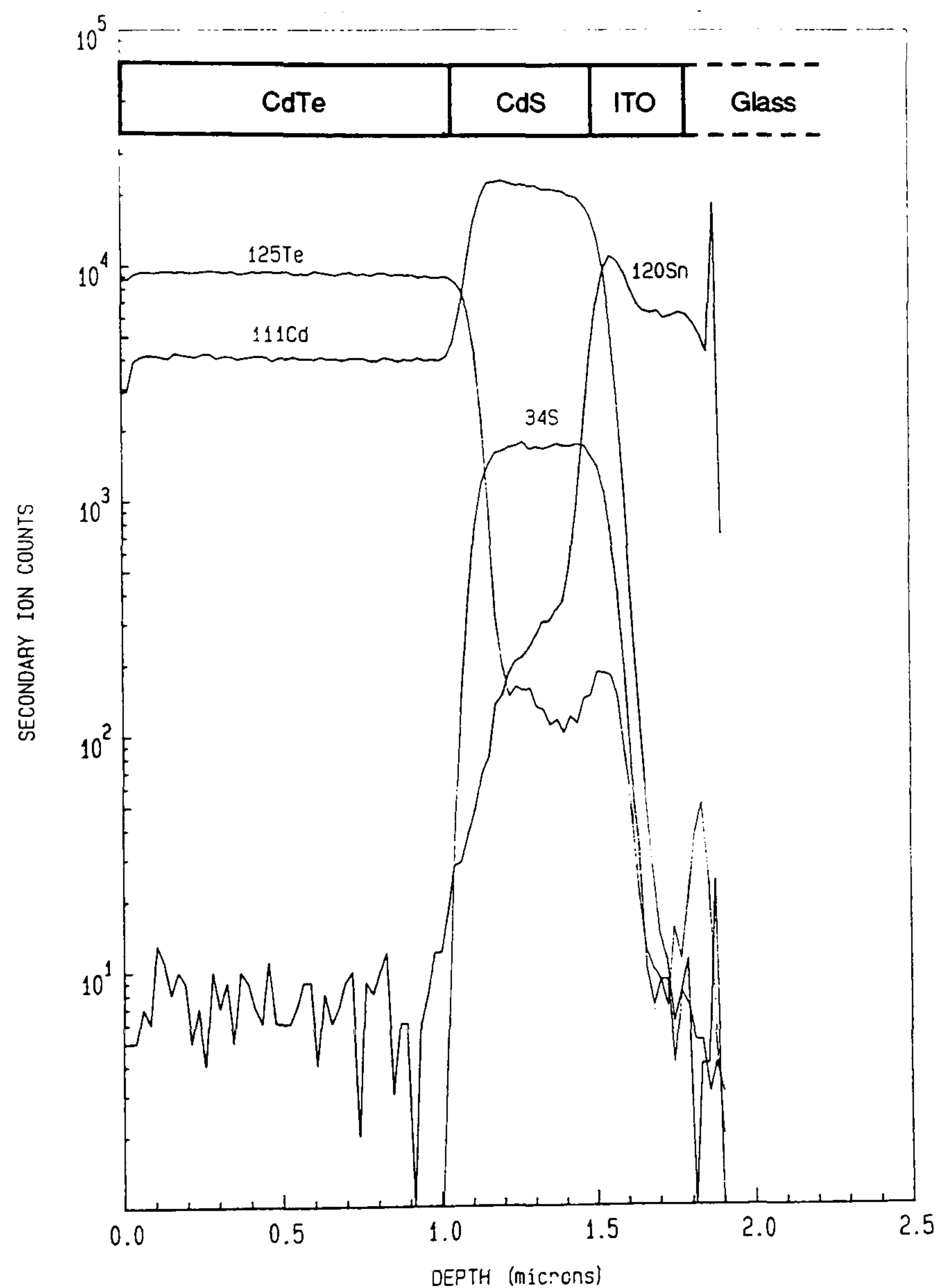


Figure 6.21 — SIMS impurity depth profile of a ITO/CdS/CdTe structure on glass substrates.

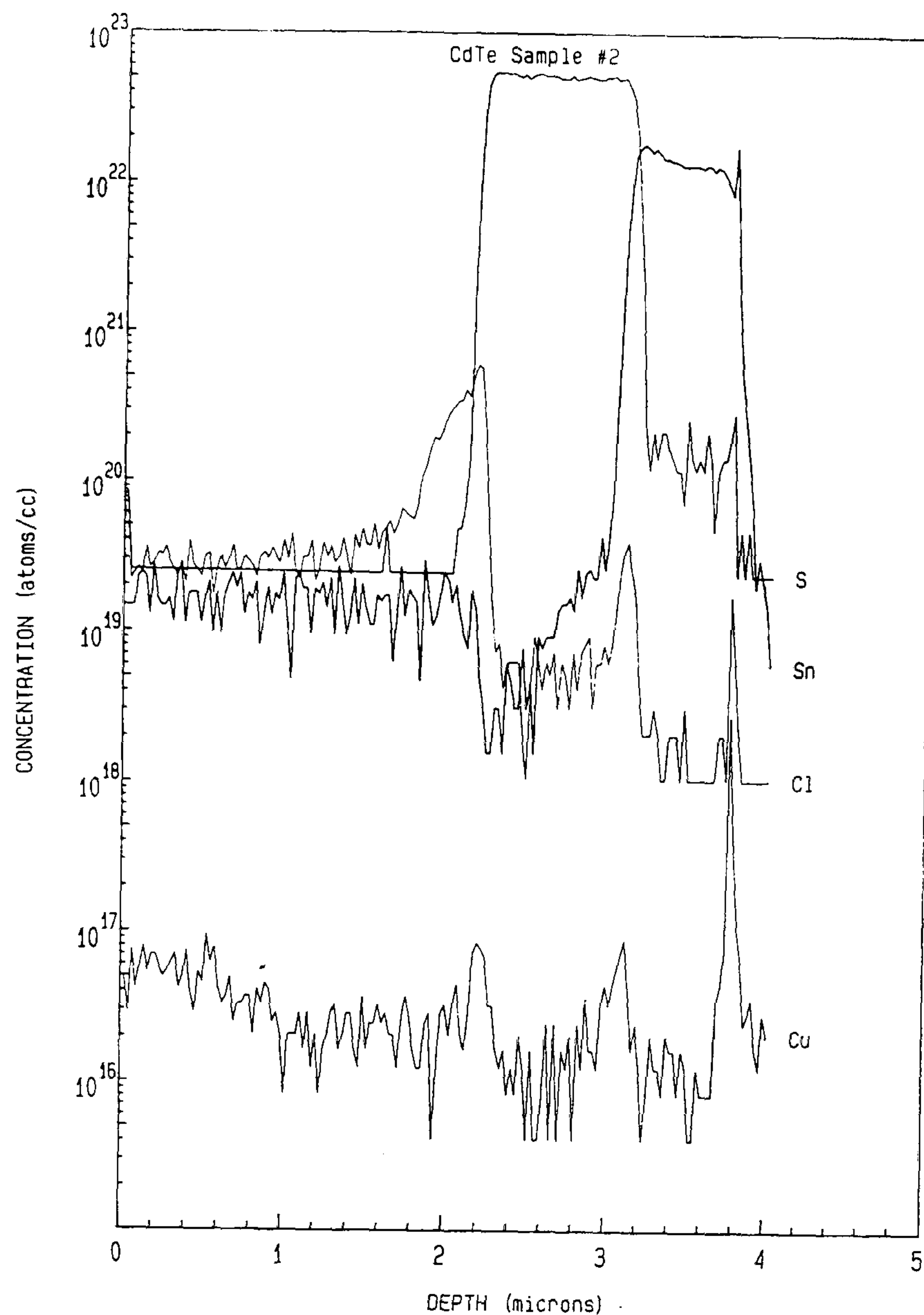


Figure 6.22 — SIMS impurity depth profile of a co-evaporated ITO/CdS/ CdTe:Cl₂ structure on glass substrates.

Due to the limits of the method, grain growth which might have occurred in Cl₂ treated layers could not be precisely estimated. Annealed layers of CdTe co-evaporated with CdCl₂, showed the presence of CdCl₂ and TeCl₂ in addition to the CdTe, suggesting that Cl₂ molecules form complexes with Te rather than Cd.

XRD spectra of CdS thin layers showed only two principal peaks at $2\theta_B$, values of 26.5° and 54.6°. The {0002} diffraction peak was narrow confirming that as-grown layers were {0002} preferred-orientation. Although the intensity of this peak increased moderately by heat treatment implying that the degree of preferred orientation was increased. The grain sizes estimates did not show any comparable change.

RHEED patterns of the surfaces of as-grown CdTe layers grown at substrate temperatures $\geq 180^\circ\text{C}$ had a random polycrystalline texture although some evidence of weak $\{111\}$ -preferred orientation was occasionally present. Whereas layers grown at a substrate temperature $\leq 170^\circ\text{C}$ had a distinct $\{111\}$ -preferred orientation (i.e. parallel to the substrate) which was stronger at the lower growth temperatures. RHEED patterns of heat treated layers were almost identical to those of as-grown $\{111\}$ -oriented layers, except that an additional arc located above the $\{111\}$ arc appeared. This may have been related to either Te or TeO_2 .

The polycrystalline nature and the $\{0002\}$ -preferred orientation of the CdS thin film layers were also confirmed by RHEED. These patterns taken from CdS thin layers deposited on ITO/glass substrates showed a $\{0002\}$ -preferred orientation, but the arcs were more diffuse, indicating that the sample surfaces were flatter.

Both CdTe and CdS displayed columnar growth with the growth axis tilted at about $\sim 15^\circ$ and $\sim 5^\circ$ to the substrate normal, respectively. Columnar structure was found to be less well developed, and the columns were less parallel and more discontinuous in CdTe than in CdS. This may affect electrical conduction. CdTe thin layers showed a smooth surface but with distinct pin-holes of about $2\mu\text{m}$ in diameter, whereas CdS thin layers exhibited smooth surfaces with no observable pin-holes at least on the scale of about $1\mu\text{m}$. EDAX scans also confirmed that CdTe and CdS thin film layers comprised only Cd and Te and Cd and S respectively.

A relative compositional depth profiling of impurity content by SIMS showed the presence of elements such as, Si, Na, Cl, Al, Cu, Cr, and K in the layers. This was associated with the glass substrates and/or desorption off hot surfaces such as crucible and etc. during the growth.

6.7 References.

1. A.Dawar, K.V.Ferdinand, C.Jagdish, P.Kumar and P.C.Mathur, J.Phys.D. in App.Phys: **16**, (1983) 2349.
2. P.Scherrer, Gött.Nachr, **2**, (1918) 98.
3. B.D.Cullity, "*Elements of X-ray Diffraction*", Addison Wesley, p.284, 1956.

4. J.Schaefer, G.A.Wolff, E.R.Hill, 2nd Quart.Tech.Progr.Rep., Contract AF33 (657) 9975, Harshaw Chem.Co., 1963.
5. A.Amitch, J.Vac.Sci.Technol., 15 (1978) 353.
6. G.R.Awan, Ph.D Thesis, University of Durham, 1987.
7. R.Wolfe, Applied Solid State Science, Advances in Materials and Device Research, Vol.5, p.251, "CdS Solar Cells", by A.G.Stanley, Academic Press, Inc., 1975.

Chapter VII

Electrical Properties of CdTe and CdS Thin Films.

7.1 Introduction.

The efficiency of a solar cell is strongly dependent on the opto-electronic properties of its constituent layers (i.e. the window and absorber layers) as well as their material properties. Hence, it was essential to investigate the electrical properties (i.e. resistivity, mobility etc.) of the CdTe and CdS thin films grown on glass substrates in an attempt to address to the n-CdS/p-CdTe cell performance and in the case of CdTe as ITO/p-CdTe:Cl₂/Au Schottky diodes. In particular, carrier scattering mechanisms in CdTe:Cl₂ layers were also investigated.

7.2 Carrier Mobility and Scattering Mechanisms.

Under the application of an external electric field, a charge carrier in free space will experience a constant acceleration with a consequent linear increase in its drift velocity with time. In a crystal, the motion of the charge carrier will be limited by scattering processes with various crystal defects or by collision with phonons, which in effect provide a “retarding force”. Under these circumstances, the carrier will experience an increased velocity, v_d (i.e. called drift velocity) which is proportional to the applied electric field, E , and may be written as [1];

$$v_d = \mu_d E \quad [7.1]$$

where μ_d is a constant of proportionality called the drift mobility.

In semiconductors, as in metals, at high temperatures (i.e. >150K), lattice vibrations and lattice deformation play a dominant role in providing the “retarding force” which limits the electron acceleration and brings it to a steady value. Imperfections due to native defects or substitutional impurities can also influence the carrier scattering, and this normally happens at lower temperatures (i.e. <100K).

Scattering phenomena influence the mean free time, τ , between the collisions which is related to the drift mobility by [2];

$$\tau = \frac{m^*}{q} \mu_d \quad [7.2]$$

There are several scattering mechanisms which can limit the carrier mobility. In this section, carrier transport in semiconductors is considered separately for two cases; -bulk single crystals and -polycrystalline thin films.

7.2.1 Carrier Transport in Bulk Single Crystals.

7.2.1.1 Lattice Scattering or Electron-Phonon Interaction.

There are three main lattice scattering mechanisms; optical, deformation and piezoelectric scattering.

i- Optical Phonon Scattering.

Optical phonon scattering is also known as polar optical mode scattering. It is associated with the vibration of two atoms in a unit cell in anti-phase which collectively produces an optical phonon. In compound semiconductors, adjacent atoms are oppositely charged forming an electrostatic potential associated with the optical phonon. Therefore, this kind of scattering could be important in II-VI compounds. The strength of the interaction between a carrier and an optical phonon is characterised by a coupling constant, α , defined by the relation;

$$\alpha = \frac{q^2}{2\hbar} \left(\frac{m^*}{2\hbar \omega_{op}} \right)^{1/2} \left[\frac{\epsilon_s - \epsilon_\infty}{\epsilon_s \epsilon_\infty} \right] \quad [7.3]$$

where ϵ_s and ϵ_∞ are the static and the optical dielectric constants respectively, and $\hbar\omega_{op}$ is the energy of the optical phonon. Due to the strong dipole moment set up by the optical modes in polar crystals, the coupling between a carrier and the optical modes is likely to be much stronger than in non-polar crystals. The mobility limited by optical mode scattering is given by [3];

$$\mu_{opt} = \frac{4}{3\sqrt{\pi}} \frac{q}{m^* \alpha \omega_{op}} f(z) \quad [7.4]$$

where,

$$f(z) = \chi(z)\{e^z - 1\}/\sqrt{z} \quad [7.4a]$$

and $z = \hbar\omega_{op}/kT$. $\chi(z)$ is a slowly varying function z having the value 1.0 for $z = 0$ and $z \cong 3$ and falling to about 0.6 for $z = 1$.

ii- Acoustic Phonon Scattering.

For a semiconductor, in which the bonding is primarily covalent, carriers are scattered predominantly by longitudinal acoustic (LA) phonons. These LA modes produce compressions and dilations which create local variations in the dielectric constant as well as the changes in the bandgap width. These produce a variation in the kinetic energy of a carrier as it passes through the crystal and the resultant interaction is known as acoustic phonon scattering. The main parameter involved is the deformation potential, E_{ac} , and the mobility limited by acoustic phonons is given by [4];

$$\mu_{ac} = \left[\frac{8\pi}{m^{*5}(kT)^3} \right]^{1/2} \left[\frac{q\hbar^4 \rho_d c_{ac}^2}{3E_{ac}^2} \right] \quad [7.5]$$

where ρ_d is the density of the semiconductor and c_{ac} is the longitudinal acoustic wave velocity.

iii- Piezoelectric Scattering.

This mechanism is confined to crystals which lack a centre of inversion symmetry. The interaction occurs as a result of the acoustic modes which generate regions of compression and rarefaction in the crystal. In piezoelectric crystals, these lead to the formation of electric fields. All II-VI compounds are piezoelectric, although those with the cubic structure are less so than the hexagonal ones. Mobility limited by piezoelectric scattering is given by [5];

$$\mu_{pie} = \frac{4.4 \times 10^{-2} \rho_d c_{ac}^2 \hbar^2 \epsilon_s^2}{q C_\alpha^2 (m^{*3} kT)^{1/2}} \quad [7.6]$$

where C_α is the piezoelectric electrochemical coupling constant.

7.2.1.2 Impurity Scattering.

i- Ionised Impurity Scattering.

This type of scattering results either from impurities deliberately introduced or from lattice defects generated by non-stoichiometry of the compounds. The defect can be positively or negatively charged and thus deflect the path of a passing electron. Conwell and Weisskopf [6] derived the first expression for the mobility limited by this kind of scattering by following a mathematical approach for the scattering of an electron in the Coulomb field of an ionised impurity atom. However, another approach was developed by Dingle [7] and Brooks [8] which took account of the screening of the Coulomb field of the ionised impurity centres by free electrons or holes. The corresponding mobility is given by;

$$\mu_I = \frac{64\epsilon^2}{N_I Z^2 q^3} \left[\frac{\pi(2kT)^3}{m^*} \right]^{1/2} \left[\ln \left\{ \frac{24m^* k^2 T^2 \epsilon}{q^2 \hbar^2 n} \right\} \right]^{-1} \quad [7.7]$$

where N_I is the total number of ionised impurities weighted with the appropriate charge (i.e. $Q_{I,A}N_{I,A} + Q_{I,D}N_{I,D}$) and n is the free carriers per unit volume.

ii- Neutral Impurity Scattering.

Although neutral impurities may be expected to contribute less to the scattering than ionised impurities, their effect may not be by any means negligible, particularly at low temperatures. The interaction of the carriers with neutral impurities is analogous to electron scattering by hydrogen atoms. Erginsoy [9] calculated the mobility limited by neutral scattering to be;

$$\mu_N = \frac{m^*}{20 N^o \epsilon_s} \left(\frac{q}{\hbar} \right)^3 \quad [7.8]$$

where N^o is the number of neutral impurity atoms per unit volume. It is well known that scattering of electrons by atomic hydrogen is spin-dependent. At very low temperatures the spins of electrons can be almost completely polarised in a strong magnetic field so that marked spin dependence of the mobility under such conditions is to be expected. This was discussed in some detail by Solomon [10].

7.2.2 Carrier Transport in Polycrystalline Thin Films.

Most analysis and modeling techniques correlating the transport properties with the polycrystallinity of thin films are based upon the consideration that the grain boundaries have an inherent space-charge region due to the interface. Band bending occurs, and potential barriers which impede charge transport result. One of the earliest models accounting for the mobility in polycrystalline semiconductor films was that of Volger [11]. His model was based on the premise that the crystal is composed of inhomogeneous domains of high conductivity and very low conductivity in which no space charge regions exist. This analysis was followed by that of Petritz [12] whose model differs from Volger's in that it is based upon the thermionic emission of carriers over grain boundary barriers. The analysis considered initially a single grain and a single boundary or barrier. The total resistivity of this case is;

$$\rho_g = \rho_1 + \rho_2 \quad [7.9]$$

where the subscripts signify grain or crystalline, 1, and boundary, 2, regions respectively. It was assumed that for the usual case, $\rho_2 > \rho_1$, then the overall conductivity, σ , is given by;

$$\sigma_g = A_g \mu_{cryst} \exp(-E_b/kT) \quad [7.10]$$

where A_g , μ_{cryst} and E_b are a constant, the perfect crystal mobility and the inter-grain potential barrier respectively. Seto [13] later, developed the most comprehensive analysis of electrical transport in polycrystalline thin films which are governed by carrier trapping at the grain boundary (see Fig.7.1). He made the following assumptions;

- i- Grains are of uniform size, L with grain boundary depletion widths, ℓ .
- ii- Only one type of impurity atom is present and uniformly distributed with a concentration N/cm^3 .
- iii- The grain boundary thickness is negligible and contains Q_t/cm^2 traps located at energy E_t with respect to the Fermi energy level, E_f .
- iv- The traps are initially neutral and become charged by trapping a free carrier.

Thus all the mobile carriers in a region between $\frac{L}{2}-\ell$ and $\frac{L}{2}$ (see Fig.7.1) are trapped, resulting in a space charge region. The model considers that thermionic emission current is the dominant current transport mechanism. Thermionic current density, J_{th} , for an applied voltage, V , across a grain boundary is;

$$J_{th} = q^2 p_a \left[\frac{1}{2\pi m^* kT} \right]^{1/2} \exp(-E_b/kT) V \quad [7.11]$$

where p_a is the average carrier concentration.

For a given crystalline size, there exist two possible conditions depending on the doping concentration;

i- The product $LN < Q_t$: crystallite is completely depleted, and traps are partially filled so that $\ell=0$.

ii- The product $LN > Q_t$: only part of the crystallite is depleted and $\ell > 0$. Hence the conductivity is given by;

$$\sigma \propto \exp \left[- \left(\frac{1}{2} E_g - E_f \right) / kT \right], \text{ if } LN < Q_t. \quad [7.12a]$$

and

$$\sigma \propto T^{-1/2} \exp(-E_b/kT), \text{ if } LN > Q_t. \quad [7.12b]$$

The plots of $\ln(\sigma)$ vs T^{-1} and $\ln(\sigma T^{1/2})$ vs T^{-1} should give a straight line with a slope $-(\frac{1}{2}E_g - E_f)/k$, if $LN < Q_t$ and $-E_b/k$, if $LN > Q_t$ respectively. In either case, providing the current transport is dominated by thermionic emission, the grain boundary limited mobility is given by;

$$\mu_g = \mu_o \exp(-E_b/kT) \quad [7.13]$$

where,

$$\mu_o = qL(A\pi m^* kT)^{-1/2} \quad [7.13a]$$

The constant A takes the value of 2 according to Seto and 8 according to Orton [14]. Considering the composite influence of the surface bulk grain and grain boundary scattering, the effective film mobility can be written as;

$$\frac{1}{\mu_f} = \frac{1}{\mu_g} + \frac{1}{\mu_b} + \frac{1}{\mu_s} \quad [7.14]$$

where, μ_b and μ_s are the bulk grain and surface mobilities respectively.

Seto [13,15] and the others [16,17,18] noted several basic limitations of the grain boundary trapping model, including the following;

i- In Seto's model, the bulk resistivity of the grain was assumed to be insignificant with respect to the resistivity of the boundary region. If the grain size is large and the doping relatively high, the grain resistivity must be considered.

ii- Rather than the discrete or fixed energy assumed in the model, it is possible that the trapping states at the grain boundaries are distributed over some energy, as reported for the surface states of a free Si [19] surface or a Si-SiO₂ [20] interface.

iii- In some cases (e.g., large-grain polycrystalline Si), the carrier concentration in the space charge layer can become appreciable, leading to inaccurate values for the barrier heights as calculated by the Seto's model.

iv- Seto's model predicts (depending upon impurity type) that the trapping states are located in either the upper or lower half of the bandgap, and excludes midgap positions [17,18].

v- A major assumption of the Seto model, that available grain boundary traps in the bandgap are always filled, is not universally true.

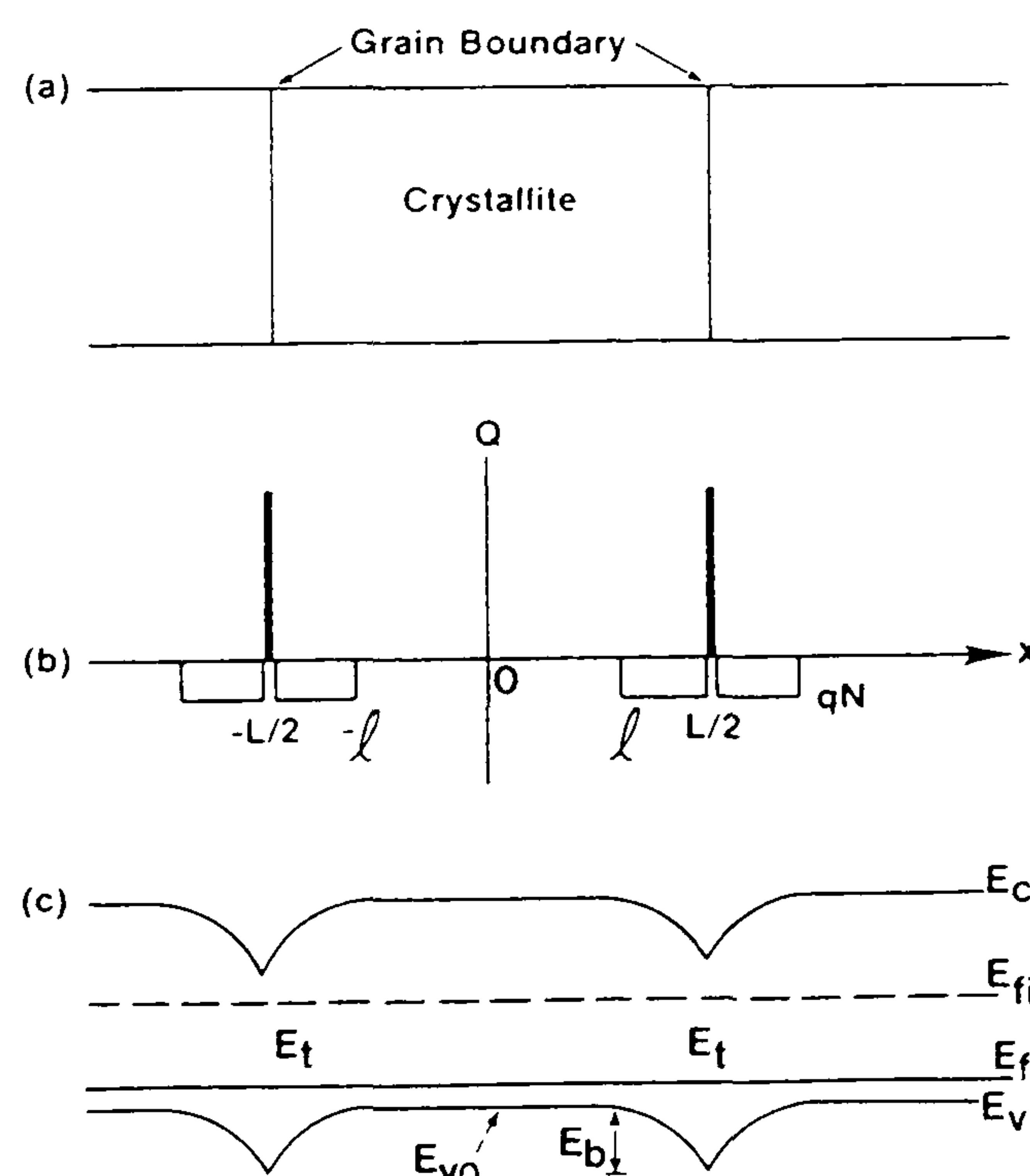


Figure 7.1 — Grain Boundary Trapping Model (Seto's [13]).

7.3 Electrical Properties of CdTe Thin Films.

7.3.1 Metal Ohmic Contacts.

Low resistance ohmic contacts are essential for the production of high efficiency solar cells. Thus far, one of the major problems encountered has been the lack of suitable low resistance contacts, due mainly to the high electron affinity of the CdTe (i.e. 5.78 eV). Two techniques appear to be particularly useful: the use of a suitable etchant, usually involving Br-Methanol and/or $K_2Cr_2O_7$ to prepare the surface followed by metallic contact formation; and the use of a particular high diffusivity impurity such as Cu, Li, Ni, or alternatively, a high conductivity p-type buffer layer, such as ZnTe between the CdTe and the metal contact (i.e. usually Au).

In the course of this study, Au was deposited onto CdTe layer surfaces that had been previously etched with 0.1–0.2% Br in Methanol solution in order to leave a Te-rich surface (i.e. p^+ layer [21,22,23]). Fig.7.2 shows the current-voltage (I–V) characteristics (on logarithmic axes) at 300K of Au contacts to CdTe. The slopes of the curves were found to vary from 1.00 to 1.03 indicating a linear response (i.e. $I \propto V^\alpha$, where $\alpha \cong 1$), and the I–V characteristics were found to be almost the same when the applied bias was reversed, indicating ohmic behaviour of the contacts in the current ranges examined.

In solar cells, the contribution of contact resistance, R_c , to the total series resistance, R_s , should be low. For instance, in the case of CdTe, the contact resistance contribution to R_s is often of the same order of magnitude as the bulk resistance or may even exceed it. Contact resistivity or specific contact resistance can be defined as [24];

$$\rho_c = \frac{1}{\left(\frac{dJ}{dV}\right)_{V=0}} = A_c R_c \quad [7.15]$$

where A_c is the contact area. This analysis gave a value for the contact resistivity for a typical low resistivity p-CdTe thin layer (i.e. $\rho \cong 2.5 \Omega\text{-cm}$) as $223 \Omega\text{-cm}^2$ at 275K. Contact resistivities generally showed rather high values. For comparison, values as low as $0.002 \Omega\text{-cm}^2$ and $0.1 \Omega\text{-cm}^2$ have been reported using Li, Cu/Au,

Ni, Ni/Au, Au/P for bulk single crystal CdTe and graphite, graphite/Cu (or Na, P), HgTe, ZnTe:Li/Au for polycrystalline thin films of CdTe respectively [25].

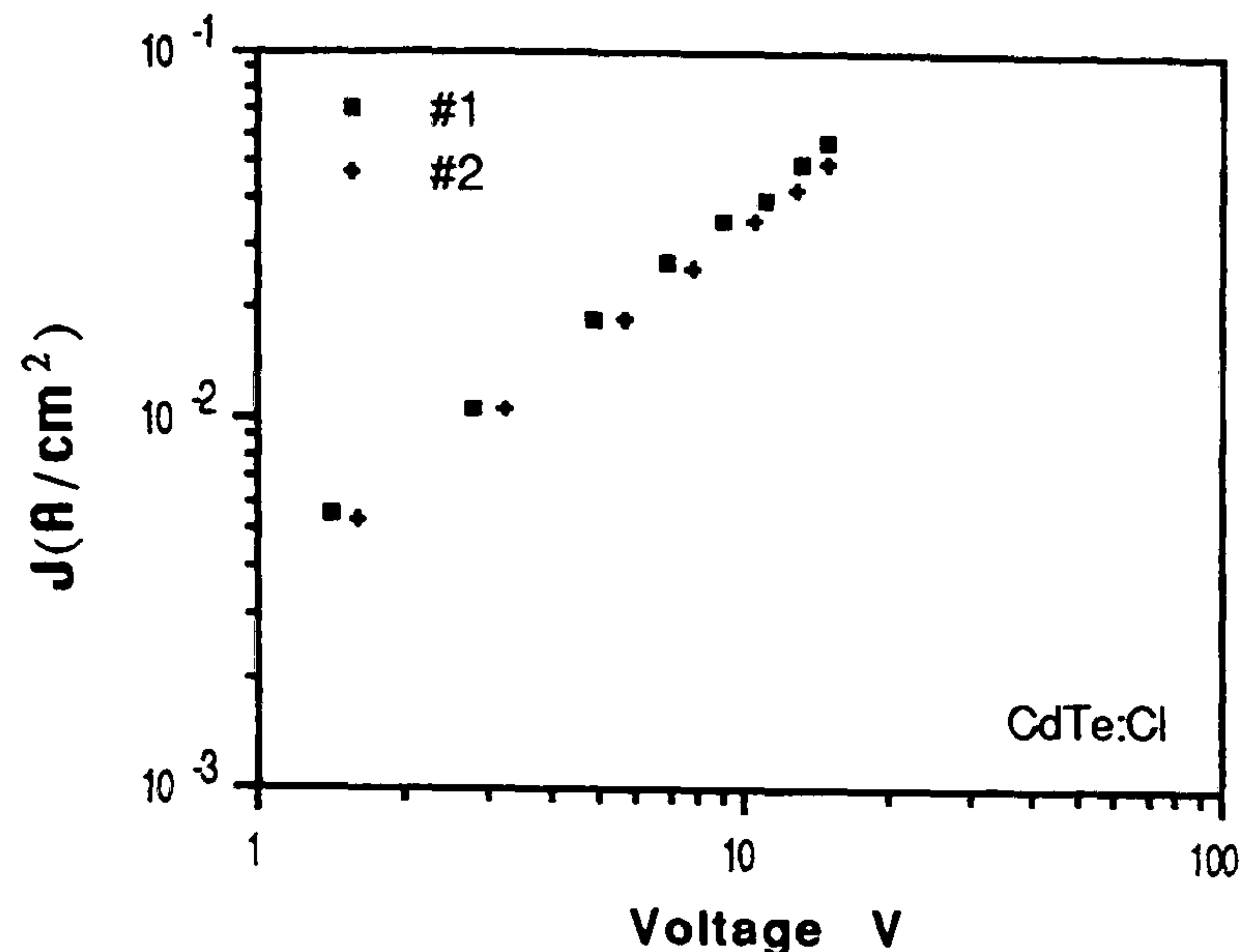


Figure 7.2 — $\log(J)$ vs $\log(V)$ characteristics of Au contact to CdTe thin layer.

7.3.2 Resistivity and Hall Measurements.

As-grown CdTe thin layers were slightly p-type as determined by the Seebeck effect and exhibited very high dark resistivities (i.e. $\sim 10^8 \Omega\text{-cm}$). More interestingly, heat treated layers (i.e. in air at about 400°C) displayed a more pronounced Seebeck effect. This could be attributed to oxygen-related Cd vacancies [26] (i.e. desorption of Cd atoms/molecules during annealing since Cd has a higher vapour pressure than Te). When measured under illumination (i.e. $\sim 80 \text{ mW/cm}^2$) the resistivity decreased by about one order of magnitude, due to electron-hole formation by the light.

During the initial stages of the study, Sb was introduced as a p-dopant element during the growth. The resistivity of the doped layers (obtained by the Van-der Pauw method) were found to be either low ($\leq 10^2 \Omega\text{-cm}$) or very high ($10^8 \Omega\text{-cm}$) at room temperature, although deposition parameters were kept the same during each growth. From this it was concluded that the introduction of Sb during growth could lead to metallic precipitates when conductivity increased discontinuously. Table 7.1 shows the resistivity and mobility results for low resistivity CdTe:Sb layers. Subsequently, CdCl_2 was introduced as a p-type dopant element to CdTe,

either during growth (pre-doping or co-evaporation) or through a post growth dipping procedure. The SIMS data (section 6.5) indicated high levels of impurity (including electrically active species). The relatively low carrier concentrations measured here, therefore, imply a high level of compensation and/or a low level of activation of the electrically active impurity species in the layer, as in commonly found in II-VI compounds.

Sample No:	$\rho(\Omega\text{-cm})$	$R_H(\text{cm}^3\text{C}^{-1})$	$\mu_H(\text{cm}^2\text{V}^{-1}\text{s}^{-1})$	$p(\text{cm}^{-3})$
3D2	48	1.3×10^3	27.1	4.8×10^{15}
3D5	157	6.8×10^3	43.4	9.9×10^{14}
3D3	210	1.1×10^4	50.5	5.9×10^{14}

Table 7.1 — Resistivity and Hall measurement results for low resistivity CdTe:Sb thin layers.

Temperature dependent resistivity and Hall measurements were also carried out for low resistivity CdTe:Cl₂ (co-evaporated) thin layers (due to the high resistivity of the undoped CdTe layers, temperature dependent measurements could not be performed). Fig.7.3 and Fig.7.4 show the $\log(\sigma)$ vs T^{-1} characteristics of CdTe:Cl₂ thin layer for the temperature ranges $3 < T < 400\text{K}$ and $10 < T < 400\text{K}$ respectively. Two values of the conductivity activation energy 0.07 meV (3–30K), and 41.8 meV (100–400K) could be obtained by extrapolating the two straight line regions of the characteristic. Fig.7.5 and 7.6 show the same data plotted on $\log(\sigma T^{1/2})$ vs T^{-1} axes. The slopes, here, give two values of activation energy of 0.33 meV (3–20K) and 35.2 meV (70–400K). The first set of plots were made to determine whether or not the grains were fully depleted, i.e. Eq.7.12a. However, the values of activation energy obtained were much small since $E_g/2 \cong 0.7\text{ eV}$ and the material was p-type (i.e. Fermi level close to the valence band). Consequently, it may be assumed that only the grain boundary regions were depleted (i.e. Eq.7.12b) and that $E_b \cong 35\text{ meV}$ for $T > 70\text{K}$ (i.e. the low temperature ($T < 70\text{K}$) characteristics suggest that other processes were limiting).

To investigate scattering mechanisms, mobility data for the same sample were plotted on linear axes (Fig.7.7), logarithmic axes (Fig.7.8) and $\log(\mu T^{-1/2})$ vs T^{-1}

axes (Fig.7.9 and Fig.7.10) to test for other scattering mechanisms. At temperatures below 240K, (see Fig. 7.7) hole mobility increased slowly with increasing temperature. At a temperature of about 260K, the mobility increased sharply and peaked at a temperature of $\sim 300\text{K}$. It dropped at higher temperature to a steady value of about $25\text{ cm}^2\text{V}^{-1}\text{s}^{-1}$. The slopes in the log-log plot (see Fig.7.8) indicated that mobility could not be limited by acoustic, piezoelectric or ionised scattering mechanisms.

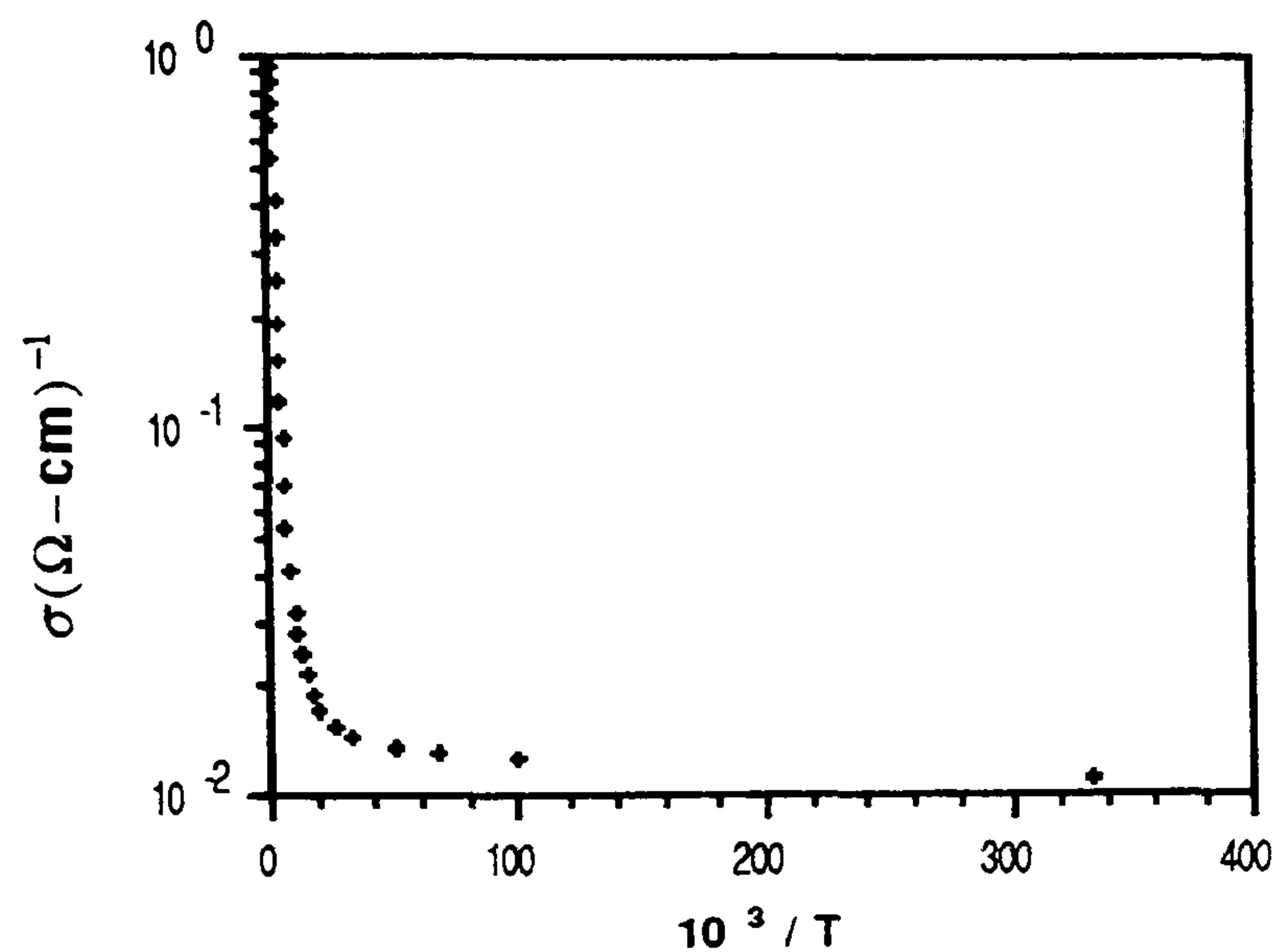


Figure 7.3 — $\log(\sigma)$ vs T^{-1} characteristic of a typical CdTe:Cl₂ thin layer, ($3 < T < 400\text{K}$).

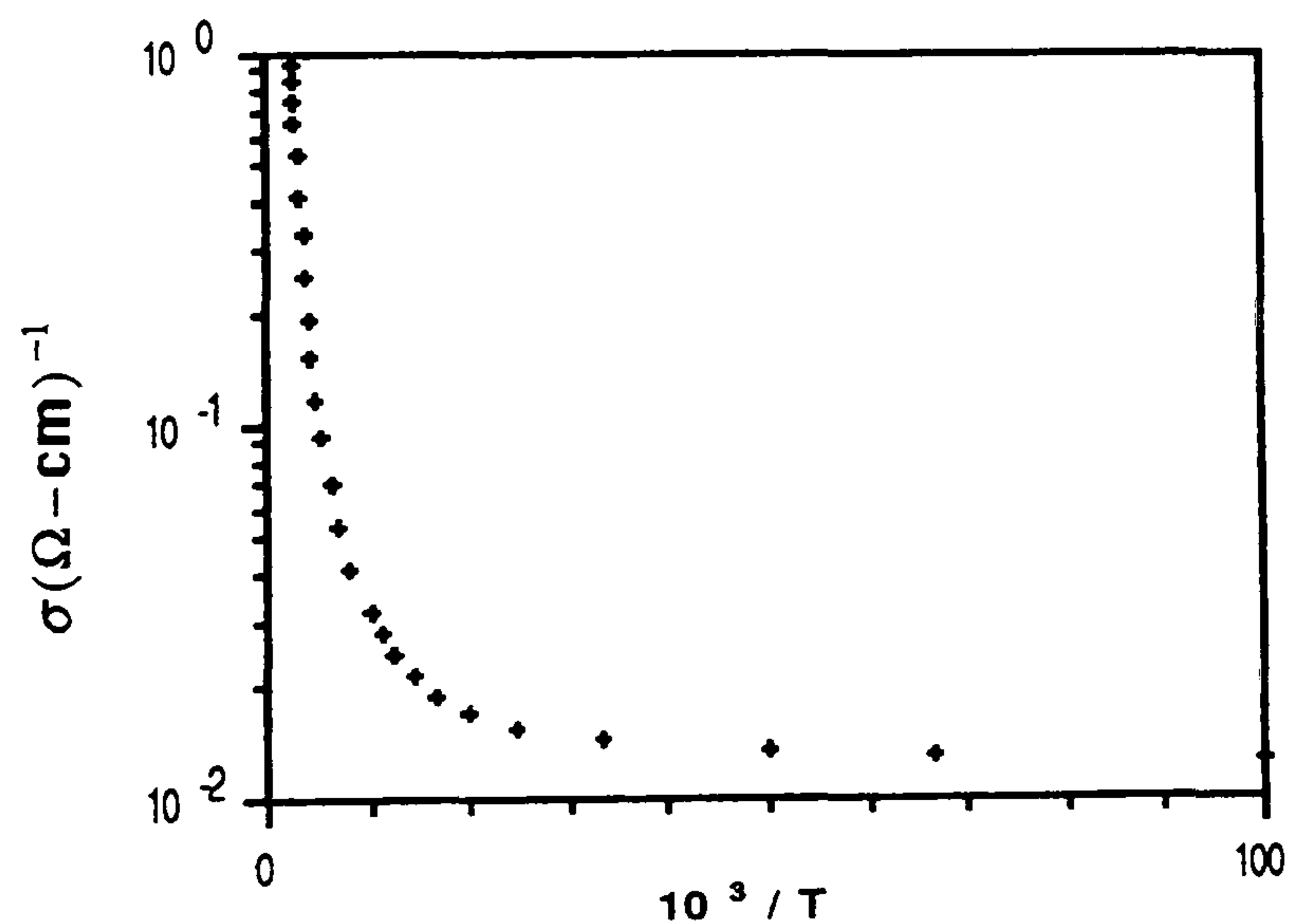


Figure 7.4 — $\log(\sigma)$ vs T^{-1} characteristic of a typical CdTe:Cl₂ thin layer, ($10 < T < 400\text{K}$).

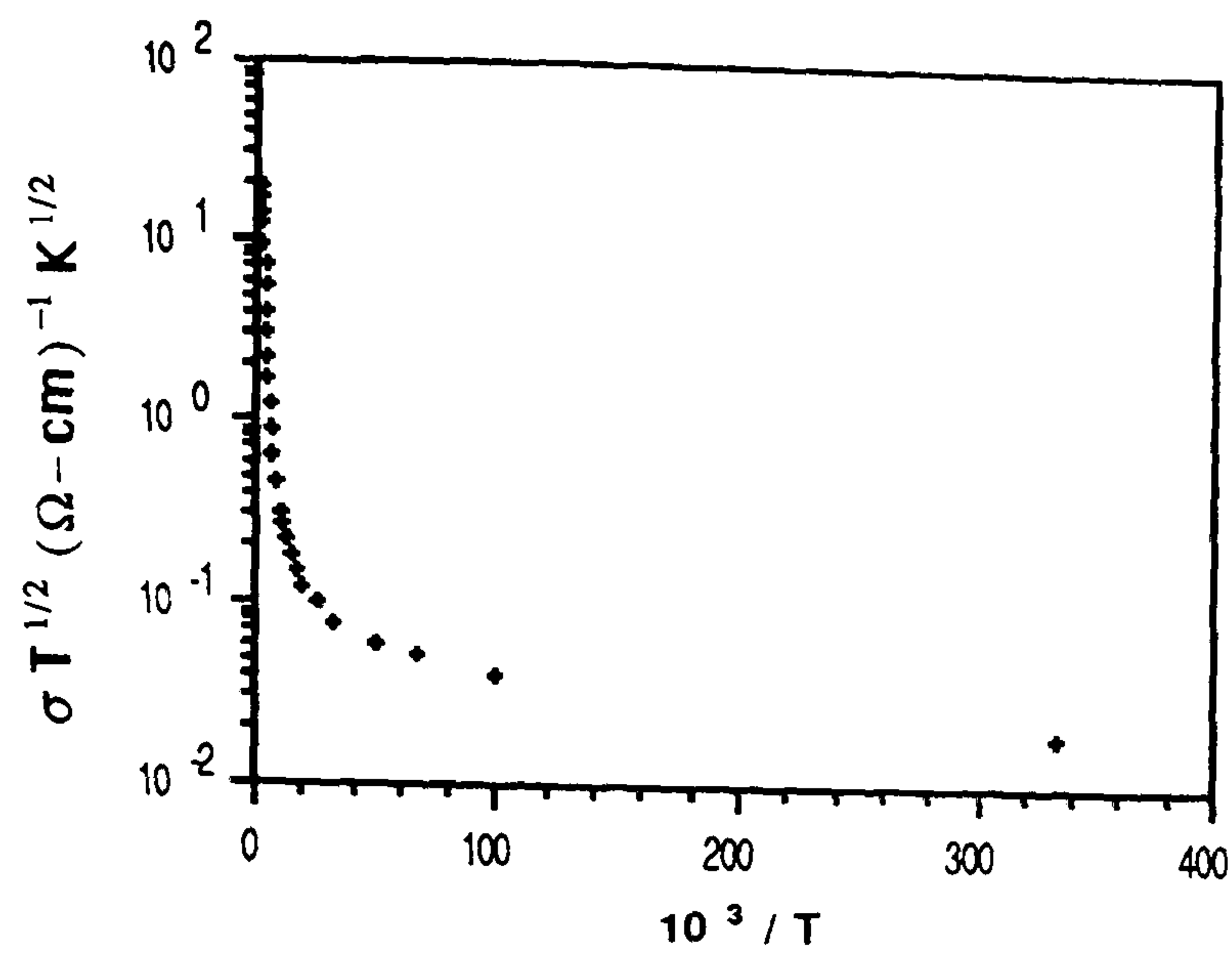


Figure 7.5 — $\log(\sigma T^{1/2})$ vs T^{-1} characteristic of typical CdTe:Cl₂ thin layer, $3 < T < 400\text{K}$.

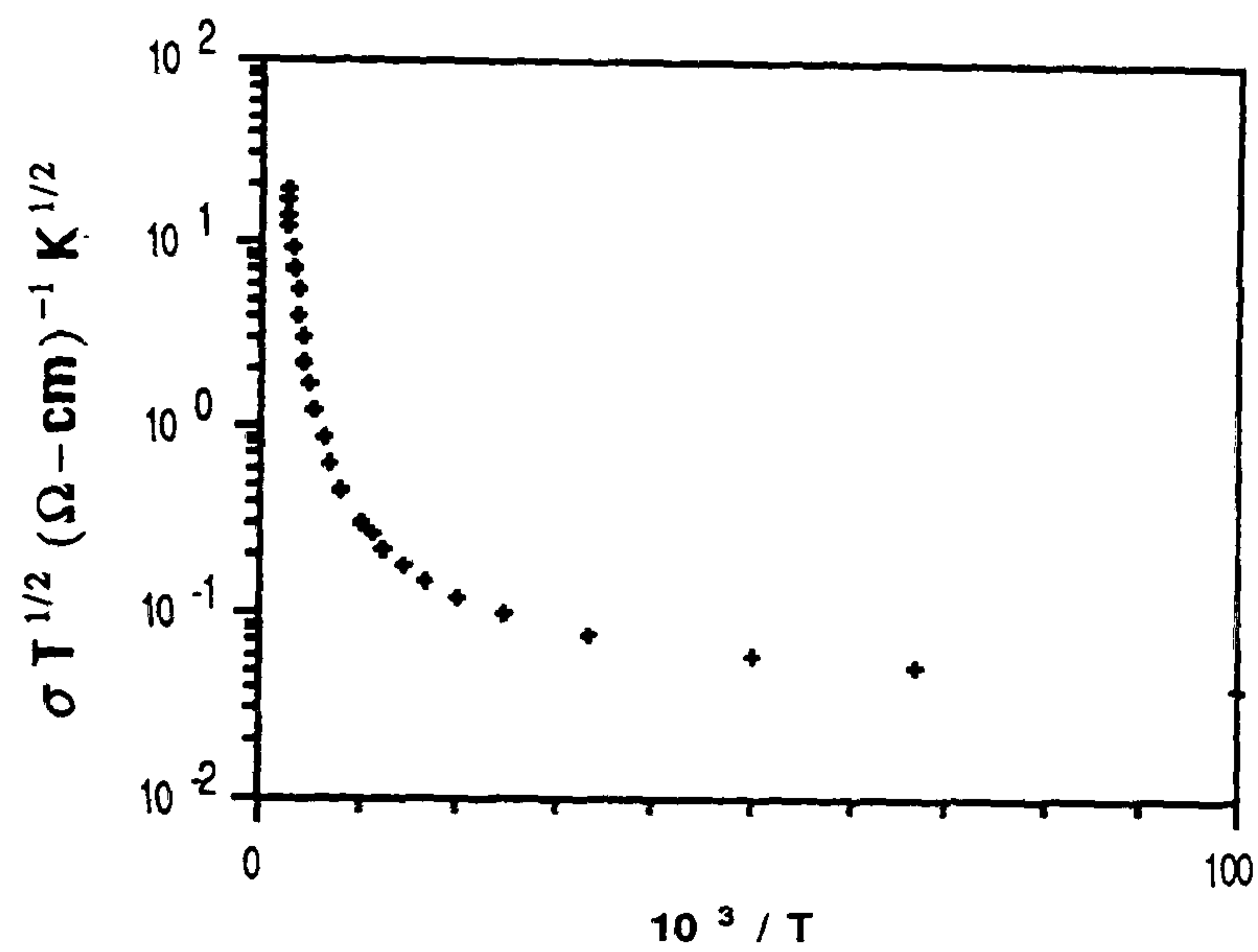


Figure 7.6 — $\log(\sigma T^{1/2})$ vs T^{-1} characteristic of typical CdTe:Cl₂ thin layer, $10 < T < 400\text{K}$.

The $\log(\mu T^{-1/2})$ vs T^{-1} characteristics (Figs. 7.9 and 7.10) displayed a slow decrease with positive slope at temperature in the range $3 < T < 25\text{K}$. However, it increased sharply with a negative slope between temperatures $25 < T < 230\text{K}$, and then decreased at temperatures, $T > 230\text{K}$. When mobility is limited by polar optical scattering in bulk single crystal CdTe, it is linearly dependent on T^{-1} with a positive slope giving $\hbar\omega_{op}$ which for CdTe is 21.7 meV [27]. However, the slope in Fig.7.9 was found to give an activation energy of 0.23 meV. At the high temperature ($T > 300\text{K}$) (Fig.7.10), the slope yielded an activation energy of 104 meV. Thus, the hole mobility did not seem to be limited by polar optical mode scattering in either range of temperature. This suggests that the mobility was limited by grain boundary rather than grain bulk effects and is consistent with the conductivity data described above (Figs. 7.5 and 7.6).

The mobility in polycrystalline films becomes thermally activated due to the effects of inter-grain potential barriers (see section 7.2.2). Fig.7.11–7.13 show $\log(\mu T^{1/2})$ vs T^{-1} characteristics of the same layer, and suggest three straight line regions of the characteristic. The barrier heights, E_b , calculated for the three regions were 0.25 meV (3–10K), 1.58 meV (15–70K) and 23.0 meV (70–200K) respectively.

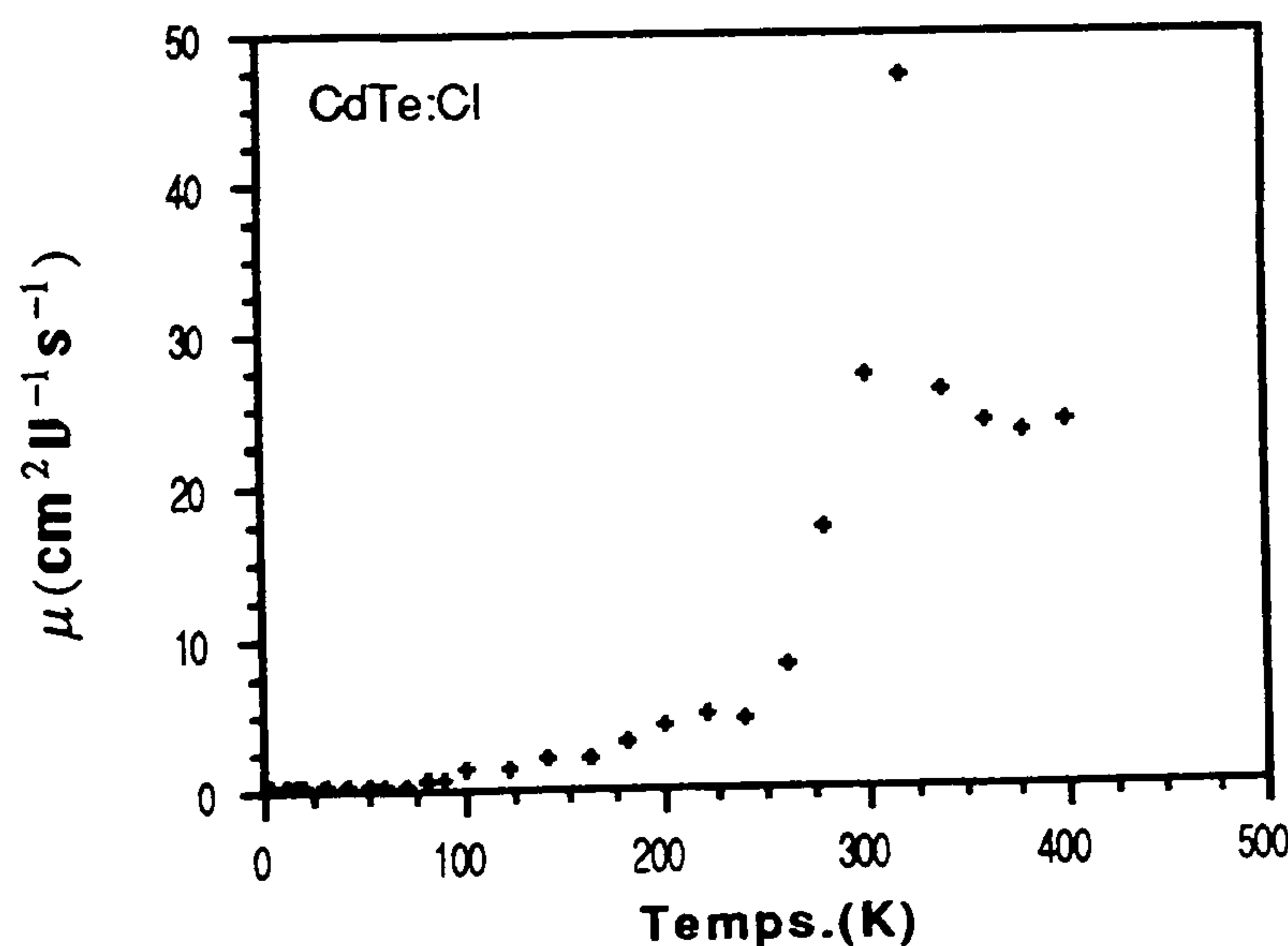


Figure 7.7 — μ vs T characteristic of a typical CdTe:Cl₂ thin layer.

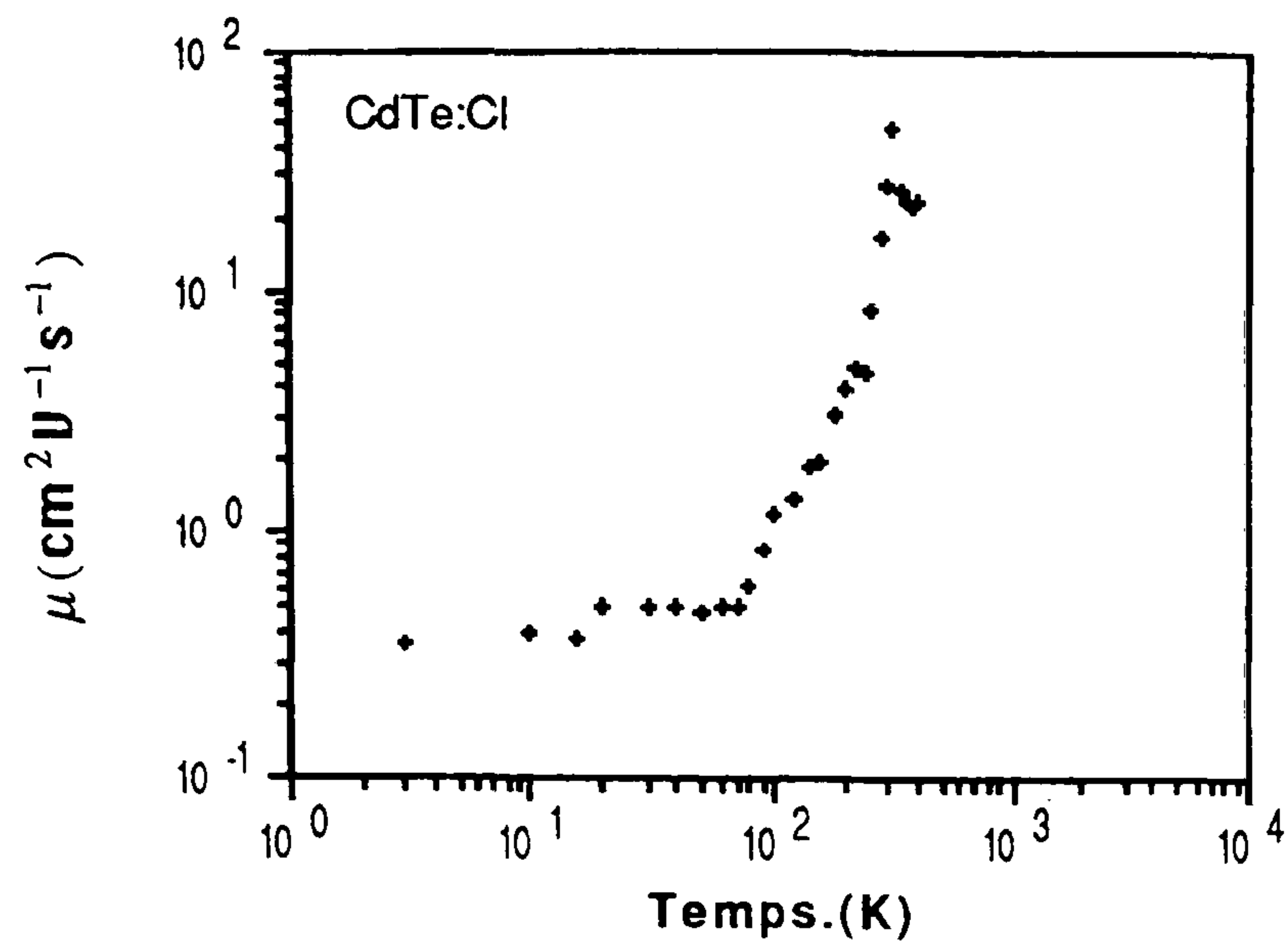


Figure 7.8 — $\log(\mu)$ vs $\log(T)$ characteristic of a typical CdTe:Cl₂ thin layer.

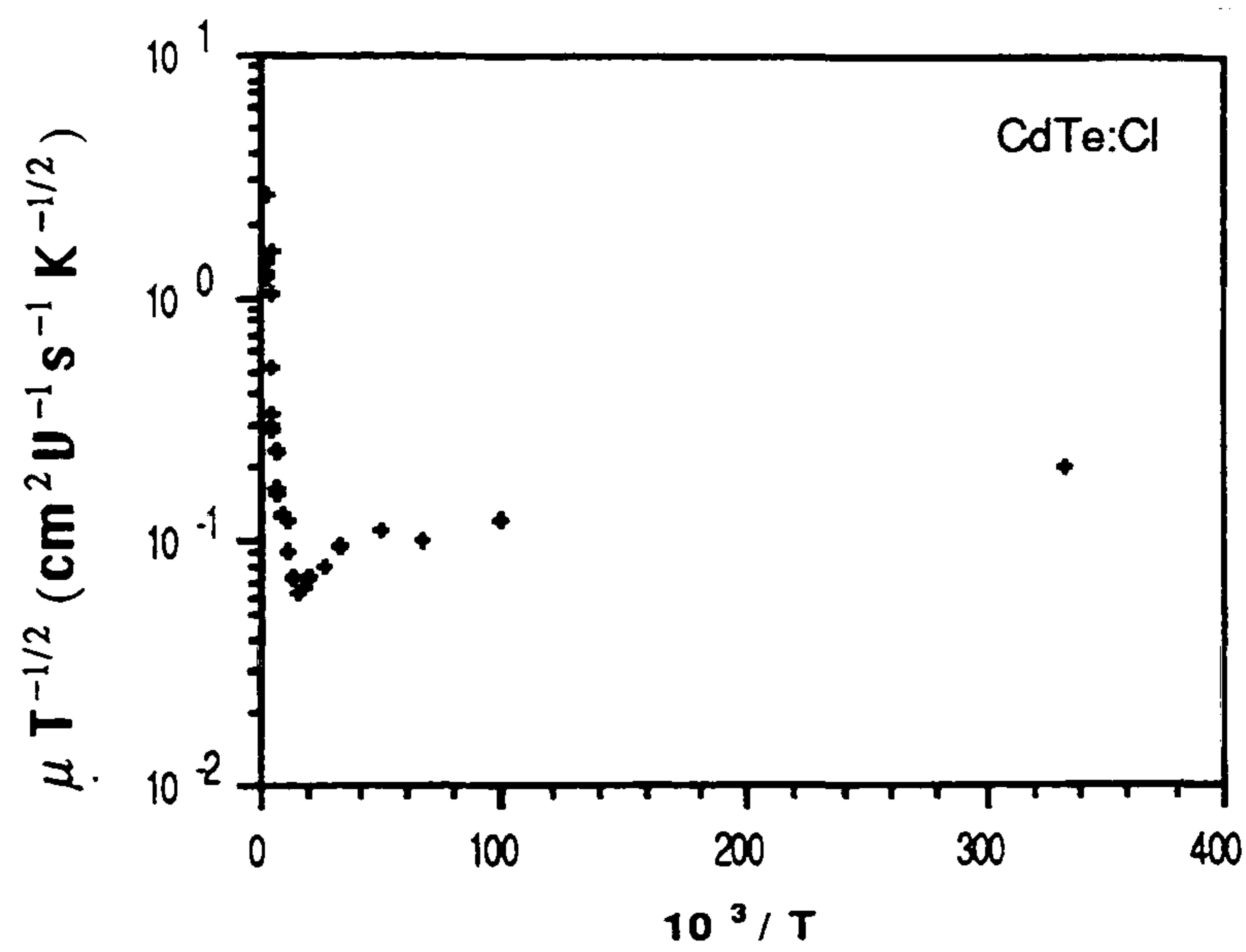


Figure 7.9 — $\log(\mu T^{-1/2})$ vs T^{-1} characteristic of a typical CdTe:Cl₂ thin layer, $3 < T < 400 \text{ K}$.

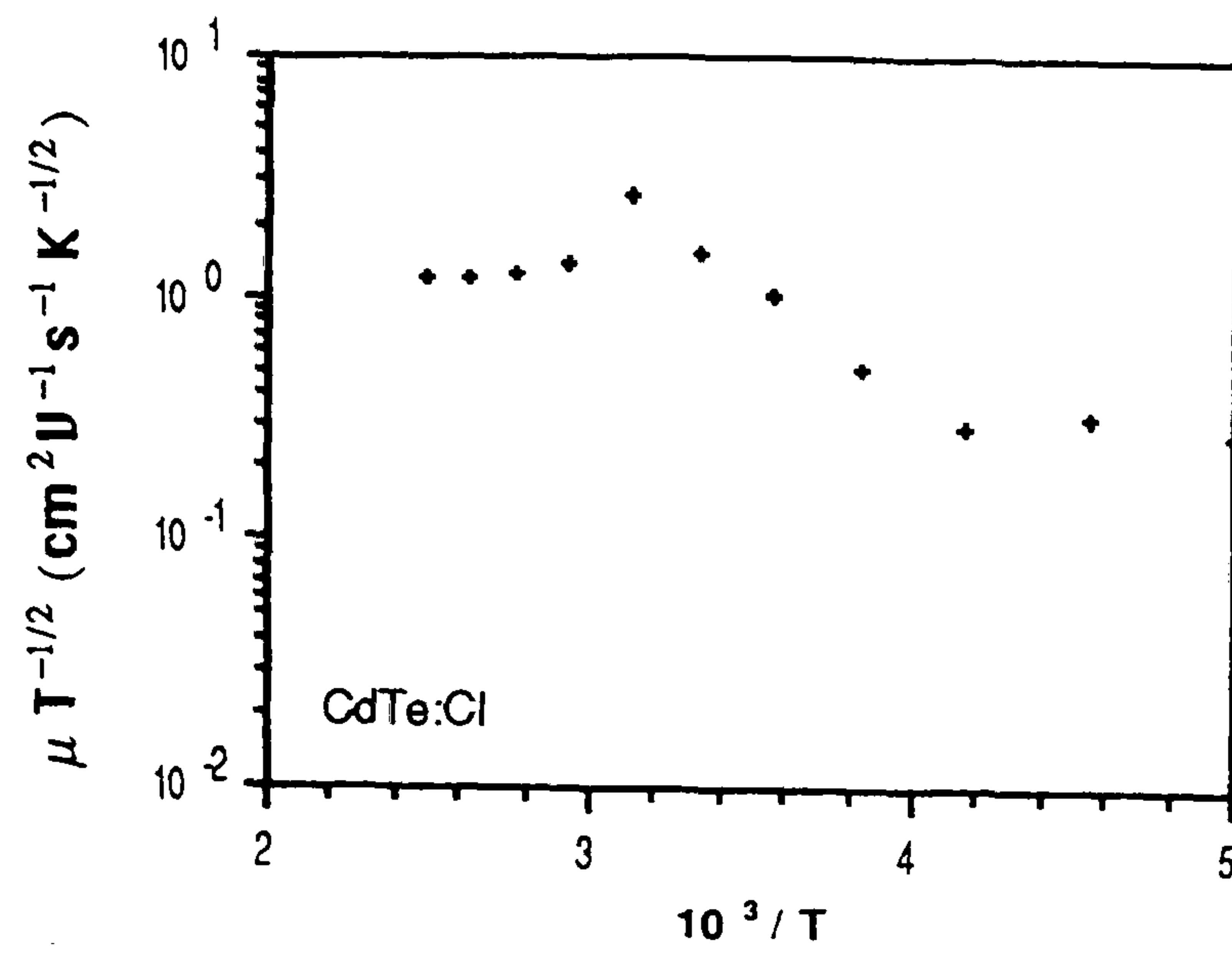


Figure 7.10 — $\log(\mu T^{-1/2})$ vs T^{-1} characteristic of a typical CdTe:Cl₂ thin layer, $200 < T < 400 \text{K}$.

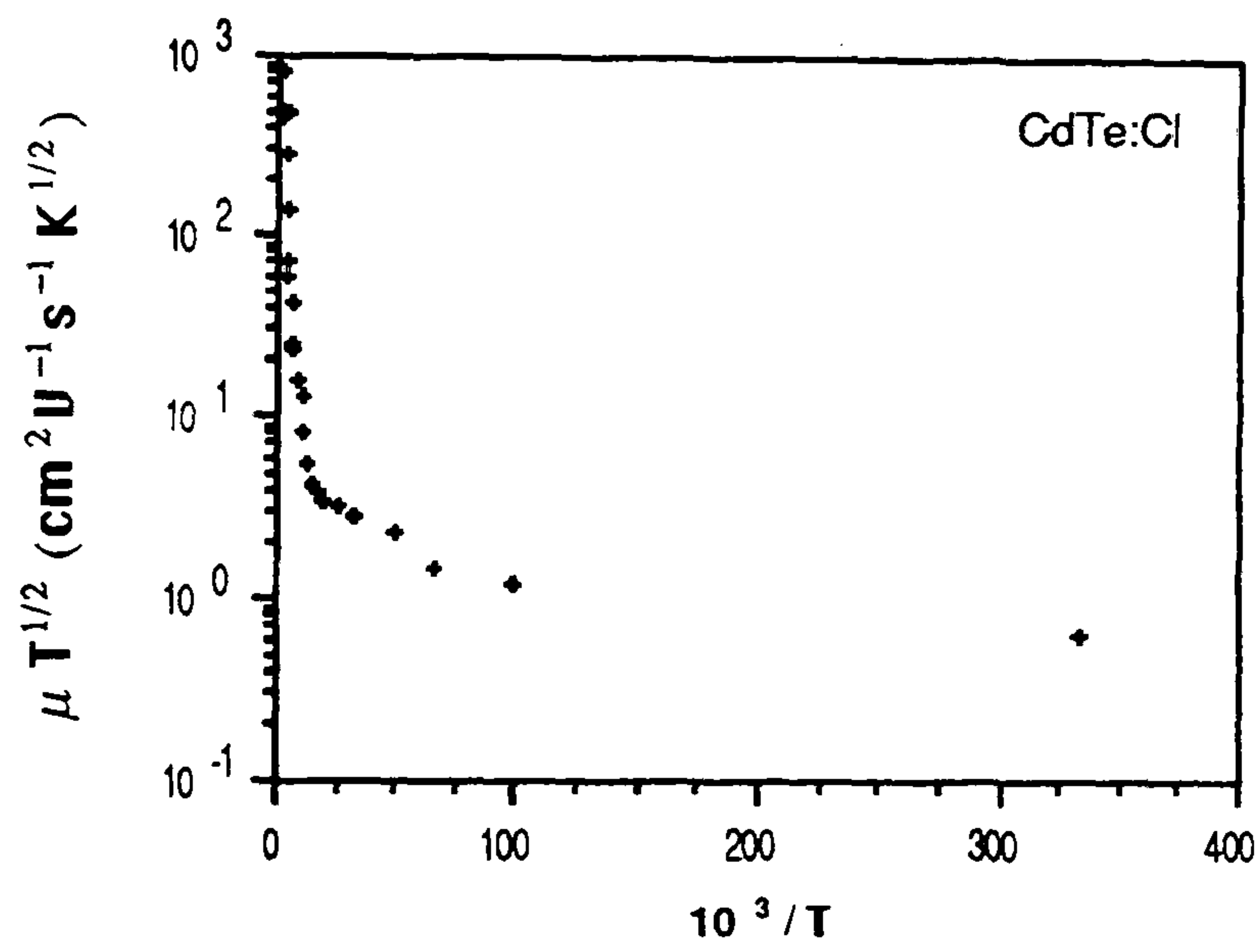


Figure 7.11 — $\log(\mu T^{1/2})$ vs T^{-1} characteristic of a typical CdTe:Cl₂ thin layer, $3 < T < 400 \text{K}$.

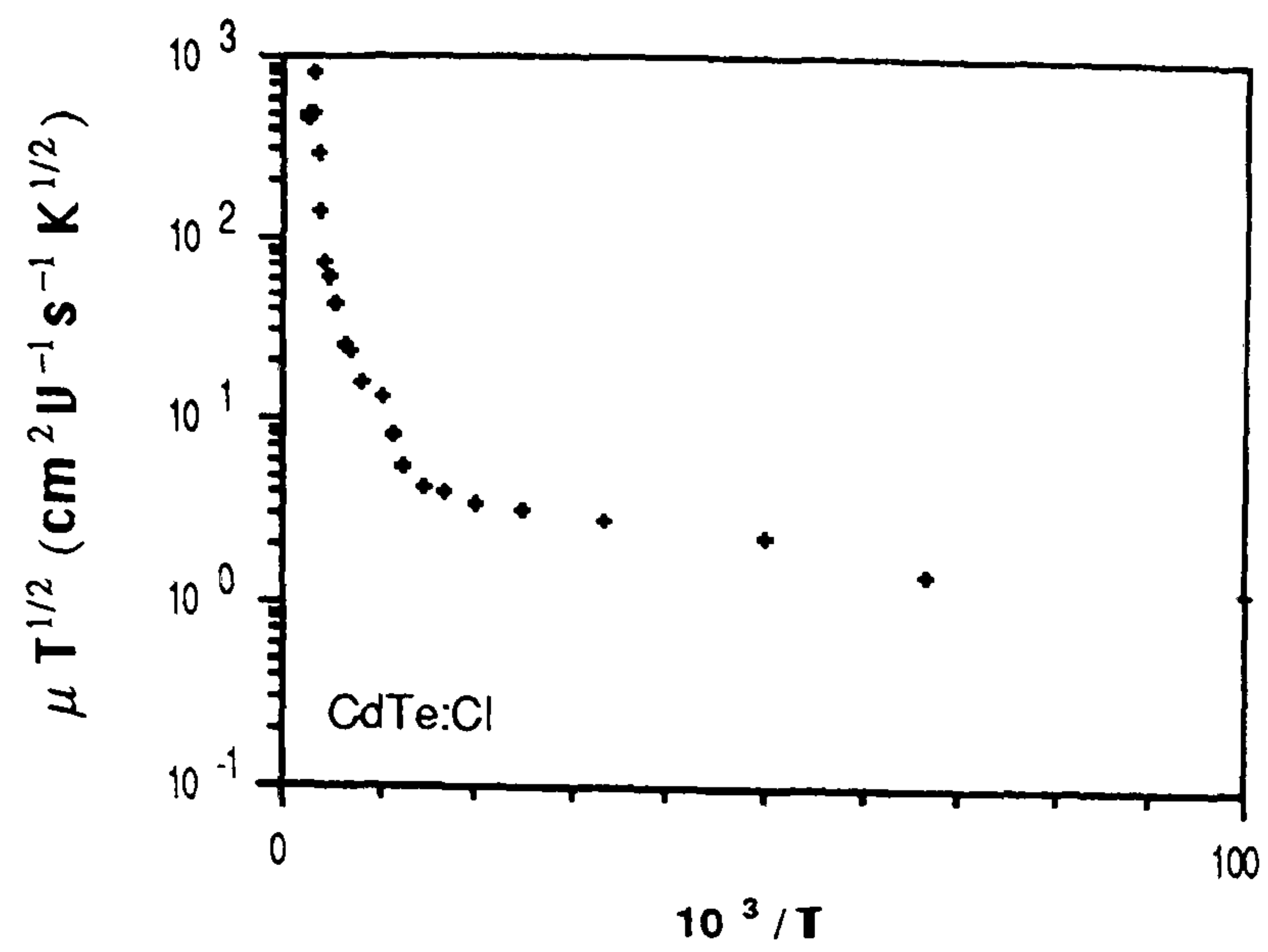


Figure 7.12 — $\log(\mu T^{1/2})$ vs T^{-1} characteristic of a typical CdTe:Cl₂ thin layer, $10 < T < 400\text{K}$.

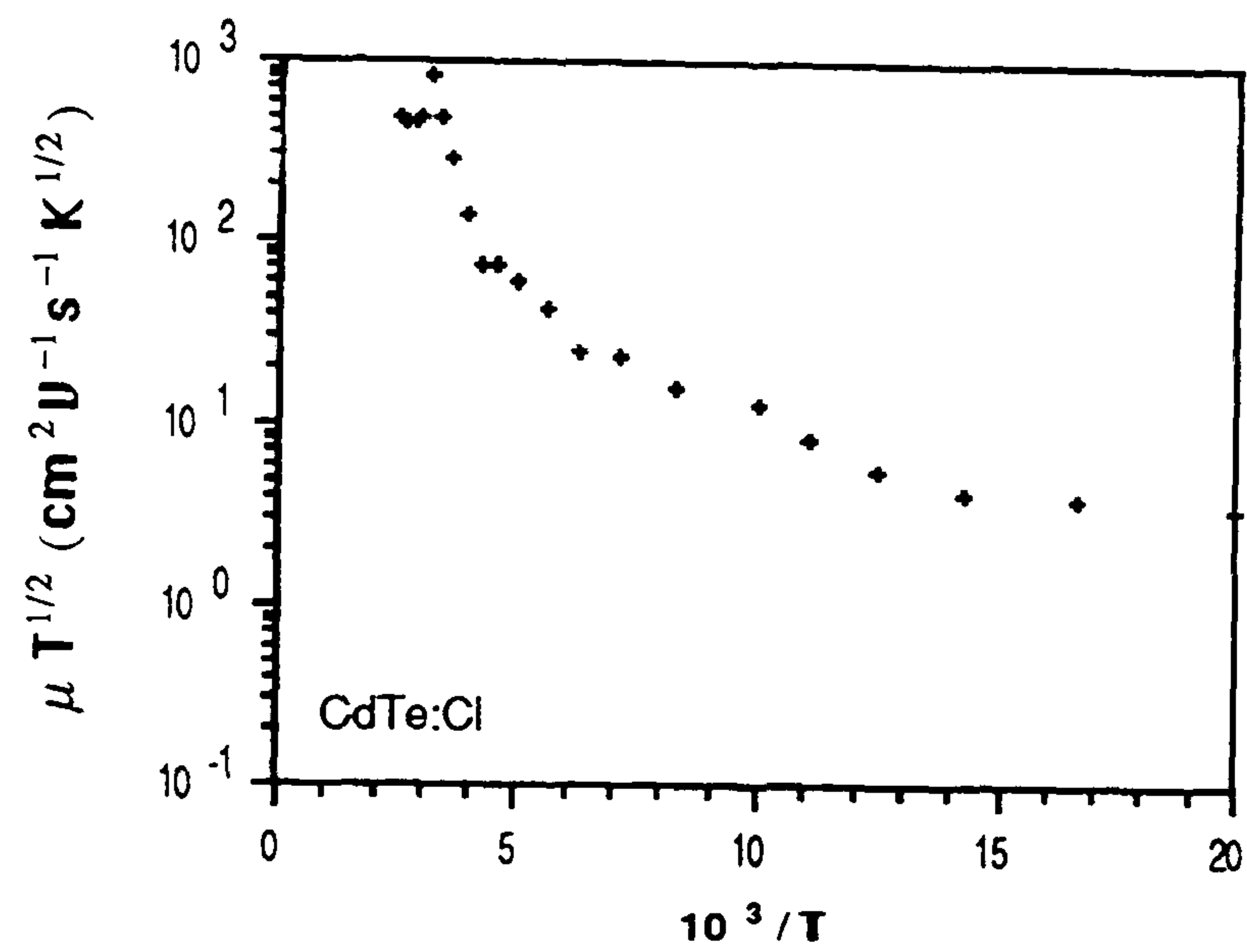


Figure 7.13 — $\log(\mu T^{1/2})$ vs T^{-1} characteristic of a typical CdTe:Cl₂ thin layer, $50 < T < 400\text{K}$.

There exists another possibility that E_b might be temperature dependent. Orton et al [28] discussed this and showed that E_b can be written as;

$$E_b = E_o(1 + \gamma T) \quad [7.16]$$

where γ is the temperature coefficient of the barrier height. Substituting Eq.7.16 in Eq.7.13 yields;

$$\mu_g = \mu'_o \exp(-E_o/kT) \quad [7.17]$$

where,

$$\mu'_o = \mu_o \exp(-\gamma E_o/k) \quad [7.18]$$

thus γ can be obtained as;

$$\gamma = \frac{k}{E_o} \ln\left(\frac{\mu_o}{\mu'_o}\right) \quad [7.19]$$

where μ'_o and E_o are determined experimentally, and μ_o is given by Eq.7.13a. At room temperature, typical temperature coefficients of barrier height were found to be 2.70 K^{-1} and 2.47 K^{-1} ($E_o=0.25 \text{ meV}$), and 0.42 K^{-1} and 0.38 K^{-1} ($E_o=1.58 \text{ meV}$), and $3.8 \times 10^{-3} \text{ K}^{-1}$ and $1.1 \times 10^{-3} \text{ K}^{-1}$ ($E_o=23.0 \text{ meV}$) for μ_o as defined by Seto and Orton respectively.

Fig.7.14 shows p vs T characteristics of the same CdTe:Cl₂ thin layer. This shows that the carrier concentration reduced at 260K sharply to about 10^{16} cm^{-3} at room temperature from a low temperature average value of 10^{17} cm^{-3} to a more modest level of $\sim 10^{16} \text{ cm}^{-3}$ at room temperature. It decreased to a steady value of about $1.5 \times 10^{16} \text{ cm}^{-3}$ for temperatures above 260K. Carrier concentration p can be expressed by similar relationships (i.e. in Seto's model). Therefore;

$$p \propto T^{1/2} \exp\left[-\left(\frac{E_g}{2} - E_f\right)/kT\right] \exp(E_b/kT), \text{ if } NL < Q_t \quad [7.20a]$$

$$p \propto \text{constant (i.e. independent of } T), \text{ if } NL > Q_t \quad [7.20b]$$

Fig.7.15 and 7.16 show $\log(pT^{-1/2})$ vs T^{-1} characteristics of the CdTe:Cl₂ layer for $LN < Q_t$. At low temperatures (i.e. $T < 40 \text{ K}$), $\log(pT^{-1/2})$ increased slowly with reciprocal temperature, but above $\sim 40 \text{ K}$, it decreased sharply with increasing T^{-1} . At low temperatures, the carrier concentration was nearly constant and consistent with Eq.7.20b. However, at higher temperature the slope was positive and $\ll E_g/2$. Clearly the high temperature regime was not well described by Eq.7.20a.

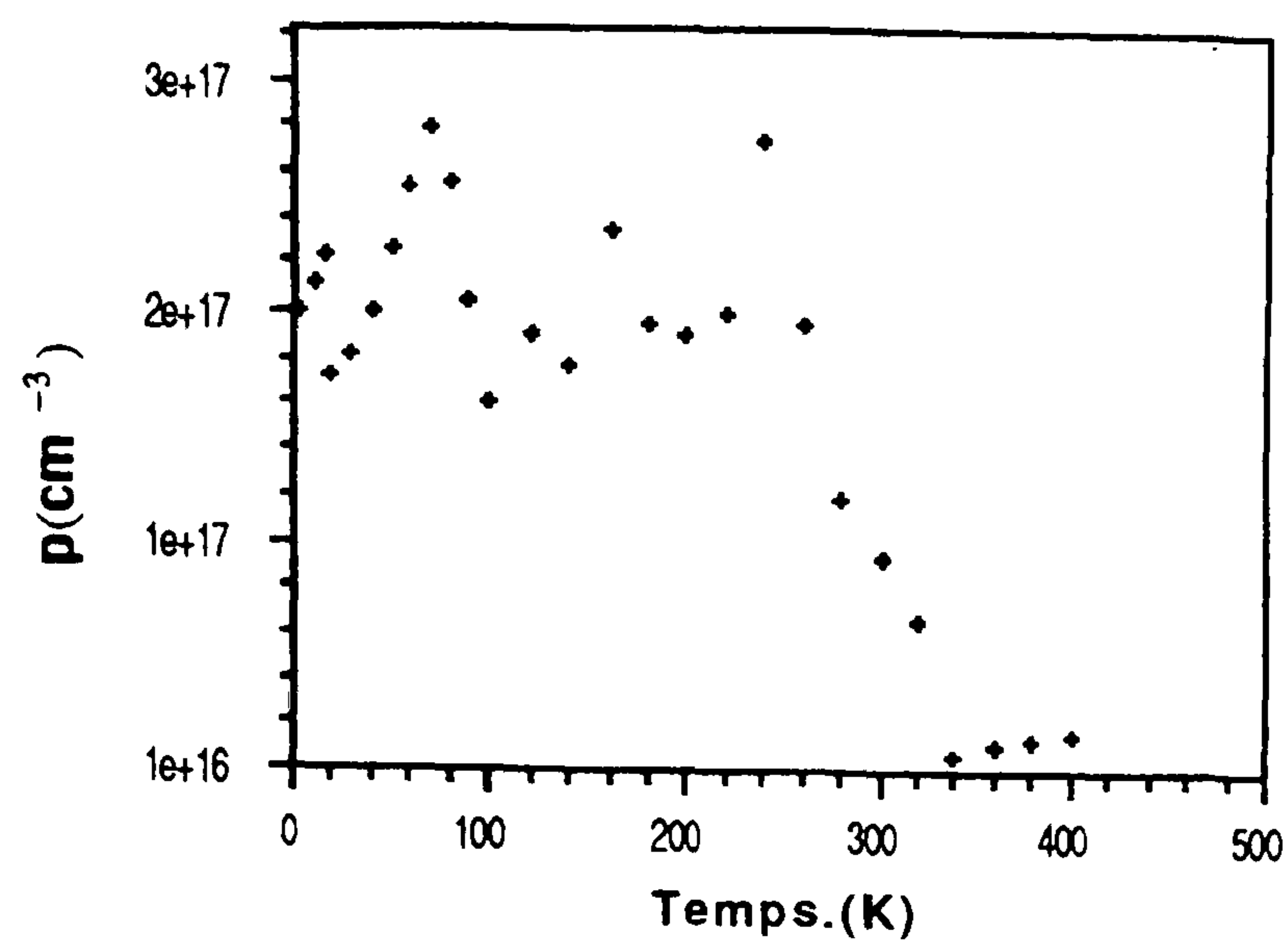


Figure 7.14 — p vs T characteristic of a typical CdTe:Cl₂ thin layer.

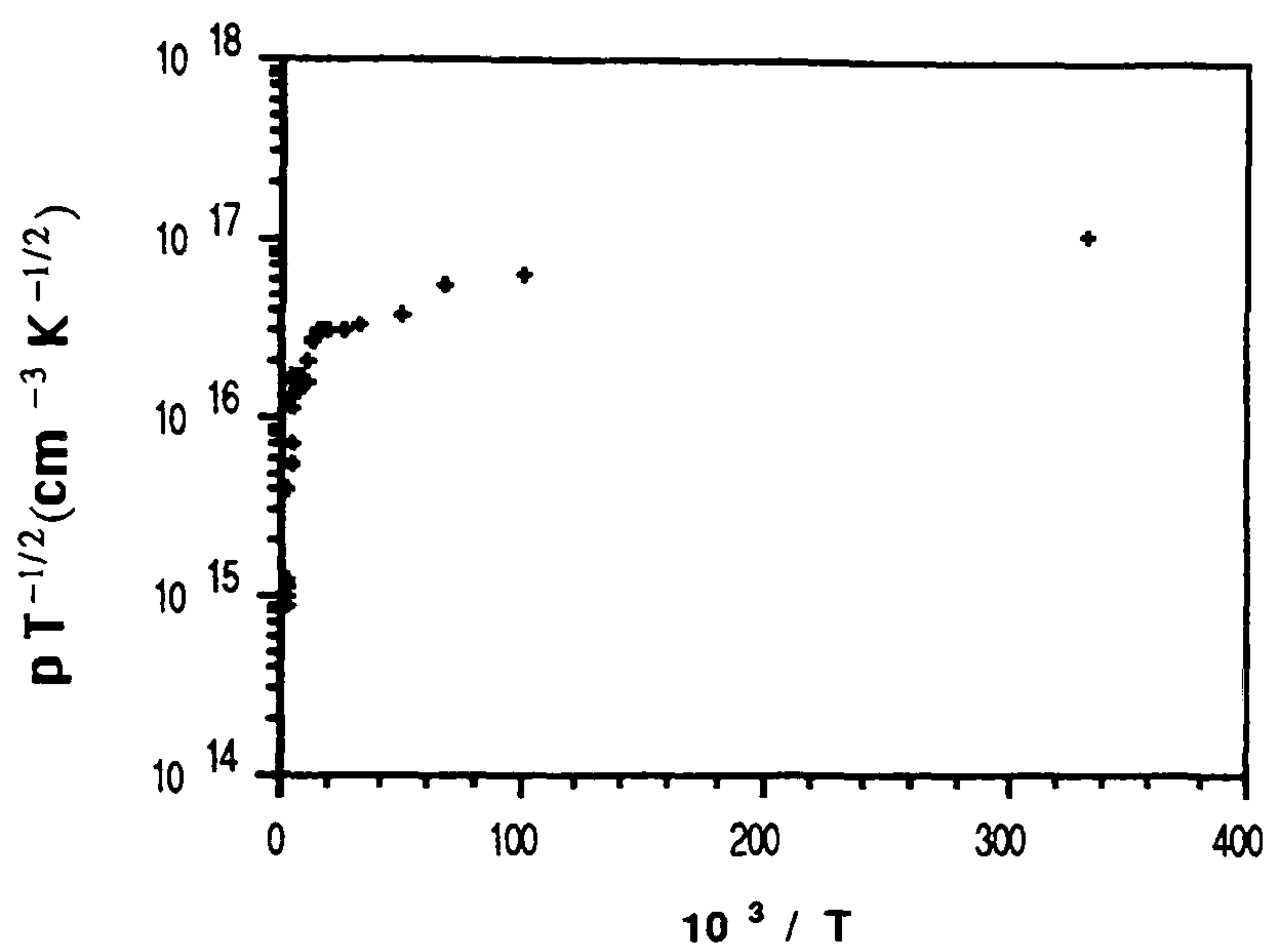


Figure 7.15 — $\log(p T^{-1/2})$ vs T^{-1} characteristic of a typical CdTe:Cl₂ thin layer, $3 < T < 400$ K.

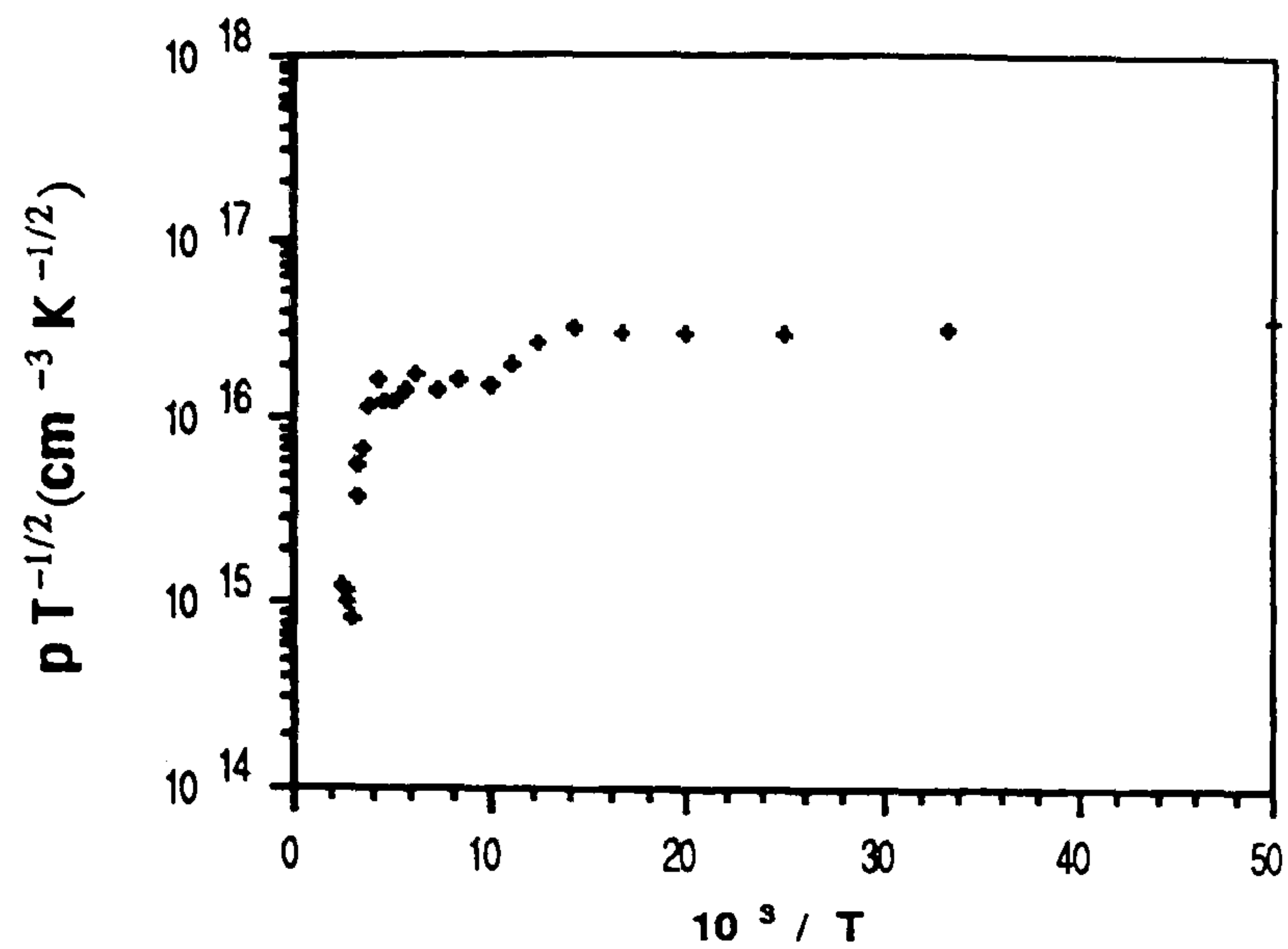


Figure 7.16 — $\log(p T^{-1/2})$ vs T^{-1} characteristic of a typical CdTe:Cl₂ thin layer, $20 < T < 400\text{K}$.

The R_H vs T characteristics of the CdTe:Cl₂ layer is shown in Fig.7.17. It changed slowly up to 250K. It then peaked at about 300K before starting to decrease exponentially to a steady value. As yet, this complex characteristic has not been explained.

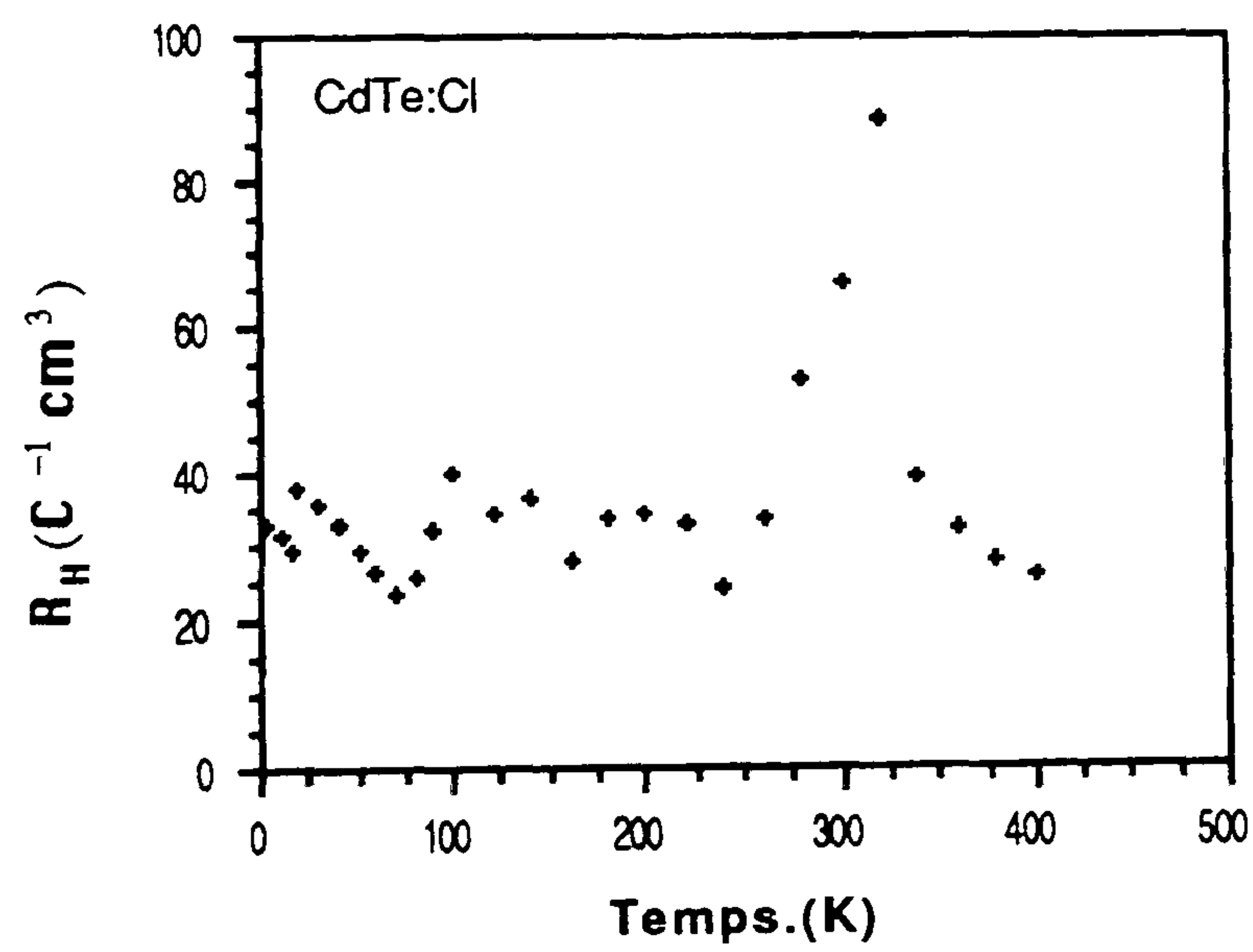


Figure 7.17 — R_H vs T characteristic of a typical CdTe:Cl₂ thin layer.

7.4 Electrical Properties of CdS Thin Films.

7.4.1 Metal Ohmic Contacts.

It is well known that metals like In, Ga, SnO_x , Zn and Au make ohmic contacts to CdS thin films. In the course of this work, In was used for the ohmic contact to the CdS thin films grown on glass substrates. The ohmicity of the In contacts was investigated by I-V measurements and the $\log(I)$ - $\log(V)$ plots were found to be straight lines with slopes 0.96 to 1.00 in both polarities.

7.4.2 Resistivity and Hall Measurements.

As expected, the CdS layers were always n-type (as shown by the Seebeck effect). At room temperature, the dark resistivity (measured by Van-der Pauw method) of the CdS thin films varied over a wide range (i.e. between 2×10^2 – $1.5 \times 10^3 \Omega\text{-cm}$) depending on growth conditions. Introduction of In as a n-type dopant element to the CdS during deposition yielded very low resistivities, although it was not possible to control the In flux. Nevertheless, the dark resistivity of CdS thin films was decreased by up to 3 orders of magnitude by co-evaporation with In.

The variation of resistivity with temperature of CdS:In thin films was investigated for temperatures between 78K to 400K. The $\log(\sigma)$ vs T^{-1} characteristics for a typical film is shown in Fig.7.18. It displayed two straight line regions, indicating that different mechanisms were operating at low and high temperatures. From the slope of two straight line regions, the corresponding activation energies were found to be 1.15 meV and 11.2 meV in the temperatures range 80–150K and 200–400K respectively. In fact, the conductivity varied little with temperature over the range examined, as would be expected for a doped layer.

However, undoped CdS thin layers showed a remarkable variation at high temperature ranges. The activation energy calculated for a typical undoped CdS layer was found to be 325 meV in the temperature ranges of 300–670K.

Fig.7.19 shows $\log(\sigma T^{1/2})$ vs T^{-1} characteristics of the same CdS:In layer, and suggest two straight line regions giving the potential barriers, E_b , (i.e. using Seto's grain boundary trapping model) as 5.75 meV (80–150K) and 23.17 meV

(200–400K), if $LN > Q_t$ respectively. E_b was calculated as 344.1 meV (300–670K) for the undoped CdS thin layer. Table 7.2 tabulates the resistivity and mobility values obtained from both undoped and In doped thin layers of CdS at room temperature.

Sample No:	Thickness(μm)	$\rho(\Omega\text{-cm})$	$R_H(\text{cm}^3\text{C}^{-1})$	$\mu_H(\text{cm}^2\text{V}^{-1}\text{s}^{-1})$	$n(\text{cm}^3)$
3CS(undop.)	3.0	212	4.8×10^2	2.3	1.3×10^{16}
4CS:In(doped)	0.6	0.12	6.5×10^{-1}	5.4	9.7×10^{18}

Table 7.2 — Resistivity and Hall measurement results of a typical undoped CdS and In doped CdS:In thin layer at room temperature.

7.5 Positron Trapping in CdTe Thin Films.

Positron diffusion and annihilation are very sensitive to negatively charged and neutral vacancy-type defects in semiconductors and provide a unique and direct method for the detection of such defects [29,30]. Significant changes in the annihilation characteristics result from positron trapping at crystal imperfections. The location of positrons at the defect sites has two important consequences;

i- The concentration of defects can be deduced from the ratio of trapped to free electrons.

ii- The annihilation characteristics of trapped positrons reflect local properties of the defects, and are to some extent specific to the particular defect configurations.

Positron annihilation in the CdTe thin films was studied as a function of depth by recording the γ - annihilation line, $E_\gamma = 511 \text{ keV} \pm \Delta E_\gamma$, as a function of positron energy E . The 511 keV annihilation line is Doppler broadened, ΔE_L , due to the momentum of the annihilation electron-positron pair [31]. As discussed in section 4.7, it is customary to characterise the momentum distribution by using the line shape parameters $S(W)$ defined as the relative number of annihilation events in the centroids (wings) of the 511 keV line.

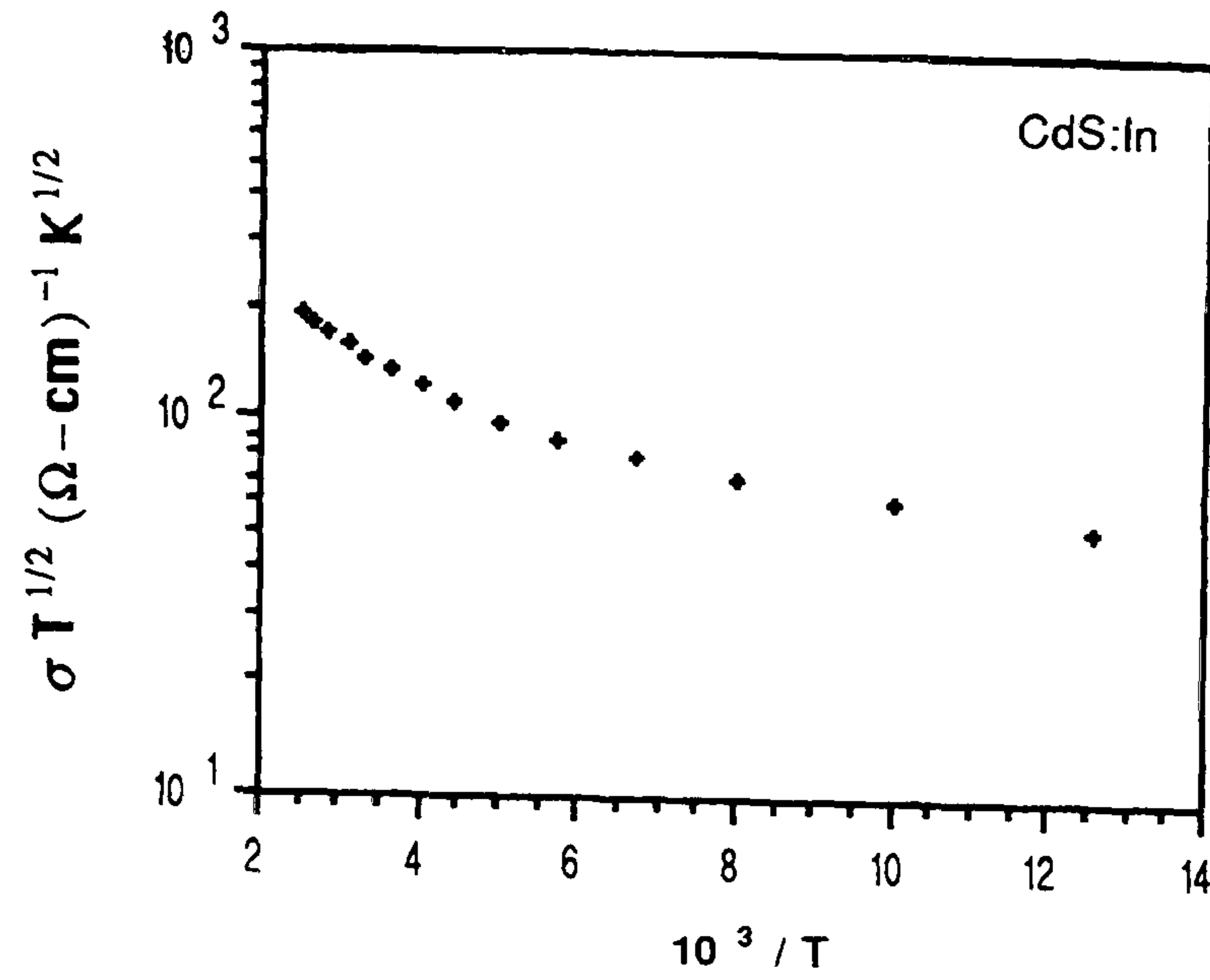


Figure 7.18 — $\log(\sigma)$ vs T^{-1} characteristic of an undoped and In-doped CdS:In thin layer, $80 < T < 400\text{K}$.

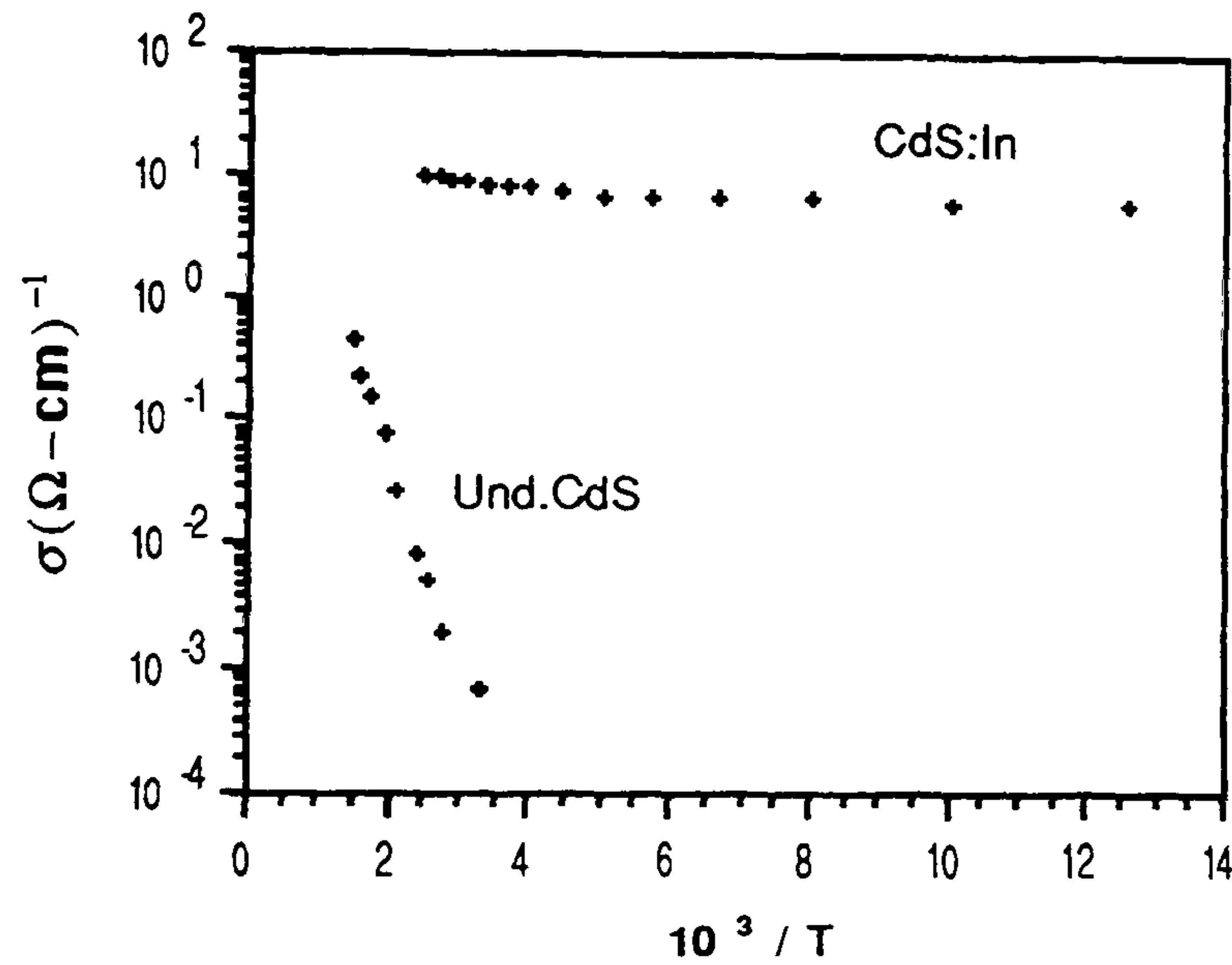


Figure 7.19 — $\log(\sigma T^{1/2})$ vs T^{-1} characteristic of In-doped CdS:In thin layer, $80 < T < 400\text{K}$.

According to the relationship $\Delta E_L = cp_L/2$ where c is the speed of light, p_L is the component of the momentum along the emission direction of the 511 keV γ -rays, annihilations with low (high) momentum electrons contribute to $S(W)$. Annihilation with valence electrons contribute mainly to S whereas annihilation with core electrons contribute to S but predominantly to W . Consequently, the S and W parameters are referred to below as valence and core annihilation parameters, respectively. Experiments were carried out with selected CdTe thin films by L.Liszkay*, C.Corbel* and P.Hautojärvi† [32]. Positron energy was varied with steps of 0.5 keV between 0.1 keV and 25 keV. This energy range corresponds to mean penetration depths of up to $1.2\mu\text{m}$ in CdTe [33,34]. Positrons were implanted only in the CdTe films and not in the substrate since all the films were $3\mu\text{m}$ thick.

7.5.1 Principles of Trapping at Small Vacancy Clusters.

Positrons can annihilate from the bulk state, i.e. delocalised in the lattice, or at vacancy-type defects where they are trapped on localised states. Trapping occurs because the positron-nucleus energy interaction is lowered in vacancy-type defects due to the missing atoms. The trapping rate, κ_d , is related to the defect concentration, c_d , and the trapping coefficient at the defect, μ_d , by;

$$\kappa_d = \mu_d c_d \quad [7.21]$$

The annihilation parameters at the defects, S_d , and, W_d , can be used as a fingerprint for the open volume of the defects. The larger the open volume, the lower the core annihilation parameter W_d and the higher the valence annihilation parameter S_d [31]. For a state i , neglecting the valence contribution in the W parameter, one can write the W_i parameter as a fraction X_i^c ($X_i^c < 1$) of the core annihilation probability: $W_i = X_i^c F_i^c$. If the fraction X_i^c remains constant for different annihilation states, then W_i/W_j is just the ratio of the core annihilation probabilities in the states i and j .

After implantation and thermalisation in the films, positrons diffuse and finally annihilate from different states, i , characterised by different annihilation parameters $S_i(W_i)$ [35,36]. Positron annihilation may occur at the surface (s), bulk (b)

* Centre d'Etudes Nucléaires de Saclay, France.

† Helsinki University of Technology, Physics Laboratory, Finland.

and defect (d) states. The probabilities $F_i(E)$ that annihilation takes place from the i state depend on the positron energy E . The analysis of the data $S(E)$ is made by iteratively fitting them to the expression;

$$S(E) = F_s(E)S_s + F_b(E)S_b + \sum_d F_d(E)S_d, \quad \sum_i F_i = 1 \quad [7.22]$$

where the annihilation probabilities $F_i(E)$ are calculated by solving the positron diffusion equation in the presence of trapping at defects. Assuming that the film is homogeneous, one can rewrite Eq.7.22 as;

$$S(E) = F_s(E)S_s + (1 - F_s)S_f \quad [7.23]$$

where S_f depends only on the annihilation probabilities in the bulk F_b and at the defects F_d . Similar equations hold for the $W(E)$ parameters.

When there is only one type, d , of defect, F_d , and, F_b , are related to the positron trapping rate, κ_d , at the defects by;

$$F_d = 1 - F_b = \kappa_d(\lambda_b + \kappa_d)^{-1} \quad [7.24]$$

where, λ_b , is the bulk annihilation rate. To determine whether positrons annihilate from the bulk state and only one other state, d , one can use the parameter, R , defined as [37];

$$R = (S - S_b)(W_b - W) \quad [7.25]$$

It can be easily established that R becomes independent of the annihilation probabilities when only one state other than the bulk exists as it takes the value, R_d [38];

$$R = R_d = (S_d - S_b)/(W_b - W_d) \quad [7.26]$$

characteristic of the annihilation state, d . In a set of samples where S and W vary, one can use the invariability of the R parameter as a proof that the different samples contain the same vacancy type-defect. When S_b and W_b are well known, one can calculate R from the S and W data and check whether R remains constant or not. This is the usual way in which the parameter R has been used. In this

work, it is proposed rather to check whether the S and W parameters were linearly related according to;

$$S = -RW + RW_b + S_b \quad [7.27]$$

If the measured (S_i, W_i) pairs lie on a straight line, then R_d (the defect parameter) is given directly by its slope.

7.5.2 Positron Trapping Analysis.

The present study was intended to show whether there were any changes in the vacancy content between as-grown and treated CdTe films grown by PVD at a substrate temperature of 220°C on both plain glass and ITO coated glass substrates. Three types of film were therefore, investigated; namely as-grown (CTD1 and CTA), heat treated (CTD2 and CTB), “dipped” in CdCl₂/MeOH followed by annealing (CTC) and a CdTe:In (ZD16) layer grown by MBE was also measured as a control. Previous experience had shown that such layers did not contain large concentration of vacancies. The electrical characteristics of CdTe films (as with other compound semiconductors) are known to be strongly influenced by stoichiometry and hence a knowledge of the vacancy distribution or at least of changes in the vacancy concentration would be important in arriving at an understanding of the effects of the dipping process.

Fig.7.20 and 7.21 show how the valence annihilation parameter S changes as a function of positron energy in CTC and CTD1. The variations are typical of those found in the other films. After a rapid change below 15 keV, the $S(W)$ parameter tends to level off as the positron energy increases above 15 keV up to 25 keV. For $E < 15$ keV, positrons can diffuse back to the surface and suffer annihilation at the surface. For $E > 15$ keV, this process is no longer possible and the probability that annihilation occurs at the surface becomes negligible. The value of S shown in Fig.7.20 and 7.21 on the plateau is nearly the same in the two films although the valence parameter at the surface S_s is much lower in the CTD2 film than in the CTC film. The plateau at $E > 15$ keV indicates that the annihilation parameters are no longer dependent on the positron implantation profile. This means that the film is homogeneous and therefore the data can be fitted to Eq.7.23 (using a programme described in [39]). Free parameters are the parameters at the surface

$S_s(W_s)$, in the film $S_f(W_f)$ and the positron diffusion length L_+ which is kept free in the fitting procedure so that inhomogeneities near the surface due to field effects or defect profile do not effect the S_f and W_f parameters. Fig.7.22 shows the valence annihilation parameter, S_f , as a function of the core annihilation parameter, W_f . It is clear that all points fit well to a straight line, implying, as discussed above that the films contain the same vacancy-type defect. The lowest S_f value was observed in the CdTe:In, MBE grown layer the highest in the as-grown CTD1 film. The W_f values also reached extrema in these two layers but, in the opposite sense to S . The W_f , S_f , S_s , L_+ , and κ are also given in Table 7.3.

Sample	W_f	S_f	S_s	L_+ (nm)	$\kappa(\text{ns}^{-1})$
CTA	0.0314	0.584	0.575	98	53.4
CTB	0.0375	0.571	0.537	51	2.5
CTC	0.0336	0.579	0.567	61	10.2
CTD1	0.0309	0.585	0.575	89	—
CTD2	0.0339	0.579	0.557	41	9.9
ZD16	0.0428	0.561	0.556	—	0.0

Table 7.3 — Annihilation parameters, W_f , S_f and S_s ; diffusion length, L_+ ; and trapping rates, κ_d , in CdTe layers. CTA: glass, as-grown; CTB: glass, heated; CTC: dipped followed by annealing; CTD1: ITO/glass, as-grown; CTD2: ITO/glass, heated; and ZD16 MBE control layer.

The parameters S_s and W_s varied between the films indicating the surfaces varied from film to film. The differing surface conditions generated different internal electrical fields in the near surface region affecting L_+ in an uncontrolled way. Thus annihilation parameters S_f and W_f only were taken into account. The variations in S_f and W_f indicated that the films contained vacancy-type defects. The films which contained the highest density of defects were the as-grown (CTA) and (CTD1) films. The MBE film where the value for $S_f(W_f)$ was the lowest (highest) contains the lowest density of defects.

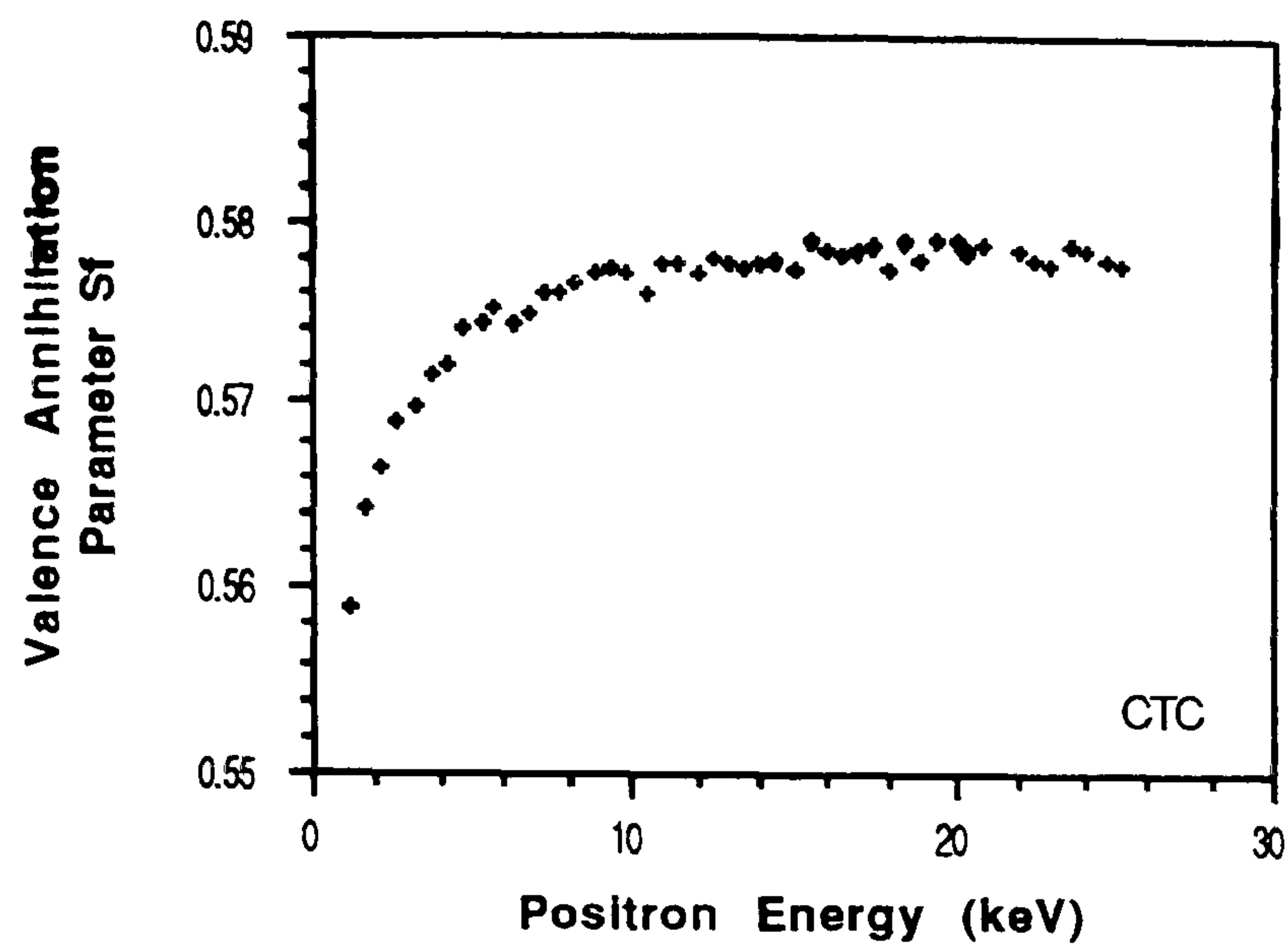


Figure 7.20 — Valence annihilation parameter, S_f , as a function of incident positron energy in CTC thin film.

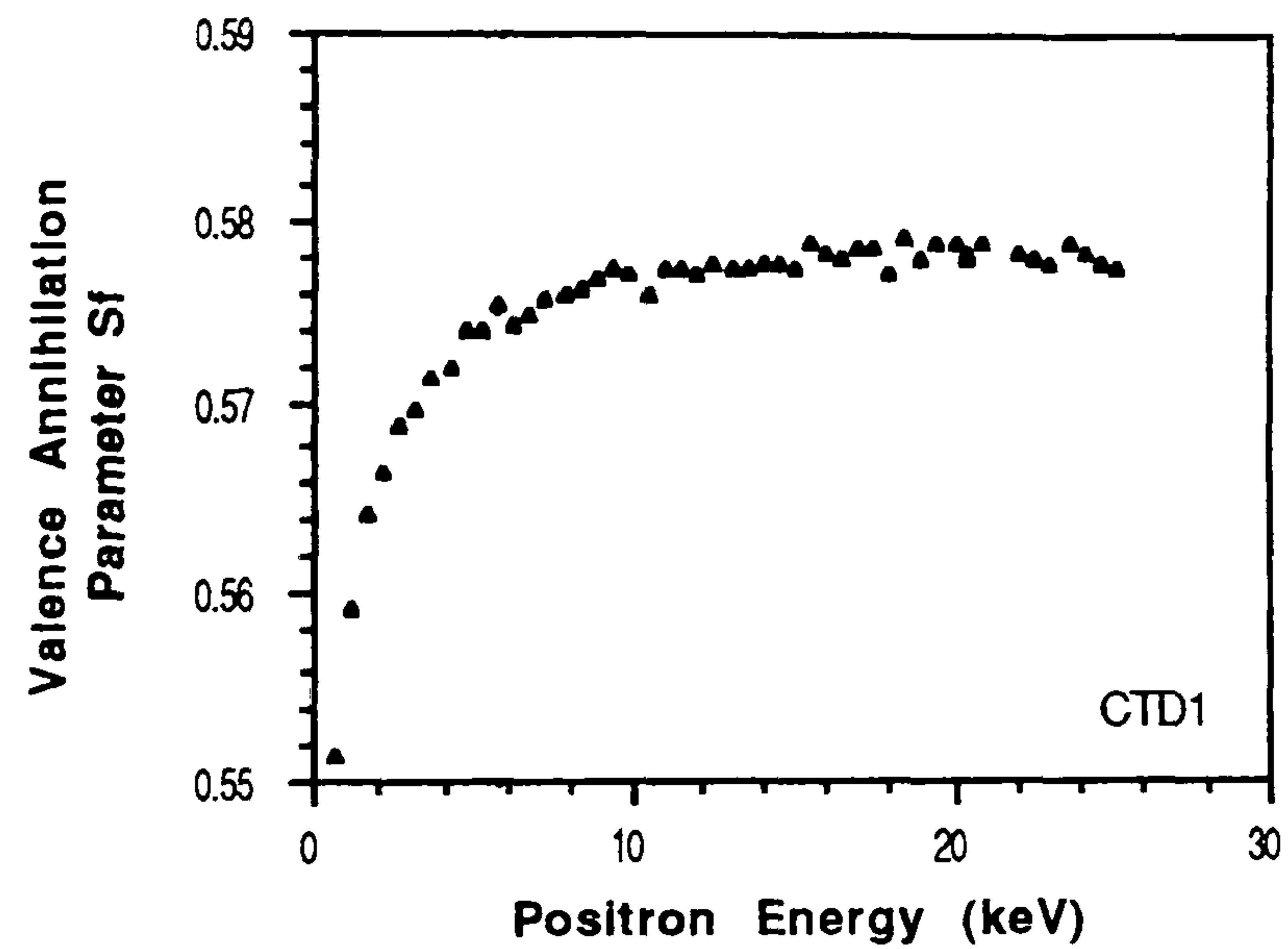


Figure 7.21 — Valence annihilation parameter, S_f , as a function of incident positron energy in CTD1 thin film.

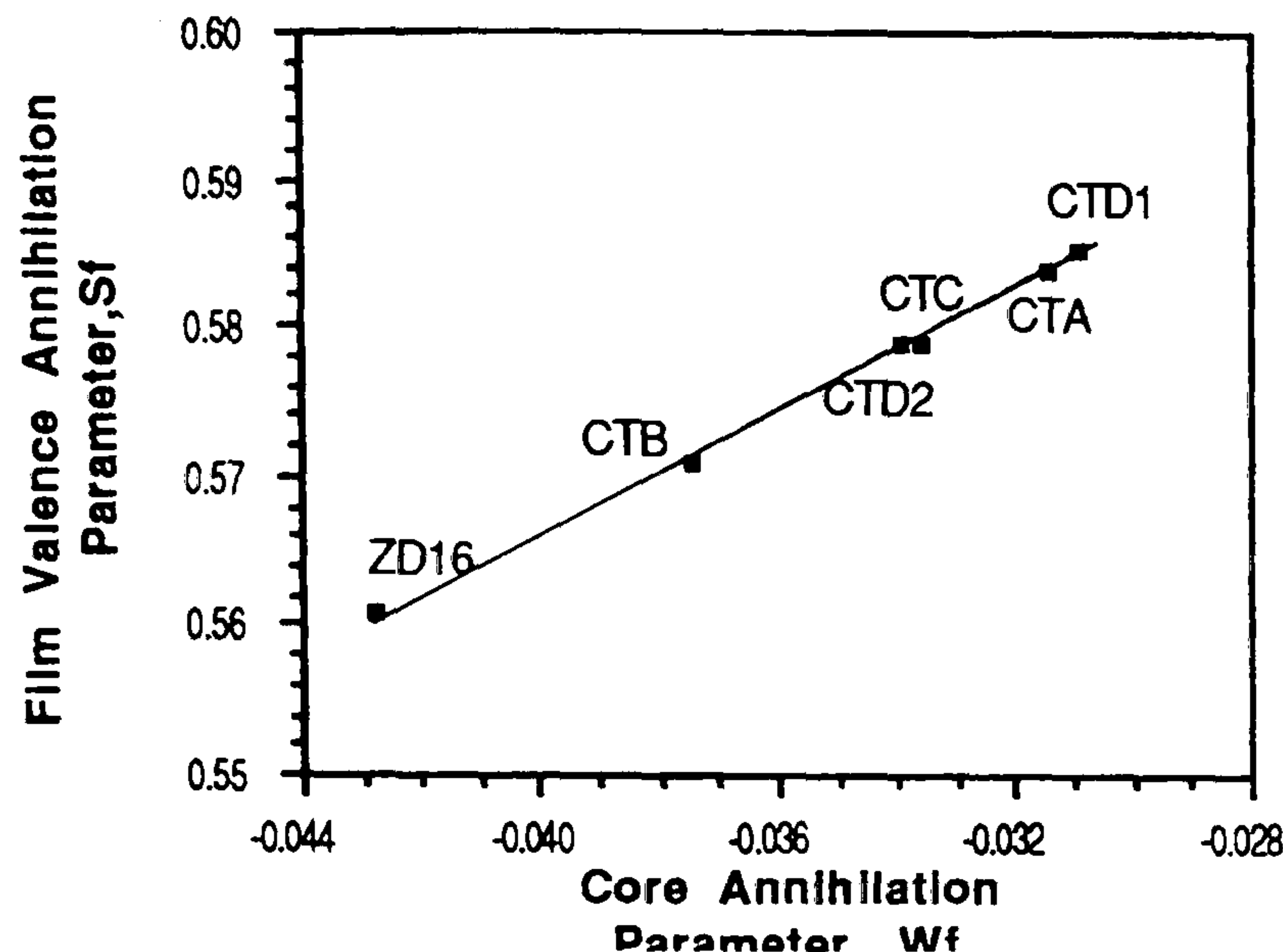


Figure 7.22 — Valence annihilation parameter, S_f , as a function of core annihilation parameter, W_f in CdTe thin films.

It is noticeable in Fig.7.22 that the MBE layer falls also on the same straight line as those for the films. This suggests that the MBE layer contains either the same vacancy cluster as the films but at a smaller concentration, or is free of them all together. It can also be seen in Fig.7.23 and 7.24 that the relative change from bulk annihilation to annihilation in the CDT1 film was 4% for S and 30% for W . This relative change was about three times larger than those measured for monovacancies in various semiconductors [38]. For instance, in CdTe bulk crystals which have been proved to be free of V_{Cd} vacancies by positron lifetime experiments [40], the relative change was measured to be only 1.5% for S . On this basis, it can be concluded that the CTD1 film contains defects where the open volume is larger than that of a vacancy. The same vacancy cluster is then the dominant positron trap in all the films. The values of $R_d = 2.02 \pm 0.02$ and after normalisation to the bulk, $R_d W_b / S_b = 0.15 \pm 0.002$ were determined from Fig.7.22 by linear regression.

Table 7.4 gives experimental values of core annihilation parameter (W_i) and theoretical core annihilation probability (F_i^c) [41] in CdTe defect free, contains monovacancies (V_{Cd} , V_{Te}) and contains divacancies ($V_{Cd} - V_{Te}$).

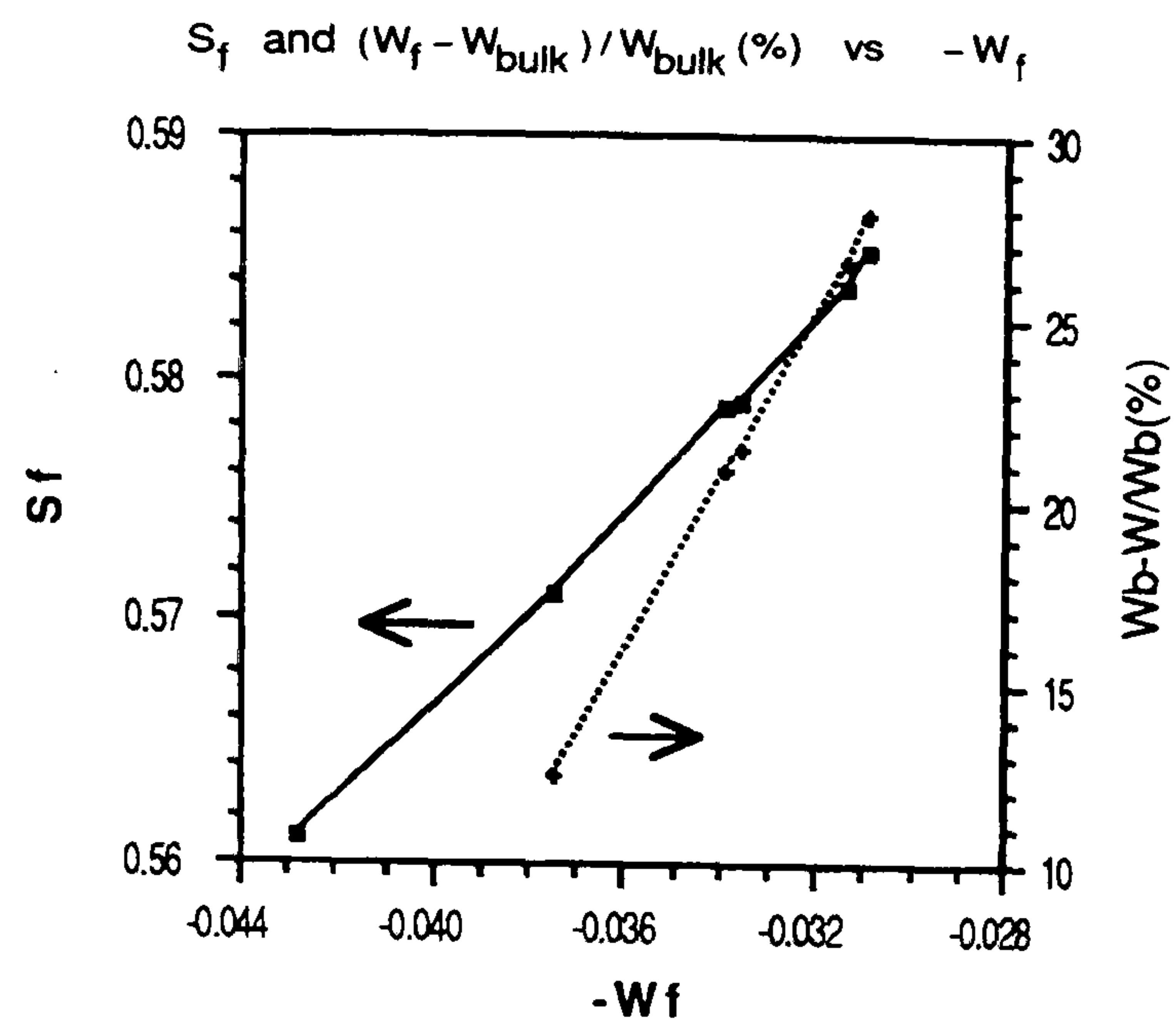


Figure 7.23 — The relative change in the annihilation parameter, W_f , compared to the bulk.

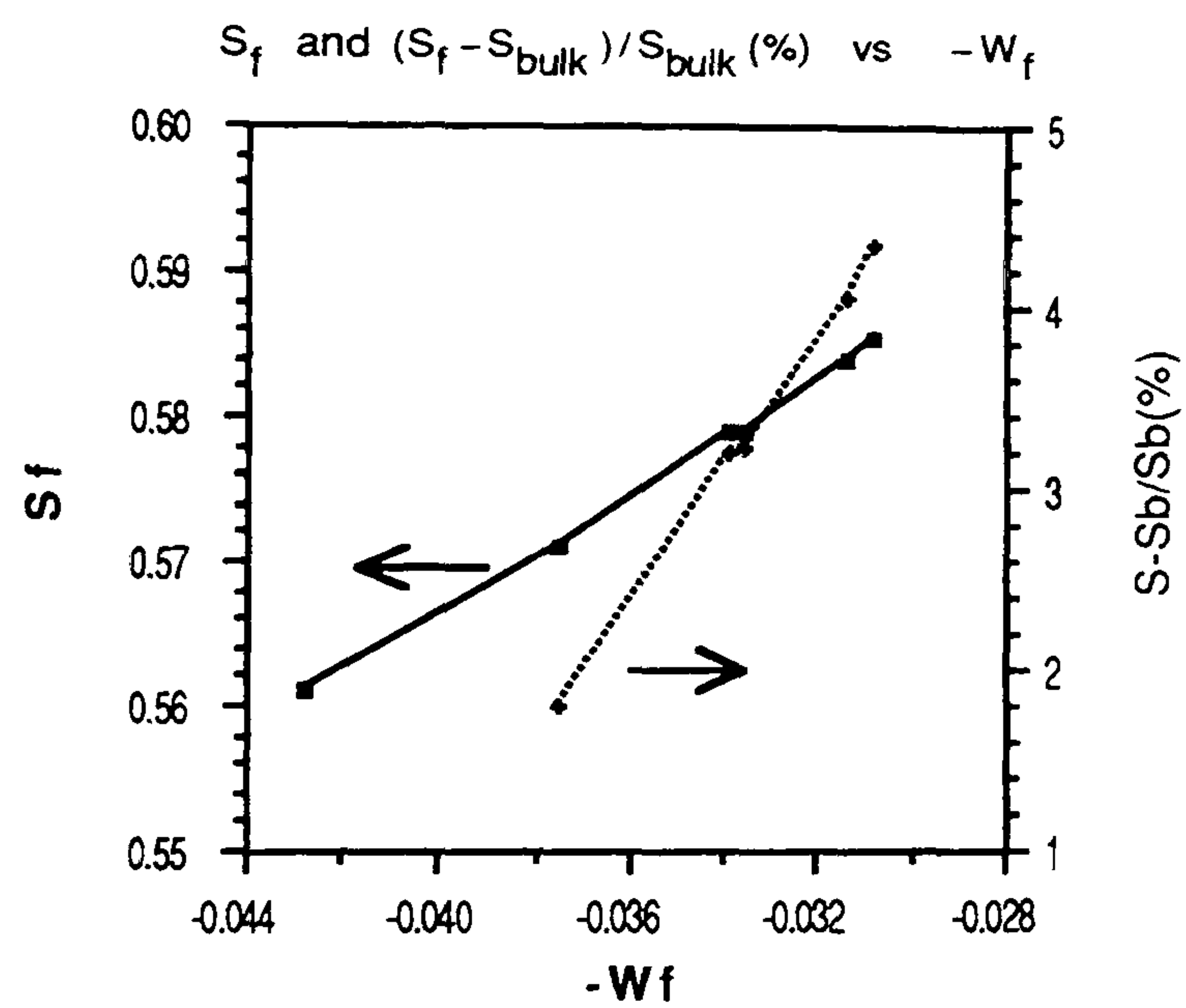


Figure 7.24 — The relative change in annihilation parameter, S_f , compared to the bulk.

As this fraction in V_{Cd} and $(V_{Cd}-V_{Te})$ is about the same, the change induced in W from the V_{Cd} vacancy to the vacancy cluster to those induced in F_c from V_{Cd} to $V_{Cd}-V_{Te}$ can be comparable. They are in rather good agreement at about 16% for W and 17% for F_c . This suggests that the divacancy can account for the change observed in W , and therefore by implication the vacancy cluster can be identified as a $V_{Cd} - V_{Te}$ divacancy.

The trapping rate, κ_d , at the divacancy in different layers can be calculated using Eq.7.24, changes in divacancy concentration to be identified since κ_d is directly proportional to it. Hence, by associating observed changes in κ_d with specific preparative procedures and treatments, it becomes possible to gain some understanding of how a given procedure affects the properties of the layer. Thus from the above results, the following conclusions may be drawn;

i- Annealed layers contain fewer divacancies than as-grown layers. This is true for layers deposited directly onto glass as well as for those layers deposited on ITO/glass substrates. Annealing at 400°C can reduce the divacancy concentration by an order of magnitude.

ii- Annealing is less effective if the film is $CdCl_2$ dipped before annealing. The divacancy decreased by a factor of 5 instead of 20. This suggests that chlorine diffused into the film and interacted with the divacancies.

iii- Deposition on ITO/glass at 220°C seems to generate as many (or even more) divacancies than deposition onto glass alone, but the reproducibility needs to be checked to confirm this conclusion.

	Defect Free	V_{Cd}	V_{Te}	$V_{Cd}-V_{Te}$
W_i	0.0428	0.0365	—	0.0309
F_i^c	0.1273	0.0725	0.0970	0.0603
$X_i^c = W_i/F_i^c$	0.3362	0.5026	0.3761	0.5117
W_i/W_{Cd}	—	1.0000	—	0.8460
F_i/F_{Cd}	—	1.0000	—	0.8310

Table 7.4 — Experimental and theoretical core annihilation probability (F_i^c) in CdTe that is: defect-free, contains monovacancies and contains divacancies.

The positron trapping coefficient at the divacancy $V_{Cd} - V_{Te}$ being unknown, divacancy concentrations can only be estimated, but nevertheless it may be assumed that the trapping coefficient at $V_{Cd} - V_{Te}$ is higher than at V_{Cd} . Taking a value of $10^{-7} \text{cm}^{-3} \text{s}^{-1}$ for the trapping coefficient, the divacancy concentration is then less than $2.5 \times 10^{16} \text{cm}^{-3}$ in the 400°C annealed CTB film which contains the lowest concentration.

7.6 ITO/CdTe:Cl₂ Diodes.

The deposition of metal on CdTe to make either ohmic or rectifying contacts has been investigated for a long time. Since there is no metal with a work function that is high enough to be comparable to the electron affinity of CdTe, all metals should create a barrier to the CdTe. However, in the literature [42,43], Au has been claimed to form both rectifying and ohmic contacts to p-type CdTe, irrespective of the value of work function of Au. The barrier height, ϕ_b , should be highly dependent on the work function of the metal and therefore larger variations in values of ϕ_b should be expected for different metals on a given semiconductor [44]. However, in practice, this is not the case for a wide range of metals on most common semiconductors, such as Si, GaAs, InP [45] and CdTe [46]. Other factors, such as depletion layer width, W_o , uncompensated donor (acceptor) density, $N_D(N_A)$, the diode ideality factor, n and the effects of the surface preparation are important too. The surface preparation is known to have a pronounced effect on the surface composition of the CdTe thin films, and these have been analysed using several spectroscopic techniques (i.e. XPS, AES, etc.). For instance, an *oxidizing etch* (i.e. bromine in methanol, followed by chromate etch; $\text{K}_2\text{Cr}_2\text{O}_7 + \text{H}_2\text{SO}_4 + \text{H}_2$) leaves a TeO_2 surface which when followed *reducing etch* (i.e. hydrazine in NaOH) leaves a Te-rich surface.

Each of the surfaces might be expected to give a different value for the barrier height. Although the work function of the metals differs quite considerably, (i.e. work function of Au is 1.0 eV larger than that of In), there is a little difference in the barrier heights observed between metals and p-CdTe. This was attributed to Fermi level pinning [47]. Interface states are also well known to influence ϕ_b [48]. Schottky barriers formed by some metals on CdTe are drastically influenced by

oxide layers whereas others are not, indicating that the differences are associated with a strong reduction of the oxide to the metal.

7.6.1 Diode Preparation and Characterisation.

ITO/CdTe:Cl₂/Au Schottky diodes were prepared by co-evaporation of CdTe and CdCl₂ onto ITO coated glass substrates. The devices were heated to 400°C for about 30 min in air (type conversion process) followed by Au contact formation (i.e. surface etching and then alloying Au followed by annealing in N₂ flow at 280°C about 15 min –note that for the rectifying contact, no surface etching of the CdTe would have been possible since the CdTe was deposited directly onto ITO coated glass substrates).

ITO/CdTe:Cl₂/Au junctions were characterised using I–V and C–V measurements in the dark at several temperatures from 300K up to 400K in 25K steps. Fig.7.25 shows a J–V characteristics of a typical ITO/CdTe:Cl₂/Au diode at 300K. The diode had a rectification value of 69 at 0.6V, a low $J_0 \cong 5.3 \times 10^{-9}$ A/cm² (extrapolated between 0 and 0.05V), and an ideality factor, n of 1.18. The reverse current characteristic is also shown. Low rectification values may be due to the relatively poor junction formation and leakage current through pin-holes present in CdTe. The series resistance resulting from the highly resistive CdTe layer and high contact resistance was high (see Fig.7.25) causing the J–V curve to bow, even at very low biases. A combination of thermionic emission and diffusion transport mechanism were thought probable due to the relatively low n values and temperature dependent slopes. Fig.7.26 is the Richardson plot of $\log(J_0 T^{-2})$ versus T^{-1} of a typical ITO/CdTe:Cl₂/Au diode, the slope of which is related to ϕ_b . A value of ϕ_b of 0.36 eV was obtained which is rather lower than what has been reported previously [49,50].

A typical C^{-2} vs V characteristic is shown in Fig.7.27 at 300K. It showed little variation with applied reverse bias. This could be attributed to leakage currents by interdiffusion of metal deposits through pin-holes and possibly to non-uniform carrier distribution. The acceptor density, N_A , and built-in potential, V_i , obtained from the C^{-2} vs V plot at low reverse bias (between –0.35V and 0) gave values of about 1.3×10^{14} cm⁻³ and 20.2 eV (which is unphysical) respectively, at room temperature. The large values of V_i obtained, clearly indicated that the device

were dominated by interface states etc. and that the conventional analysis was inappropriate.

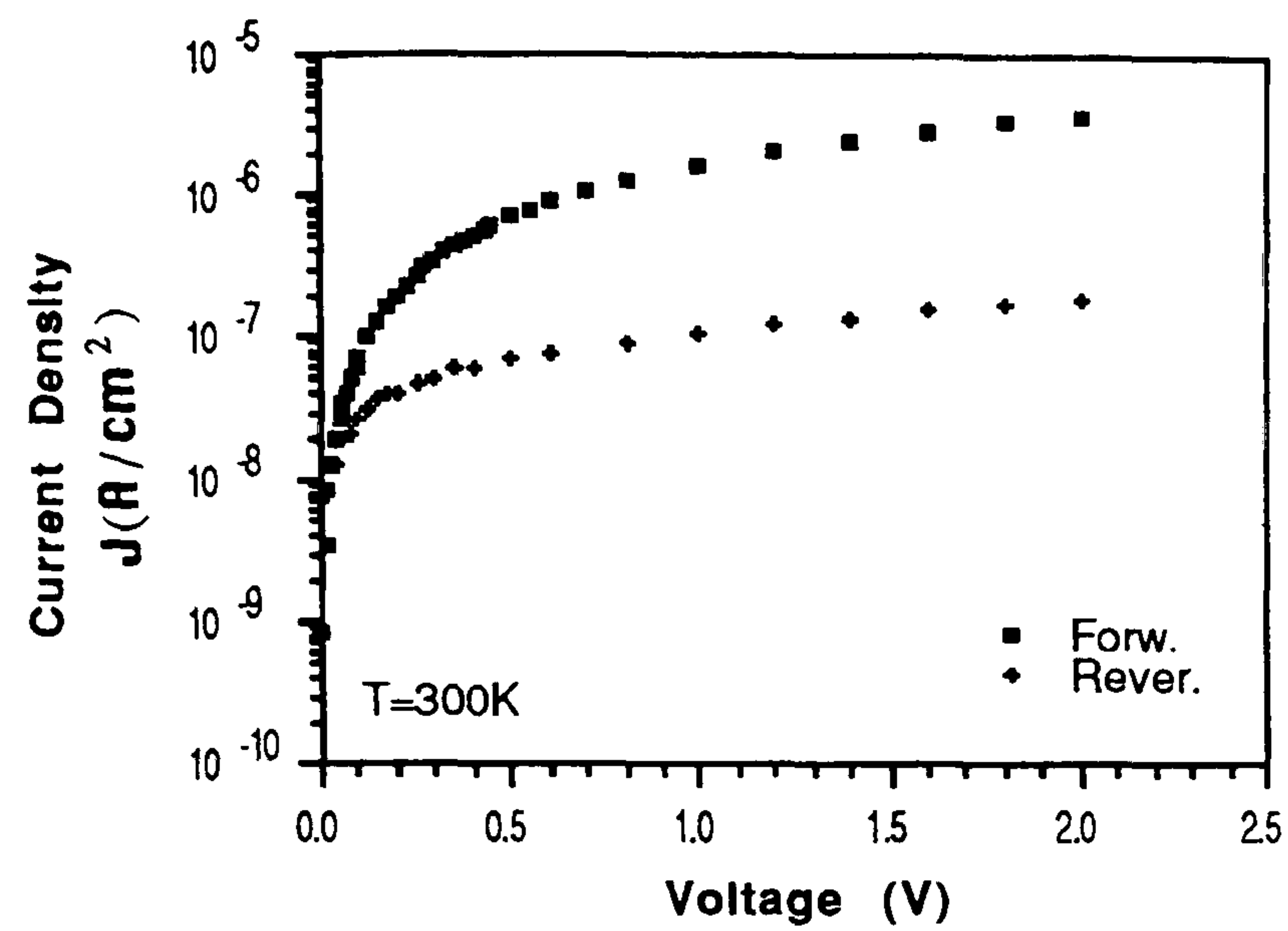


Figure 7.25 — $\log(J)$ vs V characteristics of a typical ITO/CdTe:Cl₂/Au Schottky diode at 300K.

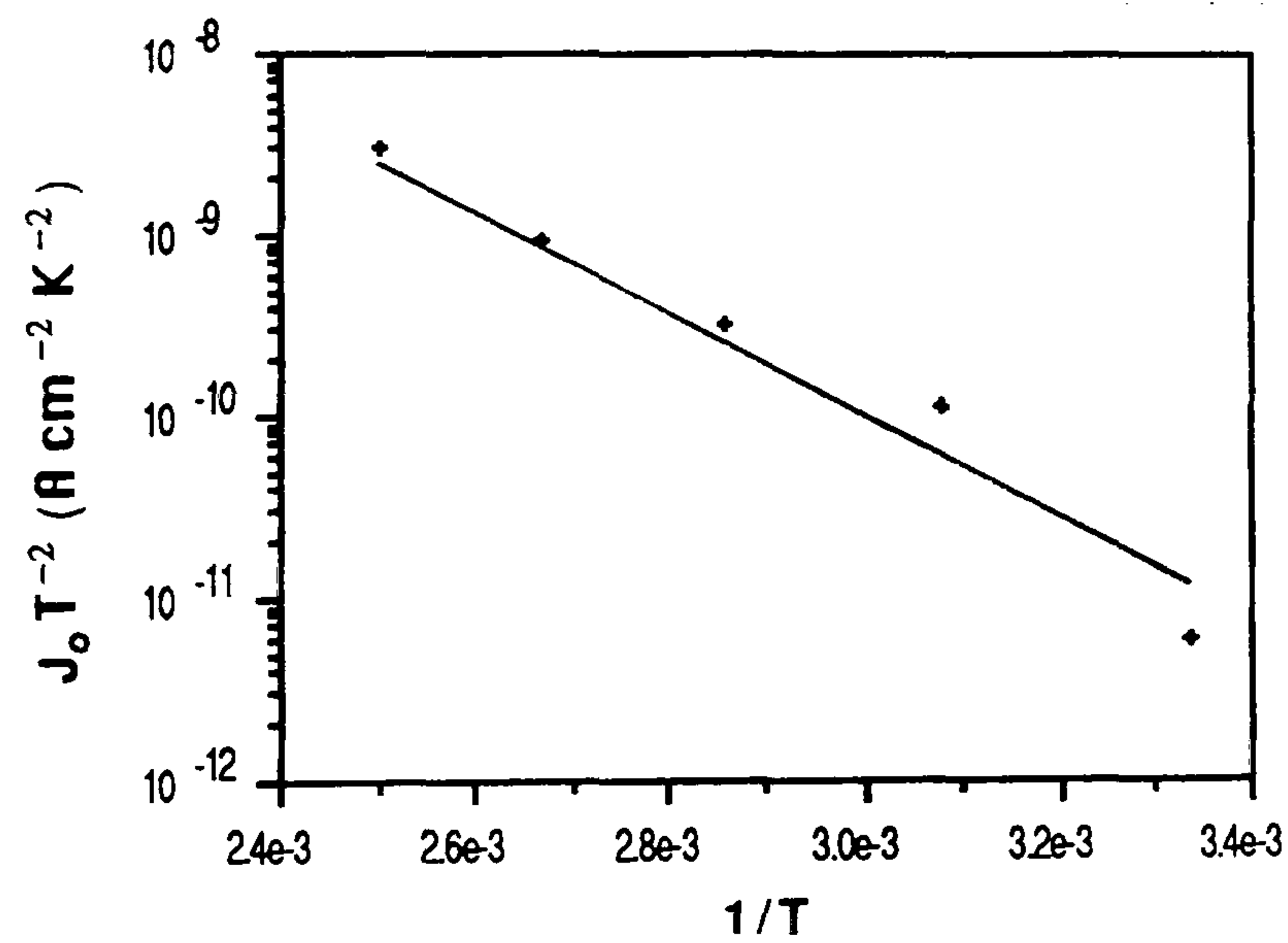


Figure 7.26 — $\log(J_0 T^{-2})$ vs T^{-1} characteristic of ITO/CdTe:Cl₂/Au Schottky diode at 300K.

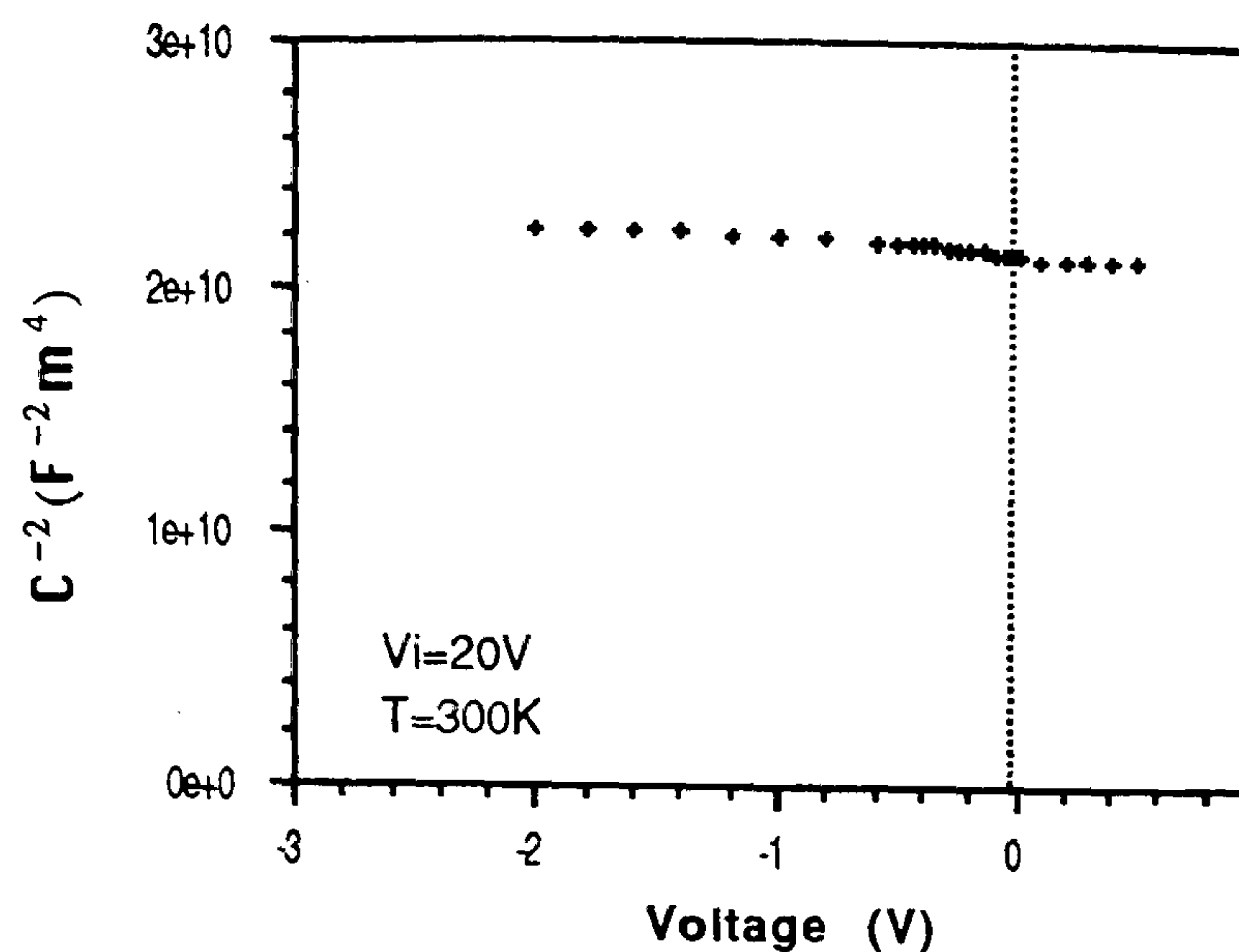


Figure 7.27 — C^{-2} vs V characteristics of ITO/CdTe:Cl₂/Au Schottky diode at 300K.

7.7 Conclusions.

Thin layers of CdTe were deposited by vacuum evaporation onto glass substrates. The as-grown CdTe thin layers were of very low p-type conductivity and several post growth and/or doping treatments were investigated in attempts to increase the conductivity. Heat treatment in air for about 30 min at 400°C, resulted in a more pronounced Seebeck effect indicating a more definite p-type conductivity, possible due to oxygen-related Cd vacancy formation. Attempts at acceptor doping with Sb produced CdTe:Sb thin layers that were either of high or of very low conductivity. This may have been due to formation of metallic precipitates. Au contacts to CdTe showed ohmic behaviour over the range of voltage examined. However, contact resistivities were generally found to be relatively high. Hence, it was concluded that surface preparation (i.e. p⁺ surface layer) prior to metallic deposition was important. In view of the high electron affinity of CdTe, it proved useful to use a high diffusivity impurity such as Cu to form a p⁺ layer under the Au contact.

Cl_2 doping was also investigated following the widely used procedure where the CdTe was dipped into a solution of CdCl_2 in methanol. The resistivity of Cl_2 doped thin layers was relatively unaffected by the dipping processes. Some changes were observed in the illumination I-V characteristics, but the effect was small.

Temperature dependent Hall measurements showed that carrier transport was dominated by grain boundary scattering.

Changes in the vacancy content between as-grown and treated layers were investigated by positron trapping. These experiments showed that post growth annealing in air lead to a reduction in the divacancy concentration and also revealed that heat treatment in air was less effective in reducing the divacancy concentration in the case of the layers dipped in CdCl_2 solution.

The J-V and C-V characteristics of ITO/CdTe: Cl_2 Schottky diodes were also investigated as a means to determine the influence of point defects and surface states. Schottky barrier heights, ϕ_b , was found to be rather lower than values reported in the literature. C^{-2} vs V characteristics showed little variation with applied reverse bias resulting in unphysical intercept voltage values, V_i , clearly indicated that the device were dominated by interface states, and leakage currents through pin-holes.

As-grown CdS layers exhibited relatively low resistivities. Introduction of In during deposition yielded very low resistivities, up to 3 orders of magnitude below comparable undoped layers. Activation energies were also calculated using the same grain boundary scattering formalism.

7.8 References.

1. N.W.Ashcroft, N.D.Mermin, "*Solid State Physics*", CBS, Publishing Asia Ltd., 1988.
2. J.P.Kelvey, "*Solid State and Semiconductor Physics*", Harper & Row, New York, Evaston & London, and John Weatherhill, Inc., Tokyo.
3. R.L.Petritz, W.W.Scanlon, Phys.Rev., **97**, 1620 (1955).
4. W.Shockley, J.Bardeen, Phys.Rev., **80**, 72 (1950).

5. W.A.Harrison, Phys.Rev., **101**, 903 (1956).
6. E.M.Conwell, V.F.Weisskopf, Phys.Rev., **77**, 388 (1950).
7. R.B.Dingle, Phil.Mag., **46**, 831 (1955).
8. H.Brooks, Advances in Electronic and Electron Physics, **7**, 85 (199).
9. C.Erginsoy, Phys.Rev., **77**, 1013 (1950).
10. I.Solomon, Proc. 12th Int.Conf.on Phys.of Semiconductors, (Polish. Sci. Publ., 1972), p.1.
11. J.Volger, Phys.Rev., **9**, 1023 (1950).
12. R.L.Petritz, Phys.Rev., **104**, 1508 (1956).
13. J.Y.W.Seto, J.Appl.Phys., **46**, 5247 (1975).
14. J.W.Orton, Thin Solid Films, **86**, 351 (1981).
15. J.Y.W.Seto, J.Electrochem.Soc., **122**, 701 (1975).
16. G.Baccarani, B.Ricco and G.Spandini, J.Appl.Phys., **49**, 5565 (1978).
17. C.H.Seager, T.G.Castner, J.Appl.Phys., **49**, 3879 (1978).
18. G.Baccarani, G.Masetti, M.Severi, and G.Spandini, Proc.Int.Symp. Silicon Mat. Sci. Technol., 3rd Philadelphia, Pennsylvania, (1977).
19. A.Many, Y.Goldstein, and N.B.Grover, "*Semiconductor Surfaces*", Chap.5 and 9, North-Holland Publ., Amsterdam, 1965.
20. S.T.Pantelides, "*The Physics of SiO₂ and its Interfaces*", Pergamon, Oxford, 1979.
21. I.M.Dharmadasa, J.M.Thorton, and R.H.Williams, Appl.Phys.Lett., **54**, 137 (1989).
22. B.M.Basol, "Method of Forming Ohmic Contacts", U.S. Patent **4 456 630**, (1984).

23. B.M.Basol, "Method of Making Multi-Layer Ohmic Contact to Thin Film p-type II-VI Semiconductors", U.S. Patent 4 666 569, (1987).
24. H.Jaeger, E.Seipp, J.Electron.Mater., 10, No:3, 605 (1981).
25. A.L.Fahrenbruch, Solar Cells, 21, 399 (1987).
26. Yuan-Sheng Tyan, Solar Cells, 23 (1988) 19.
27. A.Mitsuishi, H.Yoshinaga, and S.Fujita, J.Phys.Soc.Jpn., 13, 1235 (1958).
28. J.W.Orton, B.J.Goldsmith, J.A.Chapman, and M.J.Powell, J.Appl.Phys., 53, 1602 (1982).
29. Zs.Kajcsos, Cs.Szeles., "Positron Annihilation", Trans. Tech. Publications, (1992).
30. C.Corbel, M.Stucky, P.Hautojarvi, K.Saarinen, P.Maser, Phys.Rev B38, 8192 (1988); K.Saarinen, P.Hautojarvi, P.Lanki, C.Corbel, Phys.Rev. B44, 10585 (1991).
31. P.Hautojarvi, "Positrons in Solids", Topics in Current Physics, Springer, Vol. 12, 89 (1979).
32. J.Lahtinen, A.Vehanen, H.Huomo, J.Makinen, P. Huttunen, K. Rytsalo, in M. Bentzon, P.Hautojarvi, Nucl. Instr. Meth. Phys. Res. Sec., 17, 73 (1986).
33. A.Vehanen, K.Saarinen, P.Hautojarvi, H. Huomo, Phys. Rev., B35, 4606 (1987).
34. S.Valkealahti, R.M.Nieminen, Appl.Phys, A35, 51 (1984).
35. C.Corbel, Scanning Microsc, 1, 545 (1987).
36. P.J.Schultz, K.G.Lynn, Rev.Mod.Phys., 60, 3 (1989).
37. S.Mantl, W.Triftshauser, Phys.Rev., B17, 1645 (1978).
38. K.Saarinen, P.Hautojarvi, J.Keinonen, E.Rauhala, J. Raisanen, C. Corbel, Phys. Rev., B43, 4249 (1991).

39. A. Van Veen H, Schut J.de Vries, R.A. Hakvoort, M.R.Ljpma in "*Positron Beams for Solids and Surfaces*", (eds., P.J. Schultz, G.R. Massoumi, P.J. Simpson), AIP Conference Proceedings, **218**, p.171.
40. C. Corbel, L. Baroux, F. Kiessling, C. Gely-Sykes, R. Tribulent in "*CdTe and Related Cd-rich Alloys*", (eds., R. Triboulet, W.R. Wilcox, O. Oda), EMRS-Symposium Proceedings, Nort-Holland, p.134 (1993).
41. M.J. Puska, J. Phys. Condens. Matter, **3**, 3455 (1991).
42. H. Tubota, H. Suzuki, J. Phys. Soc., Japan **13** (1958) 538.
43. A.L. Fahrenbruch, Solar Cells, **21** (1987) 399.
44. W. Schottky, Z. Phys. **113**, 367 (1939).
45. J. Bardeen, Phys. Rev., **71**, 714 (1947).
46. J.P. Ponpon, Solid State Electron, **28**, 698 (1985).
47. R.H. Williams, M.H. Patterson, Appl. Phys. Lett., **40**, 484 (1982).
48. J.M. Dharmadasa, A.B. Mclean, M.H. Patterson, and R.H. Williams, Semicond. Sci. Technol., **2**, 404 (1987).
49. D. Kindle, J. Toušková, Phys. Stat. Sol., **A**, **106**, 297 (1988).
50. R.H. Bube, Solar Cells, **23** (1988) 1.

Chapter VIII

Bulk Single Crystal CdTe/CdS Solar Cells.

8.1 Introduction.

Although the thin film p-CdTe/n-CdS heterojunction has long been identified as one of the most likely candidates for low cost terrestrial solar cells, there is still much that is not known about the device. Consequently, a study was made to investigate the electrical and photovoltaic properties of bulk single crystal p-CdTe/n-CdS solar cells, in order to obtain a basic understanding of the junction properties, and the effects various material parameters have on performance.

The results of this study of bulk single crystal p-CdTe/n-CdS cells are presented and discussed in this chapter. Dark and illuminated I-V and capacitance-voltage characteristics were measured in an attempt to understand the current transport mechanisms and to determine the cell parameters. The influence of the p-CdTe back contact material was also studied.

8.2 Device Fabrication.

CdTe substrates were obtained from boules grown by a sealed ampoule vapour transport technique described in [1]. Dice ($5 \times 5 \times 1.4 \text{ mm}^3$) were cut from boules parallel to the (111) orientation and chemically polished in 2% Bromine/Methanol to remove surface damage. The as-grown CdTe was p-type but resistive ($\sim 10^8 \Omega\text{-cm}$). The back and front surfaces of the dice were mechanically and chemically polished prior to vacuum deposition of either Au, or Au/P contacts and the CdS window layer respectively. Indium was used as the top contact to the $\sim 0.6 \mu\text{m}$ thick CdS layer (see section 3.4.4), and was deposited in two steps: Firstly a thin transparent layer of In was deposited onto the CdS layer to cover most of the device area, then secondly a thick In spot was evaporated on the middle of the latter layer for use as a contact pad to which the top lead was to be connected. The thin transparent In layer was intended to provide a large current collection

area, and to help in offsetting the relatively high sheet resistance of the undoped CdS. Excess deposits which might cause leakage currents at the device edges were removed by a HCl etch.

8.3 Dark I-V Characteristics.

8.3.1 Room Temperature I-V Characteristics.

Fig.8.1 shows the typical forward I-V characteristics of two undoped p-CdTe/n-CdS cells which had two different back contact (i.e. CdTe) arrangements; evaporated Au, and H₃PO₄ coated/evaporated Au. The room temperature characteristics for both types of device showed good rectification (for the two devices in Fig.8.1 the rectification ratios were 4103 and 588 at 0.6V). The forward current varied exponentially with voltage for several orders of magnitude of current, while the deviation at higher current levels was due to the relatively high bulk resistance of the CdTe absorber and contact/CdTe interface states. The cell with the Au/P contact seemed to have a higher series resistance resulting in earlier onset of saturation compared to the cell with the Au contact. This appears to be in conflict with Alnajjar's results where the reverse was found to be the case [2].

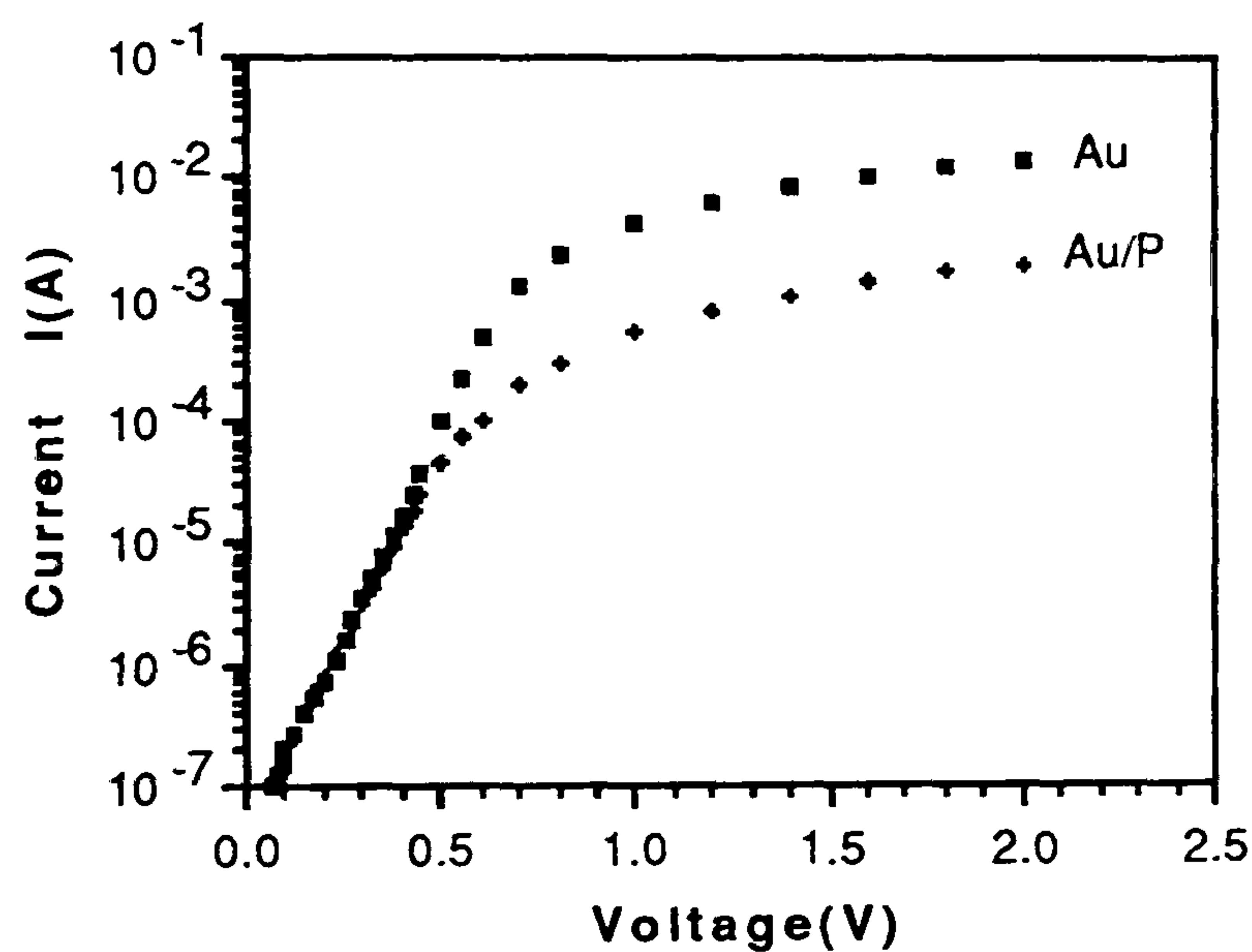


Figure 8.1 — Room temperature $\log(I)$ vs V characteristic of CdTe/CdS cells with Au and Au/P contacted.

The values of diode ideality factor, n and reverse saturation current density, J_o for the undoped p-CdTe/n-CdS cells are listed in Table 8.1. The differences observed in the n and J_o values of these CdTe based cells may be attributed to the back contact since as far as possible, all other parameters were the same. The principal differences relate to the way in which the p^+ sub-contact layer was formed.

Sample No:	n	$J_o(\text{A/cm}^2)$
BC: Au	2.4	1.5×10^{-7}
BC: Au/P	2.3	2.9×10^{-7}

Table 8.1 — n and J_o values of undoped p-CdTe/n-CdS cell with two different contacts.

The n values of the cells appeared to be relatively high which was probably related to the current transport mechanism. J_o values indicate that the junctions (i.e. CdTe/CdS interface) were relatively poor due possibly to interface states. Nevertheless, the cell with the Au/P “evaporated/coated” back contact gave a higher value of J_o which could be attributed to the presence of a high density of interface states between Au and P.

8.3.2 Temperature Dependent I-V Characteristics.

It is essential to study the I-V characteristic of the cells at a variety of temperatures in order to investigate the current-voltage mechanisms across the junction. Taking into account the effects of interface-states, the relevant current-transport mechanisms in the p-CdTe/n-CdS heterojunction devices include diffusion and emission, emission/recombination, tunnelling and tunnelling/recombination processes, represented as A, B, and C in Fig.8.2.

A- Diffusion and Emission: Anderson [3], first proposed the model, in which the diffusion current consists almost entirely of electrons injected from the conduction band of the n-type material (i.e. CdS) over the potential barrier to the p-type

material (i.e. CdTe). The current-voltage relationship is described by the usual diode equation (Eq.2.3);

$$I = I_o \left[\exp\left(\frac{qV}{kT}\right) - 1 \right] \quad [8.1]$$

B- Emission/Recombination: This model proposed by Dolega [4] which is based on the assumption that whilst injection is occurring, the electron and holes recombine at interface states (i.e. non-radiatively) giving;

$$I = I_{er} \left[\exp\left(\frac{qV}{nkT}\right) - 1 \right] \quad [8.2]$$

where I_{er} , the reverse saturation current differ from that in Eq.8.1 and is thermally activated, i.e.

$$I_{er} = I_{er,o} \exp\left(-\frac{\Delta E}{kT}\right) \quad [8.3]$$

where $I_{er,o}$ is only weakly temperature-dependent. The value of n , is an indication of junction and material imperfection, and usually lies between 1 and 2, and ΔE is the thermal activation energy.

C- Tunneling and Tunneling/Recombination: The tunneling mechanism was first introduced by Rediker, Stopek, and Ward [5]. They considered that electrons or holes might tunnel through the junction potential barrier in a single step. In this model, the current, which is the product of the tunneling probability and incident electron or hole flux is written in the form;

$$I_f(V, T) = I_o(T) \exp(AV) = I_{oo}(T) \exp(BT) \exp(AV) \quad [8.4]$$

where I_{oo} is proportional to the trap density of appropriate energy in the depletion region, A is the slope of the I_f - V characteristics, and B is a constant.

Later, Riben et al [6,7] refined the model by allowing recombination and hence relaxing the single-step tunneling constraint. This multi-step tunneling /recombination process may be expressed as;

$$I_f(V, T) = \xi N_t \exp\left[-\tau s^{1/2}(V_i - KV)\right] \quad [8.6]$$

ξ is a constant and τ is given by;

$$\tau = \left(\frac{4}{3\hbar} \right) \left(\frac{m_e^* \epsilon_n}{N_D K} \right)^{1/2} \quad [8.6a]$$

in which K is defined by;

$$K = \left[1 + \frac{N_D \epsilon_n}{N_A \epsilon_p} \right]^{-1} \quad [8.6b]$$

where s relates is the average height of the barrier surmounted per tunneling step, E_t is the electric field, N_t is the density of trapping centres in the bandgap, m_e^* is the electron effective mass, ϵ_p and ϵ_n are the dielectric constants, and N_A and N_D are the net ionised charge densities on each side of the junction.

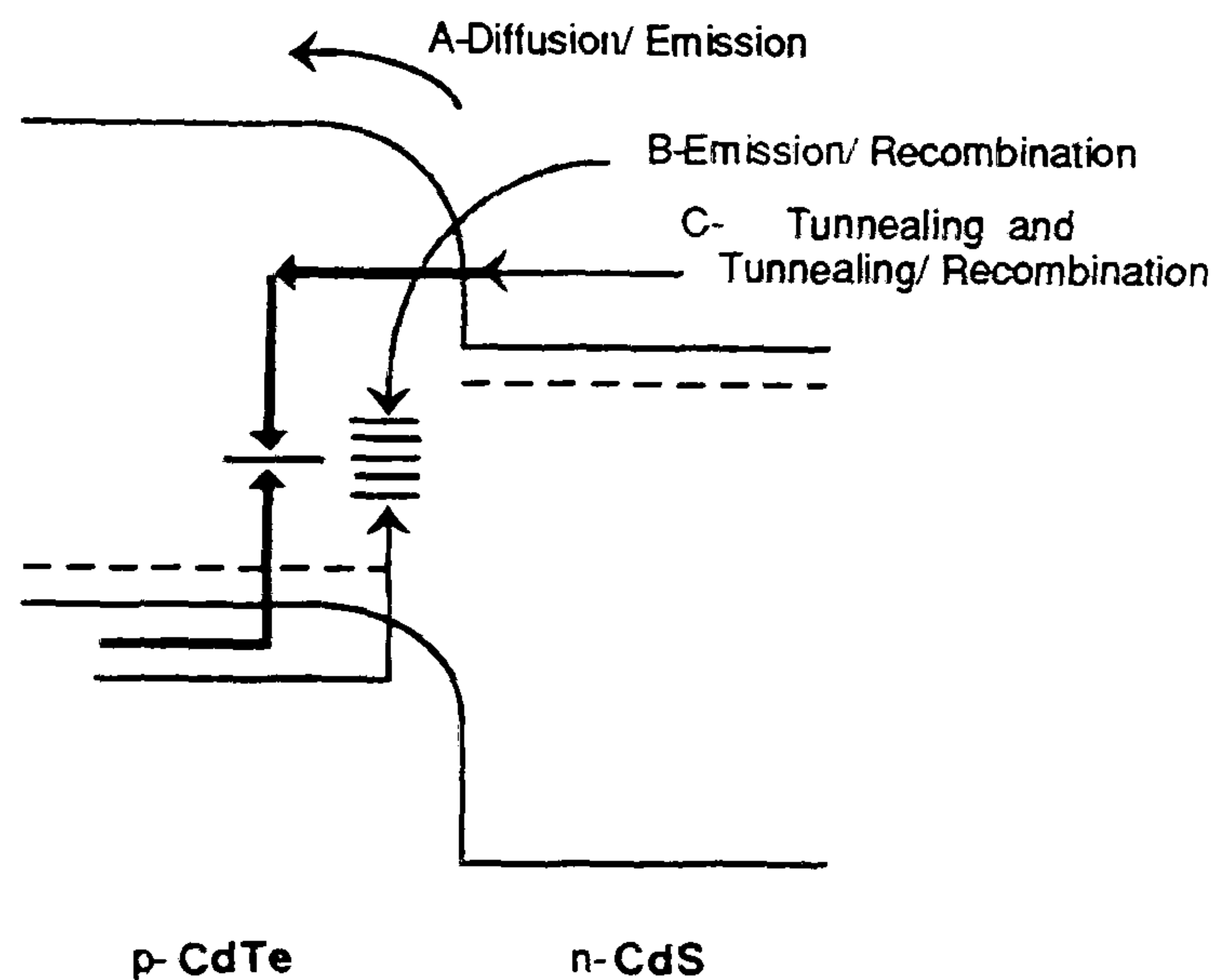


Figure 8.2 — Possible current transport mechanisms in CdTe/CdS cells.

Thus by plotting the $\log(I_f)$ vs V characteristics at different temperatures, an indication of the current transport mechanism can be obtained. The current transport across the heterojunction may be dominated by any of the three mechanisms and the dominant process may be identified from the behaviour of n . If either diffusion and emission or emission/recombination are the major process then n will be essentially constant with temperature. However if the value of n is variable while the slope (i.e. $A = \Delta(\ln I_f) / \Delta V_f$) remains constant over a range of temperatures, then the current mechanism is better explained by means of tunneling.

I-V characteristics were measured for a range of temperatures from 77K to 375K, although below 275K, no reliable current above the noise level was observed as the applied voltage was varied. The $\log(I_f)$ vs V characteristics of a typical Au/p-CdTe/n-CdS device for a range of temperatures above 275K are given in Fig.8.3. The slopes of the forward bias current characteristics were fairly parallel between the voltage range 0.2–0.4V (i.e. intermediate voltages, where series resistance was not dominant), while the ideality factor decreased with increasing temperature. The calculated values of the slope A and n are given in Table 8.2. These results suggest that current transport was probably controlled by some sort of tunneling mechanism. The temperature behaviour of the saturation current densities, J_o , are given in Fig.8.4a and Fig.8.4b which present plots of $\log(J_o)$ vs T and $\log(J_o)$ vs T^{-1} respectively for the same cell. Although J_o appeared to vary exponentially with T (see Fig.8.4a), which is consistent with tunneling transport mechanism, the inverse temperature dependence of J_o (see Fig.8.4b) was also a straight line!

This discrepancy was difficult to explain but may be due in part to the problems associated with high series and bulk resistance. Similar characteristics $\log(J_o)$ vs both T and T^{-1} were also seen for the cell with Au/P contact. The values of B , the temperature coefficient of J_o , and the activation energies, ΔE of the cells with Au and Au/P contacts were estimated from the slopes of $\log(J_o)$ vs T and $\log(J_o)$ vs T^{-1} characteristics respectively and are listed in Table 8.3.

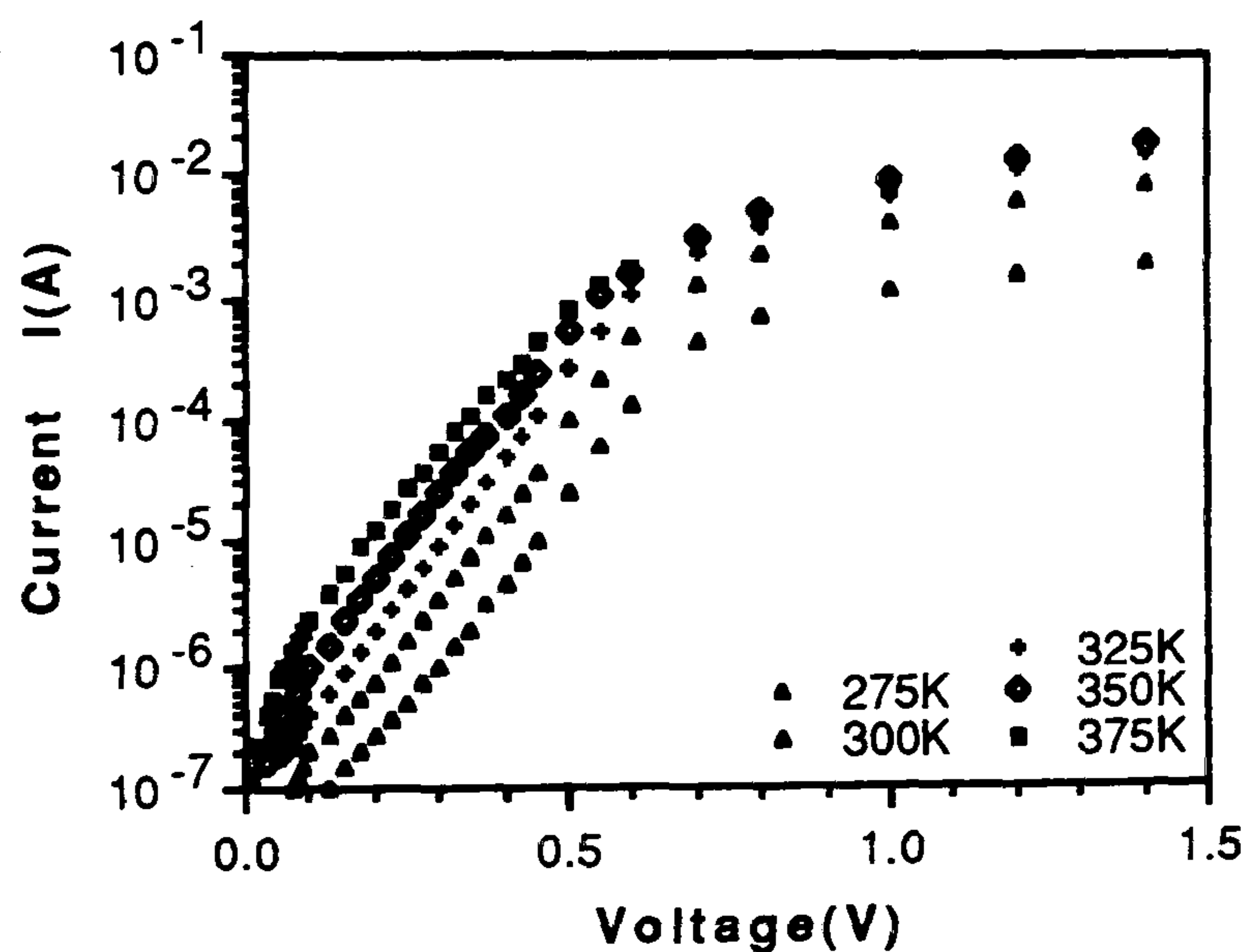


Figure 8.3 — $\log(I_f)$ vs V characteristic of CdTe/CdS cell with Au contact at several temperatures.

T(K)	$J_o(\text{A/cm}^2)$	Slope, A	n
275	4.7×10^{-8}	15.4	2.8
300	1.5×10^{-7}	16.1	2.4
325	5.2×10^{-7}	15.4	2.3
350	1.4×10^{-6}	16.1	2.1
375	3.7×10^{-6}	15.0	2.1

Table 8.2 — J_o , A , and n for the Au/p-CdTe/n-CdS cell at different temperatures.

Sample No:	$B(\text{K}^{-1})$	$\Delta E(\text{eV})$
BC: Au	0.044	0.39
BC: Au/P	0.042	0.32

Table 8.3 — The slope, B and activation energy, ΔE values for undoped CdTe cells with Au and Au/P contacts.

Values of B published in the literature vary between 0.015 K^{-1} and 0.08 K^{-1} for p-CdTe/n-CdS HJ's [8], in good agreement with the values of $\sim 0.04 \text{ K}^{-1}$ found in this study. However, values of activation energy were somewhat smaller than generally published values (0.6 eV [8]) due probably to the high bulk resistance of undoped CdTe substrates. Interestingly, Alnajjar found even lower activation energies ($\sim 0.13 \text{ eV}$) for similarly prepared bulk single crystal cells [2].

8.4 Illuminated I-V Characteristics.

The photovoltaic I-V output characteristics for the undoped CdTe cells were measured under $\sim 90 \text{ mW/cm}^2$, and are shown in Fig.8.5. The corresponding cell parameters, namely V_{oc} , J_{sc} , FF , and $\eta(\%)$ are listed in Table 8.4. The cells had relatively low light conversion efficiencies. Although the high doping concentration at the back surface (i.e. p^+ layer) might have led to a tunneling ohmic contact, with a low voltage drop across it, the low fill factor gives a clear indication that

the resistivity of the bulk was quite high. This was also apparent from the forward characteristics at voltages above V_{oc} , which show little evidence of any barrier contact, but have relatively low slopes indicating a high series resistance.

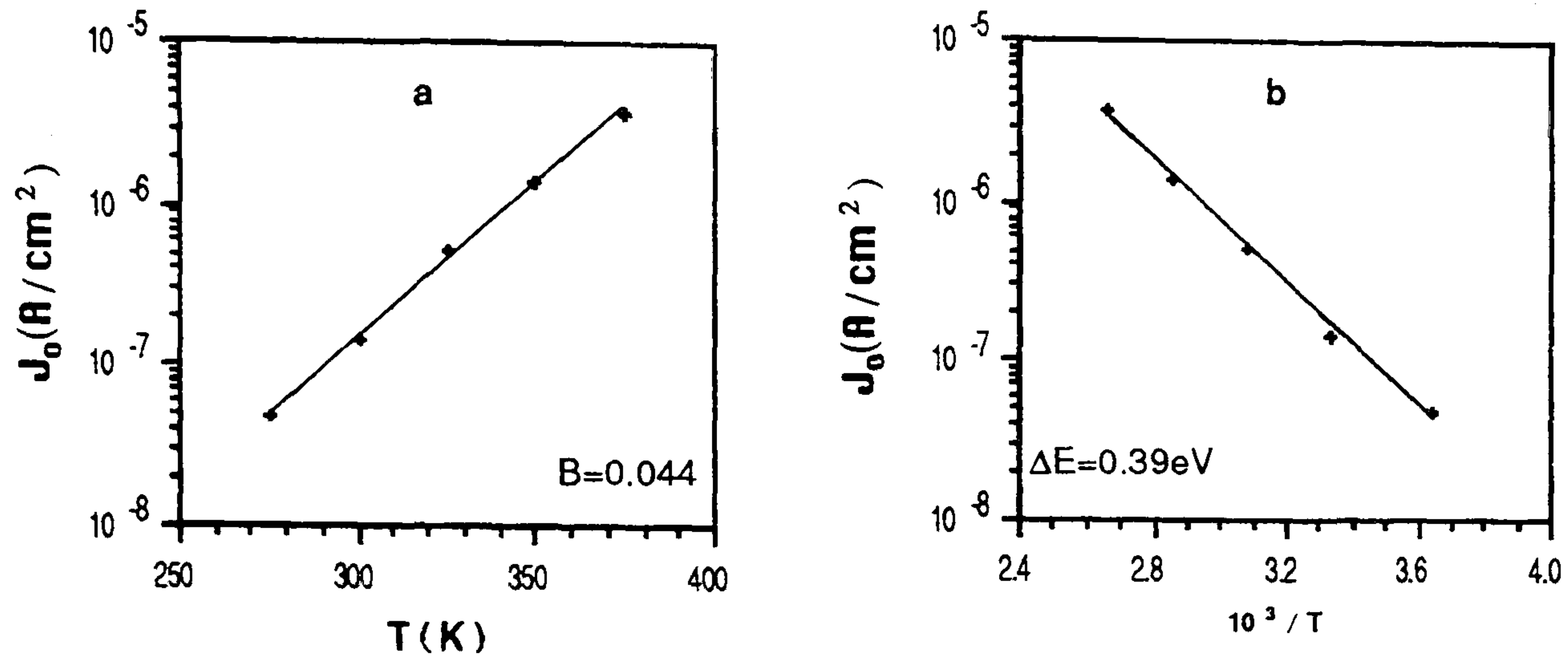


Figure 8.4 — $\log(J_0)$ vs T (a) and $\log(J_0)$ vs T^{-1} (b) characteristic of CdTe/CdS cell with Au contact.

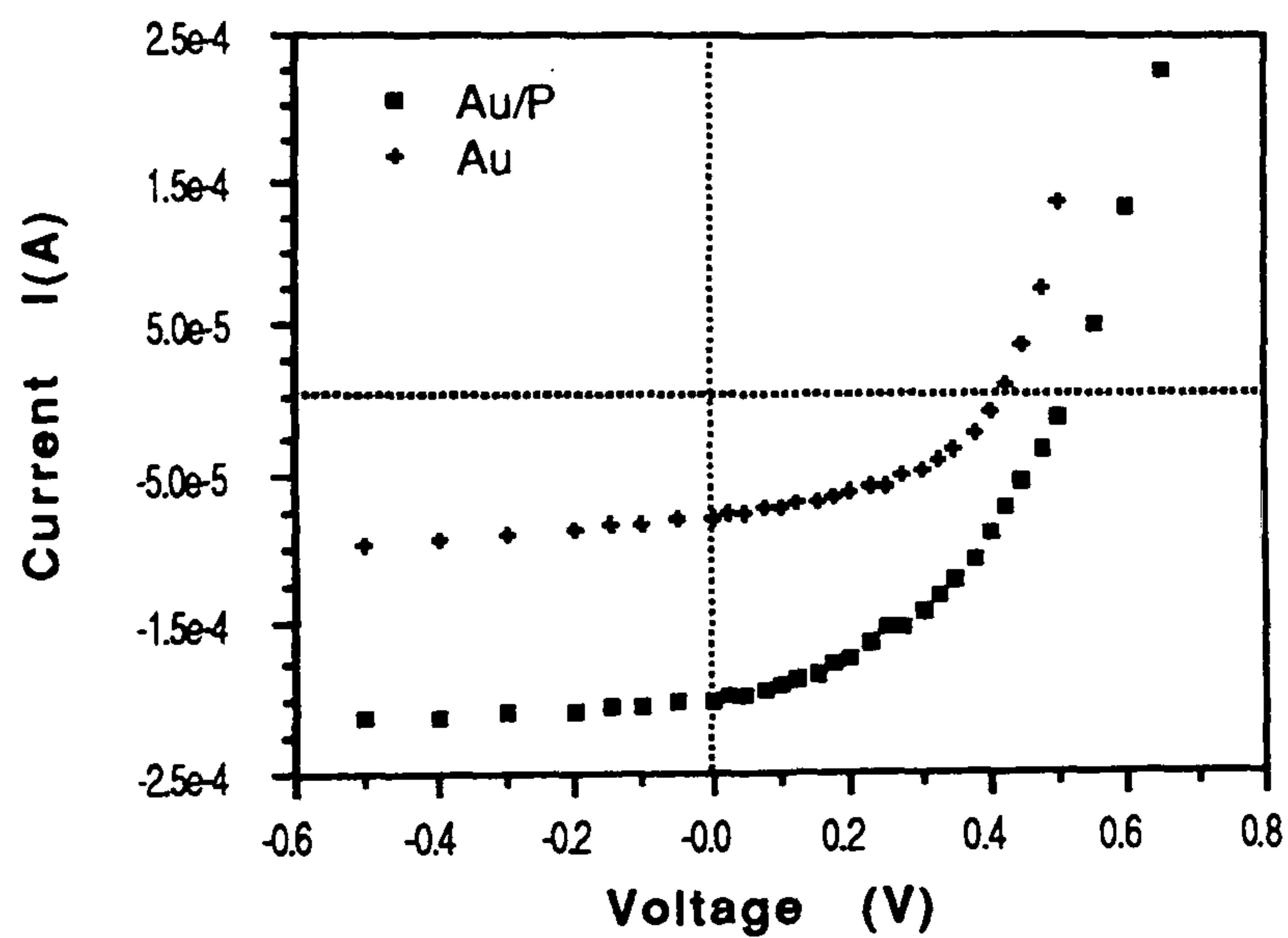


Figure 8.5 — Illuminated I-V characteristic of CdTe/CdS cells with Au and Au/P contacts under an illumination intensity of about 90mW/cm^2 .

Sample No:	V_{oc} (mV)	J_{sc} (A/cm ²)	FF	η (%)
BC:Au	420	5.2×10^{-3}	0.42	1.0
BC:Au/P	510	1.3×10^{-2}	0.42	3.1

Table 8.4 — Solar cell parameters, i.e. V_{oc} , J_{sc} , FF , and η for the cells with Au and Au/P contacts respectively.

The low efficiencies are obviously due to the highly resistive CdTe substrate. The higher values of J_{sc} and V_{oc} for the Au/P device could be attributed to back surface field (BSF) effects at the contact/CdTe interface rather than to junction effects. The back surface field (BSF) is the field associated with a space charge region at the back contact. This effect causes band bending and carrier depletion region and may be used to advantage to reduce recombination losses. As a result, it has been shown that the BSF effect may enhance J_{sc} and V_{oc} . Interestingly, better efficiencies were obtained from the Au/P contact devices, even though this gave dark I-V characteristics that were more resistive.

8.5 Determination of Device Series and Shunt Resistance.

The series, R_s and shunt, R_{sh} resistances of the undoped bulk single crystal p-CdTe/n-CdS cells have been determined approximately from their I-V characteristics. The methods used in the calculation of R_s and R_{sh} are described in detail below;

a- R_s and R_{sh} may be determined from the slopes of the forward and reversed biased dark I-V characteristics respectively;

–For R_s : at forward bias voltages where the exponential dependence of forward current has vanished, i.e. $\frac{dI}{dV}|_{V>0} = \frac{1}{R_s}$,

–For R_{sh} : at reverse bias voltages where reverse current changes linearly with reverse bias voltage, i.e. $\frac{dI}{dV}|_{V<0} = \frac{1}{R_{sh}}$.

b- R_s and R_{sh} for the illuminated cell may be determined from the slope of the illuminated I-V characteristics;

–For R_s : at forward bias voltages above V_{oc} where the forward current does not vary exponentially with the voltage, i.e. $\frac{dI}{dV}|_{V>V_{oc}} = \frac{1}{R_s}$,

–For R_{sh} : at reverse bias voltages where reverse current changes linearly with reverse bias voltage, i.e. $\frac{dI}{dV}|_{V<0} = \frac{1}{R_{sh}}$.

c- R_s may be determined from the difference between measured and ideal I–V forward characteristics (i.e. I_f vs ΔV).

d- R_s may be determined from the illuminated I–V characteristics at two levels of illumination. This method proposed by Wolf and Rauschenbach enables a more accurate determination of R_s for a solar cell [9]. For this purpose, the photovoltaic output characteristic has to be measured at two different light intensities, the magnitudes of which do not have to be known. The two characteristics will then be translated with respect to each other by the amounts ΔI_{ph} and $\Delta I_{ph} R_s$ in the y- and x-direction respectively. Corresponding points on the two characteristics will therefore show a displacement from each other equal to the translation of the coordinate systems. The displacement parallel to the ordinate gives the value of ΔI_{ph} . Since the displacement parallel to the abscissa equals $\Delta I_{ph} R_s$, the value of the internal resistance R_s is readily obtained. One practical approach to this procedure is to choose an arbitrary interval ΔI from the short circuit current I_{sc} , which determines the first characteristics. It is frequently found convenient to choose ΔI so as to obtain a point in or near the knee of the characteristic. The same ΔI value is then used for finding a second corresponding point on the second characteristic (see Fig.8.6 and Fig.8.7).

e- R_s and R_{sh} determined from I_{sc} vs V_{oc} characteristics at high and low levels of illumination intensity: I–V characteristics of a cell including the series, R_s , and shunt, R_{sh} resistances, can be given by a single diffusion/emission diode model;

$$-I = I_o \left[\exp\left(\frac{q(V + IR_s)}{nkT}\right) - 1 \right] + \frac{V + IR_s}{R_{sh}} - I_{ph} \quad [8.7]$$

where I_{ph} is the actual light generated current. The equivalent circuit is also shown in Fig.8.8. Under open circuit conditions, i.e. $V=V_{oc}$, and $I=0$, Eq.8.7 becomes;

$$0 = I_o \left[\exp\left(\frac{qV_{oc}}{nkT}\right) - 1 \right] + \frac{V_{oc}}{R_{sh}} - I_{ph} \quad [8.8]$$

Similarly, under short circuit conditions where $V=0$, and $I=I_{sc}$,

$$-I_{sc} = I_o \left[\exp\left(\frac{qI_{sc}R_s}{nkT}\right) - 1 \right] + \frac{I_{sc}R_s}{R_{sh}} - I_{ph} \quad [8.9]$$

Hence equating both Eq.8.8 and Eq.8.9 yields;

$$I_o \left[\exp\left(\frac{qV_{oc}}{nkT}\right) - 1 \right] + \frac{V_{oc}}{R_{sh}} = I_o \left[\exp\left(\frac{qI_{sc}R_s}{nkT}\right) - 1 \right] + \left(1 + \frac{R_s}{R_{sh}}\right) I_{sc} \quad [8.10]$$

Eq.8.9 cannot be solved analytically since both V_{oc} and I_{sc} appear as arguments of exponentials and also in linear terms. Detailed solution would require numerical methods. However Eq.8.10 can be solved under high and low levels of illumination when simplifying approximations can be made and hence estimates can be found for R_s and R_{sh} . At high levels of illumination (i.e. high I_{sc} and V_{oc}), the exponential terms in Eq.8.10 dominate, and linear terms may then be neglected:

$$I_o \left[\exp\left(\frac{qV_{oc}}{nkT}\right) - 1 \right] \cong I_o \left[\exp\left(\frac{qI_{sc}R_s}{nkT}\right) - 1 \right] + I_{sc} \quad [8.11]$$

providing $R_s \ll R_{sh}$ which is the case for most practical solar cells, and n remains constant at all levels of illumination. Note that there are no terms in R_{sh} in Eq.8.11 enabling an estimate to be made for R_s . Similarly at low illumination levels, (low I_{sc}) the exponential term on the RHS of Eq.8.10 becomes negligibly small since I_{sc} varies more strongly than V_{oc} ,

$$I_o \left[\exp\left(\frac{qV_{oc}}{nkT}\right) - 1 \right] + \frac{V_{oc}}{R_{sh}} \cong I_{sc} \quad [8.12]$$

where $R_s \ll R_{sh}$ and n is constant at all illumination levels. In this case, terms in R_s have been removed and R_{sh} can be obtained. Fig.8.9 shows I_{sc} vs V_{oc} characteristics for the cells with Au and Au/P contacts respectively.

Tables 8.5 and Table 8.6 tabulate the values of R_s and R_{sh} (i.e. normalized to a unit area of 1cm^2) undoped bulk single crystal p-CdTe/n-CdS cells with two different contacts, i.e. Au and Au/P respectively, determined from the methods described in detail above. Clearly, the cell with the Au/P contact exhibited higher values of R_s than the cell with the Au contact. This confirms the result observed with the dark I-V characteristics (i.e. cell with Au/P contact resulted in earlier

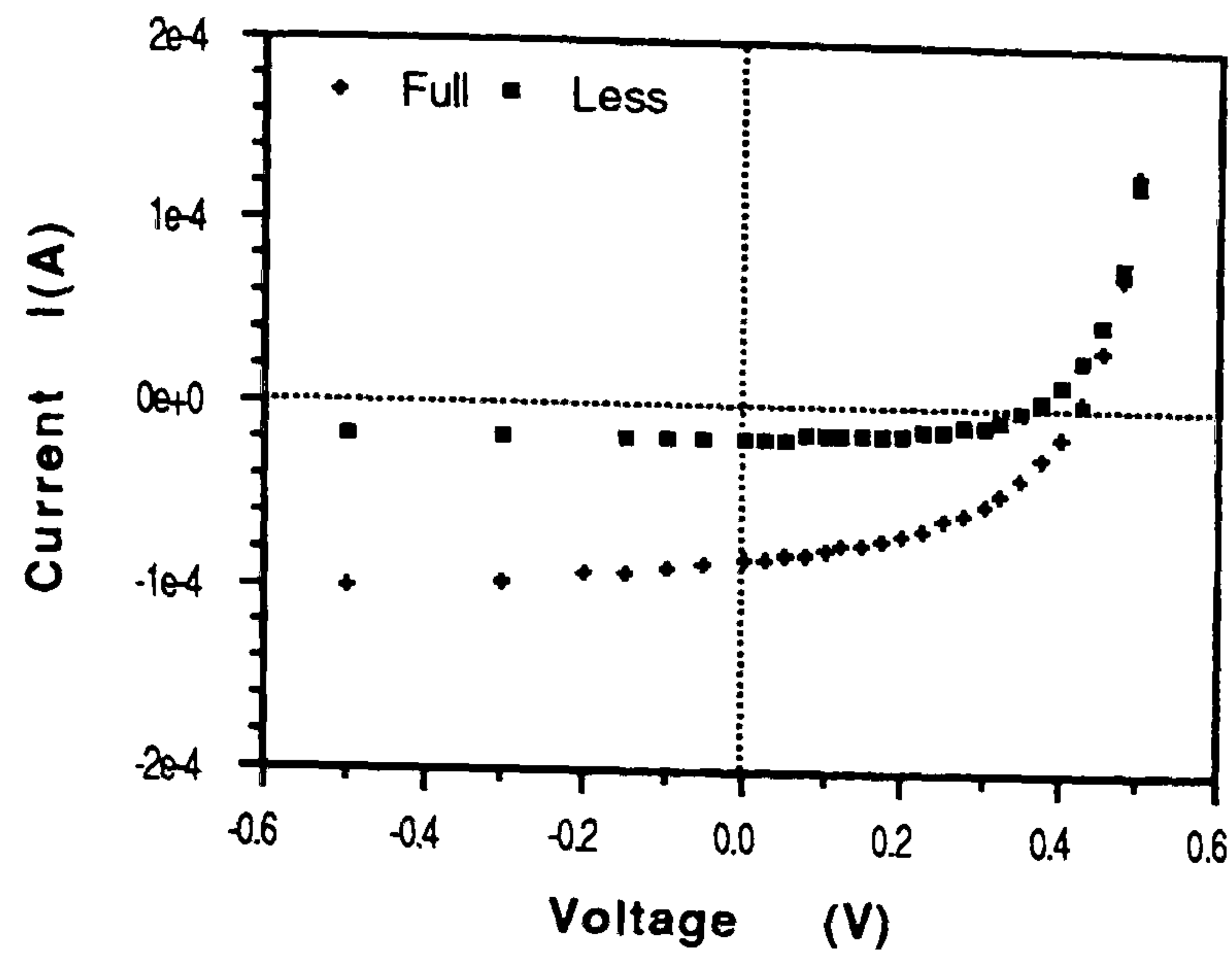


Figure 8.6 — Illuminated I-V characteristic of CdTe/ CdS cell with Au contact at two different illumination intensities.

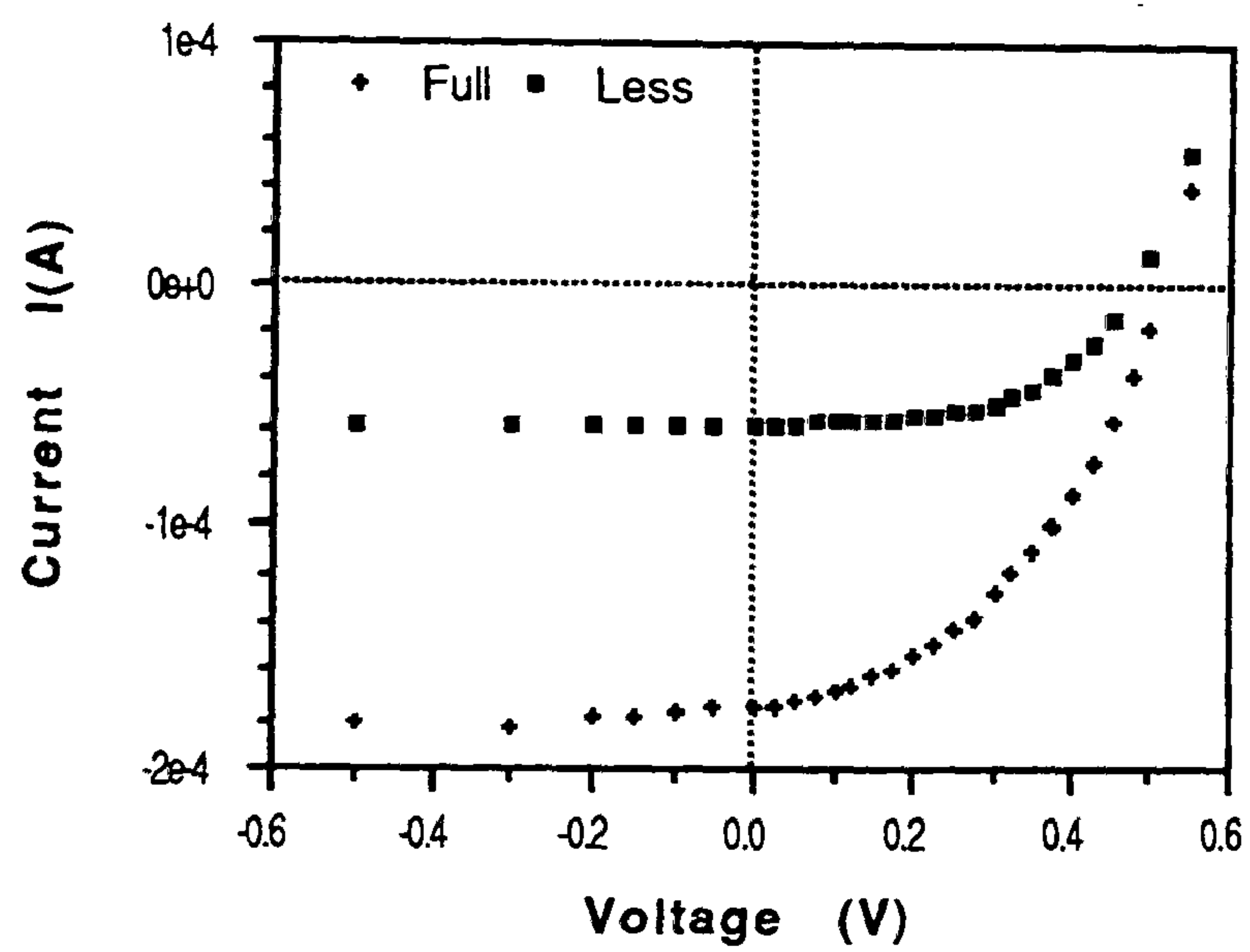


Figure 8.7 — Illuminated I-V characteristic of CdTe/ CdS cell with Au/P contact at two different illumination intensities.

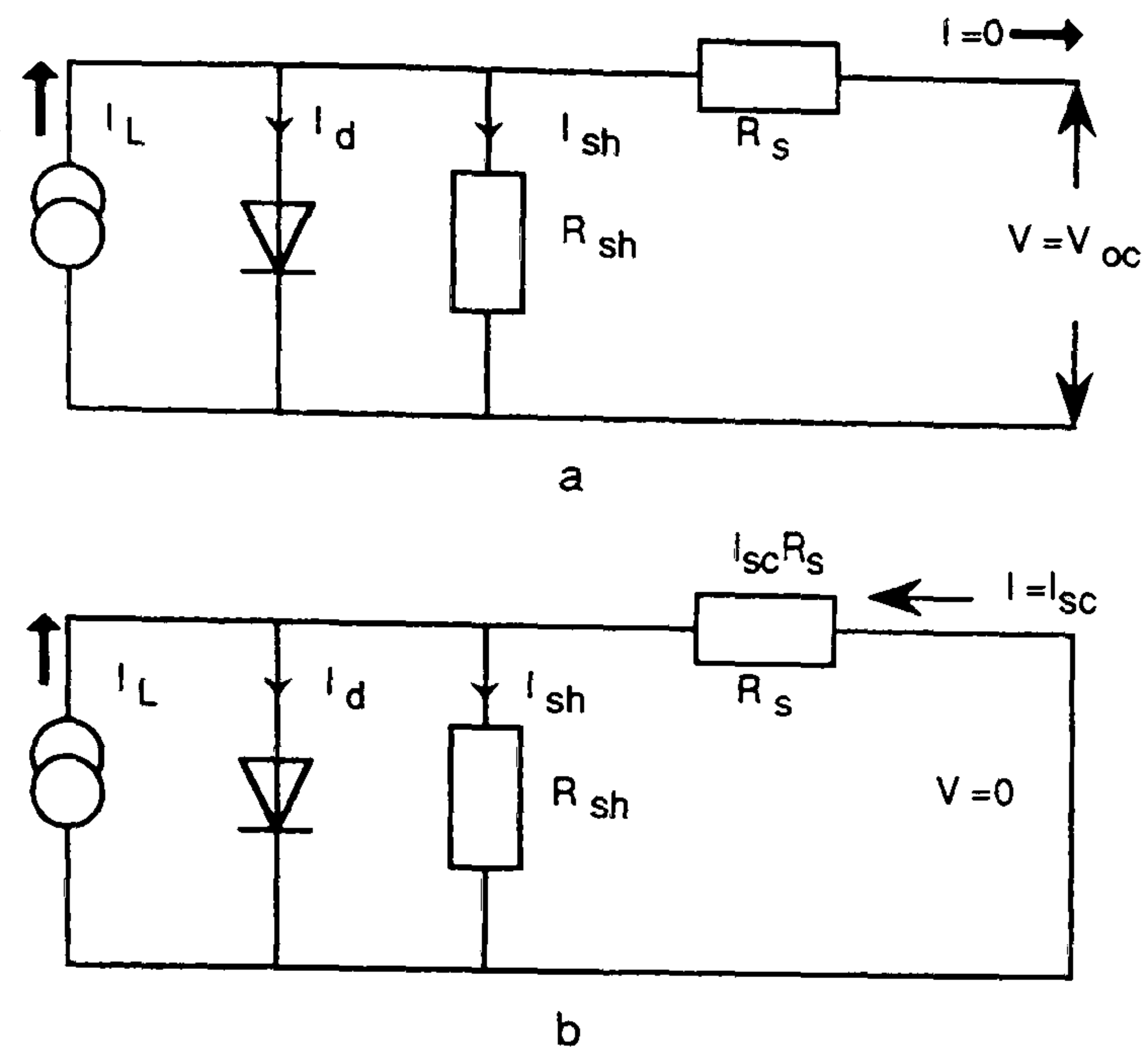


Figure 8.8 — Equivalent circuit diagrams of a cell under (a) open circuit, V_{oc} and (b) short circuit I_{sc} conditions.

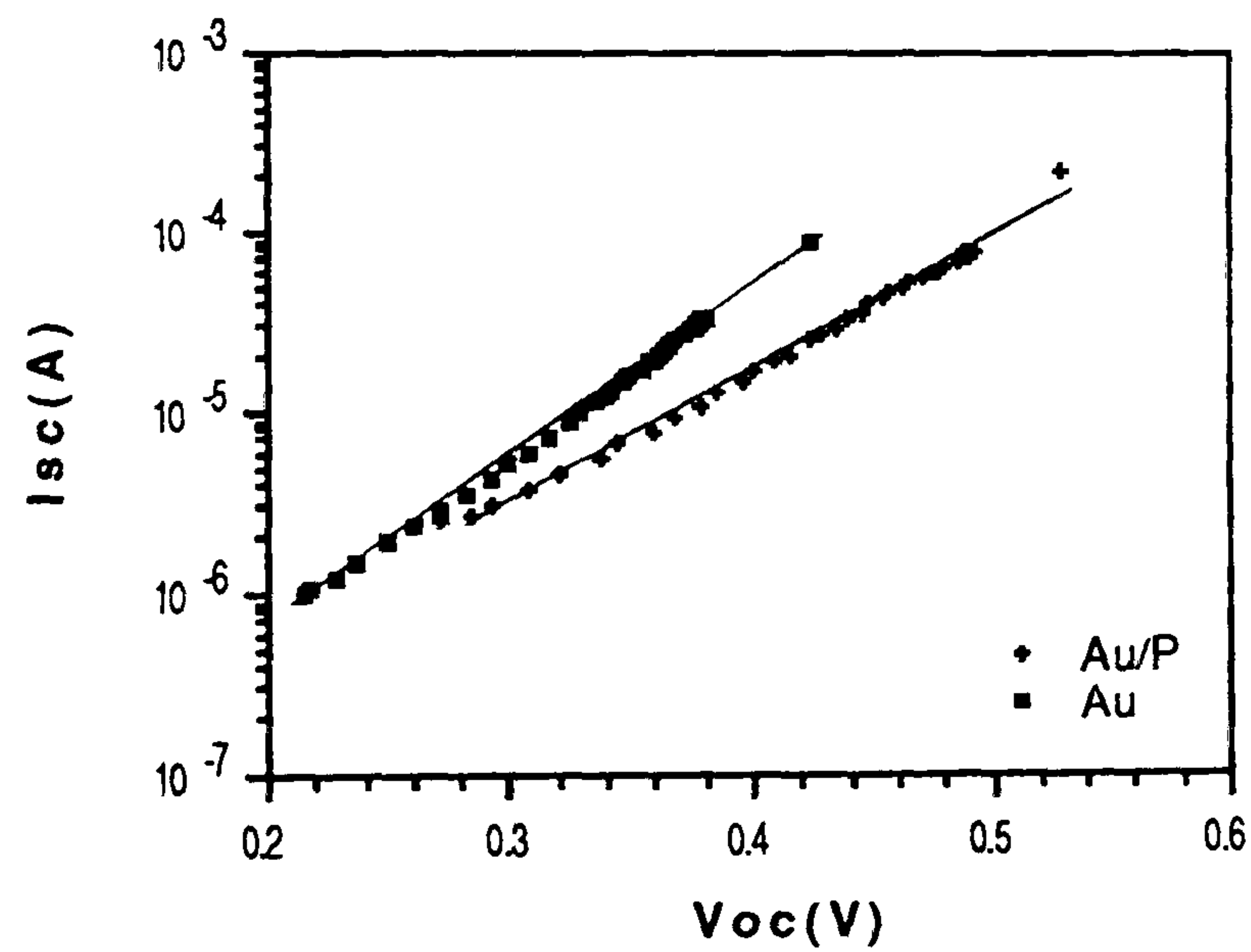


Figure 8.9 — $\log(I_{sc})$ vs V_{oc} characteristic of CdTe/CdS cell with Au and Au/P contacts.

onset of saturation than the cell with Au contact). Illuminated R_s values obtained from method b were typically one order of magnitude less than the dark values. This could be attributed to the photoconductive effect which significantly increased carrier densities and hence reduced resistivity. The method, e gave unphysical values (i.e. negative) of R_s for the cells with Au and Au/P contacts, due probably to the relatively high value of n . But if n is allowed to vary with illumination intensity [10], Eq.8.11 does give reasonable values of R_s under illumination. Method d gave very much higher values of R_s . The reasons for this are not known but are probably due to the fact that R_s was strongly dependent on illumination.

Cell Type	R_s^a (dark)	R_s^b (illum.)	R_s^c (dark)	R_s^d (illum.)	R_s^e (illum.)
BC:Au	19	1.2	16	28.5	< 0
BC:Au/P	120	4.5	99.2	19.5	< 0

Table 8.5 — R_s values (i.e., in Ohm, normalized to a unit area of 1cm^2) of undoped single crystal p-CdTe/n-CdS cells with two different contacts, i.e. Au and Au/P determined by various methods.

Cell Type	R_{sh}^a (dark)	R_{sh}^b (illum.)	R_{sh}^c (illum.)
BC:Au	9.2×10^5	4.2×10^2	3.2×10^3
BC:Au/P	1.9×10^5	6.5×10^2	2.0×10^4

Table 8.6 — R_{sh} values (i.e., in Ohm, normalized to a unit area of 1cm^2) of the undoped bulk single crystal p-CdTe/n-CdS cells with two different contacts, i.e. Au and Au/P determined by various methods.

Dark values of R_{sh} for the cells also displayed higher values than the values measured under illumination. The cell with the Au/P contact seemed to have higher R_{sh} values than the cell with Au contact under illumination due probably to a lower density of interface states. In both cases, values of R_{sh} obtained from the method e were found to be dependent on the level of illumination (i.e. an apparent

variation with V_{oc}). Accordingly, values of R_{sh} have been quoted with respect to a particular cell operating voltage, V_m .

It is important to reduce R_s to as low a value as possible in order to keep the resistive power-loss component low, although it can never be entirely eliminated. The series resistance is the sum of several components as shown in Fig.8.10, namely the substrate resistance $R_{subst.}$ (CdTe absorber), the sheet resistance, R_{sheet} (CdS, window layer), and front and back contact resistances, R_{fc} (CdS/In), and R_{bc} (Au or Au/P/CdTe).

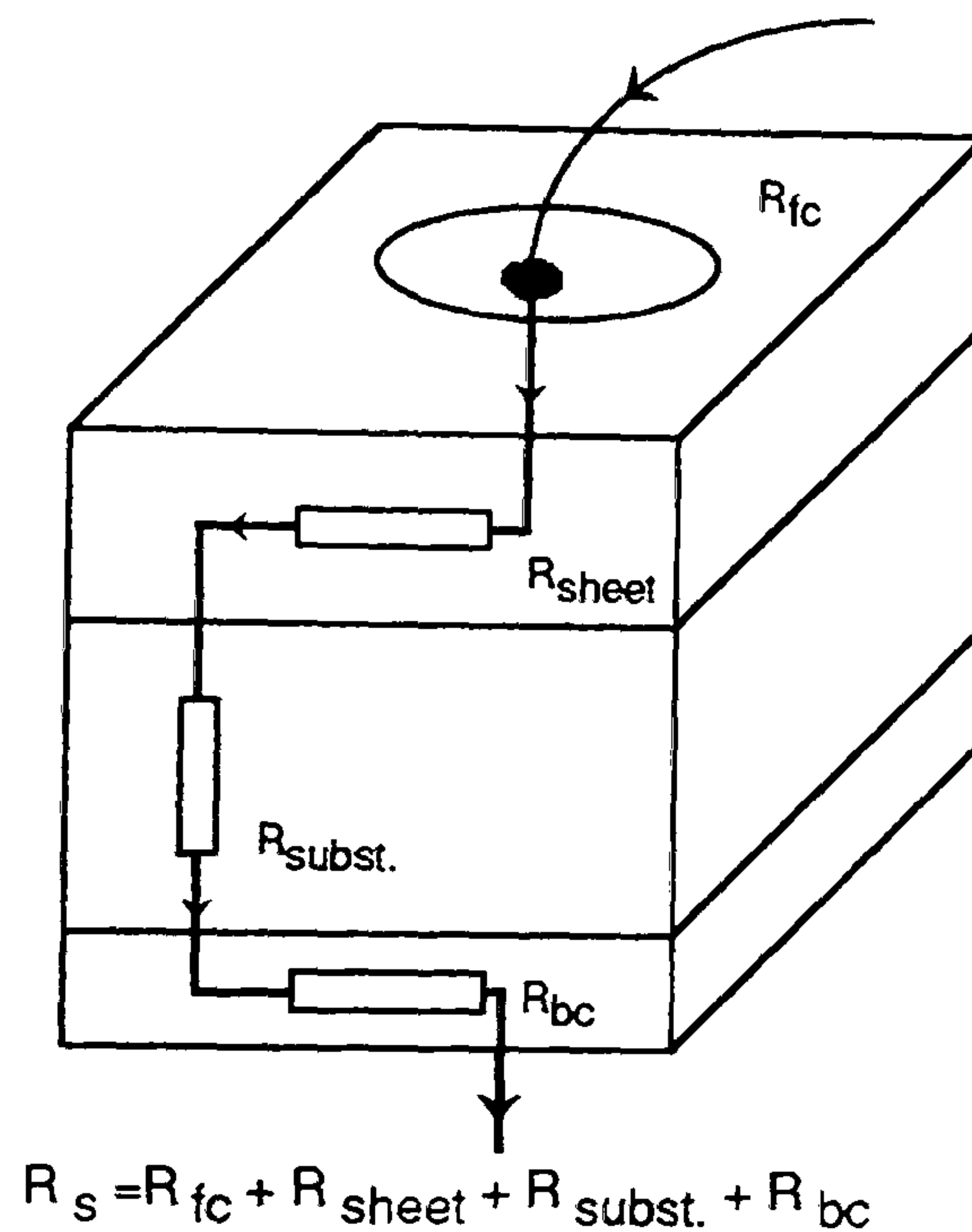


Figure 8.10 — Series resistance components of a bulk single crystal CdTe/CdS cell.

Illuminated I-V characteristics of the cells with Au and Au/P contacts shown in Fig.8.11a and Fig.8.12a were corrected for the series and shunt resistances in an attempt to determine their potential photovoltaic behaviour. The values of R_s and R_{sh} were estimated from the slope of the illuminated I-V characteristics (method b) for the forward bias voltages above V_{oc} where the forward current does not vary exponentially with the voltage and for the reverse bias voltages where reverse current changes linearly with reverse bias voltage respectively. The characteristics were then re-plotted as $I-V/R_{sh}$ vs V , and I vs $V_{dep}=V-IR_s$ in Fig.8.11b, c and Fig.8.12b, c. Fig.8.11d and Fig.8.12d show how the characteristics would appear

if both R_s and R_{sh} effects were removed. The corresponding solar cell parameters are listed in Tables 8.7 and Table 8.8 for the cells with Au and Au/P contacts respectively. This characteristic in effect is a measure of the junction quality and when compared with the theoretical maximum performance figures (Table 8.8) gives an indication of junction losses due to recombination, imperfect collection, defect effects etc.

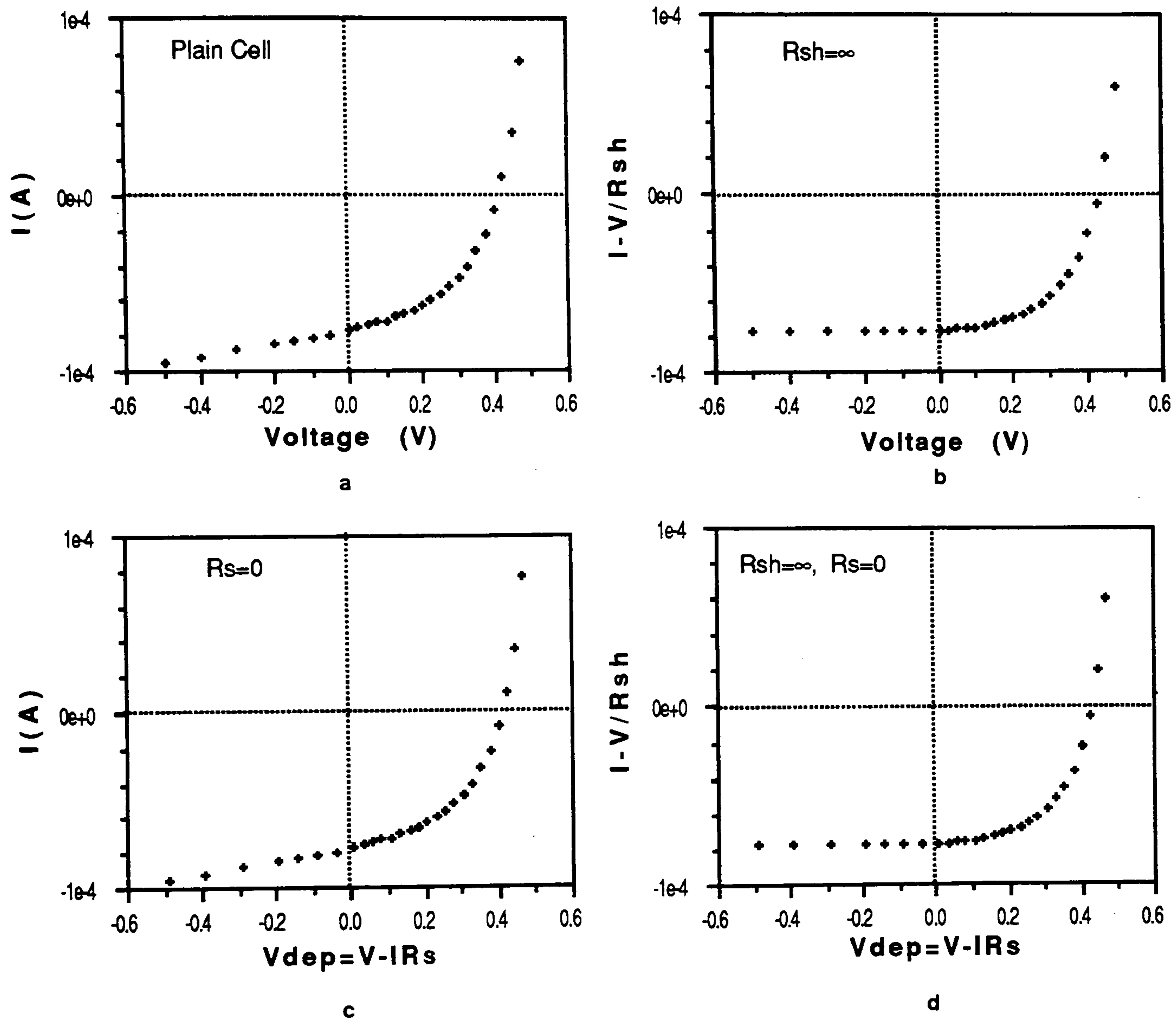


Figure 8.11 — Illuminated I-V characteristic of CdTe/CdS cell with Au contact after eliminating R_s and R_{sh} resistances, a: plain cell, b: $R_{sh} \rightarrow \infty$, c: $R_s \rightarrow 0$, d: both (b and c).

When R_{sh} was eliminated (see Table 8.7 and Table 8.8), V_{oc} , FF were increased resulting in a higher efficiency, although J_{sc} remained almost the same. Elimination of R_s as well, led to even higher values of FF with a corresponding increase in photovoltaic conversion efficiency.

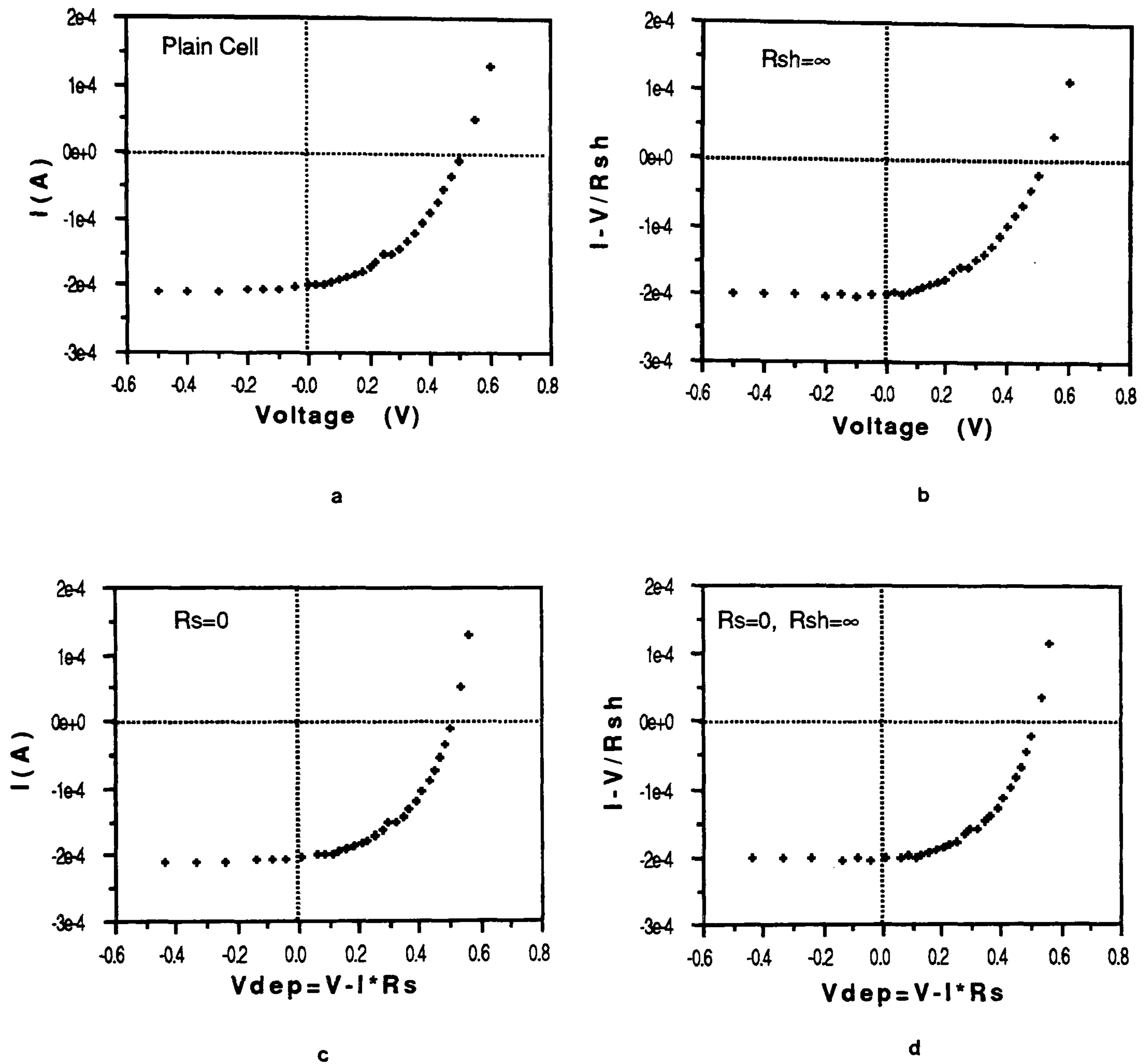


Figure 8.12 — Illuminated I-V characteristic of CdTe/CdS cell with Au/P contact after eliminating R_s and R_{sh} resistances., a: plain cell b: $R_{sh} \rightarrow \infty$, c: $R_s \rightarrow 0$, d: both (b and c).

Although the effects of both R_s and R_{sh} were removed, the new values of V_{oc} and J_{sc} remained almost half those reported for the best cells [11,12]. Clearly this revealed the existence of the problems due to junction and/or collection which has to be undertaken. The low values of V_{oc} might be attributed to the presence of interfacial recombinations at the junction resulting in poor charge separation. Generally, the CdS layers were relatively resistive and thus as a consequence, proportionately more of the depletion width lay in the CdS layer with a corresponding reduction in collection and J_{sc} . The relatively low V_{oc} may also indicate high levels of interfacial recombinations at the junction, so that charge separation was not efficient.

Cell Type	V_{oc} (V)	J_{sc} (A/cm ²)	FF	η (%)
Plain Cell	0.420	5.2×10^{-3}	0.42	1.02
$R_s \rightarrow 0$	0.400	5.2×10^{-3}	0.44	1.04
$R_{sh} \rightarrow \infty$	0.432	5.2×10^{-3}	0.49	1.22
$R_{sh} \rightarrow \infty, R_s \rightarrow 0$	0.430	5.1×10^{-3}	0.52	1.28

Table 8.7 — Re-calculated solar parameters for the cell with Au contact after removing R_s and R_{sh} effects.

Cell Type	V_{oc} (V)	J_{sc} (A/cm ²)	FF	η (%)
Plain Cell	0.510	1.3×10^{-2}	0.42	3.1
$R_s \rightarrow 0$	0.517	1.4×10^{-2}	0.44	3.41
$R_{sh} \rightarrow \infty$	0.524	1.4×10^{-2}	0.43	3.38
$R_{sh} \rightarrow \infty, R_s \rightarrow 0$	0.520	1.4×10^{-2}	0.53	4.13

Table 8.8 — Re-calculated solar parameters for the cell with Au/P contact after removing R_s and R_{sh} effects.

8.5.1 Capacitance-Voltage Characteristics.

Dark junction capacitance-voltage characteristics of the undoped CdTe based p-n devices were investigated at several temperatures. A typical C^{-2} vs V plot of a Au/CdTe/CdS device is shown in Fig.8.13. It was bowed indicating that a variation in interface state occupancy levels in the band gap might influence the estimates of carrier concentration, but nevertheless, it did indicate an abrupt junction at the interface with a uniform acceptor density in the depletion region. The ionised acceptor concentration, N_A , obtained from the slopes of linear sections between $-0.5 \leq V \leq 0$ bias of the curves in the C^{-2} vs V plots, intercept voltage, V_i , and depletion layer width, W_o , (employing a one-sided junction approximation, i.e. $(C/A)_{V=0} = \epsilon_o \epsilon_s / W_o$) are listed in Table 8.9 for a typical Au/p-CdTe/n-CdS/In device measured at 1MHz. The validity of the one-sided junction approximation in this case was open to question since the resistivity of the CdS layer was unknown, but was thought to be high as it was undoped (i.e. $\rho \cong 10^2 - 10^3 \Omega\text{-cm}$ for the layers deposited on glass substrates).

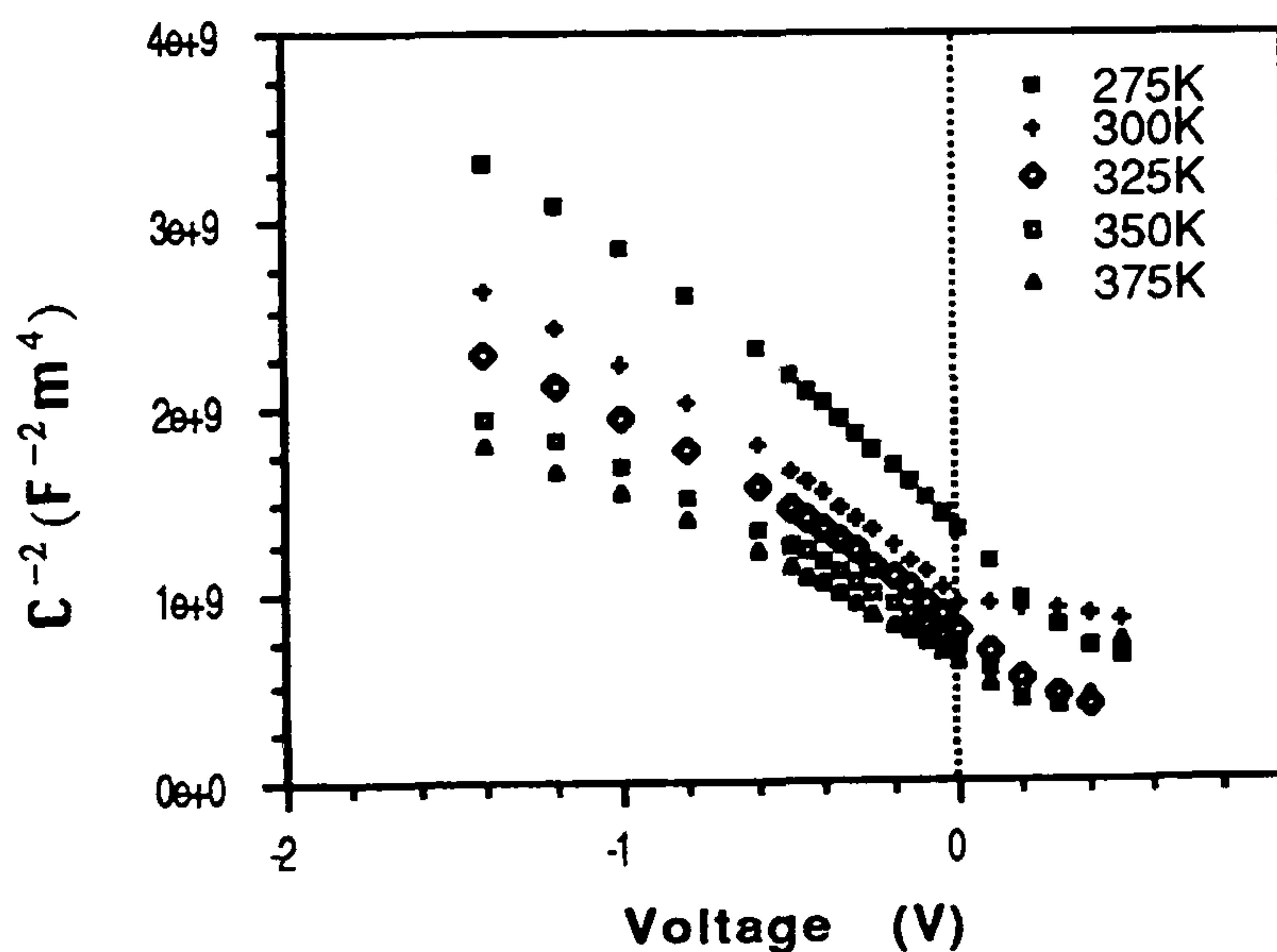


Figure 8.13 — C^{-2} vs V characteristic of CdTe/CdS cell with Au contact at several temperatures.

$T(K)$	$N_A(\text{cm}^{-3})$	$V_i(V)$	$W_o(\mu\text{m})$
275	8.3×10^{13}	0.81	3.30
300	9.6×10^{13}	0.67	2.78
325	1.1×10^{14}	0.63	2.57
350	1.3×10^{14} 1hfil	0.67	2.42
375	1.3×10^{14}	0.61	2.25

Table 8.9 — Acceptor density, N_A , intercept voltage, V_i , and depletion width, W_o , values of a typical undoped p-CdTe/n-CdS/In cell.

8.6 Conclusions.

Undoped bulk single crystal p-CdTe/n-CdS solar cells were prepared by vacuum deposition of thin film of CdS onto {111}-oriented bulk single crystal CdTe substrates. CdTe substrates were obtained from boules grown by a sealed ampoule vapour transport technique. The as-grown CdTe was p-type, but resistive (i.e. $\sim 10^8 \Omega\text{-cm}$).

Dark I-V characteristics exhibited good diode behaviour with low J_o and high rectification. At higher current levels, the deviation from ideal behaviour was mainly due to the high bulk resistance of the CdTe layer, and to Au or Au/P/CdTe interface states.

Temperature dependent I-V characteristics showed that forward bias currents were fairly parallel between the voltage range 0.2–0.4V where the series resistance was not dominant. Although, the current transport suggested by these results were more likely to be controlled by a tunneling mechanism, both $\log(J_o)$ vs T and $\log(J_o)$ vs T^{-1} gave straight line plots. This was somewhat difficult to explain but probably due to the effects of high bulk and contact resistance. Nevertheless, activation energies of the cells with Au and Au/P contact were found to be 0.39 eV and 0.32 eV respectively.

I-V characteristics under illumination displayed a relatively poor performance resulting in low cell efficiencies. In spite of the presence of a p^+ layer (i.e. BSF)

which should have led to an ohmic tunneling contact with a low voltage drop across it, the low values of FF provided clear evidence that the resistivity of the bulk was quite high. The higher values of J_{sc} and V_{oc} of the cells with Au/P contact could be attributed to the BSF effects at the contact/CdTe interface, although their dark I-V characteristics were more resistive.

C^{-2} vs V characteristics were bowed indicating that variation in interface state occupancy levels were influencing the estimation of the carrier concentration, but nevertheless, the results did indicate an abrupt junction with a uniform acceptor density. Although, V_i , and, W_o , obtained from C-V measurements gave reasonable values, acceptor densities using the one-sided junction approximation yielded relatively low carrier densities, due again to the high bulk resistance. Hence, any change in the depletion width with voltage was small. Device series and shunt resistance were calculated using various methods.

8.7 References.

1. A.A. Alnajjar, C.C.R. Watson, A.W. Brinkman and K. Durose, J. Crystal. Growth, 117 (1992) 385.
2. A.A. Alnajjar, Ph.D Thesis, University of Durham, U.K., 1992.
3. R.L. Anderson, S.S. Electron., 5 (1962) 341.
4. U. Dolega, Z. Naturf. 18a (1963) 653.
5. R.H. Rediker, S. Stopek and J.H.R. Ward, S.S. Electron, 7 (1964) 621.
6. A.R. Riben and D.L. Feucht, S.S. Electron., 9 (1966) 1055.
7. A.R. Riben and D.L. Feucht, Int. J. Electron., 20 (1966) 583.
8. K.W. Mitchell, "*Evaluation of the CdS/CdTe Heterojunction Solar Cell*", Garland Publishing, Inc. New York & London, 1979.
9. M. Wolf and H. Rauschenbach, Advance Energy Conversion, 3 (1963) 455.
10. J.C.H. Phang, D.S.H. Chan and Y.K. Wong, IEEE Transactions on Electron Devices, ED 31, No:5 (1984) 717.

11. K.Yamaguchi, H.Matsumoto, N.Nakayama and S.Ikegami, Jpn.J.Appl.Phys.,
15)1976) 1575.
12. J.G.Werthen, A.L.Fahrenbruch and R.H.Bube, J.Appl.Phys., 54 (1983) 2750.

Chapter IX

n-CdS/p-CdTe Thin Film Solar Cells.

9.1 Introduction.

Practical CdS/CdTe heterojunction solar cells are polycrystalline thin film devices, fabricated on TCO coated glass substrates. Therefore, this chapter reports on photovoltaic and electrical measurements carried out on thin film polycrystalline structure. CdS has been found to be best suited for use as a transparent conducting window for thin film CdTe cells, being superior to the usual TCO's, (SnO_2), nonstoichiometric or doped oxides (ZnO) and other sulfides, such as (Cd,Zn)S, although the crystal structures and lattice parameters of the two are different leading to potential strain at the interface. The properties of the cells produced are described and investigated in detail in this chapter, including dark and illuminated I-V, and capacitance-voltage and spectral response characteristics, and optical transmission.

9.2 I-V Characteristics.

9.2.1 Undoped cells.

$\log(I_f)$ -V characteristics of an undoped glass/ITO/n-CdS/p-CdTe/Au cell is shown in Fig.9.1. The cell exhibited poor diode behaviour dominated by series resistance. The rectification ratio was very low at about 3.2 at 0.5V. The diode ideality factor, n , was found to be 2.83 at low biases ($V \leq 0.15\text{V}$) indicating that a p-n junction had formed in spite of the polycrystalline nature of both layers. At bias voltages greater than 0.2V, the characteristics was dominated by high series resistance, due to the highly resistive layers, (especially CdTe) and the relatively high CdTe/Au contact resistance. The value of J_o was high so that a correspondingly low V_{oc} would be expected. The values of V_{oc} , I_{sc} , and, FF were found to be 0.378V, $1 \times 10^{-5}\text{A}$, and 0.20 respectively, resulting in an "efficiency" of about 0.004% measured at room temperature under an illumination of about

90mW/cm². The characteristics reflect the very high layer resistivities and also some leakage current through pin-holes in the CdTe and defects at the interface (i.e. poor junction quality).

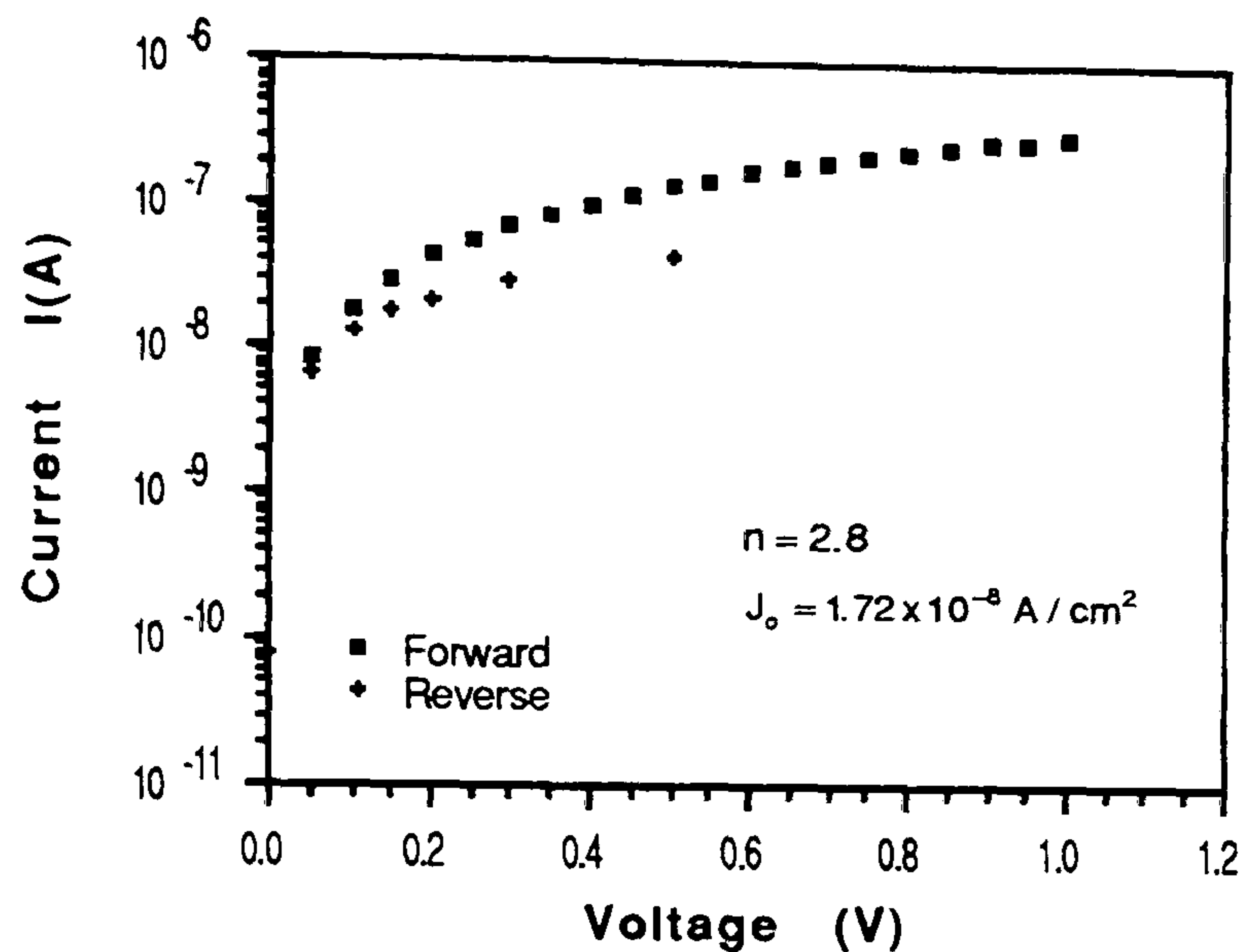


Figure 9.1 — Dark $\log(I_f)$ vs V characteristic of a typical undoped CdTe/CdS cell at room temperature.

The photovoltaic properties of the cells prepared using different CdTe source temperatures (i.e. mass fluxes) were also investigated in an attempt to address the junction formation. Fig.9.2 shows illuminated I-V characteristics of three undoped cells produced using different CdTe source temperatures. Although they displayed similar characteristics, the cell which was grown at a CdTe source temperature of 650°C exhibited a higher value of J_{sc} . This was probably a result of better junction formation, with fewer pin-holes and lower interface state densities. Nevertheless, the FF and efficiency were still low.

One of the outstanding problems to be overcome in the fabrication of highly efficient cells based on p-CdTe lies in the difficulty of preparing good low resistance ohmic contacts. One of the major approaches to achieving an ohmic contact to p-CdTe is to dope it heavily near the contact interface so that the current can be carried by tunneling through the barrier. As previously indicated, Au contacts to p-CdTe showed useable but not ideal ohmic contact behaviour, with a correspondingly high resistance. Fig.9.3 shows the illuminated I-V characteristics of a typical

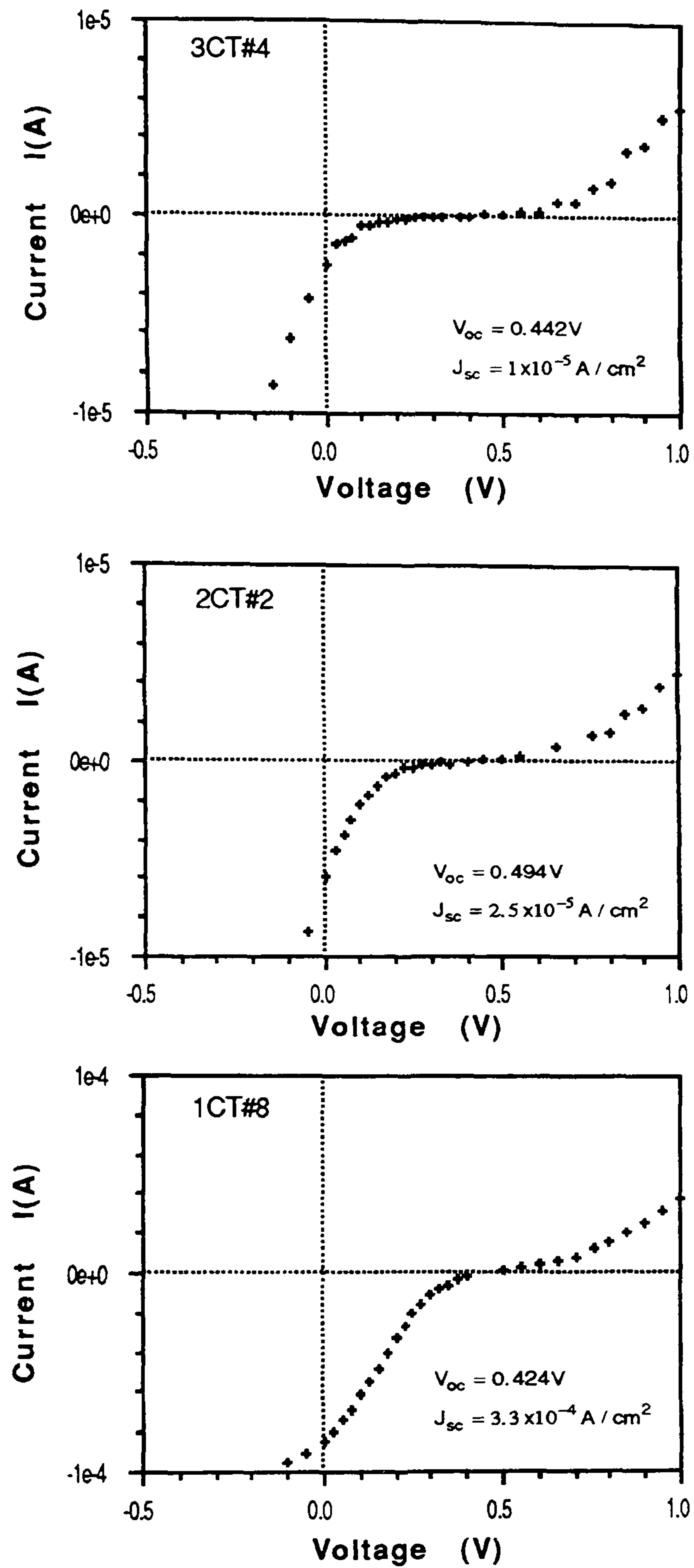


Figure 9.2 — I-V characteristic of an undoped CdTe/CdS cell under an illumination of about $90mW/cm^2$ using CdTe source temperatures of a: $650^\circ C$, b: $750^\circ C$, and c: $800^\circ C$.

undoped cell with two different types of contact, Au and Au/Cu. Although J_{sc} was increased, the forward characteristics were not significantly improved. This suggests that either the Cu layer thickness (the layer thickness ratio of Cu:Au was approximately 1:1) was not optimised or that Cu diffusion had taken place such that the tunneling barrier was not properly formed. Basol has reported that a thickness ratio (i.e. Cu:Au) of 1:20–200 is required to form a proper tunneling ohmic contact to p-CdTe, with a cell efficiency up to 10% [1].

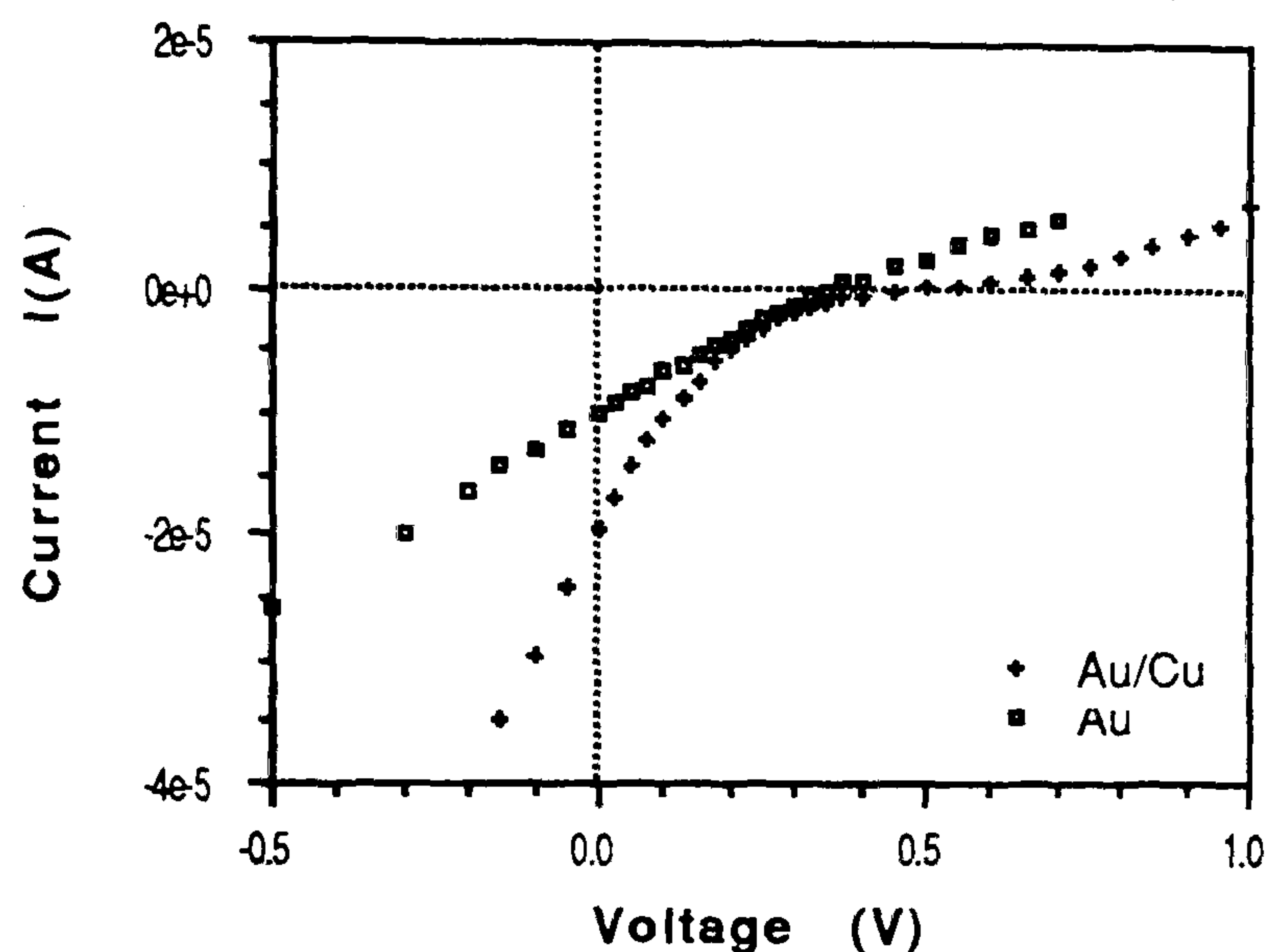


Figure 9.3 — I-V characteristic of an undoped CdTe/CdS cell with Au and Au/Cu contact under an illumination of about 90mW/cm².

9.2.2 Cl₂ doped cells.

Heat treatments of the CdTe in an oxygen containing ambient coupled with the use of a CdCl₂ as a doping element are often used in the fabrication of efficient CdTe solar cells. The treatment may result in the elimination of any excess Te through reaction with CdCl₂, and/or the creation of Cl-V_{Cd} and oxygen related acceptors resulting in a corresponding reduction in the CdTe layer resistivity [2]. As explained previously, three methods of Cl-doping were studied during the course of this project; co-evaporation with CdCl₂, pre-doping of the CdTe source material with CdCl₂ and dipping in CdCl₂/MeOH solution.

9.2.2.1 CdCl₂ co-evaporated cells.

The doping of II-VI compounds during growth (i.e. co-evaporation) is well known. Hence, CdCl₂ was introduced as a p-type dopant during the CdTe growth in an attempt to investigate the photovoltaic properties of the n-CdS/p-CdTe solar cells. Fig.9.4 and Fig.9.5 show the dark forward and illuminated I-V characteristics respectively of a co-evaporated cell. Illuminated I-V characteristics, clearly showed the incorporation of Cl₂ resulting in improved photovoltaic properties of the cells. However, the characteristics indicated that problems remained (low shunt resistance, non-ohmic contact and high series resistance) resulting in a low efficiency, and suggested that careful control of growth was still necessary.

The difficulties encountered in trying to control the co-evaporation process are typified by the characteristics of the nominally identical cell shown in Fig.9.6 and Fig.9.7. The cell displayed very similar characteristics to that of undoped cells implying that proper Cl₂ incorporation had not taken place. The effect of series resistance and related non-ohmicity of the Au/CdTe contact are clearly evident in the shape of the photovoltaic characteristics in the first quadrant.

The forward and reverse temperature dependent dark I-V characteristics of these cells were investigated in an attempt to address the current transport mechanisms. Fig.9.8 and Fig.9.9 show temperature dependent dark forward and reverse log(*I*)-V characteristics respectively of such a co-evaporated cell. The general shape was dominated by series resistance at higher biases due to the highly resistive CdTe layer. This effect became more pronounced as the temperature was lowered, since the resistivity of both the CdTe and the CdS layers increased with decreasing temperature. The slopes of the log(*I_f*)-V characteristics in the regime where the series resistance was not dominant (*V* < 0.3V) were found to be fairly constant with temperature. Table 9.1 shows the values of the slope (*A*), and *n* and *J_o* (obtained by fitting the standard diode equation to the low bias region of the characteristics).

It was observed that the diode ideality factors, *n*, required to fit the *I_f*-V data are close to or larger than 2 for the entire temperature range tested. Diode factors of 2 or greater are often taken to be indicative of interface recombination/tunneling process since an ideal emission/diffusion current mechanism would exhibit *n* ≈ 1.

Consequently, both the magnitude of n and the fact that it was temperature dependent indicate that emission/diffusion was not occurring. As discussed in Chapter 8, dark forward current, I_f limited by recombination/tunneling may be described by;

$$\begin{aligned} I_f(V, T) &= I_o(T) \exp(AV) \\ &= I_{oo}(T) \exp(BT) \exp(AV) \end{aligned} \quad [9.1]$$

where $I_o(T)$ is the temperature dependent reverse saturation current, and I_{oo} is proportional to the trap density and B is a constant. Generally, the I-V characteristic of these cells displayed constant slopes ($A \cong 21$) and the $\log(J_o)$ vs T characteristics also displayed a linear dependence. For the device of Fig.9.8, the slope, B was found to be 0.06 K^{-1} as shown in Fig.9.10. Consequently, it appeared that current transport in the co-evaporated cells was limited by recombination/tunneling mechanisms rather than by emission/diffusion processes.

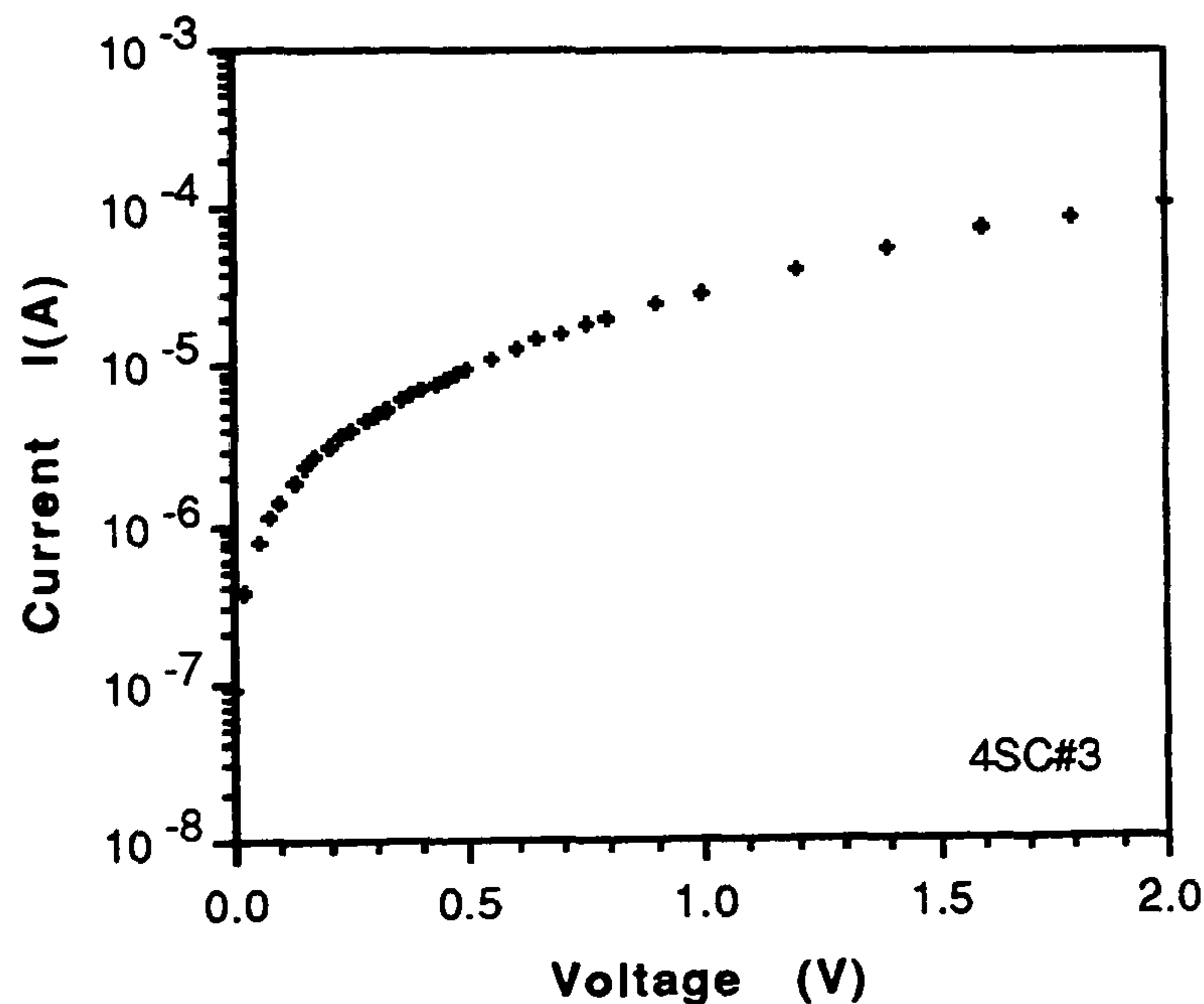


Figure 9.4 — Dark $\log(I_f)$ -V characteristic of co-evaporated CdS/CdTe:Cl₂ cell.

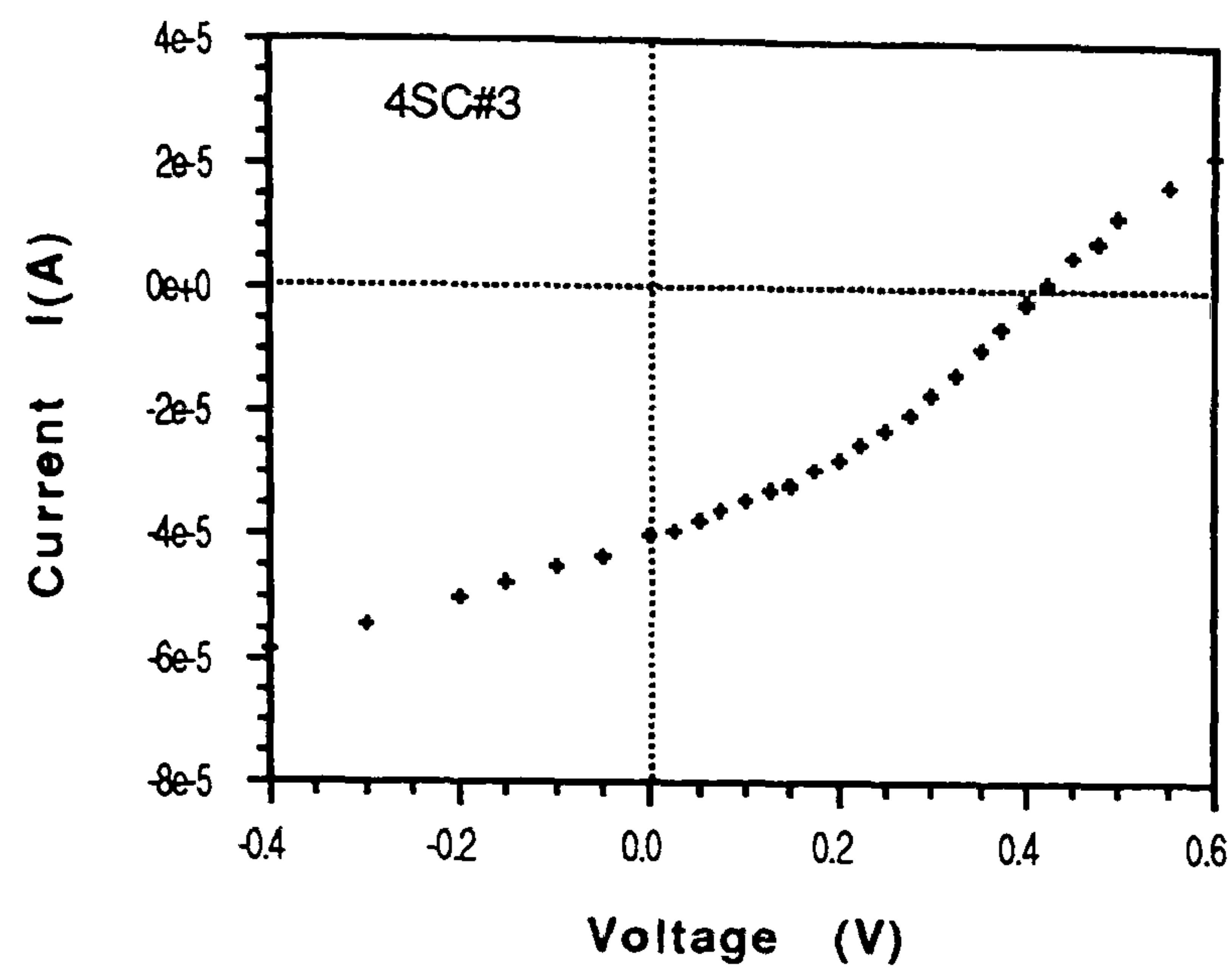


Figure 9.5 — I-V characteristic of co-evaporated CdS/CdTe:Cl₂ cell under an illumination of about 90mW/cm².

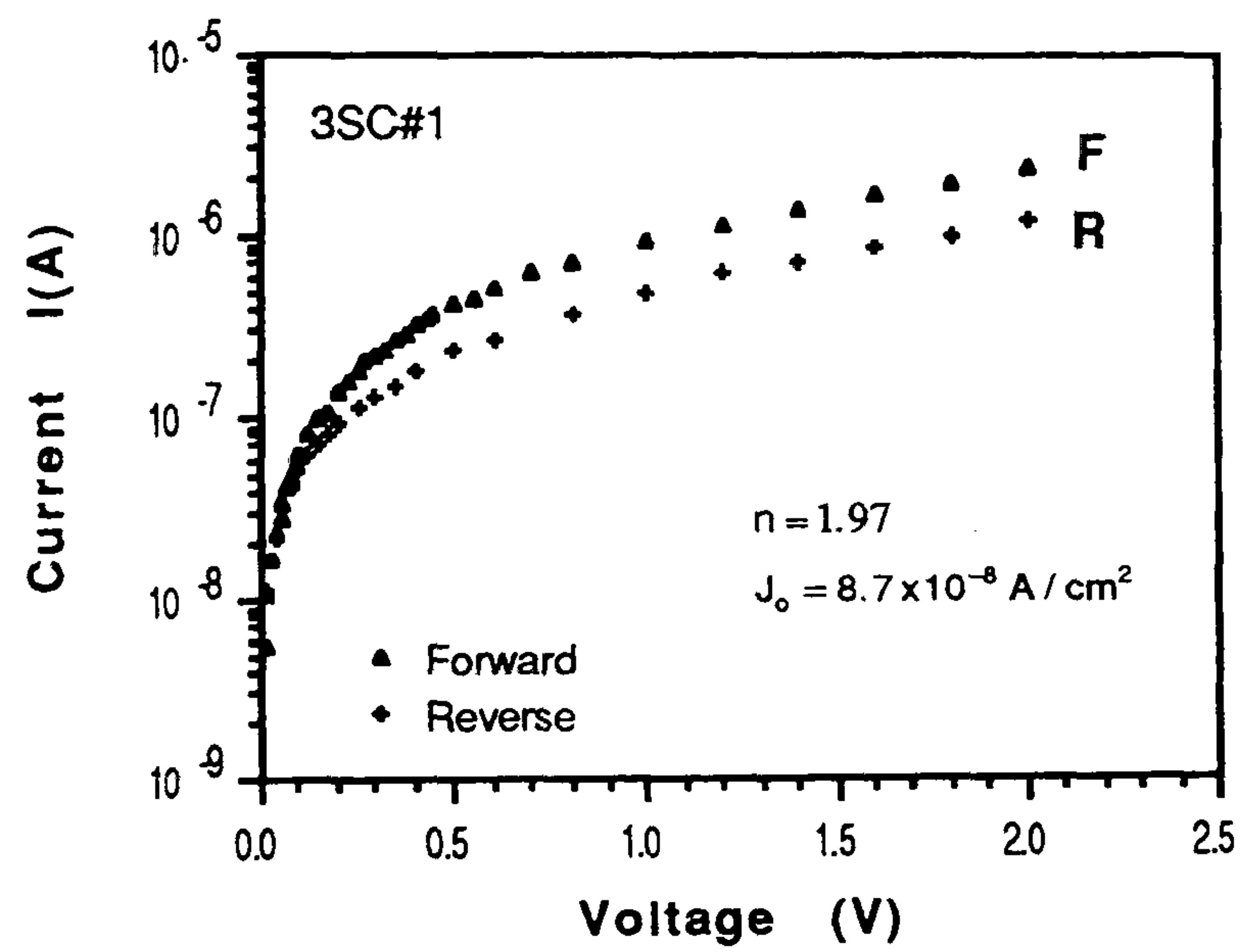


Figure 9.6 — Dark $\log(I_f)$ -V characteristic of co-evaporated CdS/CdTe:Cl₂ cell.

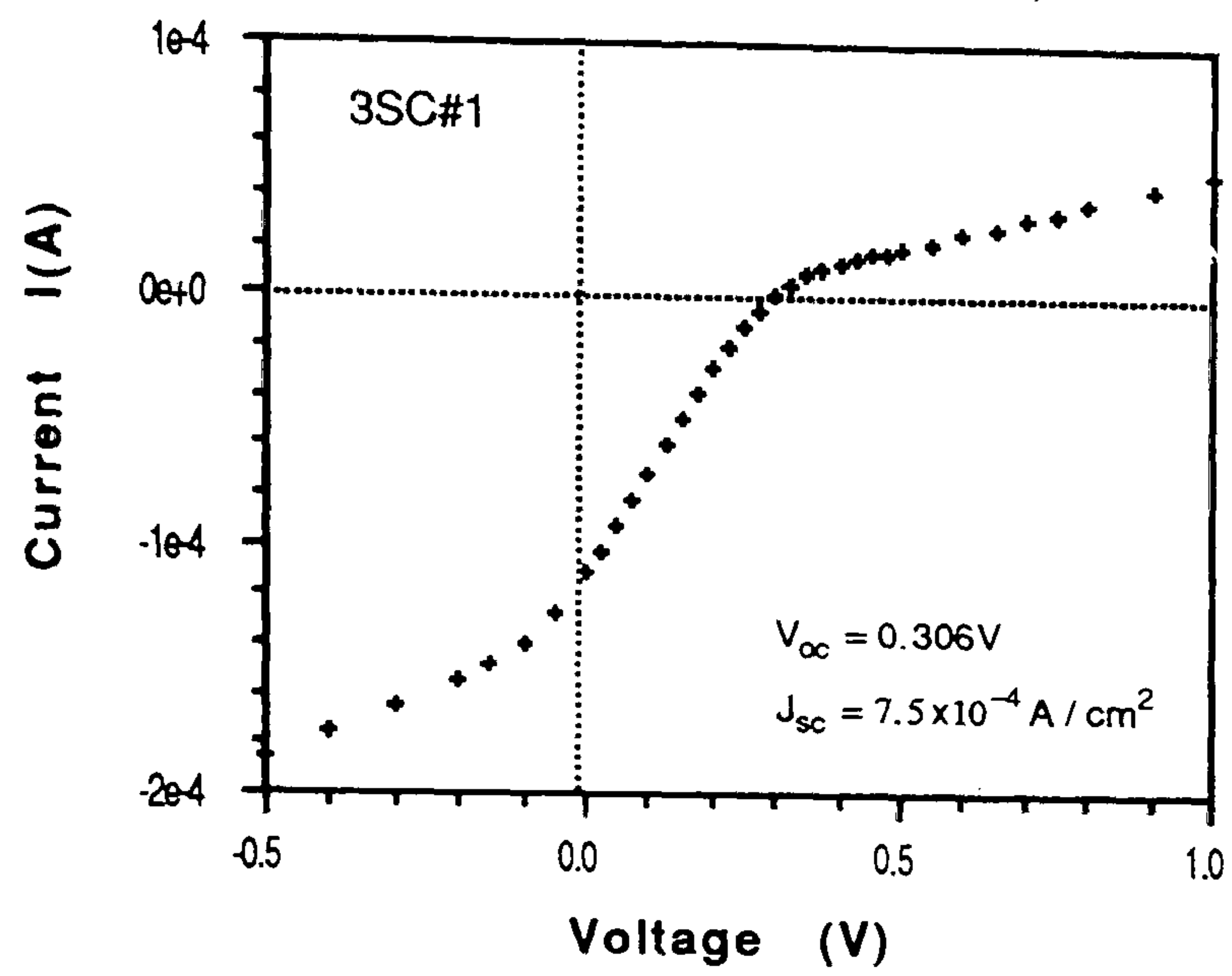


Figure 9.7 — I-V characteristic of co-evaporated CdS/CdTe:Cl₂ cell under an illumination of about 90mW/cm².

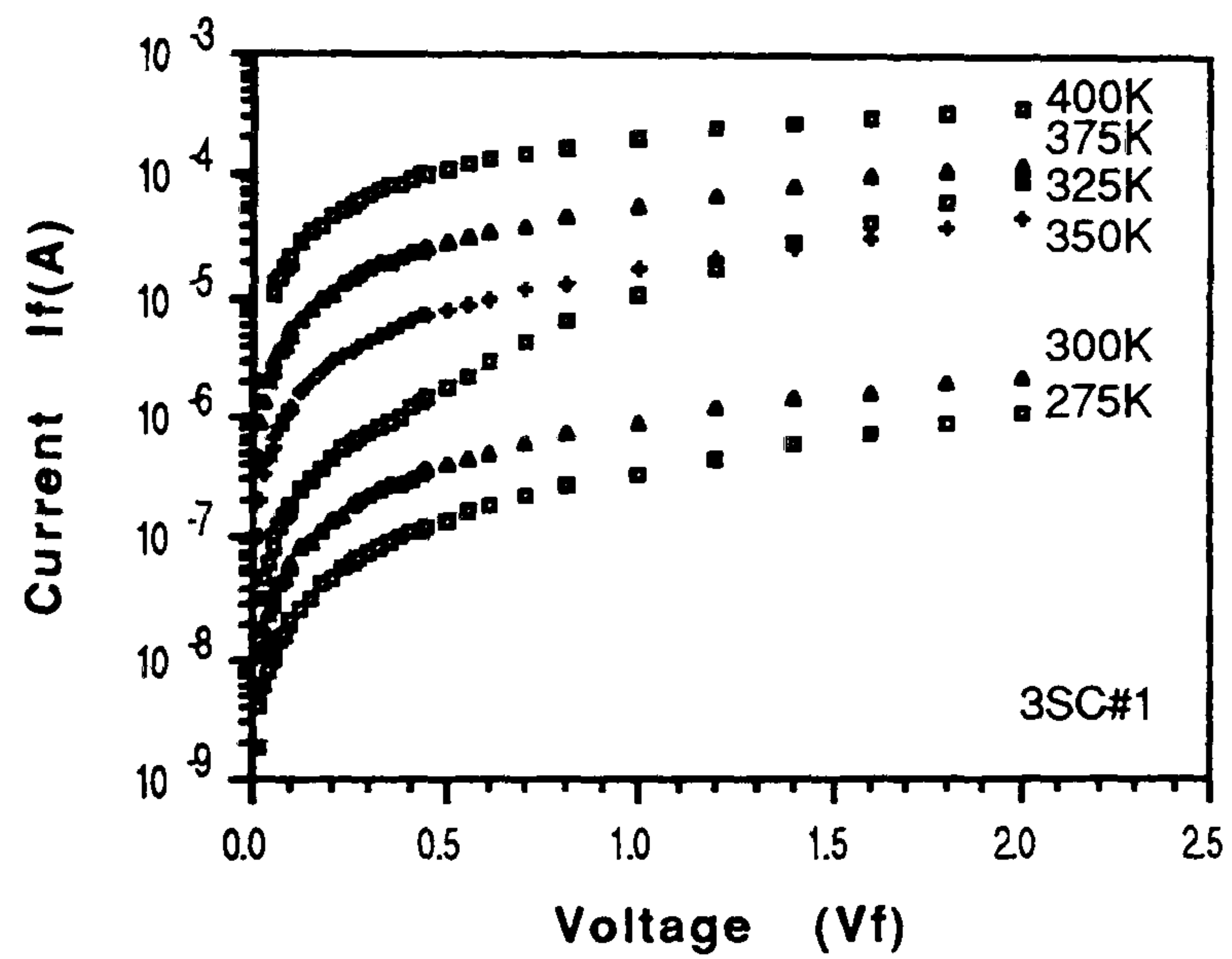


Figure 9.8 — Dark $\log(I_f)$ -V characteristic of co-evaporated CdS/CdTe:Cl₂ cell.

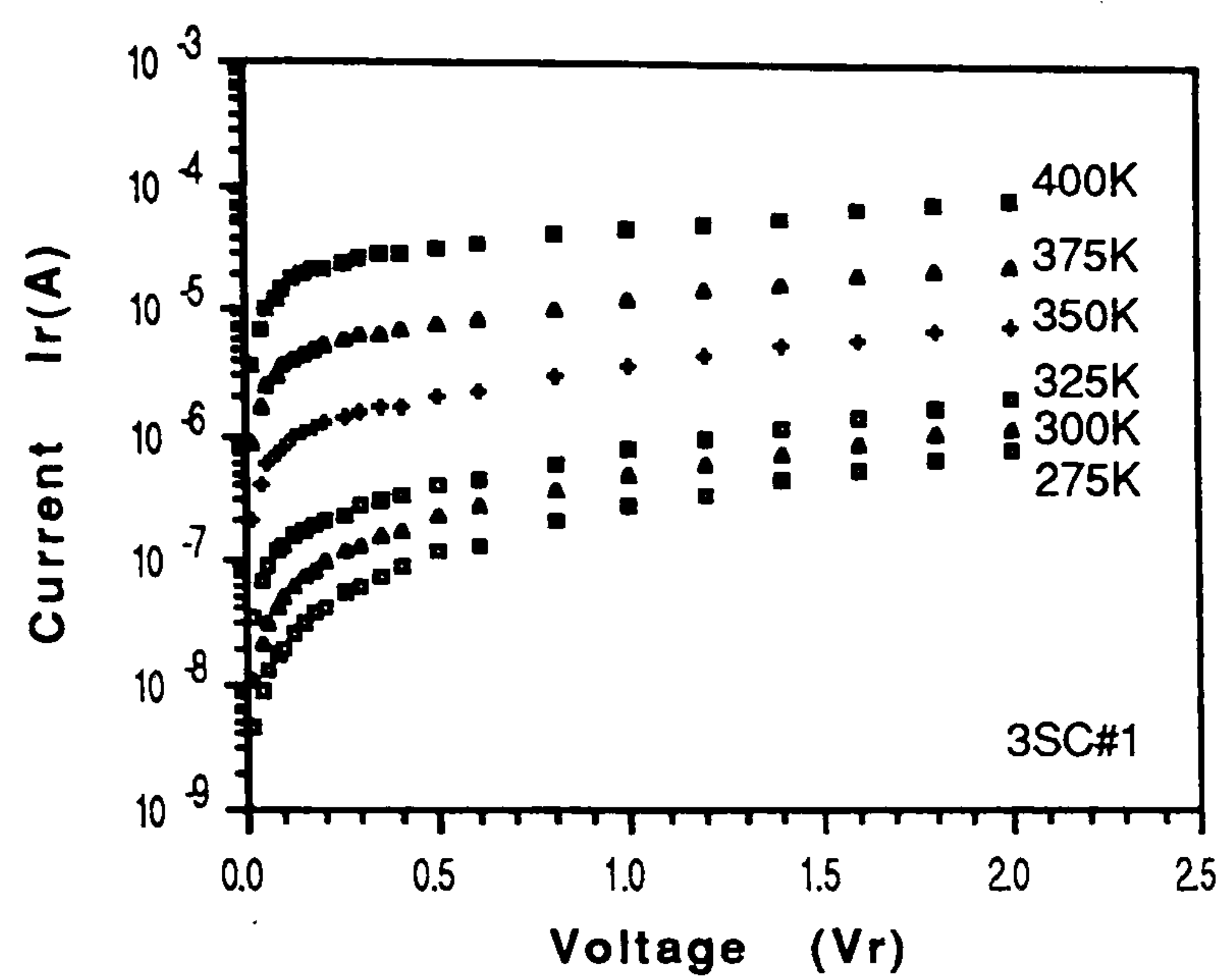


Figure 9.9 — Dark $\log(I_r)$ -V characteristic of co-evaporated CdS/CdTe:Cl₂ cell.

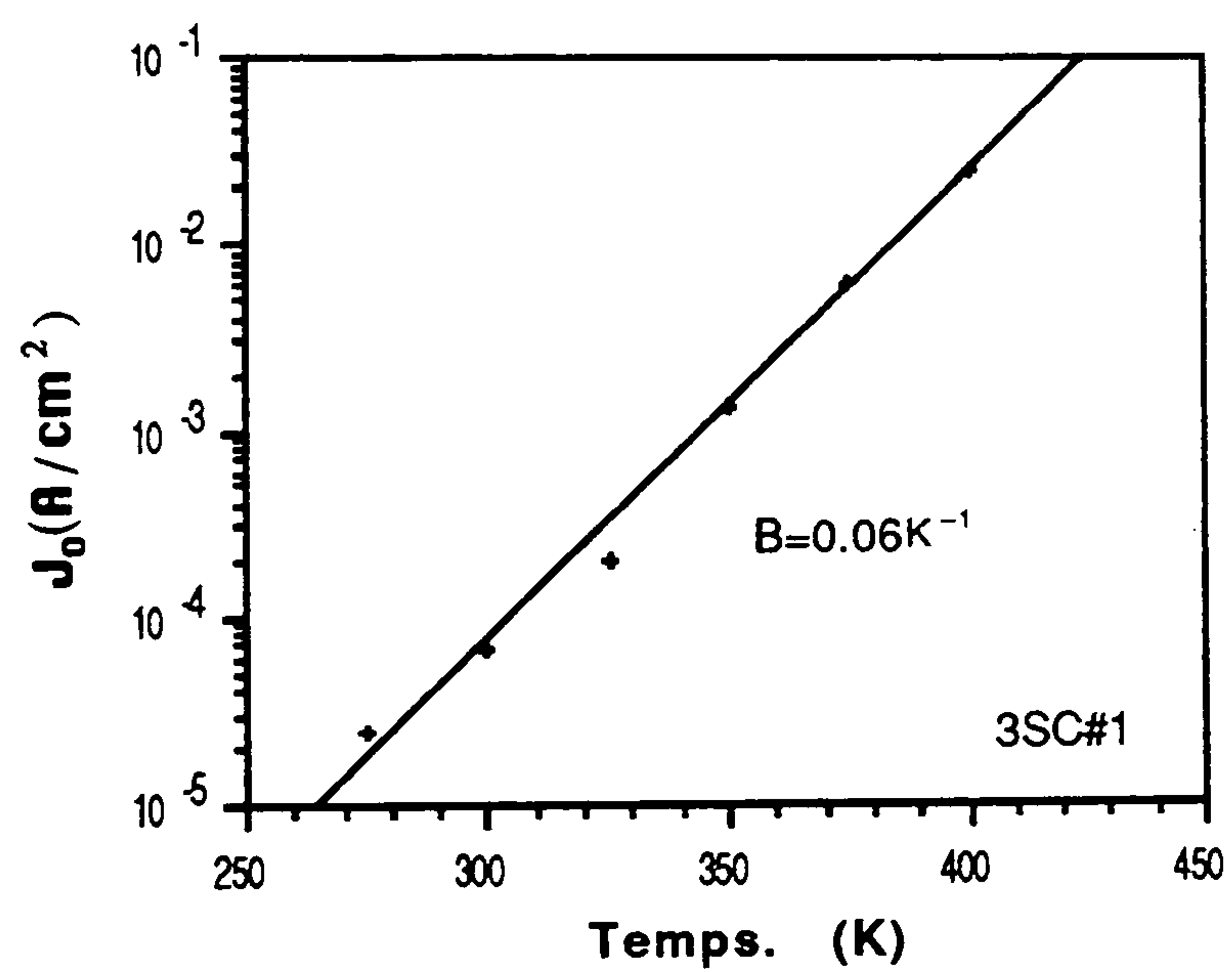


Figure 9.10 — $\log(J_0)$ vs T characteristic of a co-evaporated CdTe/CdS cell.

Temp's.(K)	$J_o(A/cm^2)$	Slope, A	n
275	2.43×10^{-5}	21.2	2.00
300	6.57×10^{-5}	21.7	1.78
325	2.00×10^{-4}	21.4	1.55
350	1.36×10^{-3}	21.7	1.53
375	6.00×10^{-3}	21.3	1.45
400	2.50×10^{-2}	21.7	1.34

Table 9.1 — Values of J_o , n and A for a typical co-evaporated cell as a function of temperature.

9.2.2.2 CdCl₂ Predoped Cells.

Cells were also fabricated using CdTe source material that had been pre-doped using CdCl₂ during the synthesis of the CdTe, as described in section 3.4.1. Fig.9.11 and Fig.9.12 show a dark $\log(I_f)$ -V and illuminated I-V characteristics respectively of a cell produced using synthesised CdTe:CdCl₂(5%). They also exhibited similar characteristics to those of undoped cells; viz low fill factor, low shunt resistance, high series resistance.

Interestingly, only layers synthesised with 0.1% CdCl₂ showed any change in the illuminated I-V characteristics. Fig.9.13 and Fig.9.14 show the dark $\log(I_f)$ -V and illuminated I-V characteristics of a cell produced using synthesised CdTe:CdCl₂ (0.1%). The cell displayed higher values of V_{oc} and J_{sc} , however, the FF was still relatively low possibly due to interface states and the high CdTe and contact resistances. It was also observed that leakage currents (probably through pin holes and/or defect induced interface states) caused an increase in J_o thus reducing J_{sc} . In forward bias the characteristics were still dominated by series resistance indicating that the contact resistance was fairly high.

In all cells, the dark and illuminated characteristics were observed to cross-over in the first quadrant. This is commonly observed in CdTe/CdS cells and is widely reported in the literature [3,4]. It has been suggested that the crossing of the light

and dark I-V curves may be due to a reduction in the depletion layer width through a photoconductive effect where excitation of carriers effectively reduces the layer resistivity under illumination. This allows an increased tunneling current to flow. The forward current under illumination was also found to saturate, (i.e. in the first quadrant of the illuminated I-V curve). This arises from the overlapping of two back-to-back Schottky diode characteristics, the p-n junction and the Au/CdTe contact interface [5,6].

9.2.2.3 BP Contacted Cells.

Some glass/ITO/n-CdS/p-CdTe:CdCl₂(0.1%) predoped cells were contacted at BP Solar Centre using their ohmic contact procedures. Fig.9.15a shows illuminated I-V characteristics of a typical pre-doped cell contacted at BP. The cell exhibited larger V_{oc} and J_{sc} values which resulted in a higher efficiency (i.e. about 1.12%). The shape of the characteristics (i.e. steeply increasing) in the first quadrant clearly demonstrates the effects of proper ohmic contact formation to the CdTe (with a low series resistance).

Although the details of the BP procedure of contact formation has not been released it is believed that the surface preparation techniques (i.e. chemical etching) as well as the metal and/or alloy deposited, play an important role in producing high efficiency cells with low contact resistance.

Illuminated I-V characteristic of the cell shown in Fig.9.15a exhibited some leakage and in an attempt to determine the potential photovoltaic behaviour, it was re-plotted after eliminating the series and shunt resistances as described in section 8.5. Fig.9.15d shows the illuminated I-V characteristics after removing the effects of both R_s and R_{sh} , and equivalent solar cell parameters are listed in Table 9.2. Clearly, it gives an indication of the junction quality and revealed the presence of junction losses due to recombination, imperfect collection, defect effects etc. when compared with the maximum performance figures.

When R_s was eliminated (see Table 9.3), J_{sc} and FF were increased resulting in a higher efficiency, although V_{oc} remained almost the same. Elimination of R_{sh} as well led to higher values of V_{oc} and FF and the efficiency was increased as a result.

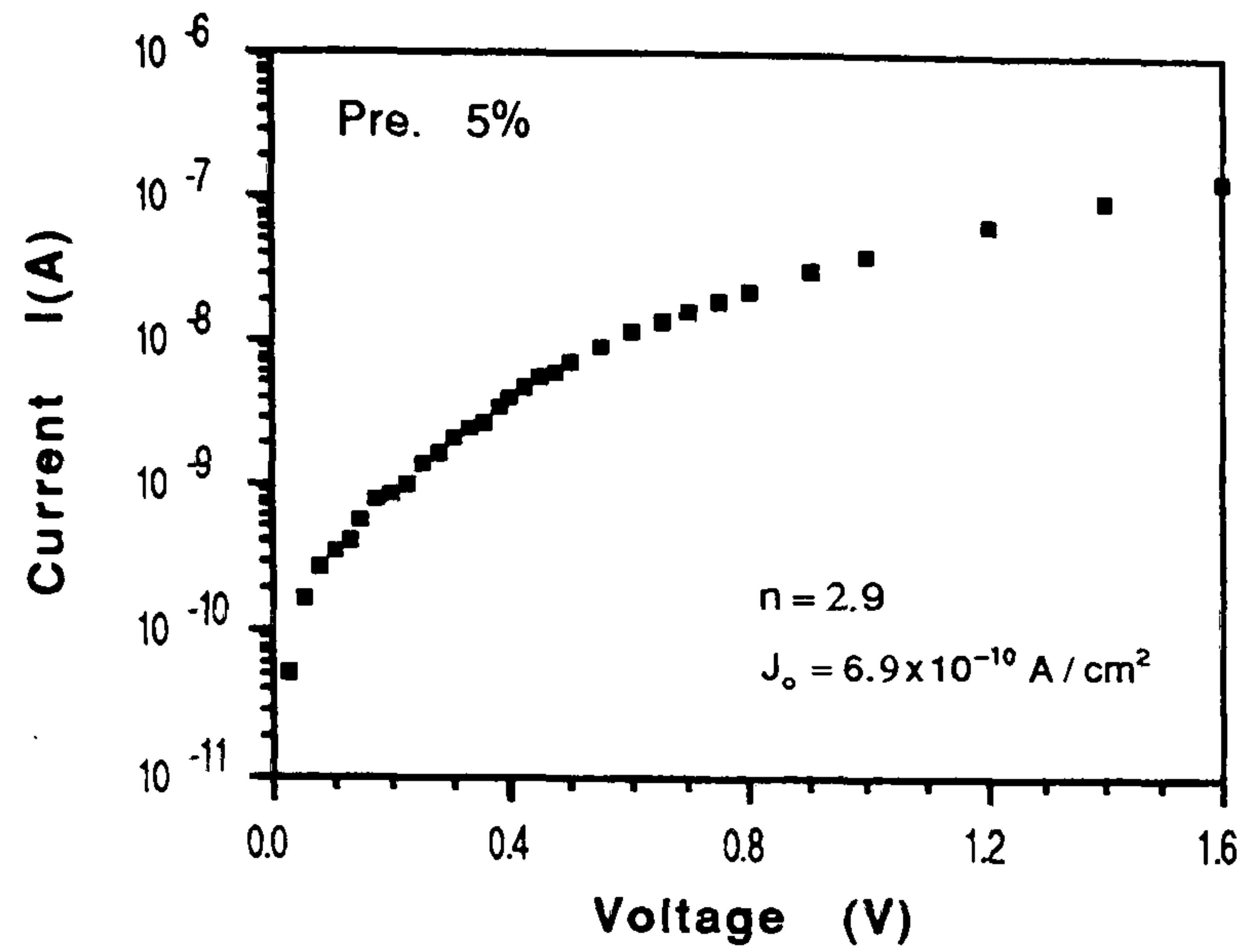


Figure 9.11 — Dark $\log(I_f)$ vs V characteristic of a pre-doped CdS / CdTe:CdCl₂ (5%) cell.

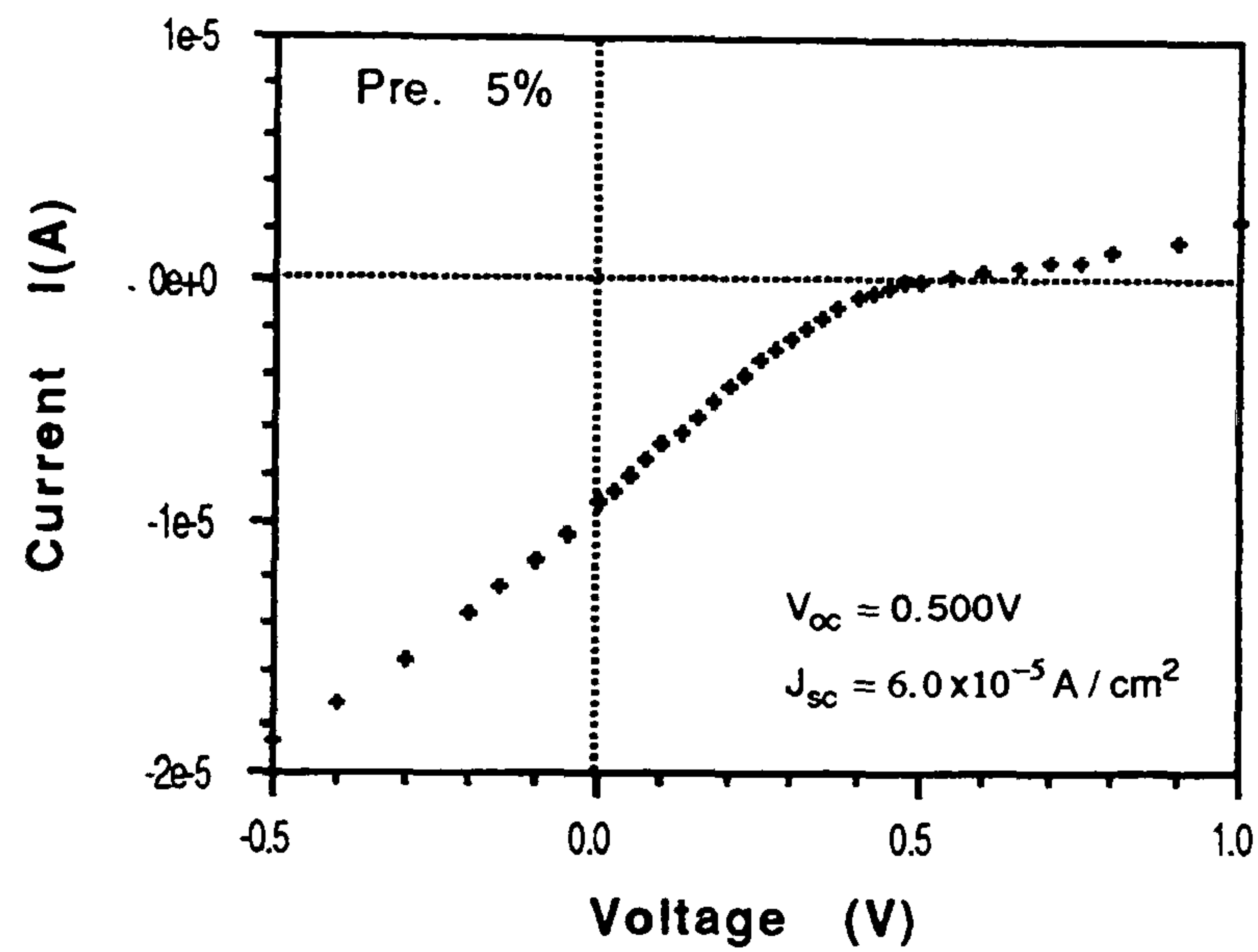


Figure 9.12 — I - V characteristic of a pre-doped CdS / CdTe:CdCl₂ (5%) cell under an illumination of 90 mW/cm^2 .

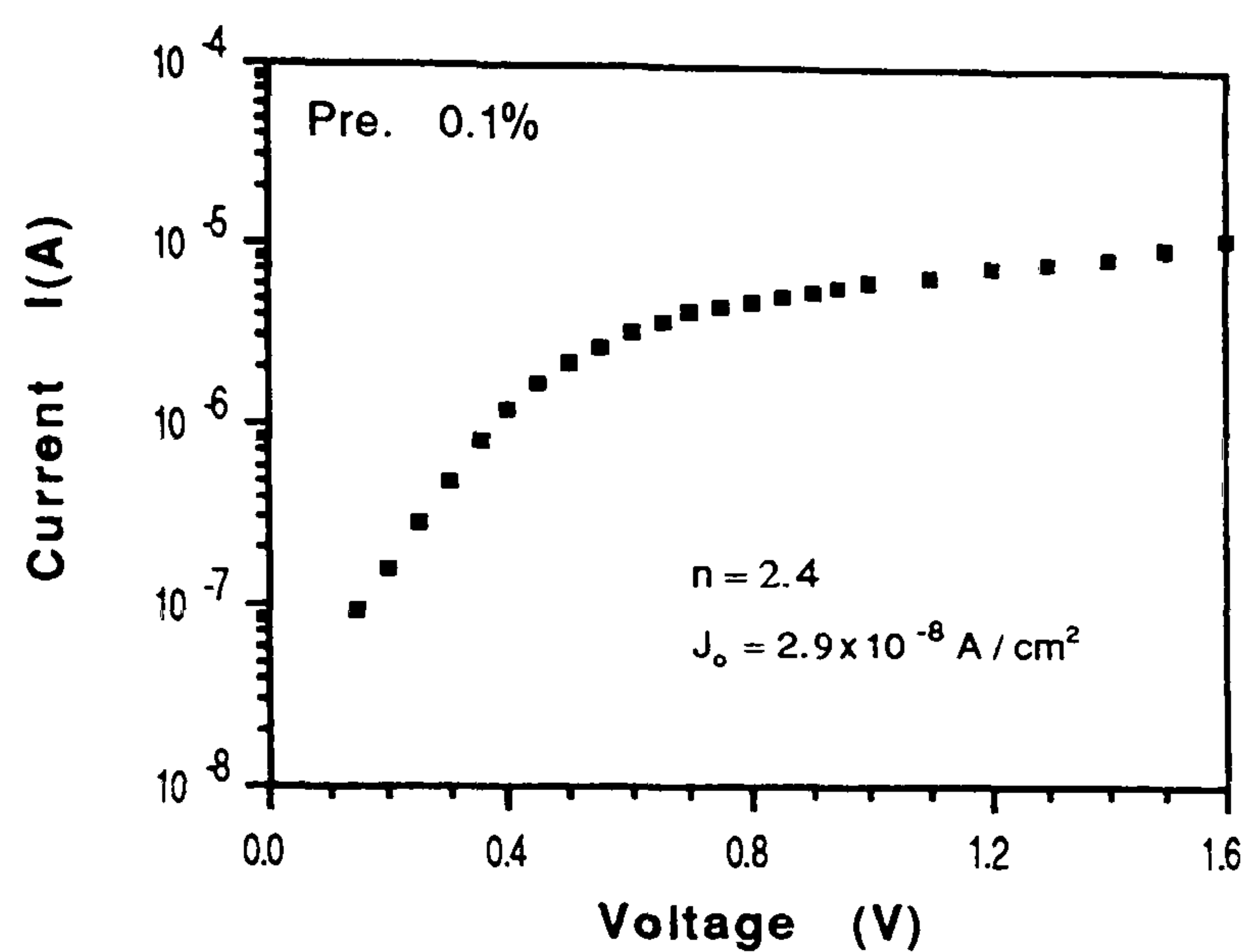


Figure 9.13 — Dark $\log(I_f)$ vs V characteristic of a pre-doped CdS/ CdTe: CdCl₂ (0.1%) cell.

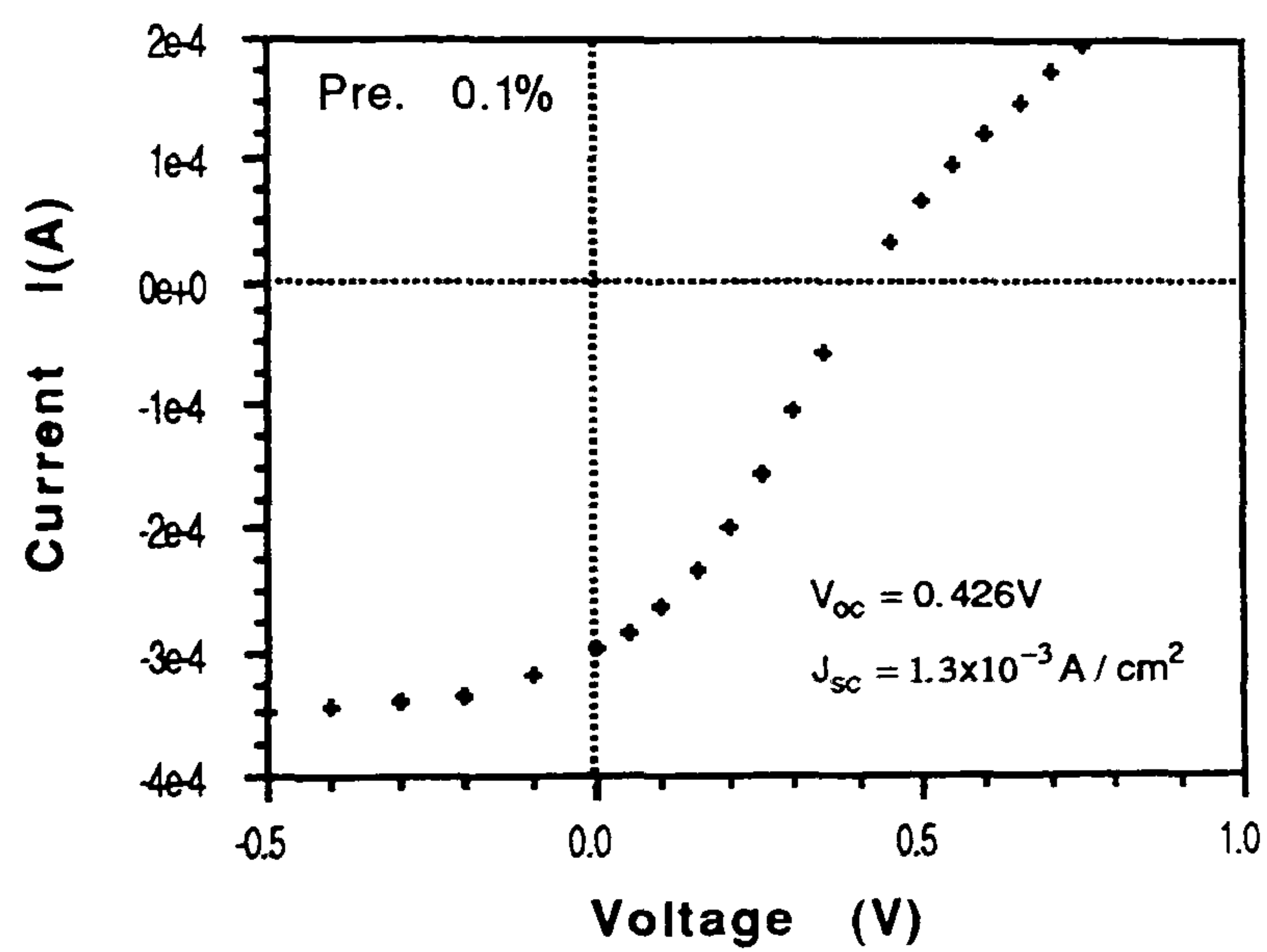
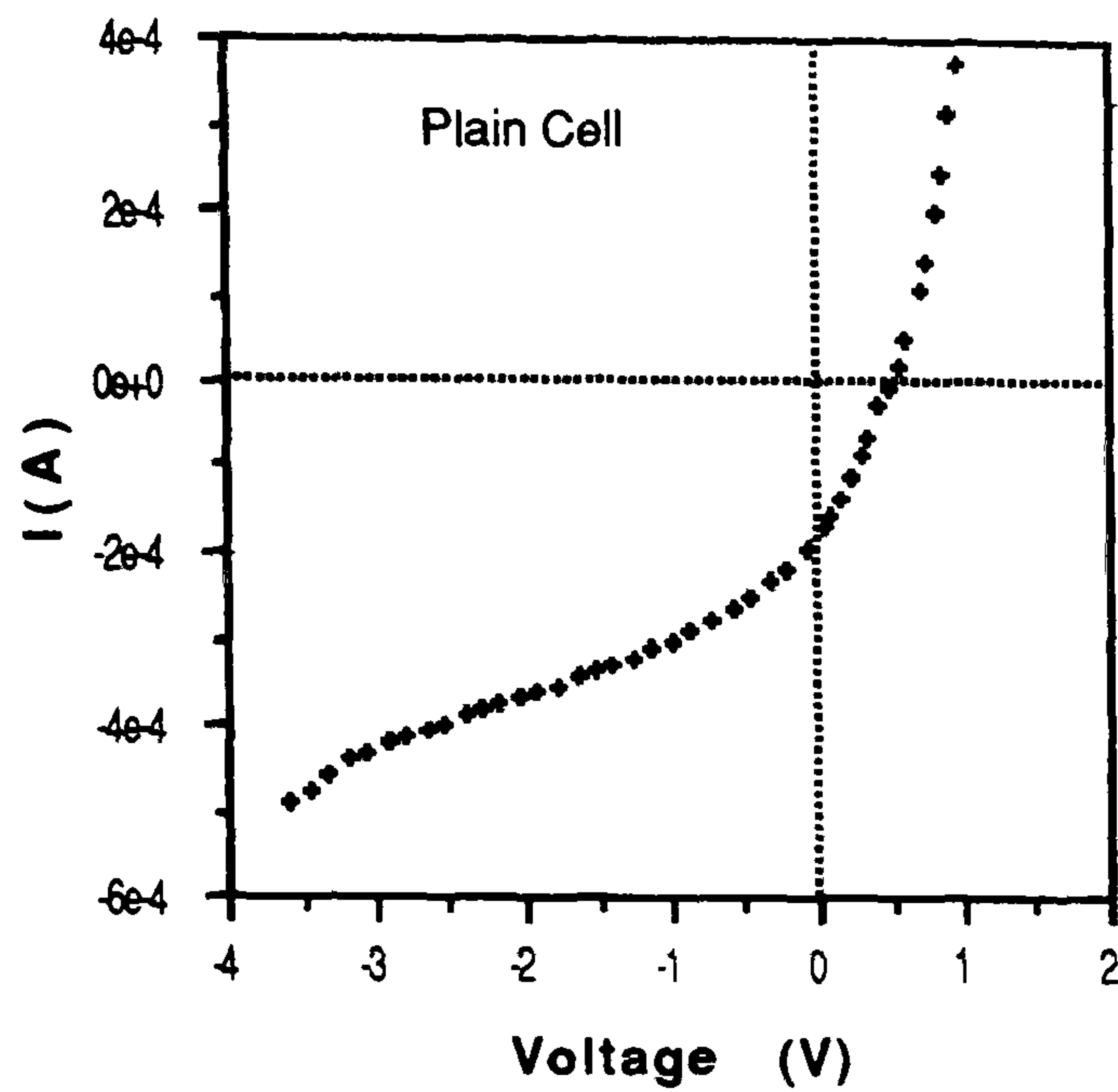
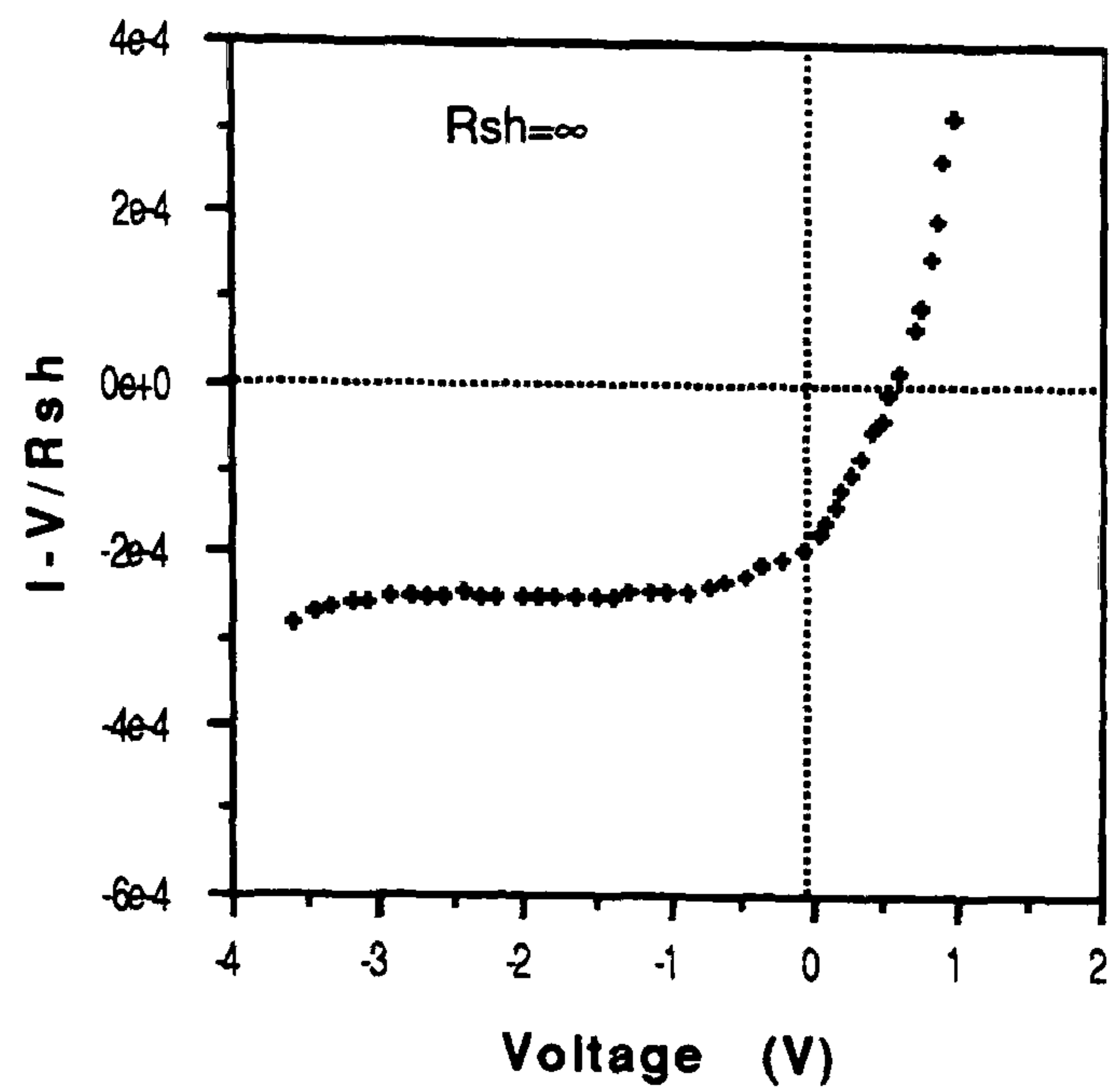


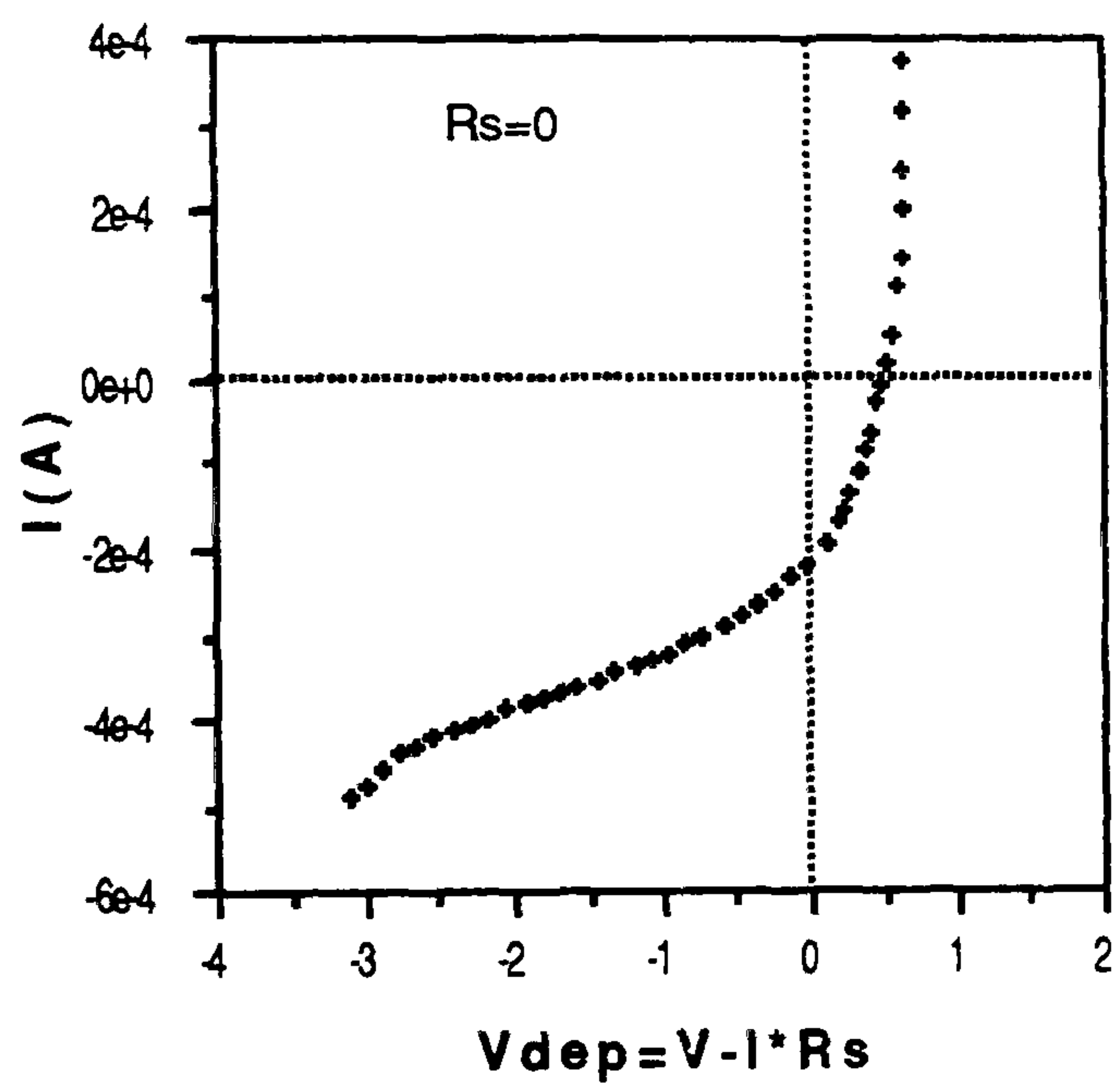
Figure 9.14 — I - V characteristic of a pre-doped CdS/ CdTe: CdCl₂ (0.1%) cell under an illumination of 90 mW/cm^2 .



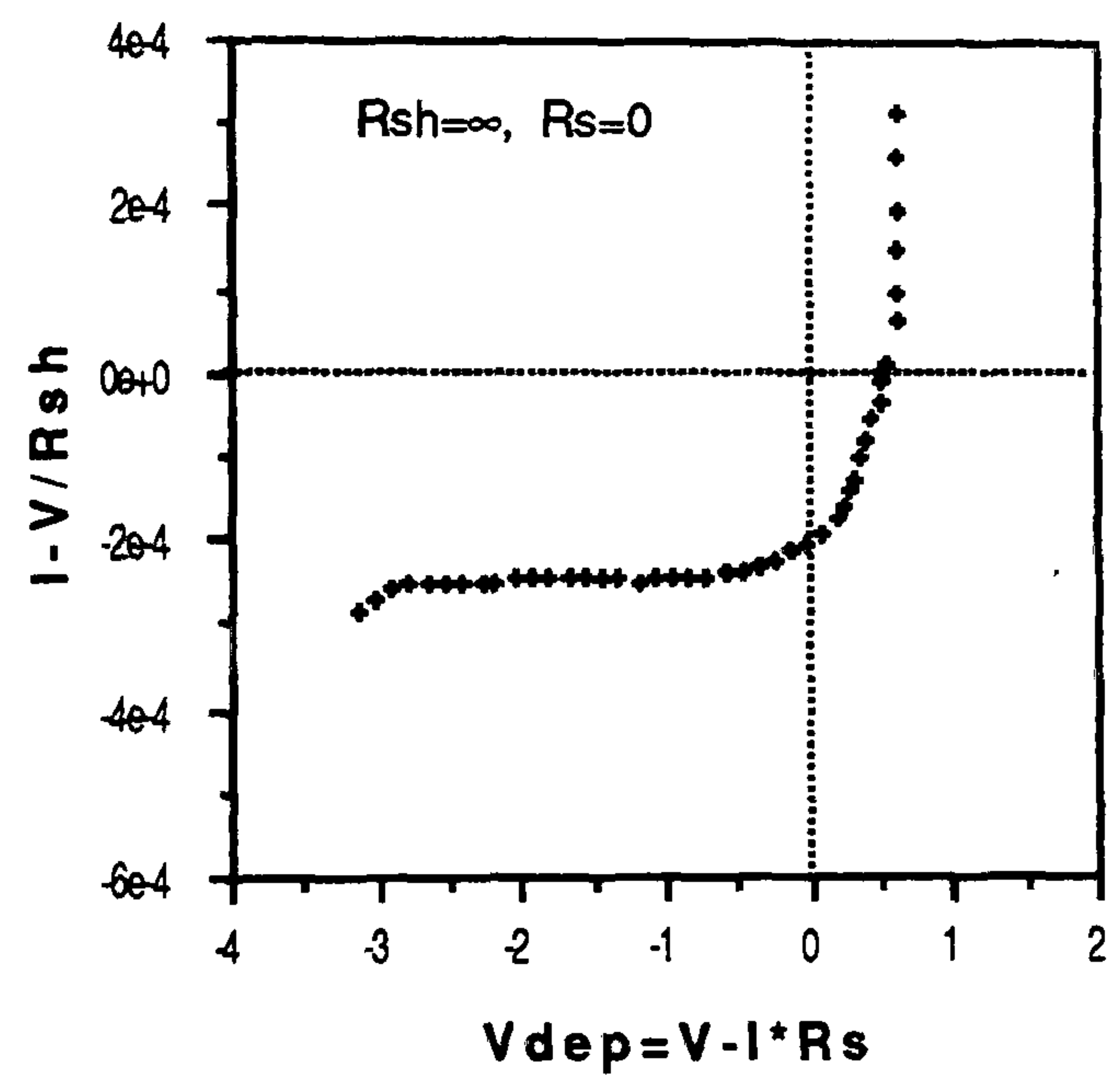
a



b



c



d

Figure 9.15 — I-V characteristics of a pre-doped CdS/CdTe: CdCl₂ (0.1%) BP contacted cell after eliminating R_{sh} and R_s , a: Plain cell, b: $R_{sh} \rightarrow \infty$, c: $R_s \rightarrow 0$, d: both (b and c).

Cell	$V_{oc}(V)$	$J_{sc}(A/cm^2)$	FF	$\eta(\%)$
Plain Cell	0.492	9.0×10^{-3}	0.26	1.16
$R_s \rightarrow 0$	0.492	1.1×10^{-2}	0.34	1.81
$R_{sh} \rightarrow \infty$	0.567	8.8×10^{-3}	0.28	1.40
$R_{sh} \rightarrow \infty, R_s \rightarrow 0$	0.538	1.0×10^{-2}	0.37	2.07
Theoretical Values	1.173	2.8×10^{-2}	0.90	29.7

Table 9.2 — Probable cell parameters after eliminating R_s and R_{sh} resistances for a typical pre-doped BP contacted cell.

Even though the data have been corrected for R_s and R_{sh} , nevertheless the value of V_{oc} and I_{sc} were approximately half those reported for the best cells [7]. This clearly indicates that there were problems associated with the junction and/or collection which remain to be addressed. Generally, the CdS layers were relatively resistive and thus as a consequence, the proportion of the depletion region that lay in the CdS layer may have been large with a corresponding reduction in collection and J_{sc} . The relatively low V_{oc} may also indicate high levels of interfacial recombinations at the junction, so that charge separation was not efficient.

9.2.2.4 CdCl₂-Coated Cells.

Fig.9.16 shows the illuminated I-V characteristics of a CdCl₂-coated cell together with those of an undoped cell, for comparison. These characteristics show that the coating procedure did lead to some improvement, although the effect was small. However, a systematic study to determine optimum coating conditions was not carried out (for lack of time) and in particular the dipping time was probably not long enough. (i.e. in the course of study, CdCl₂ concentration and dipping time were 1% and 1-2 sec respectively).

Interestingly, observations in the SEM of dipped layers (see sec.6.4.1, Fig.6.10 and 6.11) suggested that the dipping process was not uniform. The surface distribution of CdCl₂ deposits was very non-uniform which would probably lead to non-uniform junction performance (i.e. active junction would be rather smaller than the metallurgical junction area).

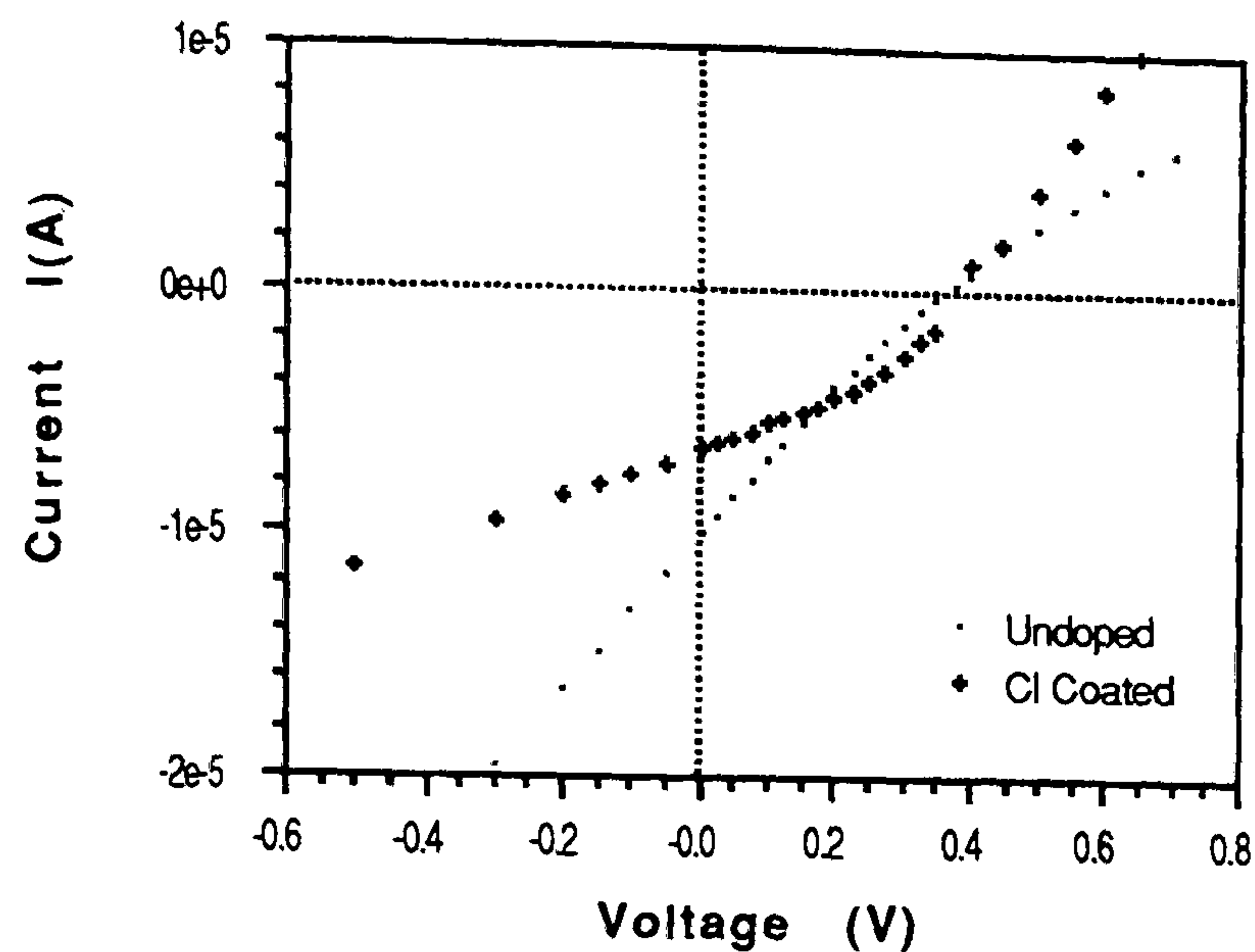


Figure 9.16 — I-V characteristic of an undoped and Cl_2 doped (by dipping) cell under an illumination of $90\text{mW}/\text{cm}^2$.

9.3 Determination of Series and Shunt Resistances.

The series, R_s , and shunt, R_{sh} resistance (i.e. normalized to a unit area of 1cm^2) of the thin film cells have been determined approximately from the dark and illuminated I-V characteristics as described previously in section 8.5. Table 9.3 tabulates the R_s values obtained from the various methods for some cells.

Sample No:	$R_s^a(\text{dark})$	$R_s^b(\text{illum.})$	$R_s^c(\text{dark})$
Undoped (1SC#1)	1.8×10^6	1.5×10^4	1.6×10^6
Co-evaporated (4SC#3)	2.6×10^3	6.1×10^2	2.6×10^3
Pre-doped (5SC#1)	8.1×10^4	5.8×10^2	8.3×10^4
Pre-doped (BP contacted)	2.1×10^2	1.8×10^1	2.1×10^2

Table 9.3 — R_s values (i.e., in Ohm, normalized to a unit area of 1cm^2) of some cells calculated by methods a, b, and c.

Briefly these are:

- a- R_s may be determined from the slope of dark I-V characteristics at forward bias voltages where the exponential dependence of forward current has vanished, i.e. $\frac{dI}{dV}|_{V>0} = \frac{1}{R_s}$;
- b- R_s may be determined from the slope of illuminated I-V characteristics at forward bias voltages above V_{oc} where the forward current does not vary exponentially with the voltage, i.e. $\frac{dI}{dV}|_{V>V_{oc}} = \frac{1}{R_s}$;
- c- R_s may be determined from the difference between measured and ideal dark characteristics, i.e. I_f vs ΔV .

R_s values measured under illumination (method b) were found to be smaller (\sim two orders of magnitude) than the corresponding values measured in the dark (methods a and c). This was probably due to photoconductive effects in the CdTe layer, i.e. the excess photogenerated carrier density was comparable or larger than the dark equilibrium carrier density, with a corresponding increase in conductivity. Methods a and c also gave values in good agreement with each other, although as the methods rest on the same assumptions (i.e. ideal diode with series resistance) they might be expected to yield similar values. These methods would be reasonable where $R_s \ll R_{sh}$, however in the present case where R_{sh} was comparable with R_s , these values may be in error.

Fig.9.17 and Fig.9.18 show I_f vs ΔV (i.e. the potential drop across the internal resistance of the device) characteristics of undoped and co-evaporated CdTe cells respectively. The plot of I_f vs ΔV for the undoped cell was quite linear whereas there exists two separate linear regions for the co-evaporated cell, as expected (i.e. barrier height lowering at higher forward biases). Fig.9.19 and Fig.9.20 show I_f - V characteristics of the undoped and co-evaporated cells respectively, where the series resistance effect has been subtracted from the plots (i.e. $V_{f,dep} = V_f - I_f R_s$). They displayed more linear characteristics in which n and J_o may be calculated more reliably. Table 9.4 lists the R_{sh} values of the cells calculated by two methods;

- a: R_{sh} may be determined from the slope of the dark I-V characteristics at reverse bias voltages where reverse current changes linearly with reverse bias voltage, i.e. $\frac{dI}{dV}|_{V<0} = \frac{1}{R_{sh}}$;

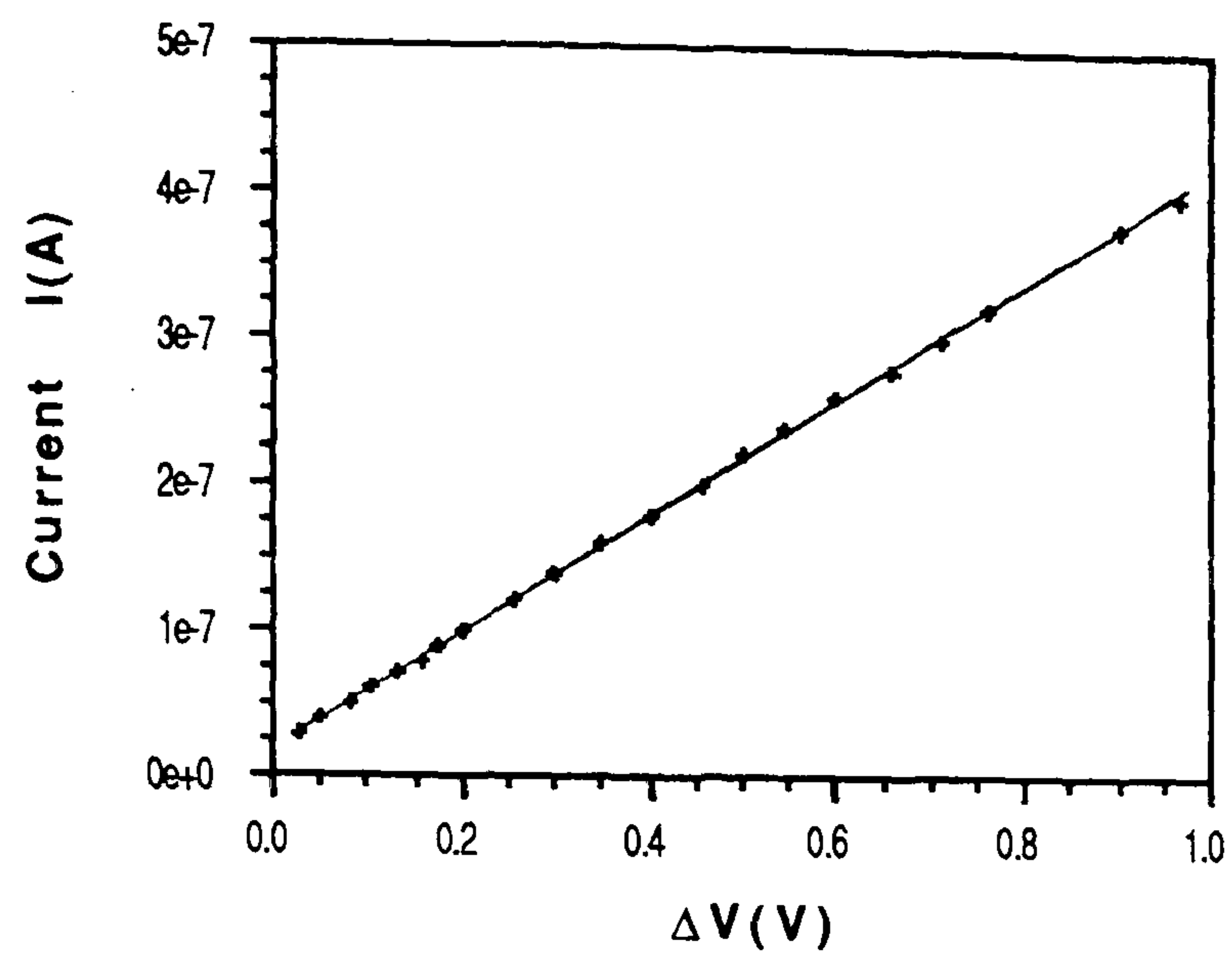


Figure 9.17 — I_f vs ΔV characteristic of an undoped CdS/CdTe cell.

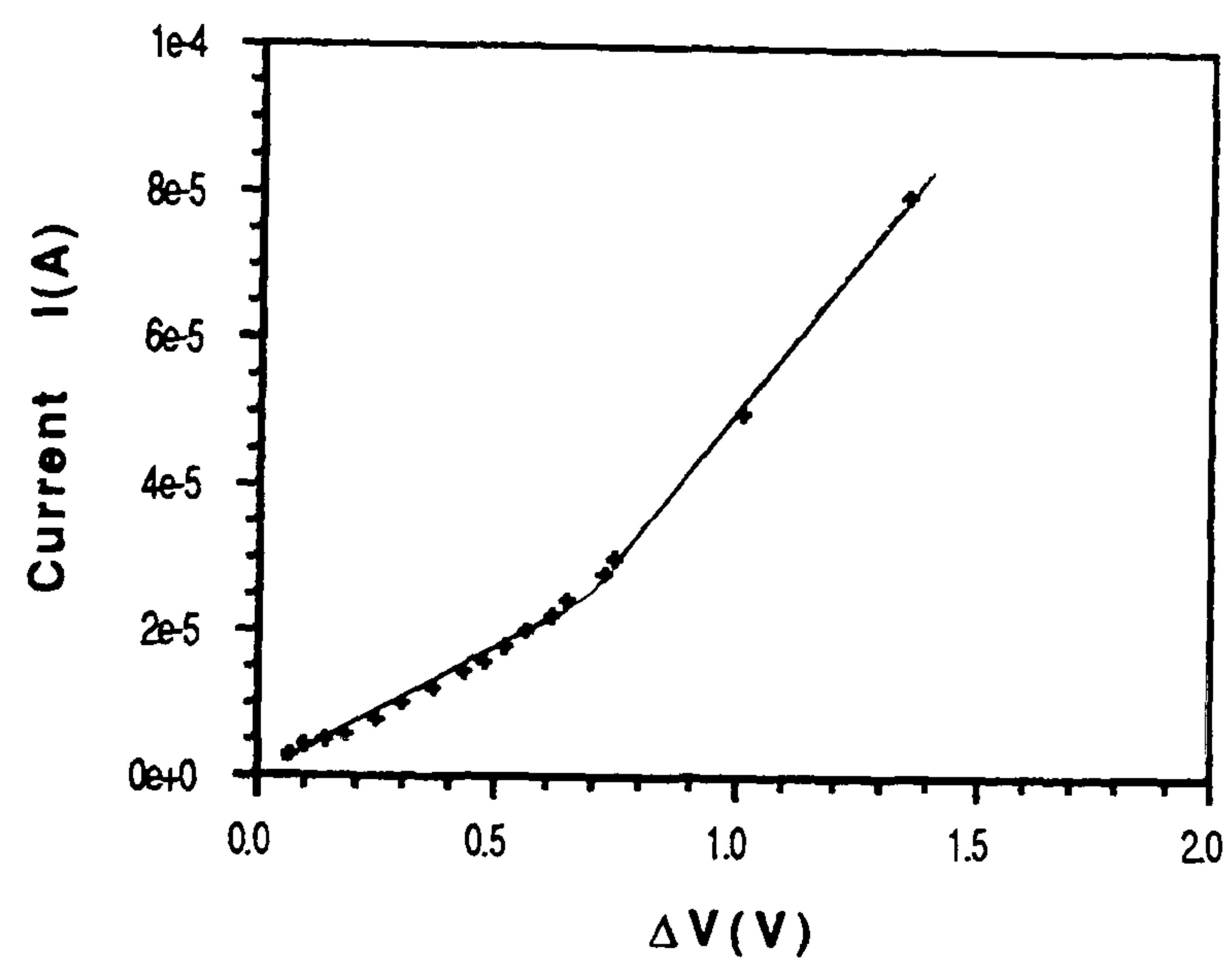


Figure 9.18 — I_f vs ΔV characteristic of a co-evaporated CdS/CdTe cell.

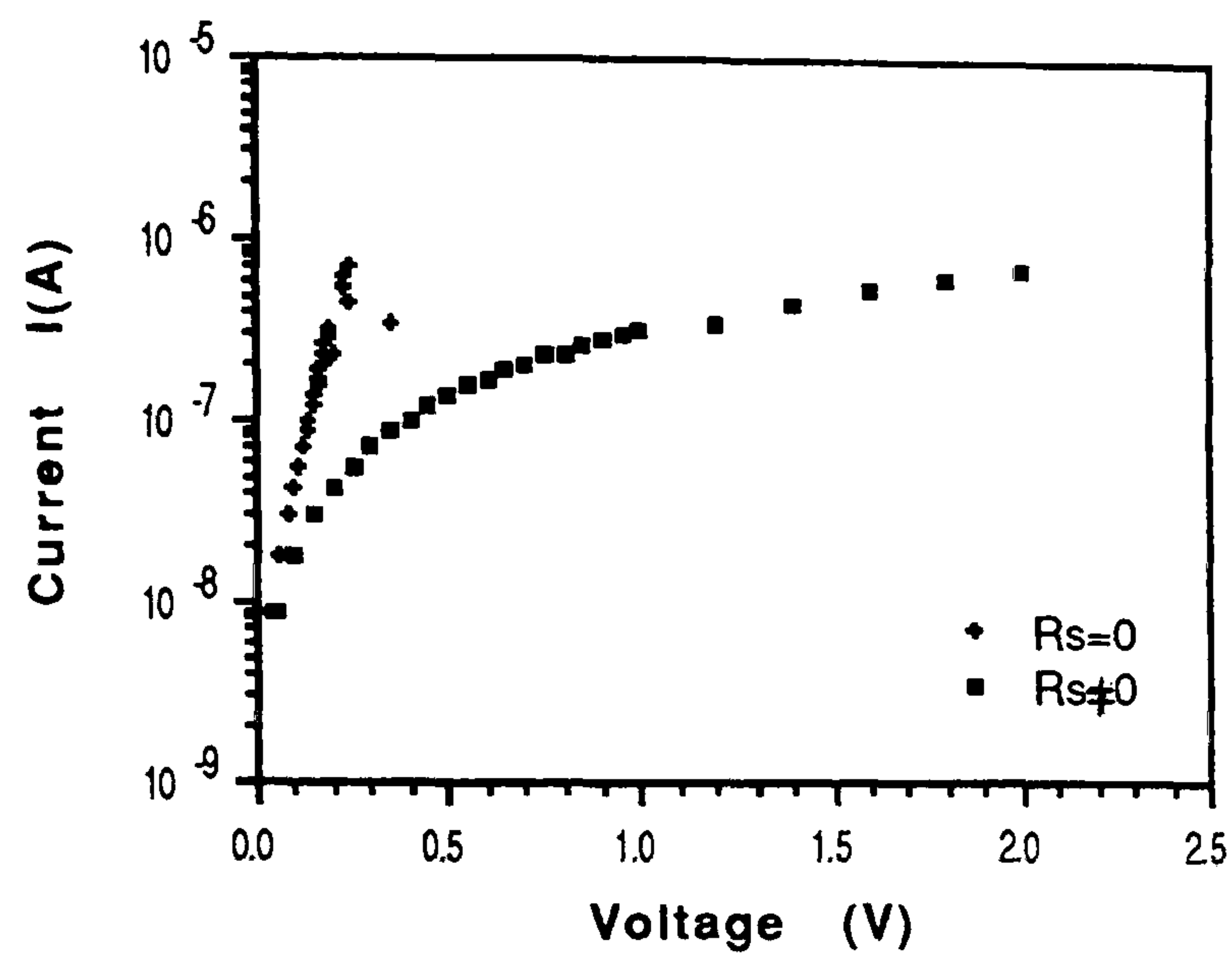


Figure 9.19 — $\log(I_f)$ vs V characteristic of an undoped CdS/CdTe cell before and after eliminating R_s .

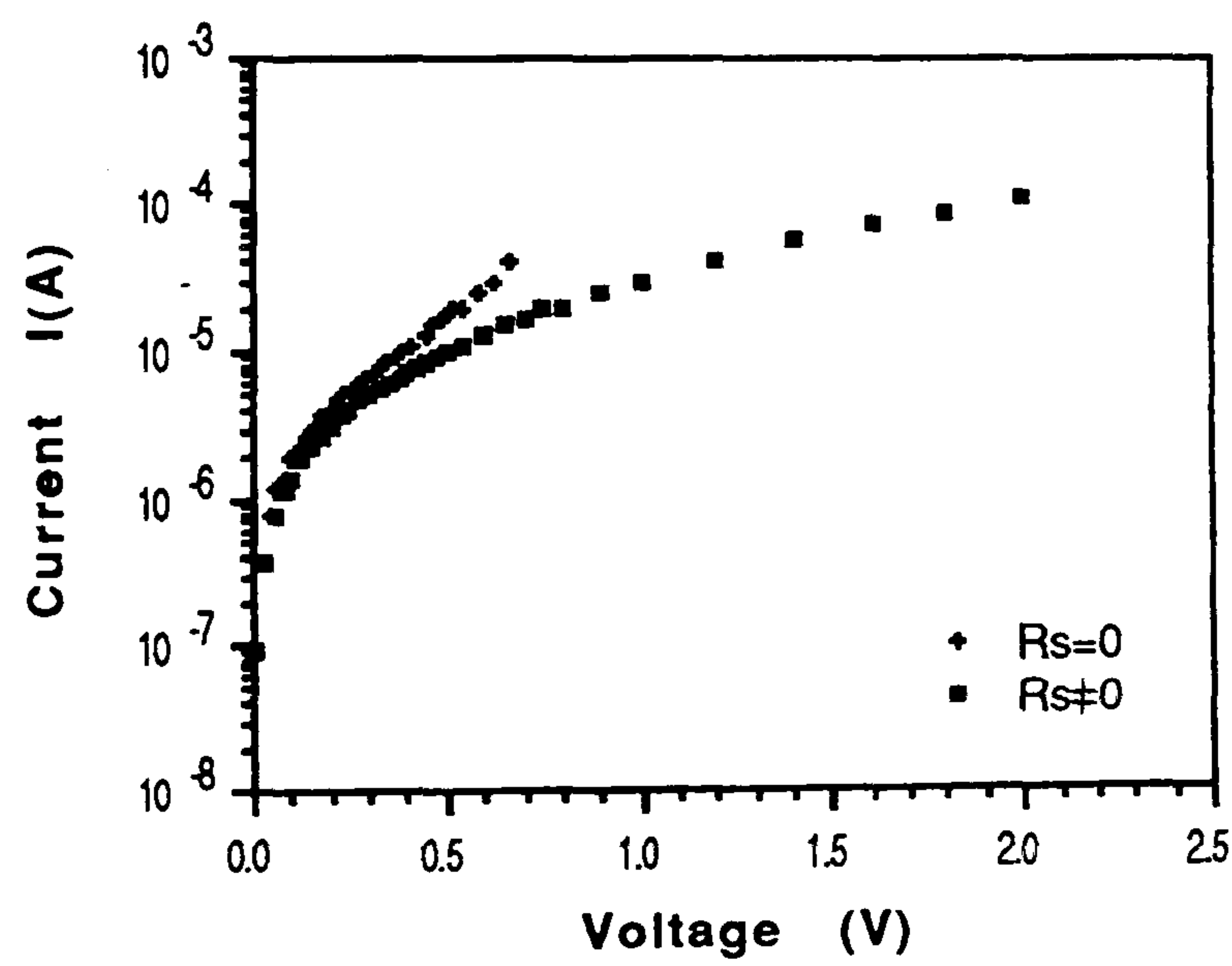


Figure 9.20 — $\log(I_f)$ vs V characteristic of a co-evaporated CdS/CdTe cell before and after eliminating R_s .

b: R_{sh} may be determined from the slope of illuminated I-V characteristics at reverse bias voltages where reverse current changes linearly with reverse bias voltage, i.e. $\frac{dI}{dV}|_{V<0} = \frac{1}{R_{sh}}$;

Sample No:	R_{sh}^a (dark)	R_{sh}^b (illum.)
Undoped (1SC#1)	8.8×10^6	7.8×10^3
Co-evaporated (4SC#3)	1.8×10^6	1.4×10^3
Pre-doped (5SC#1)	1.2×10^6	6.4×10^4
Pre-doped (BP contacted)	1.7×10^4	3.3×10^2

Table 9.4 — R_{sh} values (i.e., in Ohm, normalized to a unit area of 1cm^2) of the some cells calculated by the methods a and b.

As for the measurements of R_s , measurements of R_{sh} from the illuminated characteristics were smaller (≥ 2 orders of magnitude) than the corresponding dark values. The reasons for this are less clear but may indicate that levels of generation/recombination within the depletion region were increased on illumination. Table 9.3 and Table 9.4 show clearly the effects of improving the ohmicity of the contacts to the CdTe layer. This reduced series resistance significantly (as anticipated) by approximately 2 orders of magnitude (cf with pre-doped sample 5SC#1). The values of R_{sh} calculated from measurements made in the dark seem quite high, although the characteristics do not appear to be consistent with such values. It is not clear why the discrepancy arises, but it may be related to barrier effects at the contact which significantly alter the shape of the characteristics, leading to incorrect estimates for R_{sh} .

9.4 Spectral Response.

The spectral responses (i.e. which are directly related to the cell quantum efficiency) of the cells were measured at room temperature. Fig.9.21 and Fig.9.22 show the spectral response of a co-evaporated and a CdCl_2 coated cell. The short and long wavelength cut-off's corresponded with the absorption edges of CdS and CdTe respectively as expected for a normal window response. The CdS is transparent to photon energies less than the band gap of 2.42 eV. Electron/hole pairs

created (by those photons whose energies are greater than the band gap of CdTe) within about one diffusion length of the CdTe depletion layer will contribute to the photocurrent. The response began sharply at about 1.48 eV (i.e. CdTe absorption edge) and decreased gradually with increasing photon energy. As the photon energy increased beyond 2.42 eV (i.e. CdS band gap), the photocurrent fell sharply due to absorption occurring at the surface of the CdS and away from the junction. The relative contributions to the total response from each side of the junction depend on the relative band bending and depletion layer widths in the CdS and CdTe. This in turn depends on the doping concentrations on either side of the junction. Hence, the observed response indicated that the depletion layer was supported mostly by the CdTe (i.e. one-sided junction). The spectra are fairly similar although the co-evaporated cell had a relatively larger response near to the CdTe band gap edge than the dipped cell.

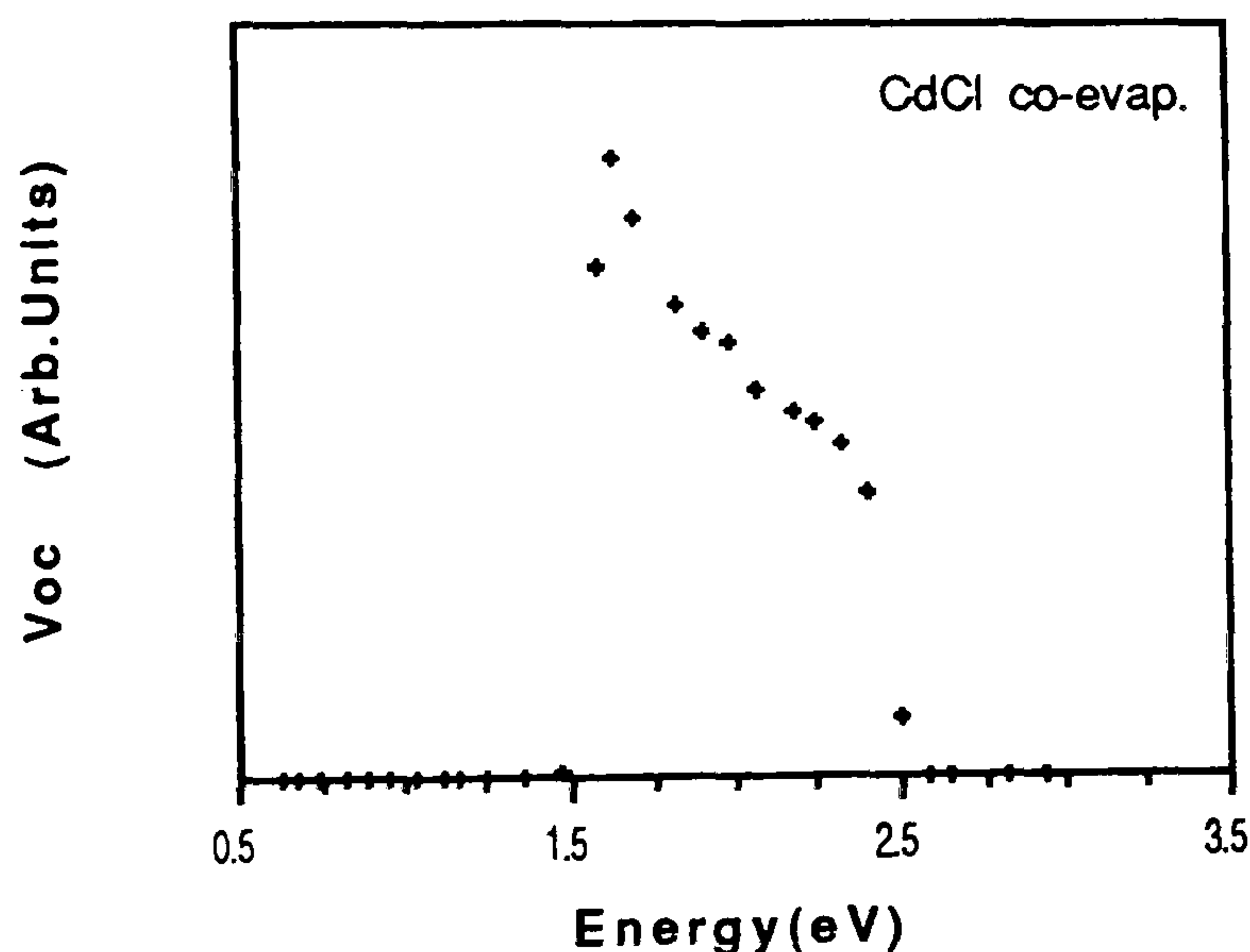


Figure 9.21 — V_{oc} as a function of photon energy of a co-evaporated CdS/CdTe: Cl_2 cell.

9.5 Optical Properties.

The optical transmission characteristics of thin layers of CdTe and CdS grown on glass substrates were reported and discussed in detail chapter 5. However, it was also important to investigate the optical transmission properties of the combined glass/ITO/CdS/CdTe multilayer structures.

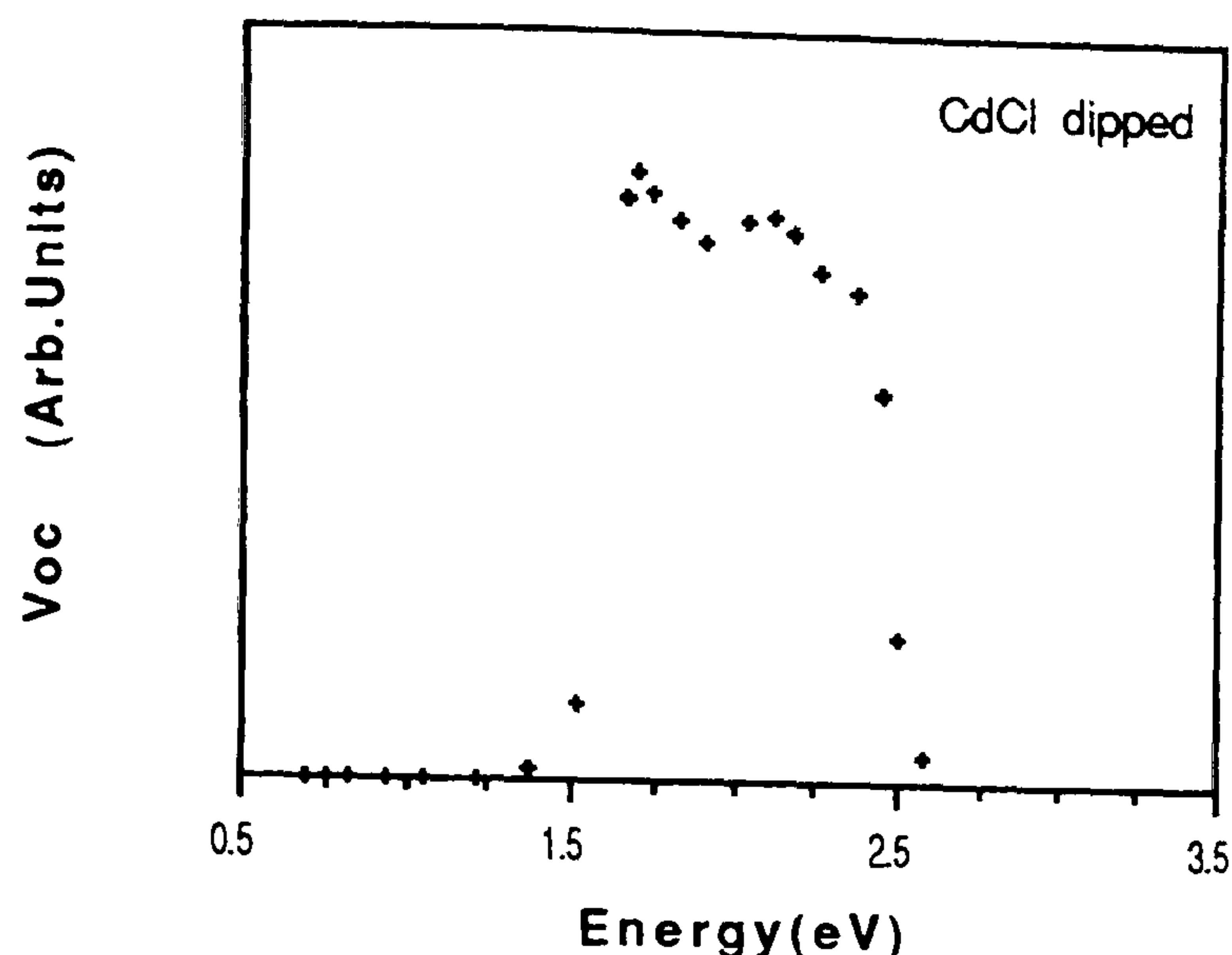


Figure 9.22 — V_{oc} as a function of photon energy of a CdCl_2 coated $\text{CdS}/\text{CdTe}:\text{Cl}_2$ cell.

In particular, an attempt was made to determine the percentage of AM1.5 solar irradiation that would be transmitted into the CdTe through the proceeding glass/ITO/CdS layers. Fig.9.23 shows the normal incidence transmission spectra for ITO, ITO/CdS and ITO/CdS/CdTe structures on glass, in the infrared and visible ranges. The transmission spectrum of the ITO/CdS/CdTe structure on glass showed a smooth cut-off at the CdTe band edge. Between the CdS and CdTe band edges (i.e. $512 \text{ nm} < \lambda < 820 \text{ nm}$), the light was mainly absorbed by CdTe. There was a steady decrease in transmission at wavelengths above 1000 nm, due mostly to the strong extinction due to the ITO.

From the glass/ITO/CdS transmission spectrum, it was possible to estimate transmission into the CdTe layer over the relevant wavelength range of 500–825 nm by integrating the area under the curve. The total transmission in this range was calculated for this cell to be 64%. However, when this is weighted to account for the AM1.5 global solar spectrum over the same spectral range, it gave an effective transmission of 86%. No attempt was made to correct for the reflection at the CdTe/CdS interface and so the actual weighted transmission in a cell would be a little less than this value.

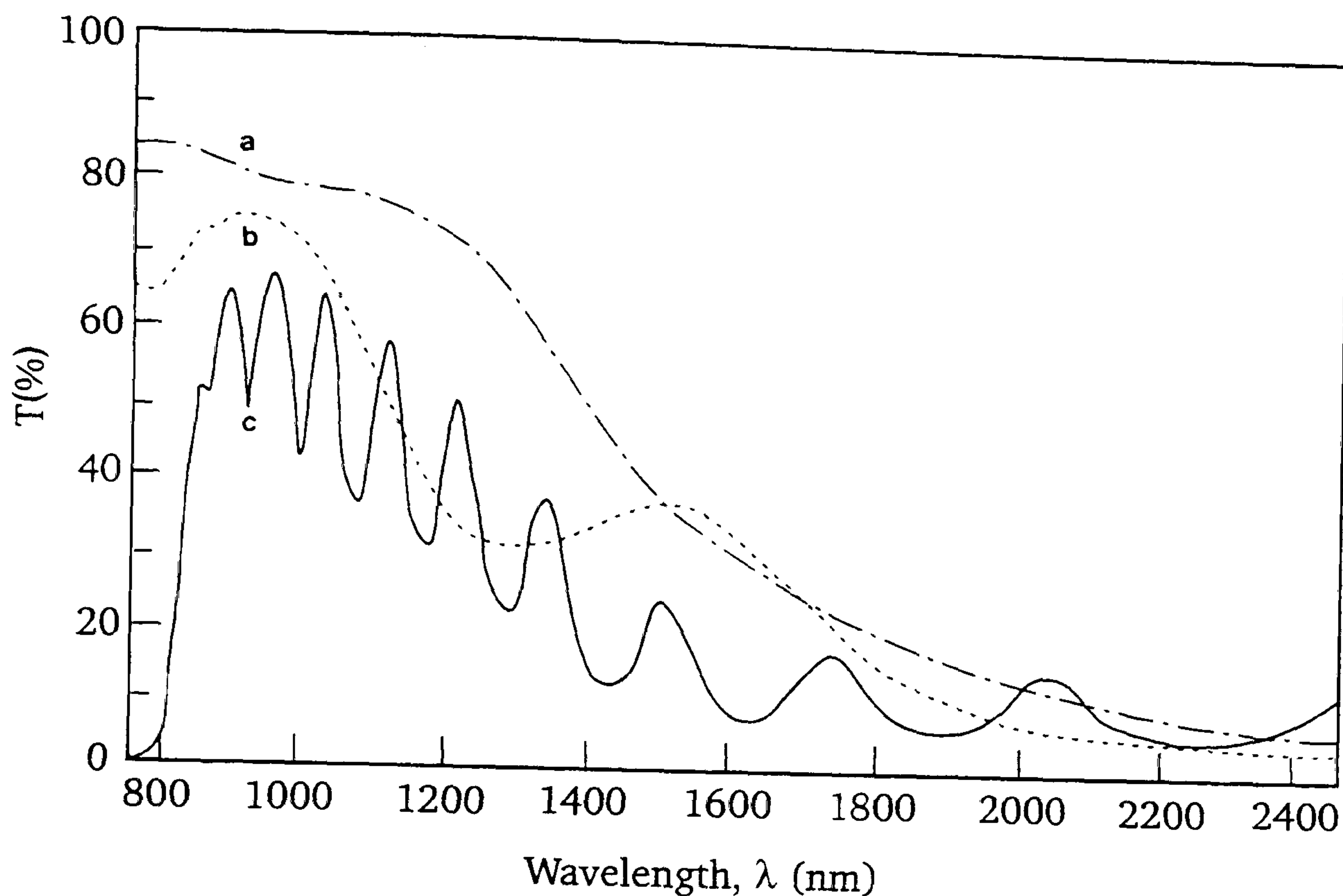


Figure 9.23 — Normal incidence transmission spectra of a: ITO, b: CdS/ITO, and c: CdTe/CdS/ITO structures on glass substrates.

9.6 C-V Characteristics.

The zero bias capacitance temperature (C-T) and C-V characteristics were measured for some cells. Fig.9.24 shows the $C|_{V=0}$ -T characteristics for a co-evaporated cell over the temperature range 170–375K. Reliable capacitance readings could not be obtained at temperatures below 170K, probably because the layers had become too resistive, as was found for the I-V measurements (sec.9.2.2.1). Over the temperature range 170–375K, the zero bias capacitance increased linearly with the temperature, indicating a progressive reduction in the depletion width, as the CdTe conductivity increased.

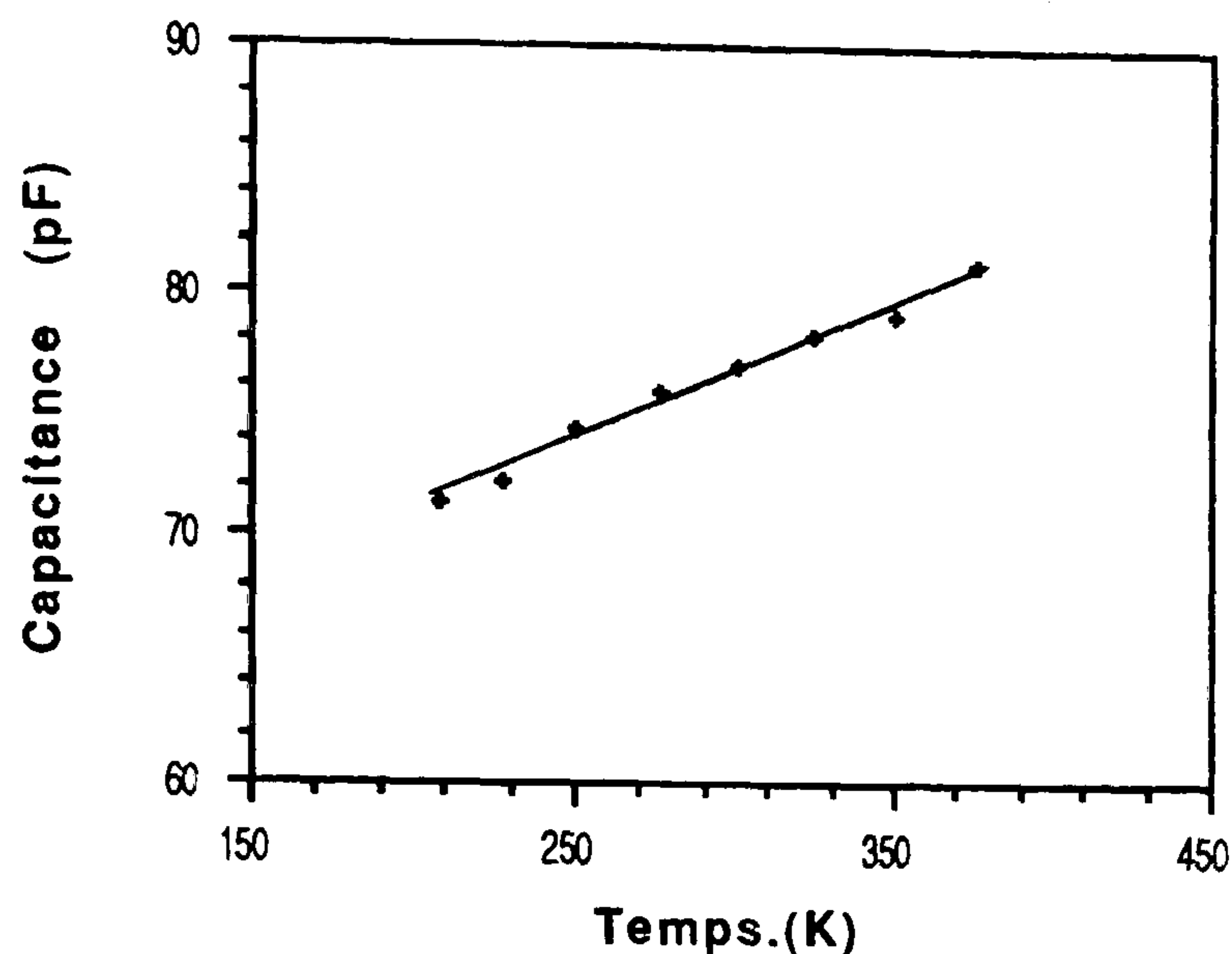


Figure 9.24 — C vs T characteristic of a co-evaporated CdS /CdTe:Cl₂ cell.

The C^{-2} vs V characteristics for the same cell are shown in Fig.9.25. These display very little change in the capacitance with reverse bias. These cells had high series resistances, across which most of the applied bias would have been dropped, rather than across the junction. As a result the junction capacitance would have been insensitive to applied bias. Alternatively, the apparent insensitivity of the C^{-2} vs V characteristics may have been due to high interface state and pin-hole densities. In practice both factors were probably contributing.

The C^{-2} vs V characteristics for a pre-doped cell (measured at BP Solar) are shown in Fig.9.26 under both dark and illuminated (100 mW/cm^2) condition. As for the co-evaporated cells, the characteristics appeared to be dominated by interface states and possibly pin-holes, leading to an unphysical value for the voltage intercept. The slope of the dark characteristic indicated a net ionised acceptor density of $3 \times 10^{16} \text{ cm}^{-3}$, although this figure was subject to a high degree of uncertainty. Under illumination photodoping should result in a decrease in the depletion region with a corresponding increase in the capacitance. This is clearly evident in the C^{-2} vs V plot. However, the increased slope of the illuminated characteristic was not expected and it is unclear how this should be interpreted.

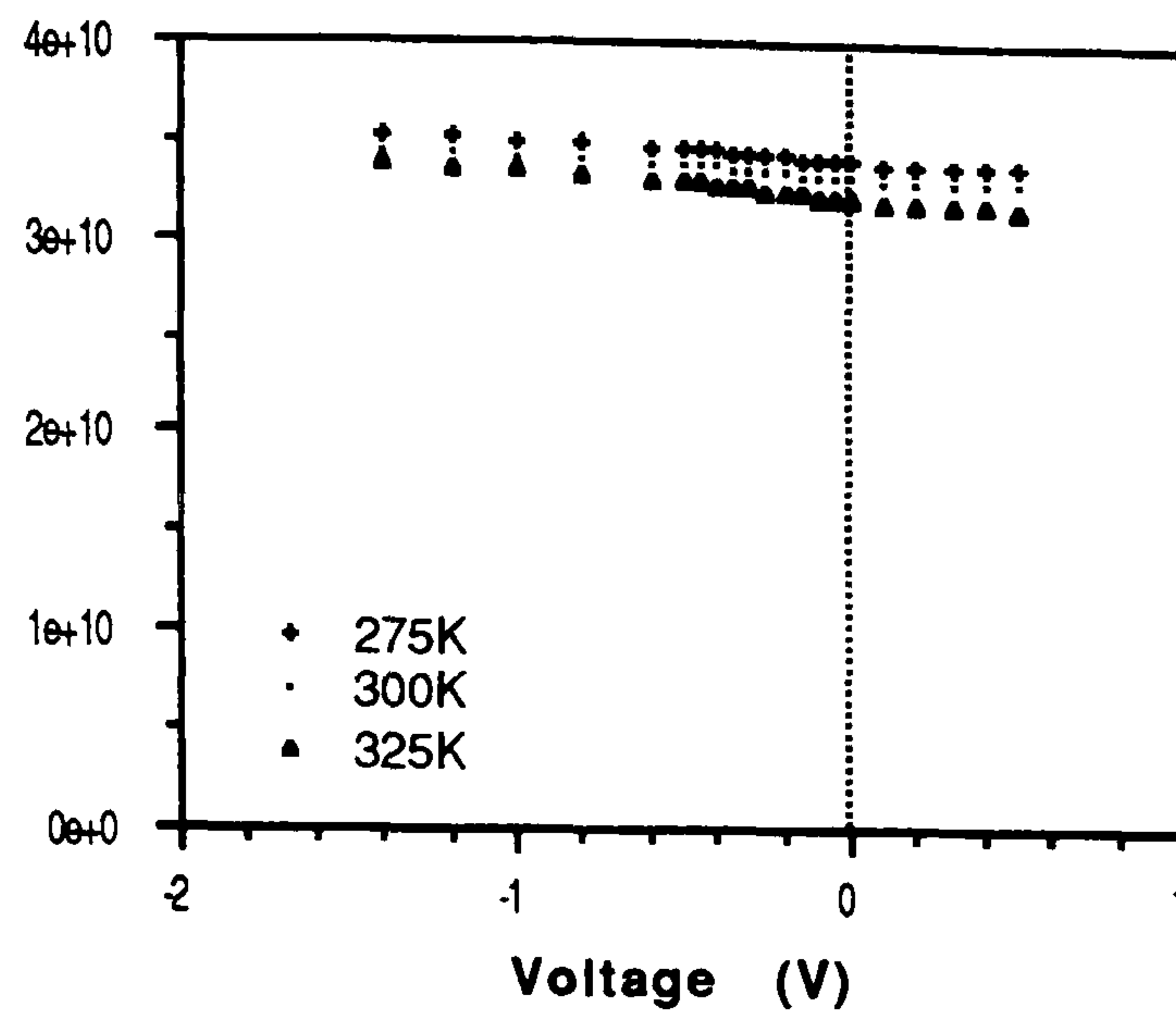


Figure 9.25 — C^{-2} vs V characteristic of a co-evaporated CdS/ CdTe:Cl₂ cell.

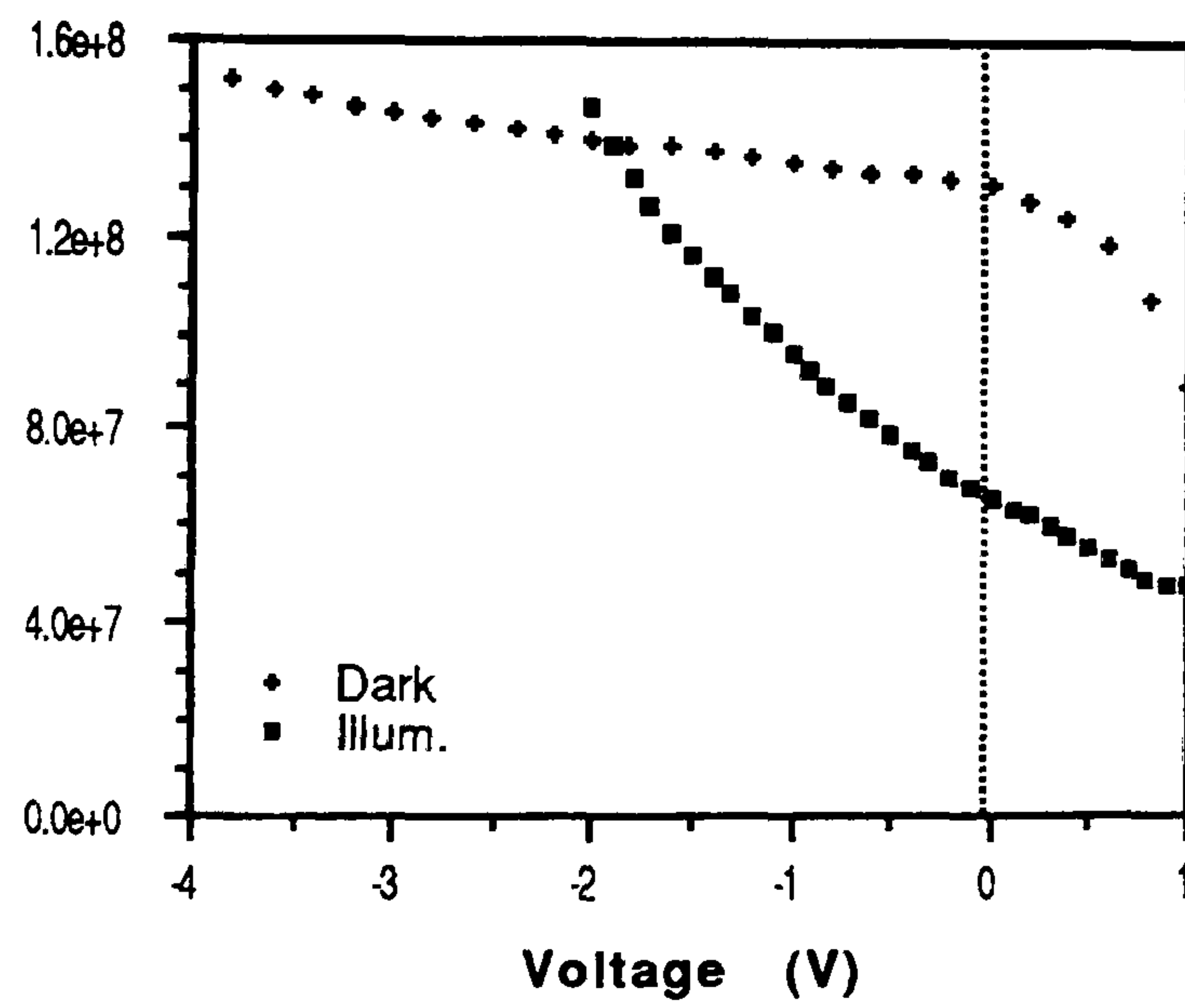


Figure 9.26 — C^{-2} vs V characteristic of BP contacted pre-doped CdS/CdTe: CdCl₂ (0.1%) cell.

9.7 Conclusion.

A range of p-CdTe/n-CdS cells have been produced by the sequential deposition of CdTe and CdS on ITO/glass substrates using vacuum evaporation. Illuminated I-V characteristics showed low J_{sc} , V_{oc} , and, FF, resulting in very low cell efficiencies. This was attributed to;

- i - the poor junction interface (i.e. high concentration of interface states),
- ii - layer quality (i.e. low grain size with poor columnar structure and high concentration of pin-holes due to poor growth),
- iii - the high resistivities of the CdTe and CdS layers.

Due to the high electron affinity of the CdTe, no simple metal can be used to make an ohmic contact to it. The use of Au as a contact metal resulted in saturation of the characteristics in the first quadrant of the I-V curve, indicating the formation of back-to-back Schottky diodes between the device and contact interface region respectively (i.e. conduction band at the interface bends downwards due to the high electron affinity of the CdTe). A thin layer of Cu was deposited onto CdTe before the Au in an attempt to make a tunneling contact. Au/Cu contacts did not noticeably improve the cell efficiency although values of J_{sc} were slightly increased. The effect was less than might be expected due possibly to pin-holes resulting in leakage currents.

The use of CdCl₂ doping achieved by pre-doping, co-evaporation and dipping resulted in improved cell performance. Illuminated I-V characteristics had a better shape which resulted in higher FF values. Best efficiencies were obtained from the CdS/CdTe:CdCl₂(0.1%) cells produced using the pre-doping method, which probably resulted in more uniform doping. However, the preparation conditions of the pre-doping method; namely concentration of CdCl₂, synthesis temperature and duration, seemed to play a very important role. Co-evaporation of CdCl₂ during growth also yielded improved illuminated characteristics, but growth control was difficult. The dipping method (i.e. dipping into CdCl₂/Methanol solution) showed the same improvement in illuminated I-V curves. Nevertheless, the concentration of the CdCl₂ in the methanol solution, solution temperature, and dipping time have to be optimised in an attempt to produce better cells with higher efficiencies.

Spectral response characteristics displayed short and long wavelength cut-offs that agreed with the absorption edges of the CdS and CdTe respectively. The response indicated that the depletion layer width was mostly inside the CdTe.

Normal incidence transmission spectra of the cell showed a smooth cut off at the CdTe band edge (i.e. ~ 820 nm) giving rise to a percentage transmission (i.e. $\sim 75\%$). Percentage transmission decreased steadily at wavelengths above 1000 nm, due mainly to the strong absorption occurring in the ITO. The percentage of solar irradiation (i.e. AM1.5) that would be transmitted into the CdTe through the glass/ITO/CdS was estimated to be 86% in the range of 500–825 nm.

In conclusion, it should be pointed out that a major reason for the low efficiencies of the cells was probably the relatively high density of pin-holes, resulting in high J_o , and low FF values. Hence, there appear to be serious problems with vacuum evaporation and this will need to be improved in future work and the causes of pin-hole formation has to be identified and eliminated. Clearly, much greater study of the relationship between layer quality and growth conditions is required.

9.8 References.

1. B.M.Basol, "Method of forming ohmic contacts.", U.S.Patent 4 456 630, (1984).
2. B.M.Basol, Int.J.Solar Energy, **12** (1992) 25.
3. G.W.Awan, A.W.Brinkman, G.J.Russell, J.Woods, 7th European Photovoltaics Conference, Seville, Spain (1986).
4. S.P.Albright, V.P.Singh, J.F.Jordon, Solar Cells, **24** (1988) 43.
5. J.W.Bowron, S.D.Damaskinos, A.E.Dixon, Solar Cells, **31** (1991) 159.
6. M.Roy, J.E.Phillips, Proc.of 21th IEEE Photovoltaic Specialist Conf. (1990) 743.
7. J.Britt, C.Ferekides, Appl.Phys.Lett., **62** (1993) 2851.

Chapter X

Conclusion.

10.1 Introduction.

The aim of the work reported in this thesis has principally been concerned with the characterisation of CdTe and CdS thin films and the photovoltaic properties of p-CdTe/n-CdS solar cells based on polycrystalline thin film and bulk single crystal CdTe substrates. Particular attention was paid to optimisation of the thin films grown by vacuum evaporation onto glass substrates.

10.2 Thin Film Characterisation.

10.2.1 Optical properties.

Optical constants of both CdTe and CdS layers were determined by the Swanepoel procedure [1] from the transmission spectra. Film thickness was also determined using α -step, graphical (Swanepoel), interference fringe, and multiple beam methods. The graphical method appeared to be the most appropriate, since the fringe index was also obtained as well as film thickness.

In CdTe thin films, transmission virtually ceased at wavelengths less than 832 nm, due to inter-band transitions occurring in the material. At slightly longer wavelengths ($1.02 < \lambda < 2.5$, λ in μm)-often referred to as the region of weak absorption- sharp distinct interference fringes due to the parallel interfaces of the layer were observed. Refractive index, n_f values were found to be in good agreement with those for bulk single crystal CdTe, confirming that the method was appropriate and also that the layers were quite uniform in thickness. Dispersion in the refractive index was well fitted by the quadratic first-order Cauchy equation (i.e. $n_f = a\lambda^{-2} + b$). There was also some absorption at long wavelengths ($2.5\mu\text{m} < \lambda$) giving rise to a reduction in transmission. This could have been due to scattering at grain boundaries or at structural imperfections, or surface scattering due

to surface roughness. It was concluded that the effects of free carrier absorption and reflection were negligible, since the layers were slightly *p-type*.

The optical bandgap, E_g (in as-grown layers) was found to be 1.53 eV corresponding to allowed direct transitions. The Urbach constant, E_o , was estimated to be 18.9 meV, somewhat below the room temperature theoretical value (i.e. 25 meV). The values of the real and imaginary parts of the dielectric constant were obtained from the optical constants and found to be 7.3 and 1.6×10^{-2} at a wavelength of about $2.5 \mu\text{m}$ respectively. The as-grown layers were quite highly resistive.

Heat treatment of layers (i.e. at 400°C for about 30 min in air) produced a remarkable change in their transmission spectrum. The absorption edge was much sharper and had shifted to a wavelength of $0.84 \mu\text{m}$. This may have been result of changes in grain size or stoichiometry due to the preferential loss of Cd, resulting in the formation of shallow oxygen-related acceptor levels, which was not well understood. The bandgap energy, E_g , was shifted by about 20 meV to 1.51 eV. There was also some additional absorption occurring near the band edge of unknown origin.

CdCl_2 *dipped* layers showed similar transmission characteristics to the heat treated layers. Refractive index values were in reasonable agreement with bulk single crystal CdTe. E_g was found to be 1.51 eV which was identical to bulk single crystal CdTe and heat treated CdTe films. However, the layers grown using Cl_2 -*predoped* starting CdTe material showed a progressive increase in absorption as the wavelength approached the band edge. This was attributed to the effects of Cl_2 associated centres, mainly $\text{Cl}-V_{\text{Cd}}$ vacancy complexes. It is also possible that pre-doped films were not as dense and that the transmission spectra were therefore affected by scattering and transmission through pin-holes. E_g was found to be 1.45 eV. Table 10.1 tabulates n_f , E_g , and, ΔE_g values (i.e. compared to an as-grown layer) of the CdTe thin layers.

Normal incidence transmission of as-grown CdS layers showed a smooth cut-off at the CdS band edge ($\lambda=0.53 \mu\text{m}$), and interference fringes due to the parallel interfaces were clearly seen in the spectra. No additional longwave absorption was observed. Heating the layers in an Ar atmosphere did not show any change in transmission. The refractive index of as-grown CdS layers was also found to

follow the first order Cauchy equation, $n_f = 5.73 \times 10^{-2} \lambda^{-2} + 2.1$, (λ in μm). E_g was found to be 2.42 eV which is very close to the bulk single crystal CdS. The Urbach constant, E_o , was calculated to be 50.3 meV, somewhat above the room temperature theoretical value.

Sample Type	$n_f(\lambda)^*$	$E_g(\text{eV})$	$\Delta E_g(\text{meV})$
As-grown	$0.16 \lambda^{-2} + 2.66$	1.53	–
Heat Treat.	$0.18 \lambda^{-2} + 2.67$	1.51	20
Cl ₂ -dipp.	$0.17 \lambda^{-2} + 2.63$	1.51	20
Cl ₂ -pred.	$0.23 \lambda^{-2} + 2.66$	1.45	80

Table 10.1 — n_f , E_g , and, ΔE_g values of CdTe thin layers. * Least-squares fitting in the region of weak absorption, λ measured in μm .

10.2.2 Structural properties.

XRD spectra of as-grown CdTe thin films showed diffraction peaks at Bragg angles, θ_B , associated with corresponding planes of cubic CdTe. However, some low intensity additional peaks were present but could not be identified, conclusively, although they may have been due to excess Te. The lattice parameter of cubic CdTe value, a_o , was calculated to be 6.48 Å which was in good agreement with the bulk single crystal CdTe value. Grain sizes of the as-grown CdTe thin layers were found to be ~ 78 nm, from the net broadening in the $\{111\}$ diffraction line. Although there was high degree of scatter in the the grain size values at low substrate temperatures, the grain size did show a maximum at a substrate temperature of about 215°C, above which the grain size decreased.

Heat treated CdTe thin layers showed a dramatic change in the XRD spectra. The intensity of the $\{111\}$ diffraction line increased probably due to grain growth, resulting in a greater degree of preferred ordering. In addition, there were peaks associated with the $\{422\}$ planes of cubic CdTe, and others which could be attributed to pure Te or TeO₂. The latter was probably due to oxygen reacting with chemi-absorbed residual free Te (i.e. from the growth) or with Te “liberated” from

the dissociation of CdTe during annealing. No diffraction peaks attributable to Cd or Cd oxides were observed, suggesting that desorption of Cd atoms/or molecules occurred during annealing.

Grain sizes in the heat treated layers were found to be larger than in the as-grown layers (i.e. 20% higher) confirming that grain growth occurred during heat treatment in air. It was possible that grain growth was more accelerated in the presence of oxygen due to some surface reaction with chemi-absorbed species. The effects of the heat treatment of Cl₂ doped layers were found to be identical to those of undoped heat treated layers. In fact, the grain sizes in former may have been higher due to the limitations of the method (i.e. max measurable grain size is about 0.1 μm). Annealing of the CdTe layer co-evaporated with CdCl₂, showed that the layer has CdCl₂ and TeCl₂ compounds additional to CdTe.

XRD spectra of as-grown CdS thin layers showed only two principal peaks which corresponded to diffraction from the {0002} (sharper) and {0004} (smaller) planes of hexagonal CdS, confirming that these layers were {0002}-preferred orientation. The intensity of this peak increased with heat treatment (i.e. 300°C for about 15 min in N₂) implying that the degree of preferred orientation also increased. This may have been due to re-crystallisation effects and probably to changes in the layer stress. No observable changes were found in the grain sizes of the heat treated CdS layers.

RHEED patterns from the surfaces of as-grown CdTe layers, grown at substrate temperatures $\geq 180^\circ\text{C}$ had a random polycrystalline texture although with some evidence of weak {111}-preferred orientation. Whereas layers grown at substrate temperatures $\leq 170^\circ\text{C}$ had a distinct {111}-preferred orientation (i.e parallel to the substrate) which was stronger at the lower growth temperatures. RHEED patterns of the heat treated layers were almost identical to those of as-grown {111}-oriented layers, except that an additional arc, located above {111} arc appeared. This could be associated with either Te or TeO₂.

The polycrystalline nature and the preferred orientation of {0002} planes of CdS thin layers were also confirmed by RHEED. RHEED patterns of CdS thin layers deposited on ITO/glass substrates were {0002}-preferred orientation, but the arcs were more diffuse, indicating that the sample surface was flatter.

Both CdTe and CdS layers displayed columnar growth with the growth axis tilted at angles of about $\sim 15^\circ$, and $\sim 5^\circ$ to the substrate normal, respectively. CdTe thin layers showed a smooth surface with distinct pin holes of about $2\mu\text{m}$ in diameter. However, surface micrographs of CdTe:Cl₂ (by co-evaporation) thin layers showed that the surface consisted of larger grains confirming that grain growth occurred during deposition by incorporation of Cl₂ molecules but also larger pores giving rise to a much rougher surface. For the CdCl₂-dipped layers, the distribution of CdCl₂ was also not uniform over the surface. CdS thin layers exhibited smooth surfaces with no observable pin holes at least on the scale of about $1\mu\text{m}$. EDAX scans also confirmed that CdTe and CdS thin film layers comprised only Cd and Te, and, Cd and S respectively.

Impurity depth profiling was carried out using SIMS and showed that elements such as, Si, Na, Cl, Al, Cu, Cr, and K were present in the layers. These may have originated from the glass substrate and/or from desorption off the surfaces of hotter growth fixtures, such as the crucible etc.

10.2.3 Electrical properties.

The as-grown CdTe layers were of high p-type resistivity (i.e. $\rho \cong 10^8 \Omega\text{-cm}$) and several post-growth and/or doping procedures were tried in attempts to increase the conductivity. Air heat treated layers resulted in a more pronounced Seebeck effect possible due to oxygen-related Cd vacancy formation. Attempts at acceptor doping with Sb produced layers that were either of high or of very low conductivity suggesting the formation of metallic precipitates. Au contacts to CdTe showed ohmic behaviour but with high contact resistance.

In view of the high electron affinity of CdTe, it proved necessary to use a high diffusivity acceptor impurity such as Cu to form a p^+ layer under the Au contact. The resistivity of Cl₂ dipped thin layers was not significantly less than heat treated undoped films, suggesting that it was the heat treatment process that was most important.

Table 10.2 tabulates the resistivity and Hall effect results for the CdTe thin layers doped by co-evaporation with Sb and CdCl₂ respectively.

Temperature dependent Hall measurements showed that the mobility could be explained in terms of the grain boundary trapping model proposed by Seto, in which carrier transport is considered to be dominated by grain boundary scattering.

Positron trapping experiments showed that post-growth annealing in air lead to a reduction in the divacancy concentration, although this procedure was less effective in reducing the divacancy concentration for the CdCl₂ dipped layers.

Sample Type	$\rho(\Omega\text{-cm})$	$R_H(\text{cm}^3\text{C}^{-1})$	$\mu_H(\text{cm}^2\text{V}^{-1}\text{s}^{-1})$	$p(\text{cm}^{-3})$
CdTe:Sb	48	1.3×10^3	27.1	4.8×10^{15}
CdTe:Cl ₂	1.8	6.5×10^1	27.2	9.6×10^{16}

Table 10.2 — Resistivity and Hall effect results for CdTe thin layers doped with Sb and Cl₂.

As-grown CdS layers exhibited relatively low resistivities (i.e. 10^2 – 10^3 $\Omega\text{-cm}$). The introduction of In during deposition yielded very low resistivities, up to 3 orders of magnitude below comparable undoped layers. Activation energies were calculated using the grain boundary trapping formalism. Table 10.3 tabulates the resistivity and Hall effect results for the undoped and In doped CdS thin layers.

Sample Type	$\rho(\Omega\text{-cm})$	$R_H(\text{cm}^3\text{C}^{-1})$	$\mu_H(\text{cm}^2\text{V}^{-1}\text{s}^{-1})$	$n(\text{cm}^{-3})$
Undoped CdS	212	4.8×10^2	2.3	1.3×10^{16}
Doped CdS:In	0.12	6.5×10^{-1}	5.4	9.7×10^{18}

Table 10.3 — Resistivity and Hall effect results for undoped and In doped CdS thin layers.

10.3 Solar Cell Characterisation.

Although the photovoltaic properties of *thin film* p-CdTe/n-CdS cells were the priority research, bulk single crystal p-CdTe/n-CdS cells were also investigated in an attempt to obtain a basic understanding of the cell performance.

10.3.1 Bulk single crystal cell characterisation.

Dark I-V characteristics of undoped cells exhibited good diode behaviour with low J_o and high rectification ratios. The deviation at higher current levels was due mainly to the relatively high bulk resistance of the CdTe layer, and Au or (Au/P)/CdTe interface states. The cell with the Au/P contact seemed to have a higher series resistance resulting in the earlier onset of saturation compared to the cell with the Au contact only.

Temperature dependent I-V characteristics showed that forward bias currents were fairly parallel between the voltage range 0.2–0.4V where after the series resistance was dominant. Although these results suggested that current transport was most probably controlled by tunneling mechanisms, both $\log(J_o)$ vs T and $\log(J_o)$ vs T^{-1} characteristics showed straight line temperature dependencies respectively. This was difficult to explain but may be associated with the high series and bulk resistances. The temperature activation energies of the cells with Au and Au/P contact were found to be 0.39 eV and 0.32 eV respectively.

Illuminated I-V characteristics displayed relatively poor photovoltaic performance resulting in low conversion efficiencies. Although the presence of a p^+ layer should have led to an ohmic tunneling contact, with a low voltage drop across it, the poor value of FF gave a clear indication that the resistivity of the bulk was quite high. The higher values of J_{sc} and V_{oc} of the cells with Au/P contact could be attributed to back-surface field effects at the contact/CdTe interface, although the dark I-V characteristics were more resistive.

C^{-2} vs V characteristics were bowed indicating that the occupancy of interface levels was changing and would influence estimates of carrier concentration made from the slope of the characteristics. Nevertheless, it did indicate an abrupt junction. Although, V_i , and, W_o , obtained from C-V measurements gave reasonable values, acceptor densities (employing one-sided junction approximation) yielded relatively low values, reflecting the high bulk resistance of the CdTe.

The series and shunt resistance of the cells are tabulated in Table 10.4. The R_s values of undoped cells with Au and Au/P gave values that varied with the

illumination intensity. This indicated a significant photoconductivity contribution to R_s (i.e. photodoping).

Sample Type	R_s (dark;illum.)	R_{sh} (dark;illum.)
Au/CdTe	1.9×10^1 ; 1.2	9.2×10^5 ; 4.2×10^2
Au/P/CdTe	1.2×10^2 ; 4.5	1.9×10^5 ; 6.5×10^2

Table 10.4 — R_s and R_{sh} resistance results (i.e., in Ohm, normalized to a unit area of 1cm^2) obtained from the dark and illuminated I–V characteristics.

10.3.2 Polycrystalline thin film cell characterisation.

p-CdTe/n-CdS cells were produced by sequential deposition of CdS and CdTe onto ITO/glass substrates using vacuum evaporation. Illuminated I–V characteristics exhibited very poor cell performance (i.e. low I_{sc} , V_{oc} , and, FF). This may have been due to:

- i- poor junction interface,
- ii- layer quality (i.e. low grain size with poor columnar growth and presence of pin holes),
- iii- highly resistive CdTe and CdS layers.

J_o was, in general quite high and varied linearly with increasing reverse voltage confirming the presence of leakage currents probably through the pin-holes. Although Au seemed to make an ohmic contact to the CdTe, saturation occurred in the first quadrant of the I–V characteristics, indicating the formation of a back-to-back Schottky diode between the device depletion and contact interface regions. This was a direct consequence of the high electron affinity value of the p-CdTe. A thin layer of Cu was deposited onto the CdTe before deposition of the Au in an attempt to make a tunneling contact. However, the Au/Cu contact did not noticeably improve the illuminated I–V characteristics, although J_{sc} increased slightly. It is possible that the Cu was diffusing through the pin-holes in the CdTe, resulting in leakage currents.

The use of CdCl_2 in the post-growth doping and pre-doping processes resulted in a slightly changed cell performance. Illuminated I-V characteristics were slightly bowed rather than linear (i.e. usually seen in undoped cells) resulted better FF values. Best cell efficiencies were obtained from the n-CdS/p-CdTe: Cl_2 (0.1%) cells due probably to the more uniform doping. However, growth parameters for the pre-doping method, such as; concentration of CdCl_2 , synthesis temperature and the way of mixturing seemed to be very important. Co-evaporation of CdTe with CdCl_2 during growth also yielded a slight change in cell performance. Reproducibility was quite a problem due to the poor control of growth. The dipping method (i.e. into CdCl_2 /Methanol solution) gave improved illuminated I-V characteristics, resulting in slightly better cell efficiencies, compared to undoped cells. Nevertheless, the concentration of CdCl_2 in the methanol, the solution temperature, and dipping time have to be optimised in attempt to produce better cells with higher efficiencies.

Table 10.5 and Table 10.6 tabulates the junction and solar parameters of a bulk single crystal and a thin film CdTe cells in dark and under illumination respectively.

Sample Type	n	$J_o(\text{A/cm}^2)$	Recf.Factor	R_s	R_{sh}
Bulk SX CdS/CdTe [†]	2.4	2.9×10^{-7}	4103	1.2×10^2	1.9×10^5
Thin Film CdS/CdTe: Cl_2 (0.1%)*	2.4	2.9×10^{-8}	10.8	8.1×10^4	1.2×10^6

Table 10.5 — Junction parameters of undoped bulk single crystal and Cl_2 doped thin film n-CdS/p-CdTe cells, R_{sh} and R_{sh} are in Ohm and were normalized to a unit area of 1cm^2 .

Sample Type	$J_{sc}(\text{A/cm}^2)$	$V_{oc}(\text{V})$	FF	$\eta(\%)$	R_s	R_{sh}
Bulk SX CdS/CdTe [†]	1.3×10^{-2}	0.510	0.42	3.1	4.5	6.5×10^2
Thin Film CdS/CdTe: Cl_2 (0.1%)*	1.3	0.426	0.31	0.2	5.8×10^2	6.4×10^4

Table 10.6 — Solar cell parameters for undoped bulk single crystal and Cl_2 doped thin film n-CdS/p-CdTe cells under illumination of $\sim 90\text{mW/cm}^2$, R_{sh} and R_{sh} are in Ohm and were normalized to a unit area of 1cm^2 , * pre-doped.

Sample Type	$J_{sc}(\text{A/cm}^2)$	$V_{oc}(\text{V})$	FF	$\eta(\%)$
Bulk SX CdS/CdTe [†]	1.4×10^{-2}	0.520	0.53	4.1
Thin Film CdS/CdTe:Cl ₂ (0.1%)*	1.0×10^{-2}	0.538	0.37	2.1

Table 10.7 — Photovoltaic potential of undoped bulk single crystal and Cl₂ doped n-CdS/p-CdTe cells after eliminating of R_s and R_{sh} resistances (i.e. $R_s \rightarrow 0$ and $R_{sh} \rightarrow \infty$), [†] (Au/P) contacted, * pre-doped BP contacted.

The spectral response displayed short and longwavelength cut-offs in agreement with the absorption edges of the CdS and CdTe respectively, and also indicated that the depletion layer width was mostly inside the CdTe.

Normal incidence transmission spectra of the cell showed a smooth cut off at the CdTe band edge (i.e. $\sim 0.83\mu\text{m}$). Progressive reduction in transmission above the wavelengths of $1\mu\text{m}$ was due mainly to absorption occurring in ITO. Percentage AM1.5 irradiation getting into the CdTe through ITO/CdS on glass substrate was calculated between CdS and CdTe band edges to be 86%.

10.4 Final Conclusion and Future Work.

It is evident from this study that in order to produce evaporated thin film p-CdTe/n-CdS solar cells, the quality of the CdTe film and the back contact resistance must be improved. In principle, it has been shown that the reduction of series and shunt resistance would lead to a significant increase in efficiency, without necessarily requiring any improvement in the junction per se. In practice better layer quality would probably result in superior junction performance as well, leading to even greater gains in the efficiency.

One of the main problems with the CdTe layer has been the presence of pinholes resulting in high current leakage due to short circuit path that form between the contact and the CdS layer. Clearly future work must address this aspect of the evaporation procedures, possibly by investigating the use of baffles in the CdTe source, and outgassing procedure, shuttering arrangements etc. Additional work

will also be required to refine doping procedures and in particular to determine why CdCl_2 dipping process seems to be relatively ineffective in evaporated films.

The back contact to the CdTe layer is a longstanding problem. A variety of etching procedures have been detailed in the literature and the applicability of some of these, to evaporated thin film, clearly needs further study. Of interest would be a detailed investigation of the use of sequential oxidizing and reducing treatments prior to deposition of the contact. Coupled with this should be a systematic study of the use of acceptor dopants, e.g., Cu and P, to form the p^+ layer. This alone would result in a significant reduction in losses due to R_s , with a corresponding increase in the efficiency. Alternatively heterogeneous contacts (e.g., p-ZnTe, HgTe) might also provide an important way of reducing contact resistance, although at the expense of increased complexity.

In conclusion, although the efficiencies achieved in this study have been lower than hoped for, nevertheless it is felt that some of the principal problem areas have been determined and possible ways of resolving these difficulties identified. There seems to be no *a-priori* reason for supposing that high efficiency evaporated thin film p-CdTe/n-CdS cells should not be realised in the near future.

Appendix A

Determination of Optical Constants Using Transmission Spectrum Only.

A.1 Introduction

The complex refractive index, n_c and absorption coefficient, α are usually determined by elaborate computer iteration procedures [1,2,3] using both the transmission and reflection spectra. A straight forward method proposed by Swanepoel [4] was used here in order to calculate the optical constants and the thickness of the layer from the interference fringes of the transmission spectrum. Two methods making use of transmission spectrum only are discussed to calculate, n_c , α and film thickness, d ; namely for a layer of uniform thickness and for a layer of varying thickness.

A.2 Method 1. Flat Film Analysis.

A.2.1 Calculation of $n_c(\lambda)$ and $\alpha(\lambda)$.

The practical situation for a thin film on a transparent substrate is shown in Fig.A.1. The film has thickness, d and complex refractive index, $n_c = n_f - ik_f$ where, n_f is the refractive index and, k_f is the extinction coefficient which can be expressed in terms of the absorption coefficient, α_f , $k_f = \alpha_f \lambda / 4\pi$, and where the subscript “ f ” indicates the film. The transparent substrate has a thickness several orders of magnitude larger than, d and has index of refraction, n_s and absorption coefficient $\alpha_s \cong 0$ in the spectral region to be examined.

Considering the thick substrate alone in the absence of a film, the interference-free transmission is given by the well-known expression as;

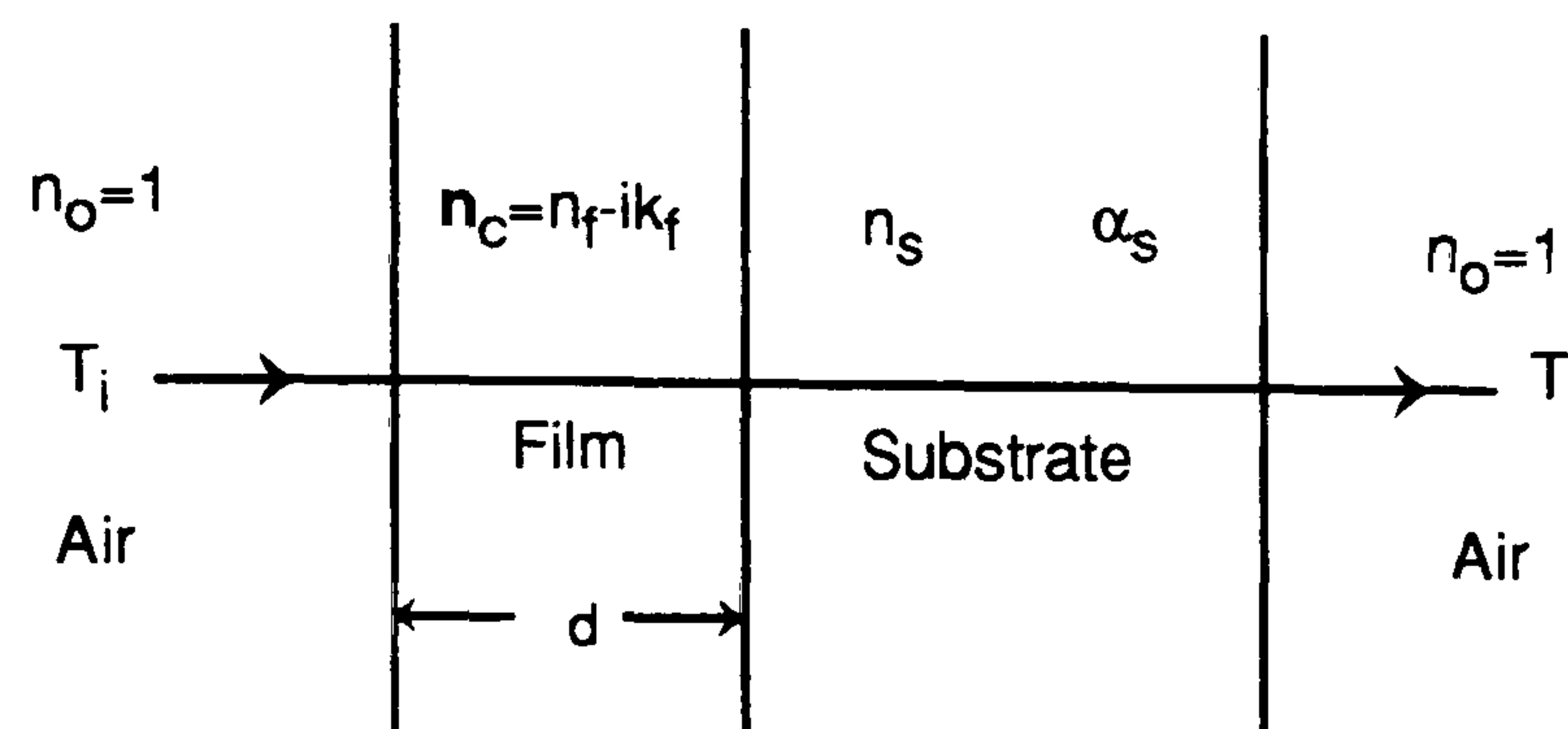
$$T_s = \frac{(1 - R_s)^2}{1 - R_s^2} \quad A1.1$$

where,

$$R_s = \left[\frac{n_s - 1}{n_s + 1} \right]^2 \quad \text{or} \quad T_s = \frac{2n_s}{n_s^2 + 1} \quad A1.1a$$

and,

$$n_s = \frac{1}{T_s} + \left[\frac{1}{T_s^2} - 1 \right]^{1/2} \quad A1.2$$



A.1 Schematic diagram for a system consisting of an absorbing thin film on a thick finite transparent substrate.

The basic equation for the formation of interference fringes due to phase changes in a plane wave propagating through a substrate of thickness, d is;

$$2 n_s d = m \lambda \quad A1.3$$

where, m is an integer for maxima and half integer for minima. Eq. A1.3 contains information on the product of n and d and there is no way of obtaining either, n_s or, d separately. The transmission, T , for a system composed of an absorbing film on a thick finite transparent substrate such as shown in Fig.A.1 is a complex function given by;

$$T = T(\lambda, n_s, n_f, d, \alpha_f) \quad A1.4$$

and can be expressed for a finite transparent substrate by;

$$T = \frac{A'x}{B' - C'x + D'x^2} \quad A1.5$$

where,

$$A' = 16n_s(n_f^2 + k_f^2) \quad A1.5a$$

$$B' = [(n_f + 1)^2 + k_f^2][(n_f + 1)(n_f + n_s^2) + k_f^2] \quad A1.5b$$

$$C' = [(n_f^2 - 1 + k_f^2)(n_f^2 - n_s^2 + k_f^2) - 2k_f^2(n_s^2 + 1)]2\cos\varphi \\ - k_f[2(n_f^2 - n_s^2 + k_f^2) + (n_s^2 + 1)(n_f^2 - 1 + k_f^2)]2\sin\varphi \quad A1.5c$$

$$D' = [(n_f - 1)^2 + k_f^2][(n_f - 1)(n_f - n_s^2) + k_f^2] \quad A1.5d$$

$$\varphi = 4\pi n_f d / \lambda \quad A1.5e$$

$$x = \exp(-\alpha_f d) \quad A1.5f$$

$$k_f = \alpha_f \lambda / 4\pi \quad A1.5g$$

The absorbance for such a system is given in terms of the interference-free transmission, T_α , by;

$$x = \frac{P + [P^2 + 2QT_\alpha(1 - R_2R_3)]^{1/2}}{2T_\alpha(R_1R_2 + R_1R_3 - 2R_1R_2R_3)} \quad A1.6$$

where,

$$P = (R_1 - 1)(R_2 - 1)(R_3 - 1) \quad A1.6a$$

$$R_1 = [(1 - n_f)/(1 + n_f)]^2 \quad A1.6b$$

$$R_2 = [(n_f - n_s)/(n_f + n_s)]^2 \quad A1.6c$$

$$R_3 = [(n_s - 1)/(n_s + 1)]^2 \quad A1.6d$$

In the case of an infinite transparent substrate, the transmission, T , is given by;

$$T = \frac{A''}{B'' - C''x + D''x^2} \quad A1.7$$

where,

$$A'' = 16n_s(n_f^2 + k_f^2) \quad A1.7a$$

$$B'' = [(n_f + 1)^2 + k_f^2][(n_f + n_s)^2 + k_f^2] \quad A1.7b$$

$$\begin{aligned} C'' &= [(n_f^2 - 1 + k_f^2)(n_f^2 - n_s^2 + k_f^2) + 4k_f^2n_s]2\cos\varphi \\ &= -k_f[2(n_f^2 - n_s^2 + k_f^2) + 2n_s(n_f^2 - 1 + k_f^2)]2\sin\varphi \end{aligned} \quad A1.7c$$

$$D'' = [(n_f - 1)^2 + k_f^2][(n_f - n_s)^2 + k_f^2] \quad A1.7d$$

The transmission spectrum for a dielectric (or semiconducting) film can be roughly divided into three regions (see Fig.A.2). In the transparent region $\alpha_f \rightarrow 0$, and the transmission is determined by n_f and n_s through the multiple reflections. In the region of weak absorption, transmission decreases slightly due to the effect of non-zero α_f . In the region of strong absorption, the transmission decreases drastically and is dominated by α_f . At all wavelengths in the spectrum, $k_f^2 \ll n_f^2$. Hence Eq.A1.5 becomes;

$$T \cong \frac{Ax}{B - Cx \cos \varphi + Dx^2} \quad A1.8$$

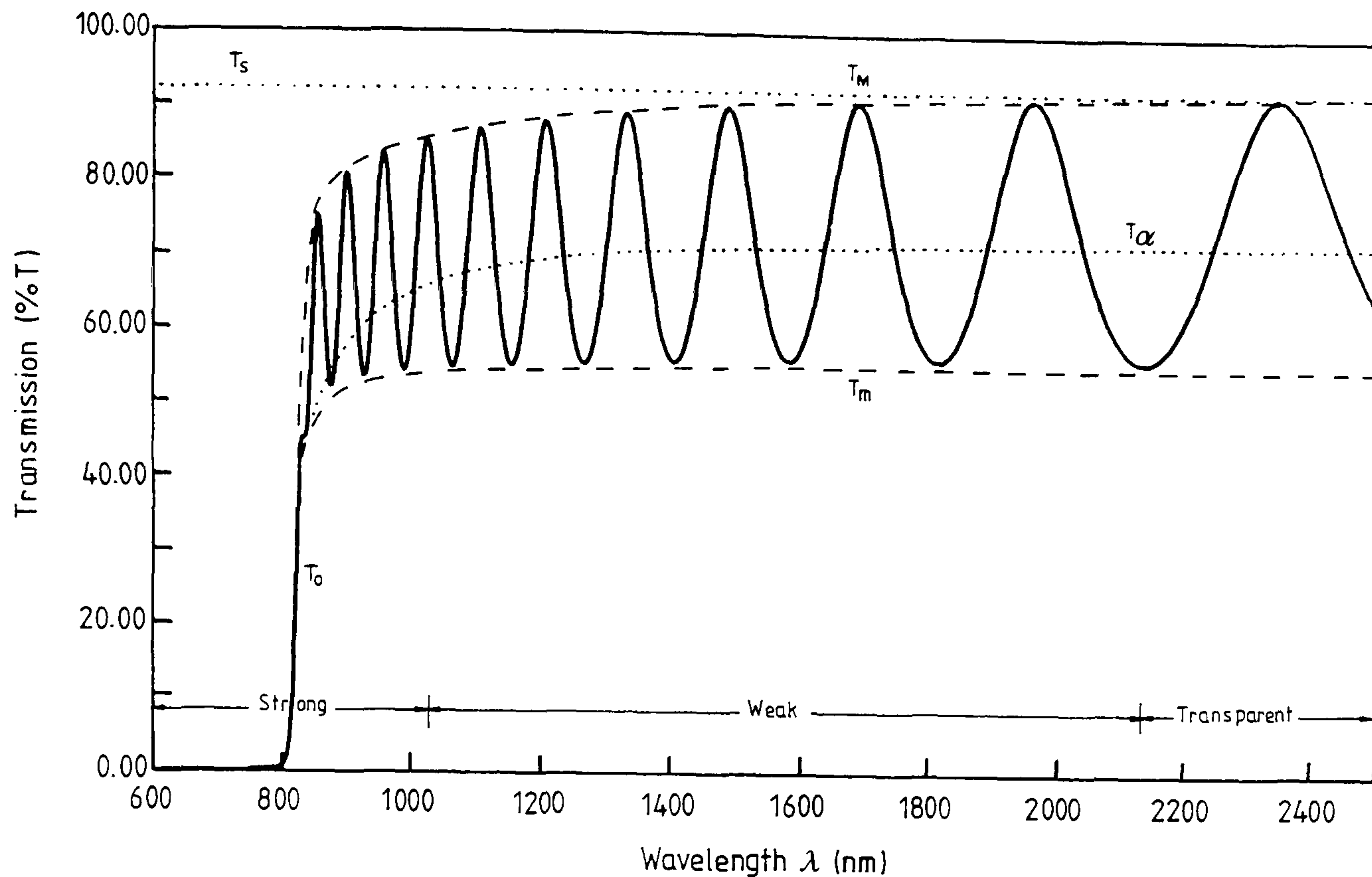
where,

$$A = 16n_f^2n_s \quad A1.8a$$

$$B = (n_f + 1)^3(n_f + n_s^2) \quad A1.8b$$

$$C = 2(n_f^2 - 1)(n_f^2 - n_s^2) \quad A1.8c$$

$$D = (n_f - 1)^3(n_f - n_s^2) \quad A1.8d$$



A.2 Transmission spectrum for a dielectric (or semiconducting) thin layer on a glass substrate.

The interference extrema are given from the Eq.A1.8 by the conditions $\cos \varphi = \pm 1$ for maxima and minima respectively, i.e;

$$T_M = \frac{Ax}{B - Cx + Dx^2} \quad A1.9$$

$$T_m = \frac{Ax}{B + Cx + Dx^2} \quad A1.10$$

In further analysis, T_M and T_m will be considered as if they were **continuous** functions of wavelength and thus of $n_f(\lambda)$ and $x(\lambda)$, i.e the envelope functions. For any wavelength T_M has a corresponding value of T_m .

A.2.2 Transparent Region.

In the transparent region, $\alpha_f \rightarrow 0$, i.e. $k_f \rightarrow 0$ or $x \rightarrow 1$. Substituting the Eq.A1.8a–A1.8d into Eq.A1.9 yields;

$$T_M = \frac{2n_s}{n_s^2 + 1} \quad A1.11$$

Eq.A1.11 is identical to Eq.A1.1b and the maxima of the interference fringes are a function of n_s only and coincide with T_s . Where the maxima depart from T_s , denotes the onset of absorption. Eq.A1.11 can be used to calculate n_s in the transparent region using the form of Eq.A1.2. Substituting Eq.A1.8a–A1.8d in Eq.A1.10 for $x = 1$ yields;

$$T_m = \frac{4n_f^2 n_s}{n_f^4 + n_f^2(n_s^2 + 1) + n_s^2} \quad A1.12$$

Solving the Eq.A1.12 for n_f , the refractive index of the film, yields;

$$n_f = [M + (M^2 - n_s^2)^{1/2}]^{1/2} \quad A1.13$$

where,

$$M = \frac{2n_s}{T_m} - \frac{1 + n_s^2}{2} \quad A1.13a$$

T_m is thus a function of both n_f and n_s , and n_f can be calculated from T_m using Eq.A1.13.

A.2.3 Weak Absorption Region.

In this region, $\alpha_f \neq 0$ and $x < 1$. However, k_f^2 is still much less than n_f^2 and Eq.A1.9 and A1.10 are still valid. Subtracting the reciprocal of Eq.A1.9 from the reciprocal of the Eq.A1.10 yields an expression which is independent of x ;

$$\frac{1}{T_m} - \frac{1}{T_M} = \frac{2C}{A} \quad A1.14$$

Substituting the Eq.A1.8a–A1.8d into Eq.A1.14 solving for n_f yields;

$$n_f = [N + (N^2 - n_s^2)^{1/2}]^{1/2} \quad A1.15$$

where,

$$N = 2n_s \frac{T_M - T_m}{T_M T_m} + \frac{1 + n_s^2}{2} \quad A1.15a$$

Once $n_f(\lambda)$ is known, all the constants in Eq.A1.8a–A1.8d were known and x can be calculated as;

$$x = \exp(-\alpha_f d) = \frac{F - [F^2 - (n_f^2 - 1)^3(n_f^2 - n_s^2)]^{1/2}}{(n_f - 1)^3(n_f - n_s^2)} \quad A1.16$$

where,

$$F = \frac{4n_f^2 n_s}{T_M T_m} (T_M + T_m) \quad A1.16a$$

and x is the attenuation of the incident light. The interference-free transmission, T_α , can be calculated from the interference fringes by integrating Eq.A1.8 between a maximum and an adjacent minimum as;

$$T_\alpha = \frac{1}{\pi} \int_0^\pi \frac{Ax}{B - Cx \cos \varphi + Dx^2} d\varphi \quad A1.17$$

Assuming all parameters are constant in the narrow integration region, the integral yields;

$$T_\alpha = \frac{Ax}{\left[(B - Cx + Dx^2)(B + Cx + Dx^2) \right]^{1/2}} \quad A1.18$$

Substituting Eq.A1.9 and Eq.A1.10 into Eq.A1.18 yields;

$$T_\alpha = \sqrt{T_M T_m} \quad A1.19$$

T_α , is just the geometric mean of T_M and T_m and Eq.A1.19 is a very useful relation. Solving Eq.A1.18 for x gives;

$$x = \frac{\left[G - \left[G^2 - (n_f^2 - 1)^6 (n_f^2 - n_s^2)^2 \right]^{1/2} \right]^{1/2}}{(n_f - 1)^3 (n_f - n_s^2)} \quad A1.20$$

where,

$$G = \frac{128n_f^4 n_s^2}{T_\alpha^2} + n_f^2 (n_f^2 - 1)^2 (n_s^2 - 1)^2 + (n_f^2 - 1)^2 (n_f^2 - n_s^2)^2 \quad A1.20a$$

Eq.A1.20 is equivalent to a well known equation often used in optical and infrared studies. It can also be used to determine n_f from T_α in the transparent region where $\alpha_f = 0$. Putting $x = 1$ in the Eq.A1.20 and solving for n_f gives;

$$n_f = [H + (H^2 - n_s^2)^{1/2}]^{1/2} \quad A1.21$$

where,

$$H = \frac{4n_s^2}{(n_s^2 + 1)T_\alpha^2} - \frac{1 + n_s^2}{2} \quad A1.21a$$

A.2.4 Strong Absorption Region.

In the region of strong absorption, the interference fringes disappear. There is no way of calculating n_f and x independently in this region from the transmission spectrum alone. For large α_f , the three curves, T_M , T_m , and, T_α converge to a single curve T_o and $k_f^2 \ll n_f^2$ still holds. If interference effects are ignored, Eq.A1.8 can be written for $x \ll 1$ as;

$$T = T_o \cong \frac{Ax}{B} \quad A1.22$$

and solving for x yields;

$$x \cong \frac{(n_f + 1)^3 (n_f + n_s^2)}{16n_f^2 n_s} T_o \quad A1.23$$

A.3 Method 2. Variable Film Analysis.

A.3.1 Calculation of $n_f(\lambda)$ and $\alpha_f(\lambda)$.

Inhomogeneties in thin films can have a large influence on the optical transmission spectrum. For a uniform film, the departure of, T_{Mo} , from, T_s , denotes the onset of absorption but in the case of non-uniform film, T_{Md} , approaches, T_s , only in the long-wavelength limit and it decreases consistently with decreasing, λ , even for the case where, $\alpha_f \cong 0$. The refractive index and absorption coefficient of non-uniform films can be calculated by transforming the observed spectrum to the spectrum of a uniform film with the same average thickness, \bar{d} , in the region of weak absorption. This can be done for the envelopes, T'_M , and, T'_m , of the non-uniform film, and the following compact relations (two independent transcendental equation) between the envelopes around the two spectra can be given;

$$T'_M = \frac{(T_{Mo}T_{mo})^{1/2}}{\theta} \tan^{-1} \left[\left(\frac{T_{Mo}}{T_{mo}} \right)^{1/2} \tan \theta \right] \quad A2.1$$

$$T'_m = \frac{(T_{Mo}T_{mo})^{1/2}}{\theta} \tan^{-1} \left[\left(\frac{T_{mo}}{T_{Mo}} \right)^{1/2} \tan \theta \right] \quad A2.2$$

where,

$$\theta = \frac{2\pi n_f \Delta d}{\lambda} \quad \text{and} \quad 0 < \theta < \pi/2 \quad A2.2a$$

Thus the same analysis applied for the layers of uniform thickness (i.e “Flat Film Analysis”) can be now employed with providing the new, T'_M , and, T'_m . The related theory for layers of non-uniform thickness is fully discussed by Swaneopel [5].

A.4 Dispersion Equations for n of an Optical Material.

The two characteristics of an optical material which are of primary interest to the optical device engineers are its transmission, absorbance, and index of refraction, all of which vary with the wavelength of the incident light. The complex refractive index of an optical material is defined as, $n_c = n_f - i k_f$ and is related

to the phase velocity, v , of a plane parallel wave by;

$$v = \frac{c}{n_f} \quad A3.1$$

The index of refraction of an optical material rises markedly at the absorption band edge before decreasing with increasing wavelength. Many investigators have attempted to describe the variation of refractive index with wavelength and several dispersion equations are listed below;

$$\text{Cauchy} \quad n = a + \frac{b}{\lambda^2} + \frac{c}{\lambda^3} + \dots \quad A3.2$$

$$\text{Hartmann} \quad n = a + \frac{b}{(c-\lambda)^{1.2}} \quad A3.3$$

$$\text{Hartmann} \quad n = a + \frac{b}{(c-\lambda)} + \frac{d}{(e-\lambda)} \quad A3.4$$

$$\text{Conrady} \quad n = a + \frac{b}{\lambda} + \frac{c}{\lambda^{3.5}} \quad A3.5$$

$$\text{Kettler-Drude} \quad n^2 = a + \frac{b}{(c-\lambda^2)} + \frac{d}{(e-\lambda^2)} + \dots \quad A3.6$$

$$\text{Sellmeier} \quad n^2 = a + \frac{b\lambda^2}{(c-\lambda^2)} + \frac{d\lambda^2}{(e-\lambda^2)} + \dots \quad A3.7$$

$$\text{Hertzberger} \quad n = a + b\lambda^2 + \frac{e}{(\lambda^2-0.035)} + \frac{d}{(\lambda^2-0.035)^2} \quad A3.8$$

The constants (a, b, etc.) are, of course, derived for each individual material by substituting known refractive index and wavelength values and solving the resulting simultaneous equations for the constants. The Cauchy equation obviously allow for only one absorption band at zero wavelength. The Hartmann formula is an empirical one, but does allow the absorption band to be located at wavelength c, and an additional term, as in Eq.A3.4 will accomodate the second band at wavelength e. The Hertzberger expression is an approximation of the Kettler-Drude equation and is reliable through the visible to about $1\mu\text{m}$ in the infrared. The Conrady equation is empirical and designed for the visible region. All these equations suffer from the drawback that the refractive index approaches infinity as the wavelength goes to absorption wavelength. Since little use is made of any material close to absorption band, this is usually of small consequence (note that the definition of the *dispersion* is given in the text books as the rate change of index of refraction with respect to wavelength, that is $dn/d\lambda$ and generally speaking, the dispersion is large at shorter wavelengths and becomes less at longer wavelengths).

A.5 References.

1. S.P. Lyashenko and V.K. Miloslavskii V.K, Opt.Spectrosc. **16**, 80, (1964).
2. J. Wales, G.J Lovitt and R.A. Hill, Thin Solids Films **1**, 137, (1967).
3. J. Szczyrbowski and A. Czapla, Thin Solid Films, **46**, 127, (1977).
4. R. Swaneopel, J.Phys.E:Sci.Instrum., **16**, 1214, (1985).
5. R. Swaneopel, J.Phys.E:Sci.Instrum., **17**, 896, (1984).
6. N.P Barnes and M.S. Piltch, J.Opt.Soc.Am., **17**, No.5 628 (1977).
7. J.E. Harvey and W.E.Wolfe, J.Opt.Soc.Am., **65**, 1267, (1975).

